

THE UNIVERSITY OF HULL

Novel Copper Coordination Compounds of Amino Acids and Pyridines:
Synthesis, Characterisation, Physical Properties, and Future Prospects for
Gas Adsorption

being a thesis submitted for the Degree of
Doctor of Philosophy in the University of Hull

by

Simon Matthew Fellows, MChem (Hons)

September 2017

Declaration

The work described in this thesis was carried out in the Department of Chemistry, The University of Hull under the supervision of Dr Timothy J. Prior between September 2013 and September 2016.

Acknowledgements

Foremost, my sincere thanks go to Dr Timothy J Prior for his guidance throughout my PhD, our talks have been a good source of inspiration and his advice both professionally and personally has been invaluable.

I would also like to thank Dr Grazia Francesconi, Naomi Jones, Kreshnik Hoxha, Chris Randles, Matthew Bennett, Shaun Johnston, Lauren Turner, and Martin Taylor for their support and encouragement through difficult times, and entertainment at all other times. In addition, I thank the numerous project students that have come through the lab during my time that have created an enjoyable and varied atmosphere, albeit adding to the mess that accompanies a chemistry laboratory.

Lastly, I would like to thank my wife Katherine for doing more than her fair share of chores around the house when time was scarce, and supporting me through my work. Hopefully I can return the favour with the completion of this thesis.

Publications and Presentations

1. S. M. Fellows and T. J. Prior, *Acta Cryst.*, 2016, **E72**, 436-439.
2. S. M. Fellows and T. J. Prior, *Cryst. Growth Des.*, 2017, **17**, 106-116.
3. S. M. Fellows, 'Structure and Reactivity of Copper Halide Complexes' (oral presentation), RSC Dalton Division Northern Regional Meeting, University of Hull, 30th June 2016.
4. S. M. Fellows, 'Structure and Reactivity of Copper Halide Complexes' (oral presentation), PhD Colloquium, University of Hull, 20th July 2016.
5. S. M. Fellows, 'Solid-gas Reactions and Polymorphism of Copper Halide Compounds' (poster presentation), RSC Dalton 2016 Joint Interest Groups Meeting, University of Warwick, 29th-31st March 2016.
6. S. M. Fellows, 'Metal-Organic Frameworks for CO₂ Capture' (poster presentation), PhD Colloquium, University of Hull, 15th-16th June 2015.
7. S. M. Fellows, 'Molecular springs - Alkyl chain order/disorder transition in copper carboxylate complexes' (poster presentation), RSC Solid State Group Christmas Meeting 2014, University of Glasgow, 18th-19th December 2014.

Abstract

The primary goal of the work discussed in this thesis was to assess the capability of cheap, readily available ligands, *e.g.* pyridines and amines, to produce new coordination compounds, primarily with copper, that could lead to the development of novel materials for gas adsorption. Chapters 1 and 2 introduce the topic and methods respectively, results are contained within chapters 3-6.

Chapter 3 describes the synthesis, polymorphism and solid-gas reactions of $[\text{CuCl}_2(\text{RPy})_2]$ and $(\text{RPy-H})[\text{CuCl}_4]$ (RPy: R = 4-CO₂H, 4-CONH₂, 3-CONH₂). The polymeric $[\text{CuCl}_2(\text{RPy})_2]$ compounds appear blue, while the equivalent $(\text{RPy-H})[\text{CuCl}_4]$ salts appear yellow or green depending on the geometry of the $[\text{CuCl}_4]^{2-}$ ion. Exchange between the two types of compound is possible through the gain and loss of HCl, although the exact mechanism and what causes the observed differences in reaction is uncertain. $[\text{CuCl}_2(\text{RPy})_2]$ compounds could be developed further into porous materials through the use of simple tris(pyridine) ligands.

Chapter 4 discusses a facile synthetic method for $[\text{Cu}_4(\mu^4\text{-O})(\mu^2\text{-Cl})_6(\text{RPy})_4]$ compounds via the oxidation of CuCl in the presence of $[\text{CuCl}_2(\text{RPy})_2]_n$ (RPy: R = 4-Me, 4-NH₂, 4-NMe₂). The production of the $[\text{Cu}_4(\mu^4\text{-O})(\mu^2\text{-Cl})_6(\text{RPy})_4]$ cluster only seems to occur for compounds where the $[\text{CuCl}_2(\text{RPy})_2]$ complex is non-polymeric or at least weakly polymeric. Only one porous $[\text{Cu}_4(\mu^4\text{-O})(\mu^2\text{-Cl})_6(\text{RPy})_4]$ compound is known with 1,4-diazabicyclo[2.2.2]octane, but there is potential for others to be discovered. However, these compounds are not as stable as other compounds that might be used for gas adsorption and are better suited for catalysis applications.

Chapter 5 focuses on the copper and zinc coordination chemistry of amino acids with general formula CO₂H-(CH₂)_n-NH₂ (where n = 1-5 and 7). Amino acids are a good

potential ligand for CO₂ capture given their similarity with monoethanolamine: the most common chemical used in industrial technologies. However, their flexibility and propensity to form zwitterions means that the majority of compounds produced were adducts of copper halides, and those which were not appeared too dense for application in CO₂ adsorption. The copper halide adducts showed similar HCl/HBr gas uptake as the [CuCl₂(RPy)₂] compounds in chapter 3, although the reverse reaction was much slower with very little change observed over several months.

Lastly, chapter 6 details the novel coordination compounds created using Cu and a combination of various benzoic acid based and pyridine-based ligands. Most of the novel compounds have only been structurally characterised and no general conclusions can be made about their structures due to the lack of data. One compound made with 4-hydroxybenzoic acid and pyrazine in methanol showed promise for methanol adsorption, however the compound could not be made reliably or quantities large enough to study the phenomenon further.

Contents

1	Introduction and Background Information	1
1.1	Requirement for Novel Capture and Storage Methods	1
1.1.1	<i>Carbon Capture and Storage</i>	1
1.1.2	<i>Hydrogen Storage</i>	3
1.1.3	<i>Capture and Storage by MOFs</i>	4
1.2	Porous Materials	4
1.2.1	<i>Definition</i>	4
1.2.2	<i>Activated Carbon</i>	5
1.2.3	<i>Porous Inorganic Materials</i>	5
1.3	Coordination Compounds, Polymers, and MOFs	7
1.3.1	<i>Definitions</i>	7
1.3.2	<i>History</i>	7
1.3.3	<i>Generations of MOFs</i>	11
1.3.4	<i>Transformation Types</i>	11
1.3.5	<i>Topology Descriptors</i>	12
1.3.5.1	<i>Schläfli symbol</i>	12
1.3.5.2	<i>Vertex symbol</i>	13
1.3.5.3	<i>RCSR codes</i>	14
1.3.6	<i>Intermolecular Interactions</i>	15
1.4	Design of MOFs	16
1.4.1	<i>Designed compounds</i>	18
1.4.2	<i>Serendipitous compounds</i>	23
1.4.3	<i>Post-synthetic modification</i>	28
1.4.4	<i>Interpenetration</i>	29
1.5	Synthetic Methods	31
1.6	Applications of MOFs	31

1.6.1	<i>Hydrogen storage</i>	32
1.6.2	<i>Carbon Dioxide Storage</i>	32
1.7	Aims	34
2	Experimental Methods	36
2.1	Solution-based reactions and crystallisations	36
2.1.1	<i>Solvent Evaporation</i>	37
2.1.2	<i>Liquid-liquid and liquid-vapour diffusion</i>	38
2.1.3	<i>Solvothermal synthesis</i>	41
2.2	Solid-solid reactions	42
2.3	Solid-gas reactions	42
2.4	X-ray diffraction	43
2.4.1	<i>Single-crystal X-ray Diffraction (SCXRD)</i>	43
2.4.2	<i>X-ray Powder Diffraction (XRPD)</i>	44
2.5	Elemental Analysis	45
2.6	Thermogravimetric Analysis (TGA)	46
2.7	Fourier Transform Infrared (FTIR) Spectrometry	46
3	Synthesis, Structure, and Solid-Gas Reactions of [CuCl₂(RPy)₂]_n and (RPy-H)[CuCl₄] Compounds	48
3.1	Experimental procedures	51
3.1.1	<i>Synthesis of INAm.HCl</i>	51
3.1.2	<i>Synthesis of [CuCl₂(INAc/INAm/NAm)₂]_n (1/3/5)</i>	52
3.1.3	<i>Synthesis of [CuCl₄](H-INAc)₂(H₂O)₂ (2a)</i>	52
3.1.4	<i>Synthesis of [CuCl₄](H-INAc)₂ (Form I) (2b)</i>	53
3.1.5	<i>Synthesis of [CuCl₄](H-INAc)₂ (Form II) (2c)</i>	53
3.1.6	<i>Synthesis of [CuCl₄](H-INAm)₂ (Form I) (4a)</i>	53
3.1.7	<i>Synthesis of [CuCl₄](H-INAm)₂ (Form II) (4b)</i>	53
3.1.8	<i>Synthesis of [CuCl₄](H-INAm)₂ (Form III) (4c)</i>	54

3.1.9	<i>Synthesis of $[\text{CuCl}_4](\text{H-NAm})_2$ (Form I) (6a)</i>	54
3.1.10	<i>Synthesis of $[\text{CuCl}_4](\text{H-NAm})_2$ (Form II) (6b)</i>	54
3.1.11	<i>Decomposition Reactions</i>	55
3.2	Crystal structure and refinement information	55
3.3	Isonicotinic acid (INAc)	58
3.3.1	<i>Summary of reactions</i>	58
3.3.2	<i>$[\text{CuCl}_2(\text{INAc})_2]_n$ (1)</i>	60
3.3.3	<i>$(\text{H-INAc})_2[\text{CuCl}_4] \cdot 2\text{H}_2\text{O}$ (2a)</i>	62
3.3.4	<i>$(\text{H-INAc})_2[\text{CuCl}_4]$ (Form I) (2b)</i>	65
3.3.5	<i>$(\text{H-INAc})_2[\text{CuCl}_4]$ (Form II) (2c)</i>	68
3.3.6	<i>Infrared spectra</i>	69
3.4	Isonicotinamide (INAm)	70
3.4.1	<i>Summary of reactions</i>	70
3.4.2	<i>$[\text{CuCl}_2(\text{INAm})_2]_n$ (3)</i>	71
3.4.3	<i>$(\text{H-INAm})_2[\text{CuCl}_4]$ (Form I) (4a)</i>	75
3.4.4	<i>$(\text{H-INAm})_2[\text{CuCl}_4]$ (Form II) (4b)</i>	78
3.4.5	<i>$(\text{H-INAm})_2[\text{CuCl}_4]$ (Form III) (4c)</i>	82
3.4.6	<i>Infrared spectra</i>	85
3.5	Nicotinamide (NAm)	86
3.5.1	<i>Summary of reactions</i>	86
3.5.2	<i>$[\text{CuCl}_2(\text{NAm})_2]_n$ (5)</i>	87
3.5.3	<i>$(\text{H-NAm})_2[\text{CuCl}_4]$ (Form I) (6a)</i>	91
3.5.4	<i>$(\text{H-NAm})_2[\text{CuCl}_4]$ (Form II) (6b)</i>	95
3.5.5	<i>Additional observations on $(\text{H-NAm})_2[\text{CuCl}_4]$ (Form I/II) (6a/6b)</i>	98
3.5.6	<i>Infrared Spectra</i>	99
3.6	Metal-free compounds and solid-gas reactions	100
3.6.1	<i>Isonicotinic Acid (INAc)</i>	101
3.6.2	<i>Isonicotinamide (INAm)</i>	105

3.6.3	<i>Nicotinamide (NAm)</i>	111
3.7	Reaction rate of solid-gas reactions	113
3.8	Conclusions and future work	118
4	Synthesis and Structure of $[\text{Cu}_4(\mu^4\text{-O})(\mu^2\text{-X})_6]$ Compounds	122
4.1	Experimental procedures	125
4.1.1	$[\text{CuCl}_2(4\text{-APy})_2]_n$ (12).....	126
4.1.2	$[\text{Cu}_4(\mu^4\text{-O})(\mu^2\text{-Cl})_6(\text{RPy})_4]$	126
4.1.3	$[\text{Cu}_4(\mu^4\text{-O})(\mu^2\text{-Cl})_6(\text{RPy})_4]\cdot(\text{Solvate})$	127
4.1.4	$[\text{CuCl}(\text{ClINAc})(\text{H}_2\text{O})_2]_n$ (18)	127
4.2	Crystal structure and refinement information	128
4.3	4-Methylpyridine	130
4.3.1	<i>Summary of Reactions</i>	130
4.3.2	$[\text{CuCl}_2(4\text{-MePy})_2]_n$	130
4.3.3	$[\text{Cu}_4(\mu^4\text{-O})(\mu^2\text{-Cl})_6(4\text{-MePy})_4]$	132
4.4	4-Dimethylaminopyridine	135
4.4.1	<i>Summary of Reactions</i>	135
4.4.2	$[\text{Cu}_2\text{Cl}_4(\text{DMAP})_4]$	137
4.4.3	$[\text{Cu}_4(\mu^4\text{-O})(\mu^2\text{-Cl})_6(\text{DMAP})_4]$	138
4.5	4-Aminopyridine	143
4.5.1	<i>Summary of Reactions</i>	143
4.5.2	$[\text{CuCl}_2(4\text{-APy})_2]_n$	144
4.5.3	$[\text{Cu}_4(\mu^4\text{-O})(\mu^2\text{-Cl})_6(4\text{-APy})_4]$	147
4.6	Non-cluster forming compounds and predicting reactivity	154
4.7	Conclusions and future work	164
5	Reactions and Complexes of $\text{H}_2\text{N}(\text{CH}_2)_n\text{CO}_2\text{H}$ Compounds	166
5.1	Experimental procedures	167
5.1.1	$\text{Cu}(\text{ABA})_2$ (19) and $\text{Cu}(\text{AHA})_2\cdot\text{H}_2\text{O}$ (21).....	168

5.1.2	$Zn(APA)_2$ (22).....	168
5.1.3	$[Cu_2L_4X_2]X_2 \cdot nH_2O$ (23-29, 31-33), $[Cu_4(Gly)_4Cl_6]_n$ (35) and $[Cu(CIMGly)(H_2O)_2]$ (36)	169
5.1.4	$[Cu_2(APA)_4Cl_2]Cl_2$ (30) and $[Cu_2(AOA)_6]Cl_2$ (34).....	170
5.1.5	$(H-L)[CuX_4]$ (37-44)	170
5.2	Crystal structure and refinement information	171
5.3	Neutral frameworks	178
5.3.1	$[Cu(ABA)_2]_n / \{[Cu(ABA)_2](H_2O)_2\}_n$ (19/20).....	180
5.3.2	$\{[Cu(AHA)_2](H_2O)_2\}_n$ (21)	182
5.3.3	$[Zn(APA)_2]_n$ (22).....	183
5.4	$[Cu_2(L)_4X_2]X_2 \cdot nH_2O$ paddlewheel compounds.....	187
5.4.1	$[Cu_2(\beta-Ala)_4Cl_2]Cl_2 \cdot H_2O$ (23).....	188
5.4.2	$[Cu_2(\beta-Ala)_4Br_2]Br_2 \cdot 2H_2O$ (24)	189
5.4.3	$[Cu_2(\beta-Ala)_4Br_2]Br_2 \cdot 3H_2O$ (25)	192
5.4.4	$[Cu_2(ABA)_4Cl_2]Cl_2 \cdot 3H_2O$ (26)	194
5.4.5	$[Cu_2(ABA)_4Cl_2]Cl_2 \cdot H_2O$ (27)	195
5.4.6	$[Cu_2(ABA)_4Br_2]Br_2$ (28)	198
5.4.7	$[Cu_2(APA)_4Cl_2]Cl_2 \cdot 2H_2O$ (29)	200
5.4.8	$[Cu_2(APA)_4Cl_2]Cl_2 / [Cu_2(APA)_4Br_2]Br_2$ (30/31)	202
5.4.9	$[Cu_2(AHA)_4Cl_2]Cl_2 \cdot 4H_2O / [Cu_2(AHA)_4Br_2]Br_2 \cdot 4H_2O$ (32/33).....	206
5.4.10	$[Cu_2(AOA)_6]Cl_4$ (34).....	208
5.4.11	X-ray powder diffraction.....	210
5.5	Glycine	211
5.5.1	$\{[Cu_2(Gly)_4][Cu_2Cl_6]\}_n$ (35)	211
5.5.2	$[Cu(CIMGly)(H_2O)_2]$ (36)	214
5.6	Thermal Experiments	216
5.6.1	Dehydration and rehydration experiments	216
5.6.1.1	$[Cu_2(ABA)_4Cl_2]Cl_2 \cdot H_2O$ (27).....	217
5.6.1.2	$[Cu_2(\beta-Ala)_4Cl_2]Cl_2 \cdot H_2O$ (23)	223

5.6.1.3	$[\text{Cu}_2(\text{APA})_4\text{Cl}_2]\text{Cl}_2 \cdot 2\text{H}_2\text{O}$ (29)	225
5.6.1.4	$[\text{Cu}_2(\text{AHA})_4\text{Cl}_2]\text{Cl}_2 \cdot 4\text{H}_2\text{O}$ / $[\text{Cu}_2(\text{AHA})_4\text{Br}_2]\text{Br}_2 \cdot 4\text{H}_2\text{O}$ (32/33)	226
5.6.2	Anisotropic thermal expansion of $[\text{Cu}_2(\text{APA})_4\text{Cl}_2]\text{Cl}_2$ / $[\text{Cu}_2(\text{APA})_4\text{Br}_2]\text{Br}_2$ (30/31)	231
5.7	Cuprate compounds and solid-gas reactions	236
5.7.1	$(\text{H-}\beta\text{-Ala})_2[\text{CuCl}_4]/(\text{H-}\beta\text{-Ala})_2[\text{CuBr}_4]$ (37/38)	238
5.7.2	$(\text{H-ABA})_2[\text{CuCl}_4]/(\text{H-ABA})_2[\text{CuBr}_4]$ (39/40)	242
5.7.3	$(\text{H-APA})_2[\text{CuCl}_4]/(\text{H-APA})_2[\text{CuBr}_4]$ (41/42)	247
5.7.4	$(\text{H-AHA})_2[\text{CuCl}_4]/(\text{H-AHA})_2[\text{CuBr}_4]$ (43/44)	250
5.8	Conclusions and future work	254
6	Copper Complexes of Benzoic Acid Based Ligands	259
6.1	Experimental procedures	261
6.1.1	$\text{Cu}_2(\text{OH})_2(\text{CO}_3)$ (Basic Copper Carbonate)	262
6.1.2	$[\text{Cu}_2(3\text{-HBA})_4(\text{H}_2\text{O})_2](3\text{-HBA})_2(\text{H-DMAP})_2$ (45)	262
6.1.3	$[\text{Cu}_2(4\text{-HBA})_4(\text{H}_2\text{O})_2] \cdot n\text{MeOH}$ (46)	262
6.1.4	$[\text{Cu}_2(4\text{-HBA})_2(\text{DMAP})_2] \cdot 1.5\text{H}_2\text{O}$ (47)	262
6.1.5	$[\text{Cu}_2(4\text{-HBA})_4(\text{Pz})_2] \cdot 2\text{MeOH}$ (48)	263
6.1.6	$[\text{Cu}_2(3,5\text{-DHBA})_4(\text{MeOH})_2] \cdot 8\text{MeOH}$ (49)	263
6.1.7	$[\text{Cu}(3,5\text{-DHBA})_2(\text{H}_2\text{O})_3] \cdot 5\text{H}_2\text{O}$ (50)	263
6.1.8	$[\text{Cu}_2(4\text{-MeBA})_4(\text{DMF})_2] \cdot 2\text{DMF}$ (51)	263
6.1.9	$\{[\text{Cu}_2(4\text{-MeOBA})_4(4,4'\text{-bipy})][\text{Cu}(4\text{-MeOBA})_2(4,4'\text{-bipy})] \cdot 2\text{EtOH}\}_n$ (52)	264
6.1.10	$[\text{Cu}_2(4\text{-ABA})_4(4,4'\text{-bipy})_2] \cdot 2\text{DMF}$ (53)	264
6.2	Crystal structure and refinement information	264
6.3	3-Hydroxybenzoic acid (3-HBA)	269
6.3.1	$[\text{Cu}_2(3\text{-HBA})_4(\text{H}_2\text{O})_2](3\text{-HBA})_2(\text{H-DMAP})_2$ (45)	270
6.4	4-Hydroxybenzoic acid (4-HBA)	274
6.4.1	$[\text{Cu}_2(4\text{-HBA})_4(\text{H}_2\text{O})_2] \cdot n\text{MeOH}$ (46)	274
6.4.2	$[\text{Cu}_2(4\text{-HBA})_2(\text{DMAP})_2] \cdot 1.5\text{H}_2\text{O}$ (47)	278

6.4.3	$[Cu_2(4-HBA)_4(Pz)_2] \cdot 2MeOH$ (48)	281
6.5	3,5-Dihydroxybenzoic acid (3,5-DHBA)	286
6.5.1	$[Cu_2(3,5-DHBA)_4(MeOH)_2] \cdot 8MeOH$ (49)	286
6.5.2	$[Cu(3,5-DHBA)_2(H_2O)_3] \cdot 5H_2O$ (50)	289
6.6	4-Methylbenzoic acid (4-MeBA)	292
6.6.1	$[Cu_2(4-MeBA)_4(DMF)_2] \cdot 2DMF$ (51)	293
6.7	4-Methoxybenzoic acid (4-MeOBA)	295
6.7.1	$\{[Cu_2(4-MeOBA)_4(4,4'-bipy)][Cu(4-MeOBA)_2(4,4'-bipy)] \cdot 2EtOH\}_n$ (52)	295
6.8	4-Aminobenzoic acid (4-ABA)	298
6.8.1	$[Cu_2(4-ABA)_4(4,4'-bipy)_2] \cdot 2DMF$ (53)	298
6.9	Conclusions and future work	302
7	References	303

Abbreviations

General

1/2/3-D	–	1/2/3-Dimensional
ATR	–	Attenuated Total Reflection
BET	–	Brunauer-Emmett-Teller
CSD	–	Cambridge Structural Database
DFT	–	Density Functional Theory
FCC	–	Face Centred Cubic
FTIR	–	Fourier Transform Infrared
HKUST	–	Hong Kong University of Science and Technology
IR	–	Infrared
IRMOF	–	Isorecticular Metal Organic Framework
IUPAC	–	International Union of Pure and Applied Chemistry
MOF	–	Metal Organic Framework
NU	–	Northwestern University
PMOF	–	Polyhedron-based Metal Organic Framework
RCSR	–	Reticular Chemistry Structure Resource
RMSD	–	Route-mean-square Deviation
SBU	–	Secondary Building Unit
SCXRD	–	Single-crystal X-ray Diffraction
SEM	–	Scanning Electron Microscope
TGA	–	Thermogravimetric Analysis
UiO	–	Universitetet i Oslo
XRPD	–	X-ray Powder Diffraction

Reagents and Compounds

3-HBA	–	3-Hydroxybenzoic acid
3-IBA	–	3-Iodobenzoic acid
3,5-DHBA	–	3,5-Dihydroxybenzoic acid
4-ABA	–	4-Aminobenzoic acid
4-APy	–	4-Aminopyridine
4-HBA	–	4-Hydroxybenzoic acid
4-MeBA	–	4-Methylbenzoic acid
4-MeOBA	–	4-Methoxybenzoic acid
4-MePy	–	4-Methylpyridine
ABA	–	4-Aminobutanoic acid
AHA	–	6-Aminohexanoic acid
AOA	–	8-Aminooctanoic acid
APA	–	5-Aminopentanoic acid
β-Ala	–	β-Alanine

BDC	–	Benzenedicarboxylate
Bipy	–	4,4'-Bipyridine
BPHZ	–	1,2-Bis(4-pyridylmethylene)hydrazine
BPDC	–	Biphenyldicarboxylate
BTB	–	1,3,5-Benzenetribenzoate
BTC	–	Benzenetricarboxylate
CIMGly	–	N-(Carboxyiminomethyl)glycine
ClINAc	–	2-Chloroisonicotinic acid
DABCO	–	1,4-Diazabicyclo[2.2.2]octane
DH	–	Dehydrated
DH3PhDC	–	2',5'-Dimethyl-3,3''-dihydroxy-[1,1':4',1''-terphenyl]-4,4''-Dicarboxylate
DMAP	–	2-Dimethylaminopyridine
DMF	–	Dimethylformamide
DMSO	–	Dimethyl sulfoxide
EtOH	–	Ethanol
Gly	–	Glycine
HX	–	Hydrogen halide (e.g. HCl HBr)
INAc	–	Isonicotinic acid
INAm	–	Isonicotinamide
MeINAc	–	Methylisonicotinate
MeOH	–	Methanol
NAm	–	Nicotinamide
NH ₂ -BDC	–	2-Aminobenzenedicarboxylate
Pz	–	Pyrazine
RH	–	Rehydrated
RPy	–	Substituted pyridine
1	–	[CuCl ₂ (INAc) ₂] _n
2a	–	(H-INAc) ₂ [CuCl ₄]·2H ₂ O
2b	–	(H-INAc) ₂ [CuCl ₄] (Form I)
2c	–	(H-INAc) ₂ [CuCl ₄] (Form II)
3	–	[CuCl ₂ (INAm) ₂] _n
4a	–	(H-INAm) ₂ [CuCl ₄] (Form I)
4b	–	(H-INAm) ₂ [CuCl ₄] (Form II)
4c	–	(H-INAm) ₂ [CuCl ₄] (Form III)
5	–	[CuCl ₂ (NAm) ₂] _n
6a	–	(H-NAm) ₂ [CuCl ₄] (Form I)
6b	–	(H-NAm) ₂ [CuCl ₄] (Form II)
7	–	[CuCl ₂ (4-MePy) ₂] _n
8	–	[Cu ₄ (μ ⁴ -O)(μ ² -Cl) ₆ (4-MePy) ₄]
9	–	[Cu ₂ Cl ₂ (μ ² -Cl) ₂ (DMAP) ₄]
10	–	[Cu ₄ (μ ⁴ -O)(μ ² -Cl) ₆ (DMAP) ₄]
11	–	[Cu ₄ (μ ⁴ -O)(μ ² -Cl) ₆ (DMAP) ₄]·(DMF)(Toluene)
12	–	[Cu ₂ Cl ₂ (4-APy) ₂] _n
13	–	[Cu ₄ (μ ⁴ -O)(μ ² -Cl) ₆ (4-APy) ₄]
14	–	[Cu ₄ (μ ⁴ -O)(μ ² -Cl) ₆ (4-APy) ₄]·(DMSO) _{5.33} (H ₂ O) _{0.88}

15	–	$[\text{CuCl}_2(\text{pz})_2]_n$
16	–	$[\text{CuCl}_2(\text{bipy})_2]_n$
17	–	$[\text{CuCl}_2(\text{MeINAc})_2]_n$
18	–	$[\text{CuCl}(\text{ClINAc})(\text{H}_2\text{O})_2]_n$
19	–	$[\text{Cu}(\text{ABA})_2]_n$
20	–	$\{[\text{Cu}(\text{ABA})_2](\text{H}_2\text{O})_2\}_n$
21	–	$\{[\text{Cu}(\text{AHA})_2](\text{H}_2\text{O})_2\}_n$
22	–	$[\text{Zn}(\text{APA})_2]_n$
23	–	$[\text{Cu}_2(\beta\text{-Ala})_4\text{Cl}_2]\text{Cl}_2 \cdot \text{H}_2\text{O}$
24	–	$[\text{Cu}_2(\beta\text{-Ala})_4\text{Br}_2]\text{Br}_2 \cdot 2\text{H}_2\text{O}$
25	–	$[\text{Cu}_2(\beta\text{-Ala})_4\text{Br}_2]\text{Br}_2 \cdot 3\text{H}_2\text{O}$
26	–	$[\text{Cu}_2(\text{ABA})_4\text{Cl}_2]\text{Cl}_2 \cdot 3\text{H}_2\text{O}$
27	–	$[\text{Cu}_2(\text{ABA})_4\text{Cl}_2]\text{Cl}_2 \cdot \text{H}_2\text{O}$
28	–	$[\text{Cu}_2(\text{ABA})_4\text{Br}_2]\text{Br}_2$
29	–	$[\text{Cu}_2(\text{APA})_4\text{Cl}_2]\text{Cl}_2 \cdot 2\text{H}_2\text{O}$
30	–	$[\text{Cu}_2(\text{APA})_4\text{Cl}_2]\text{Cl}_2$
31	–	$[\text{Cu}_2(\text{APA})_4\text{Br}_2]\text{Br}_2$
32	–	$[\text{Cu}_2(\text{AHA})_4\text{Cl}_2]\text{Cl}_2 \cdot 4\text{H}_2\text{O}$
33	–	$[\text{Cu}_2(\text{AHA})_4\text{Br}_2]\text{Br}_2 \cdot 4\text{H}_2\text{O}$
34	–	$[\text{Cu}_2(\text{AOA})_6]\text{Cl}_4$
35	–	$\{[\text{Cu}_2(\text{Gly})_4][\text{Cu}_2\text{Cl}_6]\}_n$
36	–	$[\text{Cu}(\text{CIMGly})(\text{H}_2\text{O})_2]$
37	–	$(\text{H-}\beta\text{-Ala})_2[\text{CuCl}_4]$
38	–	$(\text{H-}\beta\text{-Ala})_2[\text{CuBr}_4]$
39	–	$(\text{H-ABA})_2[\text{CuCl}_4]$
40	–	$(\text{H-ABA})_2[\text{CuBr}_4]$
41	–	$(\text{H-APA})_2[\text{CuCl}_4]$
42	–	$(\text{H-APA})_2[\text{CuBr}_4]$
43	–	$(\text{H-AHA})_2[\text{CuCl}_4]$
44	–	$(\text{H-AHA})_2[\text{CuBr}_4]$
45	–	$[\text{Cu}_2(3\text{-HBA})_4(\text{H}_2\text{O})_2](3\text{-HBA})_2(\text{H-DMAP})_2$
46	–	$[\text{Cu}_2(4\text{-HBA})_4(\text{H}_2\text{O})_2] \cdot n\text{MeOH}$
47	–	$[\text{Cu}_2(4\text{-HBA})_2(\text{DMAP})_2] \cdot 1.5\text{H}_2\text{O}$
48	–	$[\text{Cu}_2(4\text{-HBA})_4(\text{Pz})_2] \cdot 2\text{MeOH}$
49	–	$[\text{Cu}_2(3,5\text{-DHBA})_4(\text{MeOH})_2] \cdot 8\text{MeOH}$
50	–	$[\text{Cu}(3,5\text{-DHBA})_2(\text{H}_2\text{O})_3] \cdot 5\text{H}_2\text{O}$
51	–	$[\text{Cu}_2(4\text{-MeBA})_4(\text{DMF})_2] \cdot 2\text{DMF}$
52	–	$\{[\text{Cu}_2(4\text{-MeOBA})_4(4,4'\text{-bipy})][\text{Cu}(4\text{-MeOBA})_2(4,4'\text{-bipy})] \cdot 2\text{EtOH}\}_n$
53	–	$[\text{Cu}_2(4\text{-ABA})_4(4,4'\text{-bipy})_2] \cdot 2\text{DMF}$

Element colours in molecular diagrams

	–	C
	–	H
	–	N
	–	O
	–	Br
	–	Cl
	–	Cu
	–	Fe
	–	S
	–	Zn
	–	Zr
	–	Miscellaneous

1 Introduction and Background Information

Two of the greatest problems that pose a threat to humanity's future are that of climate change, and the exhaustion of fossil fuels on which we have become extremely dependent. The design of new functional materials for the capture and storage of carbon dioxide and hydrogen is a key component to the solution of these problems. Coordination/solid-state chemistry is a heavily researched topic in this regard, owing to the predictable structures of compounds in this field. This gives an aspect of control over the functionality of a compound, and the functionality can be readily altered without adversely affecting any other physical properties. This allows iterative or evolutionary improvements on previously discovered compounds; a property very rarely found, if at all, in other fields of chemistry. A family of compounds referred to as Metal-Organic Frameworks (MOFs) show great versatility in this way, making them an excellent choice for gas adsorption, and applications in many other fields as well. It is for this reason that they are currently one of the most popular research topics in chemistry. Before discussing some of the current research in the field of MOFs and the aims of this project, some general background information and history of the topics of gas storage, porous compounds, and coordination compounds/polymers is warranted.

1.1 Requirement for Novel Capture and Storage Methods

1.1.1 *Carbon Capture and Storage*

It is well established that the mass production of carbon dioxide (CO₂) is one of the leading causes of climate change.^{1,2} Containing and mitigating its release is important in diminishing the effect we have upon the environment. One of the most strategic ways of tackling the vast expulsion of the gas, is to focus on point sources where the issue is the

separation of CO₂ from gas mixtures in highly caustic environments.³ Amines are applicable in such a scenario, and are capable of reacting with CO₂ via two mechanisms as shown below with a primary amine as an example:⁴



Reaction 1 has a faster rate of reaction than that of 2, as the latter is limited by the hydrolysis of CO₂. However, reaction 2 has a higher capacity for CO₂ storage as it only requires one mole of amine per mole of the gas, whereas reaction 1 requires twice this amount. Tertiary amines are limited to reaction 2, while primary and secondary amines react predominantly by reaction 1. Due to the speed of reaction 1, aqueous monoethanolamine has become the most widely used method to capture CO₂. It efficiently binds the gas at lower temperatures (*ca.* 313 K), followed by controlled release at higher temperatures (*ca.* 393 K).⁵ The main disadvantage of this process is the energy required to raise and lower the temperature of the medium between the two states of capture and release. It has been estimated that to capture the CO₂ produced by the burning of fossil fuels with a system like that described above would consume 25 to 40% of the energy produced through burning.⁶ Additionally, the use of monoethanolamine is potentially hazardous, and substituting for other alkanolamines is currently disfavoured.⁷

Research has been conducted into the use of sterically hindered amines, such as piperazine, to replace monoethanolamine. These still react via the carbamate route (reaction 1) with a similar reactivity to that of non-sterically hindered amines, however the stability of the carbamate product is reduced. The carbamate formed therefore hydrolyses into the bicarbonate product seen in reaction 2, increasing the capacity of the solution. Such compounds have been shown to be good alternatives to monoethanolamine

and potentially less energy intensive, however they are still very energy demanding.⁸⁻¹⁰ A new, more efficient method for capture and storage of CO₂ is therefore required. A comprehensive review of the most promising emerging methods for CO₂ capture, ranging from molecular membranes to the biological production of compounds from carbon dioxide has been conducted by D'Alessandro *et al.*³

1.1.2 Hydrogen Storage

While depletion of fossil fuels is a problem, given our dependence on them, the “new” energy sources that will fulfil our requirements are already available in the form of solar, wind, hydro, and nuclear power. But how we contain and transport that energy is still an unresolved problem. Hydrogen is one possible energy carrier; with an energy content per unit mass of 143 MJ kg⁻¹ it has the capability to vastly outperform the current hydrocarbon based fuels which have a value approximately three times lower than this.¹¹ But the storage of large quantities of hydrogen is a problem that needs to be overcome to make its use feasible.

Gaseous hydrogen has a very low density of 0.089 g L⁻¹ at atmospheric pressure, meaning that in order to achieve a high storage capacity it must be highly pressurised. This is not only highly dangerous, but leads to very heavy and cumbersome containers reducing the energy capacity of the medium. On the other hand, liquid hydrogen possesses a much higher density of 70 g L⁻¹, but needs a cryogenic containment system due to its low boiling point of 20 K. This creates similar drawbacks to the high-pressure system, like weight, along with the additional energy requirement for refrigeration. A combination of the two methods, *i.e.* cryo compression, would be the best compromise, and this technique is improved further by the addition of an adsorbent material.¹² Metal hydrides are another viable route toward the storage of hydrogen via chemical bonding, and are covered in a

review of hydrogen storage strategies by McWhorter *et al.*¹³ Despite these strides towards an economically viable storage system, further work is still needed to improve them further toward commercial use.

1.1.3 Capture and Storage by MOFs

Each of the gases discussed above are capable of being captured and stored in adsorbent materials, specifically the nanoporous compounds known as MOFs. These compounds exhibit large internal surface areas which can be tailored toward the adsorption of particular molecules for increased selectivity and storage capacity. A review of MOFs for application in H₂ storage was recently reported by Langmi *et al.*¹⁴ and most of the promising compounds for application toward CO₂ are covered in the review by D'Alessandro *et al.*³ Before discussing this class of compounds in more detail, a brief description and general history of porous materials is necessary.

1.2 Porous Materials

1.2.1 Definition

The International Union of Pure and Applied Chemistry (IUPAC) defines a porous material as a solid with pores, *i.e.* cavities, channels, or interstices, which are deeper than they are wide. These pores can be terminating, also known as closed or blind, or can traverse the entire material, referred to as open. Porous solids can be categorised as either amorphous materials, such as activated carbon, or crystalline materials, such as zeolites. These materials, their synthesis, and their ability to act as adsorbents for gases are discussed briefly below.¹⁵⁻¹⁷

1.2.2 Activated Carbon

Without a doubt, the first material used for its porosity is activated carbon or charcoal. The material's adsorbent properties were first described over 200 years ago,¹⁸ and may have potentially been used in a crude form for water purification over 1000 years ago. Activated charcoal is a carbon-based material with small pores which, relative to non-porous carbon materials such as coal, increase the surface area to which chemical species can adsorb. The name is derived from the process by which it is created, referred to as activation. Synthesis is accomplished by two common methods: A carbonaceous raw material is either pyrolysed then heated in an oxidising atmosphere such as steam, or impregnated with a chemical before being pyrolysed.¹⁹ The latter method has been perfected over the years to produce highly porous activated carbon materials with very large surface areas (*ca* 5000 m²/g).²⁰

These materials can be used for the removal of heavy metals and organics from water,^{21,22} and can be modified somewhat to improve their capabilities to adsorb particular guest species such as CO₂.^{23,24} However, it is well known that the energy requirement for their creation is enormous, and this is the main disadvantage of activated carbons as gas adsorption materials.¹⁹ Additionally, the extent to which they can be tailored for selective guest adsorption is limited.

1.2.3 Porous Inorganic Materials

Porous or open-framework inorganic compounds are also known to exhibit adsorptive properties. Zeolites, for example, are well known for their adsorption of water. Similar materials include aluminium and gallium phosphates among others, Cheetham provides an excellent review on these and related compounds.²⁵ Generally these materials are

created entirely from corner-sharing TO_4 tetrahedra, with T typically being elements such as Si, Al, P, B, Ga, Be, and Ge, however other polyhedra have also been used in recent times to expand the library of potential topologies that can be created. The polymeric structures created contain pores with a typical diameter of 4-8 Å, although materials with larger pores are known.²⁶ Ions such as K^+ , Na^+ , Ca^{2+} etc. are commonly incorporated into the structures of these compounds which gives them some useful ion exchange properties,²⁷ although they can be synthesised using organic cations instead which also act as a template for the final structure. A good example of this is the MGaPOs (M = Mn, Fe, and Co) synthesised with methylimidazole, the structure of which is shown in Figure 1.1.²⁸ Such organically templated compounds can be activated by the thermal decomposition of the organic component.

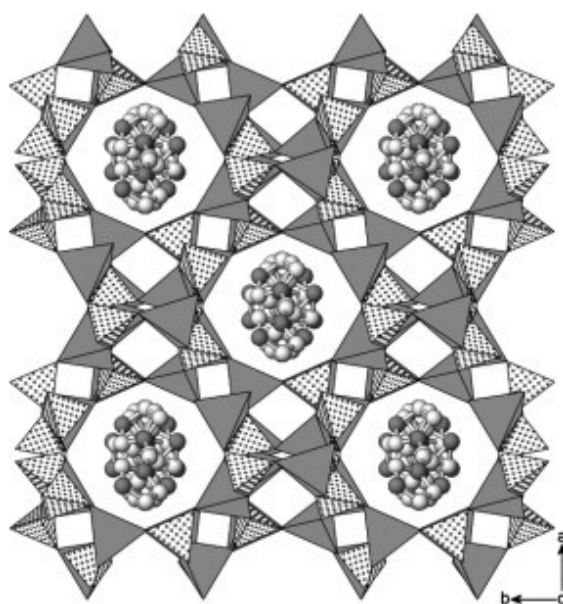


Figure 1.1 Diagram of MeGaPO (Me = Mn, Fe, and Co) as viewed down c . Taken from Gaslain *et al.*²⁸ Dark grey polyhedra = MO_4 , dotted polyhedra = PO_4 , dark spheres = N, light grey spheres = C.

Although porous inorganic materials like zeolites are commonly used for the adsorption of water and as ion exchange agents, they can also be used for catalysis, gas adsorption, and other applications, and have been heavily investigated for their adsorption of CO_2 .²⁹

Modifications can also be made to increase CO₂ adsorption of the materials while maintaining chemical stability, one example of which is loading the material with various amines.^{30,31} The disadvantage of these compounds vs. others are that, like activated carbons, the temperatures required to produce and activate the materials is high making them energy intensive, and they have limited porosity (*ca* 600 m²/g, 0.3 cm³/g maximum).³² Mesoporous silicas do have a much higher potential porosity,^{33,34} but without a periodic structure their properties are less likely to be predictable. This is where metal-organic frameworks have an edge as porosity is only limited by the size of the organic component, which is very easily increased, and require much less energy to produce.

1.3 Coordination Compounds, Polymers, and MOFs

1.3.1 Definitions

A coordination compound or complex is defined as a central atom or ion, also referred to as the coordination centre, which is surrounded by an array of bonded molecules or ions called ligands. A coordination polymer is a coordination compound with repeating coordination entities extending in 1, 2 or 3 dimensions. A coordination network is a coordination polymer extending in 1 dimension but with cross-links between two or more individual chains, loops, or spiro-links, or a coordination polymer extending in 2 or 3 dimensions. Metal-Organic Frameworks (MOFs) are a class of coordination network with organic ligands containing potential voids.³⁵

1.3.2 History

The earliest known record for the formation of a coordination compound is in Andreas Libavius' book *Alchymia* (1597) in which he described the blue colour formed when

copper containing samples come into contact with ammonia. The colour blue comes from the formation of dissolved $[\text{Cu}(\text{NH}_3)_4]^{2+}$.³⁶ Perhaps the most well-known coordination compound, however, is Prussian blue, or $\text{Fe}_4[\text{Fe}(\text{CN})_6]_3 \cdot 14\text{H}_2\text{O}$.³⁷ There is no reliable story behind the first synthesis of Prussian blue, but it is thought to have been created in 1706 by Johann Diesbach.³⁸ Prussian blue is important, not only because it was the first commercially manufactured pigment, but because it was also the first coordination polymer ever synthesised. The term coordination polymer was coined by Shibata in 1916,³⁹ although the existence of such compounds was not confirmed until the structure of Prussian blue was determined in 1936 by Keggin and Miles.⁴⁰ The more accurate, disordered structure was later determined by Buser *et al.*³⁷ As shown in Figure 1.2, Prussian blue is made up of a FCC array of Fe^{3+} ions with $[\text{Fe}(\text{CN})_6]^{4-}$ ions occupying $\frac{3}{4}$ of the octahedral holes. The CN anions bridge between the Fe^{3+} and Fe^{2+} ions. The remaining $\frac{1}{4}$ of the octahedral holes are occupied by H_2O , and H_2O also occupies all of the tetrahedral holes. The structure is an average of the disorder created by deficiency of $[\text{Fe}(\text{CN})_6]^{4-}$ ions.

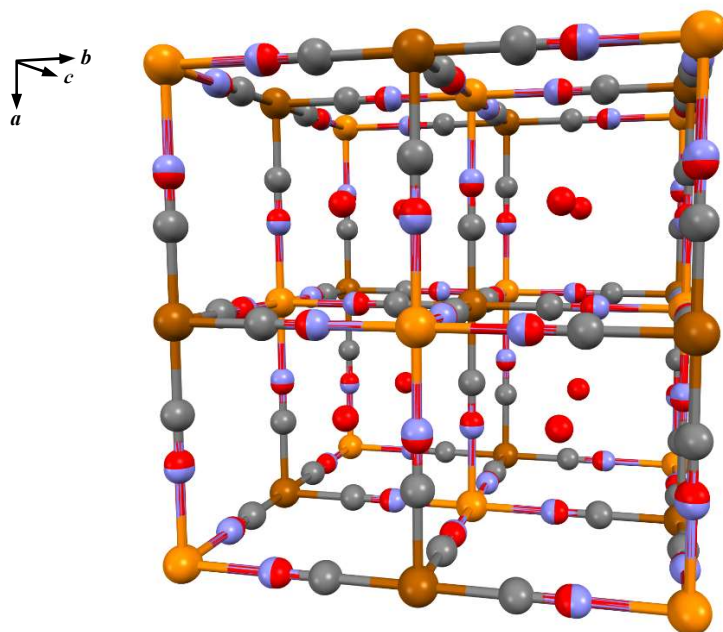


Figure 1.2 The crystal structure of Prussian blue or $\text{Fe}_4[\text{Fe}(\text{CN})_6]_3 \cdot 14\text{H}_2\text{O}$ showing the disorder of the CN and H_2O ligands.³⁷ C atoms are shown in grey, Fe^{3+} in orange, Fe^{2+} in brown, N in light grey-blue, and O in red.

The field of coordination polymers did not progress much beyond this point until the work of Hoskins and Robson in 1990. They proposed the design of scaffold-like materials created by combination of ligands acting as rod like connecting units, and coordination centres of various geometries.⁴¹ The synthesis of the similar diamond-like frameworks of $\{[\text{Cu}(4,4',4'',4'''\text{-tetracyanotetraphenylmethane})]\text{BF}_4 \cdot n\text{C}_6\text{H}_5\text{NO}_2\}_n$, and $[\text{Zn}(\text{CN})_2]_n$ led to the idea of open/porous compounds which would permit the diffusion of various molecular and ionic species. This new class of compound could be almost limitlessly expandable, provided rigid enough linkers could be discovered that would prevent their irreversible collapse.

It was the work in the late 90s by Yaghi *et al.*^{42,43} which provided the tools to create such polymers with rigid frameworks that could resist collapse. The reaction of terephthalic acid, also known as benzenedicarboxylic acid (BDC), and zinc nitrate in

dimethylformamide resulted in crystals of a compound now known as MOF-5. The compound consists of zinc-based metal clusters bridged by terephthalate groups. The clusters are constructed with four Zn^{2+} ions in a tetrahedral arrangement around a central oxide anion. The terephthalate ions are arranged in an octahedron around the Zn_4O cluster, and their carboxylate groups bridge each pair of Zn^{2+} ions in the cluster. This arrangement results in a 3-D prim

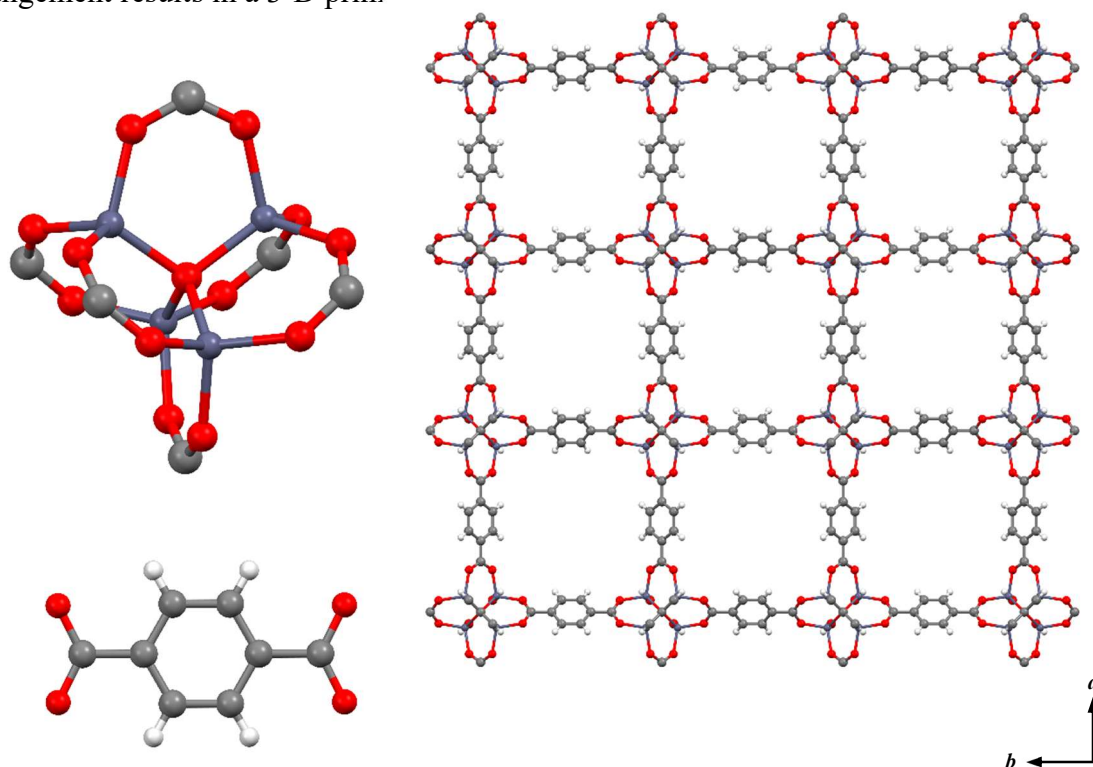


Figure 1.3 The $[\text{Zn}_4(\mu_4\text{-O})(\mu_2\text{-O}_2\text{CR})_6]$ cluster, top left, which combines with benzene dicarboxylate, bottom left, that produce the structure of MOF-5 as shown on the right as a view down one of the cell axes.
⁴² C atoms are shown in grey, H in white, O in red, and Zn in dark blue-grey.

The rigid coordination of the cluster present in MOF-5 allowed the design of topologically identical frameworks by replacing the terephthalate anion with similar rigid ligands. However, these other ligands could possess different functional groups or be longer than the terephthalate molecule, resulting in products with different pore sizes and surface properties to the original compound. The formation of such a family of related structures was termed an isorecticular series. The word reticular is defined as ‘having the form of a

net; netlike',⁴⁴ thus the term isorecticular means they have the same nets present. The discovery of the isorecticular series of MOF-5 type compounds using the same metal cluster paved the way for the secondary building unit (SBU) approach to MOF design and synthesis, discussed briefly in section 1.5. Apart from the choice of synthetic conditions, this approach simplified the process of designing new frameworks to the selection of an appropriate metal cluster and linker to create the desired topology, and is still the most widely used approach to the design of new materials today.

1.3.3 Generations of MOFs

Porous coordination polymers are generally classified into three categories: 1st, 2nd, and 3rd generation, as first described by Kitagawa *et al.*⁴⁵ 1st generation compounds have a microporous framework maintained by the guest molecules which occupy the pores, these frameworks suffer from irreversible collapse on removal of the guest molecules. 2nd generation polymers have more robust frameworks and change little on the removal of guest molecules, maintaining their porosity permanently. 3rd generation polymers have flexible frameworks and can change dynamically and reversibly in response to external stimuli such as the adsorption and desorption of guest molecules, pressure, light *etc.* A large proportion of known frameworks are 2nd generation due to the rigidity of the metal clusters and ligands that create them.

1.3.4 Transformation Types

The structural transformation of these 3rd generation materials is probably one of the most interesting aspects of MOFs. Kitagawa also gives a classification system for these phenomena, splitting them into three distinct types.⁴⁶ Type I is a “recoverable collapse” whereby the framework is destroyed on the removal of the guest but then is reproduced

on exposure to the original guest. Type II is a “guest-induced transformation” in which the framework undergoes a structural shift on exchange of one guest for another but the basic connectivity of the framework remains intact. Type III is a “guest-induced reformation” in which a framework changes structurally on desorption of a guest but is reverts to the original structural on re-adsorption. While type I is a crystal-to-amorphous transformation, types II and III are crystal-to-crystal transformations.

1.3.5 Topology Descriptors

1.3.5.1 Schläfli symbol

The simplest way to define the underlying net in a framework is with a Schläfli symbol in the format of $\{p,q\}$. This describes any array of connected points as q edge-sharing polygons of p sides meeting at each point.⁴⁷ Alternatively, p is defined as the size of the shortest circuit between any pair of links at each unique node, and q the connectivity of the node or the number of links that node makes.¹⁶ As an example, graphene is a 2-dimensional material consisting of a hexagonal array of carbon atoms, as shown in Figure 1.4. At each carbon atom or point, three six-sided polygons meet, or in other words the shortest circuit between any pair of links from each node is six and the connectivity is three, thus the structure can be described as a $\{6,3\}$ net.

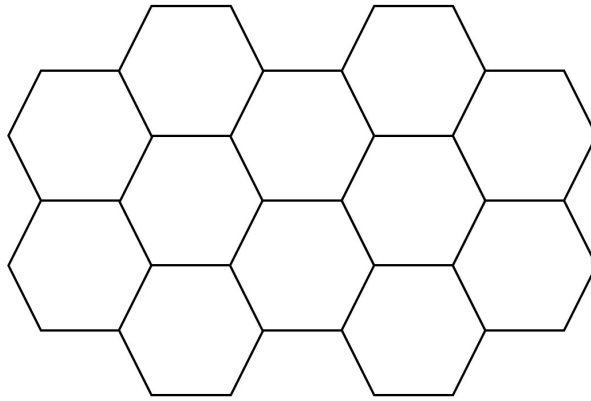


Figure 1.4 2-dimensional diagram of graphene, an example of a 6,3 net

The notation can be applied to 3-D nets in the form $\{p,q,r\}$ where r represents the number of $\{p,q\}$ meeting at an edge. The simplicity of this notation results in two major problems: No symbol can be assigned when a net has more than one type of node or different sized circuits around a node, *i.e.* a non-uniform net, and the lack of unique symbols results in multiple nets receiving the same symbol despite having very different networks. The use of a vertex symbol, sometimes incorrectly referred to as a Schläfli symbol,⁴⁷ to describe a net can alleviate these problems and is described below.

1.3.5.2 Vertex symbol

Figure 1.5 shows a 3-connected net, however there are two sizes of circuit present: one of four links and two of eight links at each node. This can be described using a vertex symbol which lists the circuit sizes at each unique node in a net with the format $p_1^{q_1}.p_2^{q_2}$. *etc.* where p is the size of the circuit and q is the number of circuits of that size. If q is 1 then no superscript is usually given. The 3-connected net would thus be given the symbol 4.8^2 . The total number of circuits at an n -connected node is determined as $n(n-1)/2$. The connectivity, n , is not given directly in the vertex symbol but can be determined using the sum of q with the calculation $\frac{(\sqrt{(8q)+1})+1}{2}$.

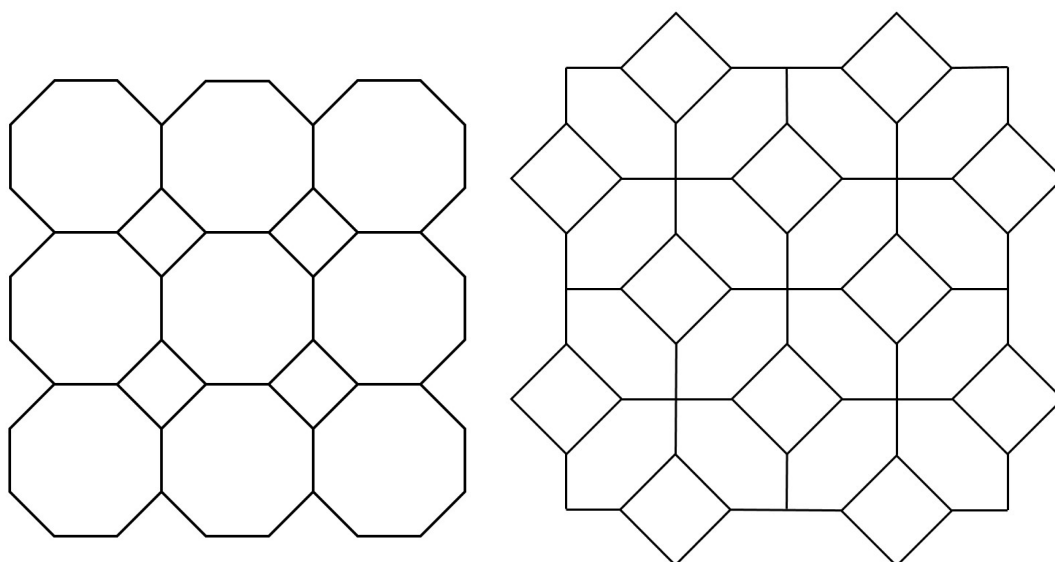


Figure 1.5 Examples of a 4.8^2 net, left, and a $(4.6^2)_4(6^4.10^2)$ net, right.

When a net possesses more than one type of node, for example the 3,4-connected net shown right in Figure 1.5, the overall vertex symbol is created by listing the individual vertex symbols for each node in parentheses, followed by subscript numbers after the parentheses to signify the ratio in which they occur in the network. The 3,4-connected net would thus be a $(4.6^2)_4(6^4.10^2)$ net. Vertex symbols give more unique names than the simple Schläfli notation, therefore reducing the problems mentioned above. But although the vertex symbol is very informative, it is much less intuitive than Schläfli symbol and it is still possible to name two very different nets with the same symbol.

1.3.5.3 RCSR codes

The Reticular Chemistry Structure Resource (RCSR) is a database of known 3-dimensional frameworks in which the frameworks are designated with three letter codes based on the compound to which they belong; *e.g.* diamond becomes **dia**, twisted boracite becomes **tbo** *etc.* The idea behind this is that unique 3-D nets are all given simple and unique names which do not result in ambiguity. It is for this reason that the use of RCSR

codes for naming the underlying net in a hydrogen or covalently bonded frameworks is prolific.

1.3.6 Intermolecular Interactions

It is not only the covalent bonding interactions which give rise to the final structure of a compound, but also the non-covalent interactions as well. In particular, the hydrogen bonding of the ligands is frequently important in MOF chemistry. The adsorption of gases onto the inner surface of MOFs is accomplished primarily by physical, non-covalent interactions, *i.e.* not chemical (covalent bonding) interactions. The choice of ligand can therefore have a great effect on the properties of the surface, and, by extension, the selectivity toward the target guest. Non-covalent interactions are electrostatic and can be categorised as ionic, hydrogen/halogen bonding, π -interactions, and dipole or induced dipole interactions also known as van der Waals forces. The majority of these are well known phenomena. However, the tool used to describe hydrogen bonding arrangements, graph-set notation, is less well known. Both simple and very complicated hydrogen bonding arrangements can be described using the straightforward symbol shown below:

$$G_d^a(r)$$

G describes the type of formation: S for an intramolecular interaction, D for a finite intermolecular interaction, C for a chain, and R for a ring. a and d are the numbers of acceptor and donor atoms respectively, and r is the degree of the interaction or the number of atoms (including non-H atoms) involved in the formation. As an example, the carboxylic acid hydrogen bonded dimer shown in Figure 1.6 would be written as $R_2^2(8)$. This graph-set notation was adopted as a descriptive tool for hydrogen bonding

arrangements, to allow easy comparison of structural features in an array of compounds and more readily identify trends.⁴⁸

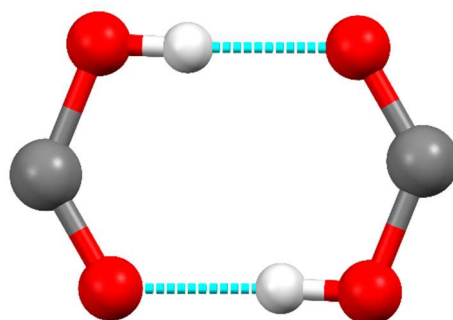


Figure 1.6 The ring-shaped carboxylic acid hydrogen bonded dimer. C atoms are shown in grey, H in white, and O in red. Hydrogen bonds are drawn as light-blue dashed lines.

1.4 Design of MOFs

The design of MOFs usually comes in the form of two choices, the ligand and the secondary building unit(s). Ligands with carboxylate (RCO_2^-) and nitrogen groups, such as pyridyl ($\text{C}_5\text{H}_4\text{N}$), feature predominantly in the design and synthesis of MOFs, and the variety of organic components incorporating these groups is vast. The unifying factor for the majority of MOF materials is the rigidity and predictable coordination of the ligands which allows for a significant amount of control over the self-assembly process, and therefore the product. The sub-units which are connected by the ligands are referred to as secondary building units and can be either singular metal ions or whole clusters. Although simple metal ions have well defined geometries dependent on the metal, they have very little directionality when it comes to the ligands as the metal-ligand bond is somewhat flexible. The latter problem is not as prevalent with the use of clusters, such as those in MOF-5, as they have much stricter bonding arrangements with the ligands around them. Metal-oxygen-carboxylate clusters are common, although examples which incorporate only metal-carboxylate and metal-nitrogen bonds also exist. Clusters are produced in situ

and usually have much more well-defined geometries than singular metal ions. Basic zinc acetate, or $[\text{Zn}_4(\mu_4\text{-O})(\mu_2\text{-O}_2\text{CR})_6]$,⁴⁹ is the cluster found in MOF-5 (R = organic substituent). Other common clusters in the literature include: copper acetate or $[\text{Cu}_2(\mu_2\text{-O}_2\text{CR})_4(\text{H}_2\text{O})_2]$;⁵⁰ basic iron acetate or $[\text{Fe}_3(\mu_3\text{-O})(\mu_2\text{-O}_2\text{CR})_6(\text{H}_2\text{O})_3]$;⁵¹ and the recently popular Zr_6O_8 “brick” carboxylate cluster or $[\text{Zr}_6(\mu_3\text{-O})_8(\mu_2\text{-O}_2\text{CR})_{12}]$.^{52–54} These clusters are shown side by side in Figure 1.7, the example for Zr is of the benzene dicarboxylate compound, CSD code RUBTAK.⁵⁴

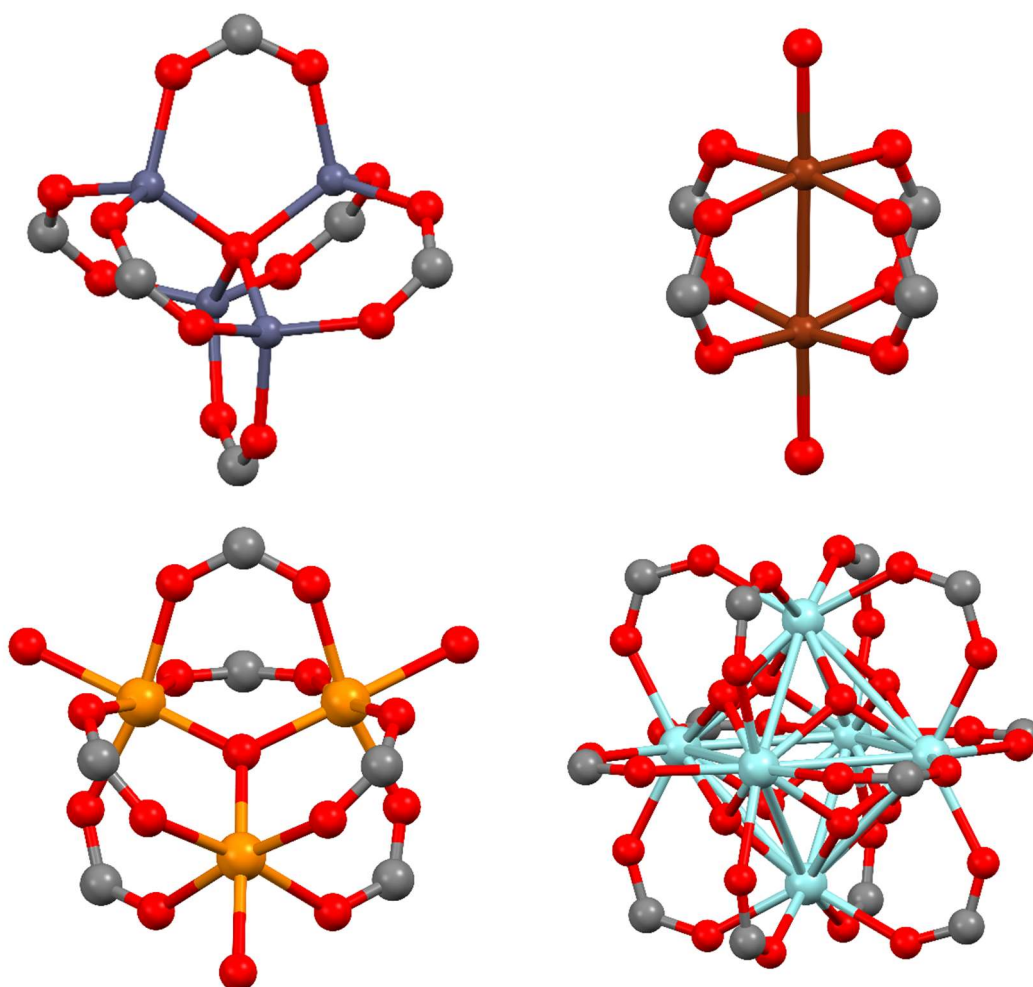


Figure 1.7 Common SBUs in MOF chemistry: top left, basic zinc acetate;⁴⁹ top right, copper acetate;⁵⁰ bottom left, basic iron acetate;⁵¹ and bottom right the zirconia “brick” carboxylate cluster.⁵² Methyl groups of acetate ligands and hydrogen atoms have been omitted for clarity. C atoms are shown in grey, H in white, Cu in dark brown, Fe in orange, O in red, Zn in dark blue-grey, and Zr in light blue.

A good review of the relative chemical and thermal stability of polymers created with these clusters was conducted by Bosch *et al.*⁵⁵ The review shows the historic transition from the not so stable $[\text{Zn}_4(\mu_4\text{-O})(\mu_2\text{-O}_2\text{CR})_6]$ -based MOFs, to those made recently with $[\text{Zr}_6(\mu_3\text{-O})_8(\mu_2\text{-O}_2\text{CR})_{12}]$ which are much more stable in comparison: they can survive temperatures upwards of 500 °C,⁵⁶ and immersion in concentrated hydrochloric acid for at least 24 hours.⁵⁷ Examples of the use of basic zinc acetate, basic iron acetate, and zirconia-based clusters in MOF synthesis are readily available.⁵⁸⁻⁶¹ Examples with other, less common SBUs, and the frameworks resulting from their combinations with various organic linkers are discussed in papers by Kitagawa *et al.*⁶² and Yaghi *et al.*⁴⁴ While zirconium clusters form the most resilient frameworks, it is copper which holds the record for the MOF with the largest surface area, known as NU-110, with a BET surface area of 7140 m²/g.⁶³ It is this metal which the majority of the work covered in this thesis is based upon, and a review of some of the MOFs created with this metal and general tools for the design of MOFs are discussed below.

1.4.1 Designed compounds

Copper acetate, and many other carboxylate salts of copper, form a paddlewheel-shaped cluster as shown in Figure 1.8. The cluster exhibits copper in either a square-pyramidal geometry with two apical ligands, or a square-planar geometry with no apical ligands. Although strictly speaking, the geometries are not truly square-pyramidal or square-planar as studies have shown the presence of a partial σ or δ bond between the copper centres at low temperatures.⁶⁴ In the formation of MOFs, the paddlewheel cluster acts as a square-planar node with no apical ligands present, or an octahedral node in the presence of apical ligands. The paddlewheel motif commonly forms *in-situ* with no special

conditions required, although some tweaking of the reaction conditions may be needed depending on the reagents in use and the desired product.

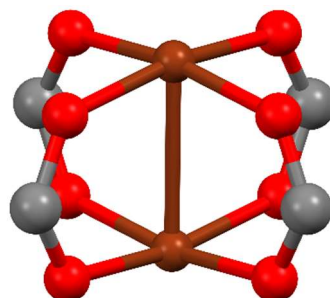


Figure 1.8 The copper carboxylate “paddlewheel” cluster, sometimes referred to as a Chinese lantern complex.⁵⁰ All extraneous have been removed for clarity, only those directly involved the cluster formation are shown. C atoms are shown in grey, Cu in dark brown, and O in red.

While complexes of this structure are most common with copper (II) and chromium (II) carboxylates, they are not exclusive to these metals and most of the other first row transition metals and zinc can form similar complexes. In fact, one of the first MOFs developed by Yaghi’s group was a zinc-based polymer with terephthalic acid or benzene dicarboxylic acid (BDC), $[\text{Zn}_2(\mu^4\text{-BDC})_2(\text{H}_2\text{O})_2]_n$ also known as MOF-2.⁶⁵ The copper equivalent to MOF-2 was not discovered until much later, although it has two monoclinic polymorphs, one with space group $C2/m$,⁶⁶ the other $P2_1/c$.⁶⁷ These three compounds are all 2-D polymers exhibiting a 4,4 net, as expected from combination of a linear linker with a square-planar node. In each, the 2-D sheets stack along one axis creating channels which the apical $\text{H}_2\text{O}/\text{DMF}$ ligands project into, as shown in Figure 1.9 with an example of the copper polymer.

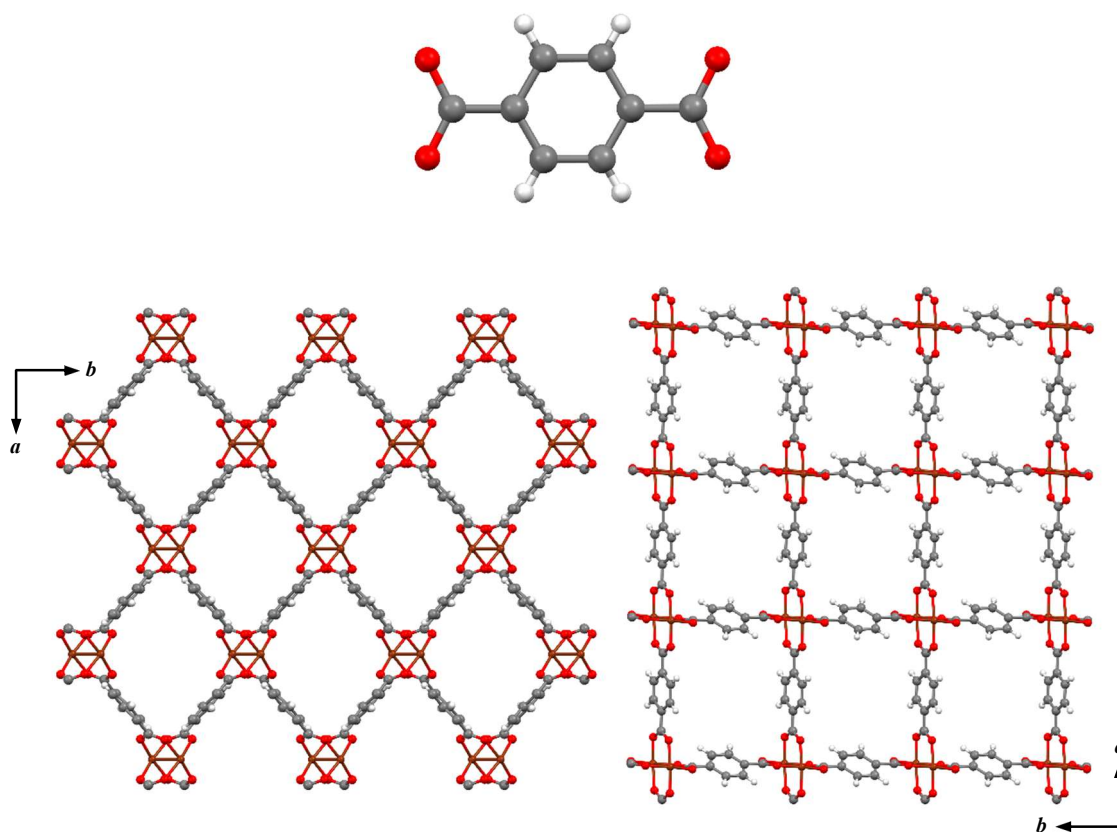


Figure 1.9 Shown top is the ligand terephthalic acid also known as benzene dicarboxylate (BDC). Shown bottom are the polymeric structures of $[\text{Cu}_2(\mu^4\text{-BDC})_2]_n$ with the $C2/m$ polymorph of the DMF solvate on the left,⁶⁶ and the desolvated structure on the right.⁶⁶ C atoms are shown in grey, H in white, Cu in dark brown, and O in red.

While MOF-2 is very unstable in air and has a somewhat poor surface area of 270-310 m^2/g , both of the copper analogues are very stable and are able to survive the removal of the DMF solvent via heating. The effect of removing the solvent is to shift the way the 4,4'-nets stack, but the overall structure is more or less the same. The BET surface area of the desolvated compound is 625 m^2/g making it more porous than MOF-2, and it is also capable of being solvated with other guest molecules.⁶⁶

The 4,4'-net of $[\text{Cu}_2(\mu^4\text{-BDC})_2]_n$ can be expanded upon by introducing a linkage between apical sites of the paddlewheel units through the use of a ligand such as 4,4'-bipy. Sakata *et al.* produced a 3-D polymer in this way, shown in Figure 1.10.⁶⁸ However, the modification of the 2-D polymer produces larger potential voids resulting in the formation

of an interpenetrated framework. This drastically reduces the available surface area compared with what would be expected for a non-interpenetrated framework. Discussion over the problem of interpenetration is conducted in the next subsection.

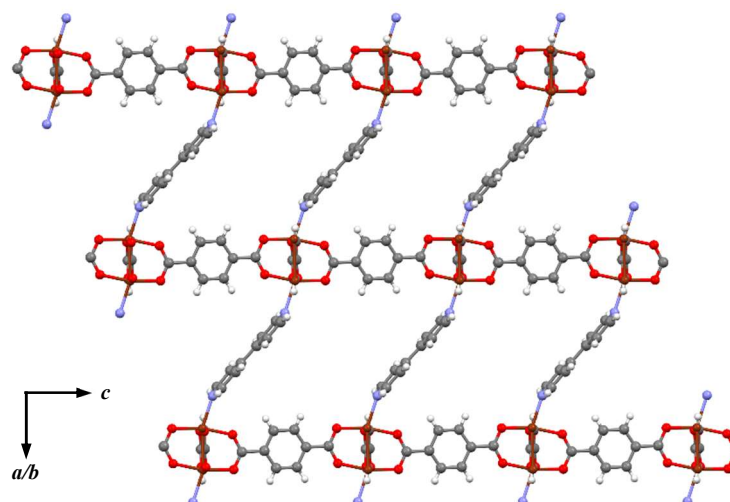


Figure 1.10 The polymeric structure of $[\text{Cu}_2(\mu^4\text{-BDC})_2(\mu^2\text{-4,4'-bipy})_2]_n$.⁶⁸ C atoms are shown in grey, H in white, Cu in dark brown, N in light grey-blue, and O in red.

A slightly different and more successful approach to the formation of a 3-D framework using the paddlewheel cluster came shortly after the discovery of MOF-5.⁶⁹ This was the compound produced by reaction of benzenetricarboxylic acid (BTC/trimesic acid) with copper nitrate. The compound, referred to as HKUST-1 after the institute at which it was discovered, features a combination of a trigonal carboxylate linker with the square-planar paddlewheel node. This results in a framework of **tbo** topology, as shown in Figure 1.11. The structure can be simply described as edge-sharing tetrahedra, each of which consists of BTC on the four faces and copper paddlewheel complexes on the six edges.

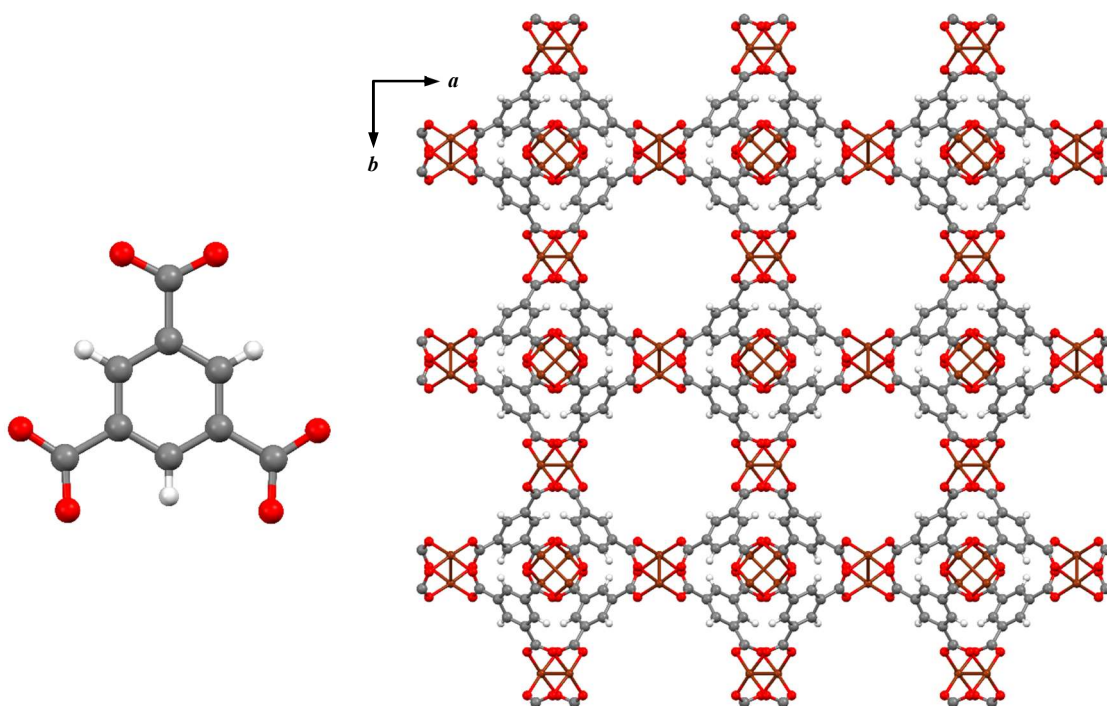


Figure 1.11 The ligand, benzene tricarboxylate (BTC), and the polymeric structure of $[\text{Cu}_3(\mu^6\text{-BTC})_2]_n$ or HKUST-1.⁶⁹ C atoms are shown in grey, H in white, Cu in dark brown, and O in red.

HKUST-1 has reported BET surface areas ranging from 692-1944 m^2/g .^{69,70} While this is less than the reported surface area of around 3800 m^2/g for MOF-5, HKUST-1 is much more stable than MOF-5 which is known to hydrolyse in moist air.⁷¹ Since its discovery, many variations on the basic structure of HKUST-1 have been developed using trigonal ligands of varying length and functionality to improve the physical properties of the material. For example, a group from Northwestern University (NU) have used hexatopic, trigonal ligands to create very similar frameworks to HKUST-1, but with much larger surface areas. This includes the MOF with the highest surface area and porosity known to date, NU-110, with a BET surface area of 7140 m^2/g .⁶³ NU-110 is produced in a similar reaction to HKUST-1 but replacing BTC with the ligand pictured in Figure 1.12, the resulting framework has **rht** topology as opposed to **tbo** as found with HKUST-1.

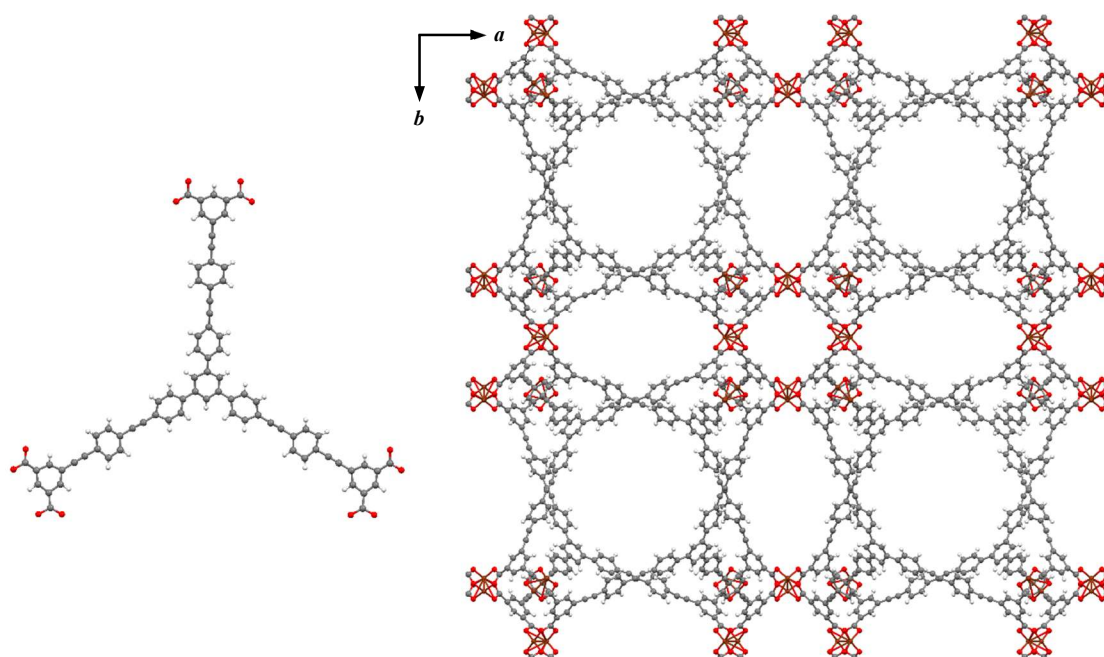


Figure 1.12 The ligand and the polymeric structure of NU-110.⁶³ C atoms are shown in grey, H in white, Cu in dark brown, and O in red.

1.4.2 Serendipitous compounds

Despite all of the examples shown above for the logical design and synthesis of MOFs, there are still many discoveries made which are completely unexpected and would have been difficult, if not impossible, to predict without prior knowledge. No other group of MOFs exemplify this more than those created with adenine. One example of this group is that of $[\text{Cu}_2(\mu_3\text{-Ade})_2(\mu_2\text{-OAc})_2]_n$ in which a paddlewheel-shaped complex is formed by a combination of adenine and acetate ions with copper.⁷² The two adenine ligands of each paddlewheel complex bridge to others producing a 3-dimensional framework exhibiting water filled channels, as shown in Figure 1.13. Pre-determination of a compound with this polymeric structure would have been extremely difficult, even though the coordination of the paddlewheel complex is well understood. This is due mainly to the formation of a mixed-ligand cluster which is very uncommon. Additionally, each adenine molecule forms three coordination bonds, even though it is more usual for

it to form one or two, and the way in which the axial-equatorial linkage occurs between the paddlewheel complexes is not straightforward.

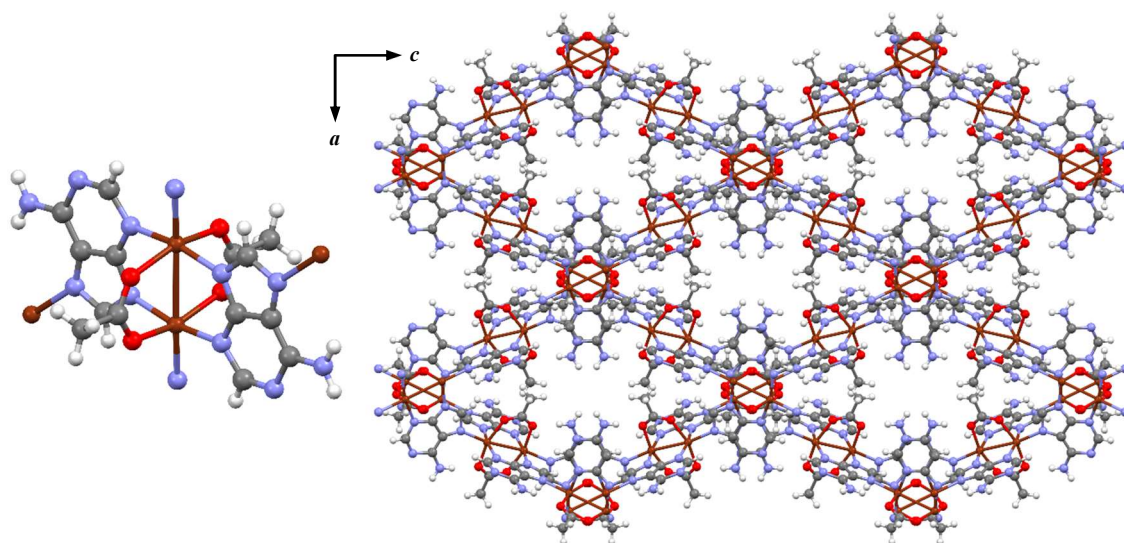


Figure 1.13 The monomeric unit and the polymeric structure of $[\text{Cu}_2(\mu^3\text{-Ade})_2(\mu^2\text{-OAc})_2]$.⁷² C atoms are shown in grey, H in white, Cu in dark brown, N in light grey-blue, and O in red.

Another example related to that above is the non-hydrated supramolecular structure of $[\text{Cu}_2\text{X}_2(\text{H-Ade})_4]\text{X}_2$ ($\text{X} = \text{Cl}, \text{Br}$).^{73,74} This complex is also paddlewheel shaped. It consists of four neutral bridging adenine ligands and two apical halide ions, as shown in Figure 1.14. Unlike the vast majority of porous metal-organic compounds, the 3-dimensional structure is a result of only hydrogen bonding interactions. Some are directly between complexes, and others are to the non-coordinated halide ions. The discrete complex in this material is remarkably simple, but the structure created from its intermolecular interactions would make it extremely difficult to predict. The fact that this structure is composed entirely of discrete complexes also questions whether porous compounds created entirely from coordinative linkages are the only option. There is a potential for much greater flexibility in such supramolecular solids given the weakness of intermolecular contacts vs covalent bonds. This may provide another route toward the

creation of more 3rd generation frameworks if such compounds could be designed as well as created by fortunate accident.

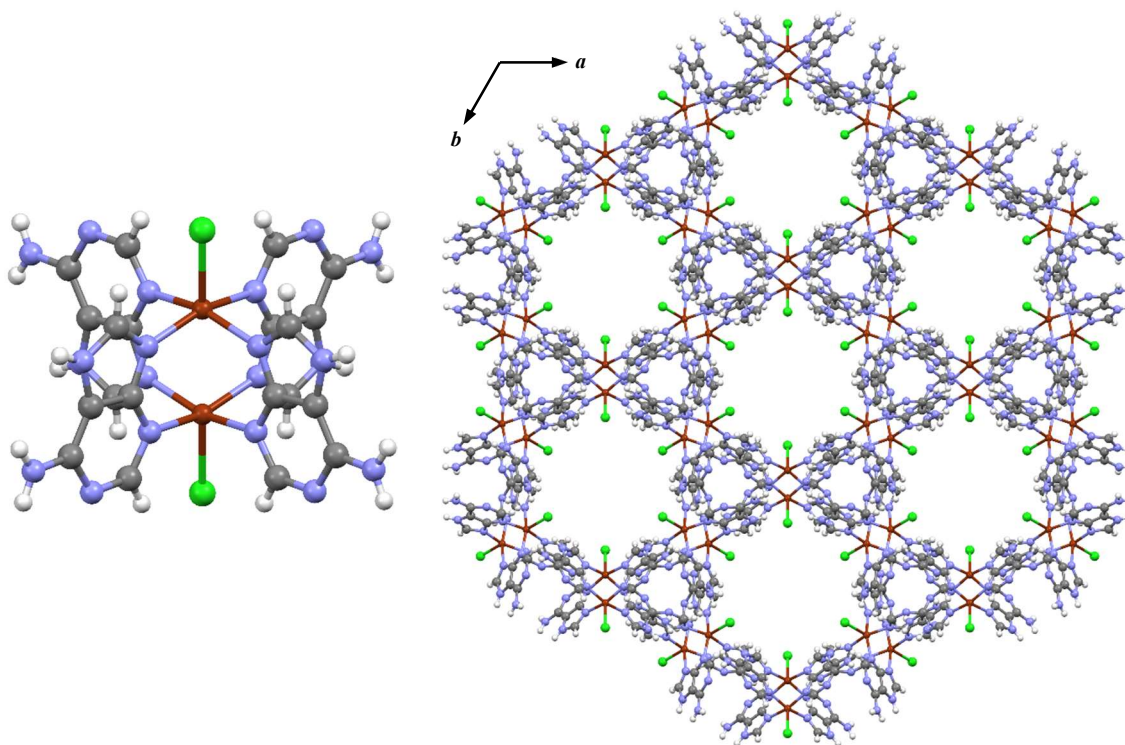


Figure 1.14 The discrete complex and overall structure of $[\text{Cu}_2\text{Cl}_2(\text{H-Adenine})_4]\text{Cl}_2$.⁷³ C atoms are shown in grey, H in white, Cl in green, Cu in dark brown, and N in light grey-blue.

The above two examples of adenine-based compounds with copper, although impressive, pale in comparison to the materials created by the reaction of carboxylates and adenine with zinc. The biomolecular cluster formed by the bridging of eight zinc cations by two O and four adenine anions, as shown in Figure 1.15, is the unit on which a number of porous materials have been created. When first produced in situ with biphenyldicarboxylic acid (BPDC), the resulting structure was a framework of tetragonal symmetry and a surface area of $\sim 1700 \text{ m}^2/\text{g}$ known as bio-MOF-1.⁷⁵ The structure of bio-MOF-1 is also shown in Figure 1.15.

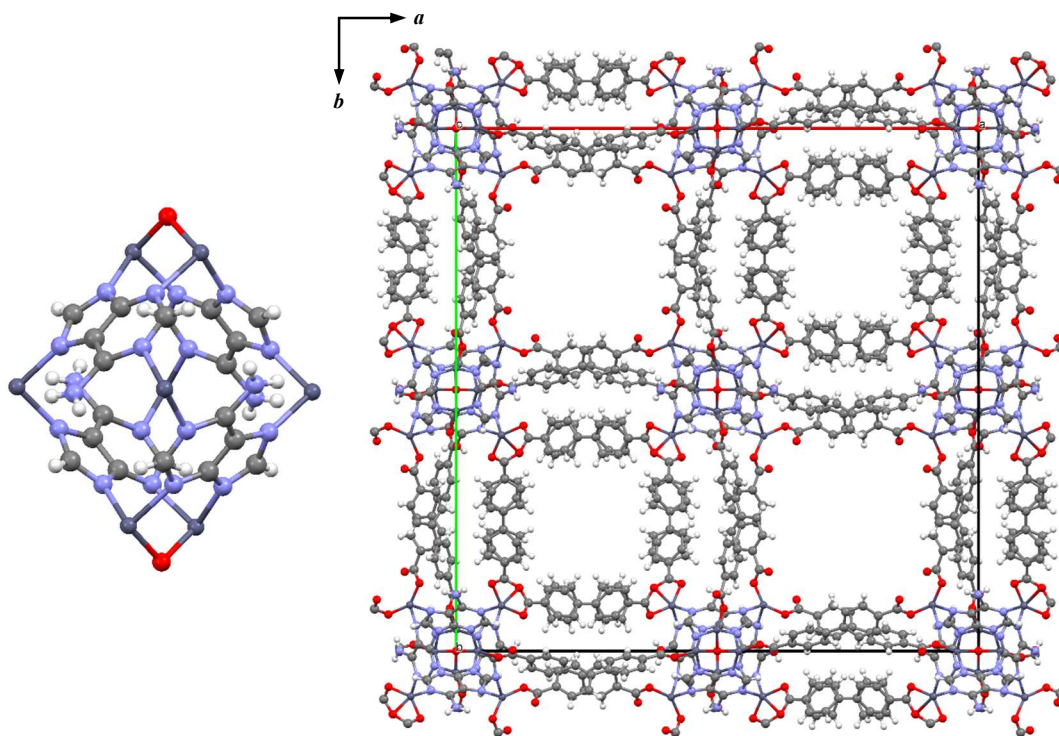


Figure 1.15 The Zn-adenine-O cluster and the overall structure of bio-MOF-1 or $\{[Zn_8(\text{adenine})_4(\text{BPDC})_6\text{O}] \cdot 2\text{Me}_2\text{NH}_2, 8\text{DMF}, 11\text{H}_2\text{O}\}_n$.⁷⁵ C atoms are shown in grey, H in white, N in light grey-blue, O in red, and Zn in dark grey-blue.

Reacting the same components in slightly different conditions to those which produce bio-MOF-1 resulted in the formation of a framework with the same Zn-adenine node but a completely different topology. This new framework, shown in Figure 1.16, was named bio-MOF-100 and has a much larger surface area than bio-MOF-1 at 4300 m²/g. Additionally, bio-MOF-100 had the largest pore volume and lowest density, 4.3 cm³/g and 0.302 g/cm³ respectively, of any known compound at the time of discovery.⁷⁶ Attempts to create isorecticular analogues of bio-MOF-100 with ligands longer than BPDC were unsuccessful using a conventional synthetic route. However, ligand exchange reactions in which the BPDC ligands in crystals of bio-MOF-100 were exchanged with azobenzene-4,4'-dicarboxylate and 2'-amino-1,1':4,1''-terphenyl-4,4''-dicarboxylate were successful, producing crystals of bio-MOF-102 and 103 respectively.⁷⁷ These two compounds are topologically identical to bio-MOF-100, and bio-MOF-102 has one of the

highest pore volumes of any currently known MOF ($4.36 \text{ cm}^3/\text{g}$).⁷⁸ However, while the BET surface areas of bio-MOF-102 and 103 were expected to be larger than the parent compound, they were in fact less at $3222 \text{ m}^2/\text{g}$ and $2704 \text{ m}^2/\text{g}$ respectively. A number of factors could have contributed to these lower values, such as improper/incomplete activation of the materials, so these measurements may not be indicative of the potential of these compounds, but they are still monumental achievements in their own rights.

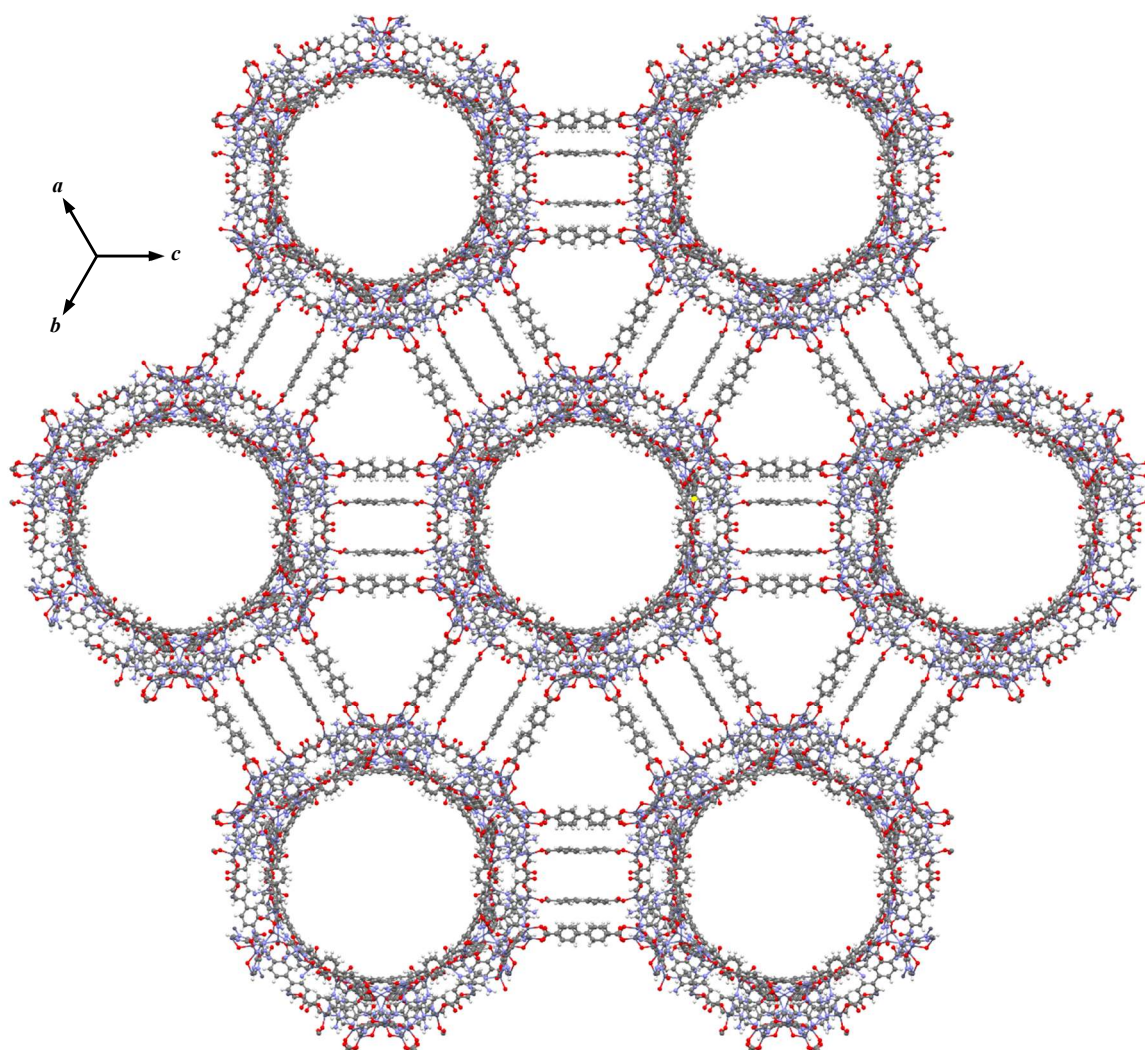


Figure 1.16 The overall structure of bio-MOF-100, or $\{[\text{Zn}_8(\text{adenine})_4(\text{BPDC})_6\text{O}_2] \cdot 4\text{Me}_2\text{NH}_2, 49\text{DMF}, 31\text{H}_2\text{O}\}_n$, as viewed down the pores.⁷⁶ C atoms are shown in grey, H in white, N in light grey-blue, O in red, and Zn in dark grey-blue.

All the examples discussed above demonstrate the ability we have to design and create MOFs with only a handful of basic units, but also exemplify the lack of knowledge which has led to the creation of some remarkably complex and previously unpredictable compounds.

1.4.3 Post-synthetic modification

In some cases, it may not be possible to directly create the desired coordination polymer due to instability of the reagent solution, competing coordinating groups on the ligand of choice, or difficulty in synthesising a single-crystalline sample due to quick precipitation. Additionally, it may be desirable to adjust the surface properties of a known material without having to conduct a crystallisation reaction. Post-synthetic modification provides one answer to these problems through direct reaction of the solid framework material.

Cohen covers some of the various modifications at our disposal and categorises them as covalent/dative when a bond is created, and deprotection when a bond is broken with the framework.⁷⁹ It is also possible for a single modification step to be included under both of these categories. These categories of reaction mainly refer to organic reactions of ligands in the framework, such as the cyanation of terephthalic acid in UiO-66-Br which replaces the Br with a CN group and other examples.⁸⁰

One can also react a solid material with an organic component to introduce a new ligand to the framework. A good example of this is the reversible reaction between $\{Zn_2(BDC)_2(DABCO) \cdot 4DMF \cdot 0.5H_2O\}_n$ (MOF-1) and $\{Zn_2(BDC)_2(H_2O)_2 \cdot (DMF)\}_n$ (MOF-2) via the exchange of 1,4-Diazabicyclo[2.2.2]octane (DABCO).⁸¹ When stored at ambient conditions, MOF-1 loses DABCO to produce MOF-2. The reaction is reversed when the MOF-2 powder is heated in a DMF solution of DABCO. Such coordinative

transformations are not limited to ligands alone, the metal component of a MOF can also be exchanged to some degree, if not entirely. One of the best examples of this is the exchange of Zn with Cu in both the Zn analogue of HKUST-1, and PMOF-2 which is similar to NU-110 discussed previously.⁸² A more in depth study of the Zn/Co/Ni/Cu transmetallation of $M_6(\text{BTB})_4(\text{bipy})_3$ (BTB = 1,3,5-benzenetribenzoate) was conducted later based on the previous work with HKUST-1 and PMOF-2.⁸³ This determined that the exchange of metals was dependent on the stability of the metals in the SBU of the MOF in use, finding in this case that the order of stability was $\text{Cu} > \text{Ni} > \text{Co} > \text{Zn}$. Such transformations would be useful toward the creation of single-crystals for structural studies as Zn analogues can be easier to grow large crystals of for analysis.⁸⁴ Not only this, but the crystals containing more than one metal could possess interesting physical properties not seen in other MOF materials, although this does not seem to have been investigated to date.

1.4.4 Interpenetration

While the design of MOFs has been simplified in the majority of cases by the use of SBUs, and adoption of the node and connector approach. The expansion of frameworks via the use of extended equivalents to the original ligands, or by increasing the dimensionality of the framework by introducing additional ligands, does not always result in the desired product. The expansion can result in a compound with pores large enough to accommodate a replicate of the desired framework, and in some cases, this produces a product containing two or more interpenetrating frameworks. The consequence of interpenetration is a material with a much lower surface area per volume than expected, as the non-primary framework(s) cannot be removed without destroying the material. This in turn reduces the capacity for gas adsorption and is obviously undesirable.

Some ways have been discovered to avoid the interpenetrated form of a framework and produce the desired material. The simplest and most obvious of these methods is control of the concentration and temperature of the synthetic procedure. An interesting study was conducted by Zhang *et al.* who controlled each of these parameters independently and found that increased concentrations and temperatures promoted the formation of the interpenetrated compound.⁸⁵ A much more interesting and ingenious solution was developed by Shekhah *et al.* referred to as liquid-phase epitaxy.⁸⁶ The method involves the surface coating of a substrate to functionalise it with appropriate organic groups, *e.g.* pyridine groups, which is thought to break the symmetry of the bulk MOF making the two or more individual networks inequivalent, therefore promoting the formation of a material with a singular framework. Using this method, they were able to produce a non-interpenetrated form of $[\text{Zn}_2(\mu^4\text{-BDC})_2(\mu^2\text{-4,4'-bipy})_2]_n$ which has an identical structure to the copper analogue discussed earlier but without the interpenetration. Another surface growth approach has since been developed by Sachdeva *et al.* who produced copper-based MOFs electrochemically using copper mesh electrodes.⁸⁷ They produced samples of the MOFs using this method, and compared the physical properties to bulk material produced solvothermally. The material produced via their method had a different BET isotherm to the bulk material, indicative of a comparison of a non-interpenetrated to an interpenetrated compound.

The properties associated with interpenetration are mostly undesirable, but it can give rise to some desirable properties such as adsorption hysteresis.^{88,89} In compounds exhibiting adsorption hysteresis, there is a difference in pressure between when adsorption and desorption of a molecular species occurs. This can mean that a compound can only adsorb at a high pressure, and not release the adsorbate until exposed to a lower pressure which could be beneficial in some applications.

1.5 Synthetic Methods

The various methods to synthesise MOFs have been categorised as slow evaporation, solvothermal (including hydrothermal), microwave-assisted, electrochemical, mechanochemical, and sonochemical by Dey *et al.*⁹⁰ However, synthesis can also be accomplished via gel, liquid-liquid, or vapour diffusion, especially where rapid precipitation is a problem.^{91,92} These methods are discussed in more detail in the next chapter on experimental details.

Generally, the solution-based syntheses (evaporation, solvothermal, diffusion *etc.*) are by far the most commonly used as these give the greatest control over the precipitation rate which is vital for the formation of large, well-formed crystals for structural analysis. Because they are somewhat slow, they are less common than quicker methods such as mechanochemical synthesis in industry. In fact, the English company MOF Technologies™ have focused heavily on mechanochemical synthesis as it allows quick production of common MOFs like HKUST-1 ($\text{Cu}_3(1,3,5\text{-benzenetricarboxylate})_2$) in large quantities without the need for solvents.

1.6 Applications of MOFs

The array of ligands capable of forming MOFs is virtually limitless. It is no wonder then, that as well as acting as porous materials for gas adsorption, MOFs also have applications in the fields of molecular separation, catalysis, luminescence, drug delivery, magnetism, spin crossover compounds, and photonic materials. A good review of how the choice of ligand gives rise to these properties is reported by Janiak.⁹³ This review also highlights the extent of rational design in this field. The majority of these properties are not of

interest for this thesis, but those of gas adsorption are. Further details on how MOFs can be designed toward the applications of hydrogen and carbon dioxide are given below.

1.6.1 Hydrogen storage

As mentioned earlier, the storage of large quantities of hydrogen is key to its use as an energy carrier to replace fossil fuels. The key issue is tailoring the binding energy of hydrogen molecules to the surface of the material, and the total surface area available for adsorption. Incorporating more exposed metal sites, which have high binding energies of around 20-30 kJ/mol,⁹⁴ seems like it would have a great effect on the adsorption of hydrogen, both in terms of quantity and the strength of binding. While studies have shown that this does have an effect on the minimum temperature at which appreciable adsorption occurs, the quantity adsorbed depends heavily on the available surface area and pore volume.⁹⁵ Although NU-110 has the largest surface area and porosity of any known MOF,⁶³ it is the very closely related compound NU-100 which holds the current record for hydrogen adsorption at 17 wt% (77 K, 70 bar).⁹⁶ As a comparative example, the zirconia based compound NU-1103 with approximately the same surface area and pore volume as NU-100 has only a 13 wt% loading under similar conditions.⁹⁷ The more effective adsorption of H₂ in NU-100 is thought to be the result of the exposed copper sites in the dehydrated form of the compound, showing the clear advantage of incorporating metal sites into the structure of compounds targeted towards hydrogen adsorption.⁹⁶

1.6.2 Carbon Dioxide Storage

While H₂ has a uniform distribution of electron density, CO₂ has a significantly anisotropic distribution due to the difference in electronegativity between C and O. This

means that while H₂ is mainly attracted to the exposed metal sites in a MOF, CO₂ can interact quite strongly with functional groups displaying similar unequal charge distribution, such as amines (-NH₂). The incorporation of such functional groups into the ligands which produce a MOF allow control over the polymer's specificity for adsorption of CO₂.

The use of ligands containing amine functional groups to increase the selectivity toward carbon dioxide adsorption/separation has been relatively successful in both recent and past examples and is why it is one of the most widely used techniques in MOF design for CO₂ capture.⁹⁸⁻¹⁰² The Cd-based MOF {[Cd(NH₂-BDC)(BPHZ)_{0.5}]·DMF·H₂O}_n (NH₂-BDC = 2-aminobenzenedicarboxylate, BPHZ = 1,2-bis(4-pyridylmethylene)hydrazine) exemplifies this well, as the research conducted on this compound showed that the primary binding site of CO₂ in the MOF is most likely the amine groups. This is supported both experimentally through blocking of the amine via post-synthetic modification, and through DFT calculations. Functionalisation of IRMOF-74, {Mg₂(DH3PhDC)}_n (DH3PhDC = 2',5'-dimethyl-3,3''-dihydroxy-[1,1':4',1''-terphenyl]-4,4''-dicarboxylate), with alkyl amine groups has also been shown to increase CO₂ selectivity and capacity over non-aminated equivalents through the formation of carbamate groups on exposure to CO₂.⁹⁹ The adenine-based compounds discussed previously also show high adsorption of CO₂ and this could be attributed to the amine group of the adenine molecule. These improvements of CO₂ capturing capability via amine functionalisation are not just isolated to MOFs, but also organic polymeric compounds as well.¹⁰⁰ As such, ligands incorporating amine groups are of key interest in the design of new materials for the capture and storage of CO₂.

1.7 Aims

The primary aim of the research discussed in this thesis was to synthesise novel MOFs using cheap and abundant ligands, such as amino acids, or to at least uncover potential areas for future research which would lead to novel MOF materials. Any new compounds discovered would be structurally characterised, and their potential for gas adsorption, specifically for CO₂, would be determined along with any other unique or interesting properties they might possess. Two areas requiring further investigation were identified to fulfil this aim.

The first of these was to determine whether aliphatic amino acids of the form CO₂H-(CH₂)_n-NH₂, such as 4-aminobutanoic acid, could be used as ligands to produce new MOFs with a great ability for CO₂ capture. This was inspired by the ability of monoethanolamine to capture CO₂. Examples of MOFs with aliphatic amine functionalisation exist and have shown some success in this application giving further credence to the idea. The use of non-rigid ligands to produce permanently porous compounds is non-conventional, as ligands with greater degrees of freedom tend to produce densely packed materials making them unattractive. However, it is exactly this property, *i.e.* flexibility, which makes them interesting to study: one of the key goals of MOF chemistry is to produce flexible materials which can respond to external stimuli.

The second area of research was to identify and explore the coordination chemistry of any underused secondary building units of copper in MOFs. This was based on the fact that copper-based MOFs are almost exclusively paddlewheel based, even though there are many more secondary building units exhibited in the literature, *e.g.* Cu₄(μ⁴-O)(μ²-Cl)₆. Limiting research to this albeit very stable and predictable cluster drastically limits the number of potential factors that can be explored to determine what makes a good or

bad material for gas adsorption: a key question to answer in order to overcome the problems of gas storage. Identification of underexplored copper-based clusters that could provide new avenues of research for porous compounds were to be identified through searches of the literature and structural databases. The ligands/conditions which lead to the formation of these clusters were to be identified, and new MOFs designed/synthesised using this knowledge.

2 Experimental Methods

Most of the work in this thesis involves the formation of coordination complexes. The synthesis of this type of compound is generally rather simple, a metal salt is selected along with one or more compounds wished to react it with, these are mixed together in some way, generally in solution, and if energetically favourable a self-assembly process takes place producing a new compound. On the following pages, the methods used to produce and characterise these compounds are described.

2.1 Solution-based reactions and crystallisations

Coordination complexes are almost always produced via one of an array of solution-based methods. One reason for this is that solutions allow quick, intimate mixing of the reactants. They can also give great control over the crystallisation of the compounds, which is important as structural characterisation by single-crystal X-ray diffraction requires crystals of sufficient size and quality to be grown.

The growth of crystals from a solution usually occurs when the concentration exceeds the saturation concentration (the maximum quantity of solute than can be dissolved in a set volume of a solvent or mixture of solvents), at which point the solution is referred to as being supersaturated. The rate of nucleation and growth of crystals depends heavily on the amount of supersaturation,^{103–106} so control of this is key to the formation of good quality, sizeable crystals. Saturation/crystallisation can be accomplished by either manipulating the solubility/concentration of the compound in solution, or, in the case of highly insoluble complexes like coordination polymers, by producing the compound

slowly by controlling the speed at which starting reagents react. There are a variety of ways to do this which are discussed below.

2.1.1 Solvent Evaporation

The most common way to achieve saturation is to simply allow the solvent in a solution to evaporate, thereby reducing the volume and increasing the concentration of the solution as time passes. The evaporation rate is directly related to the surface area where the vapour is escaping to the atmosphere, as depicted in Figure 2.1. The best quality crystals can be produced when the solvent is allowed to evaporate as slowly as possible. A good technique for this is to cap a vial of the solution with a plastic lid or Parafilm then make a singular or several pin pricks in the top, this only allows vapour to escape slowly through the holes which have a small surface area. Quick crystallisations for bulk material of good crystallinity can be done in a crystallisation/evaporation dish or half of a petri dish.

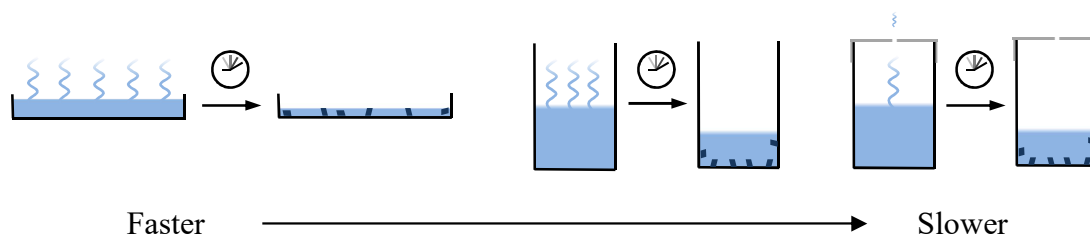


Figure 2.1 The image shows the evaporation crystallisation process. As the solvent evaporates the concentration increases to the point of precipitation. The fastest method is on the left using an evaporation dish, usually half of a petri dish, the middle is a beaker, and on the right is a beaker capped with parafilm and a hole pricked for the slowest evaporation.

In multi-solvent systems, solvents which increase and decrease the concentration required for saturation, *i.e.* increase and decrease the solubility of the compound in the solution, are referred to as a co-solvents and anti-solvents respectively. The addition of a co-solvent which is more volatile, or an anti-solvent which is less volatile, than the initial solvent

can assist in the crystallisation of a compound. This type of crystallisation relies on the fact that the solvent in which the compound is more soluble is more volatile. This more volatile, better solvent therefore contributes a larger mole fraction to the solvent vapour and evaporates faster. As a result, when the solution evaporates, not only does the concentration increase, the solubility also decreases. The solution therefore reaches saturation more quickly by these combined factors, and offers an alternative method when a singular solvent does not work.

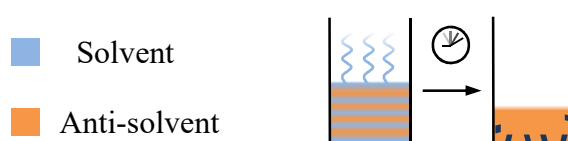


Figure 2.2 A diagram of an ideal anti-solvent/solvent crystallisation in which the anti-solvent is less volatile. As the solvent (blue) evaporates the solution left becomes more concentrated but also the fraction of anti-solvent (orange) in the solution increases resulting in precipitation. This also applies to a co-solvent/solvent crystallisation in which the co-solvent is more volatile.

2.1.2 *Liquid-liquid and liquid-vapour diffusion*

Diffusion crystallisations are closed systems which can be setup in a number of ways. They can be categorised as being either liquid/liquid or liquid/vapour diffusions depending on the phase interaction. Diffusion is a great technique to use for highly insoluble products as the slow mixing of the starting reagents that occurs allows time for the product to precipitate as single-crystals. However, it also provides an alternative technique when the only known anti-solvents for a compound are more volatile than the solvents it is soluble in.

Liquid-liquid diffusions are setup by sequential layering of different solvents/solutions in density order, with the highest density solvent/solution making up the lower layer. During

the work described in this thesis, it has been noted that the best solvent systems for layering are those with a density difference greater than 0.1 g cm^{-3} between the most and least dense solvents, and/or viscosities similar to or greater than water. The choice of vessel is also important as the rate of diffusion is proportional to the diameter of the vessel, among other factors, slower and faster diffusion taking place in narrower and wider vessels respectively, as shown in Figure 2.3. The addition of new layers usually results in a small amount of mixing with pre-existing layers, it is best to avoid this as much as possible for a clean crystallisation that produces no powdered material. To reduce mixing during layering, it is recommended that the liquid is trickled down the side of the vessel as opposed to dropping it directly onto the surface of an existing layer, choice of a narrow glass container can also help. “Buffer” layers can also be used which are either pure solvents or a mixture of the solvents being used, they prevent reaction components mixing instantly during the layering process.

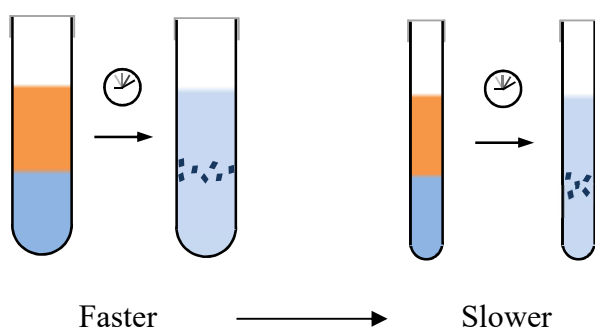


Figure 2.3 A diagram of the liquid-liquid diffusion of a solvent or solution (blue) with another solution or solvent (orange) to produce a crystalline material. Narrower vessels reduce diffusion rate which can produce fewer but larger crystals.

A typical liquid-liquid diffusion crystallisation starts with preparing a solution of the compound to be crystallised, or part of the reactants required to make the product. The solution is then layered with, or on top of, an anti-solvent or another solution containing

the remaining reactants and the diffusion vessel sealed. When the anti-solvent mixes with the solution, the solubility is reduced continuously to the point of precipitation. In the case of the diffusing reactants, the product is produced and precipitated slowly when they mix. Tweaking of the diffusion rate is usually needed to grow large crystals, this can be done by lowering the concentrations and reducing the vessel width. Typical setups are shown in Figure 2.3.

Liquid-vapour diffusions follow a similar principle to liquid-liquid diffusions, although the gaseous form of a diffusing substance results in the precipitation of the product. Control of the diffusion rate can be accomplished with the same methods used to control the evaporation rate of a solution, as shown in Figure 2.4.

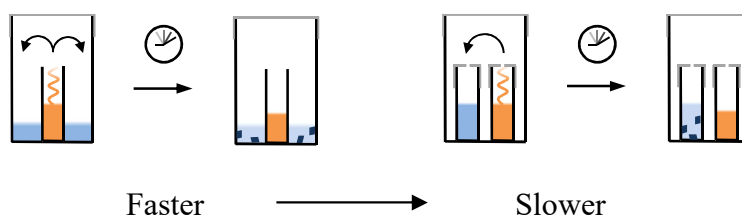


Figure 2.4 Diagram of typical vapour diffusion setups. The setup on the left has the volatile component in a small open vessel (orange) and the compound/reactant solution (blue) is in the larger vessel and has a large surface area for fast diffusion. The setup on the right is much slower as both liquids are sealed in small vials with a pin pricks in the top lowering the surface area.

A solution is first made of the reactants or compound wished to be crystallised. The volatile anti-solvent or reaction component which induces precipitation is then placed in a small glass vial capped with a lid or parafilm with a small pin hole. This is then placed in a larger glass vessel. The solution to be crystallised can then either be deposited directly into the large vessel for a quick crystallisation, or contained in a similar small glass vial as the anti-solvent/reactant capped with a lid or parafilm with a small pin hole placed inside the larger vessel. The larger vessel is then capped and sealed with Parafilm. While

this technique has been used during the studies described in this thesis, nothing of note has been produced using this method, it is just included for completeness. However, it has been particularly good for the synthesis of many pyridine-based compounds produced by Prior and Rosseinsky.^{107,108}

2.1.3 Solvothermal synthesis

Coordination polymers, metal-organic frameworks, and the reactants used to produce them tend to be rather insoluble in many common solvents. This has led to solvothermal synthesis, commonly referred to as hydrothermal if water is the solvent, being a popular method for their production. The technique involves the preparation of a mixture or solution of the reaction components in a solvent, or several solvents, then controlled heating, and sometimes cooling, of the solution to effect the crystallisation of the desired compound, as depicted in Figure 2.5.

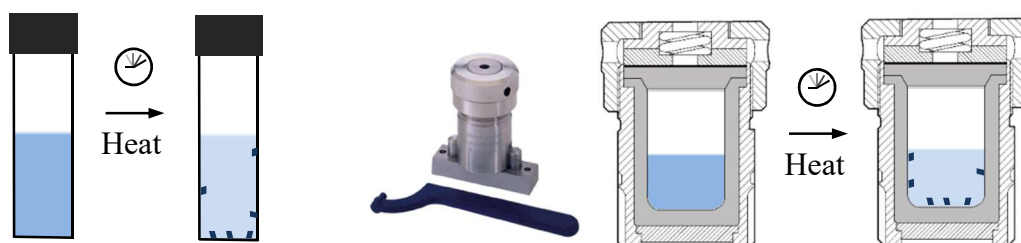


Figure 2.5 An image showing the (hydro)solvothermal synthetic method. A solution or liquid-solid mixture is loaded into a sealed glass vial (left) or autoclave (middle and right) then controllably heated and cooled to produce a crystalline material.

The use of autoclaves allows heating of a solvent above its boiling point as the vessel can withstand the vapour pressure produced at high temperatures, this gives access to reactions not possible in ambient conditions. The production of a crystalline material can occur as a result of dissolution and precipitation of the compound. Alternatively, crystals can be produced slowly in situ via a chemical reaction, *e.g.* DMF decomposes during the

course of a solvothermal reaction slowly increasing the pH which allows controlled synthesis of the desired product. It is quite common for initial procedures to produce small crystals, but large crystals can be grown by altering the reaction time, temperature, heating rate, cooling rate, concentration of reaction solution, and even the solvents in use and their ratio. As with liquid-vapour diffusion, this technique has been used during the studies described herein but nothing of note has been produced.

2.2 Solid-solid reactions

The production of compounds without any solvent at all is a technique which is becoming much more popular recently with demands for environmentally friendly syntheses. The reaction components are either ground with a pestle and mortar or ball mill. The mixing and high pressures generated by the mechanical action allow the reactions to take place. Minimal amounts of solvent (several drops) can greatly increase the reaction rate and still achieve the goal of reducing solvent waste, this is often referred to as solvent drop grinding.

2.3 Solid-gas reactions

The spontaneous reaction of some solid compounds with gases is well documented.^{109,110} Reactions can be in the form of inclusion of guest molecules into the structure of a compound with no change in bonding, or a chemical reaction where an entirely new compound is produced by the breaking and making of bonds. This type of reaction has mainly been used to investigate the reaction of various compounds with hydrohalic acids. A usual experiment is shown in Figure 2.6. and can be described as follows: the solid, in either a single-crystal or powdered form, is placed in a small glass vial; the source of the

vapour that the solid is to react with is placed in a similar vial; both vials are contained in a larger, sealed glass vessel; as time passes the vapour is released by the source and taken up by the solid.

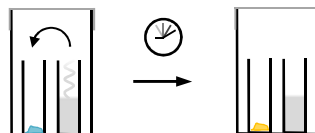


Figure 2.6 A diagram showing a typical solid-gas reaction setup. A solid (blue) and a source of vapour (grey) are placed in small glass vials contained in a larger sealed vessel, as time passes the vapour is released and reacts with the solid making a new compound (yellow).

2.4 X-ray diffraction

2.4.1 *Single-crystal X-ray Diffraction (SCXRD)*

Single-crystal X-ray diffraction data were collected routinely via a series of ω -scans on a Stoe IPDS2 image plate diffractometer with monochromated Mo K α radiation (0.71073 Å). Crystals were mounted on a glass fibre using perfluoropolyalkylether oil and cooled using an Oxford Cryosystems nitrogen cryostream set to 150(1) K. Samples measured at room temperature were mounted using epoxy resin. Data collection and reduction were performed in X-AREA, all data were subjected to a face indexed absorption correction utilising the Tompa method.¹¹¹

Crystal structures were solved and refined within the WinGX¹¹² suite of programs. Initial solutions were found using either direct or dual-space methods implemented within SHELXS and SHELXT respectively.^{113,114} Full-matrix least-squares refinement was completed with SHELXL-2014/7.¹¹⁵ Unless stated otherwise, hydrogen atoms were initially positioned geometrically then refined using a riding model with either fixed or refined (subject to restraints) X-H distances depending on the quality of data. Water

hydrogen atoms were positioned initially from electron density difference maps, they were refined subject to restraint that the two O-H bond lengths were equal with an esd of 0.03 Å and the H···H distance was $2 \times l_{O-H} \times \sin \frac{104.5}{2}$ (esd 0.03 Å) to set the H-O-H angle to 104.5°.

2.4.2 X-ray Powder Diffraction (XRPD)

X-ray powder diffraction (XRPD) was performed routinely to confirm the identity of bulk material, but also for the structural determination of novel compounds. Data were collected on a PANalytical Empyrean Series 2 diffractometer operating with monochromated Cu K α_1 radiation ($\lambda = 1.54056$ Å).

For identification, samples were scanned with the instrument set up in a Bragg-Brentano geometry (reflection) with a power setting of 40 kV and 30 mA, automatic divergence slits with an irradiated sample length of 10 mm, a step size of 0.0262°, and a net time per step of 73.4 s. Subsequent analysis of the diffraction pattern was performed in HighScore Plus¹¹⁶ using the PDF-2 2012 database of powder patterns, or patterns calculated from single-crystal structures using Mercury.¹¹⁷

For structure solution and refinement, samples were transferred to borosilicate glass capillaries of 0.5 mm internal diameter and mounted to the instrument via a goniometer for alignment. The instrument was set up in a Debye-Scherrer geometry (transmission) with a power setting of 45 kV and 40 mA, a 0.0625° divergence slit and 4° anti-scatter slit, a step size of 0.0262°, and a net time per step of 2666.8 s. Diffraction patterns were indexed using the Treor, ITO, Dicvol or Dicvol04 algorithms implemented within HighScore Plus.¹¹⁶ Candidate cells were further tested by a Pawley fit conducted in the same program. Structure solution was then attempted in each case via the global

optimisation via the simulated annealing approach in Endeavour.¹¹⁸ Initial molecule geometries were derived from similar molecules contained within the Cambridge Structural Database (CSD).¹¹⁹ The initial solutions were then used as the starting point for Rietveld refinement which was conducted using the EXPGUI interface for GSAS.¹²⁰ Atomic positions were allowed to refine subject to restraints to keep atomic distances similar to those found in similar compounds on the CSD. A single isotropic displacement parameter was refined for all atoms. In the final stage of refinement, hydrogen atoms were placed geometrically and fixed in position for the final calculation cycles with an isotropic displacement parameter set 1.2 times larger than the non-H atoms.

2.5 Elemental Analysis

Although SCXRD and XRPD provide information on the crystalline portion of a sample, confirming the purity of a sample also needs to take into account any amorphous material. Elemental analysis determines the quantity of each element present in a particular sample, and can include individual isotopes as well. Generally only CHNX analysis is performed for compounds containing organic components, which is the determination of the mass percentage of carbon (C), hydrogen (H), nitrogen (N), and any other heteroatoms (X), *e.g.* sulfur or halogens, present. Other techniques can be used for the determination of these and other elements, such as X-ray photoelectron spectroscopy (XPS) and inductively coupled plasma atomic emission spectroscopy (ICP-AES), but these are often more expensive and time consuming than simple CHNX analysis.

CHNX analysis first involves the combustion of a pre-determined mass of sample in an excess of high purity oxygen and an inert carrier gas to convert the components into their oxides (CO₂, H₂O, NO_x, SO₂ *etc.*). The products of the combustion are then passed over high purity, heated copper to remove any unconsumed oxygen and reduce nitrogen oxides

to dinitrogen (N₂), additionally, a series of filters remove any unwanted species before analysis of the composition. The N₂ and oxide species can then either be separated by gas chromatography and detected by thermal conductivity, or they can be detected individually by a series of infrared or thermal conductivity detectors tailored to the chemical species. The observed response is proportional to the quantity of the analyte, allowing one to calculate how much of each element was present in the original sample. Elemental analysis for this work was performed on a Fisons CHN Elemental Analyser (Thermo Scientific), type EA-1108.

2.6 Thermogravimetric Analysis (TGA)

Thermogravimetric analysis is the technique of measuring the mass of a sample as a function of temperature and time in varying atmospheres, and can be used to probe many properties of a sample including, but not limited to; phase transitions, chemisorption, desolvation, decomposition and solid-gas reactions. When the temperature of a sample is monitored as a function of the power input relative to a reference, called differential scanning calorimetry (DSC), the same instrument can also provide information on the energetics of a particular process. TGA measurements were performed using a Mettler TGA/DSC 1 Star System thermogravimetric balance, a typical heating regime is done under a nitrogen atmosphere with a ramping protocol starting at 50 °C increasing at 0.5 °C/s until 950 °C.

2.7 Fourier Transform Infrared (FTIR) Spectrometry

Another useful structural technique that can be used, but much less so in our group, is infrared (IR) spectroscopy. Compounds absorb photons of particular wavelengths from the IR region of the electromagnetic spectrum. This is because the energy matches that

required to make the bonds in a molecule vibrate. The energy required to effect molecular vibration is dependent on a number of factors including the mass of the atoms, the strength of the bond(s), and, in molecules with more than two atoms, the type of vibration caused *e.g.* symmetric stretch, asymmetric stretch *etc.* As such, this technique can be used to confirm structural features determined by X-ray diffraction. Most, if not all, spectrometers in use today are Fourier transform infrared (FTIR) spectrometers. These instruments irradiate the sample with every wavelength/frequency of infrared radiation simultaneously using a device known as an interferometer. The exact workings of an interferometer are beyond the scope of this thesis, but the result is a complex waveform which, when subjected to Fourier transform analysis, can be decomposed into a graph of intensity or absorption *vs.* wavelength otherwise known as a spectrum. IR spectra displayed in this thesis were collected on a Thermo Scientific Nicolet iS5 FTIR spectrometer fitted with a Thermo Scientific iD7 ATR device.

3 Synthesis, Structure, and Solid-Gas Reactions of $[\text{CuCl}_2(\text{RPy})_2]_n$ and $(\text{RPy-H})[\text{CuCl}_4]$ Compounds

The sorption of gases by solid-state compounds is currently an important topic in chemical research. A large proportion of investigations focus on compounds exhibiting permanent porosity, and specifically the sorption of hydrogen and carbon dioxide.^{121–123} However, there has recently been an upsurge in publications on both chemical and physical sorption of gases by non-porous compounds, and the associated structural transformations that take place to allow the uptake and loss of guest molecules.^{124–126} Information on these types of reactions is at present extremely limited but is key to understanding the fundamental processes involved, which is especially important from an applications standpoint.

Tetrahalometallate ($[\text{MX}_4]^{2-}$) salts are an interesting variety of compounds that can exhibit thermochromism,¹²⁷ and the ability to act as liquid crystals.¹²⁸ Adams *et al.*¹²⁹ were the first to show that release of HCl molecules from such materials is possible through thermal decomposition of Pt and Pd salts to produce the corresponding neutral coordination complexes. They also showed that the same elimination reactions occur when similar compounds of Co and Zn are heated in an inert atmosphere or ground with a basic salt, *e.g.* KOH, yielding neutral coordination polymers belonging to a family of compounds of general formula *trans*- $[\text{MX}_2(\text{RPy})_2]$ ^{130–132} (M = metal, X = Cl, Br; RPy = pyridine and substituted pyridine *e.g.* methylpyridine) which can be either discrete or polymeric in nature, through bridging halide ions, depending on the ligand.^{133–135} Additionally, they have proved that control over the polymorphic form of the product can be exerted through the choice of synthetic method,¹³¹ and that the methods they employ

can be used to achieve solvent-free synthesis of metal-carbene complexes.¹³⁶ The above reactions do not occur spontaneously in ambient conditions however, whereas Espallargas *et al.*¹⁰⁹ have demonstrated that the equivalent reactions with Cu, do. Their work focusses on the tetrahalocuprate salts of halopyridines, loss of HX from which results in neutral complexes of general formula *trans*-[CuX₂(XPy)₂]. They have also showed that the reaction is reversible through exposure to damp and anhydrous HCl and HBr gas, and that mechanochemical synthesis of the cuprate salts can be achieved through grinding of the appropriate copper and pyridinium halide salts.^{109,137–140} They have attempted to understand the mechanisms behind these reactions by utilising the difference in X-ray scattering power of chloride and bromide ions as a tracer. *E.g.* a bromide-based starting material is reacted with HCl to produce a [CuCl₂Br₂]²⁻ salt, the occupancy Cl/Br at each halide position can be calculated with X-ray diffraction data from resulting compound allowing one to determine where the Br anions have gone. However, despite these efforts, the reactions are still not fully understood.¹³⁷

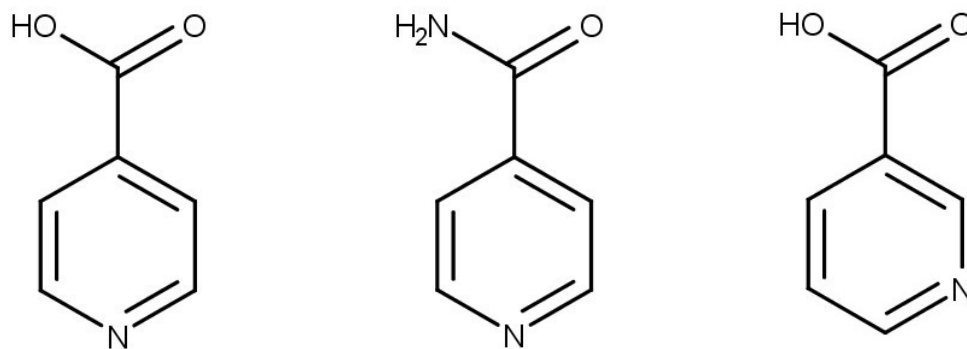


Figure 3.1 Molecular drawings of isonicotinic acid or INAc (left), isonicotinamide or INAm (middle), and nicotinamide or NAM (right).

Isonicotinic acid (INAc), isonicotinamide (INAm), and nicotinamide (NAM), shown in Figure 3.1, are three common molecules used in crystal engineering owing to the predictable but flexible hydrogen bonding arrangements they produce.^{141–143} One

example is the common $R_2^2(8)$ ring motifs produced by compounds containing carboxylic acid and amide groups, as shown in Figure 3.2. It was found that reaction of INAc with copper chloride produces a complex belonging to the *trans*-[CuX₂(RPy)₂] family and displays the predictable ring-shaped interaction. The hydrated tetrachlorocuprate salt of INAc displays a similar hydrogen bonding ring motif, but also an N-H...Cl₂-Cu interaction that is a common supramolecular synthon observed in other pyridinium tetrahalometallate compounds, also shown in Figure 3.2. The predictability of the copper chloride-INAc compounds prompted investigation of reactions with the related compounds INAm and NAm, and to conduct similar solid-gas reaction studies to those done previously. The aims of the research were threefold: to study the robustness of the hydrogen bonding interactions discussed above, to investigate the interconversion between the *trans*-[CuCl₂(RPy)₂] and (H-RPy)₂[CuCl₄] compounds by solid-gas reaction, and to compare the structures discovered to those of compounds made with other d-block metals.

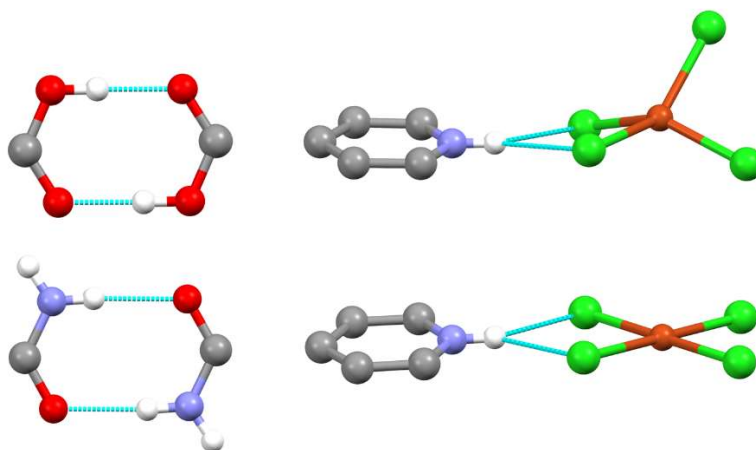


Figure 3.2 The common supramolecular synthons found in carboxylic and amide compounds, left, and pyridinium tetrachlorocuprate salts, right. C atoms are shown in grey, H in white, Cl in green, Cu in dark brown, N in light grey-blue, and O in red. Hydrogen bonds are drawn as light-blue dashed lines.

3.1 Experimental procedures

All reagents and solvents were purchased from Sigma Aldrich, BDH or Fisher Scientific and used as received. INAc.HCl¹⁴⁴ and NAm.HCl¹⁴⁵ were prepared according to the literature procedures. Elemental Analyses were conducted by the Elemental Analysis Service, Department of Chemistry, University of Hull on a Fisons CHN Elemental Analyser (Thermo Scientific), type EA-1108. Infrared (IR) spectra were collected on a Thermo Scientific Nicolet iS5 FTIR spectrometer fitted with a Thermo Scientific iD7 ATR device. Table 3.1 shows a grid of the compounds created through combination of copper chloride and/or hydrochloric acid with either INAc, INAm, or NAm. The reactions which produce these compounds are detailed below.

Table 3.1 Products resulting from the combination of copper chloride and/or hydrochloric acid with INAc/INAm/NAm. Newly discovered compounds are highlighted in bold and starred.

	INAc	INAm	NAm
CuCl₂	*[CuCl ₂ (INAc) ₂] _n (1)	*[CuCl ₂ (INAm) ₂] _n (3)	*[CuCl ₂ (NAm) ₂] _n (5)
CuCl₂ + HCl	(H-INAc) ₂ [CuCl ₄]·2H ₂ O (2a) *(H-INAc) ₂ [CuCl ₄] (Form I) (2b) *(H-INAc) ₂ [CuCl ₄] (Form II) (2c)	*(H-INAm) ₂ [CuCl ₄] (Form I) (4a) *(H-INAm) ₂ [CuCl ₄] (Form II) (4b) *(H-INAm) ₂ [CuCl ₄] (Form III) (4c)	*(H-NAm) ₂ [CuCl ₄] (Form I) (6a) *(H-NAm) ₂ [CuCl ₄] (Form II) (6b)
HCl	INAc.HCl	*INAm.HCl	NAm.HCl

3.1.1 Synthesis of INAm.HCl

Hydrochloric acid (0.08 ml, 12 M) in acetonitrile (3 ml) was added to isonicotinamide (0.2442 g, 2 mmol) dissolved in acetonitrile (25 ml). The resultant white mixture was heated until the precipitate dissolved, and the solution was left to evaporate slowly over several days. This resulted in the formation of large colourless block-shaped crystals of INAm.HCl. Replacing INAm with INAc (0.2462 g, 2 mmol) or NAm (0.2442 g, 2 mmol) produces INAc.HCl and NAm.HCl respectively, these products are comparable to those

produced via the literature methods. Elemental anal. (%) calcd for INAm.HCl: C, 45.44; H, 4.45; N, 17.66. Found: C, 45.28; H, 4.15; N, 17.47. Calcd for INAc.HCl: C, 45.16; H, 3.79; N, 8.78. Found: C, 44.77; H, 3.60; N, 8.95. Calcd for NAm.HCl: C, 45.44; H, 4.45; N, 17.66. Found: C, 45.48; H, 4.28; N, 18.04.

3.1.2 *Synthesis of [CuCl₂(INAc/INAm/NAm)₂]_n (1/3/5)*

INAc (0.2462g, 2 mmol), INAm (0.2442g, 2 mmol), or NAm (0.2442g, 2 mmol) were dissolved in methanol (25 mL) with stirring and moderate heating, CuCl₂·2H₂O (0.1705 g, 1 mmol) was then added to the solution resulting in a light blue-green precipitate of **1**, **3**, or **5**, respectively which was subsequently filtered and washed with methanol. **1**, **3** and **5** can also be prepared by grinding CuCl₂·2H₂O with two molar equivalents of INAc, INAm or NAm with several drops of water for **1**, or methanol for **3** and **5**. Single-crystals of **1** were prepared by evaporation of a dilute hydrochloric acid solution of the compound. Elemental anal. (%) calcd for **1**: C, 37.86; H, 2.65; N, 7.36. Found: C, 38.08; H, 2.40; N, 7.26. Calcd for **3**: C, 38.06; H, 3.19; N, 14.79. Found: C, 37.31; H, 3.07; N, 13.96. Calcd for **5**: C, 38.06; H, 3.19; N, 14.79. Found: C, 37.71; H, 2.76; N, 14.19.

3.1.3 *Synthesis of [CuCl₄](H-INAc)₂(H₂O)₂ (2a)*

Synthesis of **2a** by the literature procedure does not give a pure product.¹⁴⁶ Synthesis of a pure product could be achieved by grinding of CuCl₂·2H₂O (0.1705 g, 1 mmol) and INAc (0.2462g, 2 mmol) with several drops of concentrated hydrochloric acid producing a bright green powder. Elemental anal. (%) calcd for **2a**: C, 29.44; H, 3.29; N, 5.72. Found: C, 29.63; H, 3.35; N, 5.54

3.1.4 Synthesis of $[CuCl_4](H-INAc)_2$ (Form I) (2b)

A small portion of **1** was transferred to a glass vial. A similar vial was filled with concentrated hydrochloric acid. Both were placed inside a larger vessel which was capped and sealed. A colour change from light blue-green to bright green was observed with no further change in colour after 3 hours. Elemental anal. (%) calcd for **2b**: C, 31.77; H, 2.67; N, 6.18. Found: C, 32.00; H, 2.71; N, 6.11.

3.1.5 Synthesis of $[CuCl_4](H-INAc)_2$ (Form II) (2c)

The bright green powder identified as **2c** was produced via grinding of INAc.HCl (0.3191 g, 2 mmol) and $CuCl_2 \cdot 2H_2O$ (0.1705 g, 1 mmol) over several minutes, after which no further change in colour was observed. Elemental anal. (%) calcd for **2c**: C, 31.77; H, 2.67; N, 6.18. Found: C, 31.89; H, 2.73; N, 6.13.

3.1.6 Synthesis of $[CuCl_4](H-INAm)_2$ (Form I) (4a)

INAm (0.2442 g, 2 mmol) and $CuCl_2 \cdot 2H_2O$ (0.1705 g, 1 mmol) were dissolved in concentrated hydrochloric acid (3 mL). The solution was left to evaporate in a crystallising dish resulting in a few green block crystals and some unidentified material. Pure **4a** can be synthesised by prolonged reaction of **3** with hydrochloric acid vapour over 6 days. Elemental anal. (%) calcd for **4a**: C, 31.91; H, 3.12; N, 12.41. Found: C, 31.26; H, 2.64; N, 11.97.

3.1.7 Synthesis of $[CuCl_4](H-INAm)_2$ (Form II) (4b)

4b was synthesised using the same method to produce **2b**, except using **3** as the starting reagent. A colour change from light blue-green to yellow-green was observed over 3 hours, however the material continues to react and a colour change to bright green **4a**

occurs over 6 days upon prolonged exposure to the hydrochloric acid vapour. The reaction of **4b** to **4a** still occurs in ambient conditions but is significantly slower. Elemental anal. (%) calcd for **4c**: C, 31.91; H, 3.12; N, 12.41. Found: C, 31.97; H, 2.71; N, 12.03.

3.1.8 Synthesis of $[CuCl_4](H-INAm)_2$ (Form III) (4c**)**

The yellow-green powder identified as **4c** was produced via grinding of INAm.HCl and $CuCl_2 \cdot 2H_2O$ in a 2:1 molar ratio, or grinding of a 2:1 molar ratio of NAm and $CuCl_2 \cdot 2H_2O$, **3**, **4a**, or **4b** with several drops of hydrochloric acid. Grinding was continued for several minutes after which no further change in colour was observed. Elemental anal. (%) calcd for **2c**: C, 31.77; H, 2.67; N, 6.18. Found: C, 31.89; H, 2.73; N, 6.13.

3.1.9 Synthesis of $[CuCl_4](H-NAm)_2$ (Form I) (6a**)**

6a was synthesised using the same method to produce **4a** except using NAm (0.2442 g, 2 mmol). Using this method produces bright yellow crystals of **6a**, but the compound can also be prepared as a bright yellow powder via grinding of NAm.HCl and $CuCl_2 \cdot 2H_2O$ in a 2:1 molar ratio, a 2:1 ratio of NAm and $CuCl_2 \cdot 2H_2O$ with several drops of hydrochloric acid, or **6b** with several drops of hydrochloric acid. Elemental anal. (%) calcd for **6a**: C, 31.91; H, 3.12; N, 12.41. Found: C, 31.85; H, 2.81; N, 12.16.

3.1.10 Synthesis of $[CuCl_4](H-NAm)_2$ (Form II) (6b**).**

6b was synthesised using the same method to produce **2b**, except using **5** as the starting reagent. A colour change from light blue-green to yellow was observed with no further change in colour after 3 hours. Elemental anal. (%) calcd for **6b**: C, 31.91; H, 3.12; N, 12.41. Found: C, 31.54; H, 2.63; N, 11.94.

3.1.11 Decomposition Reactions

1, **3**, and **5** could also be produced via decomposition of their corresponding tetrachlorocuprate salts over several days by loss of HCl gas. This only occurred when the materials were placed on a glass dish in ambient conditions, no decomposition occurs if samples are stored in sealed containers. **2a**, **2b**, and **2c** decompose into **1**; **4a**, **4b**, and **4c** decompose into **3**; **6a** and **6b** decompose into **5**.

3.2 Crystal structure and refinement information

Crystal structures were solved and refined according to the standard procedure discussed in the experimental section, apart for the following exceptions. Data were of sufficient quality for **1** and **6b** to justify refinement of X-H distances subject to restraints to keep the bond lengths of similar chemical species similar. The crystal of **4a** was found to be a non-merohedral twin. Integration of data from each twin domain was performed. An initial solution was obtained using data from the main component followed by refinement using data from both twin domains using the hklf5 formalism. The twin fraction was found to be 0.8824(9):0.1176(9). **6a** was identified as a non-centrosymmetric structure of space group $Pca2_1$. Use of PLATON¹⁴⁷ did not reveal any missed symmetry to suggest a change of space group. Attempts to solve the structure in the equivalent centrosymmetric space group $Pbcm$ failed. The non-centric space group $Pca2_1$ was thus retained. The structure was refined as an inversion twin with a Flack parameter of 0.41(4). The highest electron density difference peak of 2.05 e/Å³, 2.313(1) Å from Cu₂, arises from minor disorder of the Cu₂ CuCl₄ unit. We have explored modelling this as a second component (refined occupancy is about 6%) but this introduces a large number of extra parameters with no improvement in the quality of fit. We have therefore retained the model with a single component for this ion. Further details for structures determined from single-

crystal X-ray diffraction data are contained in Table 3.2 and Table 3.3, while details of structures determined from X-ray powder diffraction data are contained in Table 3.4.

Table 3.2 Single-crystal structure refinement data for **1**, **4a**, and **6a**.

Compound	1	4a	6a
Empirical formula	C ₁₂ H ₁₀ Cl ₂ CuN ₂ O ₄	C ₁₂ H ₁₄ Cl ₄ CuN ₄ O ₂	C ₁₂ H ₁₄ Cl ₄ CuN ₄ O ₂
Formula weight (g mol ⁻¹)	380.66	451.61	451.61
Temperature (K)	150(1)	150(1)	150(1)
λ (Å)	1.54184	0.71073	0.71073
Crystal system	Triclinic	Triclinic	Orthorhombic
Space group	$P\bar{1}$	$P\bar{1}$	$Pca2_1$
a (Å)	3.7178(3)	7.4752(10)	14.6164(10)
b (Å)	7.4212(5)	7.7741(12)	6.9245(3)
c (Å)	12.5699(10)	8.0875(12)	33.9593(17)
α (°)	76.457(7)	77.452(12)	90
β (°)	88.766(7)	69.083(11)	90
γ (°)	85.737(7)	68.367(11)	90
V (Å ³)	336.23(5)	406.10(11)	3437.1(3)
Z	1	1	8
Density (Mg m ⁻³)	1.880	1.847	1.745
μ (mm ⁻¹)	6.126	2.015	1.904
Crystal size (mm)	0.17 × 0.05 × 0.02	0.31 × 0.22 × 0.06	0.49 × 0.25 × 0.12
Transmission factors (max/min)	0.8830 and 0.5900	0.9015 and 0.5403	0.8079 and 0.5670
$F(000)$	191	227	1816
θ range (°)	6.15 - 72.62	2.71 - 29.49	2.40 - 29.24
Index ranges	-4 ≤ h ≤ 4 -7 ≤ k ≤ 9 -15 ≤ l ≤ 10	-10 ≤ h ≤ 10 -10 ≤ k ≤ 10 -11 ≤ l ≤ 11	-20 ≤ h ≤ 16 -8 ≤ k ≤ 9 -39 ≤ l ≤ 46
Reflections collected	1764	7972	14476
Independent reflections (R_{int})	1271 (0.0157)	7972 (0.0628)	7931 (0.0454)
Completeness to $\theta = 25.242^\circ$	98.9%	100.0%	99.7%
Restraints/parameters	6/103	0/107	1/416
Goodness-of-fit on F^2	1.103	0.906	0.885
$R_1 [I > 2\sigma(I)]$	0.0280	0.0502	0.0427
wR_2 (all data)	0.0759	0.1569	0.1051
Largest diff. peak and hole (e Å ⁻³)	0.281 and -0.615	0.916 and -0.964	2.046 and -0.477

Table 3.3 Single-crystal structure refinement data for **6b**, INAc.HCl, and INAm.HCl.

Compound	6b	INAc.HCl	INAm.HCl
Empirical formula	C ₁₂ H ₁₄ Cl ₄ CuN ₄ O ₂	C ₆ H ₆ ClNO ₂	C ₆ H ₇ ClN ₂ O
Formula weight (g mol ⁻¹)	451.61	159.57	158.59
Temperature (K)	150(1)	150(1)	150(1)
λ (Å)	0.71073	0.71073	0.71073
Crystal system	Monoclinic	Monoclinic	Monoclinic
Space group	<i>P</i> 2 ₁ / <i>c</i>	<i>P</i> 2 ₁ / <i>c</i>	<i>C</i> 2/ <i>c</i>
<i>a</i> (Å)	7.6240(9)	12.9080(8)	24.960(2)
<i>b</i> (Å)	13.7623(11)	7.0479(4)	5.1055(4)
<i>c</i> (Å)	16.618(2)	14.8081(9)	12.4664(9)
α (°)	90	90	90
β (°)	94.970(10)	92.214(5)	117.545(5)
γ (°)	90	90	90
<i>V</i> (Å ³)	1737.1(3)	1346.15(14)	1408.6(2)
<i>Z</i>	4	8	8
Density (Mg m ⁻³)	1.727	1.575	1.496
μ (mm ⁻¹)	1.884	0.496	0.47
Crystal size (mm)	0.37 × 0.18 × 0.16	0.38 × 0.37 × 0.23	0.34 × 0.28 × 0.26
Transmission factors (max/min)	0.7823 and 0.5797	0.9180 and 0.8142	0.9131 and 0.8611
<i>F</i> (000)	908	656	656
θ range (°)	1.92 - 29.24	2.753 - 29.169	1.840 - 29.157
Index ranges	-10 ≤ <i>h</i> ≤ 8 -16 ≤ <i>k</i> ≤ 18 -22 ≤ <i>l</i> ≤ 22	-17 ≤ <i>h</i> ≤ 17 -9 ≤ <i>k</i> ≤ 9 -17 ≤ <i>l</i> ≤ 20	-34 ≤ <i>h</i> ≤ 34 -6 ≤ <i>k</i> ≤ 6 -17 ≤ <i>l</i> ≤ 17
Reflections collected	10952	10026	4768
Independent reflections (<i>R</i> _{int})	4571 (0.0247)	3623(0.0269)	1865(0.0471)
Completeness to $\theta = 25.242^\circ$	97.7%	99.9%	99.1%
Restraints/parameters	35/220	30/195	8/104
Goodness-of-fit on <i>F</i> ²	0.929	1.032	1.011
<i>R</i> ₁ [<i>I</i> > 2 σ (<i>I</i>)]	0.0233	0.0253	0.0337
<i>wR</i> ₂ (all data)	0.0558	0.0794	0.0931
Largest diff. peak and hole (e Å ⁻³)	0.409 and -0.376	0.394 and -0.197	0.449 and -0.484

Table 3.4 Powder structure refinement data for **2b**, **3**, **4b**, and **5**.

Compound	2b	3	4b	5
Empirical formula	C ₁₂ H ₁₂ Cl ₄ CuN ₂ O ₄	C ₁₂ H ₁₂ Cl ₂ CuN ₄ O ₂	C ₁₂ H ₁₄ Cl ₄ CuN ₄ O ₂	C ₁₂ H ₁₂ Cl ₂ CuN ₄ O ₂
Formula weight (g mol ⁻¹)	453.6	378.71	451.63	378.71
Temperature (K)	293(1)	293(1)	293(1)	293(1)
λ (Å)	1.54056	1.54056	1.54056	1.54056
Crystal system	Monoclinic	Monoclinic	Triclinic	Monoclinic
Space group, <i>Z</i>	<i>P</i> 2 ₁ / <i>c</i> , 2	<i>C</i> 2/ <i>c</i> , 4	<i>P</i> $\bar{1}$, 1	<i>P</i> 2 ₁ / <i>c</i> , 2
<i>a</i> (Å)	7.6430(5)	24.319(8)	3.9177(6)	3.7851(5)
<i>b</i> (Å)	10.8232(6)	3.7547(13)	7.7707(11)	13.8681(16)
<i>c</i> (Å)	12.2250(8)	16.432(6)	13.778(2)	13.1151(15)
α (°)	90	90	94.070(3)	90
β (°)	126.2554(10)	111.7534(34)	97.408(3)	91.6802(25)
γ (°)	90	90	100.338(2)	90
<i>V</i> (Å ³)	815.48(12)	1393.6(13)	407.27(17)	688.14(24)
Density (Mg m ⁻³)	1.847	1.841	2.101	1.828
μ (mm ⁻¹)	2.28	1.47	2.14	1.47
Sample shape (mm)	cylinder 0.12 × 0.5 × 0.5			
θ range (°)	2.5-55	2.5-55	2.5-55	2.5-55
Data	4037	3997	4037	3997
Parameters Refined	64	76	71	64
<i>R</i> _p	0.0407	0.654	0.0347	0.0412
<i>R</i> _w	0.0573	0.0975	0.0497	0.0556
χ^2	2.1000	8.9710	1.9730	2.7580

3.3 Isonicotinic acid (INAc)

3.3.1 Summary of reactions

As mentioned in the introduction to this chapter, this piece of work began with the accidental synthesis of the novel compound [CuCl₂(INAc)₂] (**1**). Single-crystals were produced by crystallisation from a dilute hydrochloric acid solution, while bulk synthesis was accomplished by mixing the starting reagents in water or methanol. The hydrated tetrachlorocuprate salt (H-INAc)₂[CuCl₄]·2H₂O (**2a**),¹⁴⁶ which had already been discovered, was synthesised from a more concentrated hydrochloric acid solution. Decomposition of **2a** to **1** occurs in approximately 2 days by loss of water and HCl molecules, however the reverse solid-gas reaction of **1** to **2a** is not possible. Reaction of **1** with hydrochloric acid vapour produces a green compound in approximately 3 hours

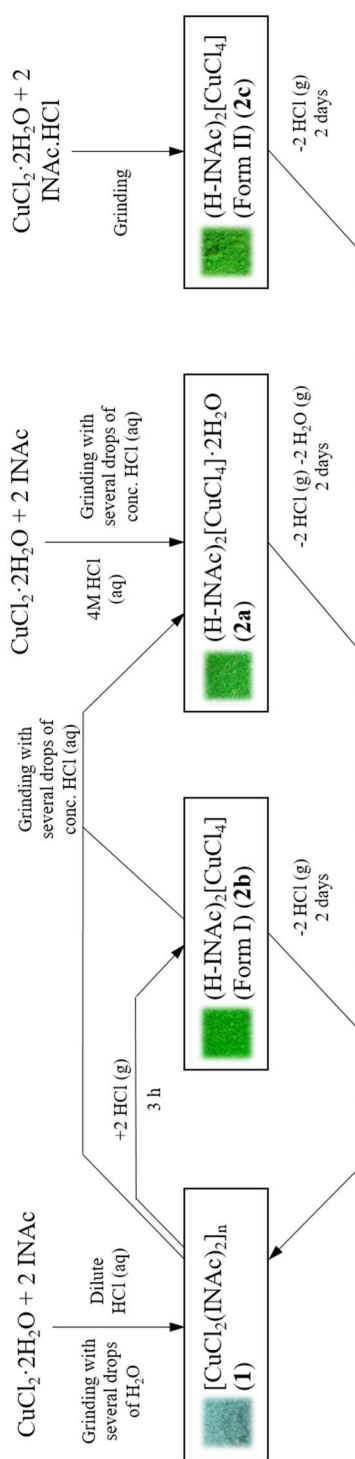


Figure 3.3 A reaction scheme for the synthesis and interconversion of copper chloride – isonicotinic acid compounds.

with a different powder X-ray diffraction pattern to that of **2a**. The unidentified compound was determined to be the anhydrous equivalent to **2a**, $(\text{H-INAc})_2[\text{CuCl}_4]$ (Form I) (**2b**), which decomposes into **1** through loss of HCl in a similar time to that of **2a**.

Mechanochemical synthesis of the three compounds, **1**, **2a**, and **2b**, was then attempted to explore the chemistry further. Grinding of copper chloride and INAc with a few drops of water was found to produce pure samples of **1**. On the other hand, grinding of the same reagents, **1**, or **2b**, with several drops of HCl(aq) produced samples of **2a** which were purer than those made via solution crystallisation. It was expected that reaction of INAc.HCl with copper chloride would produce either **2a** or **2b**, however the X-ray powder diffraction pattern of the product matched neither. It has been confirmed that this unidentified phase must be a second form of the anhydrous cuprate salt, *i.e.* $(\text{H-INAc})_2[\text{CuCl}_4]$ (Form II) (**2c**), through elemental analysis and IR spectra comparison. However, without unit-cell information it is impossible to determine the structure of this compound. A reaction scheme is shown in Figure 3.3.

3.3.2 $[\text{CuCl}_2(\text{INAc})_2]_n$ (**1**)

The single-crystals of $[\text{CuCl}_2(\text{INAc})_2]_n$ (**1**) were too small for structural analysis using the STOE IPDS II diffractometer as the detector was not sensitive enough. Samples were sent to Agilent Technologies for X-ray diffraction data collection, further crystallographic details are included in Table 3.2. The compound was found to crystallise with a centrosymmetric triclinic unit-cell. The asymmetric unit contains one chloride ion, a neutral INAc molecule, and a copper ion located on the 1a Wyckoff position, as shown in Figure 3.4. The Cu centre displays a 4+2 coordination geometry, bond distances and angles are shown in Table 3.5.

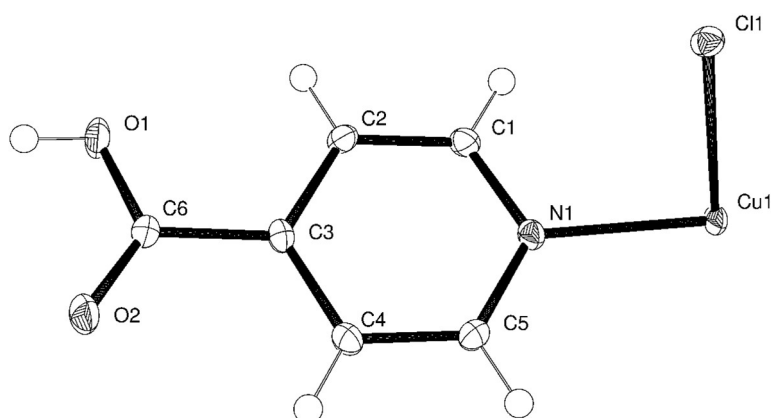


Figure 3.4 Asymmetric unit of $[\text{CuCl}_2(\text{INAc})_2]_n$ (**1**) with atoms shown as thermal ellipsoids drawn at 50% probability.

Table 3.5 Selected bond lengths (Å) and angles (°) around the Cu coordination centre for $[\text{CuCl}_2(\text{INAc})_2]_n$ (**1**).

Cu(1) – Cl(1)	2.2842(5)	N(1)-Cu(1)-Cl(1)	89.35(5)
Cu(1) – Cl(1)#1	2.8980(6)	N(1)-Cu(1)-Cl(1)#1	90.47(6)
Cu(1) – N(1)	2.0306(19)	Cl(1)-Cu(1)-Cl(1)#1	90.89(2)

#1 -1 + x, y, z

The overall structure is shown in Figure 3.5A, consisting of a chain of edge-sharing CuCl_4 rhombi along the *a* axis decorated by INAc. The orientation of the polymer is such that

the carboxylic acid groups of two INAc molecules, related by the inversion centre at $\frac{1}{2}, \frac{1}{2}, \frac{1}{2}$, create an $R_2^2(8)$ interaction composed of two O-H \cdots O contacts (O \cdots O 2.629(2) Å) which through the coordinated copper forms part of a $C_1^1(14)$ chain running in the $[\bar{1}11]$ direction. The coordination and hydrogen bonds combine to create a 2-D supramolecular framework shown in Figure 3.5B.

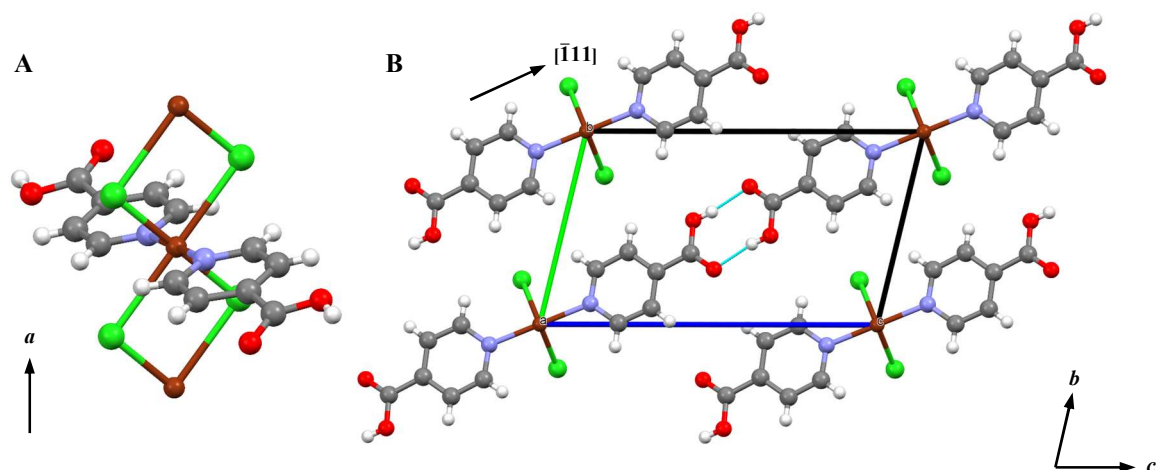


Figure 3.5 The copper chloride chain present in $[\text{CuCl}_2(\text{INAc})_2]_n$ (**1**) extending along the a axis (A), and the crystal packing of **1** showing the O-H \cdots O contacts forming a ring type hydrogen bonding arrangement, and the resulting chain which runs in the $[\bar{1}11]$ direction (B). C atoms are shown in grey, H in white, Cl in green, Cu in dark brown, N in light grey-blue, and O in red. Hydrogen bonds are drawn as light-blue dashed lines.

Amazingly, the structure of **1** is almost identical to that of $[\text{PdCl}_2(\text{INAc})_2]$ despite the absence of a polymeric metal halide chain in the latter compound (Pd-Cl 2.3051(7) Å, Pd-N 2.021(3) Å); Pd is stable in a square-planar geometry so the long Pd-Cl contacts are not formal coordination bonds (Pd-Cl 3.4516(8) Å).¹⁴⁸ Additionally, a pseudohalide analogue of **1** exists with Ni, $[\text{Ni}(\text{SCN})_2(\text{INAc})_2]_n$, although the polymeric chain of the Ni compound is not as linear as in **1** and is instead puckered which creates voids that can be filled with aromatic guest molecules.^{149,150} The aromatic guests appear to compensate for shortcomings in the crystal packing efficiency of $[\text{Ni}(\text{SCN})_2(\text{INAc})_2]_n$. Since **1** is very densely arranged, it does not possess similar host-guest properties.

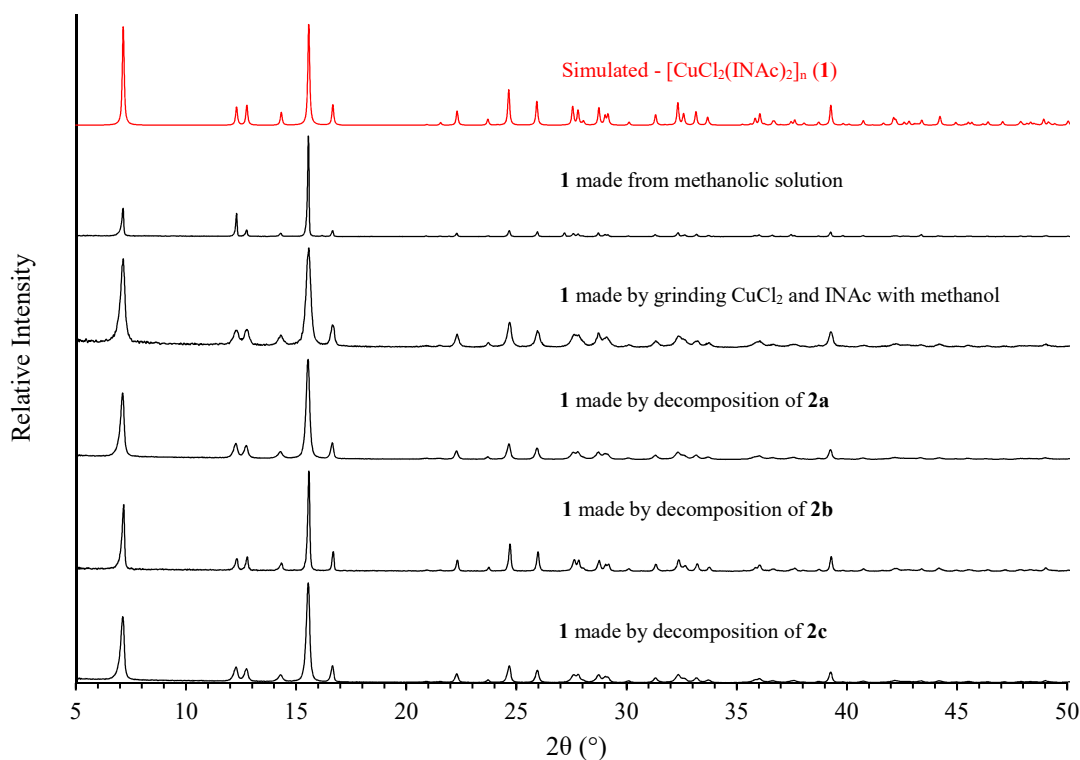


Figure 3.6 Room temperature X-ray powder diffraction data for samples of **1** made by solution and mechanochemical methods, and decomposition of the tetrachlorocuprate INAc salts (H-INAc)₂[CuCl₄]·2H₂O (**2a**), (H-INAc)₂[CuCl₄] (Form I) (**2b**) and (H-INAc)₂[CuCl₄] (Form II) (**2c**). Experimental data are shown in black while simulated data are shown in red.

Comparison of experimental powder X-ray diffraction data to that simulated from the structure confirms the purity and identification of the samples of **1** produced by the different methods of synthesis, as shown in Figure 3.6.

3.3.3 (H-INAc)₂[CuCl₄]·2H₂O (**2a**)

The structure of (H-INAc)₂[CuCl₄]·2H₂O (**2a**) has been described previously by Krishna Kumar *et al.*¹⁴⁶ The copper centre has square-planar coordination to four chloride ions, further information is contained in Table 3.6.

Table 3.6 Selected bond lengths (Å) and angles (°) around the Cu coordination centre for (H-INAc)₂[CuCl₄]·2H₂O (**2a**).¹⁴⁶

Cu(1) – Cl(1)	2.2363(19)	Cl(1)-Cu(1)-Cl(2)	89.45(5)
Cu(1) – Cl(2)	2.2663(19)		

Two water molecules and carboxylic acid groups produce an $R_4^4(8)$ ring motif on a centre of inversion. O-H and N-H moieties of water and H-INAc molecules respectively are each involved in two separate bifurcated $R_1^2(4)$ hydrogen bonding interactions through O-H \cdots Cl and N-H \cdots Cl contacts. Combination of these three ring motifs produces two distinct chain interactions, $C_4^4(20)$ and $C_4^4(12)$, which propagate along the $[3\bar{1}1]$ and $[\bar{1}11]$ crystallographic directions respectively, as depicted in Figure 3.7A. The overall effect is to produce 2-D hydrogen bonded sheets which stack in the $[\bar{1}\bar{1}1]$ direction, as shown in Figure 3.7B.

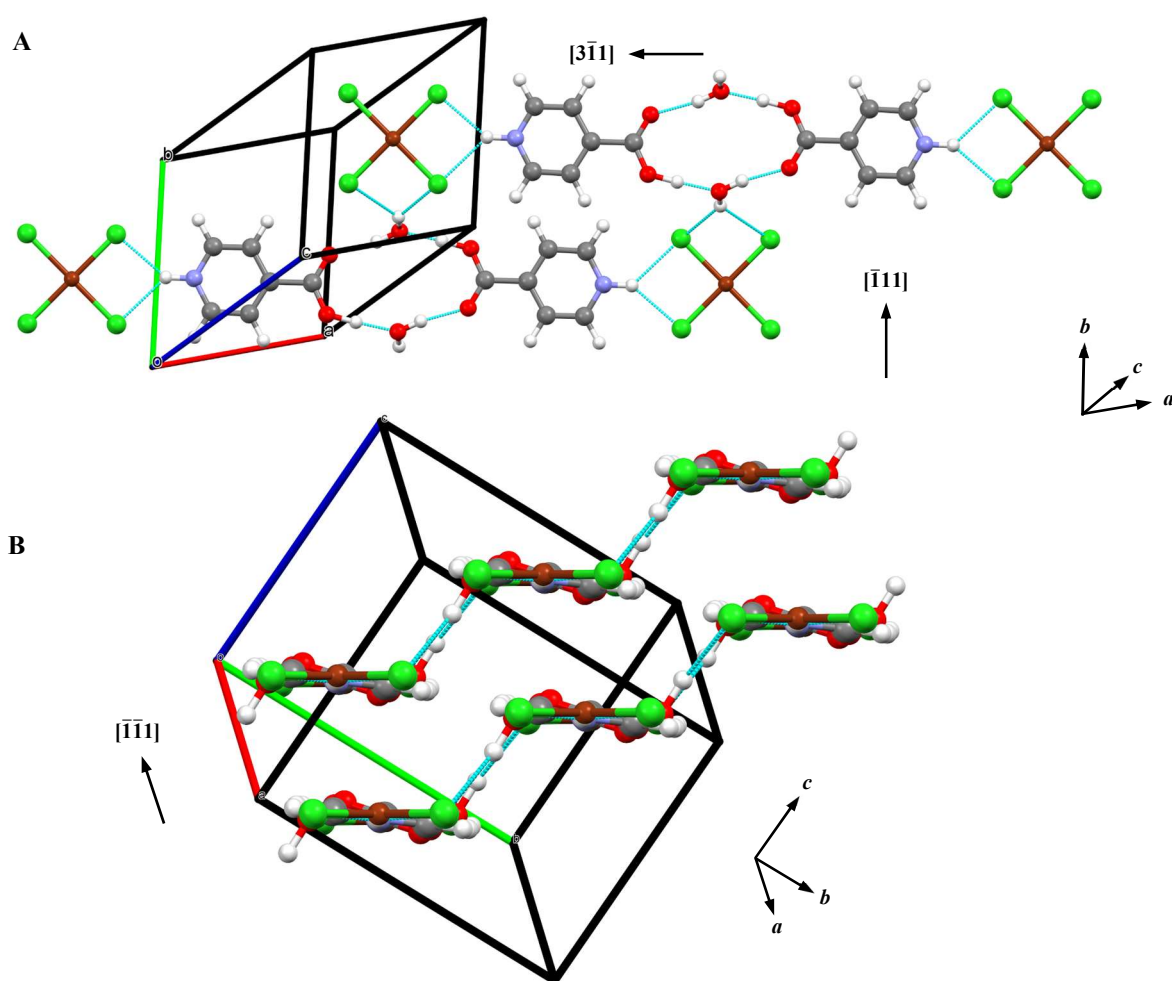


Figure 3.7 A view of the hydrogen bonded sheets in $(H-INAc)[CuCl_4] \cdot 2H_2O$ (**2a**) as viewed normal to the planar $[CuCl_4]^{2-}$ anions showing the $C_4^4(20)$ chain interactions that extend in the $[3\bar{1}1]$ direction, and the additional O-H \cdots Cl contacts which link them along the $[\bar{1}\bar{1}1]$ direction (A). The stacking arrangement of the sheets in the $[\bar{1}\bar{1}1]$ direction (B). C atoms are shown in grey, H in white, Cl in green, Cu in orange, N in blue, and O in red. Hydrogen bonds are drawn as light-blue dashed lines.¹⁴⁶

It is unexpected that Cu^{2+} adopts a square-planar geometry similar to the Pt^{2+} and Pd^{2+} analogues¹⁴⁴ as opposed to the more common 4+1 and 4+2 geometries. The geometry of Cu is most likely stabilised through strong hydrogen bonds which remove charge from the Cl^- ions reducing anion-anion repulsion, therefore allowing ligand field stabilisation energy to dictate the geometry of the Cu^{2+} ion; because of this stability, Cu forms no extra coordination bonds thus acting like Pt/Pd.

Comparison of experimental powder X-ray diffraction data to that simulated from the structure of **2a** confirms the purity and identification of the samples produced by the different methods of synthesis, as shown in Figure 3.8. The diffraction pattern of the sample produced from a dilute hydrochloric acid solution displays additional peaks which are not expected. This indicates that the sample is impure, but it has not been possible to identify this impurity. The data clearly show that synthesis of **2a** via solvent assisted mechanochemical methods produces a purer compound than that made from solution due to the absence of additional peaks.

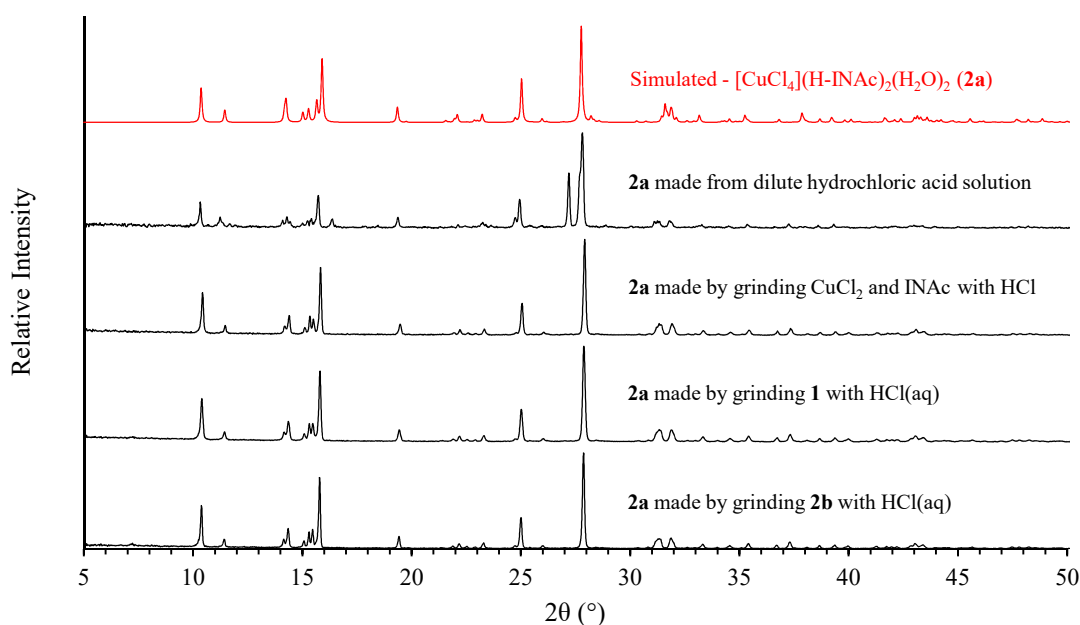


Figure 3.8. Room temperature X-ray powder diffraction data for samples of **2a** made using solution and mechanochemical methods. **1** is $[\text{CuCl}_2(\text{INAc})_2]_n$ and **2b** is $(\text{H-INAc})_2[\text{CuCl}_4]$ (Form I). Experimental data are shown in black while simulated data are shown in red.

3.3.4 (H-INAc)₂[CuCl₄] (Form I) (2b)

Although (H-INAc)₂[CuCl₄] (Form I) (**2b**) has a similar colour to **2a**, it displays a substantially different X-ray powder diffraction pattern. It was initially assumed that **2b** would be the anhydrous analogue of **2a** as a non-hydrated equivalent to the hydrated tetrachloroplatinate salt of INAc was known to exist.¹⁴⁴ This was confirmed by elemental analysis. It was not possible to create single-crystals of the compound, this therefore made it essential to attempt structure solution and refinement from X-ray powder diffraction data alone. The diffraction pattern of **2b** could be indexed with a monoclinic cell and space group *P*2₁/*c*, and volume equivalent to an asymmetric unit of one H-INAc molecule and half a [CuCl₄]²⁻ ion. The copper atom must therefore be on a centre of inversion and have a geometry with a centre of inversion, *e.g.* square-planar. *Ab initio* structure solution was performed with the global optimisation method employed in Endeavour using this simple structural model. An excellent fit to the observed data was obtained by Rietveld refinement of the crude model (*R*_{wp} = 0.0573), further crystallographic details are included in Table 3.4. An ORTEP plot of the asymmetric unit is shown in Figure 3.9, and a plot of the refinement is shown in Figure 3.10,

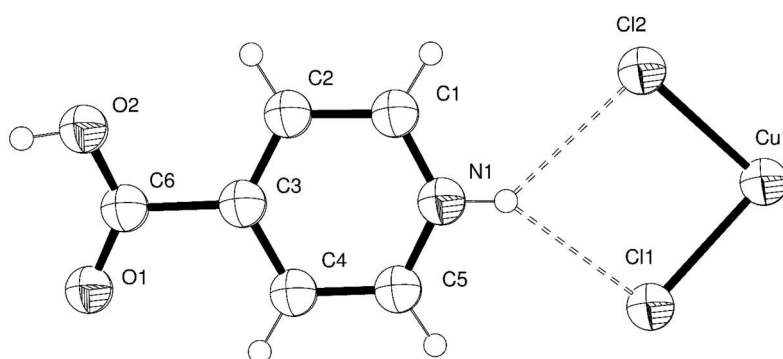


Figure 3.9 Asymmetric unit of (H-INAc)₂[CuCl₄] (Form I) (**2b**) with atoms shown as thermal ellipsoids drawn at 50% probability. Hydrogen bonds are drawn as dashed lines.

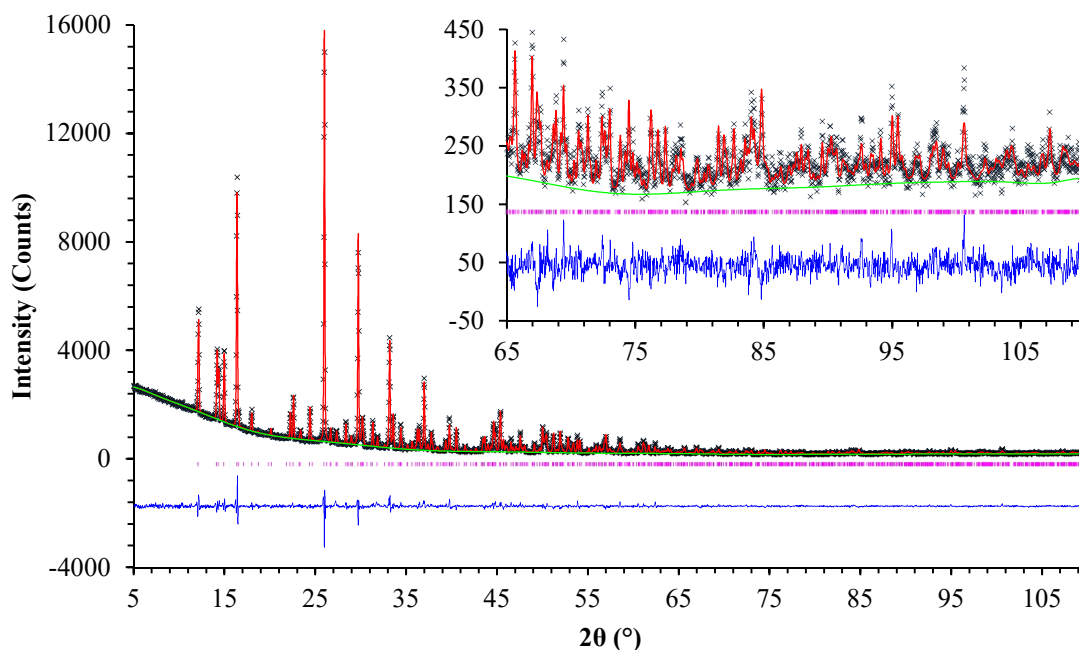


Figure 3.10 A plot of the Rietveld refinement of (H-INAc)₂[CuCl₄] (Form I) (**2b**). Black crosses represent observed data, the red line calculated data, the green line background, the pink markers peak positions, and the blue line is the difference plot [$I_{\text{obs}} - I_{\text{calc}}$]. The inset shows the portion of data between 65 and 110° 2 θ .

The pyridinium N-H group of INAc forms bifurcated hydrogen bonds to two Cl⁻ ions (N \cdots Cl 3.1808(2) Å and 3.1823(2) Å) of a [CuCl₄]²⁻ complex producing an R₁²(4) motif. Two O-H \cdots O hydrogen bonds (O \cdots O 2.6876(2) Å) between carboxylic acid groups form an R₂²(8) interaction. The two ring-shaped arrangements combine to produce a C₃³(18) chain which runs in the [102] direction, as shown in Figure 3.11. The chain motifs stack in such a way that long Cu-O bonds exist between each copper ion and the carboxylic acid groups directly above and below it in the [501] direction, meaning the Cu²⁺ ion is actually in a 4+2 coordination unlike in **2a**. Selected bond lengths and angles are shown in Table 3.7. A cursory search of the CSD shows that compounds containing Cu²⁺ in the coordination geometry found often appear green which backs up the findings.¹¹⁹

Table 3.7 Selected bond lengths (Å) and angles (°) around the Cu coordination centre for (H-INAc)₂[CuCl₄] (Form I) (**2b**).

Cu(1) – Cl(1)	2.2690(1)	O(1)#1-Cu(1)-Cl(1)	91.751(2)
Cu(1) – Cl(2)	2.2595(1)	O(1)#1-Cu(1)-Cl(2)	86.976(1)
Cu(1) – O(1)#1	3.0945(2)	Cl(1)-Cu(1)-Cl(2)	89.404(1)

#1 1 + x, y, 1 + z

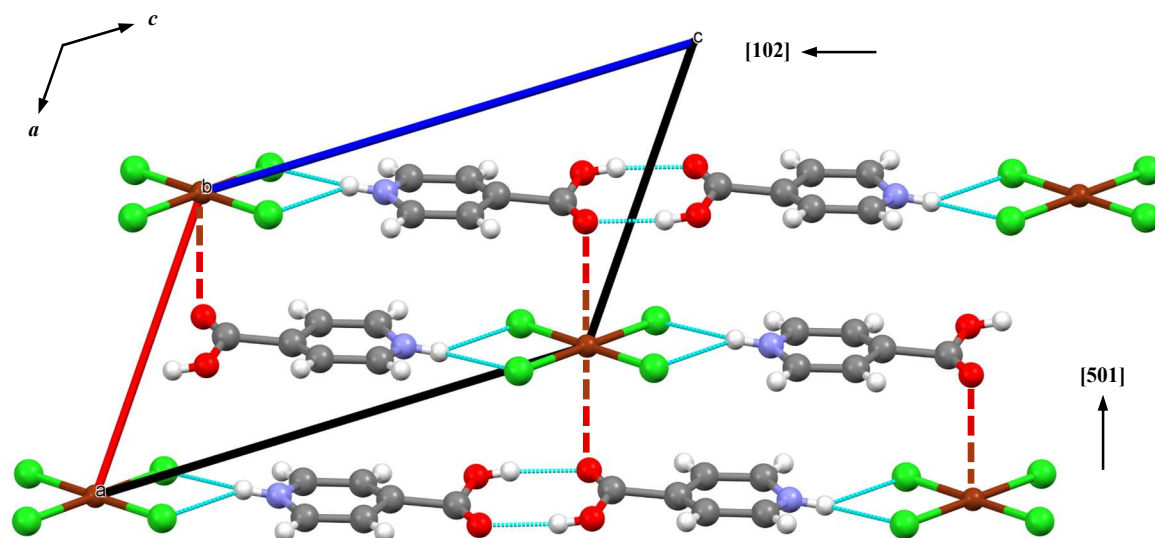


Figure 3.11. The C₃³(18) chain interactions in (H-INAc)₂[CuCl₄] (Form I) (**2b**) that extend in the [102] direction, and the stacking arrangement of the chains along the [501] direction to create long Cu-O bonds drawn as dashed lines. C atoms are shown in grey, H in white, Cl in green, Cu in dark brown, N in light grey-blue, and O in red. Hydrogen bonds are drawn as light-blue dashed lines.

The reason for the formation of the long Cu-O bonds is that the stabilisation of the square-planar geometry through hydrogen bonding is reduced relative to **2a** due to the absence of water. The Cu centre compensates for this loss by formation of long coordinate bonds. The non-hydrated [PtCl₄]²⁻ salt of INAc possesses very similar hydrogen bond interactions to that observed in **2b**, but because Pt is much more stable in a square-planar coordination geometry, no Pt-O bonds are formed and as a result the crystal packing is different.¹⁴⁴ The purity and identification of the sample produced by the solid-gas reaction of **1** with hydrochloric acid, is proven by comparison of the experimental X-ray powder diffraction data to that simulated from the structure of **2b**, as shown in Figure 3.12.

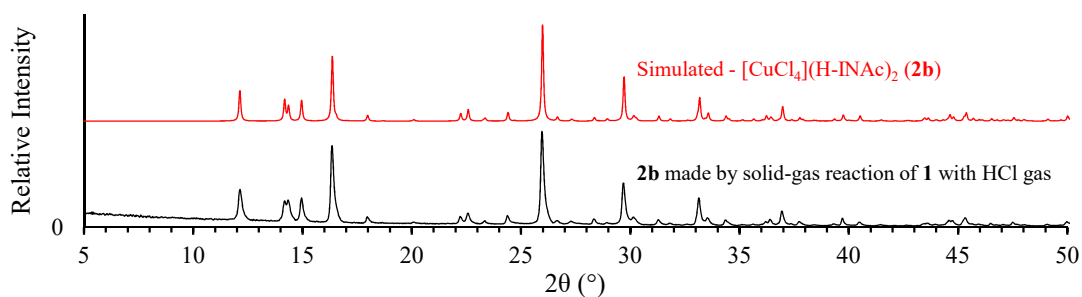


Figure 3.12. Room temperature X-ray powder diffraction data of **2b** made by solid-gas reaction of $[\text{CuCl}_2(\text{INAc})_2]_n$ (**1**) with HCl gas. Experimental data are shown in black while simulated data are shown in red.

3.3.5 $(\text{H-INAc})_2[\text{CuCl}_4]$ (Form II) (**2c**)

As mentioned previously, grinding of copper (II) chloride dihydrate with two equivalents of INAc.HCl should produce either **2a** or **2b**. However, after no changes in the colour of the sample, designated **2c**, were observed upon further grinding, an X-ray powder diffraction pattern was collected which does not match that expected for either compound, as shown in Figure 3.13. The final colour of the compound was bright green, similar to **2a** and **2b**.

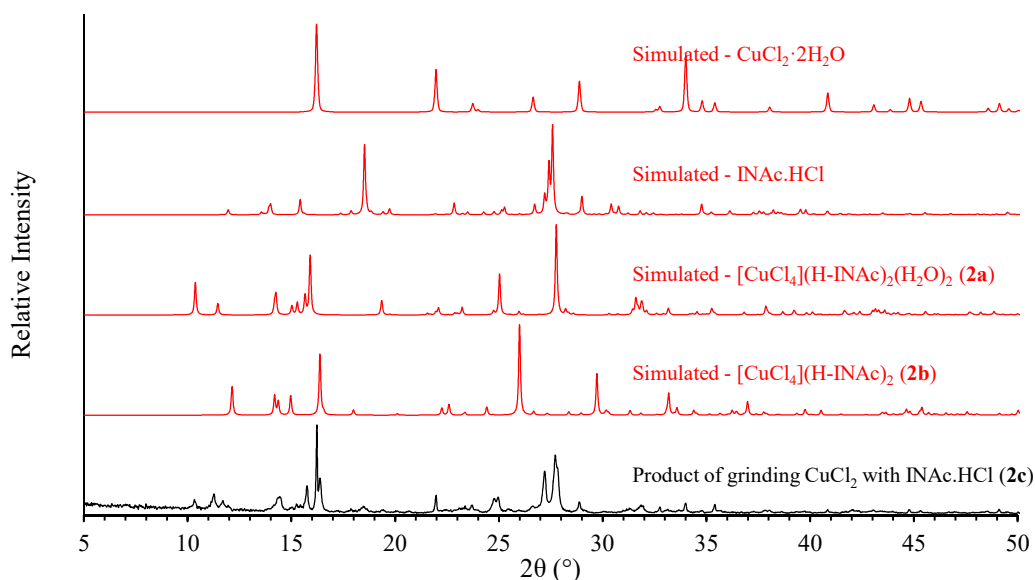


Figure 3.13. Room temperature X-ray powder diffraction data of the product made by mechanochemical reaction of copper chloride with INAc.HCl. Experimental data are shown in black while simulated data are shown in red.

Elemental analysis indicates the sample **2c** has a very similar composition to **2b** and the starting reagents. However, indexing of the sample was not possible so it can only be concluded that **2c** is most likely a polymorph of the anhydrous cuprate salt.

3.3.6 Infrared spectra

The infrared spectra of all four copper chloride coordination compounds of INAc, alongside spectra of pure INAc and INAc.HCl for comparison, are shown in Figure 3.14. **2a**, **2b**, and **2c** display very similar spectra with strong comparison to INAc.HCl, as expected, which further confirms their identification as pyridinium salts. The IR spectrum of **1** has distinct differences to these but is similar to that of pure INAc.

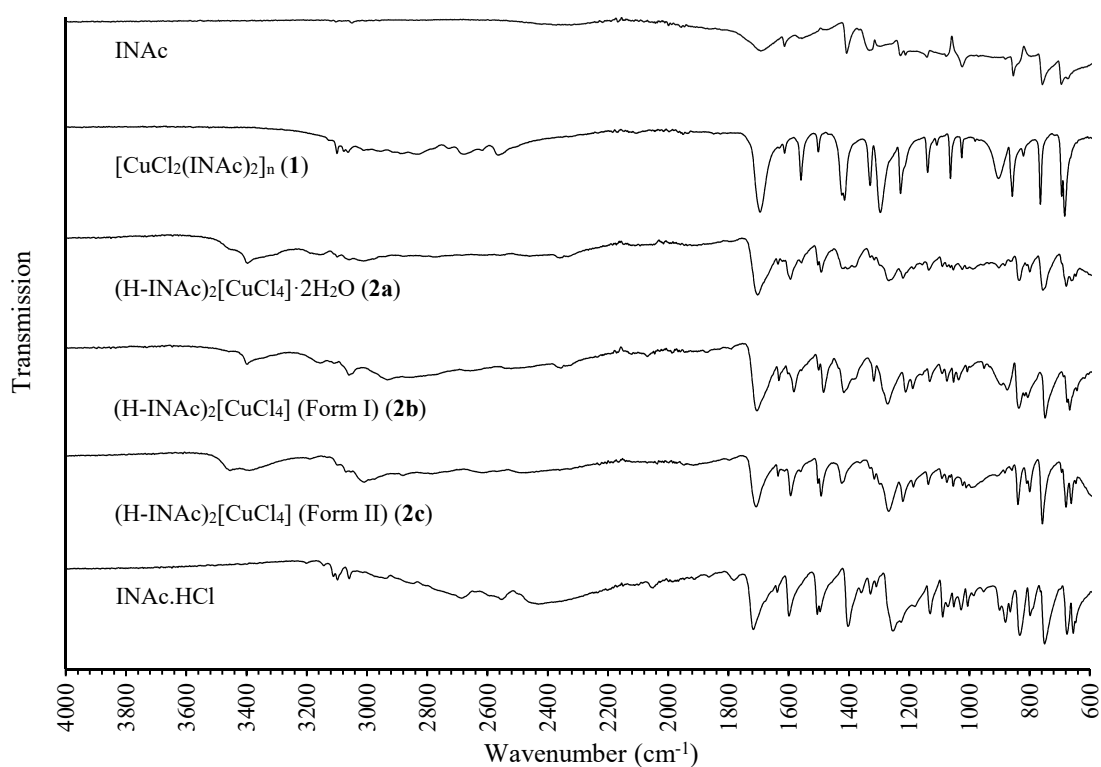


Figure 3.14. Infrared spectra for INAc, **1**, **2a**, **2b**, **2c**, and INAc.HCl.

3.4 Isonicotinamide (INAm)

3.4.1 Summary of reactions

Isonicotinamide (INAm) is an incredibly similar compound to INAc, the only difference being the exchange of a hydroxyl group for an amine. The extra hydrogen, although only a small change, can have a large effect on the hydrogen bonding arrangements of the compounds produced. It was therefore expected that the copper chloride-INAm system would be similar to that of INAc, but with some subtle differences. The reaction of INAm with copper chloride in methanol produced a blue powder, **3**, similar in appearance to **1**. Attempts to produce single-crystals of an adequate size for analysis failed, however structure solution and refinement using X-ray powder diffraction data showed that **3** was in fact $[\text{CuCl}_2(\text{INAm})_2]_n$, which has a very similar structure to **1**. Crystallisation of the same components used to make **3** from moderately concentrated hydrochloric acid (4M) produces green block crystals of $(\text{H-INAm})_2[\text{CuCl}_4]$ (Form I) (**4a**). Decomposition of **4a** to **3** occurs in approximately 3 days by loss of HCl. Reaction of **3** with HCl vapour at first produces an intermediate compound, **4b**, with a different X-ray diffraction pattern from **4a**, but produces pure **4a** after 6-7 days. In fact, the samples of **4a** made by solid-gas reaction are purer than that crystallised from hydrochloric acid. Although **4b** converts into **4a** in less than a week with exposure to HCl vapour, the process occurs naturally over 6-12 months. The structure of **4b** was determined from X-ray powder diffraction data and was shown to be a polymorph of **4a**, $(\text{H-INAm})_2[\text{CuCl}_4]$ (Form II). **4b** decomposes into **3** in a similar time to **4a**.

Mechanochemical synthesis of the three compounds was then attempted. Grinding of copper chloride and isonicotinamide with a few drops of methanol was found to produce pure samples of **3**. On the other hand, grinding of the same reagents, **3**, **4a**, or **4b**, with

several drops of concentrated hydrochloric acid, or copper chloride with INAm.HCl, produces another compound, **4c**, which could not be identified as any of the three previously discovered compounds. It was possible to index the powder X-ray diffraction pattern of **4c**, as shown by the good Pawley fit against experimental data later in this section. The unit-cell volume, elemental analysis, and comparison of the IR spectrum to **4a** and **4b** suggest that **4c** must be an additional polymorph of the tetrachlorocuprate isonicotinamide salt, *i.e.* (H-INAm)₂[CuCl₄] (Form III). However, the structure could not be determined due to the complexity of the structure, and the lack of the required computational power/time required to provide a structure solution. **4c** decomposes by loss of HCl to **3** in a similar time to **4a** and **4b**. A scheme displaying the above reactions is shown in Figure 3.15.

3.4.2 [CuCl₂(INAm)₂]_n (**3**)

As mentioned previously, [CuCl₂(INAm)₂] (**3**) could only be produced as a powder. Attempts to produce single-crystals of **3** from a dilute

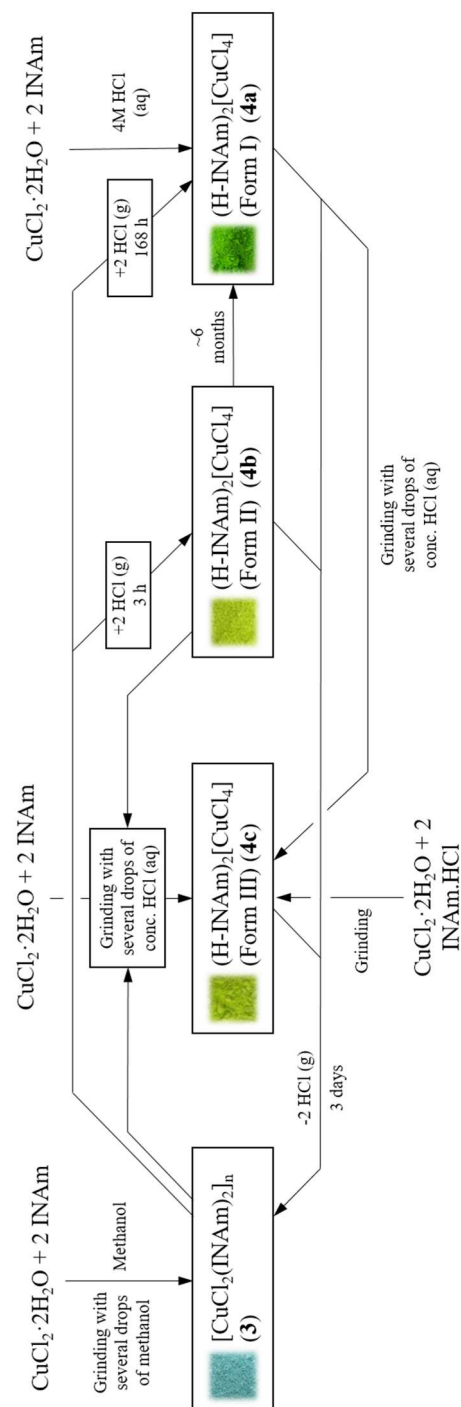


Figure 3.15. A reaction scheme for the synthesis and interconversion of copper chloride – isonicotinamide compounds.

hydrochloric acid solution and water were unsuccessful. Light blue crystals could be produced by diffusion of a methanolic solution of INAm into a propanolic solution of copper chloride, but these were too small for analysis. It was possible to index the powder X-ray diffraction pattern as belonging to a monoclinic cell of space group $C2/c$. The volume and symmetry of the unit-cell indicates **3** has a similar asymmetric unit to **1** but substituting INAc for INAm ($V = 1393.6(13) \text{ \AA}^3$, asymmetric unit has volume $174.2(2) \text{ \AA}^3$ compared with $168.1(2) \text{ \AA}^3$ for **1**). Structure solution with X-ray powder diffraction data using Endeavour was attempted by creating a molecule representing the asymmetric unit, fixing the Cu atom at the 4a Wyckoff position, and allowing rotation of the molecules around this point. Subsequent Rietveld refinement of the initial model against the observed diffraction data gave a good fit ($R_{wp} = 0.0975$), as shown in Figure 3.16, further crystallographic details are included in Table 3.4. An ORTEP plot of the asymmetric unit after refinement is shown in Figure 3.17.

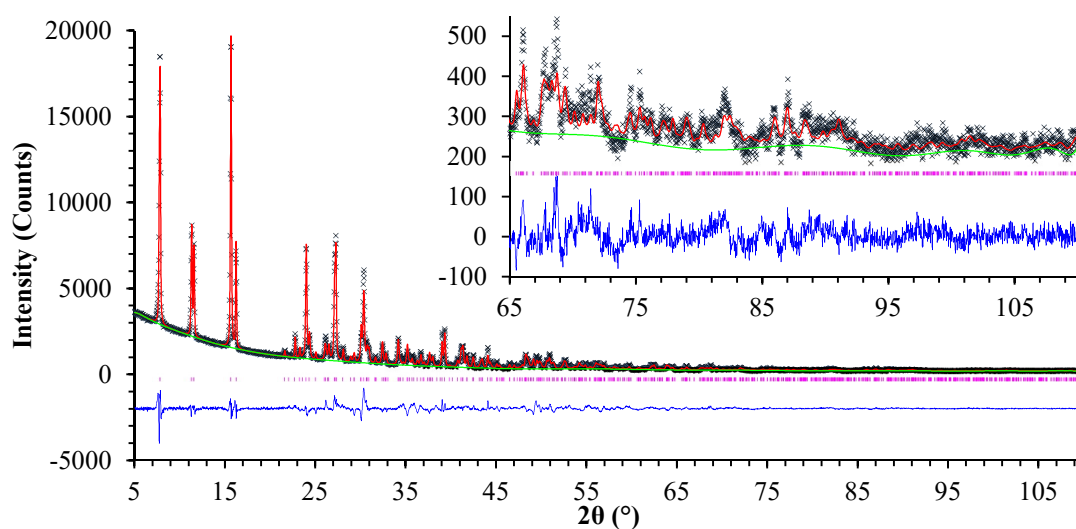


Figure 3.16 A plot of the Rietveld refinement of $[\text{CuCl}_2(\text{INAm})_2]$ (**3**). Black crosses represent observed data, the red line calculated data, the green line background, the pink markers peak positions, and the blue line is the difference plot $[(I_{\text{obs}} - I_{\text{calc}})]$. The inset shows the portion of data between 65 and $110^\circ 2\theta$.

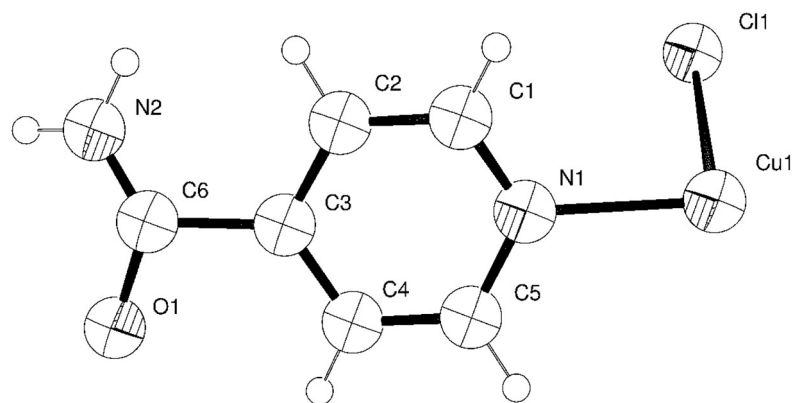


Figure 3.17 Asymmetric unit of $[\text{CuCl}_2(\text{INAm})_2]$ (**3**) with atoms shown as thermal ellipsoids drawn at 50% probability.

The structure of **3** is very similar to **1** with the Cu^{2+} ion displaying a similar 4+2 coordination geometry, bond distances and angles are shown in Table 3.8.

Table 3.8 Selected bond lengths (Å) and angles ($^\circ$) around the Cu coordination centre for $[\text{CuCl}_2(\text{INAm})_2]$ (**3**).

Cu(1) – Cl(1)	2.2842(5)	N(1)-Cu(1)-Cl(1)	91.386(7)
Cu(1) – Cl(1)#1	2.8980(6)	N(1)-Cu(1)-Cl(1)#1	90.734(5)
Cu(1) – N(1)	2.0306(19)	Cl(1)-Cu(1)-Cl(1)#1	92.326(3)

#1 x, 1 + y, z

The copper chloride polymeric chain extends along b , as seen in Figure 3.18A. The INAm molecules which decorate the chain produce an $R_2^2(8)$ interaction composed of two N-H \cdots O contacts (N \cdots O 2.9943(8) Å) between amide groups related by a centre of inversion. As shown in Figure 3.18B, this forms part of a $C_1^1(14)$ chain, via coordination to Cu^{2+} , running in the $[221]$ direction. Additionally, N-H \cdots Cl interactions (N \cdots Cl 3.3125(9) Å) between amide groups and adjacent Cl^- ions bridged by Cu^{2+} combine with the $R_2^2(8)$ ring motif to produce a $C_3^2(10)$ interaction along a . Thus **3** contains sheets in the xz plane sustained by coordination bonds and hydrogen bonds; perpendicular to these sheets are the CuCl_2 polymers, hence **3** contains a supramolecular 3-D network. The

structure of **3** is very similar to that of $[\text{CoCl}_2(\text{INAm})_2]_n$ except the Co^{2+} ion is in a non-distorted octahedral coordination geometry.¹⁵¹ A pseudohalide analogue of **3** exists, $[\text{Ni}(\text{SCN})_2(\text{INAm})_2]_n$, which contains voids filled with aromatic guest molecules due to poor packing efficiency as a result of the alternate orientations of the INAm molecules along the $\text{Ni}(\text{SCN})_2$ chain.¹⁵² Like **1**, **3** is very densely arranged so it cannot accommodate guest molecules.

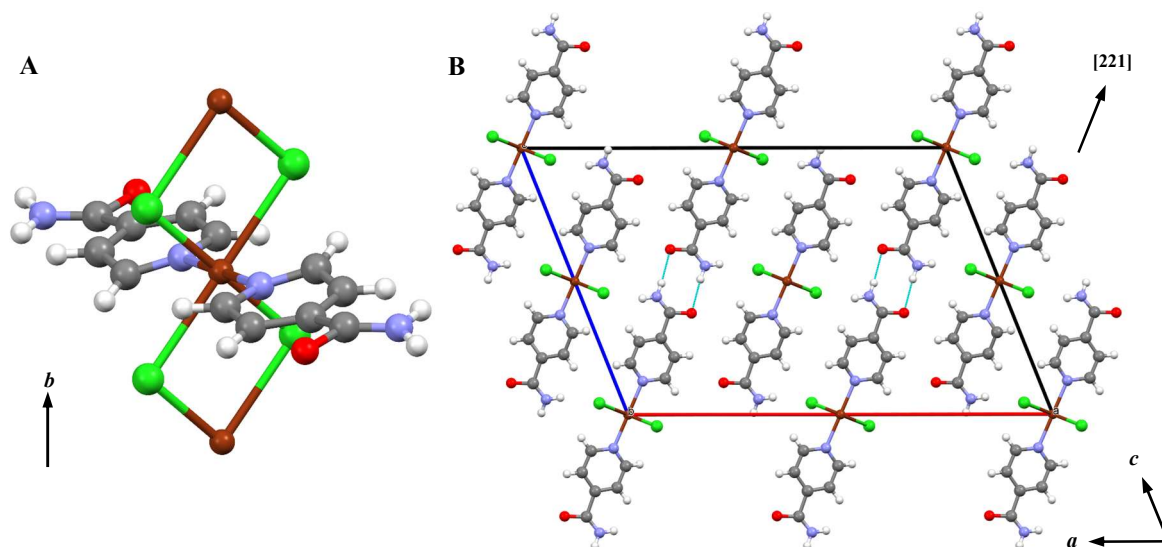


Figure 3.18 The copper chloride chain displayed in $[\text{CuCl}_2(\text{INAm})_2]_n$ (**3**) extending along the b axis (A), and the crystal packing of **3** showing the $\text{N-H}\cdots\text{Cl}$ and $\text{N-H}\cdots\text{O}$ contacts, producing the ring type hydrogen bonding arrangement and the two chain interactions that propagate along a and in the $[221]$ direction (B). C atoms are shown in grey, H in white, Cl in green, Cu in dark brown, N in light grey-blue, and O in red. Hydrogen bonds are drawn as light-blue dashed lines.

Comparison of experimental powder X-ray diffraction data to that simulated from the structure of **3** confirms the purity and identification of the samples produced by the different methods of synthesis, as shown in Figure 3.19. Additionally, elemental analysis of a representative sample of **3** also proves purity.

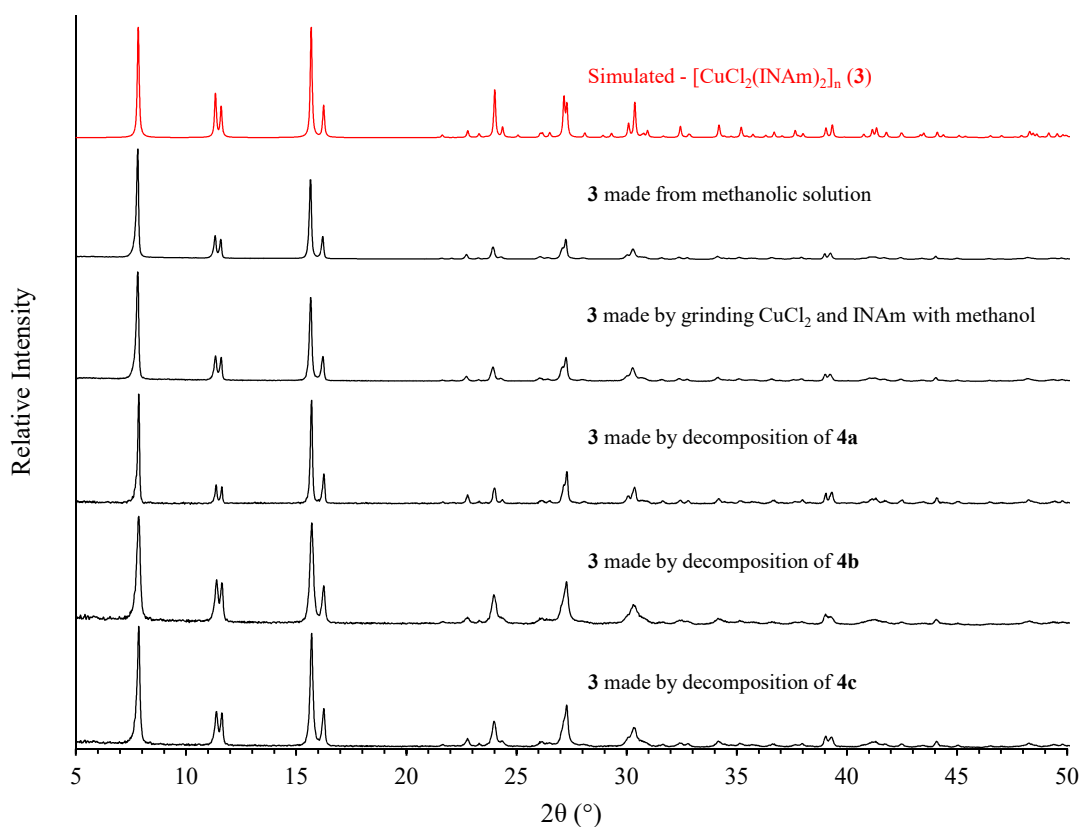


Figure 3.19 Room temperature X-ray powder diffraction data for samples of **3** made using solution and mechanochemical methods, and decomposition of the tetrachlorocuprate INAm salts (H-INAm)₂[CuCl₄] (Form I) (**4a**), (H-INAm)₂[CuCl₄] (Form II) (**4b**), and (H-INAm)₂[CuCl₄] (Form III) (**4c**). Experimental data are shown in black while simulated data are shown in red.

3.4.3 (H-INAm)₂[CuCl₄] (Form I) (**4a**)

Green crystals of (H-INAm)₂[CuCl₄] (Form I) (**4a**) were analysed by single-crystal X-ray diffraction, further crystallographic details are included in Table 3.2. **4a** adopts a triclinic cell with space group $P\bar{1}$ and has a very similar structure to **2b**. The asymmetric unit contains one protonated isonicotinamide molecule and a Cu²⁺ ion centred on the 1a Wyckoff position surrounded by four chloride ions and two oxygen atoms in a 4+2 geometry, as shown in Figure 3.20. Bond distance and angles around the Cu coordination centre are shown in Table 3.9.

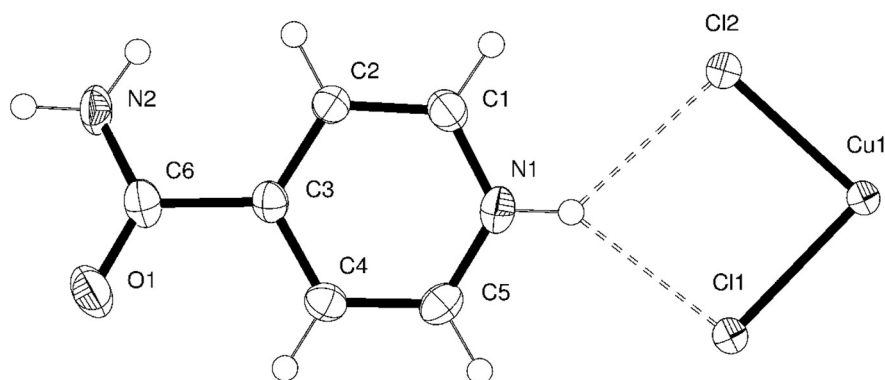


Figure 3.20 Asymmetric unit of (H-INAm)₂[CuCl₄] (Form I) (**4a**) with atoms shown as thermal ellipsoids drawn at 50% probability. Hydrogen bonds are drawn as dashed lines.

Table 3.9 Selected bond lengths (Å) and angles (°) around the Cu coordination centre for (H-INAm)₂[CuCl₄] (Form I) (**4a**).

Cu(1) – Cl(1)	2.2960(10)	O(1)#1-Cu(1)-Cl(1)	90.87(8)
Cu(1) – Cl(2)	2.2622(11)	O(1)#1-Cu(1)-Cl(2)	88.89(8)
Cu(1) – O(1)#1	2.986(5)	Cl(1)-Cu(1)-Cl(2)	89.60(4)

#1 x, 1 + y, z – 1

The pyridinium group of H-INAm forms bifurcated hydrogen bonds to two chloride ions ($N \cdots Cl$ 3.1690(5) Å and 3.1913(5) Å) of a $[CuCl_4]^{2-}$ ion producing an $R_1^2(4)$ motif, while the amide groups form an $R_2^2(8)$ interaction, as seen before ($N \cdots O$ 2.8463(5) Å). The two ring interactions produce a $C_3^3(18)$ chain which runs in the $[\bar{1}2\bar{2}]$ direction, shown in Figure 3.21A. An extra hydrogen bond is observed between amine groups and chloride ions ($N \cdots Cl$ 3.4236(6) Å) which in combination with the $C_3^3(18)$ interaction forms hydrogen bonded sheets which are parallel to the (212) crystallographic plane. As seen in Figure 3.21B, the 4+2 coordination is produced in a similar way to that in **2a**: the long Cu-O bonds occur between the carboxyl moiety of the amide groups occurring above and below each copper centre along the $[3\bar{1}1]$ direction.

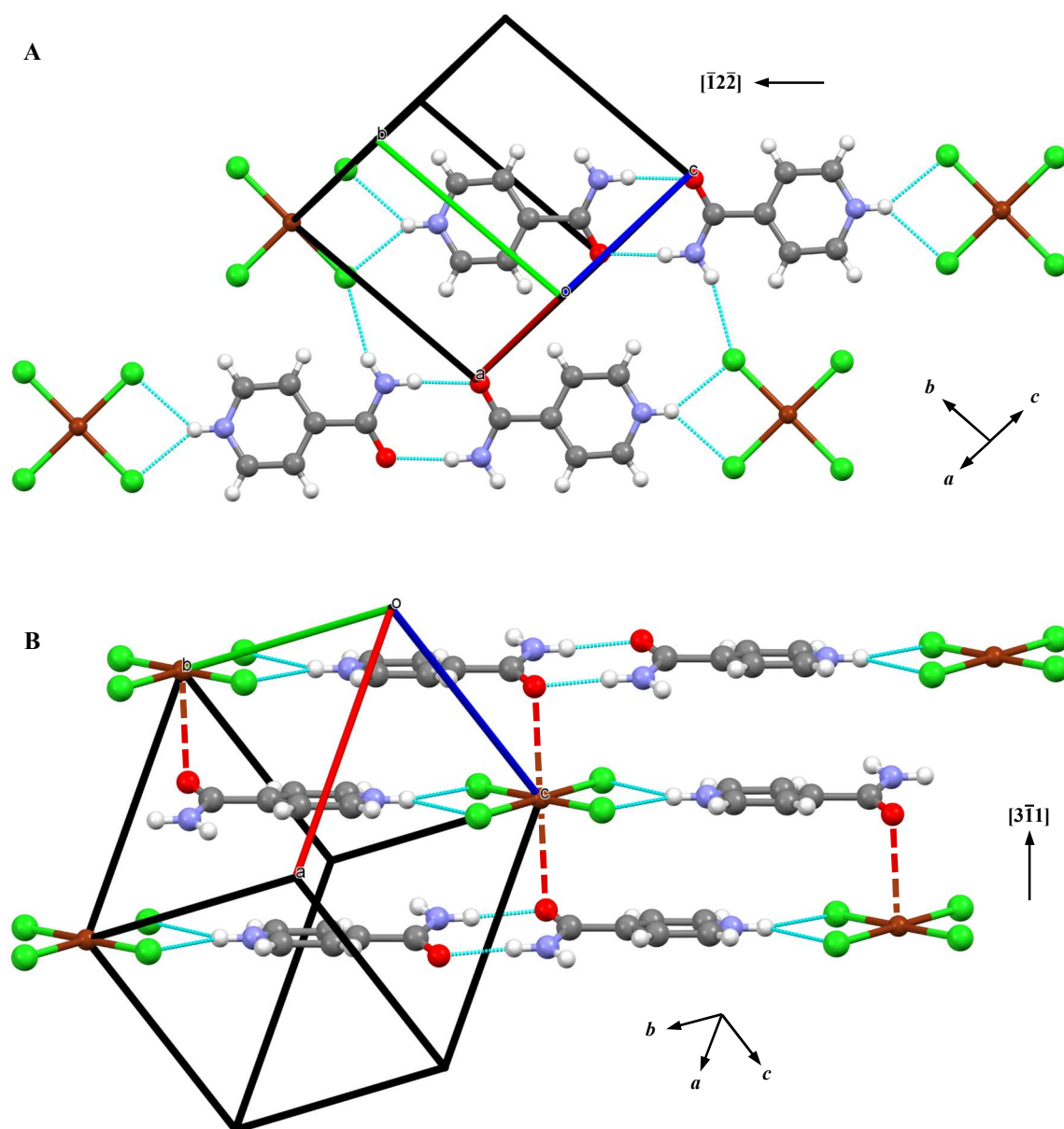


Figure 3.21. A view of the hydrogen bonded sheets in $(\text{H-INAm})_2[\text{CuCl}_4]$ (Form I) (**4a**) as viewed normal to the plane showing the $\text{C}_3^3(18)$ chain interactions that extend in the $[\bar{1}\bar{2}\bar{2}]$ direction, and the additional $\text{N-H}\cdots\text{Cl}$ contacts which link them (A). The stacking arrangement of the sheets in the $[3\bar{1}\bar{1}]$ direction to create long Cu-O bonds drawn as dashed lines (B). C atoms are shown in grey, H in white, Cl in green, Cu in dark brown, N in light grey-blue, and O in red. Hydrogen bonds are drawn as light-blue dashed lines.

Figure 3.22 shows a comparison of experimental and simulated powder X-ray diffraction data for samples of **4a**. The diffraction pattern of the sample produced by solution crystallisation displays additional peaks, and a pattern with peaks not of the same relative

intensities as those expected. This indicates that the sample is both impure and has a preferred orientation (which increases the intensity of select peaks over others) despite extensive grinding of the single-crystals. It is clear that synthesis of **4a** via solid-gas reaction produces a purer compound than that made from solution, and, due to lack of single-crystal production by the method, does not suffer from preferred orientation of crystals thus providing a much better comparison to the simulated data. The purity of **4a** is also demonstrated by elemental analysis of a representative sample.

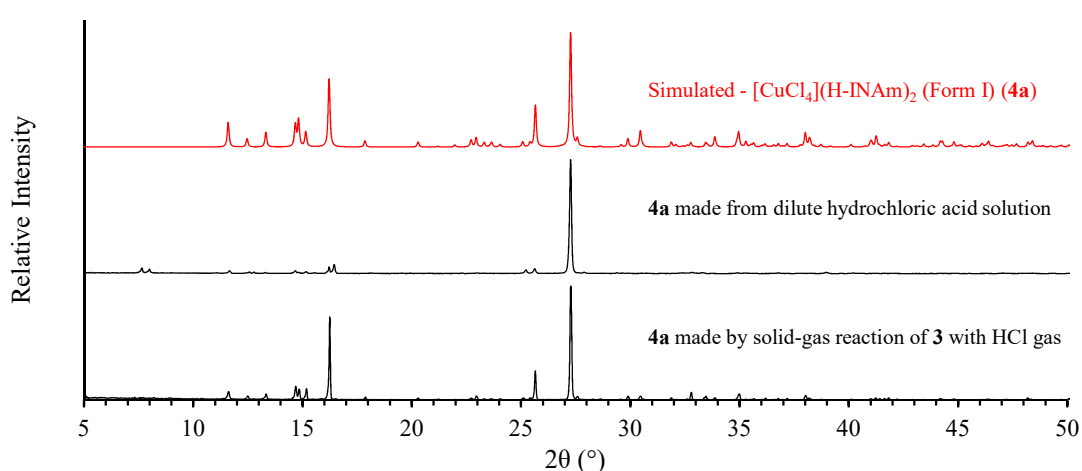


Figure 3.22. Room temperature X-ray powder diffraction data of $(\text{H-INAm})_2[\text{CuCl}_4]$ (Form I) (**4a**) made by the solution method and solid-gas reaction of $[\text{CuCl}_2(\text{INAm})_2]_n$ (**3**) with HCl gas. Experimental data are shown in black while simulated data are shown in red.

3.4.4 $(\text{H-INAm})_2[\text{CuCl}_4]$ (Form II) (**4b**)

Due to the synthetic technique required to make $(\text{H-INAm})_2[\text{CuCl}_4]$ (Form II) (**4b**), only polycrystalline samples were available for structural analysis. The structure of **4b** was therefore determined from powder diffraction data in a similar way to **2b**; the good fit observed following Rietveld refinement ($R_{\text{wp}} = 0.0497$) demonstrates the validity of the model, as shown in Figure 3.23, further crystallographic details are included in Table 3.4.

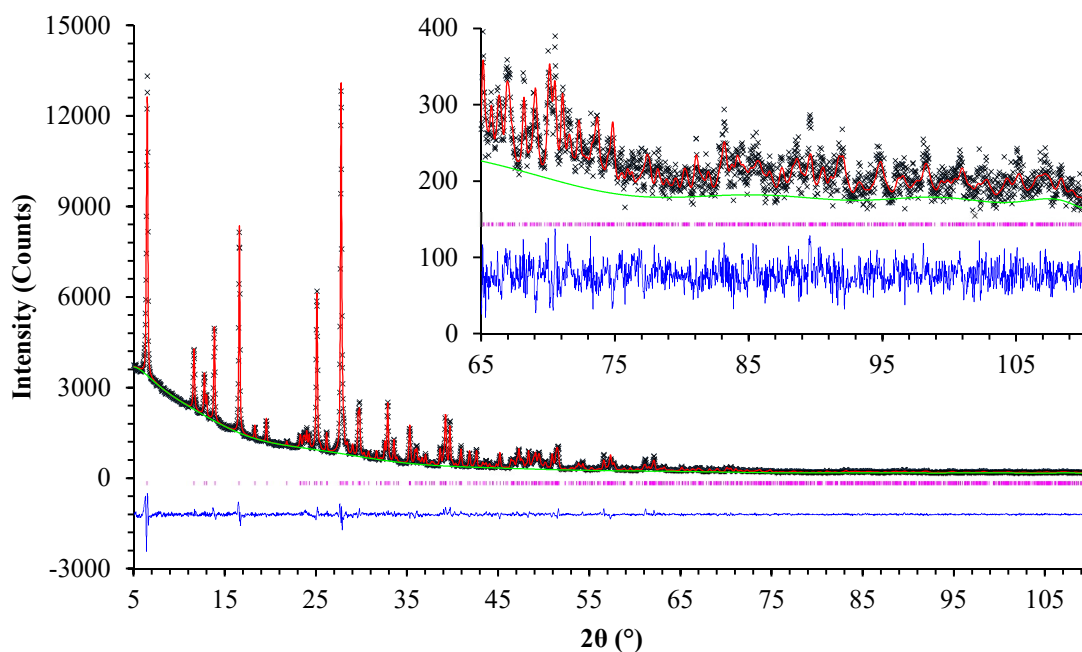


Figure 3.23 A plot of the Rietveld refinement of $(\text{H-INAm})_2[\text{CuCl}_4]$ (Form II) (**4b**). Black crosses represent observed data, the red line calculated data, the green line background, the pink markers peak positions, and the blue line is the difference plot $[(I_{\text{obs}} - I_{\text{calc}})]$. The inset shows the portion of data between 65 and 110° 2θ .

4b, like **4a**, adopts a triclinic cell with space group $P\bar{1}$ and an almost identical asymmetric unit to that of **4a** with the copper ion on an inversion centre but with the elongated Cu-O bonds replaced with Cu-Cl bonds, as shown in Figure 3.24 and Table 3.10.

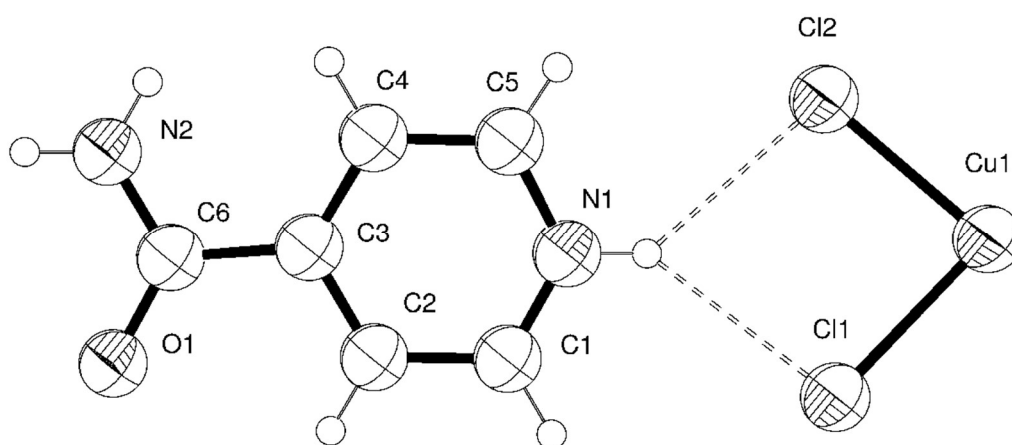


Figure 3.24 Asymmetric unit of $(\text{H-INAm})_2[\text{CuCl}_4]$ (Form II) (**4b**) with atoms shown as thermal ellipsoids drawn at 50% probability. Hydrogen bonds are drawn as dashed lines.

Table 3.10 Selected bond lengths (Å) and angles (°) around the Cu coordination centre for (H-INAm)₂[CuCl₄] (Form II) (**4b**).

Cu(1) – Cl(1)	2.2955(3)	Cl(1)-Cu(1)-Cl(2)	88.050(3)
Cu(1) – Cl(2)	2.2501(3)	Cl(1)-Cu(1)-Cl(2)#1	88.842(2)
Cu(1) – Cl(2)#1	3.2068(4)	Cl(2)-Cu(1)-Cl(2)#1	90.006(2)

#1 1 + x, y, z

The hydrogen bonding arrangement in **4b** is very similar to that in **4a**. The H-INAm pyridinium group forms a similar R₁²(4) motif through two N-H···Cl hydrogen bonds (N···Cl 3.1537(4) Å and 3.1825(3) Å) and the common R₂²(8) interaction composed of two amide groups is also present (N···O 2.8919(3) Å), although the C₃³(18) chains produced by these two components run in the [1̄21] direction, as shown in Figure 3.25A.

The hydrogen bonded sheets created by the chain interactions and additional N-H···Cl contacts between amine moieties and Cl⁻ ions (N···Cl 3.3155(4) Å) are parallel to the (11̄1) plane; the chains which make up these sheets are slightly offset from each other compared to **4a**. The sheets stack in **4b** so that long Cu-Cl bonds form between the chloride ions above and below the Cu centre in the [310] direction, as seen in Figure 3.25B. The exchange of a long Cu-O bond in **4a** with a Cu-Cl bond in **4b** is solely due to the difference in how the sheets stack. It is highly probable that the rearrangement of **4b** to **4a** occurs by the cleavage of the long Cu-Cl interaction, shifting of alternate sheets past each other such that the arrangement of matches that found in **5a**, then formation of long Cu-O bonds. The most likely movement in this rearrangement is the one with the shortest pathway which would be a shift of approximately 3.4 Å of alternate sheets in the [101] direction, with every other sheet moving a similar distance in the opposite direction.

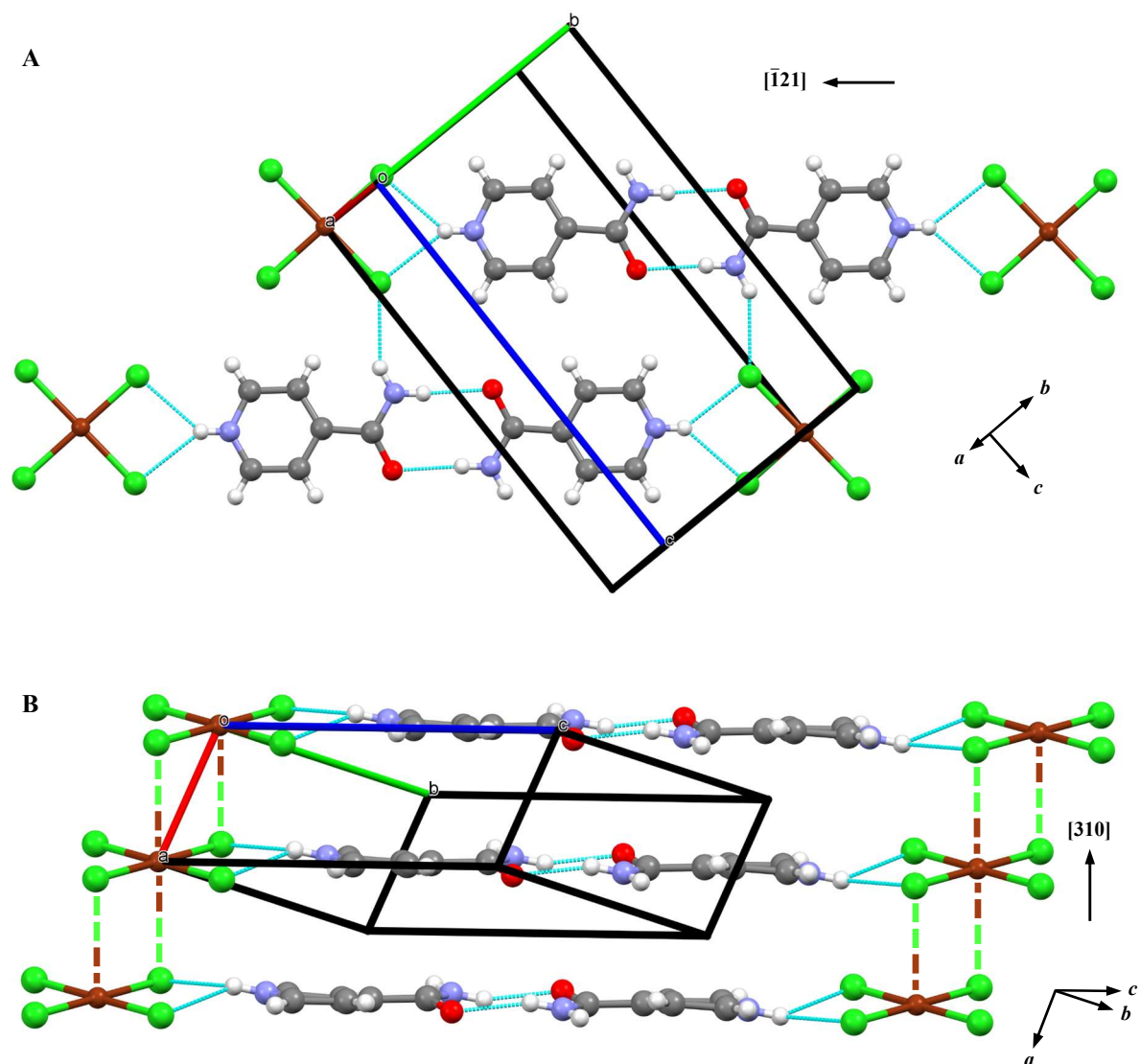


Figure 3.25. A view of the hydrogen bonded sheets in (H-INAm)₂[CuCl₄] (Form II) (**4b**) as viewed normal to the plane showing the C₃(18) chain interactions that extend in the $[\bar{1}21]$ direction, and the additional N-H...Cl contacts that link them (A). The stacking arrangement of the sheets in the $[310]$ direction that produce a copper halide polymer that extends along *a* by formation of long Cu-Cl bonds drawn as dashed lines (B). C atoms are shown in grey, H in white, Cl in green, Cu in dark brown, N in light grey-blue, and O in red. Hydrogen bonds are drawn as light-blue dashed lines.

A comparison of the experimental and simulated X-ray powder diffraction data of **4b** is shown in Figure 3.26, this proves the crystalline purity of the product produced by solid-gas reaction of **3** with HCl. The purity is further confirmed by elemental analysis.

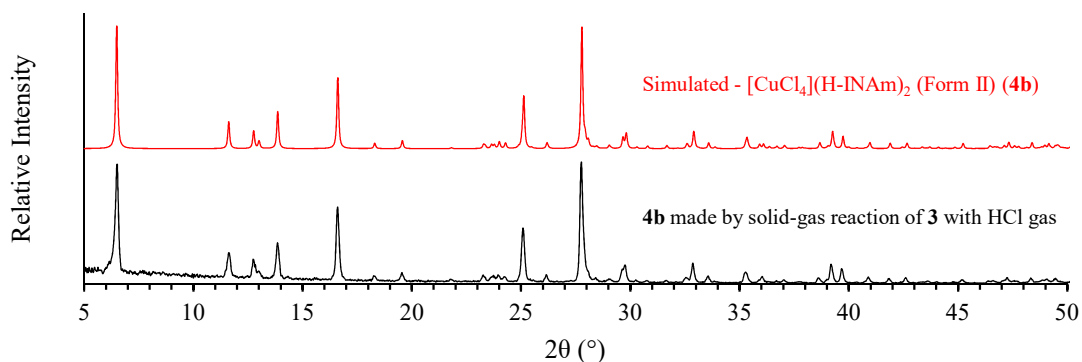


Figure 3.26. Room temperature X-ray powder diffraction data of **4b** made by solid-gas reaction of $[\text{CuCl}_2(\text{INAm})_2]_n$ (**3**) with HCl gas. Experimental data are shown in black while simulated data are shown in red.

3.4.5 $(\text{H-INAm})_2[\text{CuCl}_4]$ (Form III) (**4c**)

As mentioned in the introduction of this section, the mechanochemical reaction of all the isonicotinamide-copper chloride products and starting reagents with several drops of hydrochloric acid produces a product, **4c**, which cannot be identified as **4a** or **4b** by X-ray powder diffraction. A comparison of simulated data for structures **4a** and **4b** to the experimental data for various samples of **4c** produced by different methods is shown in Figure 3.27. There is an excellent agreement in the relative intensities and positions of the diffraction peaks observed for the different powder samples indicating that they must be pure.

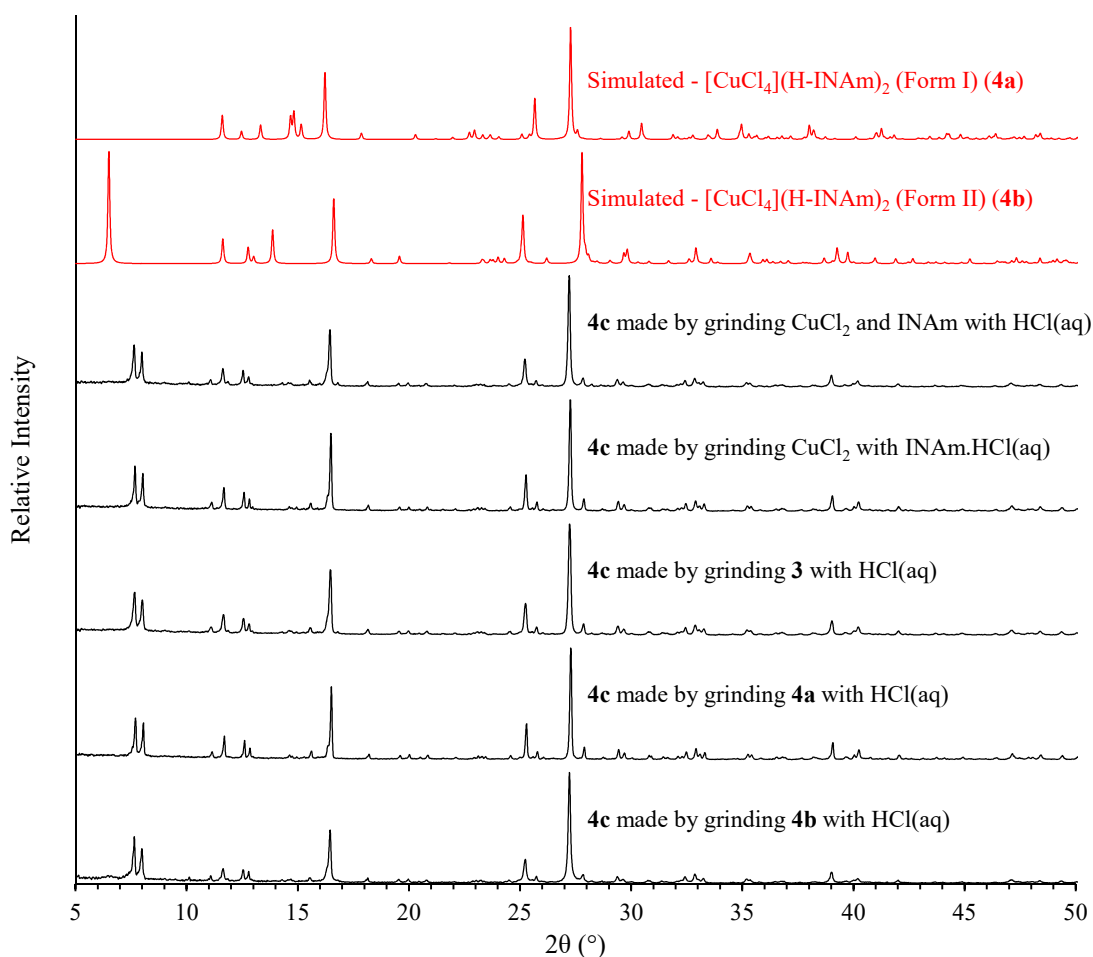


Figure 3.27. Room temperature X-ray powder diffraction data for samples of **4c** made by mechanochemical reaction of copper chloride with INAm.HCl, or copper chloride and INAm, $[\text{CuCl}_2(\text{INAm})_2]_n$ (**3**), $(\text{H-INAm})_2[\text{CuCl}_4]$ (Form I) (**4a**), or $(\text{H-INAm})_2[\text{CuCl}_4]$ (Form II) (**4b**), with HCl(aq). Experimental data are shown in black while simulated data are shown in red.

The sample produced by grinding $\text{CuCl}_2 \cdot 2\text{H}_2\text{O}$ and INAm with concentrated HCl was used for indexing. This was successful and a Pawley refinement was conducted using the candidate cell producing a good fit to the observed data ($R_{\text{wp}} = 0.0833$, $\chi^2 = 1.605$), as shown in Figure 3.28. The unit-cell was determined to be triclinic with cell parameters $a = 9.12(2) \text{ \AA}$, $b = 12.34(3) \text{ \AA}$, $c = 12.42(3) \text{ \AA}$, $\alpha = 68.92(1)^\circ$, $\beta = 82.21(1)^\circ$, $\gamma = 72.37(1)^\circ$, $V = 1243(5) \text{ \AA}^3$. The cell volume, elemental analysis, and infrared spectrum are commensurate with the sample **4c** being another tetrachlorocuprate isonicotinamide salt polymorph, $(\text{H-INAm})_2[\text{CuCl}_4]$ (Form III).

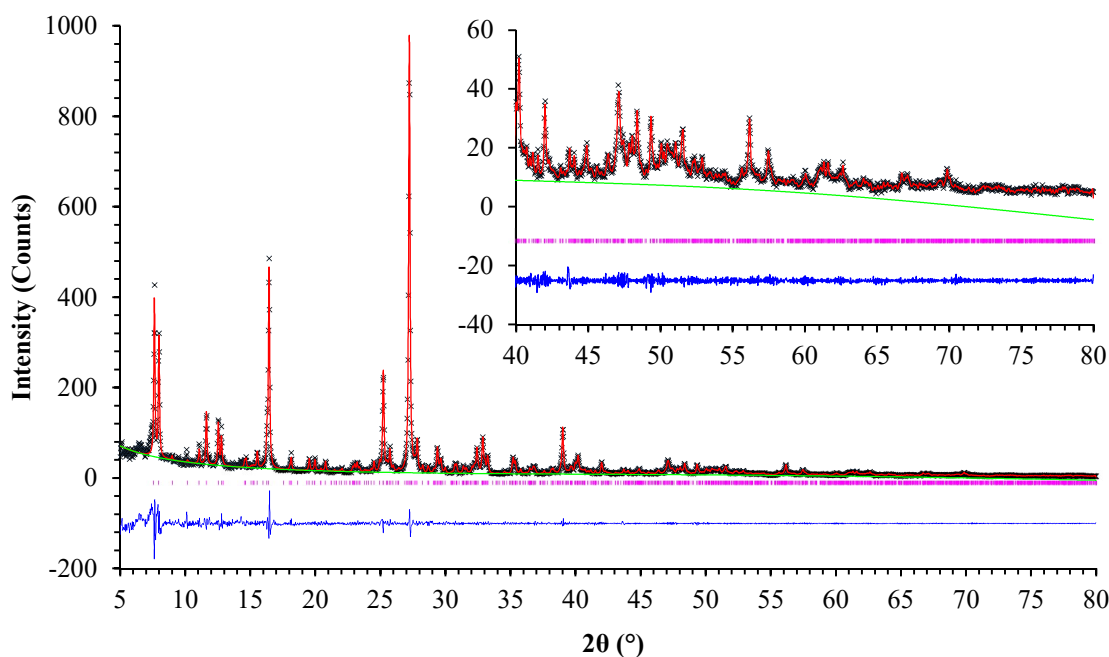


Figure 3.28. A plot of the Pawley refinement of the proposed cell for $(\text{H-INAm})_2[\text{CuCl}_4]$ (Form III) (**4c**). Black crosses represent observed data, the red line calculated data, the green line background, the pink markers peak positions, and the blue line is the difference plot $[(I_{\text{obs}} - I_{\text{calc}})]$.

The unit-cell volume of **4c** is approximately triple that of **4a** and **4b**, which are 1243(5) Å³, 406.10(11) Å³, and 407.27(17) Å³ respectively. Assuming the unit-cell is centrosymmetric, this equates to one and a half CuCl_4 units and three molecules of INAm (the asymmetric unit of **4a** and **4b** multiplied by three). In the case of the other structures determined solely from powder diffraction data, certain assumptions can be made based on the unit-cell parameters, *e.g.* fixing the position of the Cu^{2+} ions to centres of symmetry. However, this still required a certain amount of trial and error to determine the model was correct, *e.g.* trialling cuprate ions of different geometries to be certain the correct one was chosen. This example is much more complicated as it is not certain whether the unit-cell is centrosymmetric or not, whether the two cuprate ions have the same geometry or whether they are positioned on centres of inversion or not, and the number of molecules dramatically increasing the calculation time, among other factors. The attempts to provide a solution have so far been unsuccessful, although these attempts

have been based on the assumption that the unit-cell is correct, which, despite producing a good Pawley fit to the observed data, might not be true. However, if the unit-cell is correct, the problem simply requires more computational time and potentially better-quality data to solve.

3.4.6 Infrared spectra

A comparison of the infrared spectra of INAm, INAm.HCl, and all four copper chloride coordination compounds of INAm are shown in Figure 3.29. As expected, the spectrum of INAm.HCl has a good match with **4a**, **4b**, and **4c**, especially in the region of 1800-1000 cm^{-1} . Whereas the spectra of INAm and **3** are somewhat different and provide much better comparison to each other only. These observations offer further confirmation of the validity of the determined structures.

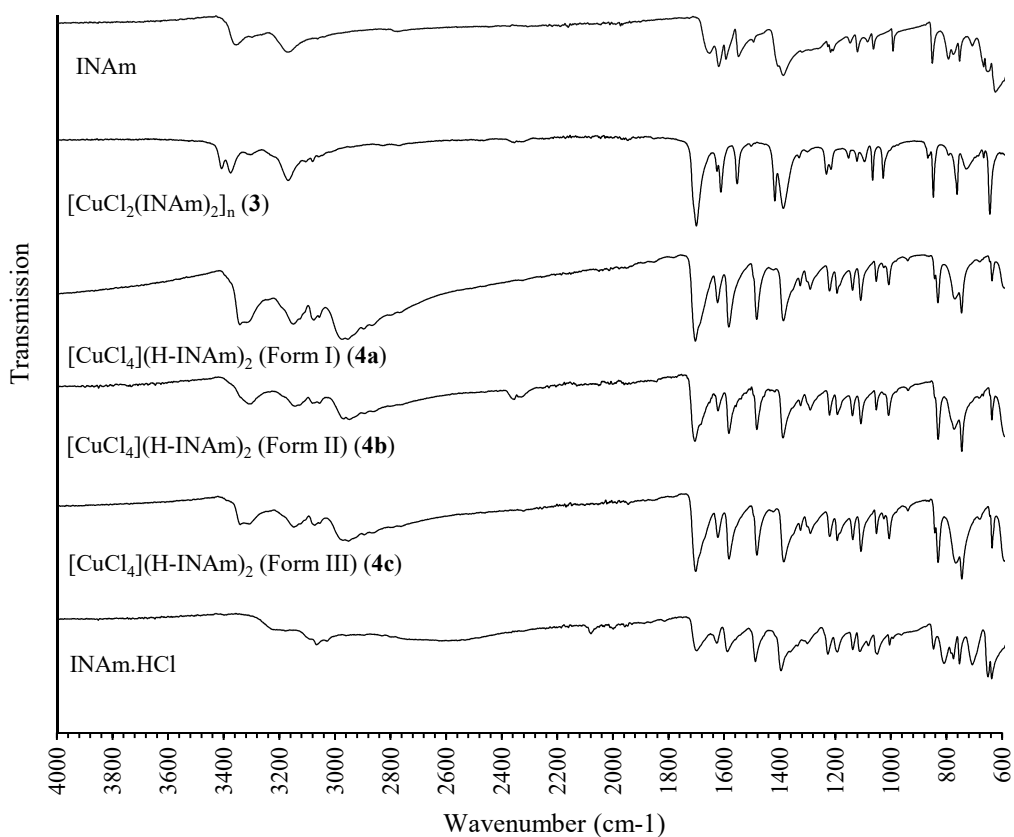


Figure 3.29. Infrared spectra for INAm, **3**, **4a**, **4b**, **4c**, and INAm.HCl.

3.5 Nicotinamide (NAm)

3.5.1 Summary of reactions

Unlike INAc and INAm which are 4-substituted pyridines, nicotinamide (NAm) is substituted in the 3 position. While the functional groups of NAm and INAm are identical, this difference in the substitution position often leads to different observed hydrogen bonding interactions. As such, it was expected that the chemistry of NAm would be distinct from that of INAc and INAm.

Reaction of copper chloride with NAm in methanol produces a blue powder, **5**. Attempts to produce crystals large enough for single-crystal X-ray diffraction analysis were unsuccessful, however structure solution and refinement using X-ray powder diffraction data showed **5** to be $[\text{CuCl}_2\text{NAm}_2]_n$, making it similar to the structures of **1** and **3**. Crystallisation of the same components used to make **5** from hydrochloric acid (4M) produces yellow block crystals of $(\text{H-NAm})_2[\text{CuCl}_4]$ (Form I) (**6a**). Decomposition of **6a** to **5** occurs in approximately 3 days by loss of HCl. The reverse of this, reaction of **5** with HCl vapour, produces a yellow powder, **6b**, possessing a different X-ray powder diffraction pattern to that expected for **6a**. Fortunately it was possible to produce single-crystals of **6b** by crystallisation of an acidified (HCl) acetonitrile solution of copper chloride and NAm, allowing identification of **6b** as $(\text{H-NAm})_2[\text{CuCl}_4]$ (Form II).

Mechanochemical synthesis of the three compounds was then attempted in a similar fashion to that attempted with INAc and INAm. Pure **5** could be produced by grinding of copper chloride and nicotinamide with a few drops of methanol. Grinding the same reagents, **5**, or **6b**, with several drops of concentrated hydrochloric acid, or copper

($R_{wp} = 0.0556$) as shown in Figure 3.31, further crystallographic details are included in Table 3.4. An ORTEP plot of the refined asymmetric unit is shown in Figure 3.32.

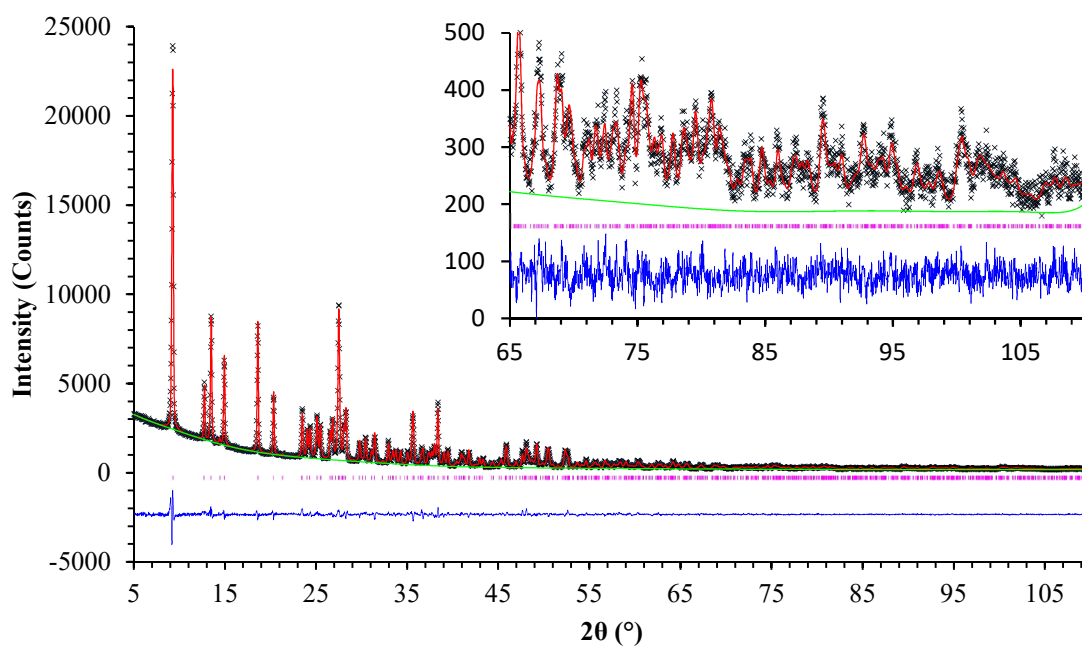


Figure 3.31 A plot of the Rietveld refinement of $[\text{CuCl}_2(\text{NAm})_2]$ (**5**). Black crosses represent observed data, the red line calculated data, the green line background, the pink markers peak positions, and the blue line is the difference plot $[(I_{\text{obs}} - I_{\text{calc}})]$. The inset shows the portion of data between 65 and $110^\circ 2\theta$.

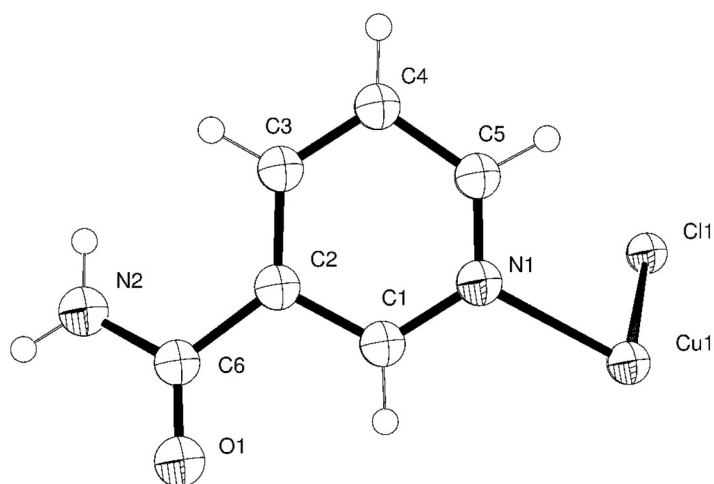


Figure 3.32 Asymmetric unit of $[\text{CuCl}_2(\text{NAm})_2]$ (**5**) with atoms shown as thermal ellipsoids drawn at 50% probability.

The structure of **5** is similar to that of $[\text{CuCl}_2(3\text{-CNpy})_2]^{133}$ and $[\text{CuCl}_2(3\text{-Xpy})_2]^{109}$, but almost identical to $[\text{PdCl}_2(\text{NAc})_2]^{148}$ (NAc = Nicotinic acid). As in **1** and **3**, a polymeric copper-chloride chain is present extending along the *a*-axis, as shown in Figure 3.33A. The Cu atom displays a 4+2 coordination geometry, bond distances and angles are shown in Table 3.11. The polymeric unit in **5** is rotated around *a* when compared to the compounds of 3-CNpy and 3-Xpy, presumably to maximise the strength of intermolecular forces.

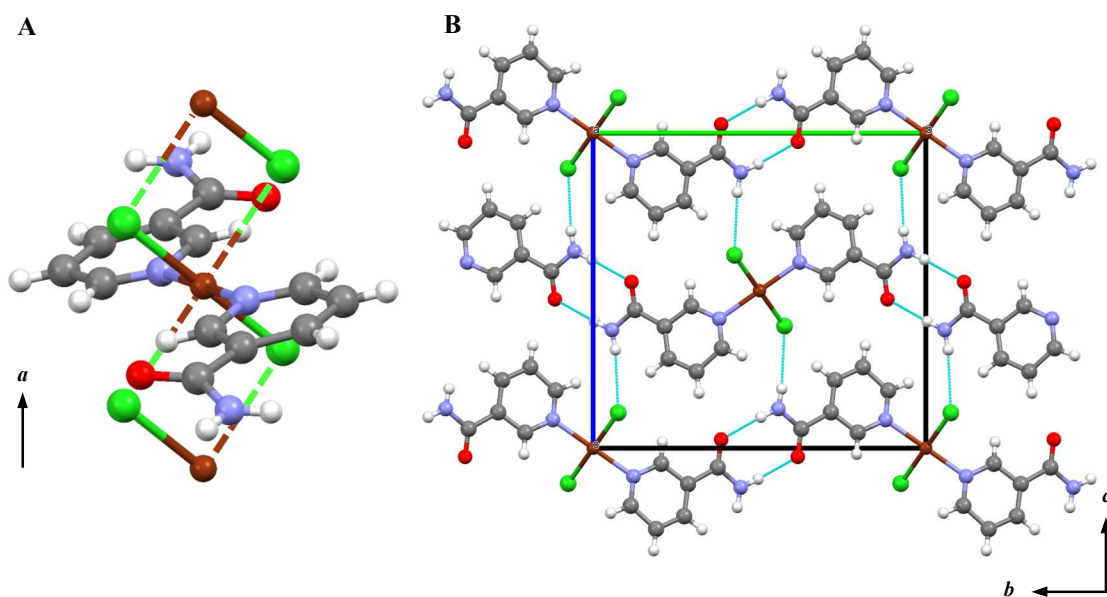


Figure 3.33. The copper chloride chain displayed in $[\text{CuCl}_2(\text{NAm})_2]$ (**5**) extending along the *a* axis (A), and the crystal packing of **5** showing the $\text{N-H}\cdots\text{Cl}$ and $\text{N-H}\cdots\text{O}$ contacts resulting in a ring type hydrogen bonding arrangement and two chain interactions running along *b* and *c* (B). Long Cu-Cl contacts are drawn as dashed lines as their length might indicate the absence of a formal bond. C atoms are shown in grey, H in white, Cl in green, Cu in dark brown, N in light grey-blue, and O in red. Hydrogen bonds are drawn as light-blue dashed lines.

Table 3.11 Selected bond lengths (Å) and angles (°) around the Cu coordination centre for $[\text{CuCl}_2(\text{NAm})_2]$ (**5**).

Cu(1) – Cl(1)	2.2842(5)	N(1)-Cu(1)-Cl(1)	90.0(3)
Cu(1) – Cl(1)#1	2.8980(6)	N(1)-Cu(1)-Cl(1)#1	89.5(3)
Cu(1) – N(1)	2.0306(19)	Cl(1)-Cu(1)-Cl(1)#1	90.8(1)

#1 1 + x, y, z

$R_2^2(8)$ interactions are present at the centres of inversion at $(\frac{1}{2}, \frac{1}{2}, 0)$ and $(\frac{1}{2}, 0, \frac{1}{2})$ between amide groups ($N\cdots O$ 2.932(11) Å), and through the coordinated Cu atoms these create $C_1^1(12)$ chains along the b axis as seen in Figure 3.33B. Furthermore, $N-H\cdots Cl$ contacts ($N\cdots Cl$ 3.506(8) Å) are observed between amine groups and nearby chloride ions, combination with the ring motifs and the bridging of Cl^- ions by Cu^{2+} produces $C_2^2(8)$ interactions along c . In a similar way to **3**, compound **5** contains a 3-D supramolecular network composed of hydrogen bonded sheets that are joined by the $CuCl_2$ chains.

The purity of the samples of **5** produced via different methods is proven in Figure 3.34 by comparison of the simulated and experimental X-ray powder diffraction data. A sample of **5** was also analysed for elemental composition to further confirm purity.

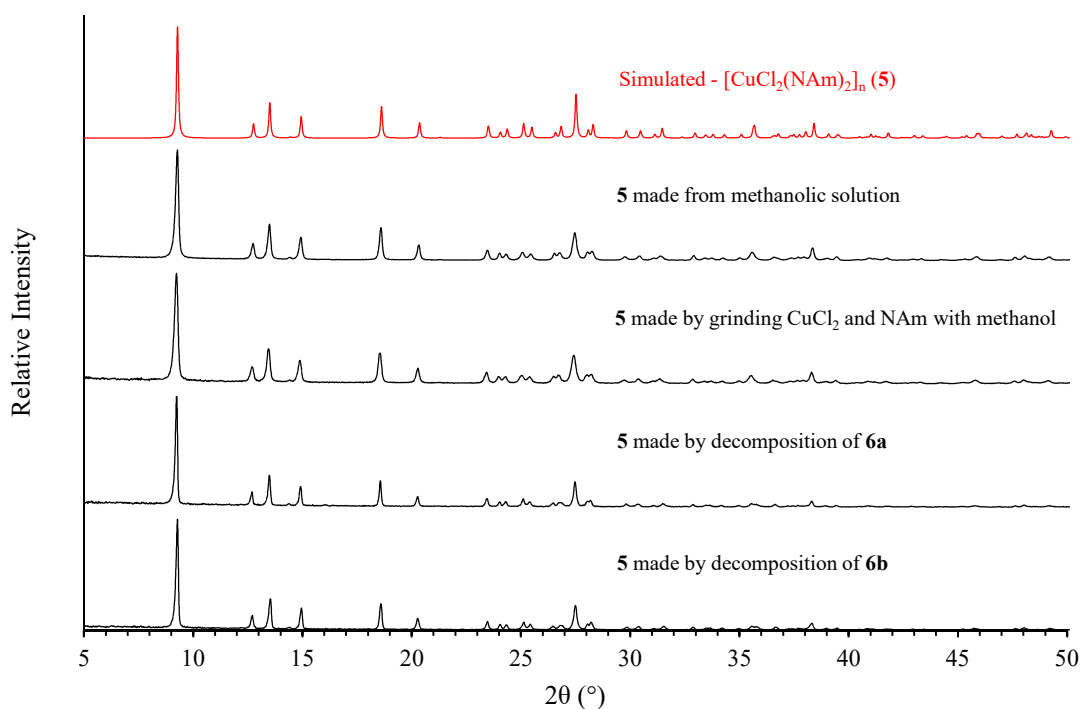


Figure 3.34. Room temperature X-ray powder diffraction data for samples of **5** made by solution and mechanochemical methods, and decomposition of the tetrachlorocuprate NAm salts $(H-NAm)_2[CuCl_4]$ (Form I) (**6a**) and $(H-NAm)_2[CuCl_4]$ (Form II) (**6b**). Experimental data are shown in black while simulated data are shown in red.

3.5.3 (H-NAm)₂[CuCl₄] (Form I) (6a)

Structure determination by single-crystal X-ray diffraction shows that (H-NAm)₂[CuCl₄] (Form I) (**6a**) adopts the orthorhombic space group *Pca*2₁, further crystallographic details are included in Table 3.2. The asymmetric unit, shown in Figure 3.35, consists of two [CuCl₄]²⁻ ions as well as four H-NAm molecules balancing the charge. Unlike the tetrachlorocuprate salts of INAc and INAm, the [CuCl₄]²⁻ units in **6a** are consistent with tetrahedral geometry, bond distance and angle data are shown in Table 3.12.

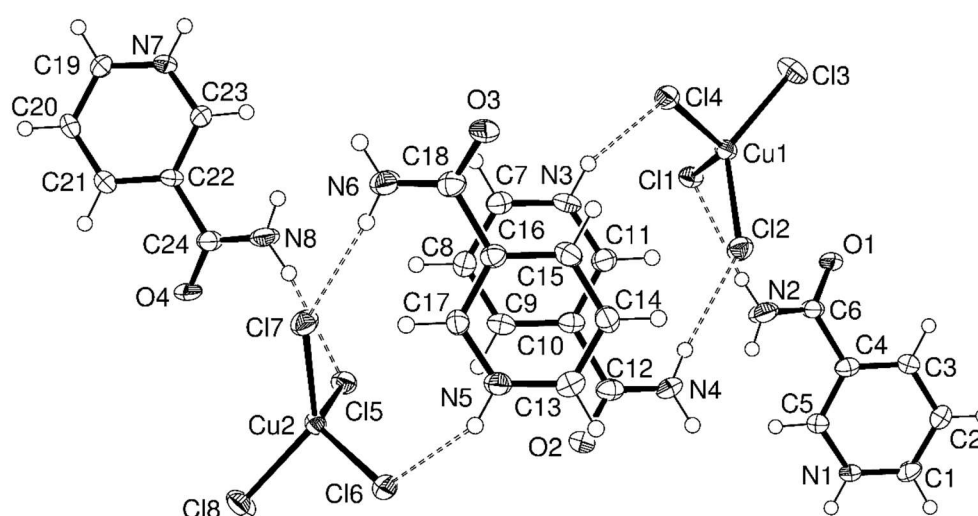


Figure 3.35 Asymmetric unit of (H-NAm)₂[CuCl₄] (Form I) (**6a**) with atoms shown as thermal ellipsoids drawn at 50% probability. Hydrogen bonds are drawn as dashed lines.

Table 3.12 Selected bond lengths (Å) and angles (°) around the Cu coordination centres for (H-NAm)₂[CuCl₄] (Form I) (**6a**).

Cu(1) – Cl(1)	2.278(2)	Cu(2) – Cl(5)	2.281(2)
Cu(1) – Cl(2)	2.232(2)	Cu(2) – Cl(6)	2.247(2)
Cu(1) – Cl(3)	2.226(3)	Cu(2) – Cl(7)	2.246(2)
Cu(1) – Cl(4)	2.261(2)	Cu(2) – Cl(8)	2.214(3)
Cl(1)-Cu(1)-Cl(2)	100.74(8)	Cl(5)-Cu(2)-Cl(6)	126.73(13)
Cl(1)-Cu(1)-Cl(3)	98.88(9)	Cl(5)-Cu(2)-Cl(7)	100.05(8)
Cl(1)-Cu(1)-Cl(4)	126.63(13)	Cl(5)-Cu(2)-Cl(8)	99.86(9)
Cl(2)-Cu(1)-Cl(3)	133.90(14)	Cl(6)-Cu(2)-Cl(7)	101.45(8)
Cl(2)-Cu(1)-Cl(4)	101.19(9)	Cl(6)-Cu(2)-Cl(8)	99.96(8)
Cl(3)-Cu(1)-Cl(4)	99.67(8)	Cl(7)-Cu(2)-Cl(8)	132.83(14)

The hydrogen bonding arrangements are much more complex and unpredictable than the previous compounds. There are two basic hydrogen bonding motifs occurring along the *a* axis. The first of these are the $C_2^2(8)$ motifs formed by each protonated nicotinamide ion by hydrogen bonds between the amine moieties and chloride ions to create chains of connected cuprate ions along *a* ($N\cdots Cl$ 3.3315(2) Å, 3.3358(2) Å, 3.3855(1) Å, 3.4127(1) Å, 3.4164(1) Å, 3.4227(1) Å, 3.4542(2) Å and 3.4852(2) Å), as seen in Figure 3.36A. The second is a $C_1^1(6)$ interaction between the pyridinium and carboxyl moieties of neighbouring H-NAm molecules ($N\cdots O$ 2.6545(2) Å, 2.6731(2) Å, 2.7890(2) Å and 2.8012(2) Å), shown in Figure 3.36B. It is important to note that while the second interaction occurs between adjacent H-NAm molecules, only alternate ones in this chain are involved in a single instance of the first interaction. The second interaction is also bifurcated for two of the H-NAm molecules in the asymmetric unit, those which form the longest $N-H\cdots O$ contacts, such that the pyridinium hydrogen sits between the carboxyl oxygen and the chloride of a cuprate ion ($N\cdots Cl$ 3.2556(1) Å and 3.2603(1) Å). The two chain motifs therefore combine to produce two similar 2-D hydrogen bonded frameworks related by a non-crystallographic centre of inversion, each composed of one $[CuCl_4]^{2-}$ and two H-NAm ions. The two frameworks stack along *c* in an interlocking zip-like fashion shown in Figure 3.36C.

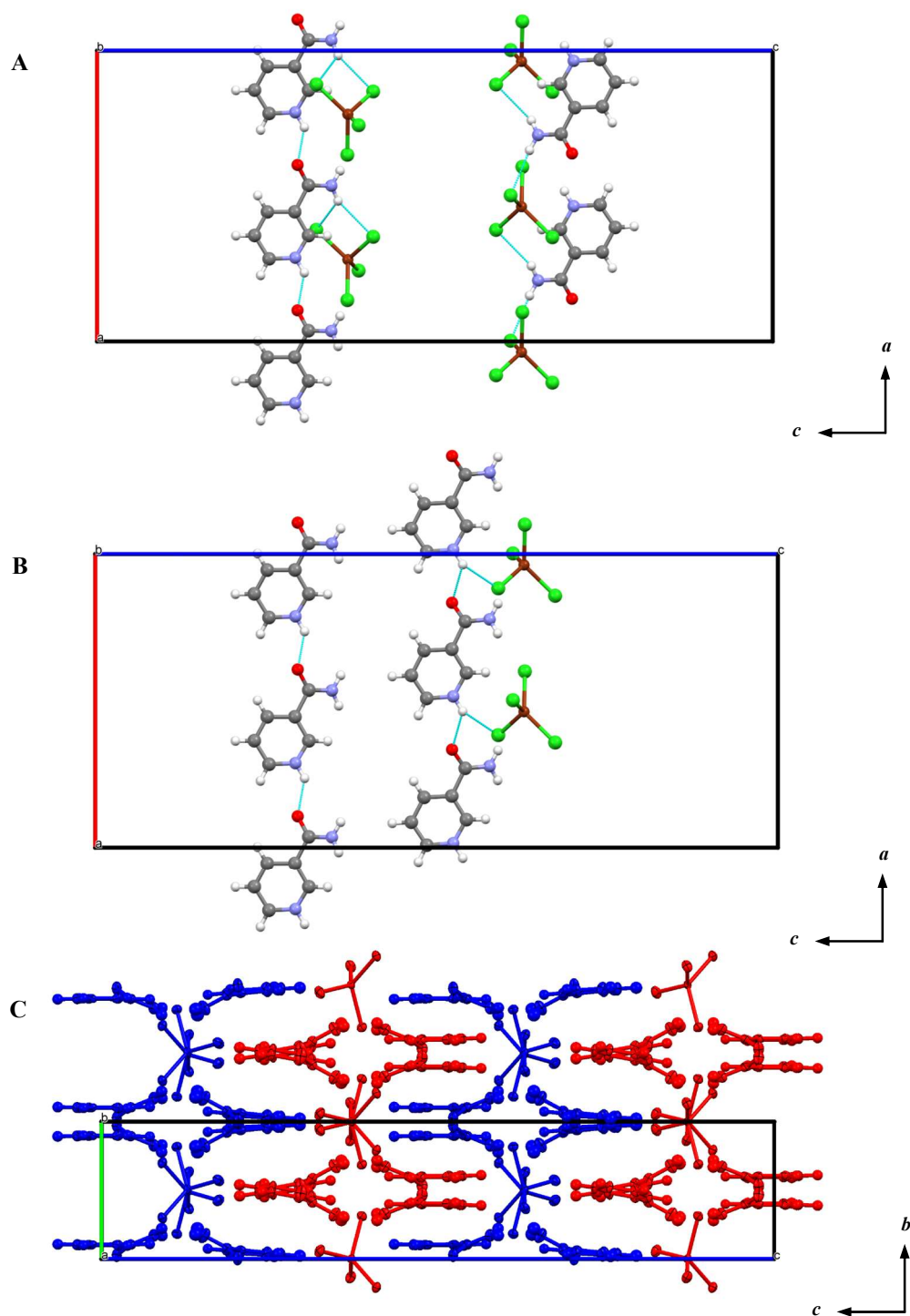


Figure 3.36. A view of some of the C₂²(6) amine-cuprate (A), and C₁¹(6) nicotinamide-nicotinamide (B) hydrogen bonded chains that occur along the *a* axis in (H-NAm)₂[CuCl₄] (Form I) (6a). Also pictured is the shape of the two 2-D hydrogen bonded frameworks coloured in red and blue to show how they pack together in the structure (C). C atoms are shown in grey, H in white, Cl in green, Cu in dark brown, N in light grey-blue, and O in red. Hydrogen bonds are drawn as light-blue dashed lines.

Figure 3.37 shows a comparison of experimental and simulated data for **6a**. It is clear that the crystalline sample produced from solution suffers from preferred orientation with specific peaks being more intense than expected, however all the observed peaks are in the predicted positions with no observed extras. The samples produced by mechanochemical synthesis provide a much better comparison to the simulated data, however the additional peak in each case at $\sim 9.25^\circ 2\theta$ is a result of partial decomposition to **5**, most likely a result of loss of HCl through the grinding process. The crystals made from solution were sent for elemental analysis to confirm purity.

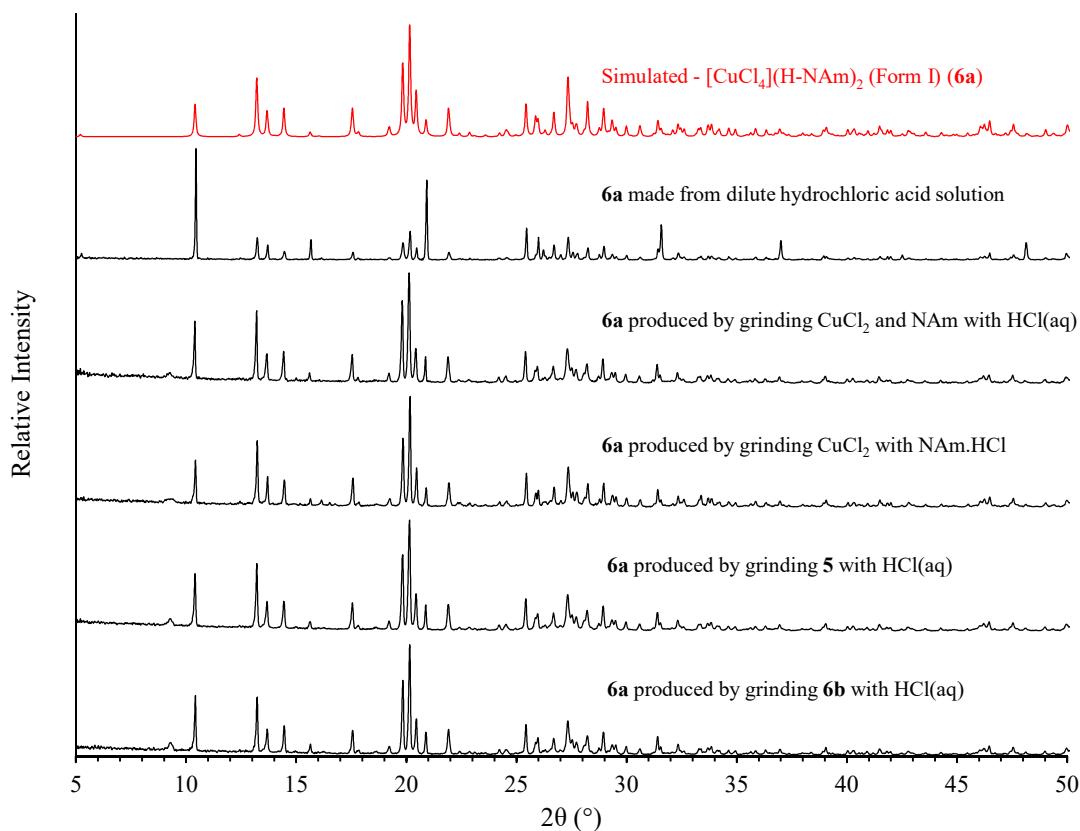


Figure 3.37. Room temperature X-ray powder diffraction data for samples of **6a** made by solution and mechanochemical methods. **5** is $[\text{CuCl}_2(\text{NAm})_2]$ and **6b** is $(\text{H-NAm})_2[\text{CuCl}_4]$ (Form II). Experimental data are shown in black while simulated data are shown in red.

3.5.4 (H-NAm)₂[CuCl₄] (Form II) (6b)

Yellow block crystals of (H-NAm)₂[CuCl₄] (Form II) (**6b**) were analysed by single-crystal X-ray diffraction analysis, further crystallographic details are included in Table 3.3. This showed that **6b** possesses a monoclinic unit-cell with the space group *P*2₁/*c*. The asymmetric unit contains only one [CuCl₄]²⁻ and two H-NAm ions, as shown in Figure 3.38, half that of **6a**. The Cu displays the same distorted tetrahedral geometry as in **6a**, bond length and angle data are shown in Table 3.13.

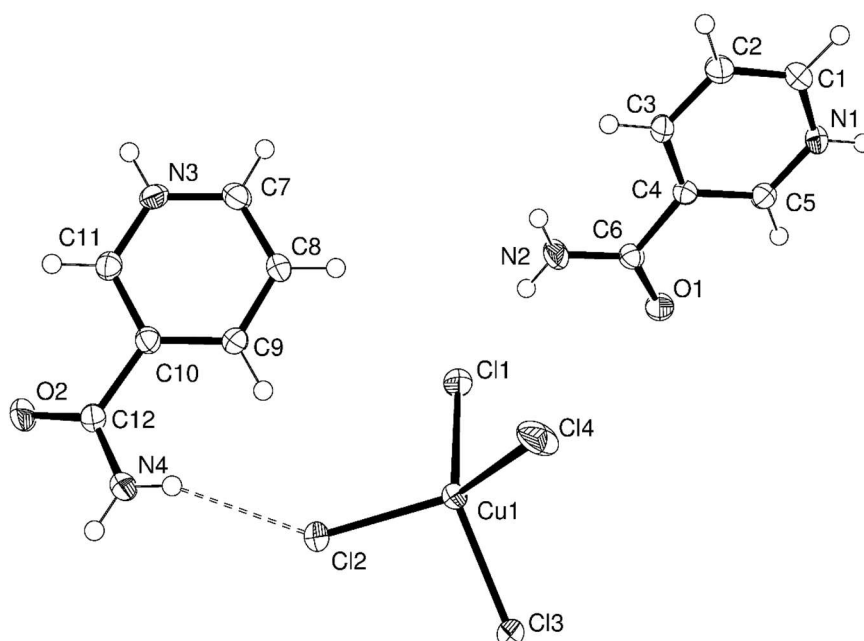


Figure 3.38 Asymmetric unit of (H-NAm)₂[CuCl₄] (Form II) (**6b**) with atoms shown as thermal ellipsoids drawn at 50% probability. Hydrogen bonds are drawn as dashed lines.

Table 3.13 Selected bond lengths (Å) and angles (°) around the Cu coordination centre for (H-NAm)₂[CuCl₄] (Form II) (**6b**).

Cu(1) – Cl(1)	2.2545(5)	Cu(1) – Cl(3)	2.2433(4)
Cu(1) – Cl(2)	2.2614(5)	Cu(1) – Cl(4)	2.2429(5)
Cl(1)-Cu(1)-Cl(2)	98.184(18)	Cl(2)-Cu(1)-Cl(3)	96.349(16)
Cl(1)-Cu(1)-Cl(3)	135.804(17)	Cl(2)-Cu(1)-Cl(4)	137.888(19)
Cl(1)-Cu(1)-Cl(4)	98.251(18)	Cl(3)-Cu(1)-Cl(4)	98.272(19)

The hydrogen bonding motifs in **6a** and **6b** are remarkably similar (for **6a** see Figure 3.36). The amine-cuprate chain ($\text{N}\cdots\text{Cl}$ 3.246(2) Å, 3.262(2) Å, 3.302(1) Å and 3.341(2) Å) is present as two crystallographically distinct $\text{C}_2^2(6)$ interactions along b and c , shown in Figure 3.39. The pyridinium-carboxyl interaction is also present ($\text{N}\cdots\text{O}$ 2.6786(2) Å and 2.7092(3) Å) as a $\text{C}_2^2(12)$ interaction along b , displayed in Figure 3.40. This is double the length of the similar $\text{C}_1^1(6)$ interaction found in **6a** as both of the H-NAm cations in the asymmetric unit are involved in a singular arrangement.

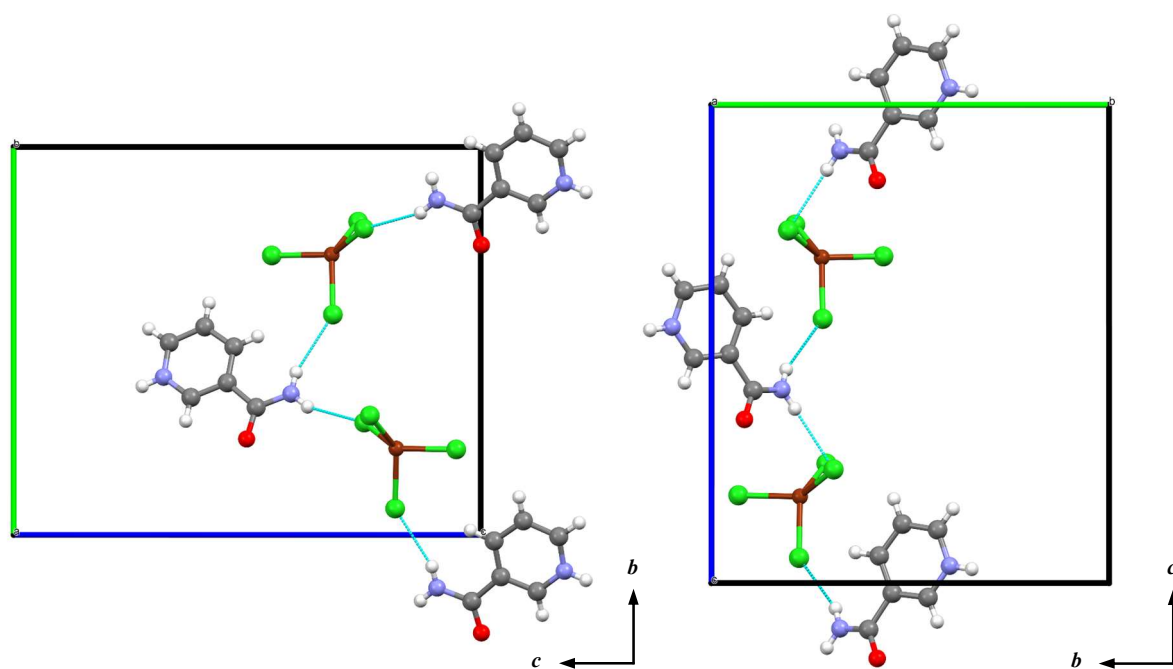


Figure 3.39 A view of the $\text{C}_2^2(6)$ amine-cuprate chains along the b and c axes in $(\text{H-NAm})_2[\text{CuCl}_4]$ (Form II) (**6b**) (B). C atoms are shown in grey, H in white, Cl in green, Cu in dark brown, N in light grey-blue, and O in red. Hydrogen bonds are drawn as light-blue dashed lines.

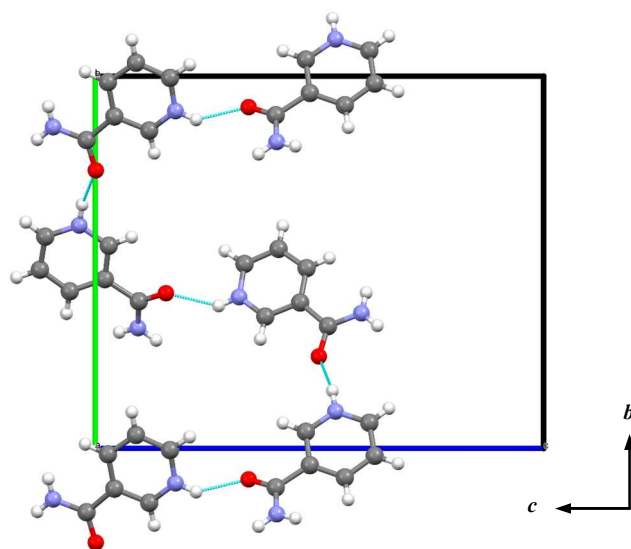


Figure 3.40. The $C_2(12)$ interactions that occur along the b axis produced by the nicotinamide molecules in $(H-NAm)_2[CuCl_4]$ (Form II) (**6b**). C atoms are shown in grey, H in white, Cl in green, Cu in dark brown, N in light grey-blue, and O in red. Hydrogen bonds are drawn as light-blue dashed lines.

The X-ray powder diffraction data for samples of **6b** produced from either solution or solid-gas reaction provide good comparison to the data simulated from the structure, as shown in Figure 3.41. Further confirmation of the purity of the samples is provided by elemental analysis.

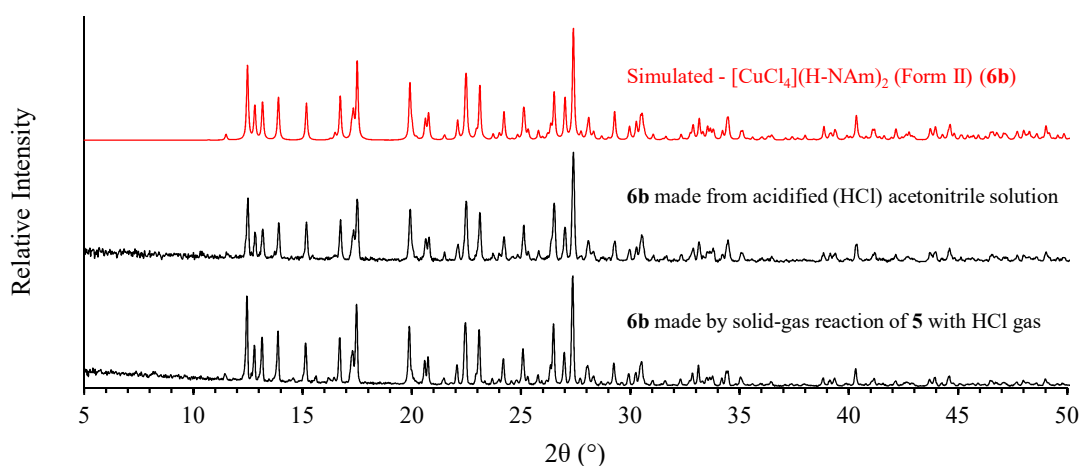


Figure 3.41. Room temperature X-ray powder diffraction data for samples of **6b** made from solution and solid-gas reaction of $[CuCl_2(NAm)_2]$ (**5**) with HCl gas. Experimental data are shown in black while simulated data are shown in red.

3.5.5 Additional observations on $(H-NAm)_2[CuCl_4]$ (Form I/II) (6a/6b)

Figure 3.42 shows the main difference between the two $(H-NAm)_2[CuCl_4]$ polymorphs; the orientation of the amide group with respect to the pyridinium ring. In form I (**6a**) the amide is orientated with the amine closest to the pyridinium N, whereas in form II (**6b**) the carboxyl group is closer. This is why despite the two forms having almost identical hydrogen bonding interactions, the structures and resulting X-ray powder diffraction patterns are substantially different.

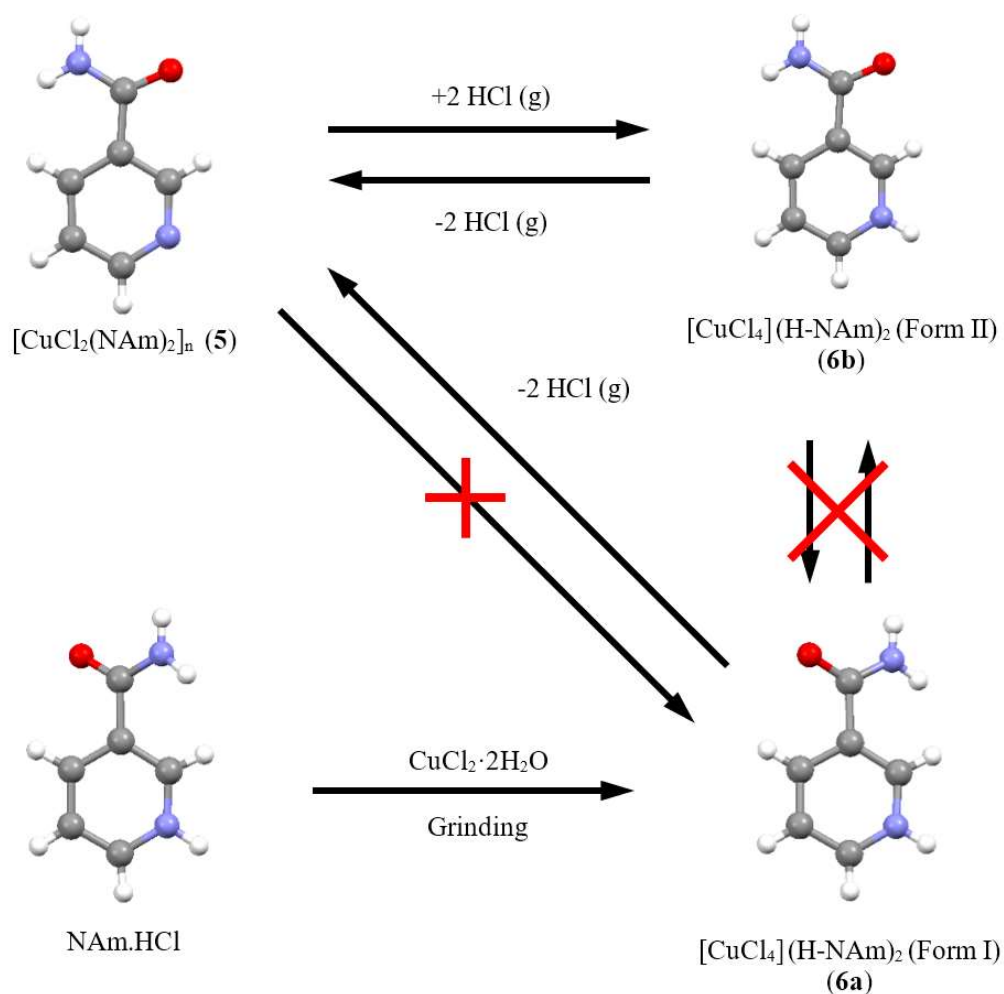


Figure 3.42. Diagram showing the orientation of the amide group relative to the pyridine ring for the nicotinamide (NAM) compounds investigated. The reaction pathways for all solid-state (not dissolution) reactions conducted are shown, and the effect the amide orientation has on controlling which polymorphic form of the NAM tetrachlorocuprate salt is produced. Reaction from **5/6b** to **6a** is possible but only via dissolution in conc. HCl (aq), not solid-state reaction. C atoms are shown in grey, H in white, N in light grey-blue, and O in red.

Interestingly, the amide orientation in $[\text{CuCl}_2(\text{NAm})_2]_n$ (**5**) and **6b** match, **6b** being the product of reaction of **5** with concentrated hydrochloric acid vapour. Additionally, the product of grinding nicotinamide hydrochloride with copper chloride is pure **6a**, and again the starting reagent, NAm.HCl, has the same orientation of the amide as the product. This leaves us with the conclusion that the amide orientation of the starting reagent controls which cuprate polymorph is produced via solid-state reaction (no dissolution), indicating that the relative stability of the two cuprates must be very similar, or at least greater than the energy required to reconfigure the NAm molecule in the solid-state. The loss of HCl from **6a** and **6b**, on the other hand, produces only one compound, **5**. The most probable reason for this is that **5** is the most thermodynamically favoured structure, no polymorph exists with the amide oriented as in **6a**. The tetrachloroplatinate salt of nicotinamide displays similar hydrogen bonding motifs to those observed in **6a** and **6b**, however the overall structure is substantially different due to the square-planar coordination of Pt.

3.5.6 *Infrared Spectra*

A comparison of the infrared spectra of NAm and NAm.HCl to the three compounds produced by reaction of copper chloride with NAm is shown in Figure 3.43. The spectra of NAm.HCl, **6a** and **6b** all show similar features, although somewhat different to those of NAm and **5**, as would be expected.

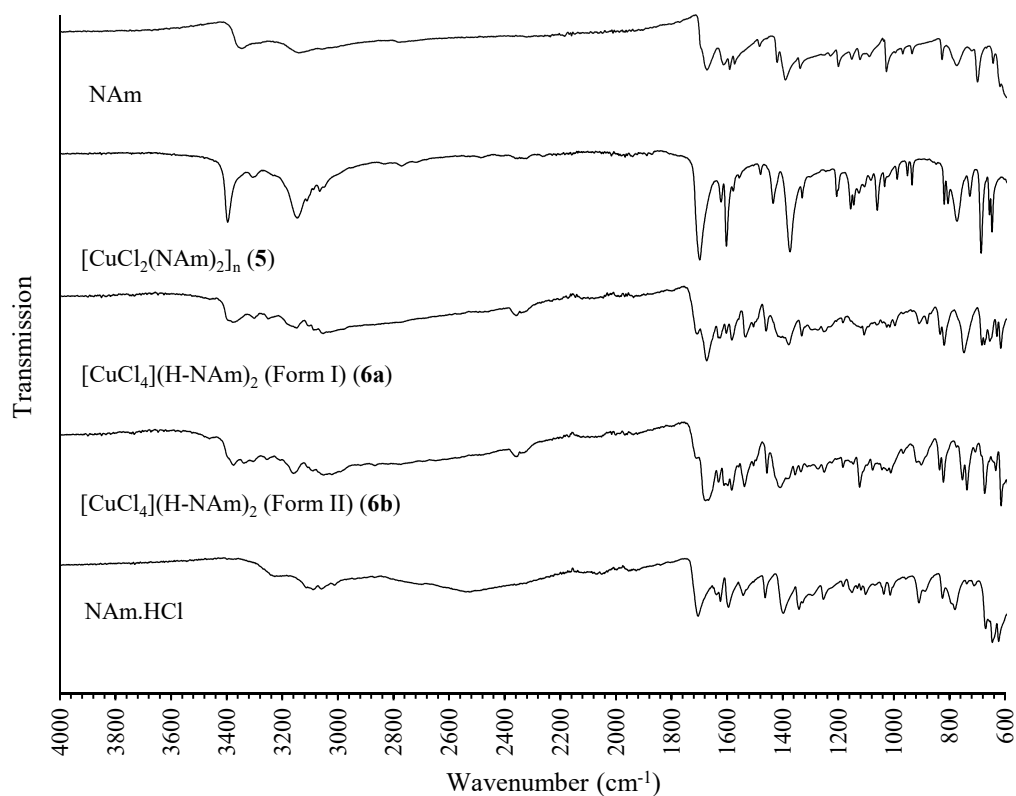


Figure 3.43. Infrared spectra for NAM, **5**, **6a**, **6b**, and NAM.HCl.

3.6 Metal-free compounds and solid-gas reactions

All of the reported research into solid-gas reactions of pyridine-based compounds with hydrohalic acids have so far been solely on coordination complexes. To investigate the phenomenon further, the equivalent metal-free solid-gas reactions with HCl of the organic components studied here were performed.

Firstly, the starting reagents, INAc, INAm, and NAM, were analysed by X-ray powder diffraction to determine their crystalline form as there are several polymorphs of these compounds. Simultaneously the same reagents were recrystallised from hydrochloric acid to produce the corresponding hydrochloride salts. While the structures of the three starting reagents and NAM.HCl were already determined accurately,^{145,153–157} the reported structure of INAc.HCl as crystallised from H₂O was found to be of poor quality,¹⁴⁴ and

that of INAm.HCl was unknown. The latter two were therefore analysed by single-crystal X-ray diffraction.

With samples and crystal structures of the neutral and hydrochloride salt forms of each compound, the solid-gas reactions could then be studied. Reaction of each neutral compound with hydrochloric acid vapour was conducted in a similar way to that used for **1**, **3**, and **5** over a period of 1 day. Meanwhile the hydrochloride salt samples which were produced via recrystallisation were left in open vessels for a period of 7 days to investigate decomposition by loss of HCl. X-ray powder diffraction patterns of the samples were used to confirm whether or not a reaction had occurred and what crystalline form was present. The structures, reactions, powder diffraction data, and elemental analyses are discussed below.

3.6.1 *Isonicotinic Acid (INAc)*

The crystal structure of INAc was originally determined and described by Takusagawa and Shimada.¹⁵³ The compound crystallises with a centrosymmetric triclinic unit-cell, and an asymmetric unit containing only one INAc molecule. There is only one strong hydrogen bonding interaction between the carboxylic acid and pyridine groups, which produces a $C_1^1(7)$ chain motif that propagates along b , as shown in Figure 3.44. Unlike INAm and NAm, which can exist in many crystalline forms, this is the only known structure of INAc. One possible reason for this lack of polymorphism could be the fact that a hydroxyl group can act as a donor group to only one acceptor atom whereas an amine can form hydrogen bonds to two. The only possible “choices” of acceptor atoms in INAc are either the pyridine N or the carboxyl O. The former atom is the acceptor in the structure of INAc, probably because an O-H \cdots N hydrogen bond is stronger and more energetically favourable than an O-H \cdots O contact.

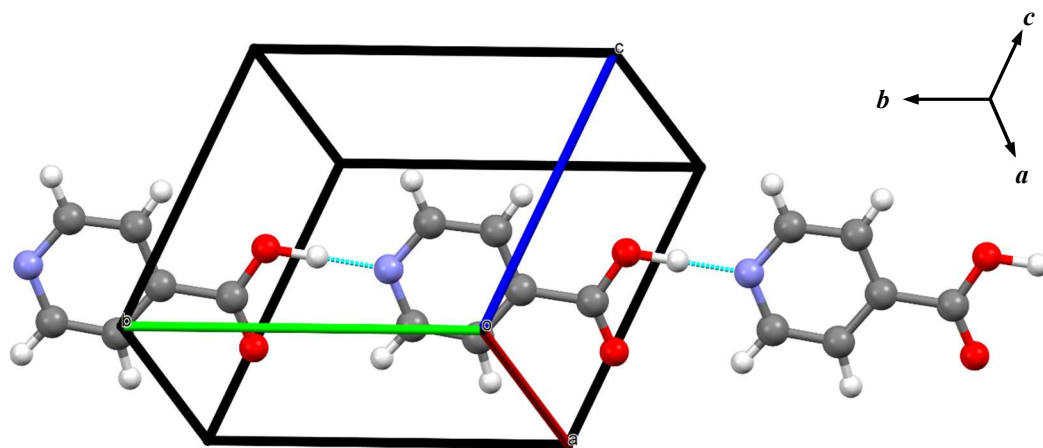


Figure 3.44 The $C_1^1(7)$ chain motif in INAc that runs parallel to b .¹⁵³ C atoms are shown in grey, H in white, N in light grey-blue, and O in red. Hydrogen bonds are drawn as light-blue dashed lines.

INAc.HCl has two known structures, one triclinic and one monoclinic. A definitive synthetic method for the production of the triclinic form has not been reported and this form has not been observed in this research so shall not be discussed (the triclinic structure is reported on the CSD only as XECDUF01, CCDC 633208). The monoclinic structure is produced by recrystallisation from aqueous hydrochloric acid and by solid-gas reaction of INAc with HCl gas. It was first determined by Adams *et al.*¹⁴⁴ who proposed a model that described the two chloride anions as being disordered over two positions, as shown in Figure 3.45.

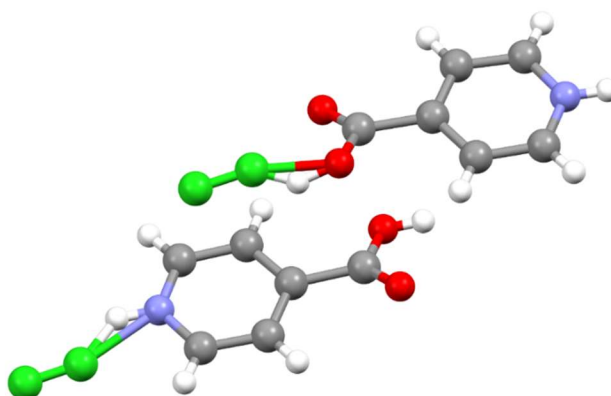


Figure 3.45 Asymmetric unit of INAc.HCl as determined by Adams *et al.*¹⁴⁴ C atoms are shown in grey, H in white, Cl in green, N in light grey-blue, and O in red.

However, the secondary positions have a very low occupancy (~3%) and are located at very short distances from N and O atoms ($N\cdots Cl$ 1.95(2) Å, $O\cdots Cl$ 1.76(2) Å) which makes the validity of the structure questionable. A redetermination of the structure was therefore conducted, and refinement using the new data did not show any discernable disorder suggesting that the original structural model was incorrect, further crystallographic details are included in Table 3.3. One possible reason for the apparent disorder might be unresolved twinning which the new crystal did not exhibit. The space group of the monoclinic structure is $P2_1/c$, and the asymmetric unit contains two protonated INAc molecules and two chloride anions balancing the charge, as shown in Figure 3.46.

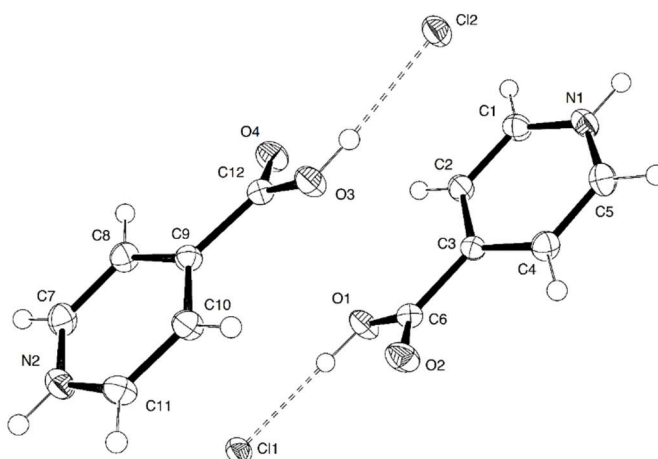


Figure 3.46 Asymmetric unit of INAc.HCl with atoms shown as thermal ellipsoids drawn at 50% probability. Hydrogen bonds are drawn as dashed lines.

The two sets of molecules are involved in almost identical hydrogen bonding arrangements. The pyridinium and carboxylic acid groups of each isonicotinic acid hydrogen bond to chloride ions ($O1\cdots Cl1$ 2.9421(9) Å, $N1\cdots Cl1$ 3.1190(10) Å, $O3\cdots Cl2$ 2.9530(9) Å, $N2\cdots Cl2$ 3.0883(10) Å) to form a $C_2^1(9)$ chain interaction that zig-zags along b , as shown in Figure 3.47.

The structural comparison of INAc and INAc.HCl is an interesting one as the connectivity of the INAc molecules is more or less the same, the only difference is that the latter contains a protonated pyridine ring and the hydrogen bonding between molecules is mediated by a Cl⁻ ion. The insertion or removal of HCl would not alter the connectivity of the INAc/H-INAc molecules.

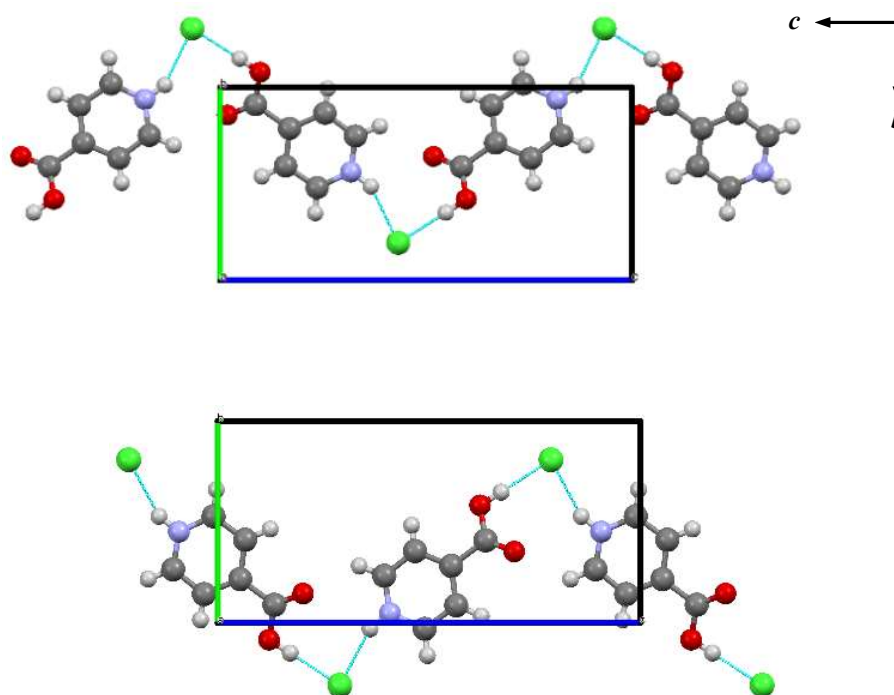


Figure 3.47 The two symmetrically independent $C_2^1(9)$ chain motifs that propagate along b in monoclinic INAc.HCl. C atoms are shown in grey, H in white, Cl in green, N in light grey-blue, and O in red. Hydrogen bonds are drawn as light-blue dashed lines.

Experimental and computed X-ray powder diffraction data are shown in Figure 3.48. The sample of INAc.HCl produced via crystallisation from solution displays gross preferred orientation despite extensive efforts to avoid this. On the other hand, the sample produced by solid-gas reaction shows no orientation preference and provides an excellent comparison to the calculated data. The comparison also proves that decomposition of INAc.HCl to INAc by loss of HCl does not occur, at least at room temperature. This is an interesting result as it indicates that metal coordination bonds could play a role in the

ready loss of HCl from tetrahalocuprate salts, but not necessarily in the gain of HCl which *has* been shown to occur in the absence of a metal.

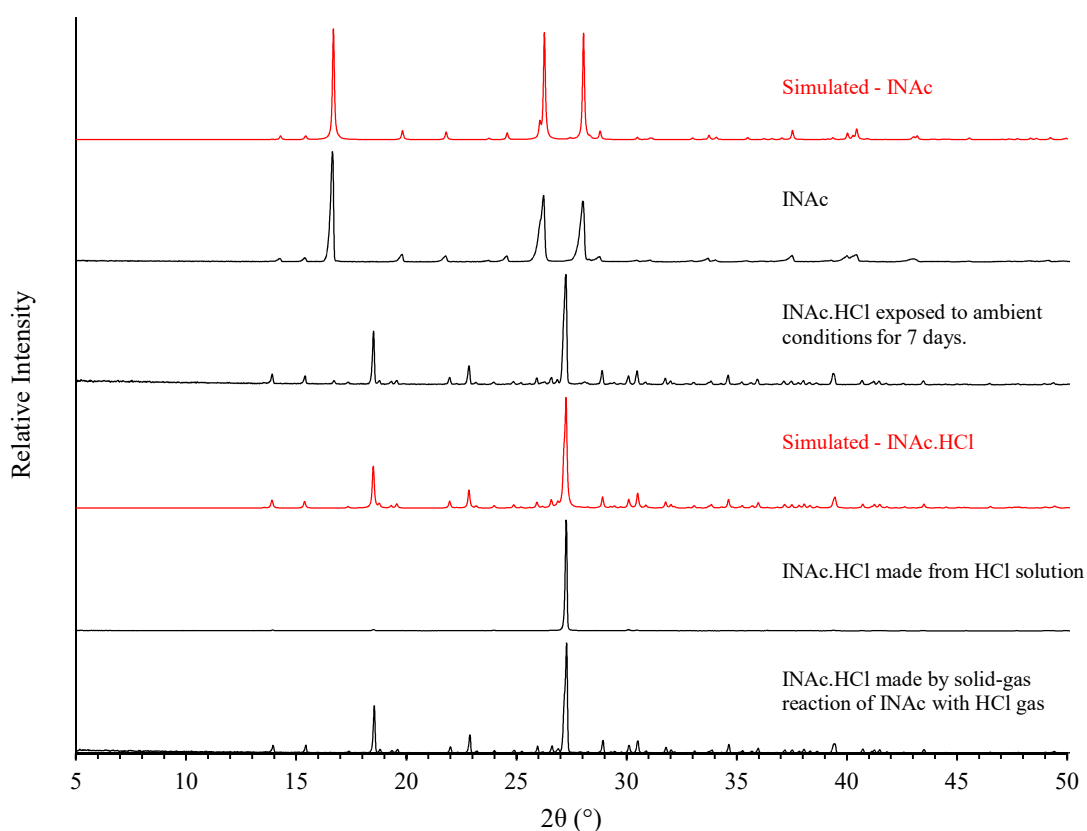


Figure 3.48. Room temperature X-ray powder diffraction data for samples of INAc.HCl made from solution, and solid-gas reaction of INAc with HCl gas. Experimental data are shown in black while simulated data are shown in red.

3.6.2 Isonicotinamide (INAm)

Isonicotinamide can crystallise in several crystalline forms, four of which are monoclinic and one orthorhombic.^{154–156} The two most common forms of INAm were reported and described by Aakeröy *et al.*, lattice parameters are given in Table 5.17.¹⁵⁴ Form I, crystallised from nitrobenzene, nitromethane, or by sublimation, possesses $R_2^2(8)$ motifs hydrogen bonded in a sheet. Form II, crystallised from most other solvents, has a hydrogen bonding arrangement more similar to INAc. Both polymorphs are monoclinic. The supplied INAm reagent has the first structural form. A crystal packing diagram of

this form is shown in Figure 3.49. The additional amine hydrogens not involved in the $R_2^2(8)$ motif hydrogen bond to adjacent carboxyl groups creating a 2-D sheet parallel to the (100) crystallographic plane. The angle between the mean planes of adjacent isonicotinamide dimers is $\sim 60^\circ$.

Table 3.14 Lattice parameters for the crystal structures of INAm form I and II.¹⁵⁴

INAm form	I	II
a (Å)	10.176(1)	15.735(3)
b (Å)	5.7319(6)	7.998(2)
c (Å)	23.008(4)	9.885(2)
β (°)	98.042(3)	105.59(2)
V (Å ³)	579.5(1)	1198.2(5)

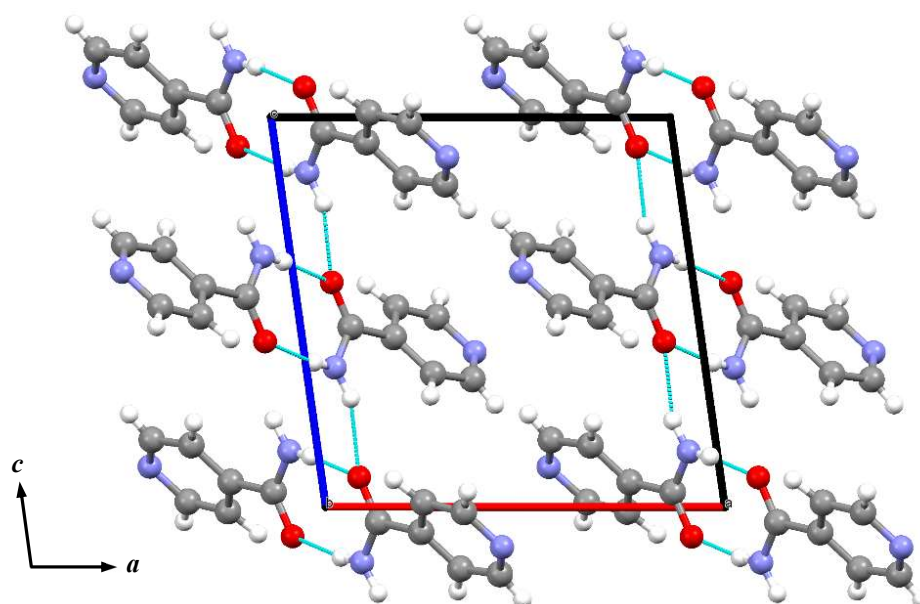


Figure 3.49 A crystal packing diagram of form I of INAm.¹⁵⁴ C atoms are shown in grey, H in white, N in light grey-blue, and O in red. Hydrogen bonds are drawn as light-blue dashed lines.

The structure of isonicotinamide hydrochloride was previously unknown before this study. Single-crystal X-ray diffraction showed that the compound possesses a monoclinic unit-cell with space group $P2_1/c$, further crystallographic details are included in Table

3.3. The asymmetric unit is shown in Figure 3.50, and consists of one chloride anion and a protonated isonicotinamide cation.

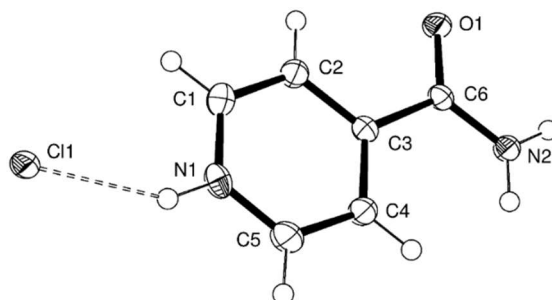


Figure 3.50. Asymmetric unit of INAm.HCl with atoms shown as thermal ellipsoids drawn at 50% probability. Hydrogen bonds are drawn as dashed lines.

The most interesting feature of the crystal structure is the intermolecular interaction between the pyridinium groups and chloride ions. Two pyridinium protons form bifurcated hydrogen bonds to two chloride ions, forming an $R_2^2(4)$ ring motif, as shown in Figure 3.51 (A), which is positioned on a centre of inversion. The interaction is similar to those found in **4a** and **4b** and the equivalent tetrachloroplatinate salt.¹⁴⁴ It is also encountered in some other pyridine-based hydrochloride salts.^{158,159} The two unique N-H \cdots Cl hydrogen bonds formed by each proton in this arrangement are usually of similar length, though one is distinctly longer than the other in this compound (N \cdots Cl = 3.0416 (12) Å and 3.4882 (13) Å). The CSD¹¹⁹ reveals that of the 426 structures of the hydrochloride salts of molecules incorporating a pyridinium group, only 16 possess the $R_2^2(4)$ ring motif. However, none of these show the same asymmetry in the hydrogen bond lengths making the observed interaction unique. Given the lack of examples of bifurcated hydrogen bonds in compounds exhibiting a pyridinium group, it seems likely that it is a compromise resulting from optimising other intermolecular interactions. In other words, one short, linear N-H \cdots Cl bond is ideal, although bifurcation is energetically more favourable than a single, weaker interaction.

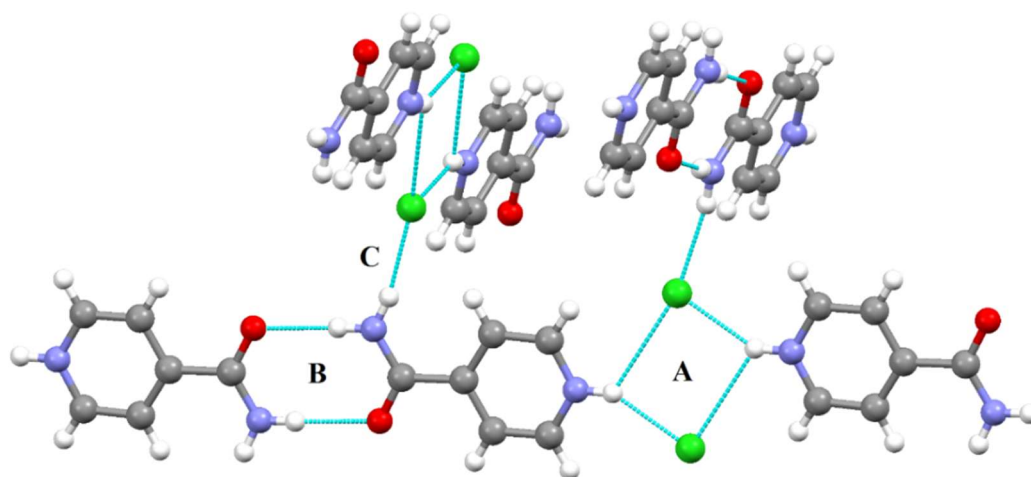


Figure 3.51. A view of the hydrogen bonding arrangements within INAm.HCl, showing the pyridinium–chloride (A) amide–amide (B) and amine–chloride (C) interactions. Possible C–H···X interactions have been omitted. C atoms are shown in grey, H in white, Cl in green, N in light grey-blue, and O in red. Hydrogen bonds are drawn as light-blue dashed lines.

The structure also exhibits a classic $R_2^2(8)$ amide–amide interaction, seen in Figure 3.51B ($N\cdots O$ 2.889(2) Å). The combination of the two ring interactions form $C_3^2(16)$ chains running in the $[150]$ and $[\bar{1}\bar{5}0]$ directions, and are related by a 2_1 screw axis. The two chain directions are almost perpendicular to each other ($\sim 80^\circ$) and are held in this respective orientation by a $C_4^3(10)$ interaction which incorporates the $R_2^2(8)$ and $R_2^2(4)$ motifs, and hydrogen bonds between the protons not involved in the amide–amide interactions and the chloride ions of neighbouring chains ($N\cdots Cl$ 3.191(1) Å), as shown in Figure 3.51C. For the overall packing arrangement, see Figure 3.52.

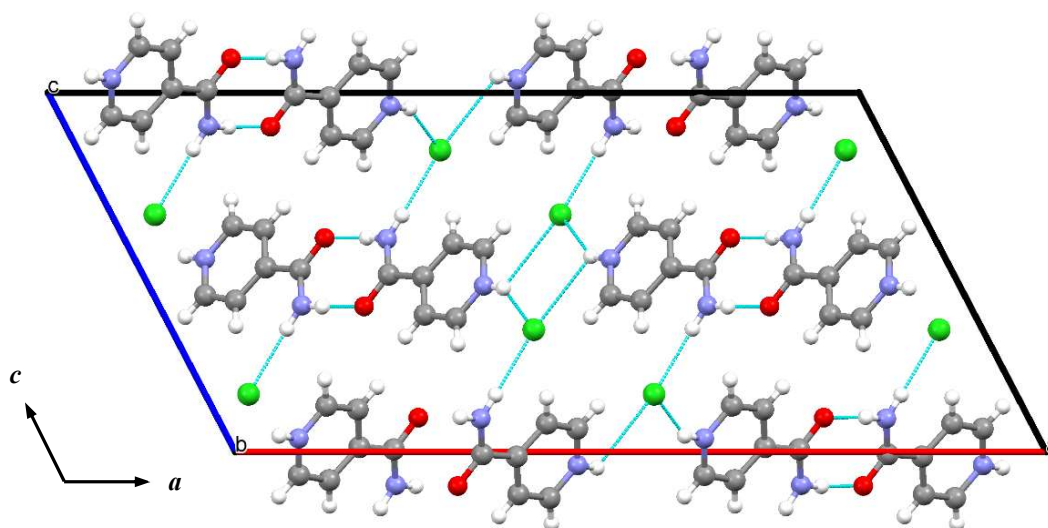


Figure 3.52. Crystal packing diagram of INAM.HCl viewed along the b axis. Hydrogen bonds are drawn as light-blue dashed lines. C atoms are shown in grey, H in white, Cl in green, N in light grey-blue, and O in red. Hydrogen bonds are drawn as light-blue dashed lines.

Figure 3.53 shows the diffractograms for samples of INAm and INAm.HCl, alongside data simulated from the crystal structures described. The data proves that the INAm starting reagent displays the monoclinic structure. Additionally, the product of solid-gas reaction of INAm with HCl gas and recrystallisation of INAm from HCl solution are the same. The sample produced by solid-gas reaction does not display as much preferred orientation as the sample made from solution, as evidenced by a better match to the relative peak intensities of the simulated data. Much like with INAc.HCl, no decomposition of INAm.HCl occurs after 7 days.

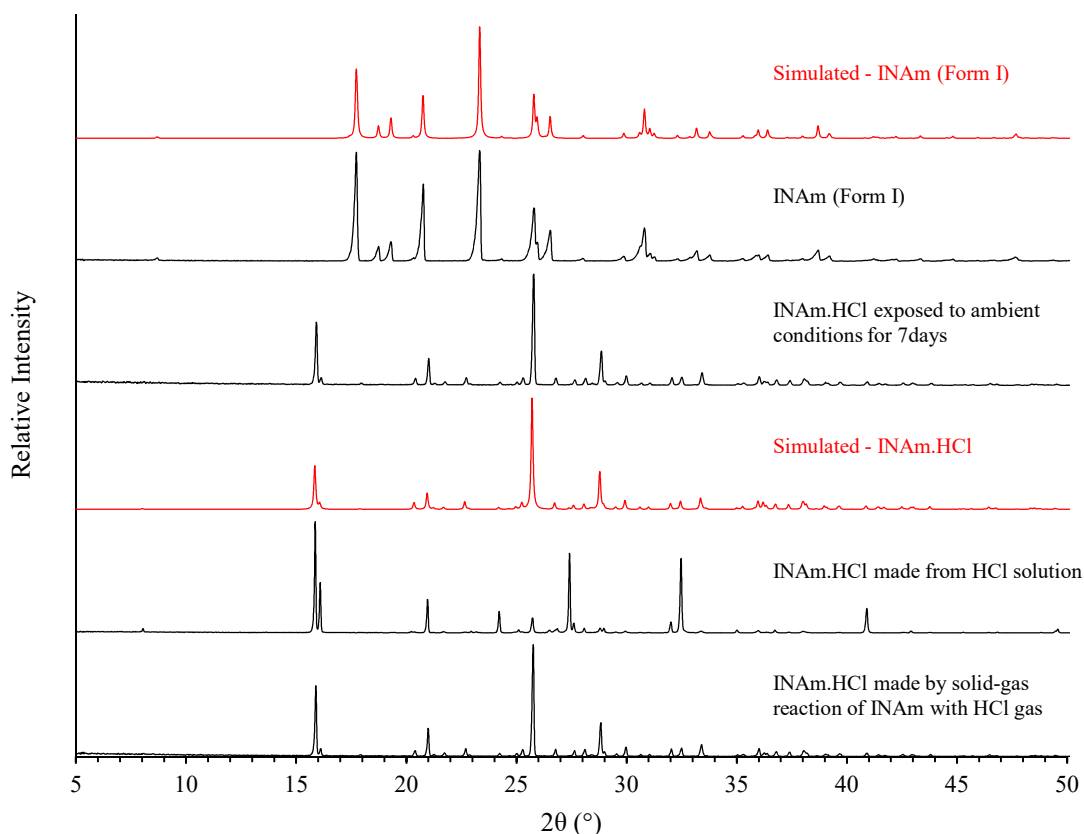


Figure 3.53. Room temperature X-ray powder diffraction data for samples of INAm.HCl made from solution, and solid-gas reaction of INAm with HCl gas. Experimental data are shown in black while simulated data are shown in red.

The comparison of INAc.HCl to INAc is similar to that of INAm.HCl to INAm, the two forms of each compound display very similar hydrogen bonding arrangements. The main differences between the neutral and hydrochloride salt forms of INAm are the extra hydrogen bonds that occur between the pyridinium groups and chloride ions in the salt. Additionally, the connectivity between the INAm.HCl chains is through N-H \cdots Cl hydrogen bonds as opposed to the N-H \cdots O hydrogen bonds between molecules in INAm. The comparable reactivity of INAm and INAc is understandable given the similarities between them, and the lack of decomposition from INAm.HCl to INAm gives further credence to the idea of metal coordination playing a pivotal role in the reversibility of reaction with HCl.

3.6.3 Nicotinamide (NAm)

Nicotinamide, much like isonicotinamide, displays polymorphism. Two structures are known, both of which are monoclinic. However, form II shall not be discussed as it is only known to crystallise in the presence of isoxyl (also known as thiocarlide or 1,3-bis[4-(3-methylbutoxy)phenyl]thiourea).¹⁵⁵ The structure of form I was first determined by Wright and King,¹⁶⁰ however it has been redetermined more recently by Miwa *et al.* including refinement of hydrogen positions.¹⁵⁷ The overall structure and hydrogen bonding arrangements are shown in Figure 3.54. The amine group hydrogen bonds to the carboxyl and pyridine groups of nearby molecules to form a 2-dimensional supramolecular arrangement parallel to the (010) crystallographic plane.

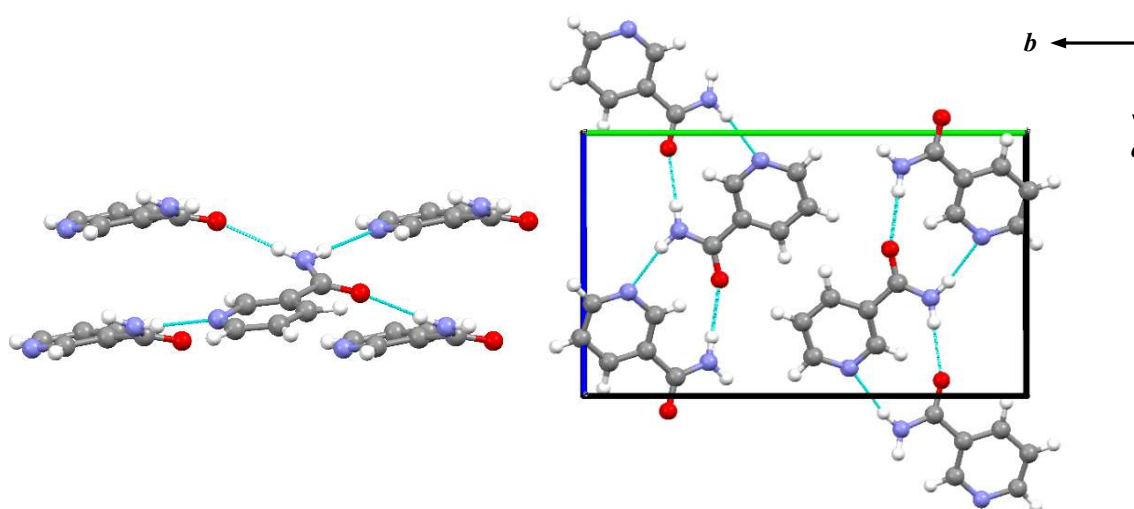


Figure 3.54 The hydrogen bonding contacts of a NAm molecule (left) and the crystal packing arrangement (right) observed in form I of NAm.¹⁵⁷ C atoms are shown in grey, H in white, N in light grey-blue, and O in red. Hydrogen bonds are drawn as light-blue dashed lines.

Nicotinamide hydrochloride only has one known structure reported by Gubin *et al.*¹⁴⁵ The structure is monoclinic with an asymmetric unit consisting of a nicotinamide cation and a chloride anion. Two hydrogen bonded amide groups create an $R_2^2(8)$ interaction. Additionally, an $R_4^2(16)$ motif is present composed of two nicotinamide molecules and

two chloride ions through pyridinium-chloride and amine-chloride hydrogen bonds. These combine to make hydrogen bonded ribbons that propagate in the $[1\bar{1}0]$ direction. Figure 3.55 displays the hydrogen bonded ribbons and how they pack to produce the crystal structure.

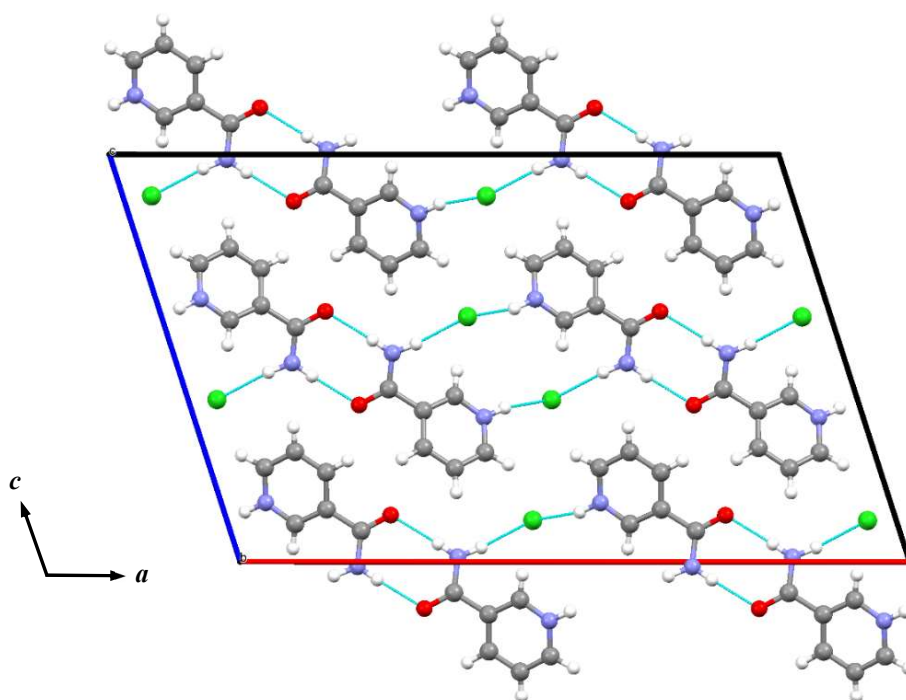


Figure 3.55 Crystal packing diagram of NAM.HCl.¹⁴⁵ C atoms are shown in grey, H in white, Cl in green, N in light grey-blue, and O in red. Hydrogen bonds are drawn as light-blue dashed lines.

X-ray powder diffraction data for all samples of NAM and NAM.HCl, including simulated data, are shown in Figure 3.56. As with INAc and INAm, comparison of simulated and experimental data proves the identity of the samples produced by solution and solid-gas methods. Additionally, the hydrochloride salt does not decompose on exposure to air for 7 days, far longer than the decomposition time of the equivalent copper coordination compounds.

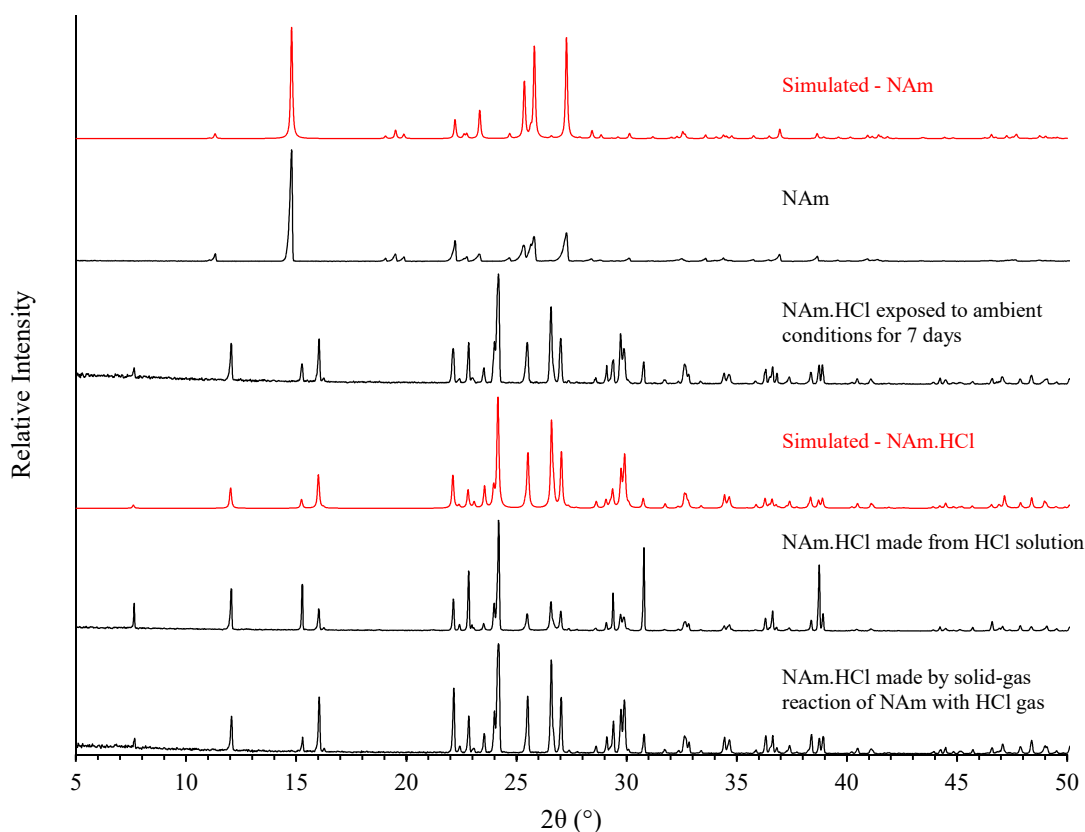


Figure 3.56 Room temperature X-ray powder diffraction data for samples of NAM.HCl made from solution, and solid-gas reaction of NAM with HCl gas. Experimental data are shown in black while simulated data are shown in red.

Unlike INAc and INAm, there is no clear comparison of the neutral and hydrochloride salt structures of NAM making it much more difficult to envisage how the reaction proceeds. Although, the fact that the NAM structures are somewhat different to INAc and INAm is fairly conclusive proof that metal coordination is a very important factor in the decomposition of the tetrachlorocuprate compounds.

3.7 Reaction rate of solid-gas reactions

Espallargas *et al.* found that $[\text{CuCl}_2(3\text{-Clpy})_2]$ and $[\text{CuCl}_2(3\text{-Brpy})_2]$ react with hydrochloric acid vapour to produce the corresponding cuprate in about 2 days, the reverse reaction taking 1 day and 7 days respectively.¹⁰⁹ They also reported that a similar

compound produced with 2-(imidazol-2-yl)pyridine reacts with HCl to completion in 1 hour with a similar setup, though they did not report on the reverse reaction.¹⁴⁰ **1**, **3** and **5** react with the acidic vapours completely in about 3 hours each, and the reverse reaction to lose HCl gas takes about 2-3 days. A few possible explanations for these observed reaction rates are differences in particle size, ligand acidity and the strength of intermolecular interactions or crystal packing.

Particle size could influence the rate if the reaction only occurs at the surface before migrating inwards: larger particles have a smaller surface area per volume than smaller particles, so conversion of the entire volume to the salt form should take longer. To address the role of particle size in this work, SEM images of the compounds both before and after HCl inclusion were taken which are shown in Figure 3.57.

Overall it appears as if there is a small increase in size and some change in shape during the process of HCl absorption. The sample of **1** has crystallites 0.5-6 μm wide initially, however the smaller crystallites are not present after reaction with HCl and the approximate size of the crystallites is 2 μm in the sample of **2b** produced. The crystallites in **3** are about 0.5-2 μm in size before exposure to HCl, and approximately 1-3 μm afterwards. **5** appears to show a larger increase in size upon reaction, the average crystallite size is approximately 0.5-1 μm before and 2-3 μm after reaction with HCl.

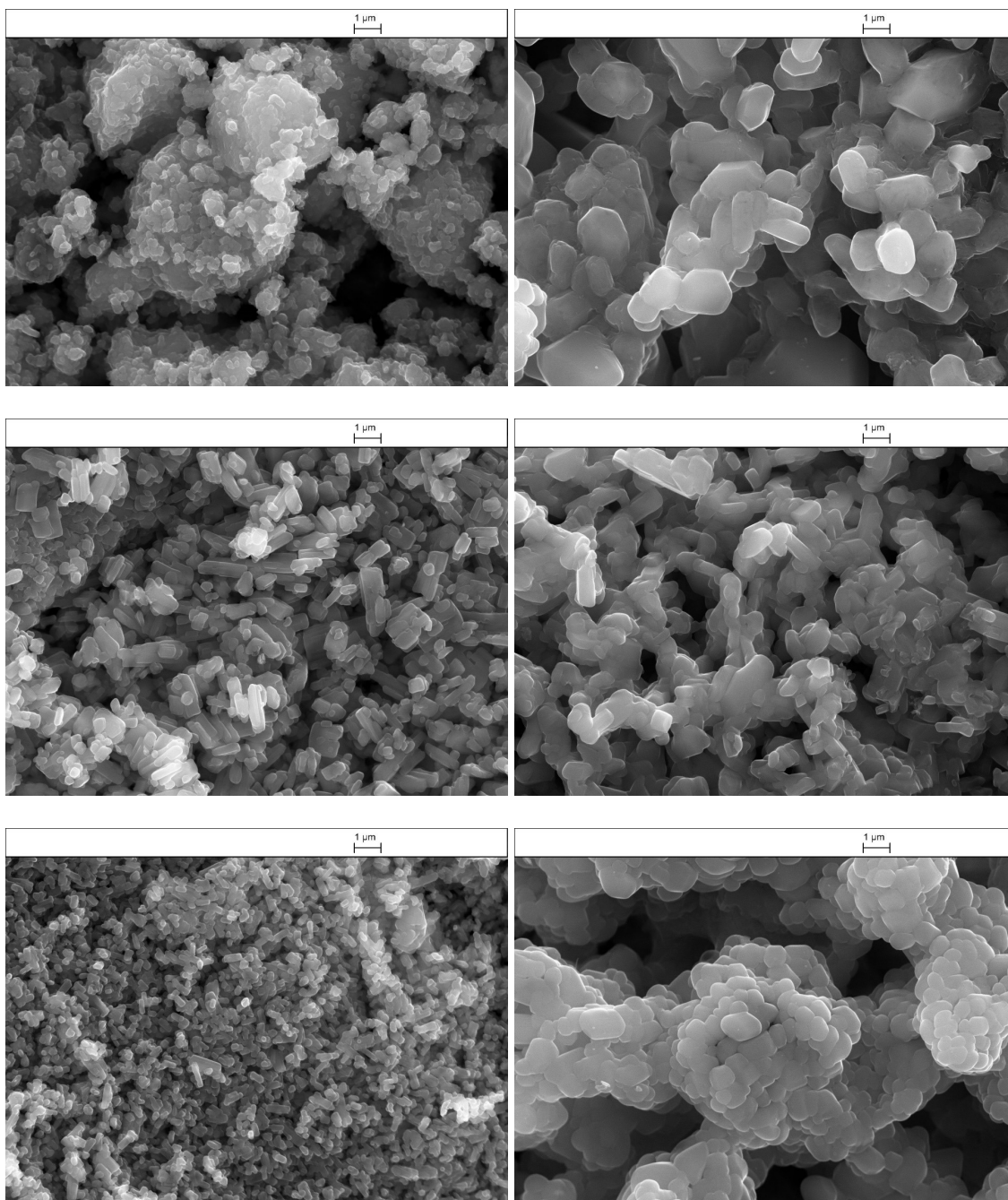


Figure 3.57 On the left are scanning electron microscope images of samples, from top to bottom, of $[\text{CuCl}_2(\text{INAc})_2]_n$ (**1**), $[\text{CuCl}_2(\text{INAm})_2]_n$ (**3**), and $[\text{CuCl}_2(\text{NAm})_2]_n$ (**5**), before exposure to HCl vapour. Images on the right were taken after exposure of the same samples to HCl vapour producing, from top to bottom, $(\text{H-INAc})_2[\text{CuCl}_4]$ (Form I) (**2b**), $(\text{H-INAm})_2[\text{CuCl}_4]$ (Form II) (**4b**), and $(\text{H-NAm})_2[\text{CuCl}_4]$ (Form II) (**6b**) respectively.

The difference in particle size increase between the samples/compounds after exposure to HCl is not congruent with the reaction rates observed. One would expect that the

difference in particle size increase between samples should result in a similar difference in reaction rate if particle size plays an important role in determining this property, although the observed reaction rates are consistent. This suggests that the reaction rates are more heavily affected by the chemical properties of the compound rather than the physical properties of the individual samples. However, a more thorough study of the effect of particle size on reaction rate would be required to rule it out entirely as a contributing factor, which is beyond the scope of this work.

The absence of very large changes in crystallite size augurs against a complete dissolution-reprecipitation mechanism. However, the clear change in crystal surface morphology and slight size increase suggests there is some dissolution occurring. One possible mechanism is the absorption of HCl on the surface of the crystallites and a reorganization near the surface. HCl then permeates through the sample until complete conversion occurs.

Ligand acidity, *i.e.* the ability to gain and lose protons, could also play a role as a more basic ligand is more likely to accept a proton than a more acidic ligand therefore displaying an increased reaction rate given the same conditions. The evidence found thus far shows that the acidity or pK_a of the ligands (referring to the reaction $R-C_5H_5N-H^+ \rightleftharpoons R-C_5H_5N + H^+$) is a bad indicator for reaction rate. INAc is substantially more acidic than INAm and NAm ($pK_a = 1.77, 3.61$ and 3.40 in water for INAc, INAm and NAm respectively) yet the copper chloride compounds react at a roughly similar rate. 3-Clpy and 3-Brpy are as acidic as each other ($pK_a = 2.84$ in water), yet while they react with HCl in a similar time scale they lose HCl at markedly different rates. However, the most basic ligand studied thus far, 2-(imidazol-2-yl)pyridine ($pK_a = 5.54, 13.4$ in water),¹⁶¹ also displays the fastest reaction rate for gain of HCl, so the idea of acidity controlling

the reaction rate may not be entirely groundless. pK_a values were taken from CRC Handbook of Biochemistry and Molecular Biology.¹⁶²

Lastly, the strength of the covalent and non-covalent interactions is likely to play a large role as the structures need to distort to facilitate the movement of HCl, stronger interactions will resist distortion increasing the activation barrier for reaction thereby slowing it down. The structures investigated presently have very similar supramolecular architectures and have comparable packing densities; volume occupied per atom is 16-16.6 Å³ for **1**, **3** and **5**, 17.7 Å³ for **2b**, **4a**, and **4b**, and 18.6-18.9 Å³ for **2a**, **6a** and **6b**. This may explain why they react within similar time frames, however, for conclusive proof the mechanism by which the uptake and loss of HCl occurs needs to be understood. Espallargas *et al.* have attempted to extract mechanistic information on how the halopyridine compounds react by utilising the similarity between bromide and chloride structures.¹³⁷ They have reacted a bromide starting material ($[\text{CuBr}_2(\text{RPy})_2]$) with HCl gas to create a $[\text{CuCl}_2\text{Br}_2]^{2-}$ salt, the occupancies of the chloride and bromide ions on each halide site could then be calculated to reveal where the chloride ions have gone. They found that halide sites which took part in hydrogen or halogen bonding interactions displayed a higher occupancy for chloride than bromide ions, leading them to conclude that insertion of HCl into the Cu-N bonds causes a reorientation of the resultant cuprate anion to maximize intermolecular interactions. Given that HBr reacts in a similar way to HCl, a more robust method would also include reaction of the equivalent chloride starting material with HBr to exclude any effect of atom size on the mechanism. Similar studies on the newly presented compounds are required before further comments can be made on the possible role of crystal packing and intermolecular forces on reaction rate. Clearly the chemistry at work is complex and the present study does not serve to clarify this. In order

to elucidate the exact causes of differences in reaction rate to create a model for prediction a systematic study of many more compounds is required.

3.8 Conclusions and future work

The reaction of INAc, INAm and NAm with copper chloride in a 2:1 ratio produces three similar polymeric copper chloride compounds, $[\text{CuCl}_2(\text{INAc})_2]_n$ (**1**), $[\text{CuCl}_2(\text{INAm})_2]_n$ (**3**), and $[\text{CuCl}_2(\text{NAm})_2]_n$ (**5**), with almost identical supramolecular frameworks and all three containing the same hydrogen bonding ring motifs. The evaporation of HCl(aq) solutions of **1**, **3** and **5** produce crystals of $(\text{H-INAc})_2[\text{CuCl}_4] \cdot 2\text{H}_2\text{O}$ (**2a**), $(\text{H-INAm})_2[\text{CuCl}_4]$ (form I) (**4a**) and $(\text{H-NAm})_2[\text{CuCl}_4]$ (form I) (**6a**) respectively. However, solid-gas reaction of the same compounds with moist HCl gas produces a different set of tetrachloro cuprate salts; **1** produces $(\text{H-INAc})_2[\text{CuCl}_4]$ (**2b**), **3** first yields $(\text{H-INAm})_2[\text{CuCl}_4]$ (form II) (**4b**) before transforming into **4a**, and **5** reacts to give $(\text{H-NAm})_2[\text{CuCl}_4]$ (form II) (**6b**). The cuprates **2a**, **2b**, **4a** and **4b** possess remarkable structural similarities, and display the same ring motif as found in **1**, **3**, and **5**. **6a** and **6b** differ substantially from these, though from each other only by the orientation of the amide group. **4a** and **4b** are found to be thermodynamic and kinetic products respectively, hence explaining the reason for the transformation of **4b** to **4a**. Additionally, the formation of **6a** or **6b** depends on the orientation of the amide group of NAm in the starting material as the orientation is maintained from reactant to product, further indicating the thermodynamic stability of each phase must be similar. All the cuprate compounds lose HCl, and water in the case of **2a**, to produce the corresponding copper halide coordination polymers.

The reaction of these compounds can be observed through a change in colour. The exact colour of the product depending on the coordination environment of the copper ion, as

illustrated in Figure 3.58. For a tetragonally elongated octahedral environment, products appear pale blue if two Cl^- ions and two N donor atoms occupy the equatorial positions and Cl^- ions occupy the axial positions (at least for pyridine-based ligands), if four Cl^- ions occupy the equatorial positions then the compound is green if O donor atoms occupy the axial positions and yellow-green if the axial positions are occupied by Cl^- . If the coordination geometry is distorted tetrahedral with Cl^- occupying all coordination sites then the compound appears yellow. There is only one compound known to break these rules, $[\text{CuCl}_2(4\text{-aminopyridine})_2]_n$, which is described in the next chapter. These observations may therefore be used as a rule of thumb for determining the coordination geometry of unknown compounds.

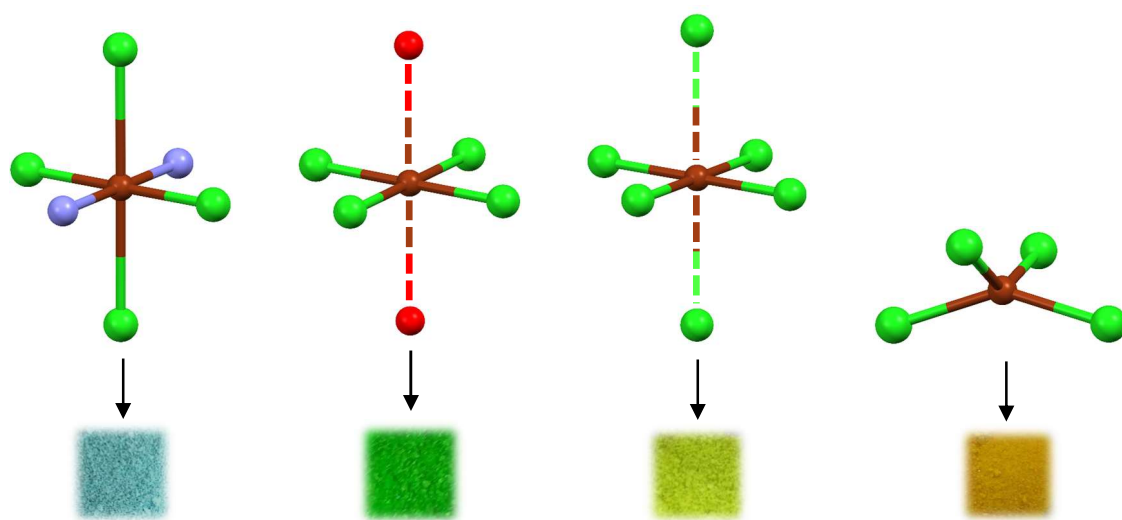


Figure 3.58 Illustration of how the coordination environment of the copper ion translates into the compound colour observed.

The equivalent metal-free reactions have also been studied. INAc.HCl , INAm.HCl , and NAm.HCl were synthesised from the neutral compounds by recrystallisation from hydrochloric acid solution, and reaction with HCl gas. However, after leaving the hydrochloride salts in the open for a week, no signs of decomposition were found in the diffraction patterns of the samples. This is a much longer time than that taken for full

decomposition of the tetrachlorocuprate salts, indicating that change in the coordination of the copper must play a pivotal role in the relatively quick and easy release of HCl from the cuprate compounds.

The rate at which HCl is gained and lost from similar copper chloride-based compounds has been found to vary depending on the ligand. Some factors that could influence this have been identified, including ligand acidity, particle size and the structure of the compound. Ligand acidity produces a reasonably accurate prediction of the rate at which HCl reacts or is extruded from the compounds. However, it is unclear what role particle size or structure might play in reaction rate as the compounds studied have similar particle sizes for similar compounds, and not enough information has been gathered thus far to postulate accurately what the mechanisms of the reactions are and therefore what effect structure might have. A systematic study covering many more pyridine-based compounds is required before firm conclusions can be made on the factors effecting the reaction rate. Clearly the copper chloride pyridine system is very complex, and despite the extensive investigations carried out thus far some questions are left unanswered. The observations made could be explored further by changing the starting materials used, *e.g.* using a different halide, metals or ligands, to understand these compounds better. This may allow materials to be engineered for the controlled uptake and release of HCl, possibly for the fast, selective, visual detection of hydrohalic acids. Additionally, the resistance of copper halide pyridine compounds to very acidic environments, and the ready reversibility of reaction with hydrohalic acids provides an interesting avenue of research into porous compounds. Combination of copper halides and multitopic ligands may result in a variety of porous compounds with unprecedented stability, and the potential for simple reconditioning by solid-gas reaction with the relevant hydrohalic acid. The reaction of 3-aminopyridine with copper chloride in methanol is already known to produce a

polymeric compound containing solvent filled channels, as shown in Figure 3.59, although the honeycomb net is only maintained by hydrogen bonds so is not stable upon solvent removal.¹³⁴ Trispyridyltriazine is thought to produce a topologically identical structure,¹⁶³ as depicted in Figure 3.59, and the much stronger covalent bonds may allow the resulting copper halide coordination compound to possess permanent porosity. This is something of keen interest with regards to gas adsorption and should be attempted in the future.

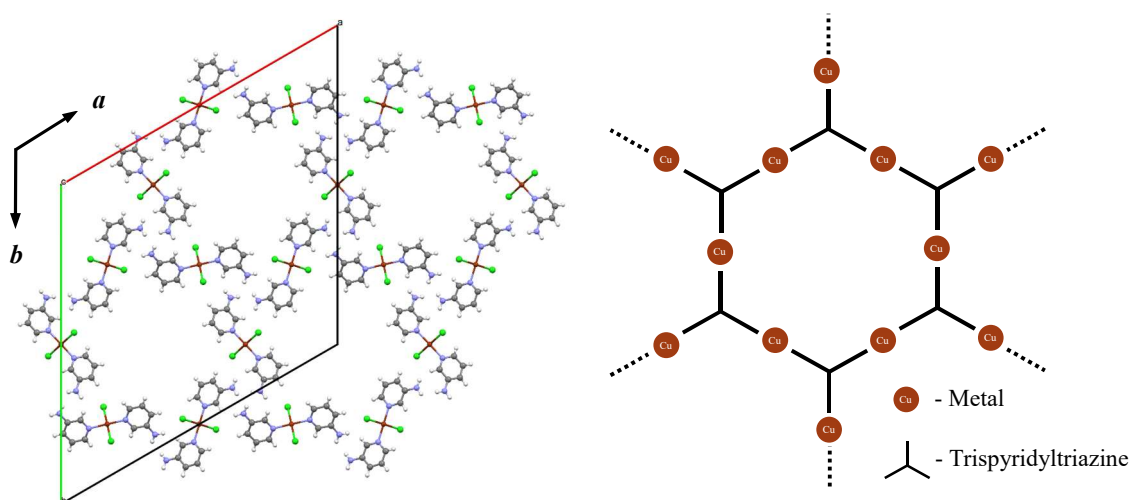


Figure 3.59 Images depicting the 2-D framework which connects the metal halide chains in the structure of $[\text{CuCl}_2(3\text{-aminopyridine})_2]_n$, left, and the proposed structure of $[\text{Cu}_2\text{Cl}_4(\text{trispyridyltriazine})_3]_n$, right, as viewed down the chains. C atoms are shown in grey, H in white, Cl in green, Cu in dark brown, and N in light grey-blue.

4 Synthesis and Structure of $[\text{Cu}_4(\mu^4\text{-O})(\mu^2\text{-X})_6]$

Compounds

The majority of research into porous compounds for gas adsorption revolves not around the coordination of singular metal ions, but of metal clusters instead. The main reason for this is that the coordination geometry of ligands around metal clusters is far more rigid than around single ions. Cluster-based compounds are less flexible as a result so are less likely collapse on solvent removal than non-cluster-based compounds, and framework topologies of cluster-based compounds are so predictable that isorecticular series of compounds can often be developed.^{43,55}

Copper can form an oxide centred, halide bridged cluster which has the general formula $[\text{Cu}_4(\mu^4\text{-O})(\mu^2\text{-X})_6(\text{L})_4]$. X is a halide (Cl or Br), L is the apical ligand which can be either a Cl or Br anion, thus requiring a positive counter-ion, or an uncharged organic ligand containing a N, O, or P donor atom which produces a neutral complex. The general structure of the cluster is shown in Figure 4.1. It consists of an oxide anion bridging four copper centres in a tetrahedron, which in turn are bridged by halide anions. The rare trigonal bipyramidal coordination geometry of each Cu is completed by coordination to the ligand L. The first compound discovered that displays this cluster was determined in 1964 by Stucky & Rundle.¹⁶⁴ The compound, $[\text{Mg}_4(\mu^4\text{-O})(\mu^2\text{-Br})_6(\text{diethyl ether})_4]$, was produced by oxidation of phenylmagnesium bromide in a diethyl ether solution. Shortly after, in 1967, Kilbourn & Dunitz, and Bertrand published structures of almost identical copper-based clusters with pyridine and triphenylphosphine oxide ligands, respectively.^{165,166} A few examples of similar clusters containing Cr and Mn have been discovered since,¹⁶⁷⁻¹⁶⁹ however the vast majority of subsequent examples contain only

copper, presumably as a result of the coordinative flexibility of Cu which other metals do not possess.

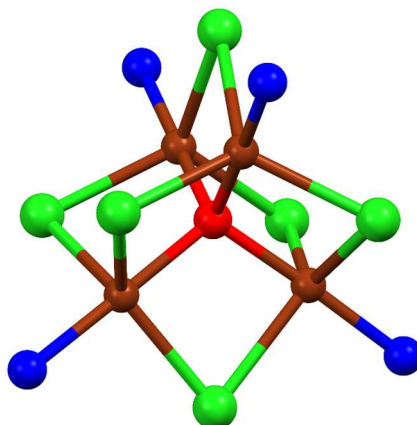


Figure 4.1 General structure of the $[\text{Cu}_4(\mu^4\text{-O})(\mu^2\text{-X})_6(\text{L})_4]$ cluster ($\text{X} = \text{Cl}, \text{Br}$). X atoms are shown in green, Cu in dark brown, O in red, and apical ligands (L) in blue.

The four apical ligands which bond to each cluster are directed in an approximate tetrahedral geometry, *i.e.* the cluster behaves as a super-tetrahedron. Combination of the cluster with a suitable multitopic ligand should give rise to frameworks through linking of tetrahedral nodes, *e.g.* a diamond-based network could be created through the use of linear linkages, and there is the possibility of substantial solvent-filled voids. Only one such compound, $[\text{Cu}_4(\mu^4\text{-O})(\mu^2\text{-Cl})_6(\text{DABCO})_4]_n$, has been created by Liu *et al.* with 1,4-diazabicyclo[2.2.2]octane (DABCO).¹⁷⁰ Our attempts to produce similar compounds using the same method as Liu *et al.* but with pyrazine and 4,4'-bipyridine have been unsuccessful. Discovering the reason for the inability to create the cluster complex with these pyridine-based ligands, and presumably similar ones, is considered paramount for using the cluster as a node to develop new porous materials.

An additional problem for use of this cluster complex is that it has not been produced in good yields without using an excess of one reagent or prolonged heating.¹⁷¹⁻¹⁷³ Three

general synthetic methods for the formation of clusters with an apical ligand (L), such as pyridine, are recorded currently: reaction of CuX_2 and CuO in the presence or followed by the addition of L,^{166,173} reaction of CuX_2 with L in the presence of a strong base *e.g.* NaOH , NaOMe *etc.*,^{165,174} and reaction of L with CuX_2 or CuX followed by oxidation by air/water.^{175,176} There are only several reported attempts to produce the cluster stoichiometrically although yields are not quite quantitative (*c* 75%) and require extensive heating in some cases.^{177–179} Based on these previous works, a novel synthetic method was theorised based on the decomposition of copper (I) halides. It is well known that copper (I) chloride and bromide oxidise quickly in certain conditions like heating while exposed to air. Additionally, a 1:1:2 mixture of CuX_2 , CuX and L contains the correct ratio of $\text{Cu}:\text{X}:\text{L}$ to produce the cluster stoichiometrically with atmospheric oxygen. Heating this ratio of components for a brief time in an appropriate solvent may produce the desired cluster readily.

The aims of the research discussed in this chapter were to establish the effectiveness of the new synthetic protocol, and to discover which ligands allow/disallow the formation of the cluster and why. Due to the amount of work already done on copper chloride compounds with pyridine-based ligands, chlorine was chosen as the halide for further work although there is no reason why the research discussed hence forth should be significantly different using bromine as the halide. Three potential ligands were chosen for testing the new method based on availability and similarity to ligands that have proved to create the clusters previously, these are 4-methylpyridine, 4-dimethylaminopyridine, and 4-aminopyridine, shown in Figure 4.2.

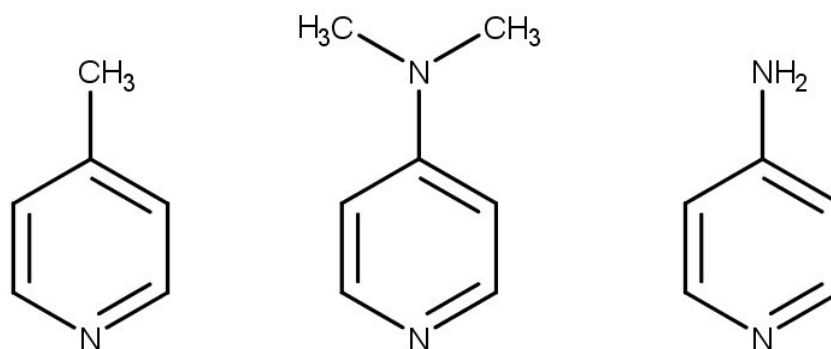


Figure 4.2 Molecular drawings of 4-methylpyridine (left), 4-dimethylaminopyridine (middle), and 4-aminopyridine (right).

4.1 Experimental procedures

All reagents and solvents were purchased from Sigma Aldrich, BDH or Fisher Scientific and used as received. Elemental Analyses were conducted by the Elemental Analysis Service, Department of Chemistry, University of Hull on a Fisons CHN Elemental Analyser (Thermo Scientific), type EA-1108. Cuprous chloride (CuCl) was synthesised by reduction of cupric chloride using sodium sulfite as described in the literature.¹⁸⁰ The new compounds developed in this piece of work are displayed in Table 4.1. The only other new compound discovered during this work was $[\text{CuCl}(\text{ClINAc})(\text{H}_2\text{O})_2]_n$ (**18**). The synthetic procedures for these compounds are discussed/detailed below.

Table 4.1 Products resulting from the reaction of 4-methylpyridine (4-MePy), dimethylaminopyridine (DMAP), and 4-aminopyridine (4-APy) with CuCl_2 , or CuCl_2 and CuCl . The solvated compounds listed are from recrystallisation. Newly discovered compounds are high in bold and starred.

	CuCl_2	$\text{CuCl}_2 + \text{CuCl}$
4-MePy	$[\text{CuCl}_2(4\text{-MePy})_2]_n$ (7)	* $[\text{Cu}_4(\mu^4\text{-O})(\mu^2\text{-Cl})_6(4\text{-MePy})_4]$ (8)
DMAP	$[\text{Cu}_2\text{Cl}_2(\mu^2\text{-Cl})_2(\text{DMAP})_4]$ (9)	* $[\text{Cu}_4(\mu^4\text{-O})(\mu^2\text{-Cl})_6(\text{DMAP})_4]$ (10) * $[\text{Cu}_4(\mu^4\text{-O})(\mu^2\text{-Cl})_6(\text{DMAP})_4] \cdot (\text{DMF})(\text{Toluene})$ (11)
4-APy	* $[\text{Cu}_2\text{Cl}_2(4\text{-APy})_2]_n$ (12)	* $[\text{Cu}_4(\mu^4\text{-O})(\mu^2\text{-Cl})_6(4\text{-APy})_4]$ (13) * $[\text{Cu}_4(\mu^4\text{-O})(\mu^2\text{-Cl})_6(4\text{-APy})_4] \cdot (\text{DMSO})_{5.33}(\text{H}_2\text{O})_{0.88}$ (14)

4.1.1 $[CuCl_2(4-APy)_2]_n$ (**12**)

4-APy (0.1882 g, 2 mmol) was dissolved in methanol (25 mL) with stirring and moderate heating, $CuCl_2 \cdot 2H_2O$ (0.1705 g, 1 mmol) was then added to the solution. Upon evaporation, green crystals of **12** grew along with some impure polycrystalline material.

4.1.2 $[Cu_4(\mu^4-O)(\mu^2-Cl)_6(RPy)_4]$

As stated in the introduction, the idea for the new synthetic method involved the reaction of a 1:1:2 mixture of CuX_2 , CuX , and L ($X = Cl, Br$; $L = RPy$ where $R = 4-Me, 4-NH_2,$ and $4-NMe_2$). Two methods were developed from this idea.

Method A - $CuCl_2$ (0.1705 g, 1 mmol) was dissolved in 25 mL MeOH to which RPy (2 mmol) was added with stirring. After addition of $CuCl$ (0.0990 g, 1 mmol) the mixture produced was heated at reflux and stirred for 30 minutes with exposure to air. **8**, **10**, and **13** were made in bulk using this method. This resulted in a brown precipitate of **8**, a bright orange precipitate of **10**, and a yellow-green precipitate of **13**. Elemental anal. (%) calcd for **8**: C, 33.70; H, 3.30; N, 6.55, found: C, 34.09; H, 3.69; N, 6.39; calcd for **10**: C, 34.61; H, 4.15; N, 11.53, found: C, 34.36; H, 4.29; N, 11.25; calcd for **13**: C, 27.95; H, 2.81; N, 13.04, found: C, 28.04; H, 2.96; N, 12.88. Exact quantities of the pyridine-based reagents used are displayed in Table 4.2.

Method B - $CuCl_2$ (0.0852 g, 0.5 mmol) was dissolved in 5 mL n-PrOH and added to a glass vial. This was layered sequentially with 10 mL of a 50/50 AcN/n-PrOH mixture, and 5 mL of an AcN solution of $CuCl$ (0.0495 g, 0.5 mmol) and RPy (1 mmol). The vessel was sealed and the layers were then allowed to diffuse creating precipitate/crystals of the desired compound. Alternatively, the two layers can be mixed instantaneously to afford

a precipitate without heating. Exact quantities of the pyridine-based reagents used are displayed in Table 4.2.

Crystals of **10** and **13** were made using the diffusion method B creating orange/yellow crystals respectively. On the other hand, crystals of **8** were made by adding 25 mL acetonitrile to the final methanolic mixture from method A described above. This afforded a brown solution which produced brown-yellow plate crystals of **8** upon evaporation.

Table 4.2 The quantities of reagents used in the synthesis of the $[\text{Cu}_4(\mu^4\text{-O})(\mu^2\text{-Cl})_6(\text{RPy})_4]$ complexes.

Reagent	Quantity	
	2 mmol	1 mmol
4-MePy	0.1863 g	0.0931 g
DMAP	0.2443 g	0.1222 g
4-APy	0.1882 g	0.0941 g

4.1.3 $[\text{Cu}_4(\mu^4\text{-O})(\mu^2\text{-Cl})_6(\text{RPy})_4]\cdot(\text{Solvate})$

The two solvated compounds, **11** and **14**, were made by recrystallisation. The bulk powder form of **10** (0.0972 g, 0.1 mmol) and **13** (0.0859 g, 0.1 mmol) were dissolved in a minimum quantity of DMF and DMSO respectively. The resulting orange/brown solutions were then layered with toluene which upon diffusion resulted in the precipitation of crystals of **11** and **14**. Elemental anal. (%): calcd for **11**: C, 40.15; H, 4.88; N, 11.09, found: C, 40.57; H, 4.74; N, 11.16; calcd for **14**: C, 28.51; H, 4.50; N, 8.67; S, 13.23, found: C, 28.66; H, 4.63; N, 8.64; S, 13.63.

4.1.4 $[\text{CuCl}(\text{ClINAc})(\text{H}_2\text{O})_2]_n$ (**18**)

CuCl (0.0495 g, 0.5 mmol) and 2-chloroisonicotinic acid (Cl-INAc, 0.1576 g, 1 mmol) were dissolved in 25 mL EtOH with heating and stirring. CuCl₂ (0.0852 g, 0.5 mmol) was added and stirring and heating was continued for approximately 30 minutes. 10-15 mL of

acetonitrile was added, and the resulting pale green solution was left to cool and evaporate resulting in pale blue-green crystals of **18**. Powder diffraction of the crystals revealed that the compound was either impure or degraded quickly in air so elemental analysis was not performed.

4.2 Crystal structure and refinement information

Crystal structures were solved and refined according to the standard procedure discussed in the experimental section, apart for the following exceptions. Due to the large unit-cells of **8** and **14** the scattering power was weak and data at high 2θ angle were essentially just noise and not used for the refinement of these structures. Data collected for **8** were cut to $50^\circ 2\theta$ while data collected for **14** were cut to $45^\circ 2\theta$. The torsion angles of the methyl groups in **8**, **10**, and **11** were determined from the electron density map. **10** was found to be non-centric, so additional data were collected to give a final Friedel coverage of 89.2%. Refinement of **10** gave a Flack parameter of 0.000(7) indicating that the absolute structure is correct. Residual electron density peaks in **12**, highest peak of $4.105 \text{ e}/\text{\AA}^3$ is 1.95 \AA away from Cu1, suggest that the structure is disordered or twinned. Modelling of the additional electron density peaks as a second component results in a refined occupancy of 6% with only a minor improvement in the quality of fit at the expense of doubling the number of parameters and resulting in a poor data to parameter ratio. Attempts to refine the structure with an appropriate twin law did not improve the fit either, but given that the structure is not grossly erroneous, and the relevant figures of merit are within acceptable limits the disorder has been left unresolved and the structure taken as is. Further details on the crystal structure refinements are contained in Table 4.3 and Table 4.4 below.

Table 4.3 Crystal structure data for compounds **8**, **10**, **11**, and **12**.

Compound	8	10	11	12
Empirical formula	C ₂₄ H ₂₈ Cl ₆ Cu ₄ N ₄ O	C ₂₈ H ₄₀ Cl ₆ Cu ₄ N ₈ O	C ₃₈ H ₅₅ Cl ₆ Cu ₄ N ₉ O ₂	C ₁₀ H ₁₂ Cl ₂ CuN ₄
Formula weight (g mol ⁻¹)	855.36	971.54	1136.77	322.68
Temperature (K)	150(1)	150(1)	150(1)	150(1)
λ (Å)	0.71073	0.71073	0.71073	0.71073
Crystal system	Triclinic	Triclinic	Triclinic	Monoclinic
Space group	$P\bar{1}$	$P1$	$P\bar{1}$	$P2_1/n$
a (Å)	18.9132(9)	10.3473(6)	9.6298(8)	9.0838(15)
b (Å)	19.3529(10)	13.7508(8)	14.9195(11)	3.9074(4)
c (Å)	20.2247(10)	14.0300(8)	16.9673(15)	17.005(3)
α (°)	78.381(4)	87.662(5)	87.417(7)	90
β (°)	64.631(4)	86.144(5)	81.473(7)	97.198(12)
γ (°)	80.362(4)	84.228(5)	81.192(6)	90
V (Å ³)	6524.2(6)	1980.5(2)	2381.7(3)	598.81(15)
Z	8	2	2	2
Density (Mg m ⁻³)	1.742	1.629	1.585	1.79
μ (mm ⁻¹)	3.089	2.557	2.141	2.25
Crystal size (mm)	0.26 × 0.25 × 0.09	0.19 × 0.17 × 0.07	0.34 × 0.15 × 0.07	0.38 × 0.04 × 0.04
Transmission factors (max/min)	0.7598 and 0.3052	0.7271 and 0.6117	0.8421 and 0.6071	0.9342 and 0.6146
$F(000)$	3408	980	1160	326
θ range (°)	1.669 - 25.000	1.982 - 29.252	1.818 - 29.294	2.414 - 29.147
Index ranges	-22 ≤ h ≤ 22 -21 ≤ k ≤ 23 -23 ≤ l ≤ 24	-14 ≤ h ≤ 14 -18 ≤ k ≤ 18 -19 ≤ l ≤ 19	-13 ≤ h ≤ 11 -20 ≤ k ≤ 20 -23 ≤ l ≤ 23	-9 ≤ h ≤ 12 -4 ≤ k ≤ 5 -23 ≤ l ≤ 23
Reflections collected	47702	63092	26684	3307
Independent reflections (R_{int})	22798 (0.1209)	20246 (0.0824)	12752 (0.0650)	1599 (0.0983)
Completeness to $\theta = 25.242^\circ$	99.3% (to 25.000°)	100.0%	99.6%	98.3%
Restraints/parameters	0/1421	3/863	0/543	0/79
Goodness-of-fit on F^2	0.897	0.807	0.805	0.869
$R_1 [I > 2\sigma(I)]$	0.0621	0.0311	0.0404	0.0748
wR_2 (all data)	0.1611	0.0563	0.0962	0.1978
Largest diff. peak and hole (e Å ⁻³)	1.549 and -1.006	0.729 and -0.298	0.850 and -1.298	4.106 and -0.795

Table 4.4 Crystal structure data for compounds **13**, **14**, and **18**.

Compound	13	14	18
Empirical formula	C ₂₀ H ₂₄ Cl ₆ Cu ₄ N ₈ O	C _{30.67} H _{57.74} Cl ₆ Cu ₄ N ₈ O _{7.22} S _{5.33}	C ₆ H ₇ Cl ₂ CuNO ₄
Formula weight (g mol ⁻¹)	859.33	1291.94	291.57
Temperature (K)	150(1)	150(1)	150(1)
λ (Å)	0.71073	0.71073	0.71073
Crystal system	Tetragonal	Tetragonal	Triclinic
Space group	$I4_1/a$	$I4_1/a$	$P\bar{1}$
a (Å)	15.8504(9)	42.4221(18)	5.7509(7)
b (Å)	15.8504(9)	42.4221(18)	8.5997(12)
c (Å)	12.1619(7)	27.6219(12)	10.4289(15)
α (°)	90	90	75.095(11)
β (°)	90	90	81.075(11)
γ (°)	90	90	73.695(10)
V (Å ³)	3055.5(4)	49709(5)	476.46(12)
Z	4	36	2
Density (Mg m ⁻³)	1.868	1.553	2.032

μ (mm ⁻¹)	3.302	2.056	2.837
Crystal size (mm)	0.52 × 0.29 × 0.23	0.34 × 0.25 × 0.12	0.34 × 0.15 × 0.13
Transmission factors (max/min)	0.6469 and 0.3449	0.8016 and 0.4357	0.7239 and 0.4461
$F(000)$	1704	22504	290
θ range (°)	2.111 - 29.159	1.618 - 22.500	2.029 - 29.178
Index ranges	-14 ≤ h ≤ 21	-45 ≤ h ≤ 35	-7 ≤ h ≤ 7
	-21 ≤ k ≤ 21	-44 ≤ k ≤ 45	-9 ≤ k ≤ 11
	-11 ≤ l ≤ 16	-28 ≤ l ≤ 29	-14 ≤ l ≤ 14
Reflections collected	8467	57787	4873
Independent reflections (R_{int})	2068 (0.0888)	16254 (0.1427)	2521 (0.1140)
Completeness to $\theta = 25.242^\circ$	99.8%	99.9% (to 22.500°)	98.7%
Restraints/parameters	0/94	0/991	6/147
Goodness-of-fit on F^2	0.987	0.884	0.909
$R_1 [I > 2\sigma(I)]$	0.0377	0.1079	0.0456
wR_2 (all data)	0.1051	0.3298	0.1236
Largest diff. peak and hole (e Å ⁻³)	1.656 and -1.039	1.549 and -1.006	1.066 and -1.395

4.3 4-Methylpyridine

4.3.1 Summary of Reactions

The 4-methylpyridine (4-MePy) cluster was produced using method A. The blue precipitate which developed upon addition of methylpyridine to the methanolic cupric chloride solution was not isolated during synthesis, but it is almost certainly $[\text{CuCl}_2(4\text{-MePy})_2]_n$ (**7**) as this procedure is similar to the method used to produce this compound in the literature.¹³⁵ After addition of cuprous chloride, this quickly converted into a brown precipitate of $[\text{Cu}_4(\mu^4\text{-O})(\mu^2\text{-Cl})_6(4\text{-MePy})_4]$ (**8**). The structures of **7** and **8** are described on the following pages.

4.3.2 $[\text{CuCl}_2(4\text{-MePy})_2]_n$ (**7**)

The copper chloride, 4-MePy adduct is part of the family of $[\text{CuX}_2(\text{RPy})_2]_n$ compounds. This compound was discovered by Marsh *et al.*¹³⁵ and displays the same general structure as many of the other members of this family: a linear chain of edge-sharing CuCl_4 rhombi decorated above and below the plane with the pyridine-based ligand, as shown in Figure

4.3. The structural features of this compound are unremarkable. The orientation of the copper chloride chains is most likely a result of weak intermolecular forces, such as C-H \cdots Cl hydrogen bonding interactions or dipole-dipole forces. The copper coordination environment is distorted octahedral, although the long Cu-Cl contact, shown along side other bond distance and angle data in Table 4.5, is too long to be considered a formal coordination bond and must be significantly weaker than a normal Cu-Cl bond. This will become important in later discussions.

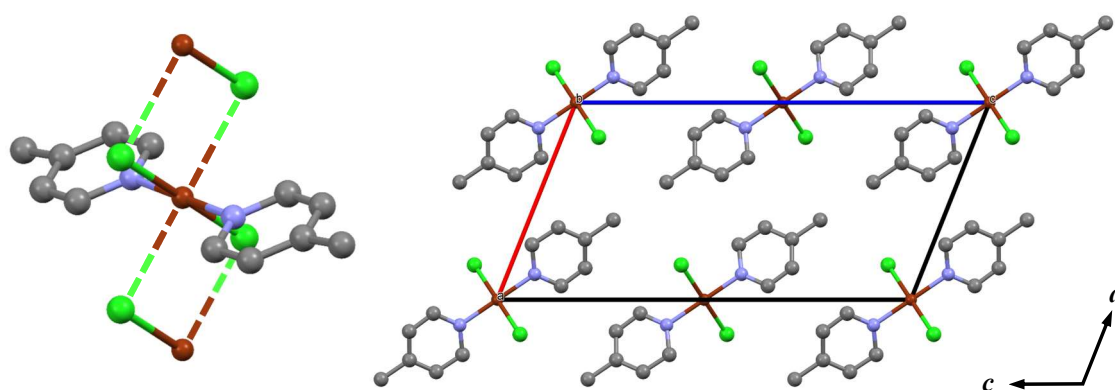


Figure 4.3 The structure of $[\text{CuCl}_2(4\text{-MePy})_2]_n$ (**7**), showing the CuCl_2 chain that extends along the b axis (left), and the overall packing (right).¹³⁵ Long Cu-Cl contacts are drawn as dashed lines as their length might indicate the absence of a formal bond. C atoms are shown in grey, Cl in green, Cu in dark brown, and N in light grey-blue.

Table 4.5 Selected bond lengths (Å) and angles ($^\circ$) around the Cu coordination centre for $[\text{CuCl}_2(4\text{-MePy})_2]_n$ (**7**).¹³⁵

Cu(1) – Cl(1)	2.352(4)	N(1)-Cu(1)-Cl(1)	89.16(4)
Cu(1) – Cl(1)#1	3.189(4)	N(1)-Cu(1)-Cl(1)#1	89.91(3)
Cu(1) – N(1)	2.081(3)	Cl(1)-Cu(1)-Cl(1)#1	89.08(2)

#1 1 + x, y, z

4.3.3 $[\text{Cu}_4(\mu^4\text{-O})(\mu^2\text{-Cl})_6(4\text{-MePy})_4]$ (**8**)

Single-crystal X-ray diffraction showed that the brown crystals of $[\text{Cu}_4(\mu^4\text{-O})(\mu^2\text{-Cl})_6(4\text{-MePy})_4]$ (**8**) displayed a centrosymmetric triclinic unit-cell. The cell volume, $6524.2(6) \text{ \AA}^3$, equates to an asymmetric unit consisting of four molecules of the complex, as confirmed by structure solution and refinement ($R_1 = 0.0621$, $wR_2 = 0.1611$), further crystallographic details are included in Table 4.3. The four symmetry independent molecules are shown separately in Figure 4.4 (although for clarity, not in the spatial arrangement within the crystal structure). Each conforms to the general description of $[\text{Cu}_4(\mu^4\text{-O})(\mu^2\text{-X})_6(\text{L})_4]$ structures given in the introduction. As the asymmetric unit contains so many molecules, the bond distance and angle data have been summarised in Table 4.6. These data show that the oxygen-centred, Cu_4 tetrahedron is relatively undistorted with Cu-O-Cu angles close to the ideal tetrahedral angle of $\approx 109.5^\circ$, however it is not uncommon for complexes of this type to show more deviation in the Cl-Cu-Cl and O-Cu-N angles away from an ideal trigonal bipyramidal geometry.^{173,181} The Cl-Cu-Cl bond angles vary far from 120° in some cases, additionally, what should be a linear arrangement of O-Cu-N has an average angle of $176(2)^\circ$. These two facts indicate a distortion towards a square-pyramidal geometry, a very common one for Cu to exhibit, in which the O, N and two Cl atoms would compose the square plane.

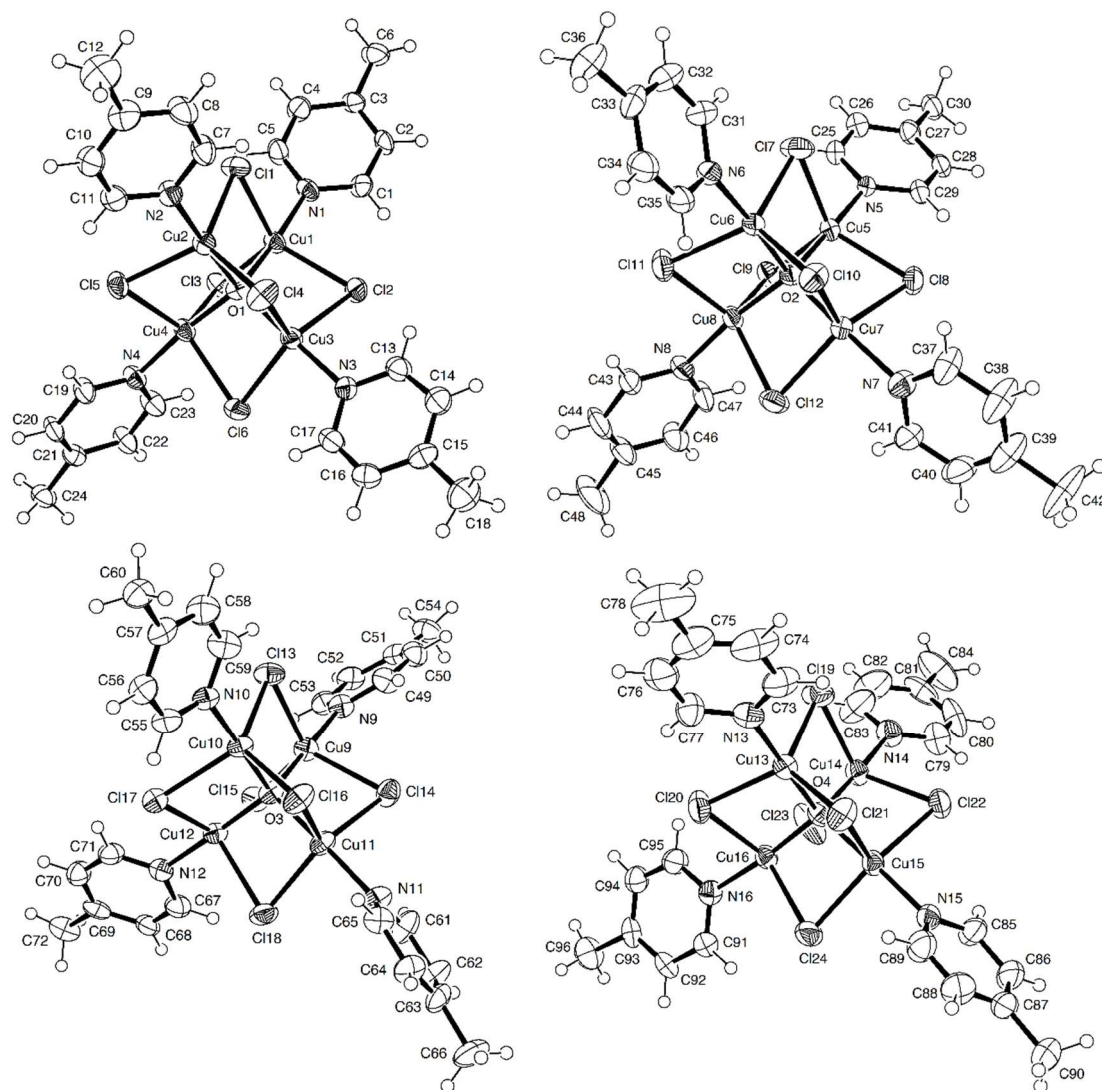


Figure 4.4 Asymmetric unit of $[\text{Cu}_4(\mu^4\text{-O})(\mu^2\text{-Cl})_6(4\text{-MePy})_4]$ (**8**) with atoms shown as thermal ellipsoids drawn at 50% probability. Symmetry independent molecules are drawn separately for clarity.

Table 4.6 Data on the bond lengths (Å) and angles (°) around the Cu coordination centres for $[\text{Cu}_4(\mu^4\text{-O})(\mu^2\text{-Cl})_6(4\text{-MePy})_4]$ (**8**).

Identity	Maximum	Minimum	Average	Median	Range
Cu – O	1.9140(5)	1.8969(5)	1.907(6)	1.9054	0.0171
Cu – N	1.988(6)	1.951(6)	1.971(11)	1.971	0.037
Cu – Cl	2.526(2)	2.359(2)	2.41(3)	2.4097	0.167
Cu – O – Cu	111.0(2)	106.9(2)	109.4(9)	109.6	4.1
O – Cu – Cl	86.7(2)	82.6(2)	84.8(9)	84.9	4.2
O – Cu – N	179.5(2)	173.3(2)	176(2)	175.7	6.2
N – Cu – Cl	101.9(2)	89.5(2)	95(3)	95.3	12.4
Cl – Cu – Cl	141.98(1)	105.82(9)	119(7)	118.85	36.16

The crystal packing of **8**, shown in Figure 4.5, is dictated entirely by weak van der Waals' interactions. There is very little evidence for the presence of any π - π stacking interactions. This is most likely due to the tetrahedral arrangement of the pyridine rings around the complex; if strong π - π interactions were present then the tetrahedral arrangement would result in a less densely packed structure which is energetically unfavourable in comparison to the adopted structure.

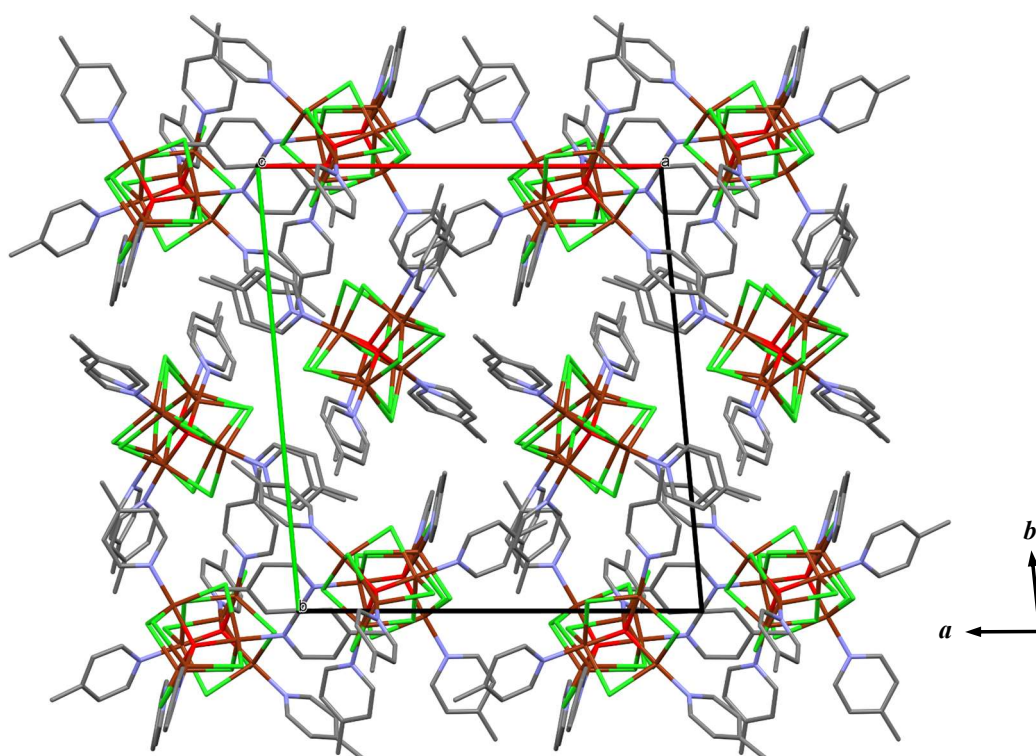


Figure 4.5 Diagram of the overall crystal packing in $[\text{Cu}_4(\mu^4\text{-O})(\mu^2\text{-Cl})_6(4\text{-MePy})_4]$ (**8**). Hydrogen atoms are omitted for clarity. C atoms are shown in grey, Cl in green, Cu in dark brown, N in light grey-blue, and O in red.

Although the crystals of **8** were produced from an acetonitrile/methanol solution, neither solvent was incorporated into the product. X-ray powder diffraction of the brown powder produced in only methanol matched the diffraction pattern simulated from the single-crystal structure, as shown in Figure 4.6. No additional peaks were observed in the experimental diffraction pattern indicating a pure product, and elemental analysis

confirms the purity. Additionally, the simulated X-ray diffraction pattern could be made to match the room-temperature experimental data by simple refinement of the cell parameters of the single-crystal structure to account for thermal expansion. This shows that the complicated structure ($Z' = 4$) described above persists even at room temperature.

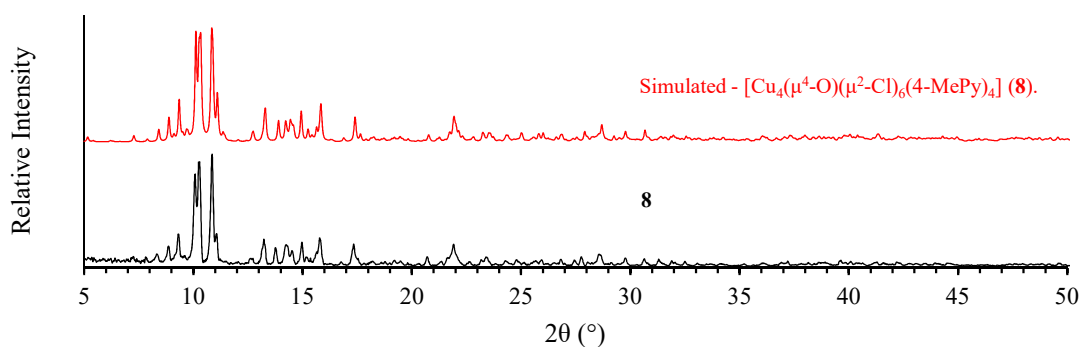


Figure 4.6 Room temperature X-ray powder diffraction data for **8**. Experimental data are shown in black while simulated data are shown in red.

4.4 4-Dimethylaminopyridine

4.4.1 Summary of Reactions

The 4-dimethylaminopyridine (DMAP) cluster was first produced using method A. Upon addition of DMAP to the methanolic cupric chloride solution, a brown-yellow precipitate in a green solution developed. The green solution is suspected to be dissolved $[\text{Cu}_2\text{Cl}_2(\mu^2\text{-Cl})_2(\text{DMAP})_4]$ (**9**) (discussed below) or some similar compound,¹⁸² however crystallisation of the green solution by evaporation was not attempted. After the addition of cuprous chloride, the supernatant became colourless, and more of the brown-yellow precipitate developed but did not dissolve upon addition of acetonitrile so was collected by filtration. The X-ray powder diffraction pattern of the solid could be indexed with a triclinic unit-cell. A Pawley refinement was conducted using the candidate cell producing a good fit to the observed data ($R_{\text{wp}} = 0.1271$, $\chi^2 = 1.753$), as shown in Figure 4.7.

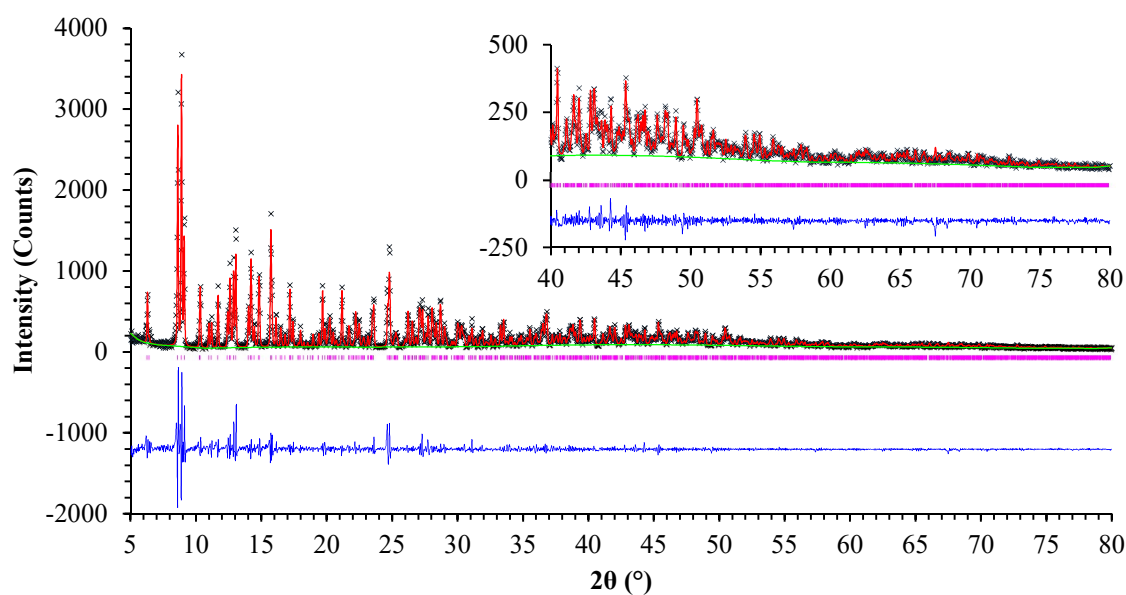


Figure 4.7 A plot of the Pawley refinement of the proposed cell for $[\text{Cu}_4(\mu^4\text{-O})(\mu^2\text{-Cl})_6(\text{DMAP})_4]$ (**10**). Black crosses represent observed data, the red line calculated data, the green line background, the pink markers peak positions, and the blue line is the difference plot $[(I_{\text{obs}} - I_{\text{calc}})]$.

The unit-cell volume of approximately 2000 \AA^3 equated to a total content of two molecules of the cluster complex with no solvent of crystallisation. This prompted the successful crystallisation of $[\text{Cu}_4(\mu^4\text{-O})(\mu^2\text{-Cl})_6(\text{DMAP})_4]$ (**10**) by method B, and the predicted structure was confirmed by single-crystal X-ray diffraction. Additionally, the simulated powder X-ray diffraction pattern of **10** matched that of the powder produced initially. Solubility experiments showed that **10** was soluble in dichloromethane, dimethylformamide (DMF), and dimethyl sulfoxide (DMSO), slightly soluble in acetone, and insoluble in methanol, acetonitrile, and toluene. The complex, $[\text{Cu}_4(\mu^4\text{-O})(\mu^2\text{-Cl})_6(\text{DMAP})_4]$, has been discovered previously as part of a piece of work into the catalysis of aerobic oxidation of alcohols, and has been shown to be catalytically active.¹⁸³ In that work, the dichloromethane solvate of **10** was discovered which displays pores filled with the guest molecules. The potential to form clathrates with large, solvent-filled pores is also of interest in gas adsorption applications, so to explore this property further solutions of the complex in DMF and DMSO were layered with methanol, acetonitrile and toluene

to induce precipitation. Only the DMF/toluene experiment produced a crystals/precipitate to analyse, although it is suspected that the other experiments only needed more of the anti-solvent in order to work. The compound, $[\text{Cu}_4(\mu^4\text{-O})(\mu^2\text{-Cl})_6(4\text{-DMAP})_4]\cdot(\text{DMF})(\text{Toluene})$ (**11**), displays small pores filled with a 1:1 mixture of DMF and toluene and is described in more detail below with a comparison to the similar structure of **10**.

4.4.2 $[\text{Cu}_2\text{Cl}_4(\text{DMAP})_4]$ (**9**)

The complex formed by reaction of cupric chloride with DMAP in acetonitrile was reported recently by Liu *et al.*¹⁸² This compound, $[\text{Cu}_2\text{Cl}_2(\mu^2\text{-Cl})_2(\text{DMAP})_4]$ (**9**), is similar to the $[\text{CuX}_2(\text{RPy})_2]_n$ family of compounds, although the Cu coordination has square pyramidal geometry for which bond lengths and angles are shown in Table 4.7. Rather than comprising a chain of $[\text{CuX}_2(\text{RPy})_2]$ monomers connected by short or long Cu-Cl contacts, **9** consists of dimers of those monomeric units as discrete molecules, shown in Figure 4.8. The shortest Cu-Cl distance between the dimer molecules is around 7 Å therefore proving **9** to be a discrete complex which will become important later.

Table 4.7 Selected bond lengths (Å) and angles (°) around the Cu coordination centre for $[\text{Cu}_2\text{Cl}_4(\text{DMAP})_4]$ (**9**).¹⁸²

Cu(1) – Cl(2)	2.3027(6)	Cu(1) – N(1)	1.9943(14)
Cu(1) – Cl(1)#1	2.7396(5)	Cu(1) – N(2)	1.9932(14)
N(1)-Cu(1)-Cl(1)	89.36(4)	N(2)-Cu(1)-Cl(2)	89.72(5)
N(1)-Cu(1)-Cl(2)	90.77(5)	N(2)-Cu(1)-Cl(1)#1	93.26(4)
N(1)-Cu(1)-Cl(1)#1	91.62(4)	Cl(1)-Cu(1)-Cl(1)#1	95.87(2)
N(1)-Cu(1)-N(2)	174.95(6)	Cl(1)-Cu(1)-Cl(2)	164.36(2)
N(2)-Cu(1)-Cl(1)	88.82(4)	Cl(2)-Cu(1)-Cl(1)#1	99.76(2)

#1 1 – x, 1 – y, 1 – z

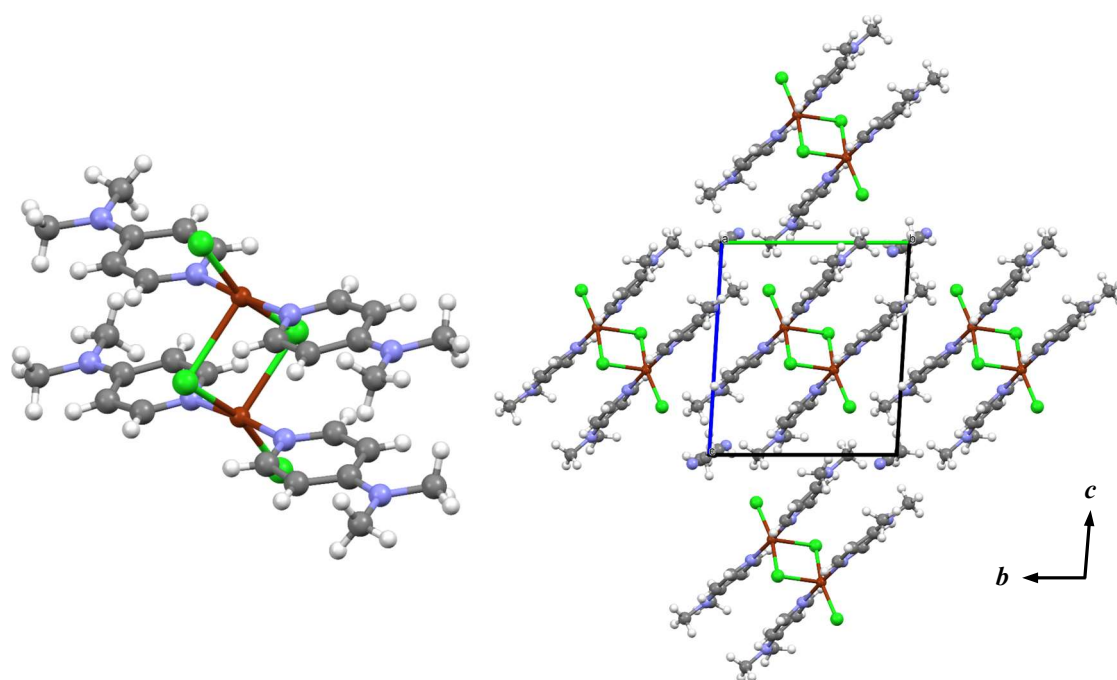


Figure 4.8 The structure of $[\text{Cu}_2\text{Cl}_4(\text{DMAP})_4]$ (**9**), showing a singular molecule of the compound (left), and how they pack to create the crystal structure (right).¹⁸² C atoms are shown in grey, H in white, Cl in green, Cu in dark brown, and N in light grey-blue.

The complexes in **9** stack in the $[011]$ direction. The similar orientations of the complexes and ligands indicates that π - π stacking interactions between the DMAP molecules is important in the crystal packing. The gaps in the structure have a solvent accessible volume of 96 \AA^3 or 11% and are filled with acetonitrile solvent.

4.4.3 $[\text{Cu}_4(\mu^4\text{-O})(\mu^2\text{-Cl})_6(\text{DMAP})_4]$ (**10/11**)

The non-solvated and solvated structures of the DMAP supertetrahedral cluster are similar so shall be discussed together. The non-solvated structure of $[\text{Cu}_4(\mu^4\text{-O})(\mu^2\text{-Cl})_6(4\text{-DMAP})_4]$ (**10**) has a non-centrosymmetric, triclinic unit-cell. The model provides an excellent fit to the observed data ($R_1 = 0.0311$, $wR_2 = 0.0563$), further crystallographic details are included in Table 4.3. The volume, $1980.5(2) \text{ \AA}^3$, is equivalent to two molecules of the cluster complex which compose the asymmetric unit of the structure, as shown in Figure 4.9.

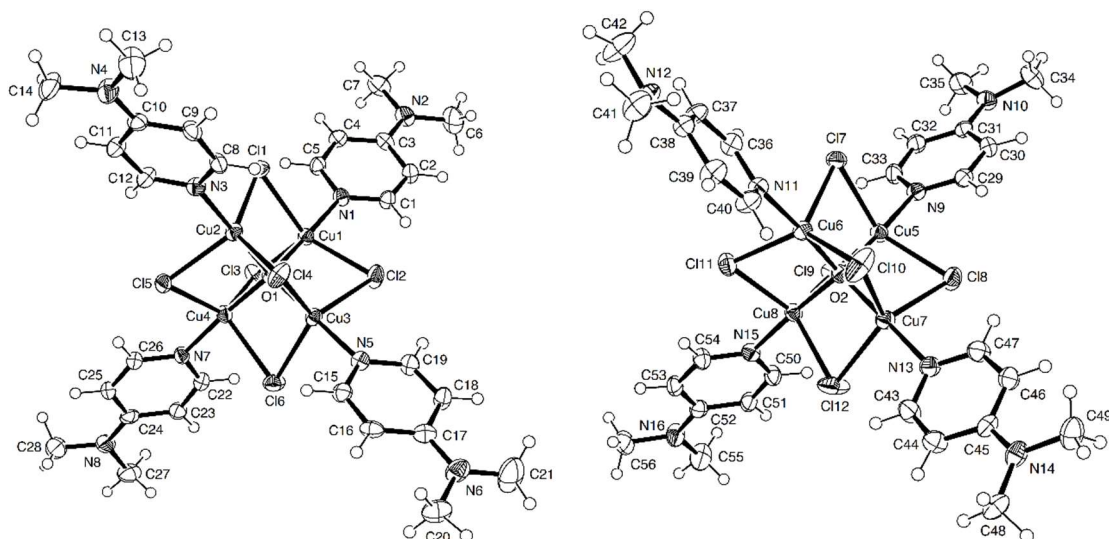


Figure 4.9 Asymmetric unit of $[\text{Cu}_4(\mu^4\text{-O})(\mu^2\text{-Cl})_6(\text{DMAP})_4]$ (**10**) with atoms shown as thermal ellipsoids drawn at 50% probability. Symmetry independent molecules are drawn separately for clarity.

The dimethylformamide (DMF) and toluene solvated structure, $[\text{Cu}_4(\mu^4\text{-O})(\mu^2\text{-Cl})_6(\text{DMAP})_4] \cdot (\text{DMF})(\text{Toluene})$ (**11**), is also triclinic. A good fit to the experimental data was obtained following refinement of the initial structure solution ($R_1 = 0.0404$, $wR_2 = 0.0962$), further crystallographic details are included in Table 4.3. Unlike **10**, the structure possesses a centre of symmetry and therefore the asymmetric unit contains only one cluster molecule in addition to molecules of DMF and toluene, as shown in Figure 4.10.

Due to the number of unique coordination bonds, bond length and angle data have been summarised in Table 4.8 and Table 4.9 for **10** and **11** respectively. The cluster complexes in **10** and **11** are distorted in a similar way to that in **8** and other compounds; the central $\text{Cu}_4(\mu^4\text{-O})$ unit is relatively undistorted compared to the ideal geometry, however the halide and apical ligands deviate much more from a true trigonal bipyramidal arrangement.

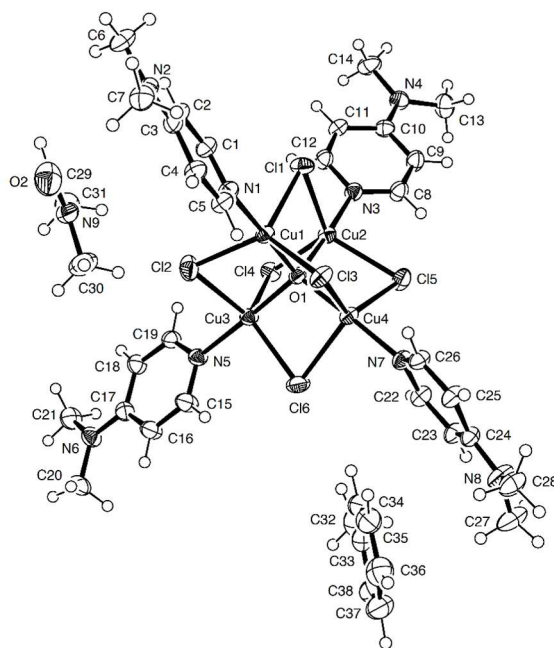


Figure 4.10 Asymmetric unit of $[\text{Cu}_4(\mu^4\text{-O})(\mu^2\text{-Cl})_6(\text{DMAP})_4]\cdot(\text{DMF})(\text{Toluene})$ (**11**) with atoms shown as thermal ellipsoids drawn at 50% probability.

Table 4.8 Selected bond lengths (Å) and angles (°) around the Cu coordination centre for $[\text{Cu}_4(\mu^4\text{-O})(\mu^2\text{-Cl})_6(\text{DMAP})_4]$ (**10**).

Identity	Maximum	Minimum	Average	Median	Range
Cu – O	1.922(3)	1.906(3)	1.914(6)	1.915	0.016
Cu – N	1.978(4)	1.963(4)	1.969(6)	1.968	0.015
Cu – Cl	2.4787(13)	2.3601(12)	2.42(4)	2.4149	0.1186
Cu – O – Cu	110.64(15)	107.75(15)	109.5(9)	109.44	2.89
O – Cu – Cl	86.95(10)	83.36(10)	84.7(10)	84.69	3.59
O – Cu – N	179.35(15)	174.45(16)	177.4(17)	177.66	4.90
N – Cu – Cl	98.81(12)	91.37(13)	95(2)	95.07	7.44
Cl – Cu – Cl	133.59(6)	106.02(5)	119(7)	118.87	27.57

Table 4.9 Selected bond lengths (Å) and angles (°) around the Cu coordination centre for $[\text{Cu}_4(\mu^4\text{-O})(\mu^2\text{-Cl})_6(\text{DMAP})_4]\cdot(\text{DMF})(\text{Toluene})$ (**11**).

Identity	Maximum	Minimum	Average	Median	Range
Cu – O	1.916(2)	1.907(2)	1.912(4)	1.913	0.009
Cu – N	1.973(3)	1.957(3)	1.965(8)	1.9645	0.016
Cu – Cl	2.4550(11)	2.3678(10)	2.42(3)	2.4205	0.0872
Cu – O – Cu	111.48(12)	107.69(11)	109.5(14)	109.6	3.79
O – Cu – Cl	86.62(8)	83.07(7)	87.9(11)	84.91	3.55
O – Cu – N	176.79(10)	178.46(11)	177.6(7)	177.56	1.67
N – Cu – Cl	98.68(9)	92.11(9)	95(2)	95.19	6.57
Cl – Cu – Cl	128.35(5)	108.49(4)	119(6)	118.78	19.86

The relative positions of the complexes in each structure are similar when viewed along *a*, each one displaying a characteristic checkerboard arrangement, as shown in Figure 4.11 and Figure 4.12. The orientation of adjacent molecules in **10** suggests there are no strong intermolecular forces dictating the packing, similar to the structure of **8**. However, the presence of solvent molecules in **11** allows π - π stacking interactions to occur for the ligands containing N1 and N5 with centroid distances of 3.843(3) Å and 3.760 Å respectively. The arrangement creates pores along *a* with a solvent accessible volume of 647 Å³ or 27% of the total volume filled with the guest molecules. A similar observation can be made about the structure of the dichloromethane solvate of the same compound discovered by Zhang *et al.*¹⁸³ However, the solvent channels in that compound occur along *c*, and the interactions between the solvent molecules and cluster complexes are unknown as the atoms constituting the solvent have not been refined. The solvent molecules in **11** are aligned to be almost parallel with the DMAP molecules. These may facilitate or even take part in the π interactions between the DMAP ligands giving rise to the observed structure.

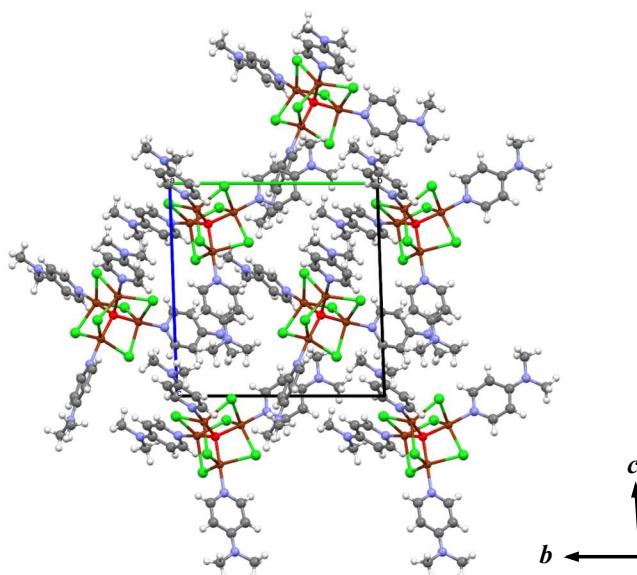


Figure 4.11 Diagram of the overall crystal packing in $[\text{Cu}_4(\mu^4\text{-O})(\mu^2\text{-Cl})_6(\text{DMAP})_4]$ (**10**). C atoms are shown in grey, Cl in green, Cu in dark brown, N in light grey-blue, and O in red.

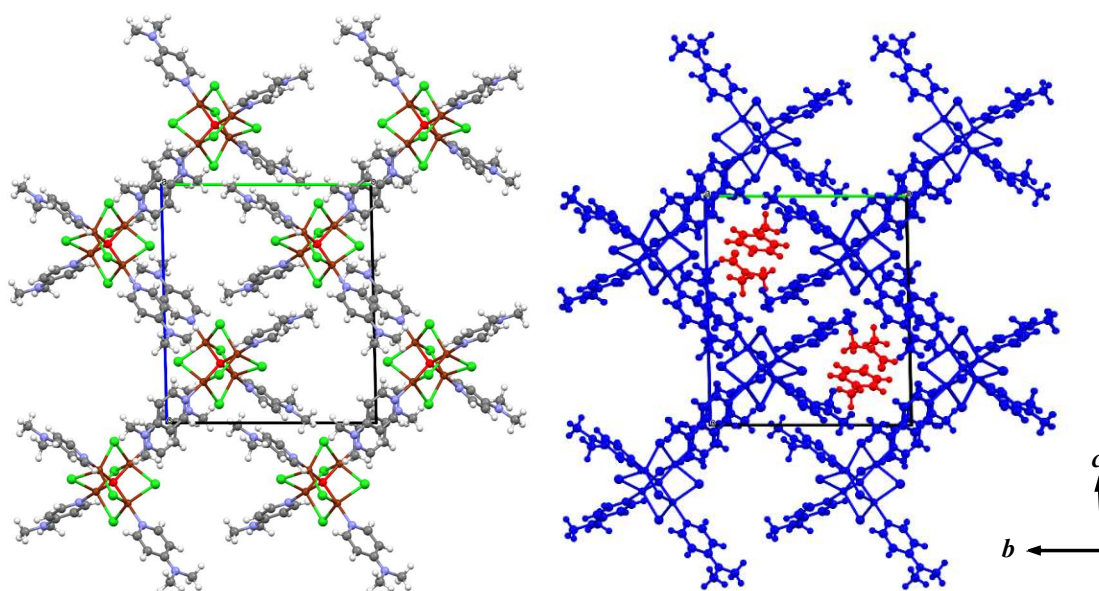


Figure 4.12 Diagrams of the overall crystal packing in $[\text{Cu}_4(\mu^4\text{-O})(\mu^2\text{-Cl})_6(\text{DMAP})_4]\cdot(\text{DMF})(\text{Toluene})$ (**11**). C atoms are shown in grey, Cl in green, Cu in dark brown, N in light grey-blue, and O in red (left). Coordination complexes are shown in blue and solvent molecules in red (right).

X-ray powder diffraction patterns of the brown powders of **10** and **11** matched the diffraction pattern simulated from the single-crystal structures, as shown in Figure 4.13. No additional peaks were observed in the experimental diffraction patterns indicating pure products were obtained, being confirmed by elemental analysis.

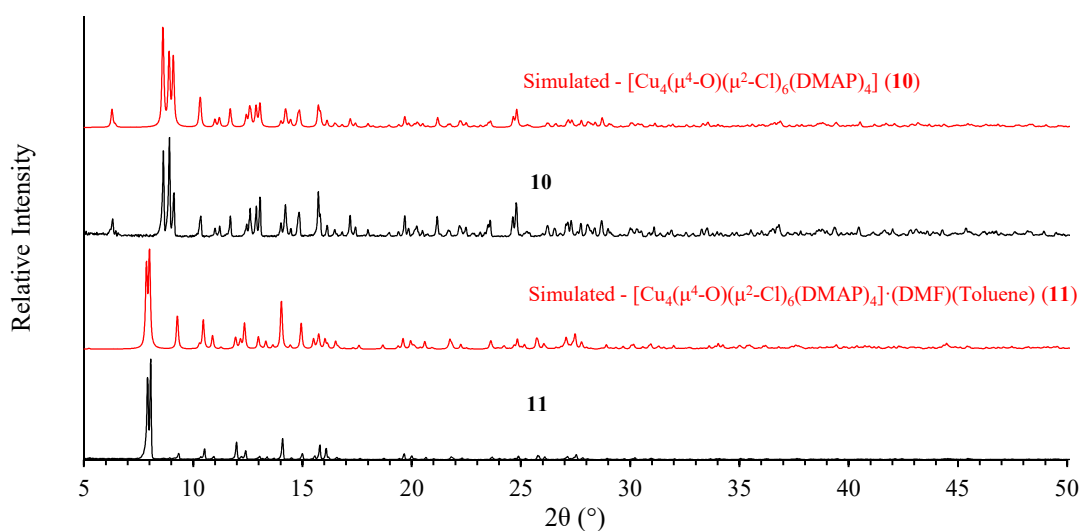


Figure 4.13 Room temperature X-ray powder diffraction data for $[\text{Cu}_4(\mu^4\text{-O})(\mu^2\text{-Cl})_6(\text{DMAP})_4]$ (**10**) and $[\text{Cu}_4(\mu^4\text{-O})(\mu^2\text{-Cl})_6(\text{DMAP})_4]\cdot(\text{DMF})(\text{Toluene})$ (**11**). Experimental data are shown in black while simulated data are shown in red.

4.5 4-Aminopyridine

4.5.1 Summary of Reactions

The 4-aminopyridine (4-APy) cluster, like in the previous two cases, was produced first using method A. The addition of 4-APy to the cupric chloride solution caused the production of a green precipitate, discoloured slightly yellow in a green solution. The green solution is almost certainly a dissolved form of $[\text{Cu}_2\text{Cl}_2(4\text{-APy})_2]_n$ (**12**) as evaporation of the green solution yields crystals of this complex. The green precipitate transforms into a yellow-green precipitate on addition of cuprous chloride, although it partially transforms without intervention. Similar to **10**, the yellow-green powder did not dissolve upon addition of acetonitrile so was collected and analysed by X-ray powder diffraction. The X-ray powder diffraction pattern of the solid was indexed with a tetragonal unit-cell. Pawley refinement of the candidate cell was conducted producing a good fit to the observed data ($R_{\text{wp}} = 0.1279$, $\chi^2 = 2.189$), as shown in Figure 4.14.

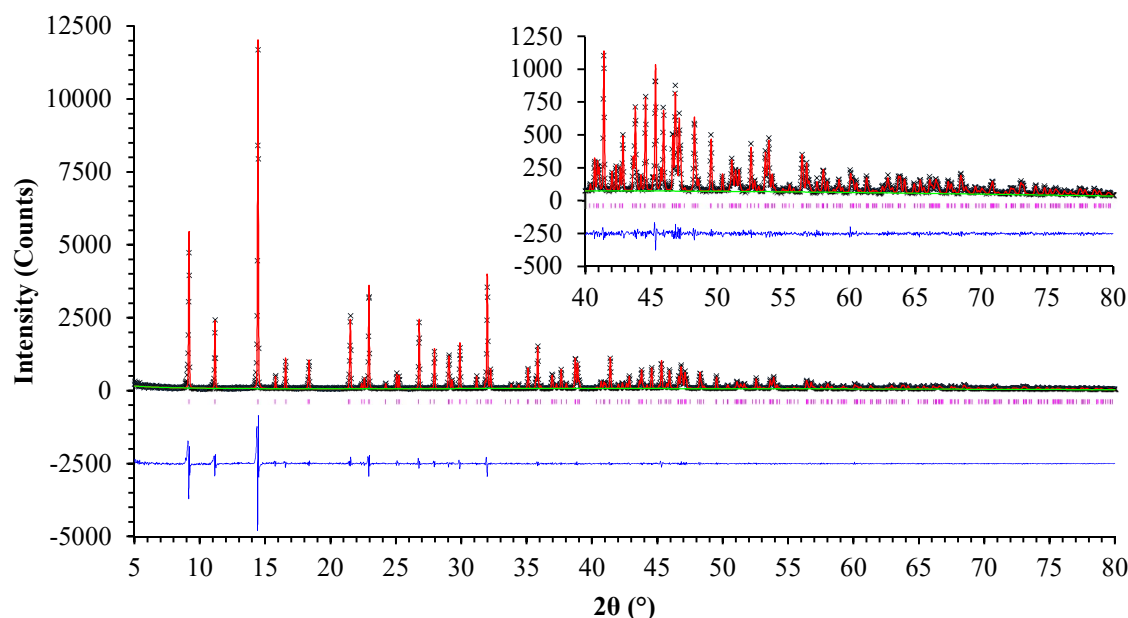


Figure 4.14 A plot of the Pawley refinement of the proposed cell for $[\text{Cu}_4(\mu^4\text{-O})(\mu^2\text{-Cl})_6(4\text{-APy})_4]$ (**13**). Black crosses represent observed data, the red line calculated data, the green line background, the pink markers peak positions, and the blue line is the difference plot $[(I_{\text{obs}} - I_{\text{calc}})]$.

The unit-cell volume of approximately 3000 Å³ is equivalent to a total cell contents of four molecules of [Cu₄(μ⁴-O)(μ²-Cl)₆(4-APy)₄] with no solvent guest molecules. The diffusion reaction used to successfully crystallise **10** was therefore attempted, resulting in the formation of yellow crystals of [Cu₄(μ⁴-O)(μ²-Cl)₆(4-APy)₄] (**13**). The simulated diffraction pattern of **13** matched the experimental diffraction pattern obtained from the earlier yellow-green precipitate confirming the solid to be pure **13**. The compound was only found to be soluble in dimethyl sulfoxide (DMSO) and dimethylformamide (DMF) in the range of solvents tested, and insoluble in everything else. The formation of structures containing guest molecules with many of the cluster based complexes prompted an investigation of the ability for **13** to produce solvated structures.^{183–185} Similar to the study conducted with the DMAP complex, solutions of **13** in DMF and DMSO were layered with methanol, acetonitrile and toluene to induce precipitation. Only the DMSO/toluene experiment produced a crystalline substance to analyse, although as with **10** it is likely that the reaction only required more anti-solvent. The brown crystals produced were found to be [Cu₄(μ⁴-O)(μ²-Cl)₆(4-APy)₄]·(DMSO)_{5.33}(H₂O)_{0.88} (**14**), although the exact solvent composition is not completely certain as disorder of the guest species made their identification difficult. **14** shows remarkable structural similarities to **13**. These compounds are discussed in more detail below including a structural description of the cupric chloride compound **12**.

4.5.2 [CuCl₂(4-APy)₂]_n (**12**)

The previously undiscovered cupric chloride compound of 4-APy, [Cu₂Cl₂(4-APy)₂]_n (**12**), displays a monoclinic unit-cell with space group *P*2₁/*n*. A second set of atoms in the Fourier difference map was observed but modelling this as disorder or with a twin rule did not improve the quality of the model so was left unresolved. Despite this, the model

gave a relatively good fit to the observed data ($R_1 = 0.0748$, $wR_2 = 0.1978$), further crystallographic details are included in Table 4.3. The asymmetric unit contains one chloride ion, a neutral 4-APy molecule, and a copper ion located on the 2d Wyckoff position, as shown in Figure 4.15. The Cu has a 4+2 coordination geometry, bond distances and angles are shown in Table 4.10.

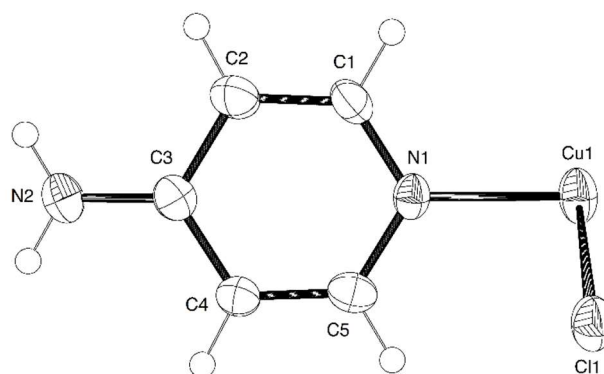


Figure 4.15 Asymmetric unit of $[\text{CuCl}_2(4\text{-APy})_2]_n$ (**12**) with atoms shown as thermal ellipsoids drawn at 50% probability.

Table 4.10 Selected bond lengths (\AA) and angles ($^\circ$) around the Cu coordination centre for $[\text{CuCl}_2(4\text{-APy})_2]_n$ (**12**).

Cu(1) – Cl(1)	2.334(2)	N(1)-Cu(1)-Cl(1)	90.6(2)
Cu(1) – Cl(1)#1	3.305(2)	N(1)-Cu(1)-Cl(1)#1	88.8(2)
Cu(1) – N(1)	1.968(6)	Cl(1)-Cu(1)-Cl(1)#1	85.9(1)

#1 $x, 1 + y, z$

The overall structure conforms to that presented by many of the $[\text{CuX}_2(\text{RPy})_2]_n$ family of compounds, as shown in Figure 4.16. The $[\text{CuX}_2(\text{RPy})_2]$ monomeric units align themselves in a chain along b , although the distance between Cu and Cl atoms of adjacent $[\text{CuCl}_2(4\text{-APy})_2]$ units is too great to suggest a formal bond between them, it is more likely a weak contact. The amine groups on the 4-APy ligands form hydrogen bonds to nearby chloride ions ($\text{N}\cdots\text{Cl}$ 3.532(6) \AA and 3.563(7) \AA). These hydrogen bonds produce a $C_2^1(4)$ motif which propagates along b in spiral configuration due to the symmetry relationship between chains on the $(\bar{1}03)$ crystallographic plane (2-fold rotation). The

coordination and hydrogen bonds combine to create a 3-D supramolecular framework. Potential reasons for the increased length of the long $\text{Cu}\cdots\text{Cl}$ contact are discussed later. Attempts to produce pure samples of **12** were unsuccessful. Additional, unexpected peaks were observed in the experimental X-ray powder diffraction patterns which were not in the simulated data, as shown in Figure 4.17. The additional peaks could not be identified at the time of synthesis of **12**. No method has yet been found to produce pure samples of the complex.

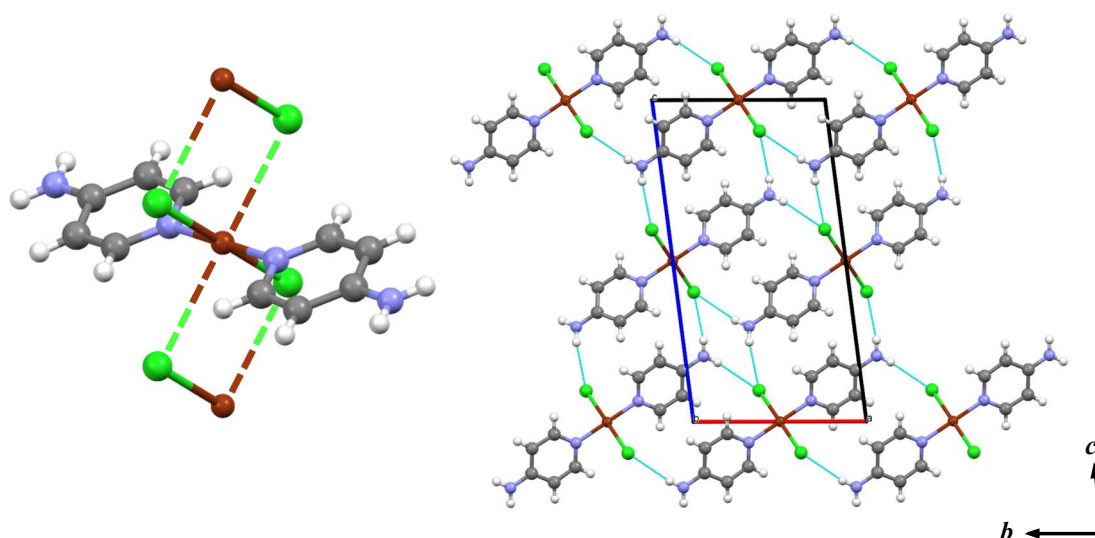


Figure 4.16 The structure of $[\text{CuCl}_2(4\text{-APy})_2]_n$ (**12**), showing the CuCl_2 chain that extends along the b axis (left), and the overall packing (right). Long Cu-Cl contacts are drawn as dashed lines as their length might indicate the absence of a formal bond. C atoms are shown in grey, H in white, Cl in green, Cu in dark brown, and N in light grey-blue. Hydrogen bonds are drawn as light-blue dashed lines.

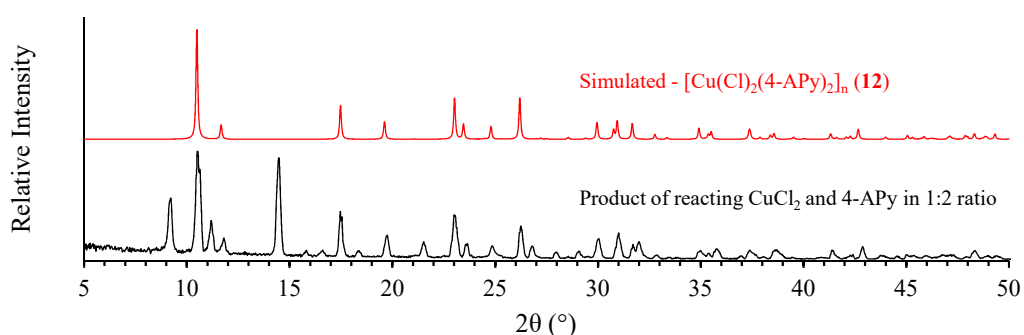


Figure 4.17 Room temperature X-ray powder diffraction data for the powder produced by reaction of $\text{CuCl}_2 \cdot 2\text{H}_2\text{O}$ with two molar equivalents of 4-APy. Experimental data are shown in black while simulated data are shown in red.

4.5.3 $[\text{Cu}_4(\mu^4\text{-O})(\mu^2\text{-Cl})_6(4\text{-APy})_4]$ (13/14)

The non-solvated and DMSO/H₂O solvated structures of $[\text{Cu}_4(\mu^4\text{-O})(\mu^2\text{-Cl})_6(4\text{-APy})_4]$ are very similar, therefore the two structures will be described and discussed together like with **10** and **11**. Each structure has a tetragonal unit-cell with space group $I4_1/a$. The non-solvated structure, $[\text{Cu}_4(\mu^4\text{-O})(\mu^2\text{-Cl})_6(4\text{-APy})_4]$ (**13**), has a unit-cell volume of 3055.5(4). The refined model of **13** gave an excellent fit to the experimental data ($R_1 = 0.0377$, $wR_2 = 0.1051$), further crystallographic details are included in Table 4.4. The asymmetric unit is composed of one 4-APy molecule, one Cu^{2+} ion, two chloride ions, one of which is on the 8e Wyckoff site, and an oxide ion on the 4a Wyckoff site. This is exactly $\frac{1}{4}$ of a $[\text{Cu}_4(\mu^4\text{-O})(\mu^2\text{-Cl})_6(4\text{-APy})_4]$ complex which is created from the asymmetric unit by the four-fold symmetry occurring on the O position. The fragment and whole complex are shown in Figure 4.18, bond distance and angle data are shown in Table 4.11.

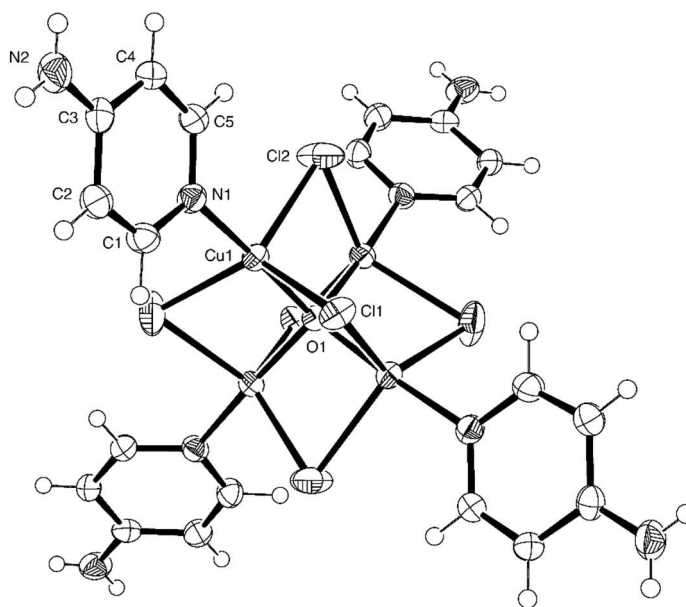


Figure 4.18 The structure of the complex in $[\text{Cu}_4(\mu^4\text{-O})(\mu^2\text{-Cl})_6(4\text{-APy})_4]$ (**13**) with atoms shown as thermal ellipsoids drawn at 50% probability. The asymmetric unit is labelled and creates the complete complex by the symmetry operators: $\frac{3}{4} + y, \frac{5}{4} - x, \frac{1}{4} - z; \frac{5}{4} + y, -\frac{3}{4} + x, \frac{1}{4} - z; 2 - x, \frac{1}{2} - y, z$.

Table 4.11 Selected bond lengths (Å) and angles (°) around the Cu coordination centre for $[\text{Cu}_4(\mu^4\text{-O})(\mu^2\text{-Cl})_6(4\text{-APy})_4]$ (**13**).

Cu(1) – O(1)	1.9117(3)	Cu(1) – Cl(2)#1	2.3636(9)
Cu(1) – Cl(1)	2.4701(9)	Cu(1) – N(1)	1.952(2)
Cu(1) – Cl(2)	2.4349(9)		
O(1) – Cu(1) – Cl(1)	84.72(2)	Cl(1) – Cu(1) – N(1)	91.69(8)
O(1) – Cu(1) – Cl(2)	83.90(2)	Cl(2) – Cu(1) – Cl(2)#1	120.054(16)
O(1) – Cu(1) – Cl(2)#1	85.90(2)	Cl(2) – Cu(1) – N(1)	99.92(7)
O(1) – Cu(1) – N(1)	175.50(7)	Cl(2)#1 – Cu(1) – N(1)	94.16(7)
Cl(1) – Cu(1) – Cl(2)	110.32(3)	Cu(1) – O(1) – Cu(1)#1	108.617(11)
Cl(1) – Cu(1) – Cl(2)#1	127.24(3)	Cu(1) – O(1) – Cu(1)#2	111.20(2)

#1 $\frac{3}{4} + y, -\frac{3}{4} + x, \frac{1}{4} - z$

#2 $2 - x, \frac{1}{2} - y, z$

#3 $\frac{3}{4} + y, \frac{3}{4} - x, \frac{1}{4} - z$

As mentioned previously, the DMSO/H₂O solvated structure $[\text{Cu}_4(\mu^4\text{-O})(\mu^2\text{-Cl})_6(4\text{-APy})_4] \cdot (\text{DMSO})_{5.33}(\text{H}_2\text{O})_{0.88}$ (**14**) also has a tetragonal unit-cell with the same space group as **13**, however the unit-cell volume is approximately 16 times larger (49709(5) Å³) due to a loss of symmetry. This structure gave a relatively poor fit to the observed data, but that is most likely due to weak scattering from the sample and insensitivity of the detector used for data collection giving rise to a large merging R-factor ($R_{\text{int}} = 0.1427$, $R_1 = 0.1079$, $wR_2 = 0.3298$), further crystallographic details are included in Table 4.4. The refined structure does not contain any gross errors, is chemically sensible, and bears many resemblances to the non-solvated structure indicating the model is correct. The asymmetric unit is composed of $\frac{1}{4}$ of one whole cluster complex with the Cl⁻ and O²⁻ ions on the same Wyckoff positions as in **13**, in addition to two whole cluster molecules not positioned on centres of symmetry, twelve DMSO molecules, and two water molecules, as shown separately in Figure 4.19. Due to the number of unique complexes in **14**, the individual bond distances and angles within the inner coordination sphere of the Cu²⁺ ions have not been reported but are summarised in Table 4.12.

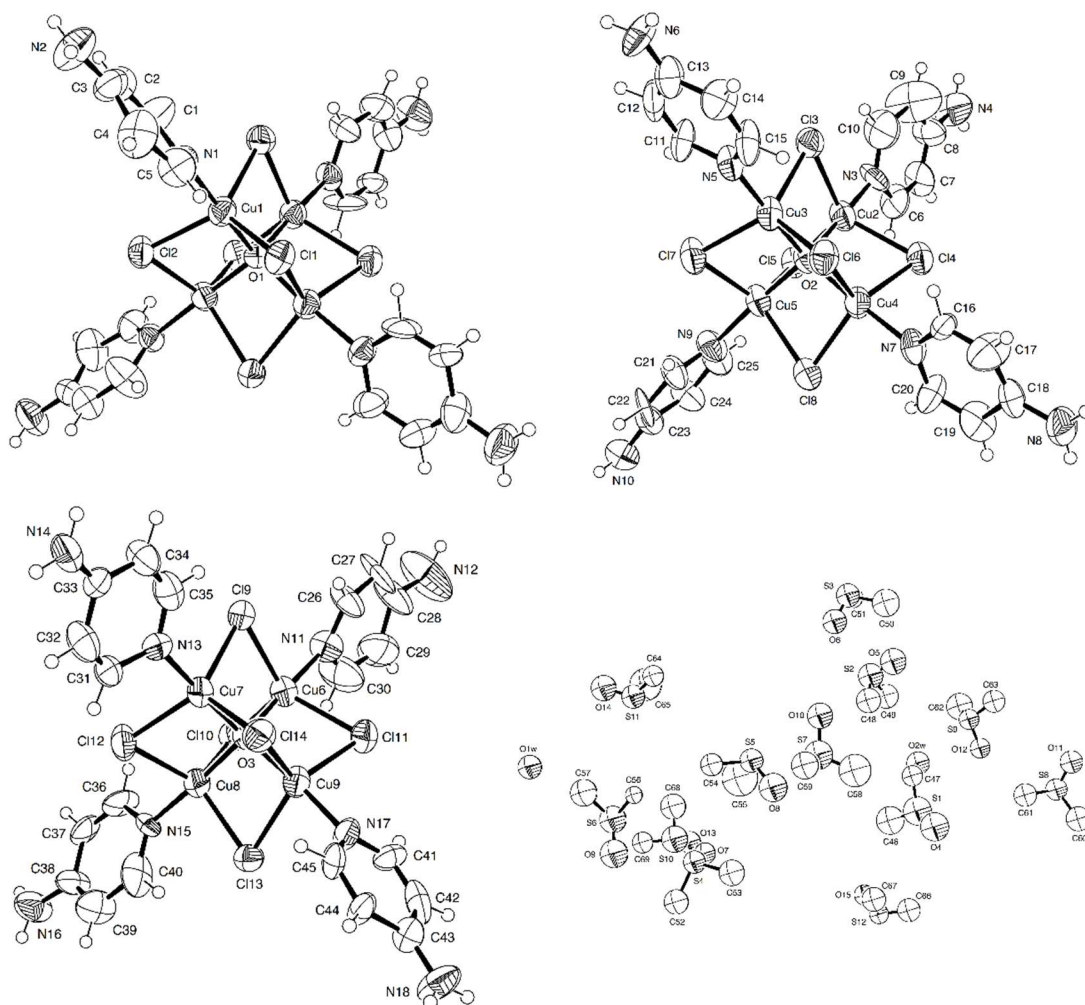


Figure 4.19 The whole molecules within $[\text{Cu}_4(\mu^4\text{-O})(\mu^2\text{-Cl})_6(4\text{-APy})_4]\cdot(\text{DMSO})_{5.33}(\text{H}_2\text{O})_{0.88}$ (**14**) with atoms shown as thermal ellipsoids drawn at 50% probability. Symmetry independent molecules are drawn separately for clarity. Atoms within the asymmetric unit are labelled, the fragment containing Cu1 creates the complete molecule by the symmetry operators: $7/4 - y, -1/4 + x, 7/4 - z; 1/4 + y, 7/4 - x, 7/4 - z; 2 - x, 3/2 - y, z$.

Table 4.12 Selected bond lengths (Å) and angles (°) around the Cu coordination centre for $[\text{Cu}_4(\mu^4\text{-O})(\mu^2\text{-Cl})_6(4\text{-APy})_4]\cdot(\text{DMSO})_{5.33}(\text{H}_2\text{O})_{0.88}$ (**14**).

Identity	Maximum	Minimum	Average	Median	Range
Cu – O	1.936(13)	1.894(11)	1.919(13)	1.921	0.042
Cu – N	1.977(18)	1.924(16)	1.947(17)	1.943	0.053
Cu – Cl					
Cu – O – Cu	110.5(6)	108.2(5)	109.5(6)	109.7	2.3
O – Cu – Cl	86.0(4)	83.3(4)	84.8(6)	84.9	2.7
O – Cu – N	178.1(6)	175.1(6)	176.4(10)	176.6	3.0
N – Cu – Cl	98.9(6)	91.1(5)	95(2)	95.5	7.8
Cl – Cu – Cl	124.0(2)	115.5(2)	119.2(16)	118.9	8.5

The cluster complexes **8**, **10**, and **11** are all distorted in a similar way. Despite the higher symmetry displayed in **13** and **14**, the clusters still display distortions akin to those described on the preceding pages. The central $\text{Cu}_4(\mu^4\text{-O})$ moieties are effectively undistorted, Cu-Cu and Cu-O bond lengths are normal and not particularly varied, and the Cu-O-Cu bond angles do not vary greatly either. The Cu-Cl bond lengths and the Cl-Cu-Cl and O-Cu-N bond angles show a much larger variation which are comparable to those in the previously discussed compounds.

The 3-D arrangement of the clusters is primarily controlled by a single hydrogen bonding motif in each structure. The amine groups of the 4-APy ligands around each cluster hydrogen bond to a chloride ion in an adjacent complex ($\text{N}\cdots\text{Cl}$ in **13** is 3.326(3) Å, and the average in **14** is 3.39(6) Å with a range of 0.16(4) Å), and a 4-APy ligand in the acceptor complex hydrogen bonds back in the same way therefore forming an $\text{R}_2^2(16)$ motif in **13** and a $\text{R}_2^2(20)$ motif in **14**, as shown in Figure 4.20.

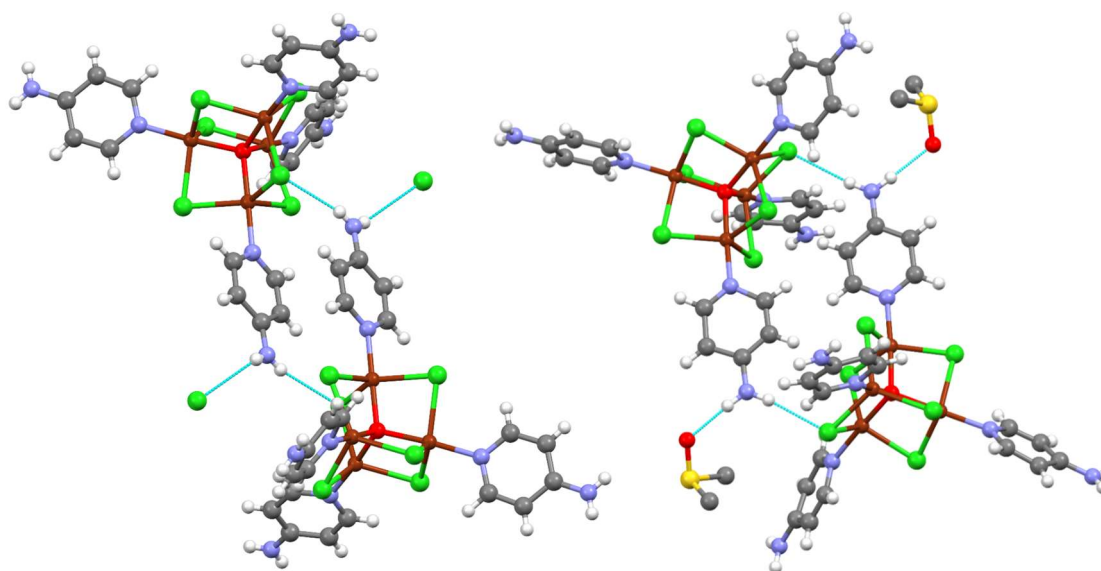


Figure 4.20 The hydrogen bonding arrangements between cluster complexes in $[\text{Cu}_4(\mu^4\text{-O})(\mu^2\text{-Cl})_6(4\text{-APy})_4]$ (**13**) (left) and $[\text{Cu}_4(\mu^4\text{-O})(\mu^2\text{-Cl})_6(4\text{-APy})_4]\cdot(\text{DMSO})_{5.33}(\text{H}_2\text{O})_{0.88}$ (**14**) (right). C atoms are shown in grey, H in white, Cl in green, Cu in dark brown, N in light grey-blue, O in red, and S in yellow. Hydrogen bonds are drawn as light-blue dashed lines.

Since every 4-APy ligand bonded to each cluster is involved in the aforementioned ring motif, and the ligands are in an approximate tetrahedral arrangement, the result is that **13** and **14** contain a distorted diamond-like hydrogen bonded framework, as shown in Figure 4.21 and Figure 4.22 respectively. The difference between the two structures is what else the amine group of the 4-APy ligands hydrogen bond to in each structure. In **13**, the amine group also hydrogen bonds to the chloride ions of additional clusters belonging to two separate but identical hydrogen bonded frameworks to the original one ($N \cdots Cl$ 3.354(3) Å). In other words, **13** is composed of a triply interpenetrated hydrogen bonded diamond-like framework which is also shown in Figure 4.21 by blue, red, and green stick models. Each framework in **13** is related to the others by a unit translation along *c*.

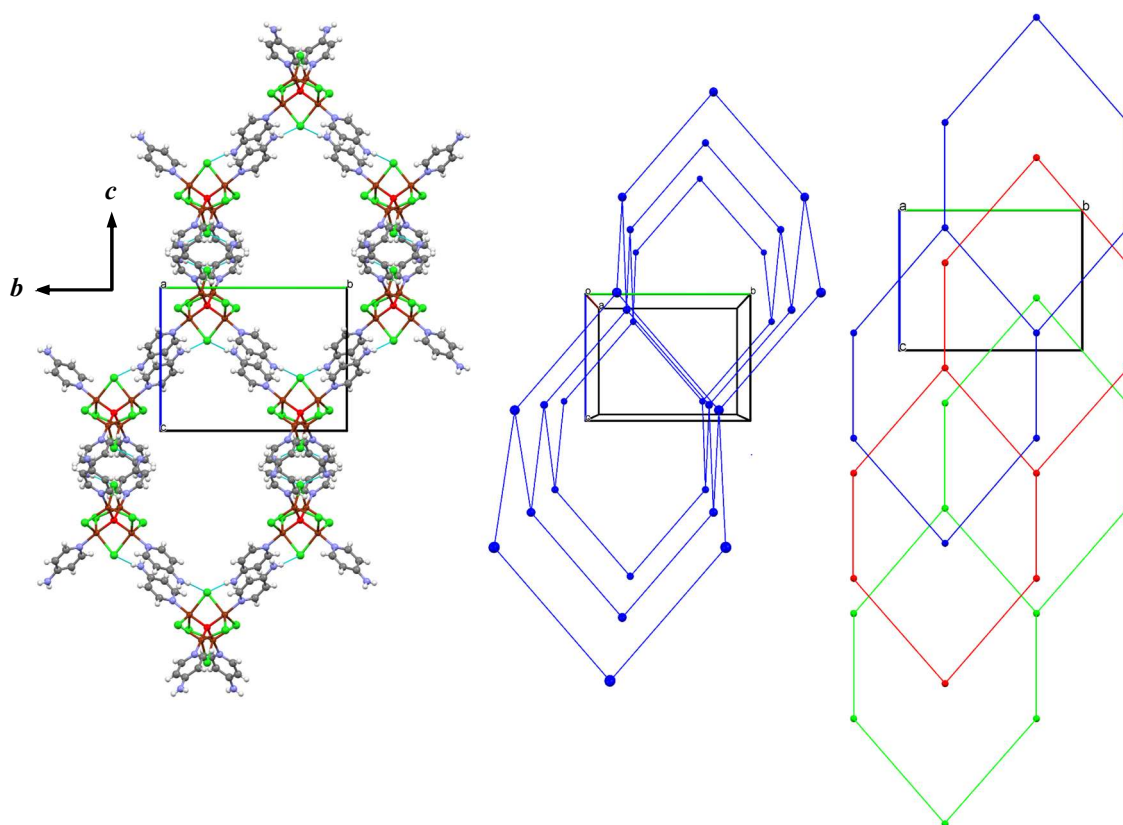


Figure 4.21 The distorted diamond-like hydrogen bonded framework in $[Cu_4(\mu^4-O)(\mu^2-Cl)_6(4-APy)_4]$ (**13**). Left is a ball and stick diagram with C atoms shown in grey, H in white, Cl in green, Cu in dark brown, N in light grey-blue, and O in red. Hydrogen bonds are drawn as light-blue dashed lines. Middle is a simplified single framework in blue. Right is a diagram of the triple interpenetration of the framework with individual 3-D nets coloured red, green and blue, these are shown in 2-D for clarity.

14 contains only a single diamond-like hydrogen bonded framework. Instead of the amine groups of the 4-APy ligands hydrogen bonding to two chloride ions, as in **13**, the additional hydrogen bond is to either a DMSO or water molecule contained within channels which extend along *a* and *b* (average N···O 2.87(9) Å with a range of 0.16(5) Å). This effectively “caps off” the amine group and avoids the formation of an interpenetrated network. The channels present in **14** have a solvent accessible volume of approximately 26500 Å³ per unit-cell, or 53% of the total volume, and are filled with DMSO and H₂O as shown in Figure 4.22.

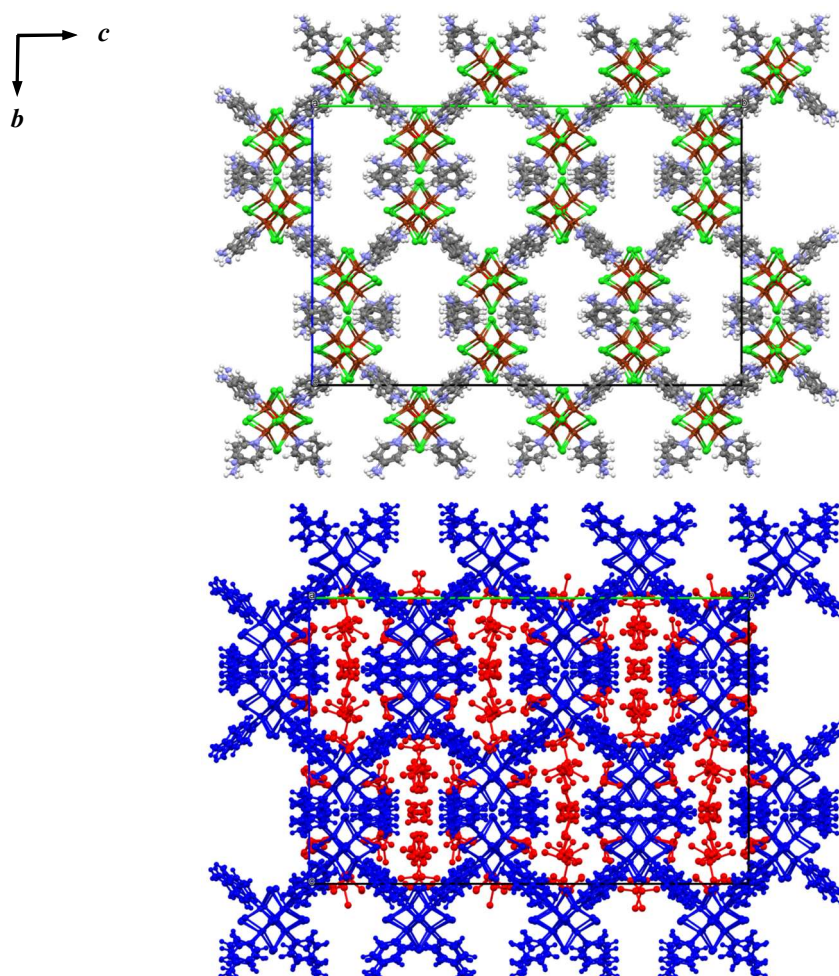


Figure 4.22 Shown left is the distorted diamond-like hydrogen bonded framework in $[\text{Cu}_4(\mu^4\text{-O})(\mu^2\text{-Cl})_6(4\text{-APy})_4] \cdot (\text{DMSO})_{5.33}(\text{H}_2\text{O})_{0.88}$ (**14**). C atoms are shown in grey, H in white, Cl in green, Cu in dark brown, N in light grey-blue, and O in red. Right shows how the channels within the framework (blue) are filled with the solvent molecules (red).

X-ray powder diffraction patterns of the yellow/brown powders of **13** and **14** matched the diffraction patterns simulated from the single-crystal structures, as shown in Figure 4.23. No additional peaks were observed in the experimental diffraction patterns, and although elemental analysis is not accurate enough to confirm the solvent composition of **14**, the experimental data matched the predicted compositions therefore confirming the purity of the samples.

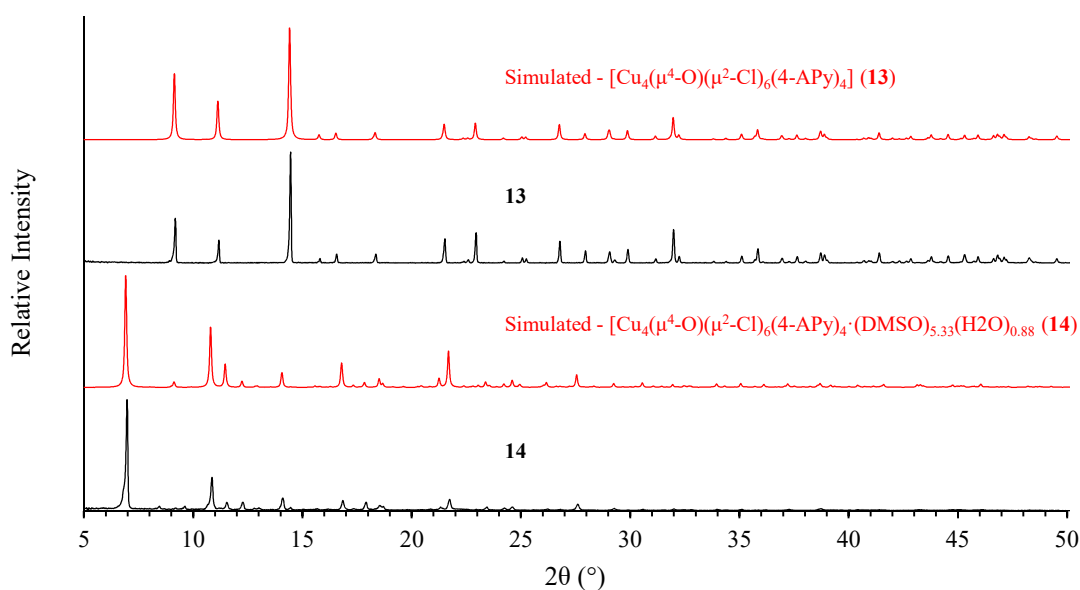


Figure 4.23 Room temperature X-ray powder diffraction data for **13** and **14**. Experimental data are shown in black while simulated data are shown in red.

As mentioned earlier, the attempts to produce pure samples of **12** failed and the experimental X-ray powder diffraction patterns of the samples possessed peaks belonging to an additional phase that was unknown at the time of synthesis. Additionally, samples of **14** degraded over time from a brown to a deep green powder. Analysis of the powders from the above reactions by X-ray diffraction showed them each to be a mixture of **12** and **13** by comparison to the simulated powder diffraction patterns of these two compounds as shown in Figure 4.24. Therefore, **14** decomposes over time by loss of oxygen from some of the cluster molecules, or in other words reduction, presumably

brought on by a loss of DMSO by evaporation and subsequent collapse of the hydrogen bonded framework. Conversely, the contamination of **12** with **13** in the attempts to produce pure **12** indicate self-oxidation occurs. Using this information, perhaps one method of producing pure **12** might be the addition of a very mild and non-coordinating reducing agent to prevent the formation of the cluster complex.

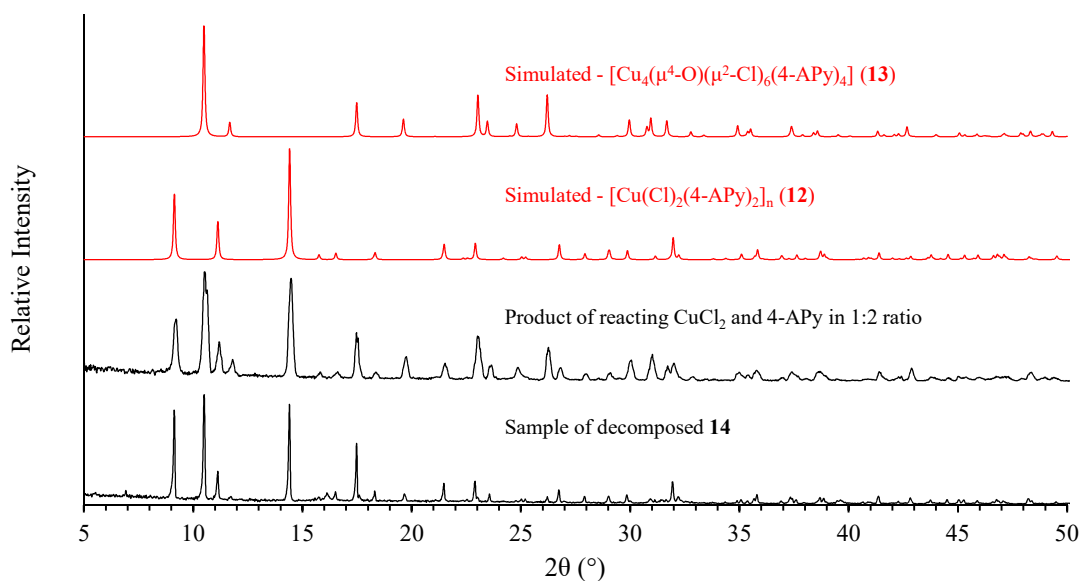


Figure 4.24 Room temperature X-ray powder diffraction data for $[\text{Cu}_4(\mu^4\text{-O})(\mu^2\text{-Cl})_6(4\text{-APy})_4] \cdot (\text{DMSO})_{5.33}(\text{H}_2\text{O})_{0.88}$ (**14**) after storage for one month, and the powder produced by reaction of $\text{CuCl}_2 \cdot 2\text{H}_2\text{O}$ with two molar equivalent of 4-APy. Experimental data are shown in black while simulated data are shown in red.

4.6 Non-cluster forming compounds and predicting reactivity

Spurred on by the successful tests described above producing copper-oxide-chloride clusters by oxidation of a stoichiometric mixture of CuCl , CuCl_2 , and a pyridine-based ligand, similar reactions were attempted with isonicotinic acid (INAc), isonicotinamide (INAm), nicotinamide (NAm), pyrazine (pz), and 4,4'-bipyridine (bipy) to test whether the method would work with other ligands.

On addition of two molar equivalents of each of these compounds to a cupric chloride solution, a blue/green precipitate developed as expected for the production of a $[\text{CuCl}_2(\text{RPy})_2]_n$ type compound. However, no change was observed following addition of cuprous chloride, even after heating. The blue/green precipitates were collected and analysed by X-ray powder diffraction, and all samples were shown to be the $[\text{CuCl}_2(\text{RPy})_2]_n$ compound for that particular ligand, as shown in Figure 4.25.

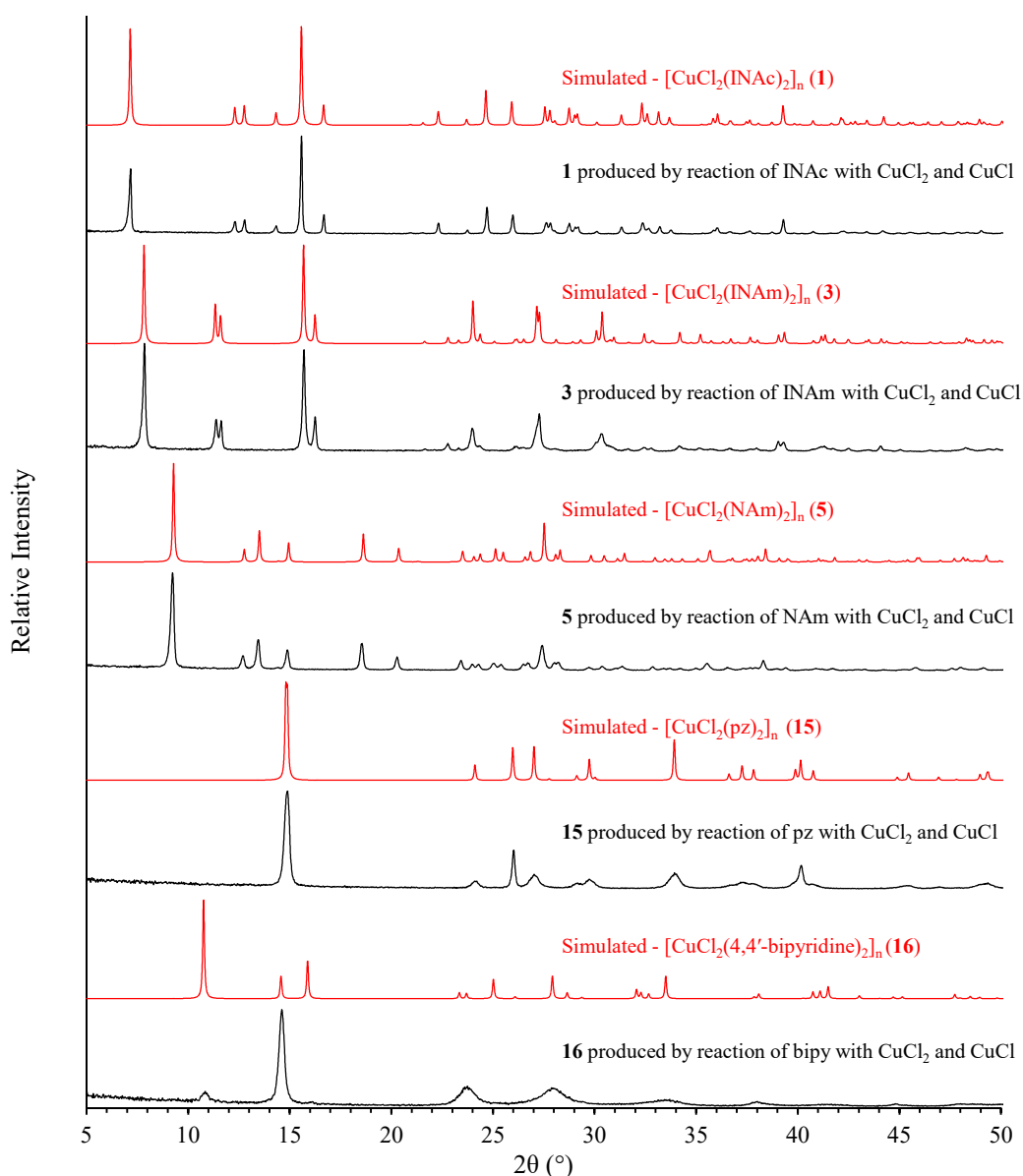


Figure 4.25 Room temperature X-ray powder diffraction data for the products from reaction of INAc, INAm, Nam, pz, and bipy with cupric and cuprous chloride in methanol. Experimental data are shown in black while simulated data are shown in red.

The structures of the INAc, INAm, and NAm copper chloride compounds (**1**, **3**, and **5**) were described in detail in chapter 3, so shall not be described again. The pz (**15**) and bipy (**16**) compounds were initially discovered by Lapidus *et al.* and Masciocchi *et al.* respectively and are shown in Figure 4.26 and Figure 4.27.^{186,187} Each consists of the same polymeric CuCl₂ chain that is prolific in this family of compounds, however the inorganic chains are bridged through the pz/bipy molecules to create 2-D sheets which stack in an alternating ABAB fashion along *a*. Bond distance and angle data are contained within Table 4.13 and Table 4.14.

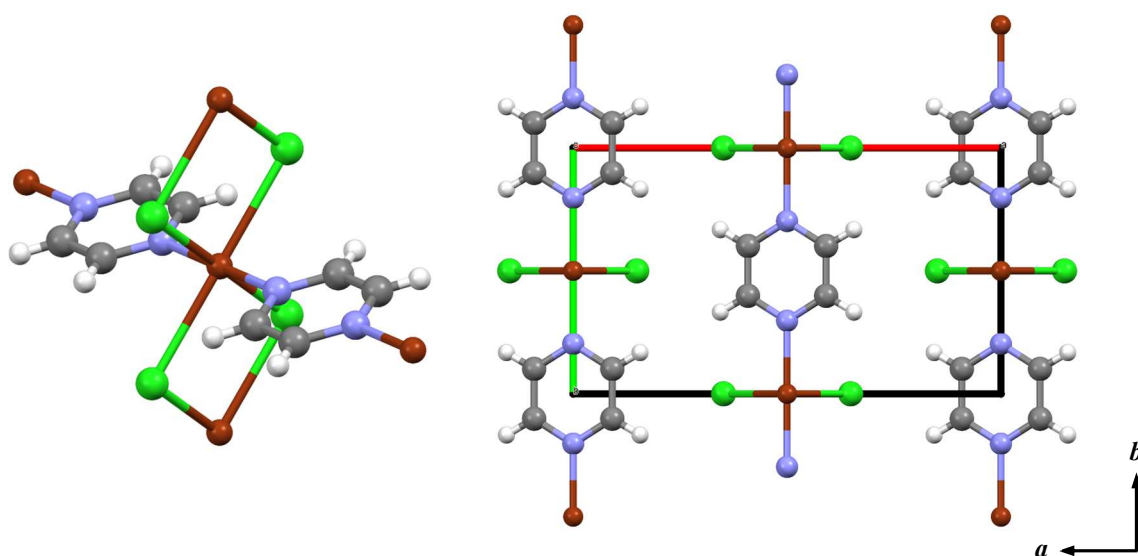


Figure 4.26 The structure of $[\text{CuCl}_2(\text{pz})_2]_n$ (**15**), showing the CuCl_2 chain that extends along the *c* axis (left), and the overall packing (right).¹⁸⁶ C atoms are shown in grey, H in white, Cl in green, Cu in orange, and N in blue.

Table 4.13 Selected bond lengths (Å) and angles (°) around the Cu coordination centre for $[\text{CuCl}_2(\text{pz})_2]_n$ (**15**).¹⁸⁶

Cu(1) – Cl(1)	2.2871(3)	Cl(1)-Cu(1)-Cl(1)#1	91.115(12)
Cu(1) – Cl(1)#1	2.8732(4)		
Cu(1) – N(1)	2.0376(13)		

#1 *x*, *y*, *z* – 1

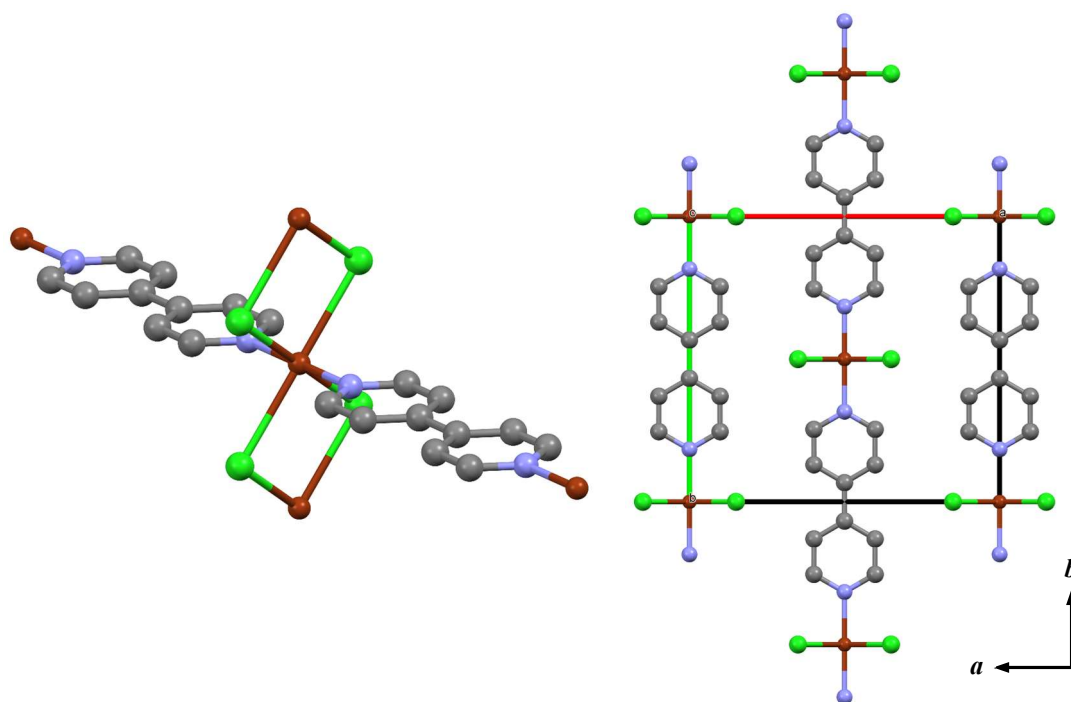


Figure 4.27 The structure of $[\text{CuCl}_2(\text{bipy})_2]_n$ (**16**), showing the CuCl_2 chain that extends along the c axis (left), and the overall packing (right).¹⁸⁷ C atoms are shown in grey, H in white, Cl in green, Cu in orange, and N in blue.

Table 4.14 Selected bond lengths (Å) and angles (°) around the Cu coordination centre for $[\text{CuCl}_2(\text{bipy})_2]_n$ (**16**).¹⁸⁷

Cu(1) – Cl(1)	2.347(7)	Cl(1)-Cu(1)-Cl(1)#1	90.6(2)
Cu(1) – Cl(1)#1	2.905(7)		
Cu(1) – N(1)	2.051(5)		

#1 1 + x, y, z – 1

It was evident that only some $[\text{CuCl}_2(\text{RPy})_2]$ compounds react to produce the oxide-centred cluster, but what allowed/disallowed the reaction to take place was unknown. It was suspected that the non-reactivity was either a result of the polymeric nature of the $[\text{CuCl}_2(\text{RPy})_2]$ complexes, or the presence of strong hydrogen bonding interactions or covalent linkages between the pyridine groups; two features present in the above non-reactive compounds. A simple experiment designed to probe this further is described below.

The methyl ester of INAc (MeINAc) cannot participate in the same hydrogen bonding interactions as the carboxylic acid as it is missing the necessary hydrogen atom to do so. Additionally, the structure of the copper chloride compound of this molecule discovered by Ahadi *et al.*,¹⁸⁸ $[\text{CuCl}_2(\text{MeINAc})_2]_n$ (**17**), has a similar polymeric structure to that of **1** as shown in Figure 4.28 above, bond length and angle data are shown in Table 4.15. The main difference between **1** and **17** is that the packing in **17** is directed only by weak intermolecular forces. Therefore, attempting the reaction of **17** with cuprous chloride would reveal which of the above two suggested causes for differences in reactivity are true. The reaction proceeded much like with INAc, producing only a blue-green precipitate. This was collected and analysed by X-ray powder diffraction, showing the material to be the pure cupric chloride compound, as shown in Figure 4.29 by a comparison of simulated and experimental data.

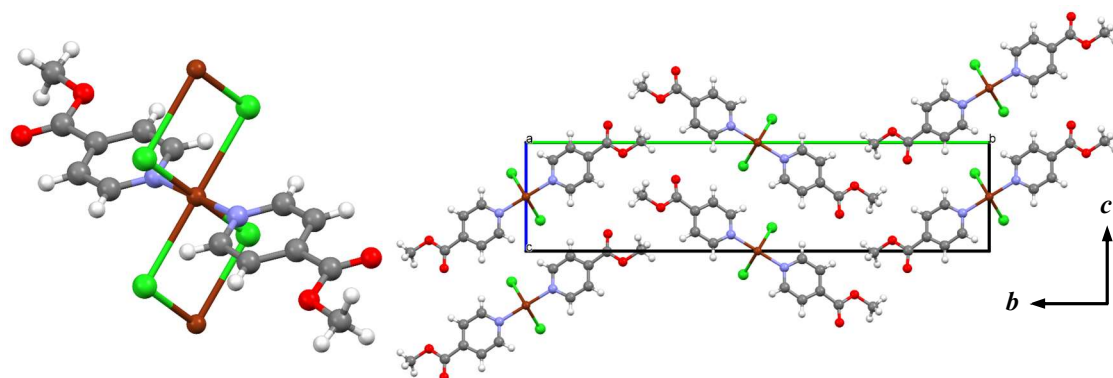


Figure 4.28 The structure of $[\text{CuCl}_2(\text{MeINAc})_2]_n$ (**17**), showing the CuCl_2 chain that extends along the a axis (left), and the overall packing (right).¹⁸⁸ C atoms are shown in grey, H in white, Cl in green, Cu in dark brown, N in light grey-blue, and O in red.

Table 4.15 Selected bond lengths (Å) and angles (°) around the Cu coordination centre for $[\text{CuCl}_2(\text{MeINAc})_2]_n$ (**17**).¹⁸⁸

Cu(1) – Cl(1)	2.2962(7)	N(1)-Cu(1)-Cl(1)	90.78(6)
Cu(1) – Cl(1)#1	2.9215(7)	N(1)-Cu(1)-Cl(1)#1	89.30(6)
Cu(1) – N(1)	2.025(2)	Cl(1)-Cu(1)-Cl(1)#1	92.03(2)

#1 $x - 1, y, z$

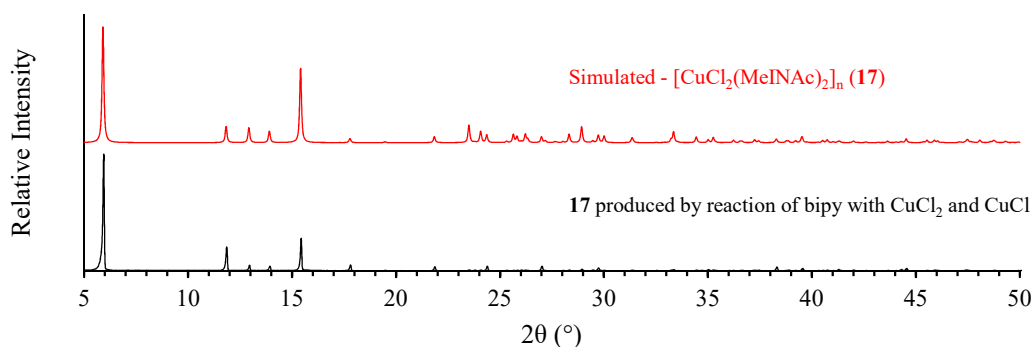


Figure 4.29 Room temperature X-ray powder diffraction data for **17**. Experimental data are shown in black while simulated data are shown in red.

Since neither of the cupric chloride compounds of INAc or MeINAc react to produce the oxide centred cluster, and both are polymeric coordination compounds, this implies that ligands producing non-polymeric compounds are the only ones capable of also forming a cluster compound, this raises other questions however. For example, is the only requirement to form the cluster that the ligand must not form a polymeric cupric chloride compound? Or is there some physical property of the ligand which simultaneously allows the formation of the cluster, but also weakens/lengthens the long Cu-Cl contact in the cupric chloride complex with that ligand?

Pyridine ligands possessing functional groups on the carbon adjacent the pyridine N are known to produce discrete copper halide compounds, regardless of other properties the ligand may possess.^{189–192} The steric hindrance around the N donor atom is so large it effectively caps the apical sites of the copper centre giving only square-planar complexes. So, to answer the first of the questions above, another simple experiment was designed based on this information, reaction of cupric chloride with 2-chloroisonicotinic acid (ClINAc). The standard procedure of method A was followed; reaction of two molar equivalents of ClINAc with cupric chloride, followed by addition of one molar equivalent of cuprous chloride. This resulted in a green solution which when left to evaporate

produced blue parallelogram-shaped blocks. Single-crystal X-ray diffraction showed that these crystals were of triclinic symmetry and centrosymmetric. Further crystallographic details are included in Table 4.4.

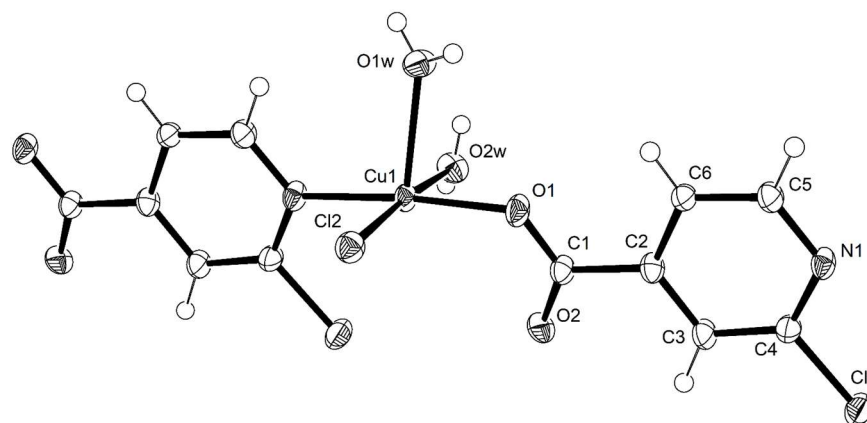


Figure 4.30 The asymmetric unit of $[\text{CuCl}(\text{CIINAc})(\text{H}_2\text{O})_2]_n$ (**18**) with atoms shown as thermal ellipsoids drawn at 50% probability. The fragment is completed by the symmetry operator: $-1+x, 1+y, z$.

The asymmetric unit, shown in Figure 4.30, consists of a copper centre coordinated to one chloride ion, two water molecules, and a deprotonated CIINAc molecule through both the N and one carboxylate O. The Cu atom therefore has a square-pyramidal coordination geometry, and produces a 1-D polymeric chain via coordination to the CIINAc molecule as shown in Figure 4.31, bond length and angle data are shown in Table 4.16. The structure can therefore be described as $[\text{CuCl}(\text{CIINAc})(\text{H}_2\text{O})_2]_n$ (**18**).

Table 4.16 Selected bond lengths (Å) and angles (°) around the Cu coordination centre for $[\text{CuCl}(\text{CIINAc})(\text{H}_2\text{O})_2]_n$ (**18**).

Cu(1) – Cl(2)	2.2699(12)	Cu(1) – O(2W)	1.996(3)
Cu(1) – O(1)	1.944(2)	Cu(1) – N(1)#1	2.024(3)
Cu(1) – O(1W)	2.236(3)		
O(1) – Cu(1) – Cl(2)	91.02(10)	O(1W) – Cu(1) – O(2W)	85.17(13)
O(1) – Cu(1) – O(1W)	85.92(11)	O(1W) – Cu(1) – N(1)#1	99.94(12)
O(1) – Cu(1) – O(2W)	87.62(13)	O(2W) – Cu(1) – Cl(2)	174.76(9)
O(1) – Cu(1) – N(1)#1	173.68(12)	O(2W) – Cu(1) – N(1)#1	90.50(13)
O(1W) – Cu(1) – Cl(2)	99.79(10)	N(1)#1 – Cu(1) – Cl(2)	90.31(10)

#1 $-1+x, 1+y, z$

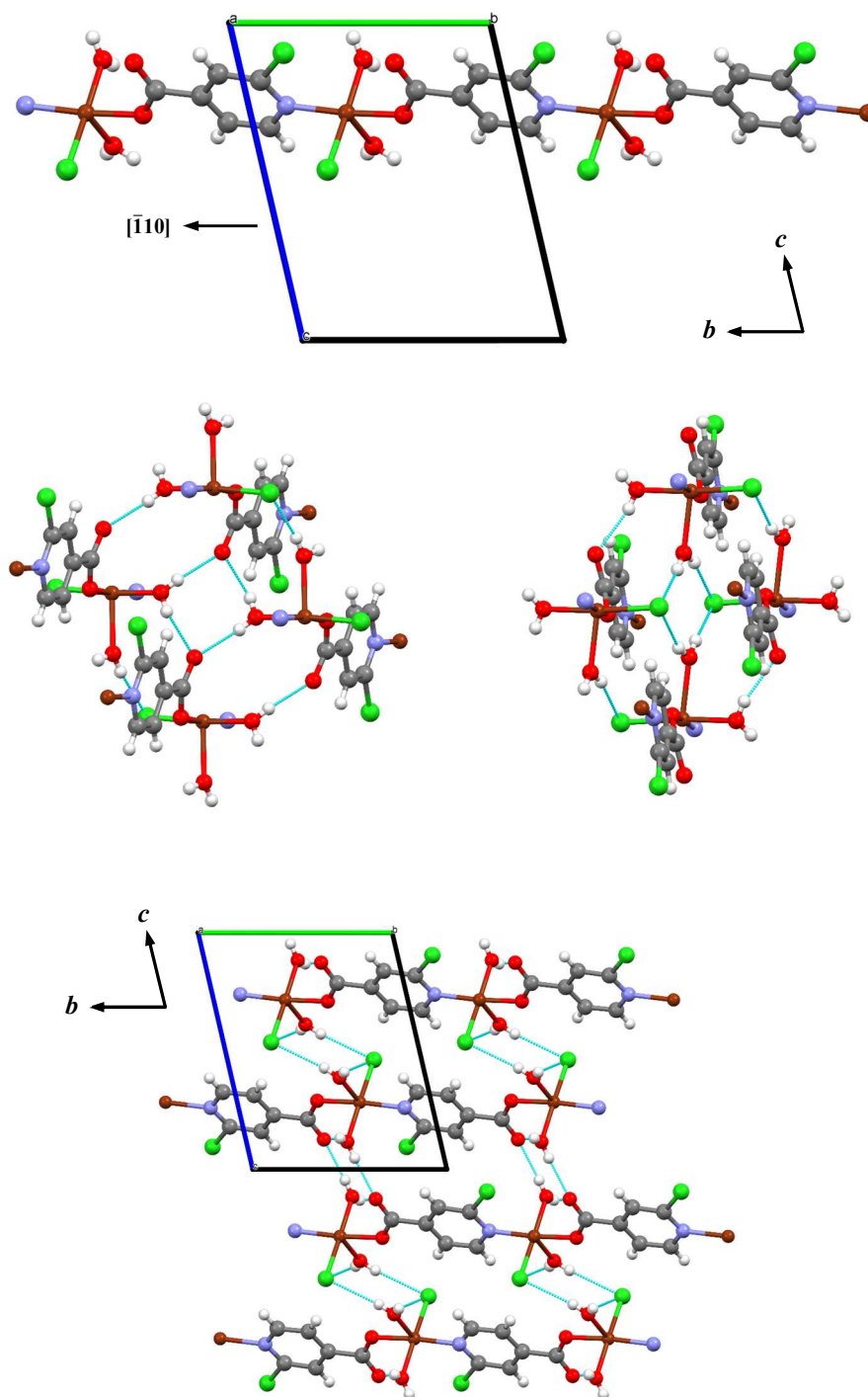


Figure 4.31 Structural images of $[\text{CuCl}(\text{ClINAc})(\text{H}_2\text{O})_2]_n$ (**18**). The Cu-ClINAc polymeric chain is shown top. $\text{H}_2\text{O}-\text{CO}_2\text{H}$ and $\text{H}_2\text{O}-\text{Cl}$ $R_4^2(8)$ interactions are shown middle left and right respectively, and the overall structure created by the Cu-ClINAc chain and these interactions is shown bottom. C atoms are shown in grey, H in white, Cl in green, Cu in dark brown, N in light grey-blue, and O in red. Hydrogen bonds are drawn as light-blue dashed lines.

The two symmetrically independent water molecules in the structure are each involved in similar $R_4^2(8)$ hydrogen bonding interactions which shall be referred to as R1 and R2. R1 consists of two water molecules, O1w, hydrogen bonding to two chloride ions, Cl2 ($O\cdots Cl$ 3.275(3) Å and 3.178(3) Å). R2 is similar but the water molecules, O2w, hydrogen bond to the carboxyl O of two carboxylic acids instead ($O\cdots O$ 2.763(4) Å and 2.719(4) Å). The ring interactions occur in a repeating fashion along *a*, R1 and R2 creating $C_1^1(4)$ and $C_1^1(6)$ chain interactions respectively through coordination to Cu. However, they alternate along *c* producing a singular $C_2^2(10)$ interaction. The 1-D Cu-ClINAc chain combines with these chain interactions to give a 3-D supramolecular network consisting of coordination and hydrogen bonds.

It has not been possible yet to make **18** in a pure form as exposure to air causes a change in the structure/identity of the compound and therefore the experimental diffraction pattern doesn't match the simulated pattern from the crystal structure. Evidently the reaction above does not answer the proposed question of whether steric hindrance can play a role in deciding reactivity as neither a $[Cu_4(\mu^4-O)(\mu^2-X)_6(L)_4]$ or $[CuCl_2(RPy)_2]$ type compound was produced. Further work is needed to find an answer to this question.

The second question posed about the reactivity of non-polymeric $[CuCl_2(RPy)_2]$ compounds was whether another property gave rise to both the reactivity and lengthening of the long Cu-Cl contact. Cl^- is a relatively good π -donor ligand, whereas pyridine (and presumably its derivatives) can act as a π -acceptor. The former would therefore be likely to be involved in ligand-to-metal π bonding while the latter would have metal-to-ligand π bonds, each complimenting the other, *i.e.* if the metal-to-ligand π bonds are stronger so are the ligand-to-metal π bonds. The differences in the length of the long Cu-Cl contact could be explained by differences in the degree of π backbonding by the pyridine ligand,

and this should be evidenced by a correlation between the Cu-N and Cu-Cl bond lengths. Alternatively, the angle between the Cl-Cu-Cl line and the pyridine ring plane may also affect the strength of the bond through differences in orbital overlap. However, as seen in Figure 4.32, there is no observed correlation between any of these parameters and the long Cu-Cl contact in any of the Cl-based structures currently published on the CSD. The linear correlation coefficients are low, and there doesn't appear to be a clear nonlinear correlation. This doesn't necessarily rule out the ideas proposed as there is very little data available, and what is available has not been collected in a systematic/identical way which may have introduced too much variance to show a correlation if one does exist.

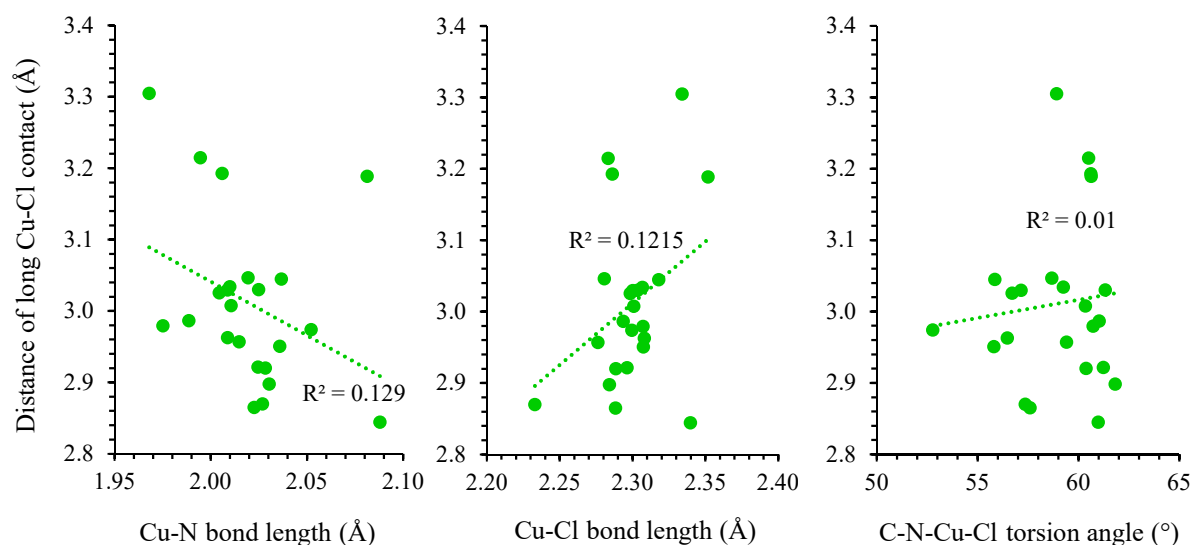
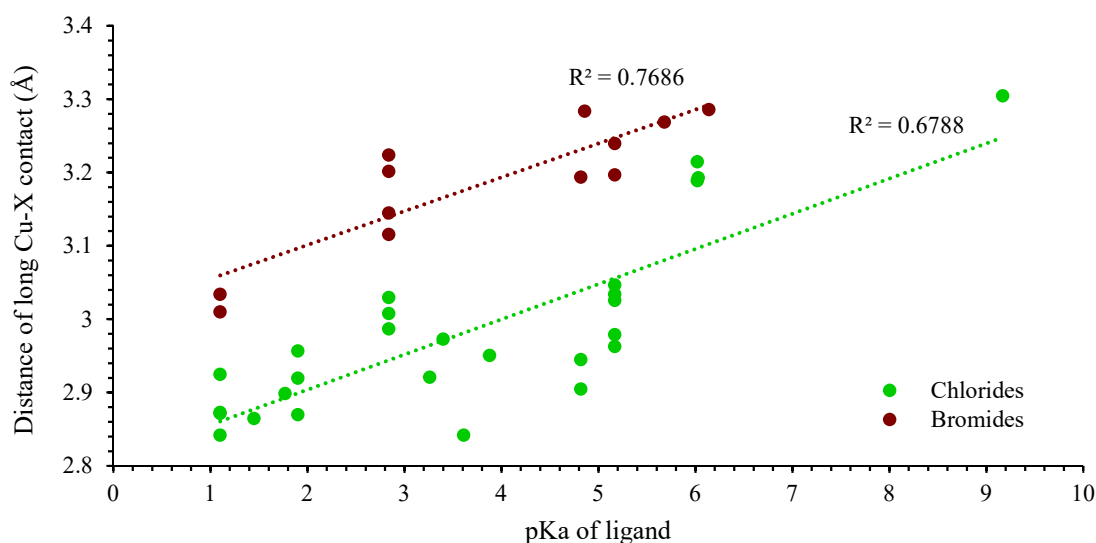


Figure 4.32 Plots of the long Cu-Cl contact distance (y-axis in each case) vs. various parameters. All values are taken from the CSD.¹¹⁹

Although no correlations were found in the analysis above, one good correlation was found between the pK_a of the ligand (referring to the reaction $R-C_5H_5N-H^+ \rightleftharpoons R-C_5H_5N + H^+$) and the length of the long Cu-X contact, as shown in Figure 4.33. The graph contains the long Cu-X contact distance data for all $[CuX_2(RPy)_2]_n$ type compounds on the CSD and discovered as part of this thesis vs. the pK_a values of each ligand as taken

from the CRC Handbook of Biochemistry and Molecular Biology.^{119,162} There is no clear connection between pK_a and the observed reactivity, so the correlation could just be coincidence. Further reactions of a wider array of ligands is necessary to produce a clear picture of what is going on, additionally, spectroscopic analysis would provide further insight into the bonding within these compounds and therefore clues as to the driving forces behind the reactivity or lack thereof.



$[\text{Cu}_4(\mu^4\text{-O})(\mu^2\text{-Cl})_6(4\text{-APy})_4] \cdot (\text{DMSO})_{5.33}(\text{H}_2\text{O})_{0.88}$ (**14**) which have all been structurally characterised. Additionally, $[\text{Cu}_2\text{Cl}_2(4\text{-APy})_2]_n$ (**12**) and $[\text{CuCl}(\text{ClINAc})(\text{H}_2\text{O})_2]_n$ (**18**) were also synthesised and the structures of these compounds determined.

An investigation into why only certain ligands allow the formation of $[\text{Cu}_4(\mu^4\text{-O})(\mu^2\text{-X})_6(\text{L})_4]$ type complexes has also been conducted. This revealed that only ligands which form cupric halide complexes without a polymeric copper halide chain can form the cluster complex. No correlations could be found between the coordination bond lengths in the $[\text{CuX}_2(\text{RPy})_2]_n$ family of compounds. The only correlation that could be found with the length of the long Cu-X bond, the governing factor in these reactions, was with the acid dissociation constant of the ligand. However, this may be pure coincidence as there doesn't seem to be any link between ligand acidity/basicity and reactivity toward producing the cluster complex. If this correlation did turn out to be true, then it is predicted that only basic pyridine-based ligands are capable of forming $[\text{Cu}_4(\mu^4\text{-O})(\mu^2\text{-X})_6(\text{L})_4]$ clusters, *e.g.* piperazine. However, if the cupric halide complex of the ligand just needs to be non-polymeric to form the corresponding cluster complex then pyridine-oxide based ligands would be of interest as the only examples on the CSD for compounds of this type are discrete molecules.

Further study is warranted to investigate these compounds and the reasons behind their formation, also an investigation into the capability of these cluster complexes to form clathrates with solvent molecules or gases would be of interest. Additionally, $[\text{Cu}_4(\mu^4\text{-O})(\mu^2\text{-X})_6(\text{L})_4]$ complexes are known to be catalytically active,^{182,183} a systematic investigation into the effect of ligand functional group on catalytic activity could be easily conducted with the knowledge of which pyridine ligands have the potential to form the complex and would be an interesting avenue of research to pursue.

5 Reactions and Complexes of $\text{H}_2\text{N}-(\text{CH}_2)_n-\text{CO}_2\text{H}$ Compounds

The use of ligands that contain amine functional groups to increase the selectivity of a compound toward carbon dioxide adsorption/separation (relative to the non-aminated equivalent), has proved to be a successful design strategy for metal-organic frameworks.^{100,101,193,194} The majority of examples in the literature focus on the functionalisation of pre-existing rigid frameworks by the addition of amine groups to the ligand, usually an aromatic polycarboxylic acid, which produces the desired structure. The lone pair of electrons on the amine in such ligands is easily donated into the conjugated π system, however monoethanolamine, the primary compound used for CO_2 capture in industrial applications, displays a much greater reactivity towards the target molecule but does not exhibit conjugation as it is aliphatic. Therefore, it was of interest to explore whether coordination polymers incorporating aliphatic amines possessed higher reactivity toward CO_2 as these mimic the amine group in monoethanolamine better. However, rather than functionalising known compounds, the desire was to create new compounds using known, cheap materials that are available en masse. A series of amino acids with different methylene chain lengths were chosen for investigation.

A generic structural diagram is shown in Figure 5.1 and names and abbreviations are shown in Table 5.1. The plan for the work was to attempt to react the amino acids with various metal salts and determine the structures of the compounds produced. Additionally, the physical properties of the compounds produced would be investigated, regardless of the applicability of the compounds/structures to the overall aim of producing novel compounds for gas adsorption.

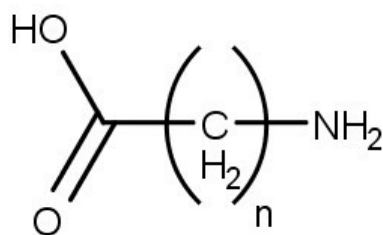


Figure 5.1 A generic diagram of the amino acids. $n = 1-5$ and 7 .

Table 5.1 The names and abbreviations of the amino acids used.

Chain Length (n)	Name	Abbreviation
1	2-aminoethanoic acid, glycine	Gly
2	3-aminopropanoic acid, β -alanine	β -Ala
3	4-aminobutanoic acid	ABA
4	5-aminopentanoic acid	APA
5	6-aminohexanoic acid	AHA
7	8-aminooctanoic acid	AOA

5.1 Experimental procedures

All reagents and solvents were purchased from Sigma Aldrich, BDH or Fisher Scientific and used as received. Elemental Analyses were conducted by the Elemental Analysis Service, Department of Chemistry, University of Hull on a Fisons CHN Elemental Analyser (Thermo Scientific), type EA-1108. Four neutral compounds were investigated containing the amino acids in a non-zwitterionic state: $[\text{Cu}(\text{ABA})_2]_n$ (**19**), $\{[\text{Cu}(\text{ABA})_2](\text{H}_2\text{O})_2\}_n$ (**20**),¹⁹⁵ $\{[\text{Cu}(\text{AHA})_2](\text{H}_2\text{O})_2\}_n$ (**21**),¹⁹⁶ and $[\text{Zn}(\text{APA})_2]_n$ (**22**). Only **22** was previously undiscovered. All other compounds created contained amino acids in the zwitterionic state and were halide salts, these are shown in Table 5.2. The table shows the reagents used, and which salt compounds were created using those reagents. The procedures used to create all compounds are discussed below.

Table 5.2 Products resulting from the combination of copper halides and hydrohalic acids with the amino acids mentioned in Table 5.1. Newly discovered compounds are highlighted in bold and starred.

	CuCl ₂	CuCl ₂ + HCl	CuBr ₂	CuBr ₂ + HBr
Gly	*{[Cu ₂ (Gly) ₄][Cu ₂ Cl ₆]} _n (35)	-	*[Cu(CIMGly)(H ₂ O) ₂] (36)	-
β-Ala	[Cu ₂ (β-Ala) ₄ Cl ₂]Cl ₂ ·H ₂ O (23)	(H-β-Ala) ₂ [CuCl ₄] (37)	*[Cu ₂ (β-Ala) ₄ Br ₂]Br ₂ ·2H ₂ O (24) *[Cu ₂ (β-Ala) ₄ Br ₂]Br ₂ ·3H ₂ O (25)	(H-β-Ala) ₂ [CuBr ₄] (38)
ABA	[Cu ₂ (ABA) ₄ Cl ₂]Cl ₂ ·3H ₂ O (26) *[Cu ₂ (ABA) ₄ Cl ₂]Cl ₂ ·H ₂ O (27)	(H-ABA) ₂ [CuCl ₄] (39)	*[Cu ₂ (ABA) ₄ Br ₂]Br ₂ (28)	*(H-ABA) ₂ [CuBr ₄] (40)
APA	*[Cu ₂ (APA) ₄ Cl ₂]Cl ₂ ·2H ₂ O (29) *[Cu ₂ (APA) ₄ Cl ₂]Cl ₂ (30)	*(H-APA) ₂ [CuCl ₄] (41)	*[Cu ₂ (APA) ₄ Br ₂]Br ₂ (31)	*(H-APA) ₂ [CuBr ₄] (42)
AHA	[Cu ₂ (AHA) ₄ Cl ₂]Cl ₂ ·4H ₂ O (32)	*(H-AHA) ₂ [CuCl ₄] (43)	*[Cu ₂ (AHA) ₄ Br ₂]Br ₂ ·4H ₂ O (33)	*(H-AHA) ₂ [CuBr ₄] (44)
AOA	*[Cu ₂ (AOA) ₆]Cl ₄ (34)	-	-	-

5.1.1 Cu(ABA)₂ (19) and Cu(AHA)₂·H₂O (21)

Cu(OAc)₂·H₂O (0.0250 g, 0.125 mmol) and ABA (0.0258 g, 0.25 mmol) or AHA (0.0328 g, 0.25 mmol) were dissolved in a 1:2 mixture of DMSO and water (7.5 mL). The solution was transferred to a sample vial and maintained at 40 °C in an oven to expedite the evaporation of water and prevent the DMSO from freezing. Purple crystals of **19** and **21** grew respectively from these solutions in addition to bulk polycrystalline material. Only **21** could be made pure via this method: Elemental anal. (%) calcd for **21**: C, 40.05; H, 7.84; N, 7.78. Found: C, 39.69; H, 7.75; N, 7.66.

5.1.2 Zn(APA)₂ (22)

22 was made in an identical way to **19** and **21** but using Zn(OAc)₂·2H₂O (0.0274 g, 0.125 mmol) and APA (0.0293 g, 0.25 mmol). Colourless blade-shaped crystals were obtained after a week. Elemental anal. (%) calcd for **22**: C, 40.35; H, 6.77; N, 9.41. Found: C, 39.81; H, 6.90; N, 8.75.

5.1.3 $[Cu_2L_4X_2]X_2 \cdot nH_2O$ (23-29, 31-33), $[Cu_4(Gly)_4Cl_6]_n$ (35) and $[Cu(CIMGly)(H_2O)_2]$ (36)

The general synthesis of the paddlewheel and glycine-based compounds of the amino acids that were studied is as follows. The amino acid (4 mmol), L, was dissolved in a 1:1 mixture of MeOH and water (25 mL). The copper halide salt (2 mmol), CuX_2 , was then dissolved in 10 mL of an identical solvent mixture and added slowly to the former solution. The resulting solution was then left to evaporate slowly affording intense green parallelogram shaped block crystals upon almost complete evaporation of the solvent. Exact quantities of each reagent used are listed in Table 5.3.

Table 5.3 The quantities of reagents used in the synthesis of the amino acid paddlewheel-shaped complexes and glycine-based complexes.

Reagent		Quantity
CuX ₂	CuCl ₂ ·2H ₂ O	0.3410 g
	CuBr ₂	0.4451 g
L	Gly	0.3003 g
	BAL	0.3564 g
	GABA	0.4125 g
	APA	0.4686 g
	AHA	0.5247 g

Of the compounds created, only the following were made as a pure phase: $Cu_2(ABA)_4Cl_2]Cl_2 \cdot H_2O$ (**27**), $[Cu_2(ABA)_4Br_2]Br_2$ (**28**), $[Cu_2(APA)_4Br_2]Br_2$ (**31**), $[Cu_2(AHA)_4Br_2]Br_2 \cdot 4H_2O$ (**33**). Elemental anal. (%) calcd for **27**: C, 27.48; H, 5.48; N, 8.01, found: C, 27.71; H, 5.71; N, 8.10; calcd for **28**: C, 22.37; H, 4.22; N, 6.52, found: C, 22.53; H, 4.10; N, 6.39; calcd for **31**: C, 26.24; H, 4.85; N, 6.12, found: C, 26.48; H, 4.86; N, 6.01; calcd for **33**: C, 27.63; H, 5.80; N, 5.37, found: C, 27.86; H, 5.55; N, 5.28.

5.1.4 $[Cu_2(APA)_4Cl_2]Cl_2$ (**30**) and $[Cu_2(AOA)_6]Cl_2$ (**34**)

Identical reactions to those in the above subsection were conducted for **30** and **34** but only water was used instead of a 1:1 mixture of MeOH and water. For **34** the quantity of reagents used was 0.0398 g (0.25 mmol) AOA, and 0.0213 g (0.125 mmol) of $CuCl_2 \cdot 2H_2O$. **30** could be made pure via this procedure but **34** could not. Elemental anal. (%) calcd for **30**: C, 32.57; H, 6.01; N, 7.60. Found: C, 32.94; H, 5.93; N, 7.64.

5.1.5 (H-L)[CuX₄] (37-44)

For general synthesis of the tetrahalocuprate salts of the amino acids studied, the following procedure was used. The amino acid (4 mmol), L, and the copper halide salt (2 mmol), CuX_2 , were dissolved in the corresponding concentrated hydrohalic acid (3 mL). The resulting solution was left to evaporate in a crystallising dish. Upon almost complete evaporation of the solvent, large yellow or black-purple crystals grew for the chloride and bromide salts respectively. Exact quantities of each reagent used are listed in Table 5.3.

This method was used to create (H- β -Ala)₂[CuCl₄] (**37**), (H- β -Ala)₂[CuBr₄] (**38**), (H-ABA)₂[CuCl₄] (**39**), (H-ABA)₂[CuBr₄] (**40**), (H-APA)₂[CuCl₄] (**41**), (H-APA)₂[CuBr₄] (**42**), (H-AHA)₂[CuCl₄] (**43**), and (H-AHA)₂[CuBr₄] (**44**), all of which were made pure. Elemental anal. (%) calcd for **37**: C, 18.69; H, 4.18; N, 7.27, found: C, 18.51; H, 4.57; N, 7.05; calcd for **38**: C, 12.79; H, 2.86; N, 4.97, found: C, 13.02; H, 2.91; N, 4.61; calcd for **39**: C, 23.23; H, 4.87; N, 6.77, found: C, 22.89; H, 4.51; N, 7.00; calcd for **40**: C, 16.25; H, 3.41; N, 4.74, found: C, 16.40; H, 3.15; N, 4.78; calcd for **41**: C, 27.19; H, 5.48; N, 6.34 found: C, 27.31; H, 5.79; N, 6.46; calcd for **42**: C, 19.39; H, 3.90; N, 4.52, found: C, 19.19; H, 4.06; N, 4.76; calcd for **43**: C, 30.68; H, 6.01; N, 5.96, found: C, 30.91; H, 6.29; N, 6.13; calcd for **44**: C, 22.26; H, 4.36; N, 4.33. Found: C, 22.56; H, 4.60; N, 4.65.

5.2 Crystal structure and refinement information

Crystal structures were solved and refined according to the standard procedure discussed in the experimental section or as described in the above sections, apart for the following exceptions. The crystal of **25** was found to be non-centrosymmetric and racemically twinned. Refinement was conducted using the default twin command (inversion) and the twin fraction was found to be 0.776(14):0.224(14). The crystal of **40** was also found to be twinned with a twin law of $-1, 0, 0, 0, -1, 0, 0.99, 0.96$. Refinement with this twin law calculated the twin fraction as 0.898(2):0.102(2). **41** was found to scatter poorly at high angle meaning the collected data were effectively just noise at these angles, therefore the data were omitted from $51^\circ 2\theta$ onwards to give a much better R_{int} . Further details on the crystal structure refinements are contained in Table 5.4 to Table 5.10.

Table 5.4 Crystal structure data for compounds **22**, **24**, and **25**.

Compound	22	24	25
Empirical formula	C ₁₀ H ₂₀ N ₂ O ₄ Zn	C ₁₂ H _{34.25} Br ₄ Cu ₂ N ₄ O _{11.125}	C ₁₂ H ₃₂ Br ₄ Cu ₂ N ₄ O ₁₀
Formula weight (g mol ⁻¹)	297.65	859.38	839.13
Temperature (K)	150(1)	150(1)	150(1)
λ (Å)	0.71073	0.71073	0.71073
Crystal system	Monoclinic	Orthorhombic	Monoclinic
Space group	<i>I</i> 2/ <i>a</i>	<i>C</i> 222 ₁	<i>P</i> 2 ₁ / <i>n</i>
<i>a</i> (Å)	8.7338(9)	27.5474(10)	10.2319(9)
<i>b</i> (Å)	12.6678(9)	29.6697(9)	9.7111(6)
<i>c</i> (Å)	11.4820(15)	27.0281(9)	13.5609(12)
α (°)	90	90	90
β (°)	97.862(9)	90	98.909(7)
γ (°)	90	90	90
<i>V</i> (Å ³)	1258.4(2)	22090.7(13)	1331.20(19)
<i>Z</i>	4	32	2
Density (Mg m ⁻³)	1.571	2.067	2.093
μ (mm ⁻¹)	1.957	7.381	7.65
Crystal size (mm)	0.3 × 0.13 × 0.12	0.19 × 0.17 × 0.06	0.48 × 0.11 × 0.11
Transmission factors (max/min)	0.8023 and 0.6324	0.5302 and 0.3166	0.4931 and 0.1447
<i>F</i> (000)	624	13280	820
θ range (°)	2.407 - 29.179	1.259 - 25.444	2.328 - 29.190
Index ranges	-11 ≤ <i>h</i> ≤ 11 -17 ≤ <i>k</i> ≤ 17 -15 ≤ <i>l</i> ≤ 15	-30 ≤ <i>h</i> ≤ 33 -32 ≤ <i>k</i> ≤ 35 -22 ≤ <i>l</i> ≤ 32	-12 ≤ <i>h</i> ≤ 14 -11 ≤ <i>k</i> ≤ 13 -18 ≤ <i>l</i> ≤ 18
Reflections collected	6100	29962	9230
Independent reflections (<i>R</i> _{int})	1697 (0.0389)	20028 (0.0659)	3581 (0.0985)
Completeness to $\theta = 25.242^\circ$	100.0%	99.4%	100.0%
Restraints/parameters	0/78	0/1158	3/155
Goodness-of-fit on <i>F</i> ²	0.918	0.834	0.854
<i>R</i> ₁ [<i>I</i> > 2 σ (<i>I</i>)]	0.0193	0.0477	0.0347
<i>wR</i> ₂ (all data)	0.0446	0.0979	0.0854
Extinction coefficient	-	-	0.0069(4)
Largest diff. peak and hole (e Å ⁻³)	0.381 and -0.280	1.961 and -0.605	1.162 and -0.753

Table 5.5 Crystal structure data for the compound **27**, and **27** after the first and second steps of dehydration (**DH1** and **DH2**).

Compound	27	DH1	DH2
Empirical formula	C ₁₆ H ₃₈ Cl ₄ Cu ₂ N ₄ O ₉	C ₁₆ H _{37.16} Cl ₄ Cu ₂ N ₄ O _{8.58}	C ₁₆ H _{36.7} Cl ₄ Cu ₂ N ₄ O _{8.35}
Formula weight (g mol ⁻¹)	699.4	691.83	687.69
Temperature (K)	150(1)	150(1)	150(1)
λ (Å)	0.71073	0.71073	0.71073
Crystal system	Monoclinic	Monoclinic	Monoclinic
Space group	<i>P</i> 2 ₁ / <i>c</i>	<i>P</i> 2 ₁ / <i>c</i>	<i>P</i> 2 ₁ / <i>c</i>
<i>a</i> (Å)	9.1318(6)	9.0870(5)	9.0697(4)
<i>b</i> (Å)	21.1712(9)	21.0787(13)	21.0400(12)
<i>c</i> (Å)	15.1158(10)	15.0875(8)	15.0755(7)
α (°)	90	90	90
β (°)	106.274(5)	106.529(4)	106.656(4)
γ (°)	90	90	90
<i>V</i> (Å ³)	2805.3(3)	2770.5(3)	2756.1(2)
<i>Z</i>	4	4	4
Density (Mg m ⁻³)	1.656	1.658	1.657
μ (mm ⁻¹)	1.946	1.969	1.978
Crystal size (mm)	0.22 × 0.2 × 0.11	0.48 × 0.44 × 0.1	0.48 × 0.44 × 0.1
Transmission factors (max/min)	0.8142 and 0.6930	0.8145 and 0.4454	0.8135 and 0.4436
<i>F</i> (000)	1440	1418	1411
θ range (°)	1.701 - 29.209	1.707 - 29.169	1.710 - 29.172
Index ranges	-12 ≤ <i>h</i> ≤ 9 -28 ≤ <i>k</i> ≤ 28 -20 ≤ <i>l</i> ≤ 20	-12 ≤ <i>h</i> ≤ 12 -28 ≤ <i>k</i> ≤ 24 -20 ≤ <i>l</i> ≤ 16	-12 ≤ <i>h</i> ≤ 12 -28 ≤ <i>k</i> ≤ 24 -20 ≤ <i>l</i> ≤ 17
Reflections collected	21735	14129	15838
Independent reflections (<i>R</i> _{int})	7554 (0.0808)	7267 (0.0544)	7341 (0.0377)
Completeness to $\theta = 25.242^\circ$	99.9%	97.2%	98.8%
Restraints/parameters	3/327	0/321	0/323
Goodness-of-fit on <i>F</i> ²	0.833	0.928	0.888
<i>R</i> ₁ [<i>I</i> > 2 σ (<i>I</i>)]	0.0313	0.0429	0.0298
<i>wR</i> ₂ (all data)	0.0694	0.1025	0.0657
Largest diff. peak and hole (e Å ⁻³)	0.775 and -0.693	0.657 and -0.785	0.534 and -0.524

Table 5.6 Crystal structure data for the compound **27** after full dehydration and partial rehydration (**DH3** and **RH1**), and **28**.

Compound	DH3	RH1	28
Empirical formula	C ₁₆ H _{36.1} Cl ₄ Cu ₂ N ₄ O _{8.04}	C ₁₆ H _{37.2} Cl ₄ Cu ₂ N ₄ O _{8.60}	C ₁₆ H ₃₆ Br ₄ Cu ₂ N ₄ O ₈
Formula weight (g mol ⁻¹)	682.12	692.19	859.21
Temperature (K)	150(1)	150(1)	150(1)
λ (Å)	0.71073	0.71073	0.71073
Crystal system	Monoclinic	Monoclinic	Triclinic
Space group	<i>P</i> 2 ₁ / <i>c</i>	<i>P</i> 2 ₁ / <i>c</i>	<i>P</i> $\bar{1}$
<i>a</i> (Å)	9.0418(4)	9.0882(5)	8.5589(9)
<i>b</i> (Å)	20.9813(12)	21.0797(14)	8.9229(10)
<i>c</i> (Å)	15.0562(7)	15.0986(7)	10.486(2)
α (°)	90	90	100.722(11)
β (°)	106.749(4)	106.493(4)	106.343(10)
γ (°)	90	90	110.957(8)
<i>V</i> (Å ³)	2735.1(2)	2773.5(3)	679.91(17)
<i>Z</i>	4	4	1
Density (Mg m ⁻³)	1.656	1.657	2.098
μ (mm ⁻¹)	1.992	1.967	7.487
Crystal size (mm)	0.48 × 0.44 × 0.1	0.48 × 0.44 × 0.1	0.28 × 0.25 × 0.15
Transmission factors (max/min)	0.8117 and 0.4416	0.8336 and 0.4372	0.3832 and 0.1867
<i>F</i> (000)	1401	1419	422
θ range (°)	1.714 - 29.210	1.706 - 25.982	2.136 - 29.155
Index ranges	-12 ≤ <i>h</i> ≤ 12 -28 ≤ <i>k</i> ≤ 25 -20 ≤ <i>l</i> ≤ 18	-11 ≤ <i>h</i> ≤ 11 -23 ≤ <i>k</i> ≤ 25 -18 ≤ <i>l</i> ≤ 18	-11 ≤ <i>h</i> ≤ 11 -12 ≤ <i>k</i> ≤ 12 -14 ≤ <i>l</i> ≤ 14
Reflections collected	17334	23908	7399
Independent reflections (<i>R</i> _{int})	7348 (0.0426)	23908 (0.0409)	3619 (0.1095)
Completeness to $\theta = 25.242^\circ$	99.6%	99.5%	99.3%
Restraints/parameters	0/318	0/319	0/155
Goodness-of-fit on <i>F</i> ²	0.873	0.987	0.970
<i>R</i> ₁ [<i>I</i> > 2 σ (<i>I</i>)]	0.0336	0.0695	0.0379
<i>wR</i> ₂ (all data)	0.0801	0.1972	0.1027
Largest diff. peak and hole (e Å ⁻³)	0.605 and -1.001	0.633 and -1.144	2.169 and -1.880

Table 5.7 Crystal structure data for **29**, and **30** at 150, 298, and 333 K.

Compound	29	30	30	30
Empirical formula	C ₂₀ H ₄₈ Cl ₄ Cu ₂ N ₄ O ₁₀	C ₂₀ H ₄₄ Cl ₄ Cu ₂ N ₄ O ₈	C ₂₀ H ₄₄ Cl ₄ Cu ₂ N ₄ O ₈	C ₂₀ H ₄₄ Cl ₄ Cu ₂ N ₄ O ₈
Formula weight (g mol ⁻¹)	773.5	737.47	737.47	737.47
Temperature (K)	150(1)	150(1)	298(1)	333(1)
λ (Å)	0.71073	0.71073	0.71073	0.71073
Crystal system	Triclinic	Monoclinic	Monoclinic	Monoclinic
Space group	$P\bar{1}$	$P2_1/c$	$P2_1/c$	$P2_1/c$
a (Å)	8.0302(11)	9.0041(6)	8.9843(7)	8.9854(7)
b (Å)	9.1126(11)	19.5885(14)	19.8343(17)	19.8807(17)
c (Å)	12.2504(16)	9.4018(7)	9.6807(8)	9.7594(8)
α (°)	74.418(10)	90	90	90
β (°)	80.299(11)	115.711(5)	117.045(6)	117.371(6)
γ (°)	83.810(10)	90	90	90
V (Å ³)	849.3(2)	1494.08(19)	1536.4(2)	1548.2(2)
Z	1	2	2	2
Density (Mg m ⁻³)	1.512	1.639	1.594	1.582
μ (mm ⁻¹)	1.617	1.83	1.779	1.766
Crystal size (mm)	0.24 × 0.2 × 0.07	0.29 × 0.28 × 0.1	0.31 × 0.31 × 0.11	0.31 × 0.31 × 0.11
Transmission factors (max/min)	0.8952 and 0.7145	0.7767 and 0.5969	0.8246 and 0.6064	0.8256 and 0.6091
$F(000)$	402	764	764	764
θ range (°)	1.744 - 27.786	2.079 - 29.196	2.545 - 29.210	2.553 - 29.167
Index ranges	-9 ≤ h ≤ 10 -11 ≤ k ≤ 11 -16 ≤ l ≤ 16	-12 ≤ h ≤ 12 -26 ≤ k ≤ 26 -12 ≤ l ≤ 12	-12 ≤ h ≤ 12 -27 ≤ k ≤ 22 -13 ≤ l ≤ 13	-12 ≤ h ≤ 12 -27 ≤ k ≤ 22 -13 ≤ l ≤ 13
Reflections collected	8962	11601	10866	11125
Independent reflections (R_{int})	3957 (0.1035)	4020 (0.0563)	4122 (0.0498)	4158 (0.0523)
Completeness to $\theta = 25.242^\circ$	98.7%	99.7%	99.4%	99.5%
Restraints/parameters	3/197	0/174	4/174	4/174
Goodness-of-fit on F^2	0.891	0.835	0.890	0.894
R_1 [$I > 2\sigma(I)$]	0.0529	0.0266	0.0343	0.0338
wR_2 (all data)	0.1501	0.0637	0.0888	0.0891
Largest diff. peak and hole (e Å ⁻³)	1.342 and -1.300	0.600 and -0.820	0.647 and -0.813	0.523 and -0.659

Table 5.8 Crystal structure data for **31** at 150, 298, and 333 K, and **33**.

Compound	31	31	31	33
Empirical formula	C ₂₀ H ₄₄ Br ₄ Cu ₂ N ₄ O ₈	C ₂₀ H ₄₄ Br ₄ Cu ₂ N ₄ O ₈	C ₂₀ H ₄₄ Br ₄ Cu ₂ N ₄ O ₈	C ₂₄ H ₆₀ Br ₄ Cu ₂ N ₄ O ₁₂
Formula weight (g mol ⁻¹)	915.31	915.31	915.31	1043.48
Temperature (K)	150(1)	298(1)	333(1)	150(1)
λ (Å)	0.71073	0.71073	0.71073	0.71073
Crystal system	Monoclinic	Monoclinic	Monoclinic	Monoclinic
Space group	<i>P</i> 2 ₁ / <i>c</i>	<i>P</i> 2 ₁ / <i>c</i>	<i>P</i> 2 ₁ / <i>c</i>	<i>P</i> 2 ₁ / <i>n</i>
<i>a</i> (Å)	8.8923(9)	8.9505(7)	8.9615(7)	9.5204(7)
<i>b</i> (Å)	20.0101(17)	20.1051(14)	20.1319(14)	12.2505(6)
<i>c</i> (Å)	9.7160(9)	10.0922(8)	10.1514(8)	17.8516(16)
α (°)	90	90	90	90
β (°)	114.846(7)	116.778(5)	117.038(5)	105.284(6)
γ (°)	90	90	90	90
<i>V</i> (Å ³)	1568.8(3)	1621.3(2)	1631.3(2)	2008.4(3)
<i>Z</i>	2	2	2	2
Density (Mg m ⁻³)	1.938	1.875	1.863	1.725
μ (mm ⁻¹)	6.496	6.286	6.247	5.093
Crystal size (mm)	0.25 × 0.25 × 0.24	0.25 × 0.25 × 0.24	0.25 × 0.25 × 0.24	0.4 × 0.38 × 0.24
Transmission factors (max/min)	0.3362 and 0.2439	0.3766 and 0.2640	0.3563 and 0.2522	0.3235 and 0.2208
<i>F</i> (000)	908	908	908	1052
θ range (°)	2.035 - 29.206	2.026 - 29.163	2.023 - 29.213	2.040 - 29.239
Index ranges	-10 ≤ <i>h</i> ≤ 12 -24 ≤ <i>k</i> ≤ 27 -13 ≤ <i>l</i> ≤ 13	-12 ≤ <i>h</i> ≤ 11 -25 ≤ <i>k</i> ≤ 27 -13 ≤ <i>l</i> ≤ 13	-12 ≤ <i>h</i> ≤ 10 -25 ≤ <i>k</i> ≤ 27 -13 ≤ <i>l</i> ≤ 13	-13 ≤ <i>h</i> ≤ 12 -16 ≤ <i>k</i> ≤ 14 -24 ≤ <i>l</i> ≤ 24
Reflections collected	10431	12902	11373	13407
Independent reflections (<i>R</i> _{int})	4199 (0.0543)	4350 (0.0686)	4348 (0.0692)	5378 (0.1102)
Completeness to $\theta = 25.242^\circ$	99.3%	99.9%	98.8%	99.9%
Restraints/parameters	0/174	4/174	4/174	6/223
Goodness-of-fit on <i>F</i> ²	0.833	0.842	0.809	0.916
<i>R</i> ₁ [<i>I</i> > 2 σ (<i>I</i>)]	0.0229	0.0354	0.0381	0.0464
<i>wR</i> ₂ (all data)	0.0492	0.0899	0.0966	0.1178
Largest diff. peak and hole (e Å ⁻³)	0.414 and -0.814	0.649 and -1.034	0.610 and -1.041	1.160 and -1.004

Table 5.9 Crystal structure data for compounds **34**, **35**, **36**, **37**.

Compound	34	35	36	37
Empirical formula	C ₄₈ H ₁₀₂ Cl ₄ Cu ₂ N ₆ O ₁₂	C ₈ H ₂₀ Cl ₆ Cu ₄ N ₄ O ₈	C ₄ H ₈ CuN ₂ O ₆	C ₆ H ₁₆ Cl ₄ CuN ₂ O ₄
Formula weight (g mol ⁻¹)	1224.23	767.14	243.66	385.55
Temperature (K)	150(1)	150(1)	150(1)	150(1)
λ (Å)	0.71073	0.71073	0.71073	0.71073
Crystal system	Triclinic	Triclinic	Monoclinic	Monoclinic
Space group	$P\bar{1}$	$P\bar{1}$	$P2_1/c$	$I2/a$
a (Å)	8.8726(8)	8.2377(11)	7.0481(6)	7.3735(6)
b (Å)	14.0656(11)	8.3801(11)	7.8049(7)	7.7223(4)
c (Å)	14.1451(10)	8.5255(12)	13.9638(15)	24.080(2)
α (°)	67.083(6)	84.875(11)	90	90
β (°)	73.027(6)	79.783(11)	90.845(8)	91.485(7)
γ (°)	76.748(6)	64.958(10)	90	90
V (Å ³)	1541.7(2)	524.69(13)	768.06(13)	1370.66(17)
Z	1	1	4	4
Density (Mg m ⁻³)	1.319	2.428	2.107	1.868
μ (mm ⁻¹)	0.921	4.809	2.846	2.376
Crystal size (mm)	0.26 × 0.24 × 0.08	0.13 × 0.12 × 0.04	0.11 × 0.1 × 0.04	0.48 × 0.4 × 0.38
Transmission factors (max/min)	0.9314 and 0.8047	0.8159 and 0.4939	0.8798 and 0.6987	0.4707 and 0.3961
$F(000)$	654	378	492	780
θ range (°)	1.586 - 29.257	2.428 - 29.232	2.890 - 29.290	2.770 - 29.157
Index ranges	-12 ≤ h ≤ 10 -19 ≤ k ≤ 19 -18 ≤ l ≤ 19	-11 ≤ h ≤ 10 -11 ≤ k ≤ 11 -11 ≤ l ≤ 11	-9 ≤ h ≤ 9 -9 ≤ k ≤ 10 -19 ≤ l ≤ 16	-10 ≤ h ≤ 8 -10 ≤ k ≤ 10 -27 ≤ l ≤ 32
Reflections collected	12255	6004	4317	4748
Independent reflections (R_{int})	7583 (0.0506)	2822 (0.0879)	2058 (0.0673)	1723 (0.0479)
Completeness to $\theta = 25.242^\circ$	93.1%	99.7%	99.4%	94.6%
Restraints/parameters	0/325	0/138	6/131	0/82
Goodness-of-fit on F^2	0.822	0.927	0.846	1.125
R_1 [$I > 2\sigma(I)$]	0.0379	0.0335	0.0392	0.0299
wR_2 (all data)	0.0889	0.0876	0.0860	0.0810
Extinction coefficient	-	-	-	0.040(2)
Largest diff. peak and hole (e Å ⁻³)	0.998 and -0.651	0.876 and -0.920	0.903 and -0.609	0.887 and -1.104

Table 5.10 Crystal structure data for compounds **38**, **40**, **41**, **43**.

3	38	40	41	43
Empirical formula	C ₆ H ₁₆ Br ₄ CuN ₂ O ₄	C ₈ H ₂₀ Br ₄ CuN ₂ O ₄	C ₁₀ H ₂₄ Cl ₄ CuN ₂ O ₄	C ₁₂ H ₂₈ Cl ₄ CuN ₂ O ₄
Formula weight (g mol ⁻¹)	563.39	591.44	441.65	469.7
Temperature (K)	150(1)	150(1)	150(1)	298(1)
λ (Å)	0.71073	0.71073	0.71073	0.71073
Crystal system	Monoclinic	Triclinic	Triclinic	Monoclinic
Space group	<i>I</i> 2/ <i>a</i>	<i>P</i> $\bar{1}$	<i>P</i> $\bar{1}$	<i>P</i> 2 ₁ / <i>c</i>
<i>a</i> (Å)	7.7324(7)	11.0761(11)	7.1827(13)	18.766(3)
<i>b</i> (Å)	8.0011(9)	11.1901(16)	7.5193(12)	7.3824(7)
<i>c</i> (Å)	24.087(2)	15.772(2)	16.597(3)	7.5660(8)
α (°)	90	109.223(11)	86.525(13)	90
β (°)	92.062(7)	109.689(10)	87.155(14)	98.719(10)
γ (°)	90	91.967(10)	89.188(14)	90
<i>V</i> (Å ³)	1489.2(2)	1714.6(4)	893.6(3)	1036.1(2)
<i>Z</i>	4	4	2	2
Density (Mg m ⁻³)	2.513	2.291	1.641	1.506
μ (mm ⁻¹)	12.202	10.604	1.833	1.586
Crystal size (mm)	0.4 x 0.27 x 0.12	0.29 x 0.21 x 0.03	0.45 x 0.19 x 0.12	0.4 x 0.15 x 0.11
Transmission factors (max/min)	0.2080 and 0.0670	0.6976 and 0.0812	0.8222 and 0.5275	0.8168 and 0.5728
<i>F</i> (000)	1068	1132	454	486
θ range (°)	1.692 - 29.232	1.954 - 29.594	2.462 - 25.500	2.970 - 29.178
Index ranges	-8 \leq h \leq 10 -10 \leq k \leq 9 -32 \leq l \leq 32	-11 \leq h \leq 15 -14 \leq k \leq 15 -21 \leq l \leq 21	-8 \leq h \leq 8 -9 \leq k \leq 9 -20 \leq l \leq 20	-25 \leq h \leq 15 -9 \leq k \leq 10 -10 \leq l \leq 10
Reflections collected	4436	17934	6481	5275
Independent reflections (<i>R</i> _{int})	1994 (0.1136)	9053 (0.0915)	3293 (0.0996)	2731 (0.0708)
Completeness to $\theta = 25.242^\circ$	99.2%	99.9%	98.7%	97.3%
Restraints/parameters	0/82	0/313	0/197	0/103
Goodness-of-fit on <i>F</i> ²	0.957	1.112	0.810	0.918
<i>R</i> ₁ [<i>I</i> > 2 σ (<i>I</i>)]	0.0486	0.0834	0.0512	0.0515
<i>wR</i> ₂ (all data)	0.1263	0.2939	0.1214	0.1538
Extinction coefficient	0.0046(4)	-	-	0.040(5)
Largest diff. peak and hole (e Å ⁻³)	1.644 and -1.736	2.613 and -2.109	0.771 and -0.847	0.378 and -0.509

5.3 Neutral frameworks

Before commencing any work, a thorough search of the Cambridge Structural Database (CSD)¹¹⁹ was conducted. This showed three neutral coordination polymers had already been reported for copper with ABA and AHA by Takenaka *et al.* and Sjöberg *et al.* respectively.^{195,196} Two of these polymers, $\{[\text{Cu}(\text{ABA})_2](\text{H}_2\text{O})_2\}_n$ and $\{[\text{Cu}(\text{AHA})_2](\text{H}_2\text{O})_2\}_n$, are 2-D frameworks, and the other, $[\text{Cu}(\text{ABA})_2]_n$, is a 1-D chain.

While Sjöberg *et al.* synthesised $\{[\text{Cu}(\text{AHA})_2](\text{H}_2\text{O})_2\}_n$ via air oxidation of an aqueous solution containing copper (I) perchlorate and AHA, Dan and Rao synthesised the compound by evaporation of ammoniacal solution of copper (II) chloride and AHA.¹⁹⁷ Additionally, the latter group investigated the loss and gain of water from the framework and found that while the water could be removed from the compound, the change was irreversible.

The first experiments in the present work attempted to replicate the results/methods already reported, but also to expand the library of compounds by attempting experiments using iron, cobalt, nickel, and zinc instead of copper. The experiments were conducted in water systematically testing different metal salts, metal to amino acid ratios, and quantities of base added, but all experiments failed to produce any crystalline material; the majority of the solvent evaporated before leaving a viscous syrup. Although no crystalline material was produced to be analysed, it is likely that a reaction did take place. Firstly, the inability of the solutions to produce crystals in the presence of water is indicative of a compound containing neutral amine groups; amines are commonly crystallised as their salts due to their affinity for water, compounds exhibiting lots of free, neutral amine groups would potentially be very soluble to the point of deliquescence. Secondly, the majority of the metals show a slight colour change, however iron (III) nitrate solutions show a clear colour change from yellow to dark red-orange in water when mixed with a basic solution of the acids; the same colour change observed on reaction of iron (III) salts with sodium acetate producing the common tri-iron oxo-centred cluster. This again indicates that a reaction does take place, at least with iron.

In order to overcome the extreme solubility of the potential compounds, a solvent that is less volatile than water but in which the ligand is not soluble was required to perform

crystallisation by evaporation of a solvent/anti-solvent solution. There were not many options to choose from due to water being somewhat non-volatile, but experimentation showed DMSO to be a good candidate. Additionally, DMSO seemed to prevent the decomposition reaction that occurs when solutions of copper salts and amino acids are heated for a prolonged period; the solution would turn green and cloudy then produce an unidentified amorphous brown powder. The procedure was to first dissolve the reaction components in water, then add an equal quantity of DMSO creating a 50:50 mixture of the two solvents before placing the solution in an oven maintained at 60 °C until precipitation/crystallisation was observed. The majority of the DMSO/water reactions again failed to produce any crystalline material, but those using zinc and copper produced some material. Unfortunately, the single-crystals produced with copper were of the known complexes with ABA and AHA mentioned above, although a new compound was produced with zinc and APA. The structures of these compounds are discussed below.

5.3.1 $[Cu(ABA)_2]_n/\{[Cu(ABA)_2](H_2O)_2\}_n$ (19/20)

The structures of the two polymeric compounds formed by reaction of copper with ABA are shown in Figure 5.2. Both structures were discovered originally by Takenaka *et al.* from crystals produced by reaction of copper chloride and ABA in a water/methanol/ethanol solution.¹⁹⁵ $[Cu(ABA)_2]_n$ (**19**) displays a 1-D polymeric structure whereby a chain of Cu atoms along *a* are bridged by amino acids with two between each pair. $\{[Cu(ABA)_2](H_2O)_2\}_n$ (**20**) is instead a 2-D polymer as each pair of Cu atoms is bridged by only one ABA molecule. The 2-D polymeric sheets stack in such a way along *a* as to create channels filled with water molecules which hydrogen bond to the surrounding structure. In both structures the Cu has a distorted octahedral environment whereby two N and two O donor atoms form a square planar coordination geometry (for

19: Cu-N = 2.0197(9) Å, Cu-O = 1.9837(10) Å, O-Cu-N = 91.981(10)°; for **20**: Cu-N = 2.0146(3) Å, Cu-O = 1.9593(4) Å, O-Cu-N = 86.057(8)°, and the two additional carboxylate O donor atoms form extended Cu-O bonds that are not perpendicular to the plane (for **19**: Cu-O = 2.6423(4) Å, O-Cu-O = 54.687(2)°; for **20**: Cu-O = 2.7958(7) Å, O-Cu-O = 51.793(2)°).

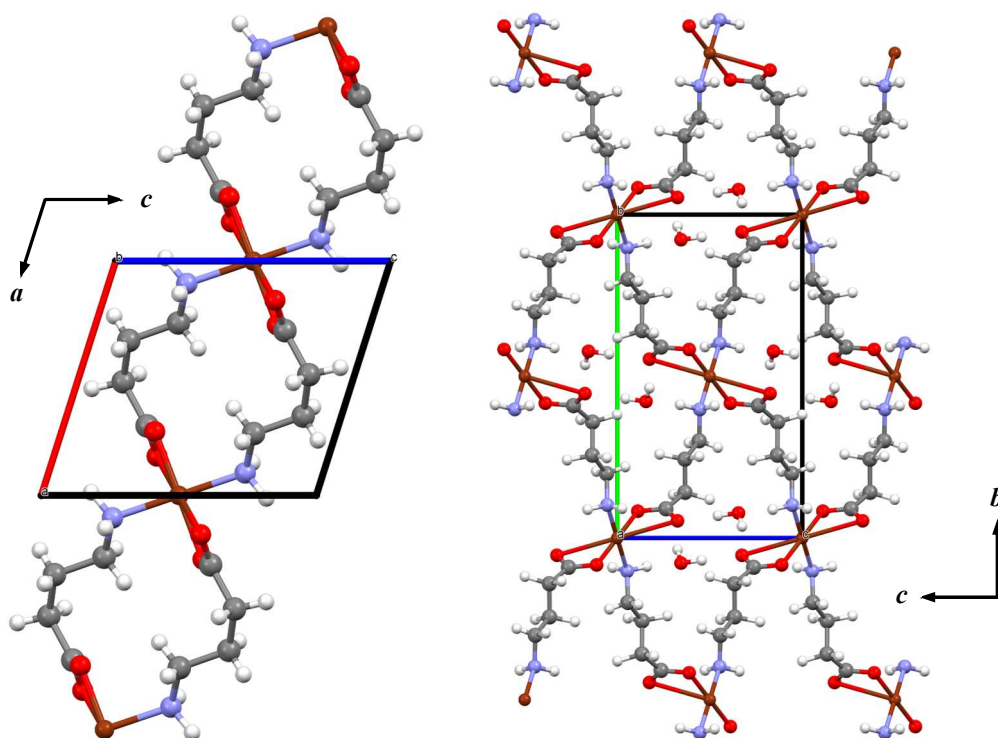


Figure 5.2 Crystal structures of $[\text{Cu}(\text{ABA})_2]_n$ (**19**), left, and $\{[\text{Cu}(\text{ABA})_2](\text{H}_2\text{O})_2\}_n$ (**20**), right, as viewed down the *b* and *a* axes respectively.¹⁹⁵ C atoms are shown in grey, H in white, Cu in dark brown, N in light grey-blue, and O in red.

The lack of details in the original report by Takenaka *et al.* has meant efforts to replicate the results have been unsuccessful. The DMSO/H₂O reaction described above resulted in a few crystals that displayed the same unit-cell as the non-hydrated structure. Although the resulting material is not pure as shown by comparison of simulated and experimental X-ray powder diffraction data shown in Figure 5.3.

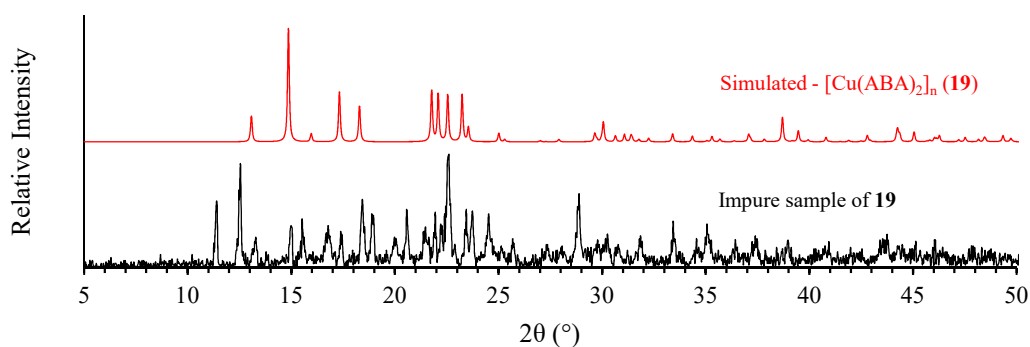


Figure 5.3 Room temperature X-ray powder diffraction data for **19**. Experimental data are shown in black while simulated data are shown in red.

5.3.2 $\{[Cu(AHA)_2](H_2O)_2\}_n$ (**21**)

The hydrated 2-D polymer $\{[Cu(AHA)_2](H_2O)_2\}_n$ (**21**) displays a remarkably similar structure to that of the ABA compound, **20**, as shown in Figure 5.4.¹⁹⁷ The Cu centre also has the same distorted octahedral environment as **20**: two N and two O donor atoms form a square plane (Cu-N = 1.9934(2) Å, Cu-O = 1.9661(3) Å, O-Cu-N = 93.258(7)°) and the other two O donor atoms form extended Cu-O bonds non-perpendicular to the plane (Cu-O = 2.7679(6) Å, O-Cu-O = 51.793(6)°). Additionally, a similar occupancy of the 1-D channels by water is observed. Since it was feasible that the water could be removed from such a structure, Dan and Rao attempted dehydration/rehydration experiments.¹⁹⁷ On removal of the water, the X-ray powder diffraction pattern showed an unknown change in the structure of the compound which was irreversible; re-exposure to water did not alter the sample any further. Similar experiments have not yet been conducted on **20** given the difficulty of synthesising the compound, but it may be worthwhile as a comparative study would allow observation of how extending the carbon chain in the ligand affects the physical properties.

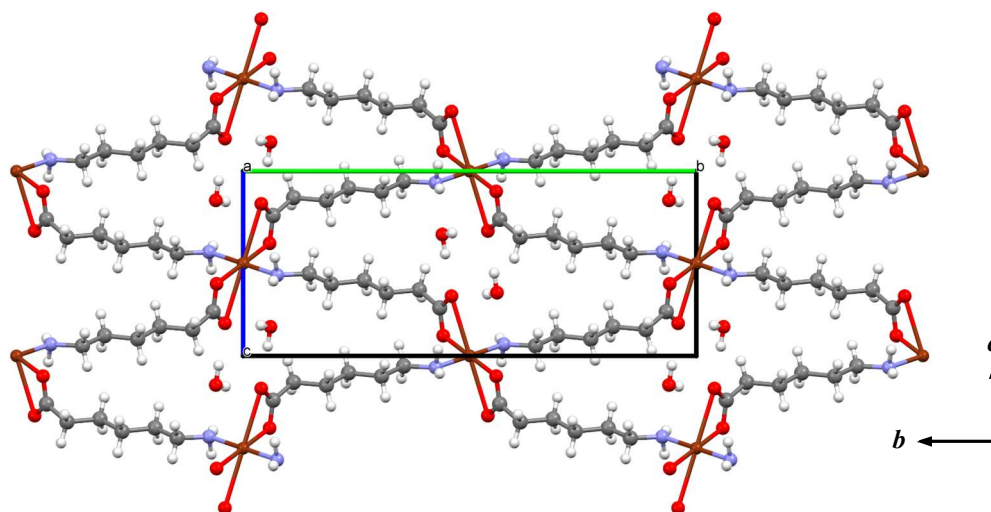


Figure 5.4 Crystal structure of $\{[\text{Cu}(\text{AHA})_2](\text{H}_2\text{O})_2\}_n$ (**21**) as viewed down the a axis. C atoms are shown in grey, H in white, Cu in dark brown, N in light grey-blue, and O in red.¹⁹⁷

X-ray powder diffraction of the purple powder matched the diffraction pattern simulated from the single-crystal structure, as shown in Figure 5.5. No additional peaks were observed in the experimental diffraction pattern indicating a pure product, elemental analysis also confirmed this.

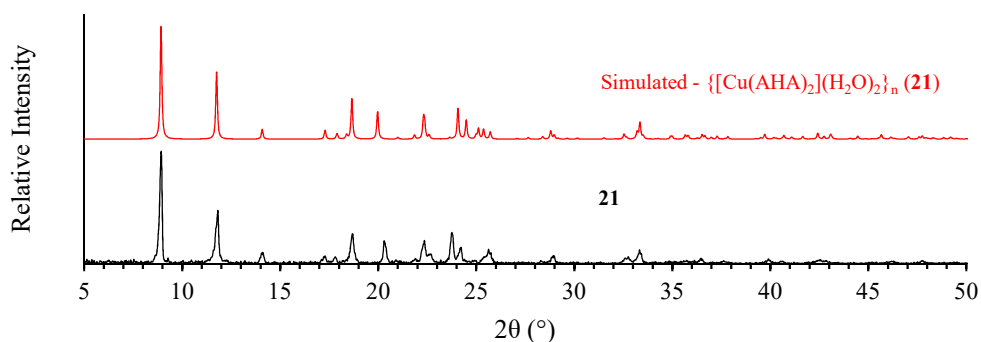


Figure 5.5 Room temperature X-ray powder diffraction data for $\{[\text{Cu}(\text{AHA})_2](\text{H}_2\text{O})_2\}_n$ (**21**). Experimental data are shown in black while simulated data are shown in red.

5.3.3 $[\text{Zn}(\text{APA})_2]_n$ (**22**)

Colourless blade-like crystals were produced by reaction of zinc acetate, $[\text{Zn}(\text{OAc})_2(\text{H}_2\text{O})_2]$, with APA in DMSO/ H_2O as described above. Single-crystal X-ray

diffraction analysis showed the compound to be $[\text{Zn}(\text{APA})_2]_n$ (**22**). **22** displays a monoclinic unit-cell with space group $I2/a$. The choice of a non-standard setting was based on the smaller β angle relative to that in the equivalent C-centred cell; $\beta = 97.862(8)^\circ$ in the I -centred cell as opposed to $\beta = 122.202(7)^\circ$ in the equivalent C-centred cell. The advantages of the choice of a conventional cell over a standard cell are covered in a paper by Mighell.¹⁹⁸ Further crystallographic details are included in Table 5.4. The asymmetric unit consists of one zinc cation on the 4e Wyckoff site and one APA anion, as shown in Figure 5.6. Each Zn^{2+} ion bonds to four APA molecules via two O and two N atoms in a distorted-tetrahedral geometry, bond distances and angles are given in Table 5.11.

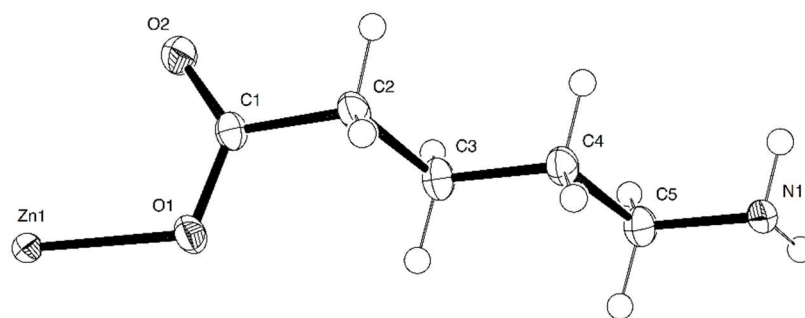


Figure 5.6 Asymmetric unit of $[\text{Zn}(\text{APA})_2]_n$ (**22**) with atoms shown as thermal ellipsoids drawn at 50% probability.

Table 5.11 Selected bond lengths (Å) and angles ($^\circ$) around the Zn coordination centre for $[\text{Zn}(\text{APA})_2]_n$ (**22**).

Zn(1) – O(1)	1.9909(9)	Zn(1) – N(1)#2	2.0298(12)
O(1) – Zn(1) – O(1)#1	107.29(6)	O(1) – Zn(1) – N(1)#3	101.45(4)
O(1) – Zn(1) – N(1)#2	109.99(4)	N(1)#2 – Zn(1) – N(1)#3	125.77(7)

#1 $\frac{1}{2}-x, y, -z$

#2 $x-\frac{1}{2}, y-\frac{1}{2}, z-\frac{1}{2}$

#3 $1-x, y-\frac{1}{2}, \frac{1}{2}-z$

Each APA ligand bonds to two Zn^{2+} ions thus a 4,4 net is formed which runs parallel to the $(10\bar{1})$ crystallographic plane. The 4,4 nets stack along a in an ABAB fashion, and the two unique orientations of the net are related by the glide plane symmetry element of the space group that runs parallel to the ac plane, as shown in Figure 5.7.

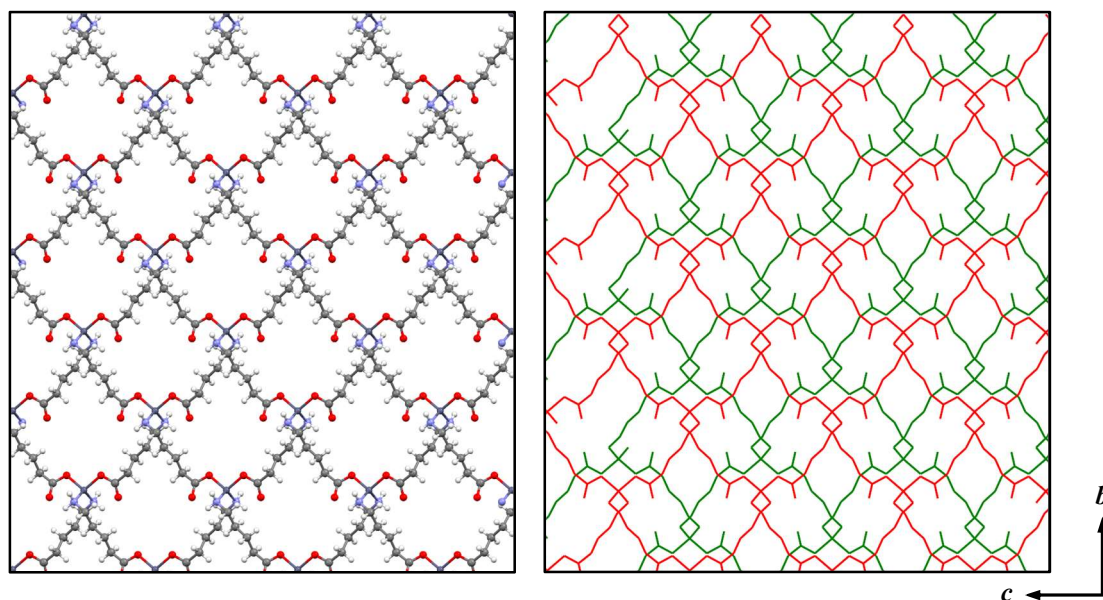


Figure 5.7 The 4,4 nets formed in the crystal structure of $[\text{Zn}(\text{APA})_2]_n$ (**22**) as shown down the a axis. Displayed left is the structure of one net shown as a ball and stick model. C atoms are shown in grey, H in white, N in light grey-blue, O in red, and Zn in dark grey-blue. Displayed right is the same net drawn as a red wireframe, and its symmetry related net coloured green showing the alternate ABAB stacking.

The distortion away from a true tetrahedral environment is shown most clearly by the N1-Zn1-N2 angle of $125.77(7)^\circ$, and the angular separation between the N1-Zn1-N2 and O1-Zn1-O3 planes of $84.04(9)^\circ$. The distortion appears to be a result of optimisation of hydrogen bonding interactions between the coordination polymer sheets, shown in Figure 5.8, which operate in the directions expected to give rise to the observed deviations: the N-H \cdots O hydrogens bonds of N2 and N1 operate in opposite directions which would result in them moving away from each other, and the same bonds from the perspective of O1 and O3 appear to be directing in such a way that a reduction in the angle shown in Figure 5.8 is required.

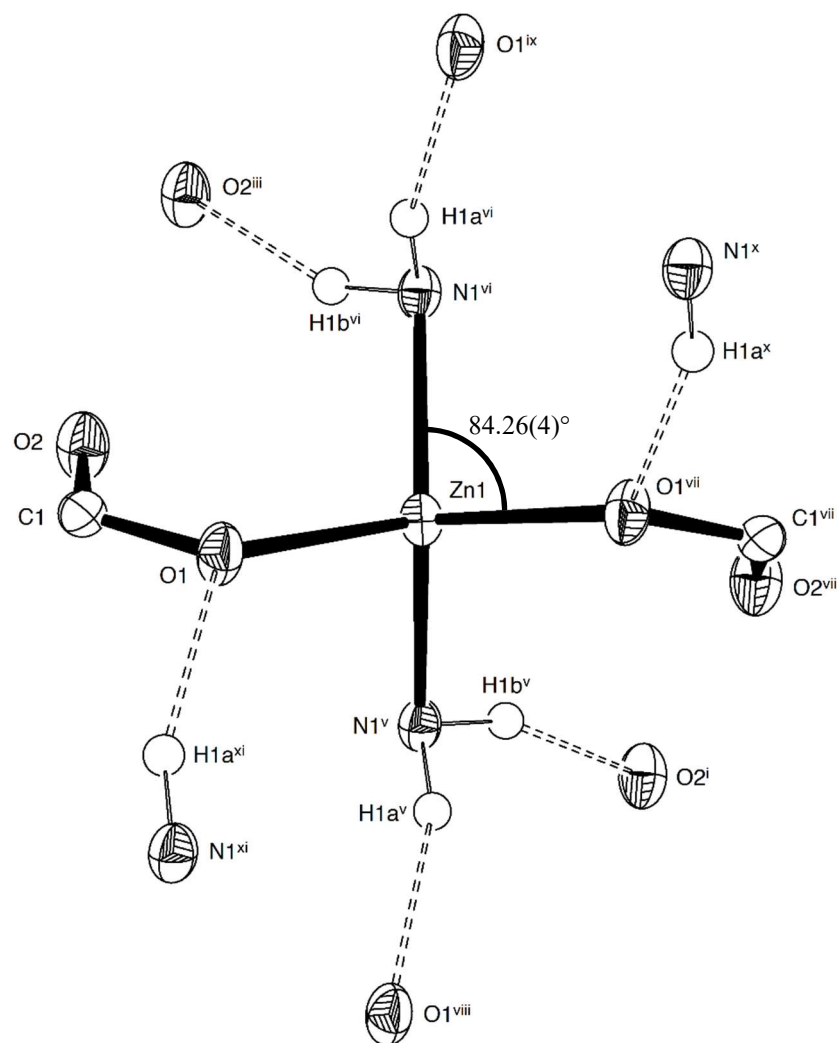


Figure 5.8 Hydrogen bonding interactions within $[\text{Zn}(\text{APA})_2]_n$ (**22**) as viewed down the N2-Zn1-N1 plane, also showing the angle between the N-Zn-N and O-Zn-O planes due to the tetrahedral distortion.

X-ray powder diffraction of the colourless powder matched the diffraction pattern simulated from the single-crystal structure, as shown in Figure 5.9. The difference in the relative intensities between the experimental and simulated data is most likely a result of preferred orientation due to the shape of the crystals, this can artificially increase the intensity of some peaks relative to others. The fact there are no additional peaks observed in the experimental diffraction pattern compared with the simulated data indicates a pure product was obtained, and this was confirmed by elemental analysis.

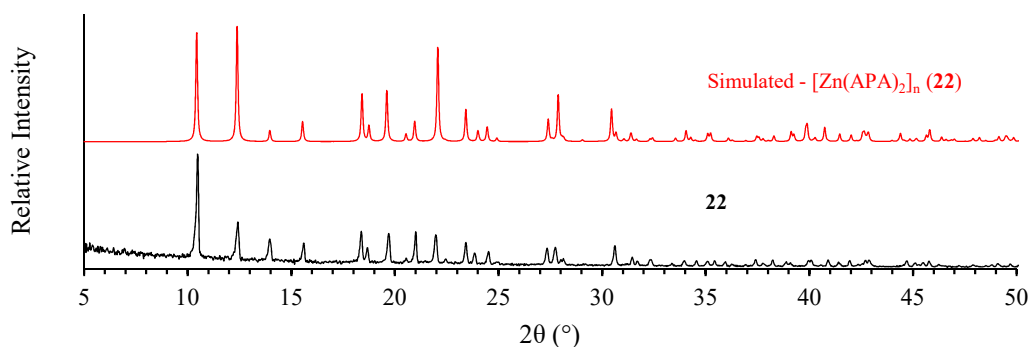


Figure 5.9 Room temperature X-ray powder diffraction data for **22**. Experimental data are shown in black while simulated data are shown in red.

5.4 $[\text{Cu}_2(\text{L})_4\text{X}_2]\text{X}_2 \cdot n\text{H}_2\text{O}$ paddlewheel compounds

Unlike the attempted formation of neutral coordination compounds with amino acids which was fraught with problems, the complexation of amino acids (L) with CuX_2 ($\text{X} = \text{Cl}, \text{Br}$) was very straightforward producing a variety of dichroic green-blue crystals. The majority of the compounds formed by this combination of metal salt and ligand type follow the general formula in the title of this subsection, along with n water of crystallisation where n is any integer 0-4. All the crystal structures with this general formula consist of four molecules of the given ligand in the zwitterionic state bridging two copper (II) ions, via the carboxylate group, in a paddlewheel type configuration: two copper centres with opposing square-pyramidal coordination, four oxygen atoms occupying each basal plane with apical sites capable of further coordination. The charge is balanced by four halide counterions, two for each copper centre, of which two bond to the vacant apical sites of the paddlewheel, as shown in Figure 5.10.

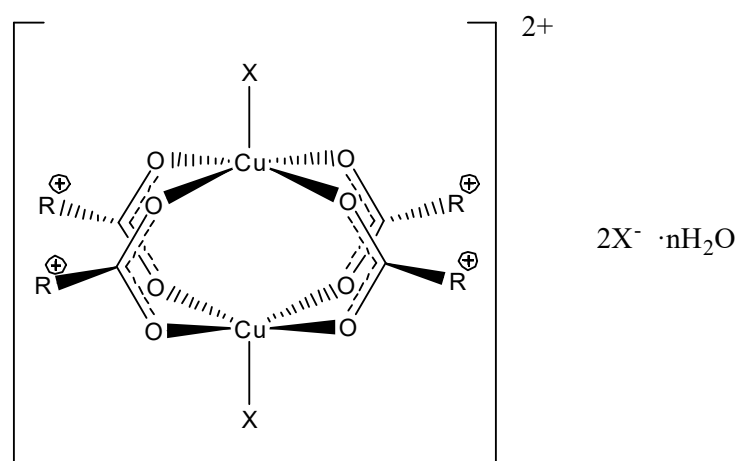


Figure 5.10 General structure of the $[\text{Cu}_2(\text{L})_4\text{X}_2]\text{X}_2 \cdot n\text{H}_2\text{O}$ type complexes showing the coordination about each copper centre. L = Ligand (Amino acid), X = Cl^- , Br^- and R^+ is an alkyl ammonium group with a varying methylene chain length.

The differences in these systems lie in the conformational changes of the alkyl ammonium chain, and the hydrogen bonding interactions between complexes including those mediated via free halide ions and water molecules. Descriptions will therefore focus on these two properties. As a reminder, the abbreviations used for the amino acids in the next two sections are shown in Table 5.1.

5.4.1 $[\text{Cu}_2(\beta\text{-Ala})_4\text{Cl}_2]\text{Cl}_2 \cdot \text{H}_2\text{O}$ (**23**)

The structure of $[\text{Cu}_2(\beta\text{-Ala})_4\text{Cl}_2]\text{Cl}_2 \cdot \text{H}_2\text{O}$ (**23**) was originally determined and described by Jezierska *et al.* so a full description will not be given here.¹⁹⁹ It has a triclinic unit-cell and is centrosymmetric, but the asymmetric unit contains two symmetry independent molecules which differ mainly in the orientations of the alkylammonium chains which are part of the bridging $\beta\text{-Ala}$ ligands. An image of the overall crystal packing is shown in Figure 5.11.

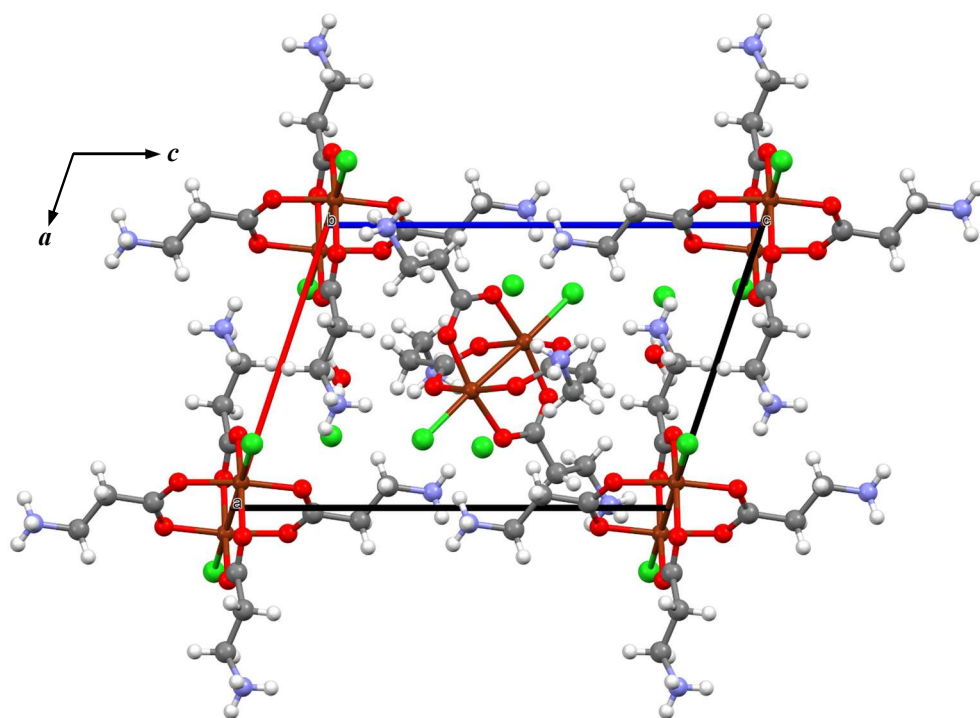


Figure 5.11 Crystal structure of $[\text{Cu}_2(\beta\text{-Ala})_4\text{Cl}_2]\text{Cl}_2\cdot\text{H}_2\text{O}$ (**23**) as viewed down the b axis. C atoms are shown in grey, H in white, Cu in dark brown, Cl in green, N in light grey-blue, and O in red.¹⁹⁹

The compound was produced within this body of work in a 1:1 mixture of methanol and water, while originally it was produced in pure water. This would seem to suggest that no other phase exists with a different level of hydration so no further experiments were attempted.

5.4.2 $[\text{Cu}_2(\beta\text{-Ala})_4\text{Br}_2]\text{Br}_2\cdot 2\text{H}_2\text{O}$ (**24**)

The synthesis of $[\text{Cu}(\beta\text{-Ala})_4\text{Br}_2]\text{Br}_2\cdot 2\text{H}_2\text{O}$ (**24**) was accomplished by evaporation of an aqueous solution of copper bromide to which two molar equivalents of $\beta\text{-Ala}$ were added. The unit-cell is monoclinic and has the space group $P2_1/n$, further crystallographic details are included in Table 5.4. Figure 5.12 shows the structure of the complex in **21** with the asymmetric unit labelled, it is composed of the basic paddlewheel motif located on a centre of inversion and the Cu centre has a square-pyramidal coordination geometry.

Bond distances and angles are shown in Table 5.12. One alkylammonium chain is in a simple planar zig-zag formation (RMSD from planarity = 0.0673 Å), while the other is only approximately planar (RMSD from planarity = 0.1301 Å) with a C4-C5-C6-N2 torsion angle of 96.0(5)°.

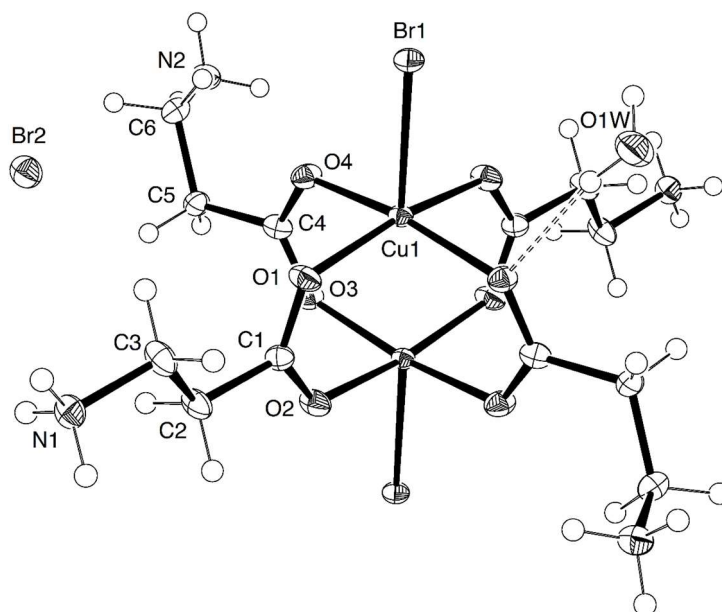


Figure 5.12 Asymmetric unit of $[\text{Cu}(\beta\text{-Ala})_4\text{Br}_2]\text{Br}_2 \cdot 2\text{H}_2\text{O}$ (**24**) with atoms shown as thermal ellipsoids drawn at 50% probability. The fragment is completed by the symmetry operator: $1-x, -y, 1-z$.

Table 5.12 Selected bond lengths (Å) and angles (°) around the Cu coordination centre for $[\text{Cu}(\beta\text{-Ala})_4\text{Br}_2]\text{Br}_2 \cdot 2\text{H}_2\text{O}$ (**24**).

Cu(1) – O(1)	1.980(3)	Cu(1) – O(4)#1	1.972(3)
Cu(1) – O(2)#1	1.963(3)	Cu(1) – Br(1)	2.5938(6)
Cu(1) – O(3)	1.977(3)	Cu(1) – Cu(1)#1	2.6498(10)
O(1) – Cu(1) – O(2)#1	168.32(12)	O(2)#1 – Cu(1) – Br(1)	93.51(9)
O(1) – Cu(1) – O(3)	88.10(13)	O(3) – Cu(1) – O(4)#1	168.04(12)
O(1) – Cu(1) – O(4)#1	92.76(13)	O(3) – Cu(1) – Br(1)	94.63(9)
O(1) – Cu(1) – Br(1)	98.04(9)	O(4)#1 – Cu(1) – Br(1)	97.06(9)
O(2)#1 – Cu(1) – O(3)	89.27(14)	Br(1) – Cu(1) – Cu(1)#1	175.60(3)
O(2)#1 – Cu(1) – O(4)#1	87.50(13)		

#1 $1-x, -y, 1-z$

N1 forms a bifurcated hydrogen bond, via H1c, to O2 and Br1 in an adjacent complex, while also simultaneously forming hydrogen bonds to the free halide ion and water

molecule via the two other hydrogen atoms. N2 also hydrogen bonds to these latter groups forming a bifurcated hydrogen bond to O1w and Br1 but also hydrogen bonds directly to another symmetry related Br1 atom. The effect is to produce an overall 3-D hydrogen bonded network in which the free bromide ion and water molecules occur in channels along *b* as shown in Figure 5.13. It is strange that a simple change in the halide ion gives rise to a very different structure to **23** with a greater number of waters of crystallisation. One possibility may be compensation for the weaker N-H...Br hydrogen bonds *i.e.* the Br equivalent to **23** is less energetically favourable than **24** as the latter contains more O-H...Br/O hydrogen bonds, whereas the N-H...Cl hydrogen bonds in **23** are strong enough that no extra water is incorporated. Alternatively, the size of Br⁻ ions is great enough that they push the complexes in **24** apart leaving voids that are filled with the available H₂O molecules in solution.

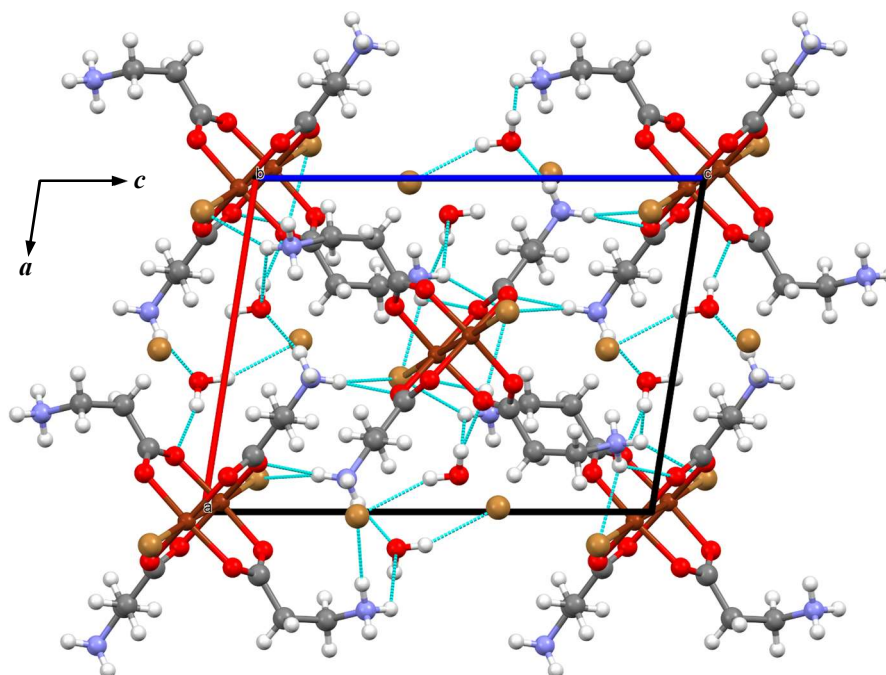


Figure 5.13 Crystal structure of $[\text{Cu}(\beta\text{-Ala})_4\text{Br}_2]\text{Br}_2 \cdot 2\text{H}_2\text{O}$ (**24**) as viewed down the *b* axis. C atoms are shown in grey, H in white, Br in light-brown, Cu in dark brown, N in light grey-blue, and O in red. Hydrogen bonds are drawn as light-blue dashed lines.

5.4.3 $[\text{Cu}_2(\beta\text{-Ala})_4\text{Br}_2]\text{Br}_2 \cdot 3\text{H}_2\text{O}$ (**25**)

$[\text{Cu}(\beta\text{-Ala})_4\text{Br}_2]\text{Br}_2 \cdot 3\text{H}_2\text{O}$ (**25**) was synthesised in a similar way to **24** but using a 1:1 mixture of methanol and water. The green crystal selected for analysis scattered predominantly at low 2θ angle ($\sim 5\text{-}30^\circ$) indicating a large unit-cell. The diffraction pattern was indexed with a non-centrosymmetric C -centred orthorhombic unit-cell with space group $C222_1$, further crystallographic details are included in Table 5.4. The asymmetric unit contains six symmetry independent paddlewheel motifs, as shown in Figure 5.14, two lack a centre of symmetry and are located in general positions, the other four are located on centres of inversion. The Cu^{2+} ions have a square-pyramidal coordination geometry, due to the large number of molecules the unique bond distances and angles have not been reported but are summarised in Table 5.13.

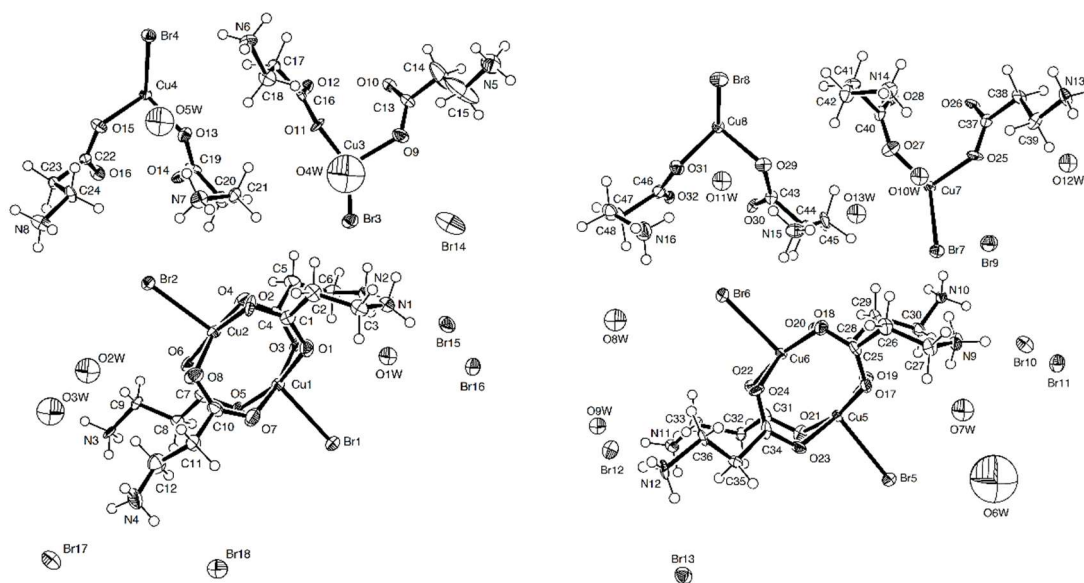


Figure 5.14 Asymmetric unit of $[\text{Cu}(\beta\text{-Ala})_4\text{Br}_2]\text{Br}_2 \cdot 3\text{H}_2\text{O}$ (**25**) with atoms shown as thermal ellipsoids drawn at 50% probability. For clarity, the asymmetric unit has been split into two components, related by the pseudosymmetrical operator: $x, y + \frac{1}{2}, z$.

Table 5.13 Selected bond lengths (Å) and angles (°) around the Cu coordination centre for [Cu(β -Ala)₄Br₂]Br₂·3H₂O (**25**).

Identity	Maximum	Minimum	Average	Median	Range
Cu – O	2.049(11)	1.927(11)	1.98(2)	1.981	0.122
Cu – Br	2.677(2)	2.607(2)	2.63(2)	2.627	0.070
Cu – Cu	2.678(4)	2.646(4)	2.668(12)	2.672	0.032
O – Cu – O (cis)	92.8(5)	86.5(5)	89(2)	89.1	6.3
O – Cu – O (trans)	171.2(5)	164.3(4)	167(2)	166.8	6.9
O – Cu – Br	106.0(3)	88.9(3)	96(3)	96.4	17.1
Br – Cu – Cu	179.30(8)	175.87(11)	177.1(12)	176.9	3.4

The symmetry independent molecules are related by pseudosymmetry with a visually identifiable pseudotranslation of $y + \frac{1}{2}$ between the two groupings of the molecules. Stark differences in the conformation of the alkylammonium chains and positions of the solvent molecules/free ions, in addition to more subtle differences in the orientation of the complexes are the reason the structure deviates from strict symmetry giving such a large unit-cell. The differences are highlighted best in Figure 5.15 which is an overlay of the two components related by the previously mentioned pseudotranslation.

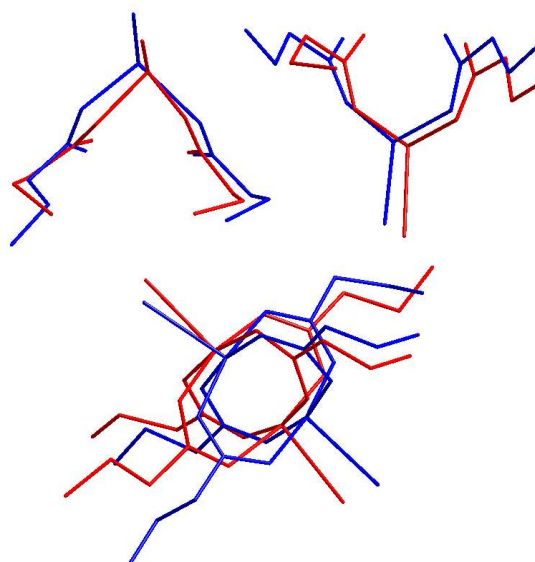


Figure 5.15 The two components of the asymmetric unit in [Cu(β -Ala)₄Br₂]Br₂·3H₂O (**25**) related by the pseudosymmetry after performing the operator $x, y + \frac{1}{2}, z$ on one component. All solvent molecules and free counter-ions have been omitted for clarity.

It is difficult to determine, and show graphically, the exact reasons for the differences between the symmetrically independent molecules due to the complexity of the structure. However, as shown in Figure 5.14, the local environment each complex occupies with respect to the solvent molecules and free halide ions is substantially different, meaning the most probable reason is optimisation of hydrogen bonding interactions.

A variable temperature study was later conducted to determine whether the pseudosymmetry dissipates through a heat induced transformation. At 298 K, the crystal still showed peaks corresponding to the previously determined unit-cell, and further heating to 333 K caused the crystal to melt. Further studies have not yet been conducted, but the lack of an identifiable phase change upon heating from 150 K to 298 K may indicate there will be no change approaching the melting point.

5.4.4 $[\text{Cu}_2(\text{ABA})_4\text{Cl}_2]\text{Cl}_2 \cdot 3\text{H}_2\text{O}$ (**26**)

Sabirov *et al.* conducted the original structure determination of $[\text{Cu}_2(\text{ABA})_4\text{Cl}_2]\text{Cl}_2 \cdot 3\text{H}_2\text{O}$ (**26**).²⁰⁰ They determined that the compound had a non-centrosymmetric monoclinic unit-cell. The asymmetric unit contains a whole paddlewheel complex. Two of the alkylammonium chains exhibit a planar zig-zag formation with almost mirror symmetry, however the other two are markedly different which is most likely what gives rise to the observed pseudosymmetry and non-centrosymmetric unit-cell. An image of the overall crystal packing is shown in Figure 5.16. Attempts were made to resynthesise the compound via the original reported method to investigate whether the structure was correct, however the synthetic details for the production of **26** were lacking which makes the work very difficult to replicate.²⁰⁰ The attempts were unsuccessful and therefore it has not been possible to conduct further studies on the compound.

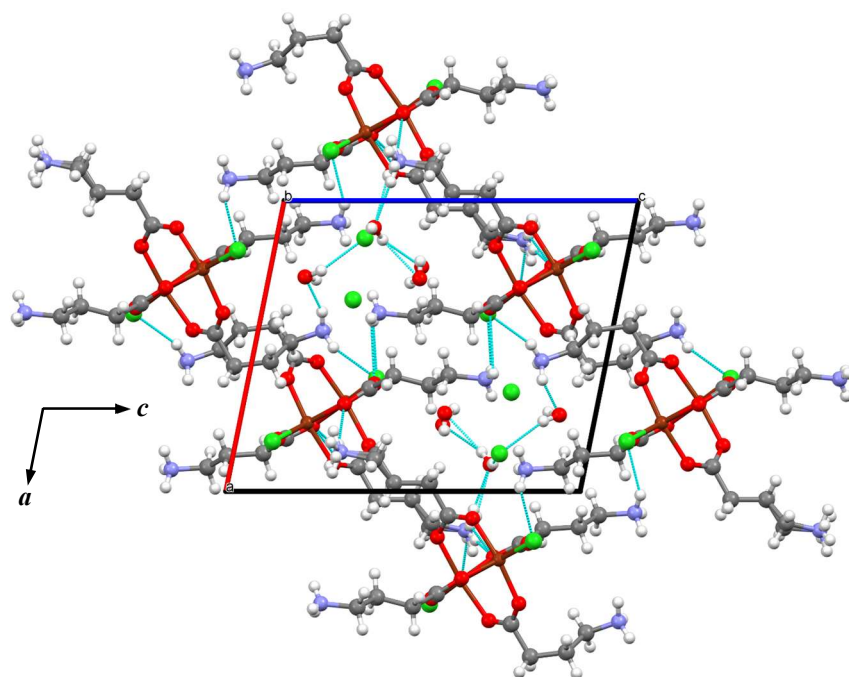


Figure 5.16 Crystal structure of $[\text{Cu}(\text{ABA})_4\text{Cl}_2]\text{Cl}_2 \cdot 3\text{H}_2\text{O}$ (**26**) as viewed down the b axis. C atoms are shown in grey, H in white, Cu in dark brown, Cl in green, N in light grey-blue, and O in red.²⁰⁰

5.4.5 $[\text{Cu}_2(\text{ABA})_4\text{Cl}_2]\text{Cl}_2 \cdot \text{H}_2\text{O}$ (**27**)

The attempts to produce crystals of **26** in 1:1 methanol:water produced a new phase with a different extent of hydration, $[\text{Cu}_2(\text{ABA})_4\text{Cl}_2]\text{Cl}_2 \cdot \text{H}_2\text{O}$ (**27**). **27** crystallises in a monoclinic cell with space group $P2_1/c$, further crystallographic details are included in Table 5.5. The asymmetric unit consists of one paddlewheel motif without a centre of inversion, two free chloride ions, and a single water of crystallisation, as shown in Figure 5.17. The Cu centres have square-pyramidal geometry and further data for the inner coordination sphere are given in Table 5.14.

The alkylammonium chains for all four ligands are approximately planar, the RMSD of this portion of the ligands containing N1-N4 are 0.0530 Å, 0.0913 Å, 0.0578 Å, and 0.0585 Å respectively. The difference in configuration of the ligands lies in the angle between the carboxylate group plane, and the plane the alkylammonium chain of each

ligand; for the ligands containing N1-N4 this is 10.3(4)°, 31.0(2)°, 9.7(4)°, and 52.4(2)° respectively. The lack of symmetry in these configurations is why the complex, unlike most of the other examples, is not situated on a centre of inversion.

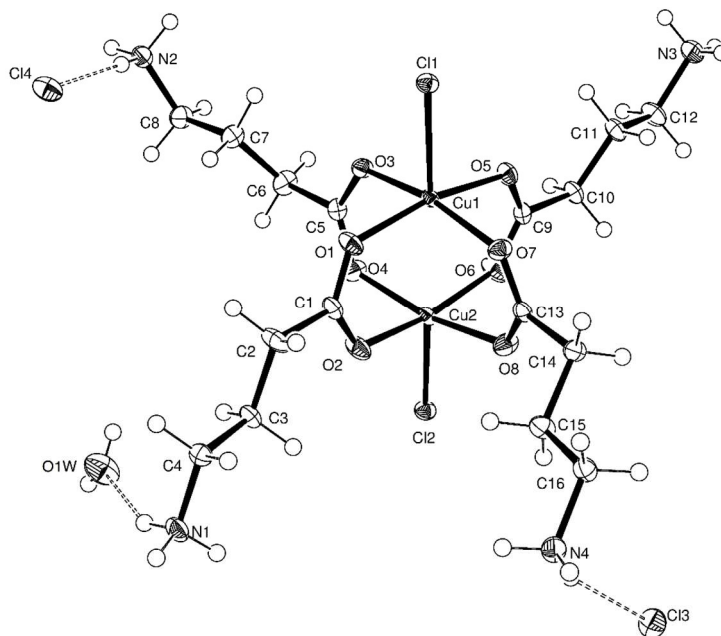


Figure 5.17 Asymmetric unit of $[\text{Cu}_2(\text{ABA})_4\text{Cl}_2]\text{Cl}_2 \cdot \text{H}_2\text{O}$ (**27**) with atoms shown as thermal ellipsoids drawn at 50% probability. Hydrogen bonds are drawn as dashed lines.

Table 5.14 Selected bond lengths (Å) and angles (°) around the Cu coordination centre for $[\text{Cu}_2(\text{ABA})_4\text{Cl}_2]\text{Cl}_2 \cdot \text{H}_2\text{O}$ (**27**).

Cu(1) – O(1)	1.9775(16)	Cu(2) – O(2)	1.9428(17)
Cu(1) – O(3)	1.9882(17)	Cu(2) – O(4)	1.9805(17)
Cu(1) – O(5)	1.9981(16)	Cu(2) – O(6)	1.9536(17)
Cu(1) – O(7)	1.9831(17)	Cu(2) – O(8)	1.9838(18)
Cu(1) – Cl(1)	2.4780(6)	Cu(2) – Cl(2)	2.4726(6)
Cu(1) – Cu(2)	2.6488(4)		
O(1) – Cu(1) – O(3)	90.16(7)	O(2) – Cu(2) – O(4)	89.91(8)
O(1) – Cu(1) – O(5)	167.74(7)	O(2) – Cu(2) – O(6)	168.02(8)
O(1) – Cu(1) – O(7)	87.47(7)	O(2) – Cu(2) – O(8)	90.15(8)
O(1) – Cu(1) – Cl(1)	93.25(5)	O(2) – Cu(2) – Cl(2)	101.52(5)
O(3) – Cu(1) – O(5)	89.20(7)	O(4) – Cu(2) – O(6)	89.59(8)
O(3) – Cu(1) – O(7)	168.27(7)	O(4) – Cu(2) – O(8)	167.36(7)
O(3) – Cu(1) – Cl(1)	96.31(5)	O(4) – Cu(2) – Cl(2)	90.25(5)
O(5) – Cu(1) – O(7)	90.69(7)	O(6) – Cu(2) – O(8)	87.74(8)
O(5) – Cu(1) – Cl(1)	99.00(5)	O(6) – Cu(2) – Cl(2)	90.46(6)
O(7) – Cu(1) – Cl(1)	95.29(5)	O(8) – Cu(2) – Cl(2)	102.11(5)
Cl(1) – Cu(1) – Cu(2)	176.633(19)	Cl(2) – Cu(2) – Cu(1)	171.972(19)

There is a noticeable increase in the number of direct hydrogen bonding interactions between molecules in **27** vs. **26**: N2 and N4 both hydrogen bond directly to C11 and C12 of adjacent molecules, N1 also hydrogen bonds with C11 but O3 and O8 as well. In addition to these, two N3 ammonium groups form the central component of a centrosymmetric cluster of free halide ions and water molecules which in turn hydrogen bond to N1, N3 and N4, as shown in Figure 5.18. This gives rise to a 3-D hydrogen bonded framework.

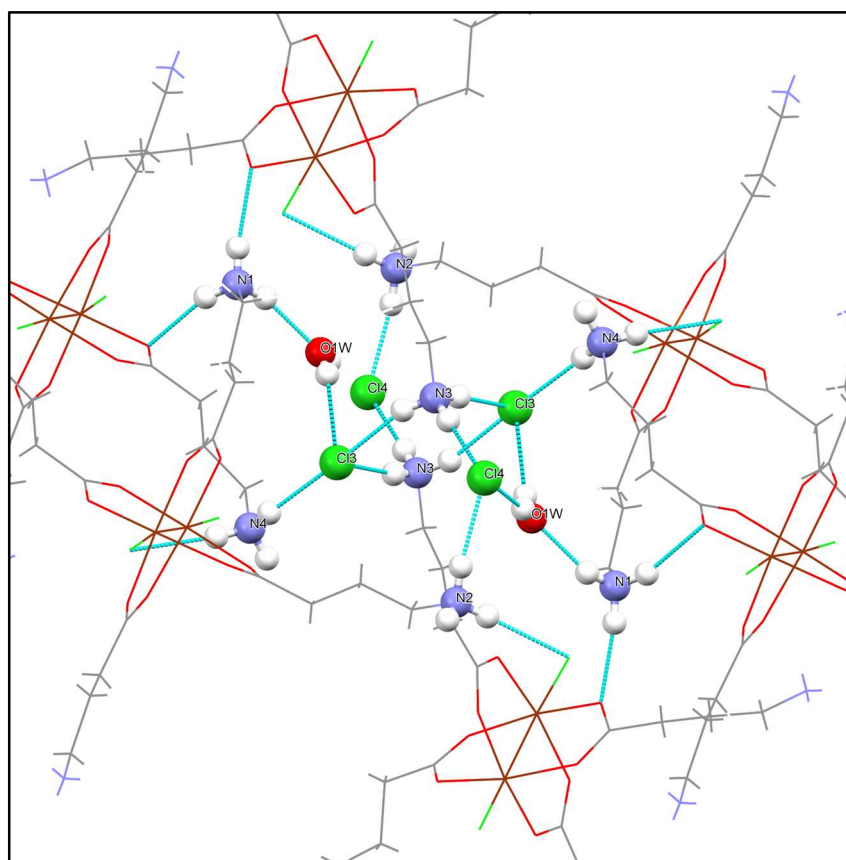


Figure 5.18 The centrosymmetric cluster of chloride ions and water molecules within the structure of $[\text{Cu}_2(\text{ABA})_4\text{Cl}_2]\text{Cl}_2 \cdot \text{H}_2\text{O}$ (**27**), showing the hydrogen bonding interactions. C atoms are shown in grey, H in white, Cu in dark brown, Cl in green, N in light grey-blue, and O in red. Hydrogen bonds are drawn as light-blue dashed lines.

5.4.6 $[\text{Cu}_2(\text{ABA})_4\text{Br}_2]\text{Br}_2$ (**28**)

Only an anhydrous product is obtained from the reaction of ABA with CuBr_2 , $[\text{Cu}(\text{ABA})_4\text{Br}_2]\text{Br}_2$ (**28**). The structure has a triclinic unit-cell with space group $P\bar{1}$, further crystallographic details are included in Table 5.6. The asymmetric unit consists of half a paddlewheel motif which lies on a centre of inversion completing the molecule by symmetry, and one uncoordinated bromide ion, as shown in Figure 5.19. Bond distance and angle data for the square-pyramidal Cu coordination are shown in Table 5.15. The ammonium alkyl chains are in a standard planar zig zag conformation, the RMSD from planarity of the ligands containing N1 and N2 is 0.0230 Å and 0.0624 Å respectively. Each is twisted around the C1-C2 and C5-C6 bonds by $53.3(4)^\circ$ and $30.2(4)^\circ$ respectively. The net result is that the ammonium groups are twisted toward each other on two sides of the complex which allows the formation of hydrogen bonded sheets.

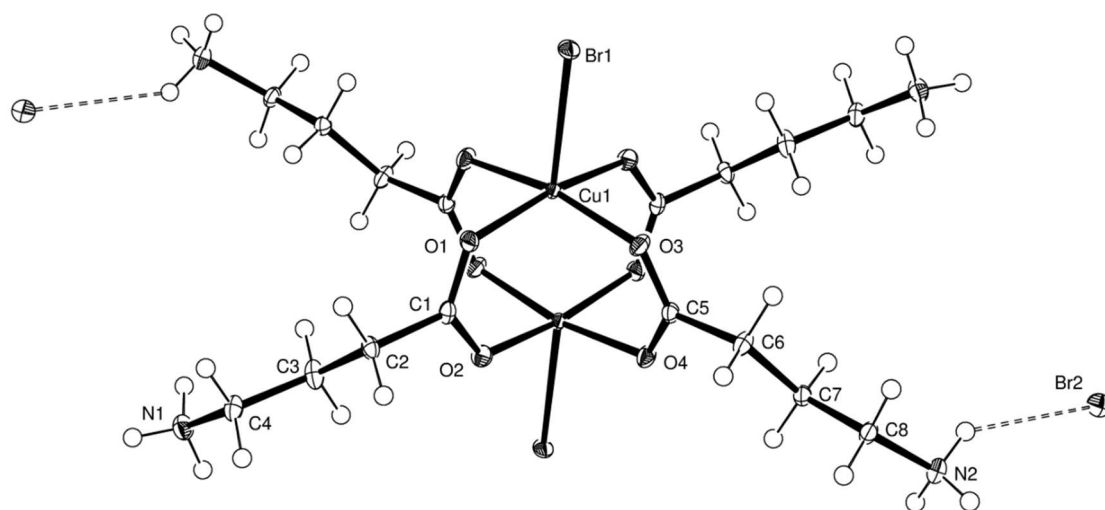


Figure 5.19 Asymmetric unit of $[\text{Cu}(\text{ABA})_4\text{Br}_2]\text{Br}_2$ (**28**) with atoms shown as thermal ellipsoids drawn at 50% probability. Fragment is completed by the symmetry operator: $1-x, 2-y, 1-z$. Hydrogen bonds are drawn as dashed lines.

Each ammonium group forms an $R_4^4(8)$ interaction by hydrogen bonds to two bromide ions which in turn are hydrogen bonded by another ammonium related by inversion.

These alternate in the [101] crystallographic direction with hydrogen bonds between the N1 and N2 ring formations (N1 \cdots Br2) to form 2-D sheets that run parallel to the ($\bar{1}21$) plane, as shown in Figure 5.20. The sheets stack in the [021] direction, perpendicular to the ($\bar{1}21$) plane, and interact by hydrogen bonds between N2 and O2, and N1 bifurcated between Br1/O3.

Table 5.15 Selected bond lengths (Å) and angles (°) around the Cu coordination centre for [Cu(ABA)₄Br₂]₂Br₂ (**28**).

Cu(1) – O(1)	1.971(3)	Cu(1) – O(4)#1	1.987(3)
Cu(1) – O(2)#1	1.968(3)	Cu(1) – Br(1)	2.6071(6)
Cu(1) – O(3)	1.981(3)	Cu(1) – Cu(1)#1	2.6511(9)
O(1) – Cu(1) – O(2)#1	167.69(11)	O(2)#1 – Cu(1) – Br(1)	99.69(8)
O(1) – Cu(1) – O(3)	90.87(12)	O(3) – Cu(1) – O(4)#1	167.93(11)
O(1) – Cu(1) – O(4)#1	89.51(12)	O(3) – Cu(1) – Br(1)	94.61(8)
O(1) – Cu(1) – Br(1)	92.38(8)	O(4)#1 – Cu(1) – Br(1)	97.43(8)
O(2)#1 – Cu(1) – O(3)	90.61(12)	Br(1) – Cu(1) – Cu(1)#1	171.67(3)
O(2)#1 – Cu(1) – O(4)#1	86.51(12)		

#1 -x, 1 -y, 1 -z

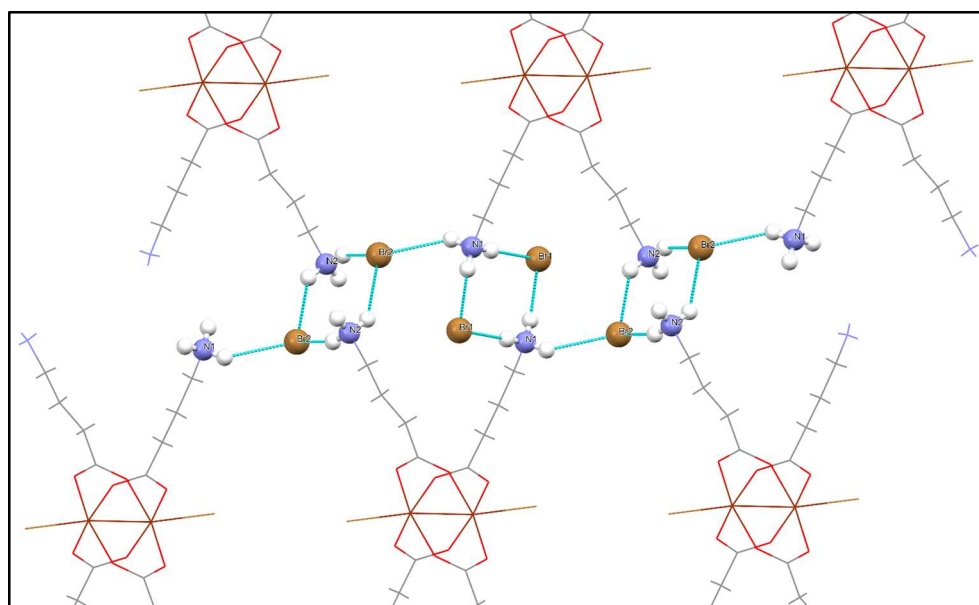


Figure 5.20 Sheets of [Cu(ABA)₄Br₂]₂Br₂ (**28**) as viewed perpendicular to the ($\bar{1}21$) crystallographic plane showing the two R₄^s(8) interactions formed by N1 and N2. C atoms are shown in grey, H in white, Br in

light-brown, Cu in dark brown, N in light grey-blue, and O in red. Hydrogen bonds are drawn as light-blue dashed lines.

5.4.7 $[\text{Cu}_2(\text{APA})_4\text{Cl}_2]\text{Cl}_2 \cdot 2\text{H}_2\text{O}$ (**29**)

The reaction of APA and CuCl_2 yields two products, one anhydrous the other hydrated, $[\text{Cu}_2(\text{APA})_4\text{Cl}_2]\text{Cl}_2 \cdot 2\text{H}_2\text{O}$ (**29**). Strangely, the hydrated compound was synthesised in 1:1 methanol:water, whereas the anhydrous compound was synthesised in pure water. The asymmetric unit consists of half a paddlewheel motif that lies upon an inversion centre, in addition to a water molecule and one chloride anion disordered over two positions labelled A and B, as shown in Figure 5.21. One of the positions for the disordered chloride ion, A, is located on the 1c Wyckoff position. The site occupancies were refined as a single free variable calculated as 0.417(3) and 0.583(3) for A and B respectively. The Cu coordination has square-pyramidal geometry and bond distances and angles are shown in Table 5.16. Further crystallographic details are included in Table 5.7.

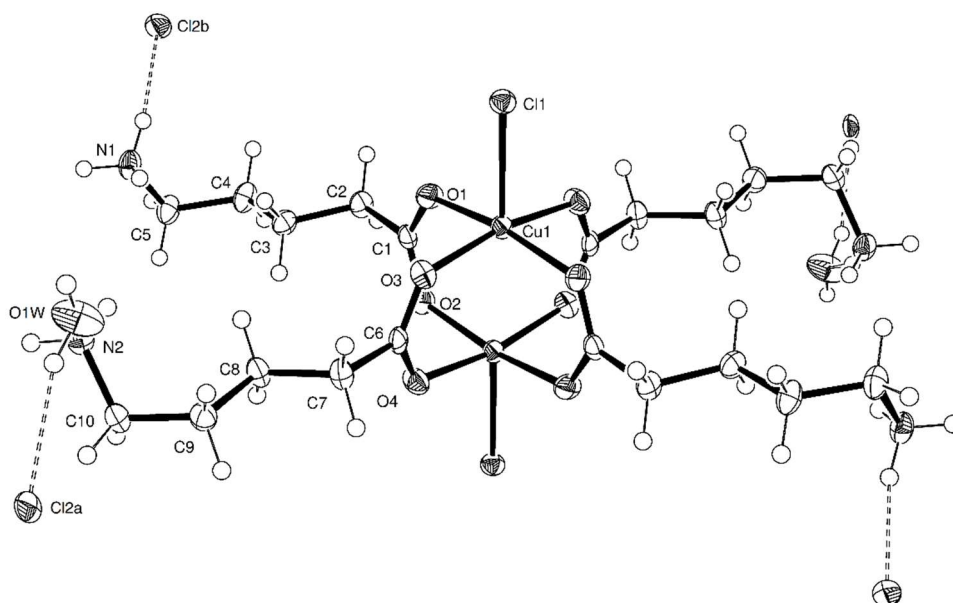


Figure 5.21 Asymmetric unit of $[\text{Cu}_2(\text{APA})_4\text{Cl}_2]\text{Cl}_2 \cdot 2\text{H}_2\text{O}$ (**29**) with atoms shown as thermal ellipsoids drawn at 50% probability. The fragment is completed by the symmetry operator: $-x, -y, 1-z$. Hydrogen bonds are drawn as dashed lines.

Table 5.16 Selected bond lengths (Å) and angles (°) around the Cu coordination centre for [Cu₂(APA)₄Cl₂]Cl₂·2H₂O (**29**).

Cu(1) – O(1)	1.979(3)	Cu(1) – O(4)#1	1.971(3)
Cu(1) – O(2)#1	1.967(3)	Cu(1) – Cl(1)	2.5068(11)
Cu(1) – O(3)	1.982(3)	Cu(1) – Cu(1)#1	2.6275(10)
O(1) – Cu(1) – O(2)#1	168.95(12)	O(2)#1 – Cu(1) – Cl(1)	96.63(9)
O(1) – Cu(1) – O(3)	92.71(14)	O(3) – Cu(1) – O(4)#1	168.57(12)
O(1) – Cu(1) – O(4)#1	87.44(14)	O(3) – Cu(1) – Cl(1)	95.38(9)
O(1) – Cu(1) – Cl(1)	94.39(9)	O(4)#1 – Cu(1) – Cl(1)	96.01(9)
O(2)#1 – Cu(1) – O(3)	86.99(14)	Cl(1) – Cu(1) – Cu(1)#1	177.09(4)
O(2)#1 – Cu(1) – O(4)#1	90.67(14)		

#1 -x, -y, 1 - z

Two N1 ammonium groups and two water molecules hydrogen bond to a single Cl_{2a} ion, although strangely the four hydrogen bonds are in a square plane almost at right angles to each other. The water molecules in turn act as a hydrogen bond acceptor to an ammonium group in another complex in the same plane. Each Cl_{2a} ion therefore connects four paddlewheel motifs together through direct and indirect (through water molecules) hydrogen bonding, forming a 2-D sheet parallel to the (120) crystallographic plane. The sheets stack in the [110] direction. The water molecules which form interactions within the sheets also hydrogen bond to Cl_{2b} which in turn accepts a hydrogen bond from an ammonium group belonging to the sheet either directly above or below with respect to [110]. In addition to this, rotations about C1-C2 and C6-C7 as well as C4-C5 and C9-C10 bring two hydrogen atoms of the N1 and N2 groups both close enough to hydrogen bond to Cl₁, O1 and O3 of a paddlewheel in the sheet directly above or below. All interactions are shown in Figure 5.22, and overall create a 3-D supramolecular network.

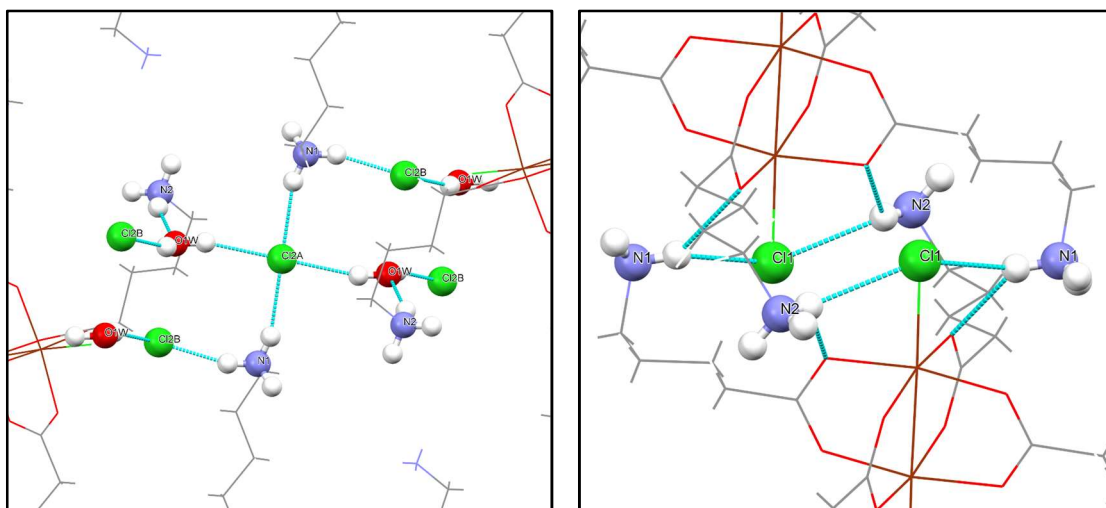


Figure 5.22 Shown left are the hydrogen bonds that form the 2-D sheets, and the O1W-Cl2b interactions which occurs between the stacks of sheets in $[\text{Cu}_2(\text{APA})_4\text{Cl}_2]\text{Cl}_2 \cdot 2\text{H}_2\text{O}$ (**29**). Shown right are the direct interactions of the N1 and N2 ammonium groups with Cl1, O1 and O3 which occur mutually between each complex and the complexes belong to the 2-D sheets directly above and below with respect to [120]. C atoms are shown in grey, H in white, Cu in dark brown, Cl in green, N in light grey-blue, and O in red. Hydrogen bonds are drawn as light-blue dashed lines.

5.4.8 $[\text{Cu}_2(\text{APA})_4\text{Cl}_2]\text{Cl}_2 / [\text{Cu}_2(\text{APA})_4\text{Br}_2]\text{Br}_2$ (**30/31**)

As mentioned in the previous subsection, the reaction of CuCl_2 and APA yields a hydrated product (**29**) and an anhydrous product, $[\text{Cu}_2(\text{APA})_4\text{Cl}_2]\text{Cl}_2$ (**30**), the former being produced in 50:50 MeOH/ H_2O and the former in pure water. The reaction using CuBr_2 in 50:50 MeOH/ H_2O yields only the anhydrous bromide compound $[\text{Cu}_2(\text{APA})_4\text{Br}_2]\text{Br}_2$ (**31**). The structures of **30** and **31** are very similar. The cell parameters for **30** and **31** are shown side by side in Table 5.17. Both structures are centrosymmetric monoclinic with the space group $P2_1/c$, further crystallographic details are included in Table 5.7 and Table 5.8.

Table 5.17 Unit-cell parameters for the crystal structures of $[\text{Cu}_2(\text{APA})_4\text{Cl}_2]\text{Cl}_2$ (**30**) and $[\text{Cu}_2(\text{APA})_4\text{Br}_2]\text{Br}_2$ (**31**).

Compound	30	31
a (Å)	9.0041(6)	8.8923(9)
b (Å)	19.5885(14)	20.010(2)
c (Å)	9.4018(7)	9.7160(9)
β (°)	115.711(5)	114.846(7)
V (Å ³)	1494.1(4)	1568.8(6)

Table 5.18 Selected bond lengths (Å) and angles (°) around the Cu coordination centre for $[\text{Cu}_2(\text{APA})_4\text{Cl}_2]\text{Cl}_2$ (**30**).

Cu(1) – O(1)	1.9775(14)	Cu(1) – O(4)#1	1.9821(13)
Cu(1) – O(2)#1	1.9810(14)	Cu(1) – Cl(1)	2.5071(6)
Cu(1) – O(3)	1.9709(13)	Cu(1) – Cu(1)#1	2.6262(5)
O(1) – Cu(1) – O(2)#1	168.73(6)	O(2)#1 – Cu(1) – Cl(1)	96.61(4)
O(1) – Cu(1) – O(3)	88.39(6)	O(3) – Cu(1) – O(4)#1	168.73(6)
O(1) – Cu(1) – O(4)#1	90.99(6)	O(3) – Cu(1) – Cl(1)	93.33(4)
O(1) – Cu(1) – Cl(1)	94.35(4)	O(4)#1 – Cu(1) – Cl(1)	97.80(5)
O(2)#1 – Cu(1) – O(3)	88.36(6)	Cl(1) – Cu(1) – Cu(1)#1	175.766(18)
O(2)#1 – Cu(1) – O(4)#1	90.12(6)		

#1 1 – x, 1 – y, 1 – z

Table 5.19 Selected bond lengths (Å) and angles (°) around the Cu coordination centre for $[\text{Cu}_2(\text{APA})_4\text{Br}_2]\text{Br}_2$ (**31**).

Cu(1) – O(1)	1.9772(16)	Cu(1) – O(4)#1	1.9789(19)
Cu(1) – O(2)#1	1.9784(16)	Cu(1) – Br(1)	2.6656(4)
Cu(1) – O(3)	1.9627(19)	Cu(1) – Cu(1)#1	2.6206(6)
O(1) – Cu(1) – O(2)#1	168.93(6)	O(2)#1 – Cu(1) – Br(1)	96.76(5)
O(1) – Cu(1) – O(3)	89.34(7)	O(3) – Cu(1) – O(4)#1	169.06(7)
O(1) – Cu(1) – O(4)#1	90.38(7)	O(3) – Cu(1) – Br(1)	92.55(5)
O(1) – Cu(1) – Br(1)	94.12(5)	O(4)#1 – Cu(1) – Br(1)	98.37(5)
O(2)#1 – Cu(1) – O(3)	88.19(7)	Br(1) – Cu(1) – Cu(1)#1	174.898(19)
O(2)#1 – Cu(1) – O(4)#1	90.00(8)		

#1 1 – x, 1 – y, 1 – z

Despite some very slight differences in the bond angles and lengths, shown in Table 5.18 and Table 5.19, the structures are identical, thus the description of the structures will be conducted using examples from the bromide analogue which possesses lower R-factors

(**30**: $R_1 = 0.0266$, $wR_2 = 0.0637$; **31**: $R_1 = 0.0229$, $wR_2 = 0.0492$). Similar to **24**, **28**, and **29**, the asymmetric unit contains half a paddlewheel on an inversion centre with a singular bromide ion in a general position, as shown in Figure 5.23. The Cu coordination geometry is square-pyramidal in each case.

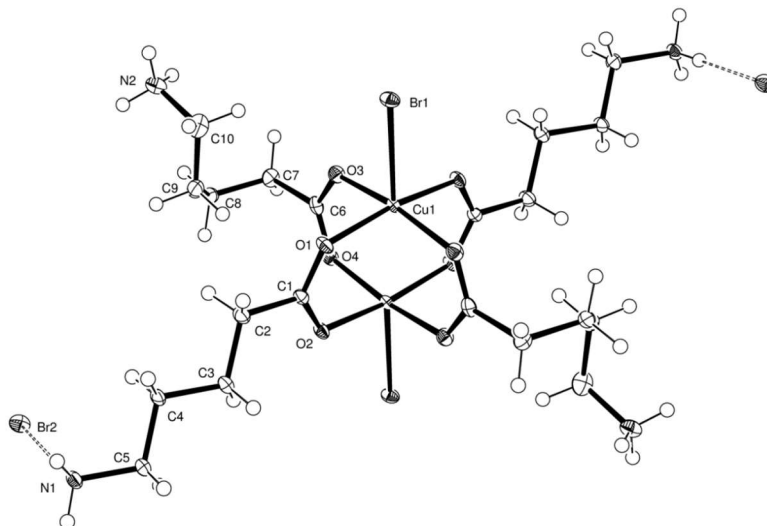


Figure 5.23 Asymmetric unit of $[\text{Cu}_2(\text{APA})_4\text{Br}_2]\text{Br}_2$ (**31**) with atoms shown as thermal ellipsoids drawn at 50% probability. Fragment is completed by the symmetry operator: $1-x, 1-y, 1-y$. Hydrogen bonds are drawn as dashed lines.

One ligand of the coordination complex is in the standard approximately planar zig zag conformation, the RMSD from planarity is 0.1563 \AA in **30**, and 0.1190 \AA in **31**. Additionally, the alkylammonium chain twisted around the C1-C2 bond by $37.3(3)^\circ$ and $35.3(3)^\circ$ in **30** and **31** respectively. The other ligand is coiled in a way not dissimilar to a spring. The average torsion angle throughout the ligand is $60.1(4)^\circ$ in **30** and $63.6(6)^\circ$ in **31**. The configuration of this ligand leads to some interesting anisotropic thermal expansion properties discussed further in section 5.4.

The N2 ammonium group of every paddlewheel motif hydrogen bonds to the Br1 atoms of two adjacent complexes in the *ac* plane, but also to Br2 which in turn acts as a hydrogen bond acceptor to N1. This creates 2-D hydrogen bonded sheets which stack along the *b*

axis. The sheets interact with each other via involvement in a hydrogen bonded chain that occurs down the *c* axis. The chain is made up of alternating N1 and Br2 atoms. The N1 ammonium groups in this chain also hydrogen bond to the Br1 atoms of complexes in an adjacent sheet, and as mentioned above the Br2 atoms are hydrogen bonded by the N2 ammonium groups increasing the involvement of each sheet in this chain interaction. Overall, as with the other compounds, this creates 3-D hydrogen bonded network. All interactions are shown in Figure 5.24.

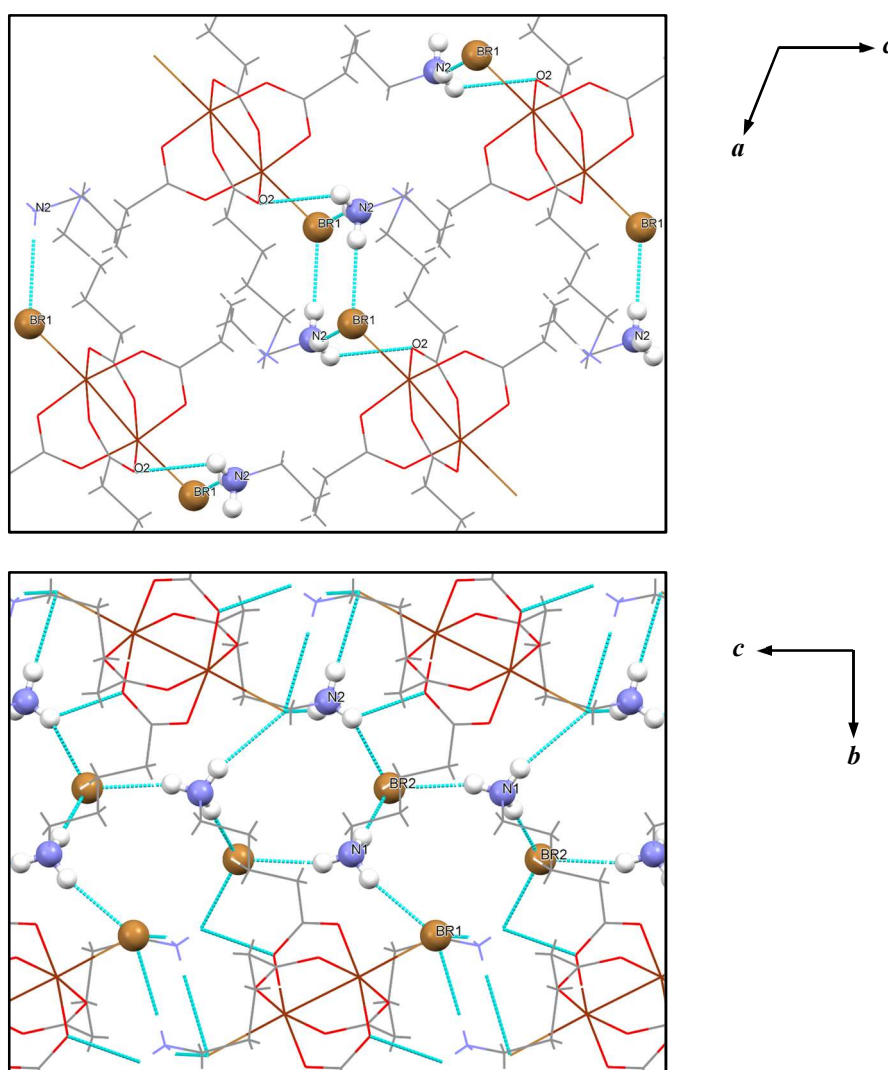


Figure 5.24 Shown left are the hydrogen bonding interactions between molecules in the *ac* plane in $[\text{Cu}_2(\text{APA})_4\text{Br}_2]\text{Br}_2$ (**31**). Shown right is the 1-dimensional chain interaction which hold the hydrogen bonded sheets together. C atoms are shown in grey, H in white, Br in light-brown, Cu in dark brown, N in light grey-blue, and O in red. Hydrogen bonds are drawn as light-blue dashed lines.

5.4.9 $[\text{Cu}_2(\text{AHA})_4\text{Cl}_2]\text{Cl}_2 \cdot 4\text{H}_2\text{O}$ / $[\text{Cu}_2(\text{AHA})_4\text{Br}_2]\text{Br}_2 \cdot 4\text{H}_2\text{O}$ (32/33)

Lah and Leban documented the structure of $[\text{Cu}_2(\text{AHA})_4\text{Cl}_2]\text{Cl}_2 \cdot 4\text{H}_2\text{O}$ (**32**) previously.²⁰¹ It is a dimeric paddlewheel type complex comprising four molecules of the ligand which, along with the uncoordinated chloride ions and water molecules, form extensive hydrogen bonding interactions. A full description of the structure was originally given by Lah and Leban so will not be duplicated here. A comparison of the unit-cell parameters of the two structures is shown in Table 5.26, further crystallographic details are included in Table 5.8. The bromide analogue $[\text{Cu}_2(\text{AHA})_4\text{Br}_2]\text{Br}_2 \cdot 4\text{H}_2\text{O}$ (**33**) reported here is identical to **32** apart from the expected slight changes in bond lengths and angles, shown in Table 5.21, associated with a change in halide anion, therefore no description will be given for this structure either. No other phases with a different level of hydration were identified for AHA. The asymmetric unit of **33** is shown in Figure 5.25 showing the Cu coordination to be of square-pyramidal geometry.

Table 5.20 Unit-cell parameters for the crystal structures of $[\text{Cu}_2(\text{AHA})_4\text{Cl}_2]\text{Cl}_2 \cdot 4\text{H}_2\text{O}$ (**32**)²⁰¹ and $[\text{Cu}_2(\text{AHA})_4\text{Br}_2]\text{Br}_2 \cdot 4\text{H}_2\text{O}$ (**33**).

Compound	32	33
a (Å)	9.4122(1)	9.5204(7)
b (Å)	12.1852(2)	12.2505(6)
c (Å)	17.5851(2)	17.8807(14)
β (°)	105.440(1)	105.621(6)
V (Å ³)	1944.04(4)	2088.4(4)

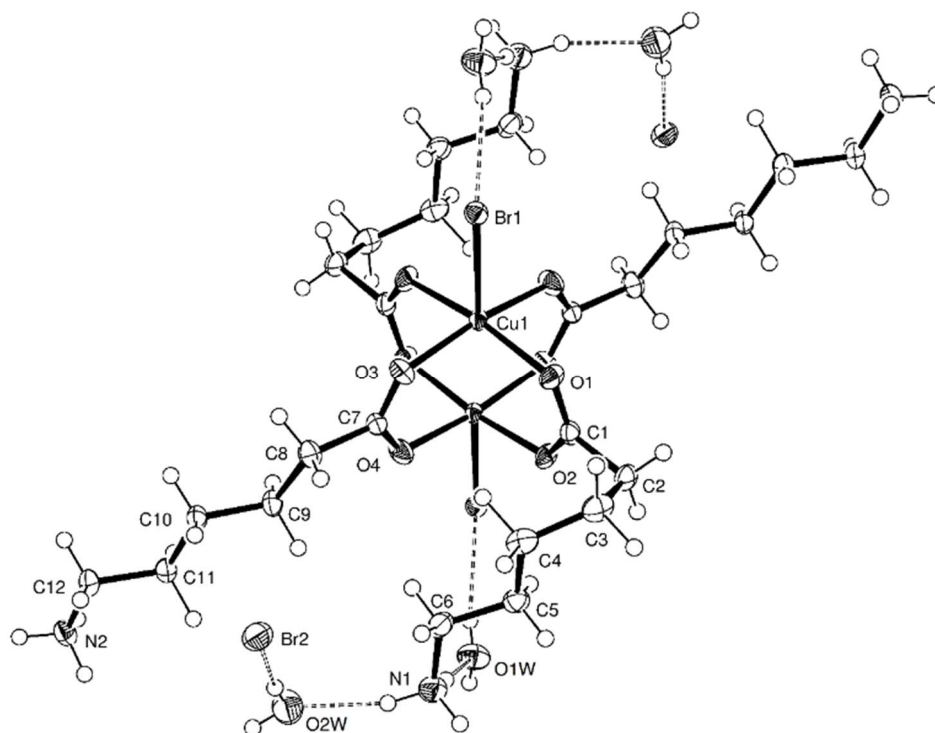


Figure 5.25 Asymmetric unit of $[\text{Cu}_2(\text{AHA})_4\text{Br}_2]\text{Br}_2 \cdot 4\text{H}_2\text{O}$ (**33**) with atoms shown as thermal ellipsoids drawn at 50% probability. Fragment is completed by symmetry operator: $-x, 1-y, 1-z$. Hydrogen bonds are drawn as dashed lines.

Table 5.21 Selected bond lengths (\AA) and angles ($^\circ$) around the Cu coordination centre for $[\text{Cu}_2(\text{AHA})_4\text{Br}_2]\text{Br}_2 \cdot 4\text{H}_2\text{O}$ (**33**).

Cu(1) – O(1)	1.973(3)	Cu(1) – O(4)#1	1.967(3)
Cu(1) – O(2)#1	1.974(3)	Cu(1) – Br(1)	2.6312(7)
Cu(1) – O(3)	1.973(3)	Cu(1) – Cu(1)#1	2.6266(10)
O(1) – Cu(1) – O(2)#1	168.56(13)	O(2)#1 – Cu(1) – Br(1)	93.73(9)
O(1) – Cu(1) – O(3)	91.47(13)	O(3) – Cu(1) – O(4)#1	168.76(13)
O(1) – Cu(1) – O(4)#1	87.76(14)	O(3) – Cu(1) – Br(1)	94.32(9)
O(1) – Cu(1) – Br(1)	97.69(9)	O(4)#1 – Cu(1) – Br(1)	96.90(10)
O(2)#1 – Cu(1) – O(3)	86.99(13)	Br(1) – Cu(1) – Cu(1)#1	176.07(3)
O(2)#1 – Cu(1) – O(4)#1	91.55(14)		

#1 $1-x, 1-y, 1-z$

5.4.10 $[\text{Cu}_2(\text{AOA})_6]\text{Cl}_4$ (**34**)

Only one single-crystalline material was identified in the product produced by the reaction of AOA with CuCl_2 , $[\text{Cu}_2(\text{AOA})_6]\text{Cl}_4$ (**34**). The structure has a centrosymmetric triclinic unit-cell, further crystallographic details are included in Table 5.9. The asymmetric unit, shown in Figure 5.26, contains half a paddlewheel motif located on an inversion centre, and the carboxylate group of a zwitterionic AOA molecule is coordinated to the apical position of the complex. Two free chloride ions balance the charge. The Cu centre has square-pyramidal geometry and bond length/angle data are shown in Table 5.22.

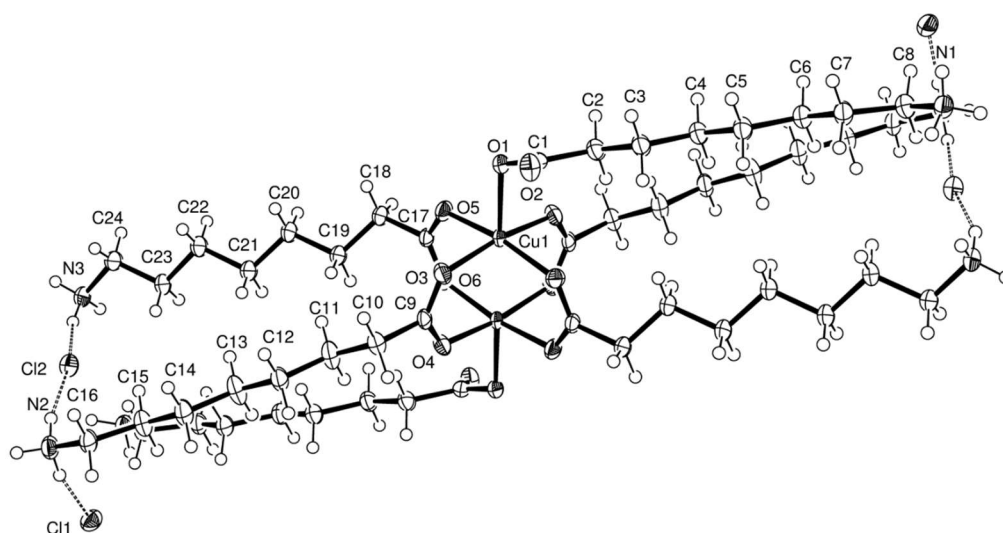


Figure 5.26 Asymmetric unit of $[\text{Cu}_2(\text{AOA})_6]\text{Cl}_4$ (**34**) with atoms shown as thermal ellipsoids drawn at 50% probability. Fragment is completed by the symmetry operator: $1-x, 1-y, 2-z$. Hydrogen bonds are drawn as dashed lines.

This is an uncommon paddlewheel structure with a limited number, ~ 70 , of examples in the literature. The displacement of the apical chloride ion could be due to either the long alkyl chain donating enough electron density to allow AOA to act as a better ligand than a chloride ion, or better packing of the long alkyl chains being possible in this configuration, or possibly a combination of the two. All the AOA ligands are in the planar zig-zag conformation, the RMSD from planarity is 0.0351 Å, 0.0577 Å, and 0.1118 Å for

the ligands containing N1, N2, and N3 respectively. All three ammonium groups hydrogen bond to Cl1 and Cl2, they also hydrogen bond to the carboxylate group of the apical ligand on the paddlewheel complex, therefore creating a 3-D hydrogen bonded network. An image of the overall crystal packing is shown in Figure 5.27. Unfortunately, the compound could not be made in pure form despite efforts to do so. Additionally, no further crystallographic analysis was conducted beyond the structural study at 150 K, *e.g.* studying the effect of temperature on the structure.

Table 5.22 Selected bond lengths (Å) and angles (°) around the Cu centre for [Cu₂(AOA)₆]Cl₄ (**34**).

Cu(1) – O(1)	2.1641(15)	Cu(1) – O(5)	1.9587(16)
Cu(1) – O(3)	1.9807(19)	Cu(1) – O(6)#1	1.9768(16)
Cu(1) – O(4)#1	1.9602(18)	Cu(1) – Cu(1)#1	2.6027(6)
O(1) – Cu(1) – O(3)	95.04(7)	O(3) – Cu(1) – O(5)	88.38(7)
O(1) – Cu(1) – O(4)#1	95.36(7)	O(3) – Cu(1) – O(6)#1	89.36(8)
O(1) – Cu(1) – O(5)	92.56(6)	O(4)#1 – Cu(1) – O(5)	91.04(7)
O(1) – Cu(1) – O(6)#1	97.72(6)	O(4)#1 – Cu(1) – O(6)#1	89.36(8)
O(1) – Cu(1) – Cu(1)#1	177.26(5)	O(5) – Cu(1) – O(6)#1	169.63(7)
O(3) – Cu(1) – O(4)#1	169.60(7)		

#1 1 – x, 2 – y, 1 – z

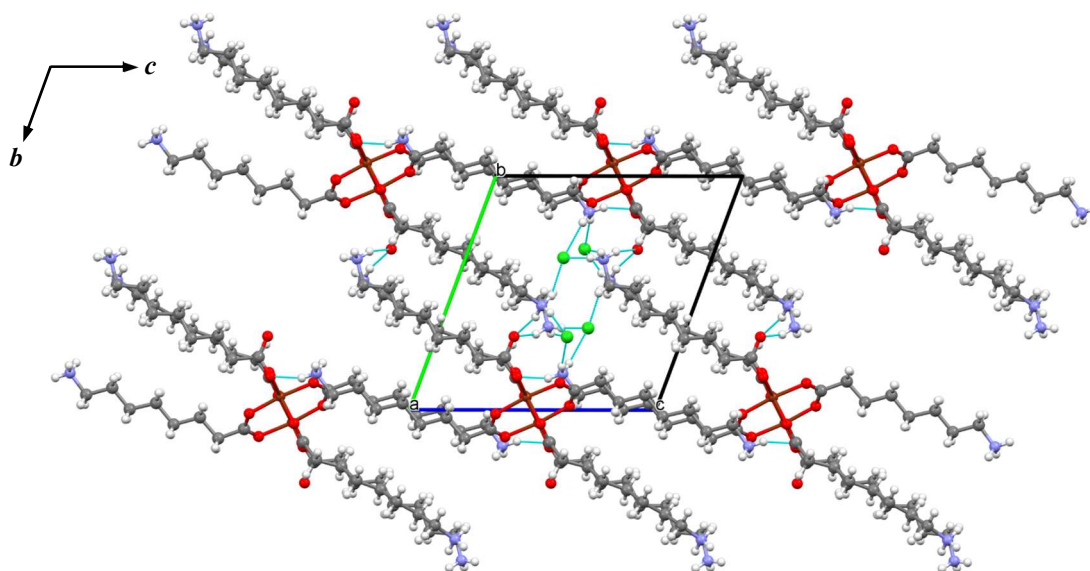


Figure 5.27 Crystal structure of [Cu₂(AOA)₆]Cl₄ (**34**) as viewed down the *a* axis. C atoms are shown in grey, H in white, Cu in dark brown, Cl in green, N in light grey-blue, and O in red. Hydrogen bonds are drawn as light-blue dashed lines.

5.4.11 X-ray powder diffraction

In total, nine new complexes of the general formula $[\text{Cu}_2(\text{L})_4\text{X}_2]\text{X}_2 \cdot n\text{H}_2\text{O}$ were produced in the above work, of these only five could be made pure: **27**, **28**, **30**, **31**, and **33**. Figure 5.28 shows a comparison of the simulated and experimental X-ray powder diffraction data.

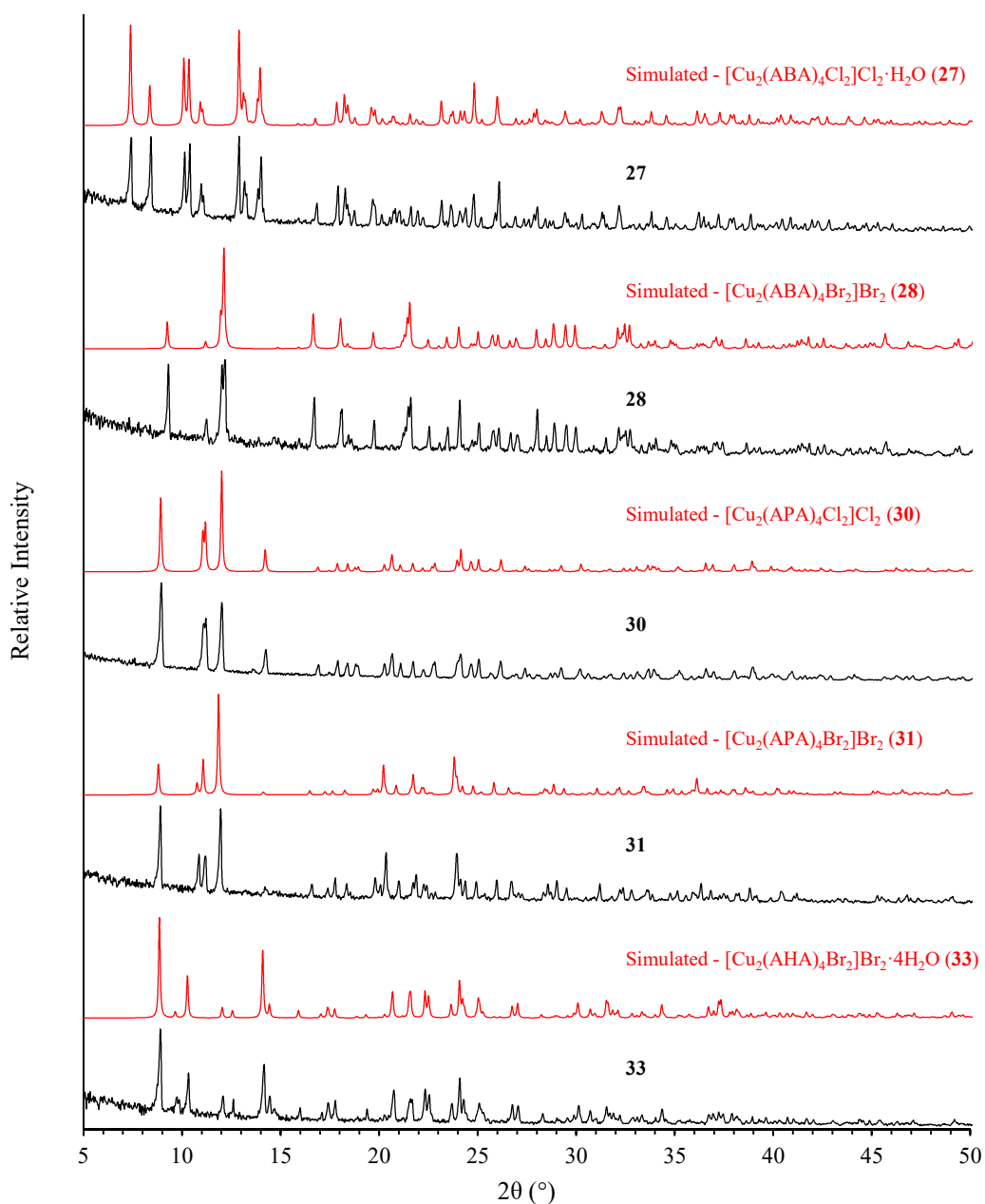


Figure 5.28 Room temperature X-ray powder diffraction data for samples of **27**, **28**, **30**, **31**, and **33**. Experimental data are shown in black while simulated data are shown in red.

The absence of additional peaks in the experimental data is what indicates pure products were obtained, but purity was also confirmed by elemental analysis. All other novel compounds exhibited many additional peaks in the X-ray powder diffraction pattern, or an entirely different pattern to that simulated from the structure determined from a single-crystal.

5.5 Glycine

Glycine (Gly) shows some interesting chemistry with copper halides which is distinctly different from that of the other amino acids described above. The coordination complexes of glycine have been well studied with many examples present on the Cambridge structural database,¹¹⁹ though much less attention seems to have been paid to glycine as a zwitterionic ligand, and none of these compounds show the same type of chemistry as presented here.

5.5.1 $\{[Cu_2(Gly)_4][Cu_2Cl_6]\}_n$ (35)

Reaction of cupric chloride with glycine yields two types of parallelogram shaped crystals, one green and the other colourless. The latter was identified as glycine glycinium chloride, while the green crystals were shown to be a new phase possessing a centrosymmetric triclinic unit-cell, further crystallographic details are included in Table 5.9. The asymmetric unit consists of two copper cations, three chloride anions and two glycine molecules, as shown in Figure 5.29. The two glycine molecules coordinate through the carboxylic acid group to one of the copper atoms to form a paddlewheel type structure positioned at $(\frac{1}{2}, \frac{1}{2}, 0)$, the paddlewheel is capped by a chloride anion bridging to the other copper atom which is coordinated by the remaining two chlorides.

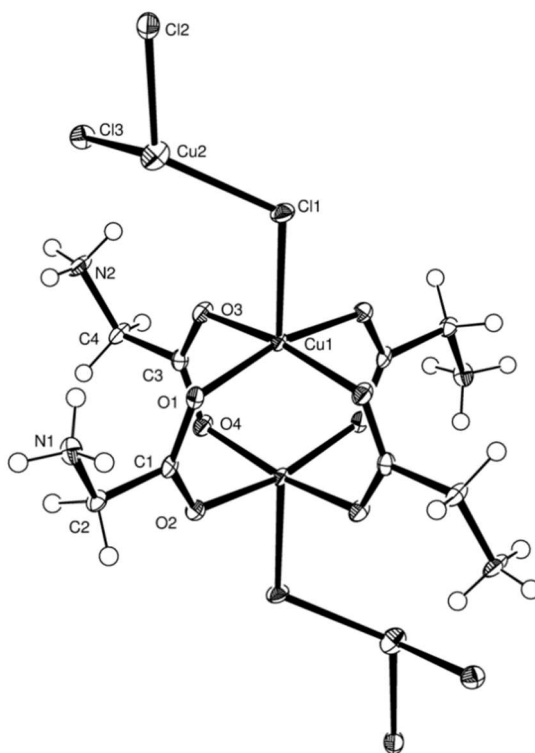


Figure 5.29 Asymmetric unit of $\{[\text{Cu}_2(\text{Gly})_4][\text{Cu}_2\text{Cl}_6]\}_n$ (**35**) with atoms shown as thermal ellipsoids drawn at 50% probability. The paddlewheel fragment is completed by the symmetry operator: $1 - x, 1 - y, \bar{z}$.

Table 5.23 Selected bond lengths (Å) and angles (°) around the Cu coordination centre for $\{[\text{Cu}_2(\text{Gly})_4][\text{Cu}_2\text{Cl}_6]\}_n$ (**35**).

Cu(1) – O(1)	1.982(2)	Cu(2) – Cl(1)	2.3551(9)
Cu(1) – O(2)#1	1.970(2)	Cu(2) – Cl(2)	2.3309(10)
Cu(1) – O(3)	1.992(2)	Cu(2) – Cl(3)	2.4148(9)
Cu(1) – O(4)#1	1.977(2)	Cu(2) – Cl(3)#2	2.3997(9)
Cu(1) – Cl(1)	2.4489(9)	Cu(2) – Cu(2)#2	2.8880(10)
Cu(1) – Cu(1)#1	2.7055(9)		
O(1) – Cu(1) – O(2)#1	166.30(9)	Cl(1) – Cu(1) – Cu(1)#1	177.84(3)
O(1) – Cu(1) – O(3)	91.69(9)	Cl(1) – Cu(2) – Cl(2)	119.45(3)
O(1) – Cu(1) – O(4)#1	89.09(9)	Cl(1) – Cu(2) – Cl(3)	109.23(3)
O(1) – Cu(1) – Cl(1)	99.68(7)	Cl(1) – Cu(2) – Cl(3)#2	110.36(3)
O(2)#1 – Cu(1) – O(3)	89.32(9)	Cl(2) – Cu(2) – Cl(3)	105.05(3)
O(2)#1 – Cu(1) – O(4)#1	86.87(9)	Cl(2) – Cu(2) – Cl(3)#2	105.63(3)
O(2)#1 – Cu(1) – Cl(1)	93.71(7)	Cl(3) – Cu(2) – Cl(3)#2	106.28(3)
O(3) – Cu(1) – O(4)#1	166.80(9)	Cl(1) – Cu(2) – Cu(2)#2	124.36(3)
O(3) – Cu(1) – Cl(1)	98.00(7)	Cu(1) – Cl(1) – Cu(2)	116.47(3)
O(4)#1 – Cu(1) – Cl(1)	94.86(7)		

#1 $1 - x, 1 - y, -z$

#2 $-x, 1 - y, 1 - z$

Cu1 has a square-pyramidal coordination geometry while Cu2 has a tetragonal coordination geometry, bond lengths and angles are shown in Table 5.23. The “CuCl₃” capping group of the paddlewheel is part of a centrosymmetric Cu₂Cl₆ dimer consisting of two copper centres (Cu2) doubly bridged by two chlorides (Cl3). This group bridges the paddlewheel motifs forming an organic-inorganic polymeric chain in the (1̄01) direction. Fourier difference maps, shown in Figure 5.30, clearly show the presence of three H atoms around each N atom, meaning the glycine ligands are in the zwitterionic state. In order for the overall structure to be neutral, one copper ion must be in the +1 oxidation state which is most likely to be the tetrahedrally coordinated Cu2 atom, therefore the Cu₂Cl₆ bridging group is more accurately described as a [Cu₂Cl₆]⁴⁻ ion.

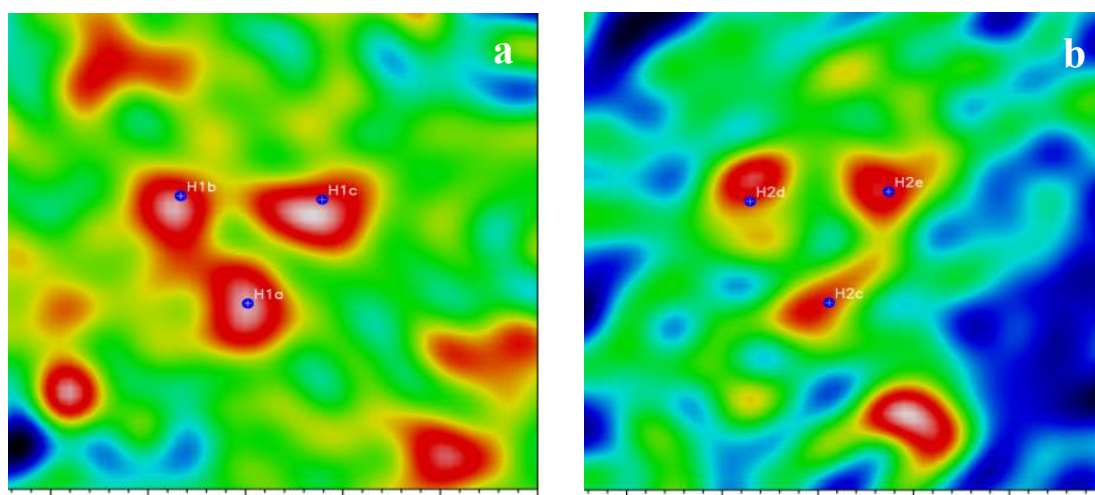


Figure 5.30 Fourier difference maps of $\{[\text{Cu}_2(\text{Gly})_4][\text{Cu}_2\text{Cl}_6]\}_n$ (**35**) ($F_o - F_c$) as calculated across planes passing through (a) H1a/b/c (b) H2c/d/e. The atoms the plane pass through have been omitted from the calculated structure factors.

Interestingly, dimethylglycine forms a very similar non-polymeric complex, however there is a large distortion of the Cl-Cu··Cu-Cl axis away from linearity, which is approximately linear in **35**, and the paddlewheel unit is terminated with tetrahedral CuCl₄ ions. Hydrogen bonding interactions in **35** between N1 and Cl3, and N2 and Cl2 may have a stabilising effect on the inorganic components of the polymer, and explain why

the compound forms without oxidising to a similar material to the dimethylglycine analogue. The chains are also held together by mutual interactions between the ammonium groups and the O atoms of the carboxylate functional group which may provide further stabilisation.

A reaction scheme for the reaction between copper chloride and glycine is shown in Figure 5.31. In order to balance the observed products, **35** and glycine glycinium chloride, with the starting reagents, an additional proton and electron are required. The source of the extra proton and electron is unknown, but a plausible source would be interaction of the sample solution with UV irradiation from the sun which is not blocked by the glass installed in the lab in which the reaction took place. Further experiments are required to determine the exact cause of the reaction, and the role that glycine plays in it.

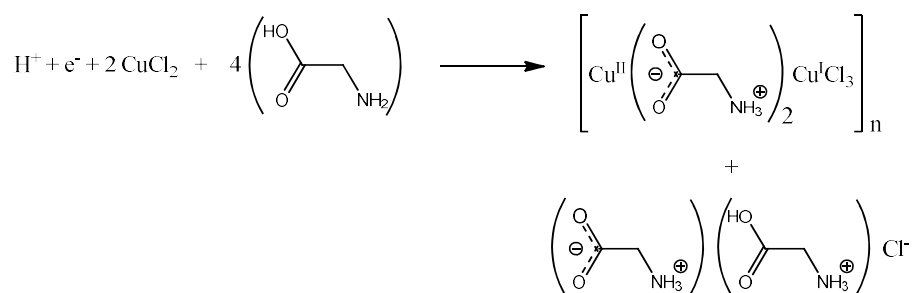


Figure 5.31 Reaction scheme for the reaction of CuCl₂ with Gly.

5.5.2 [Cu(CIMGly)(H₂O)₂] (36)

The same reaction that forms **35** but in the presence of bromide ions results in small green crystals that show a very different unit-cell of monoclinic symmetry. Structure solution and refinement were performed readily in space group *P2*₁/*c*, further crystallographic details are included in Table 5.9. It appeared at first to be a diglycine ligand bound to copper through the two amine N atoms and a carboxylate O atom along with two water molecules. However, none of the known hydrates have similar cell parameters to those

found for this sample, and a large electron density peak was located near what should be the terminal amine. Additionally, the O atom of the peptide bond showed two electron density peaks which appeared to be hydrogen atoms. The only sensible assignment was for the ligand to be based on iminodiacetic acid and the extra non-hydrogen atom to be an imine group with two hydrogen atoms. The true ligand is therefore carboxyiminomethylglycine (CIMGly) which coordinates to the Cu centre through the two carboxylate functional groups each through an O atom, and the deprotonated secondary amine, shown in Figure 5.32. Assignment of the two other atoms coordinated to Cu as water molecules was correct, the Cu therefore has square-pyramidal coordination geometry and bond distances/angles are listed in Table 5.24.

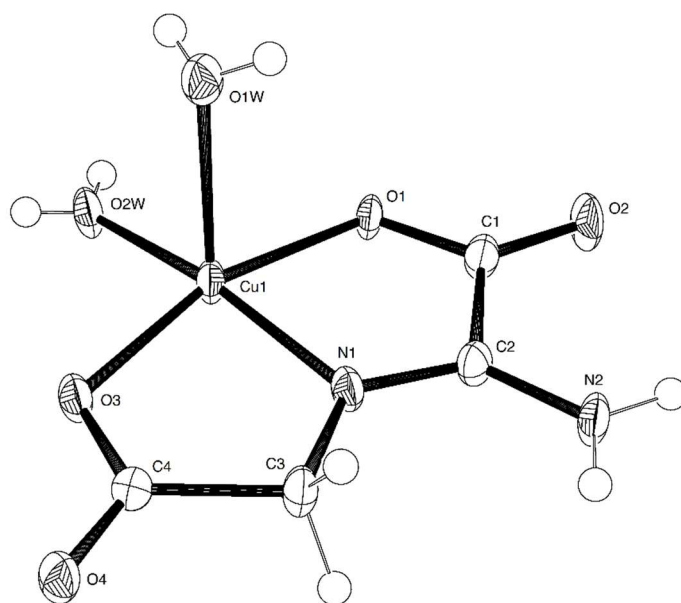


Figure 5.32 Asymmetric unit of $[\text{Cu}(\text{CIMGly})(\text{H}_2\text{O})_2]$ (**36**) with atoms shown as thermal ellipsoids drawn at 50% probability.

Hydrogen bonding interactions occur between the O2w and CIMGly ligands in the [104] crystallographic plane creating a 2-D sheet. Further interactions between O1w and CIMGly allow the sheets to stack, similar to the interactions in $[\text{Cu}(\text{Gly-Gly})(\text{H}_2\text{O})]$.

Table 5.24 Selected bond lengths (Å) and angles (°) around the Cu coordination centre for [Cu(CIMGly)(H₂O)₂] (**36**).

Cu(1) – O(1)	2.022(2)	Cu(1) – O(2W)	1.918(3)
Cu(1) – O(3)	1.995(2)	Cu(1) – N(1)	1.896(3)
Cu(1) – O(1W)	2.306(3)		
O(1) – Cu(1) – O(3)	163.73(11)	O(3) – Cu(1) – O(2W)	97.44(11)
O(1) – Cu(1) – O(1W)	92.49(12)	O(3) – Cu(1) – N(1)	83.00(11)
O(1) – Cu(1) – O(2W)	95.58(11)	O(1W) – Cu(1) – O(2W)	92.99(14)
O(1) – Cu(1) – N(1)	82.09(11)	O(1W) – Cu(1) – N(1)	100.20(13)
O(3) – Cu(1) – O(1W)	96.51(12)	O(2W) – Cu(1) – N(1)	166.68(16)

One theory of how the ligand has been formed is that a coordinated glycine molecule has undergone a bromination reaction, most likely through a free radical mechanism involving UV irradiation, then another glycine molecule acts as a nucleophile reacting with the brominated species releasing a bromide ion and producing the secondary amine. This is purely speculative, and further information is required before a true reaction mechanism can be determined. Additional observations were that the brown, oily supernatant did not mix with perfluoropolyether oil, and there were few and very small crystals of the product indicating a very low undeterminable yield.

5.6 Thermal Experiments

As a reminder before the thermal experiments are discussed, the abbreviations used for the amino acids in this section are shown in Table 5.1.

5.6.1 Dehydration and rehydration experiments

The structures of [Cu₂(β-Ala)₄Cl₂]Cl₂·H₂O (**23**), [Cu₂(ABA)₄Cl₂]Cl₂·H₂O (**27**), [Cu₂(APA)₄Cl₂]Cl₂·2H₂O (**29**), [Cu₂(AHA)₄Cl₂]Cl₂·4H₂O (**32**), and [Cu₂(AHA)₄Br₂]Br₂·4H₂O (**33**) consist partially of water-filled channels. It is feasible that the water could be removed from such compounds leaving the channels vacant allowing them to be filled with another component, like a gas, albeit very poorly due to the lack of

substantial internal surface area/volume. Additionally, there is a possibility that HX could be driven off from the same compounds by combination of a halide ion and a proton from an ammonium group resulting in the formation of a new neutral compound.

Thermogravimetric analysis of the materials was therefore conducted in order to deduce:

1. If there is a plateau of stability following an apparent weight loss corresponding to the loss of all, or close to all, the water molecules or HCl.
2. The temperature at which the solvent molecules/HCl are readily lost.

These pieces of information would indicate whether the crystal is stable upon the loss of water/HX, and the approximate temperature/time requirements to achieve dehydration/dehydrohalogenation allowing the creation of a protocol for studying the reactions. Apart from **29**, which loses water naturally at room temperature, each compound was subjected to this analysis. In each case, the thermogravimetrogram is presented and subsequent studies of the reactions/decompositions are discussed.

5.6.1.1 $[Cu_2(ABA)_4Cl_2]Cl_2 \cdot H_2O$ (**27**)

The thermogravimetrogram of **27** is shown in Figure 5.33. There is a steady drop in weight up to approximately 325 °C, at which point the sample loses weight rapidly, most likely from a loss of the organic component. No plateau occurs in the decomposition, although the shallow gradient up to 325 °C indicates the dehydration step indicates that dehydration could be performed without adversely affecting the structure of the complex (removal of the ligands).

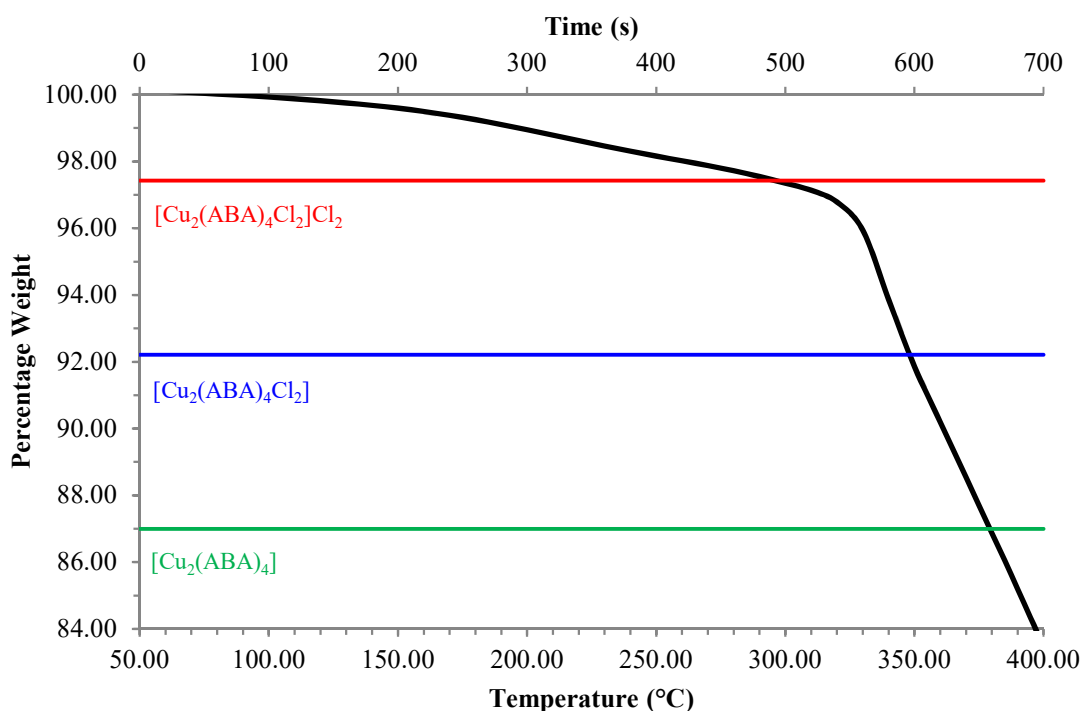


Figure 5.33 TGA results of $[\text{Cu}_2(\text{ABA})_4\text{Cl}_2]\text{Cl}_2 \cdot \text{H}_2\text{O}$ (**27**) heated at $5\text{ }^\circ\text{C}/\text{min}$ in N_2 as a graph of temperature/time vs. percentage weight. The black line indicates the weight of the sample as time/temperature increase. The red, blue, and green lines show the approximate % weight expected for the chemical species indicated next to the line.

Using the above data, it was decided that heating the sample to 393 K ($120\text{ }^\circ\text{C}$) should be sufficient to drive the water out of the material. A crystal of **27** was mounted on the goniometer using epoxy resin, and the sample heated to 393 K ($120\text{ }^\circ\text{C}$) for a set period of time before cooling back down to 150 K for analysis. The sample was initially heated for 30 mins, then for a further hour, and finally a further 3 hours to afford almost complete dehydration. As the crystal was glued to the fibre, the orientation was maintained during the heating regime meaning the same data collection method could be used each time for consistency. These data sets are labelled **DH1**, **DH2**, and **DH3** respectively (**DH** = Dehydrated), further crystallographic details are included in Table 5.5 and Table 5.6.

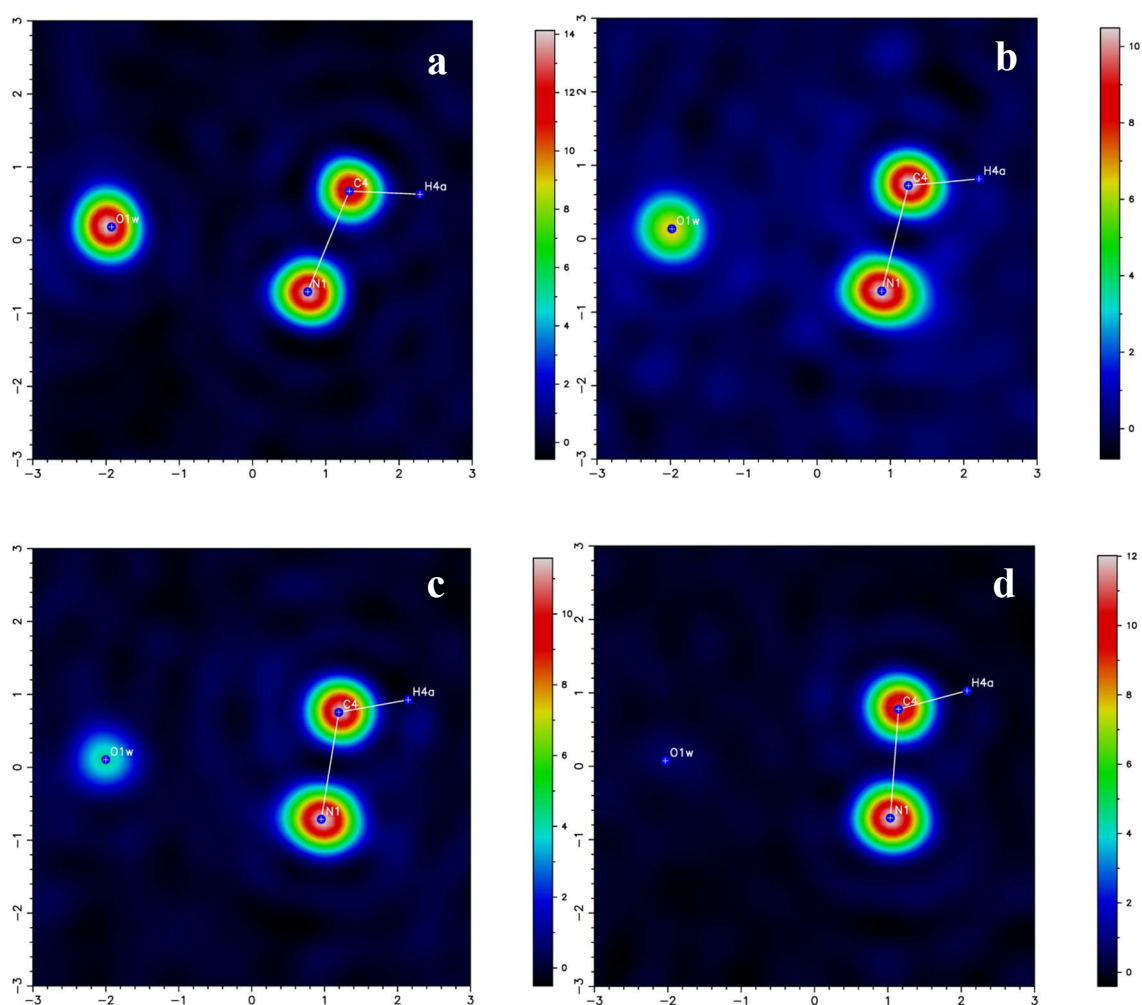


Figure 5.34 Difference Fourier map calculated as a plane passing through N1 C4 O1w of the original sample of $[\text{Cu}_2(\text{ABA})_4\text{Cl}_2]\text{Cl}_2 \cdot \text{H}_2\text{O}$ (**27**) (a), and the same sample after successive dehydrations **DH1** (b), **DH2** (c), and **DH3** (d).

The starting model for refinement was taken from the structure of **27** with O1w fully occupied. Each subsequent refinement used the model from the previous refinement, *e.g.* **DH2** used the model from **DH1**. The O1w atom's occupancy was allowed to refine freely, and the water-bound hydrogens were omitted. The occupancy was calculated to be 0.584(10), 0.345(7), and 0.043(8) for **DH1**, **DH2**, and **DH3** respectively. Figure 5.34 shows the Fourier difference maps of the fully hydrated sample and **DH1**, **DH2**, and **DH3** as a 2-D slice through N1 C4 and O1w. There is a clear reduction in the electron density at the O1w atomic position upon heating, which reinforces the above mentioned

calculated occupancies. In order to determine the effect of water removal from the structure, the refined cell parameters at each level of hydration were plotted as a fraction of the cell parameters for the fully hydrated compound vs. water occupancy, as shown in Figure 5.35.

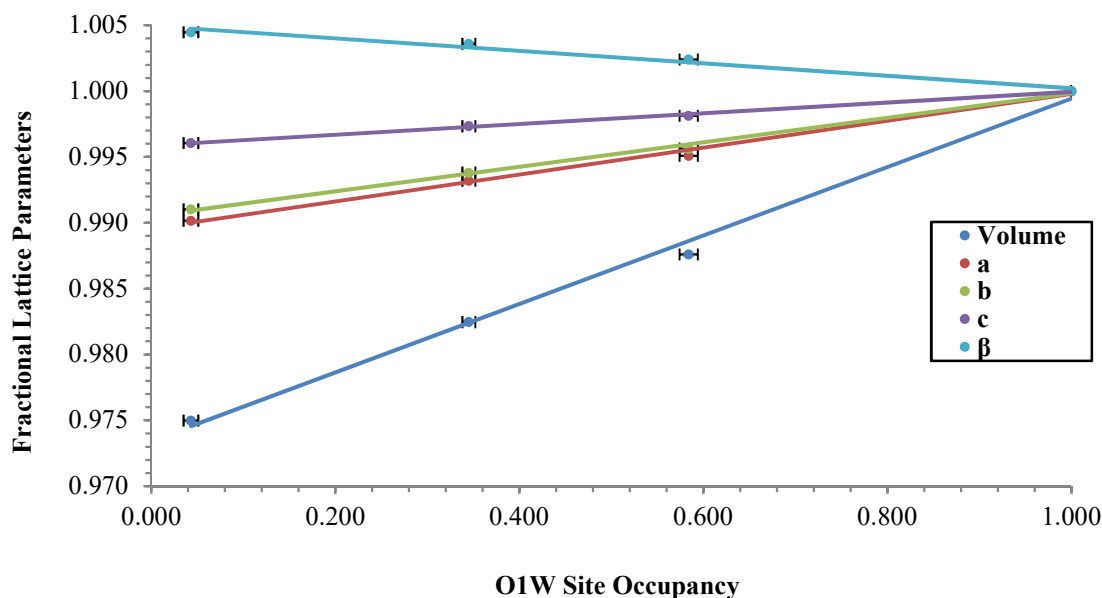


Figure 5.35 Plot of refined cell parameters of $[\text{Cu}_2(\text{ABA})_4\text{Cl}_2]\text{Cl}_2\cdot\text{H}_2\text{O}$ (**27**) as a fraction of the fully hydrated parameters vs. water occupancy. The typical error on the y-axis is ± 0.0001 , this is not easily shown on the same scale as the data so y-axis error bars have not been included.

Interestingly, as occupancy reduces, a , b , and c reduce while at the same time the β angle increases. There is a much greater effect upon the a and b axes lengths than the c axis on removal/gain of water, as shown by the increased gradient for the former two. The exact reasons for these observations are unclear, but it may be that as water is removed the packing efficiency of the remaining material is improved by a greater reduction of a and b than c . The volume reduction of the unit-cell on going from fully hydrated to all water of crystallisation removed equates to the volume occupied by the water within the structure. Therefore, no void is left of removal that could be filled with a gas without distorting the structure in some way.

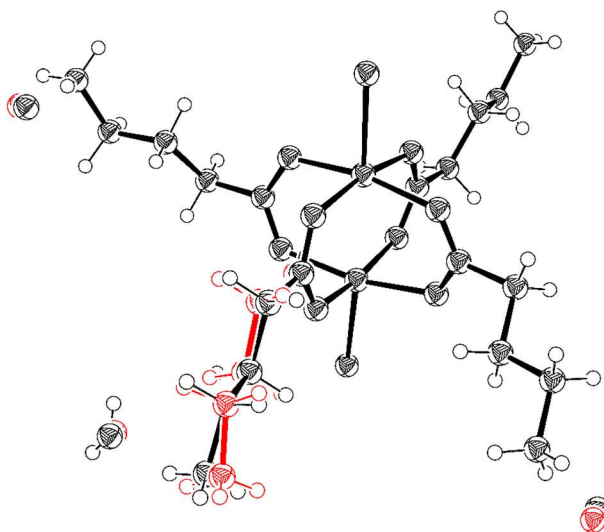


Figure 5.36 Asymmetric unit of $[\text{Cu}_2(\text{ABA})_4\text{Cl}_2]\text{Cl}_2 \cdot \text{H}_2\text{O}$ (**27**) with atoms shown as thermal ellipsoids drawn at 50% probability. Original atomic positions are shown in black, while those after dehydration of the compound are shown in red.

In addition to the changes in cell parameters, there is also an observed movement of the N1 ammonium alkyl chain as depicted in Figure 5.36 via an overlay of the hydrated and non-hydrated structures. Upon desolvation, the chain moves in the opposite direction to that of the hydrogen bond with the water molecules. As the water is removed there is a reduced chance of the hydrogen bond occurring between O1w and N1 atoms throughout the crystal. Therefore, the movement could be explained by a weakening of the $\text{O1w} \cdots \text{N1}$ hydrogen bond causing the chain to be pulled toward the remaining strong hydrogen bonds.

To explore the possibility of resolating the structure with a different guest, a desolvated crystal secured to a glass fibre via epoxy resin was sealed within a chamber filled with ethanol vapour. A similar data collection to those conducted for **DH1/2/3** was performed, however the diffraction patterns showed signs the crystal had split. To rectify the splitting, the data reduction was performed using two orientation matrices which covered all the observed data for the two domains. The **DH3** model was used as the starting point for

refinement, but with O1w removed from the atom list. The Fourier difference map clearly showed only a singular extra peak in the structure corresponding to O1w with no other new peaks in close proximity that could be C atoms. The occupancy of O1w was freely refined as before giving a value of 0.60(2). The cell parameters for the resolved structure (**RH1**) all correspond to those predicted for an occupancy of 0.6, showing a predictable (with respect to the cell parameters) and reversible water desolvation/resolution process.

As further confirmation of the reversible desolvation/resolution process, bulk material was analysed by powder diffraction being conducted on untreated, dehydrated, and rehydrated samples. The diffraction data, and simulated data for the hydrated and dehydrated structures, are shown in Figure 5.37. There is very little difference between the diffraction diagrams, although the peaks at 11° and 13.2° 2θ are split in the hydrated samples, but singular peaks in the dehydrated sample. This clearly shows the above conclusions based on the single-crystal studies apply to the bulk material as well.

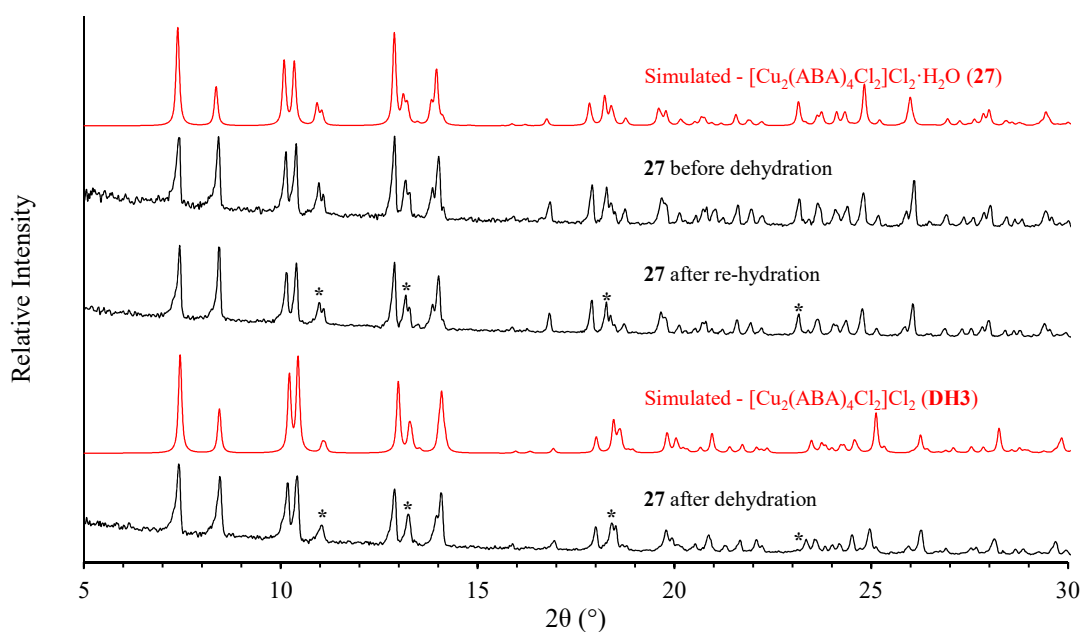


Figure 5.37 Room temperature X-ray powder diffraction data for samples of **27** Before and after dehydration, and after rehydration. Experimental data are shown in black while simulated data are shown in red. As the differences are only subtle, some of the main peaks affected in the dehydrated and rehydrated samples have been marked with *.

5.6.1.2 $[\text{Cu}_2(\beta\text{-Ala})_4\text{Cl}_2]\text{Cl}_2\cdot\text{H}_2\text{O}$ (**23**)

The thermogravimetrogram of **23** is shown in Figure 5.38. There is a steady decrease in weight up to approximately 150 °C, at which point the sample appears stable slowly losing weight up to 325 °C at which point the mass rapidly reduces with no plateaus to indicate a stable compound forming by loss of HCl. The plateau from 150-325 °C occurs at the approximate weight corresponding with the loss of all water molecules (red).

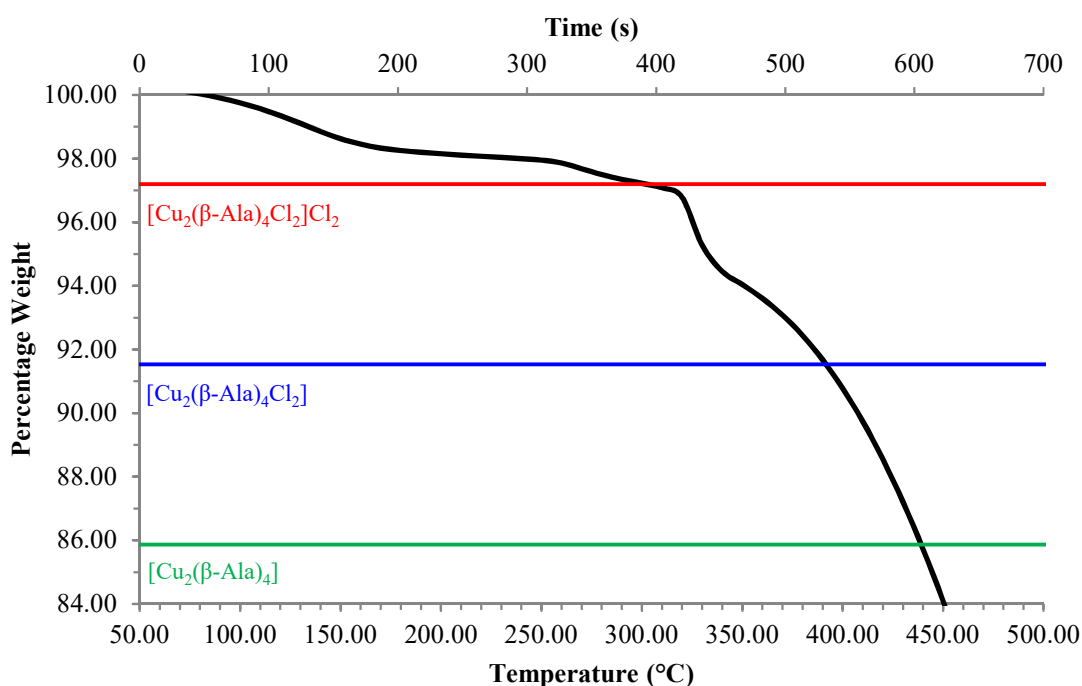


Figure 5.38 TGA results of $[\text{Cu}_2(\beta\text{-Ala})_4\text{Cl}_2]\text{Cl}_2\cdot\text{H}_2\text{O}$ (**23**) heated at 5 °C/min in N_2 as a graph of temperature/time vs. percentage weight. The black line indicates the weight of the sample as time/temperature increase. The red, blue, and green lines show the approximate % weight expected for the chemical species indicated next to the line.

Given the lack of any drastic change in the structure of **27** on the loss of H_2O from the structure, the transformation of **23** from hydrated to dehydrated was not investigated using single-crystal X-ray diffraction but just X-ray powder diffraction alone. The X-ray

powder diffractograms of a sample of **23** before and after dehydration and after subsequent rehydration alongside simulated data are shown in Figure 5.39.

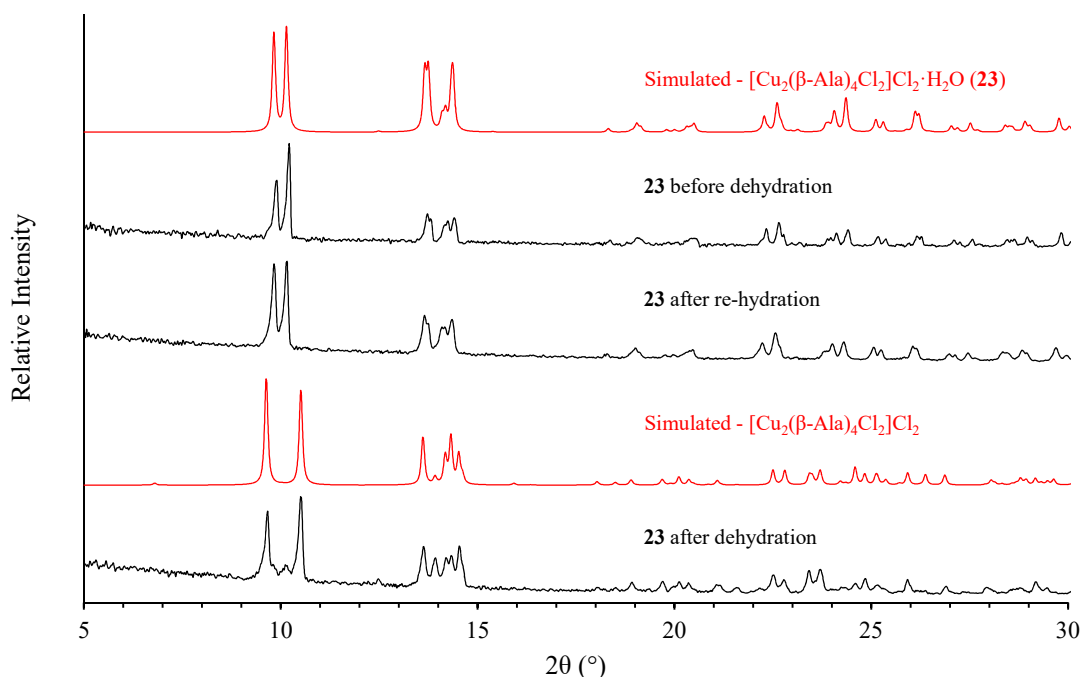


Figure 5.39 Room temperature X-ray powder diffraction data for samples of **23** Before and after dehydration, and after rehydration. Experimental data are shown in black while simulated data are shown in red.

The unit-cell parameters of the hydrated structure were refined to give a better fit to the observed data for the dehydrated sample. The unit-cell parameters for each sample are shown in Table 5.25. The simulated data for the dehydrated structure were created by importing the unit-cell parameters into the structure file for the hydrated compound and removing the atoms constituting the water molecule in the asymmetric unit. This gave an excellent fit to the observed data despite only being an approximation. The X-ray powder diffraction data plotted above clearly show that the dehydrated compound has a different structure to that before dehydration, and on re-hydration the diffraction pattern appears to revert back to that obtained originally. This shows that a reversible dehydration-rehydration process is also exhibited by **23**, so this property is not unique to the structure of **27**.

Table 5.25 Unit-cell parameters for the crystal structures of hydrated and dehydrated $[\text{Cu}_2(\beta\text{-Ala})_4\text{Cl}_2]\text{Cl}_2 \cdot \text{H}_2\text{O}$ (**23**).

Compound	Hydrated	Dehydrated
a (Å)	9.444(2)	8.984(2)
b (Å)	9.498(2)	9.726(2)
c (Å)	14.107(3)	14.165(3)
α (°)	104.04(3)	103.64(3)
β (°)	105.90(3)	106.14(3)
γ (°)	97.15(3)	99.05(3)

Interestingly, while the structure of **26** shows only a reduction in all variable unit-cell parameters upon dehydration, **23** shows an increase of b with a simultaneous decrease of a and all other parameters more or less maintained. The water molecules in **23** occupy the space between paddlewheel complexes stacking along a and b . It is likely the removal of the water allows better packing of the complexes along a , while the loss of hydrogen bonds to water causes a shift of the molecules to compensate, increasing the distance between complexes along b .

5.6.1.3 $[\text{Cu}_2(\text{APA})_4\text{Cl}_2]\text{Cl}_2 \cdot 2\text{H}_2\text{O}$ (**29**)

As mentioned earlier, $[\text{Cu}_2(\text{APA})_4\text{Cl}_2]\text{Cl}_2 \cdot 2\text{H}_2\text{O}$ (**29**) could not be made in a pure form. X-ray powder diffraction of the crystals of **29** produced by solvent evaporation and subsequent grinding showed the samples to be a mixture of **29** and $[\text{Cu}_2(\text{APA})_4\text{Cl}_2]\text{Cl}_2$ (**30**), as shown in Figure 5.40. Following storage of this sample of **29** for one month in a sealed container, further degradation occurred resulting in an X-ray powder diffraction pattern of only **30**. Further tests showed that grinding of the starting reagents that make both **29** and **30**, with water produced only **30**. Therefore, one explanation for the observed degradation and lack of pure samples of **29** is that the hydrated structure is less thermodynamically stable than **30** and only under special but not fully understood

conditions is **29** produced in an appreciable quantity. It is interesting that only the complex of APA exhibits this property, whereas all other hydrated compounds are stable at room temperature for some years. TGA studies on **29** have not yet been attempted and further experiments are required to understand the conditions that give rise to **29** in order to make pure samples for analysis.

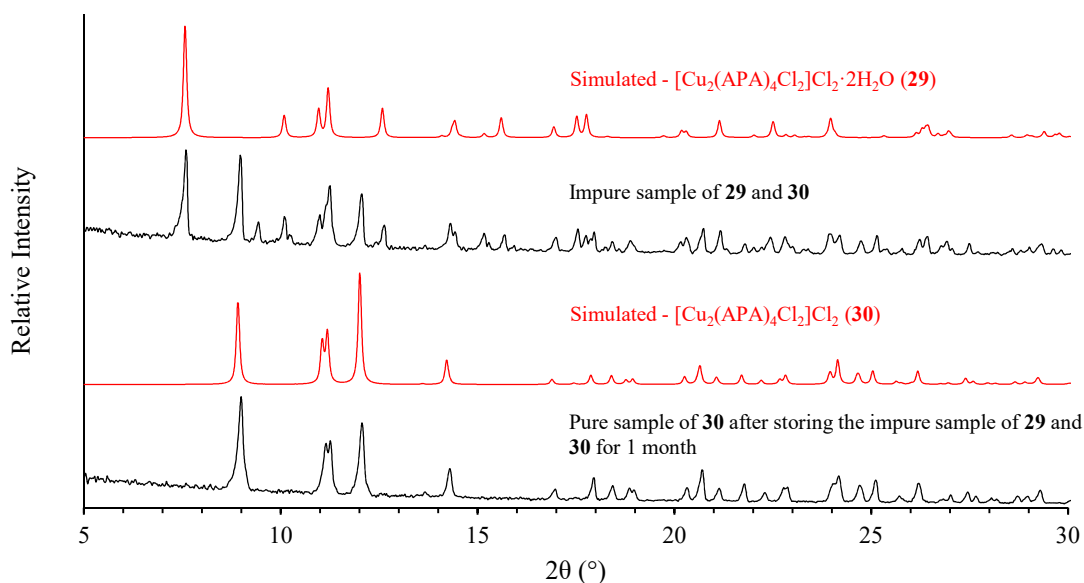


Figure 5.40 Room temperature X-ray powder diffraction data for a sample of **29** immediately after synthesis and grinding, and after storage for a month. Experimental data are shown in black while simulated data are shown in red.

5.6.1.4 [Cu₂(AHA)₄Cl₂]Cl₂·4H₂O / [Cu₂(AHA)₄Br₂]Br₂·4H₂O (**32/33**)

The result of thermogravimetric analysis of **32** is shown in Figure 5.41. The results appear similar to those of **23** and **27**. There is a steady loss of mass up to approximately 175 °C at which point a very steady plateau occurs until around 325 °C at which point the mass decreases rapidly most likely to be decomposition of the ligand. The plateau indicates that a fully dehydrated compound is formed and is very stable as the weight corresponds to that expected for a fully dehydrated form (red). As with the other experiments, there does not appear to be a stable compound formed from loss of HCl.

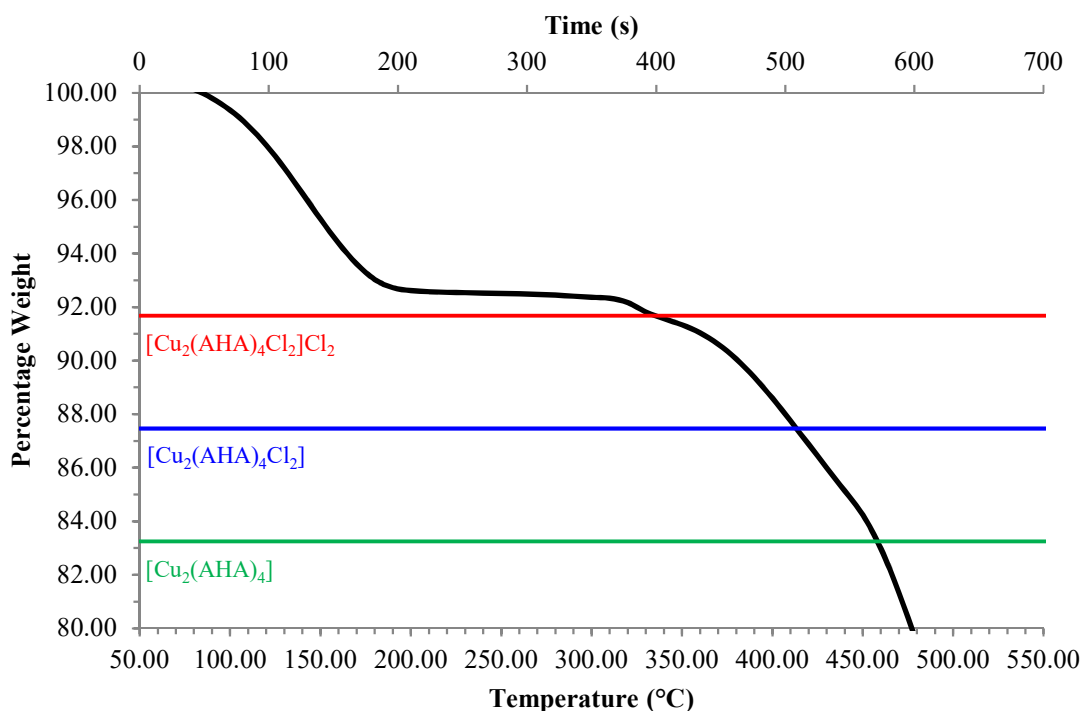


Figure 5.41 TGA results of $[\text{Cu}_2(\text{AHA})_4\text{Cl}_2]\text{Cl}_2 \cdot 4\text{H}_2\text{O}$ (**32**) heated at 5 °C/min in N_2 as a graph of temperature/time vs. percentage weight. The black line indicates the weight of the sample as time/temperature increase. The red, blue, and green lines show the approximate % weight expected for the chemical species indicated next to the line.

The thermal decomposition of **33**, the bromide equivalent to **32**, is very similar to that of the chloride counterpart. The thermogravimetrogram is shown in Figure 5.42. The water molecules appear to be lost much more readily than in **32**, with complete loss occurring by approximately 150 °C. A plateau occurs from 150 °C until the loss of mass becomes much more rapid at around 350-375 °C, a similar temperature to the final decomposition of **32**. This further indicates that the ligand is destroyed at this point as this is the unifying feature for the two compounds. No stable compound forms corresponding to the loss of HBr from the paddlewheel complex.

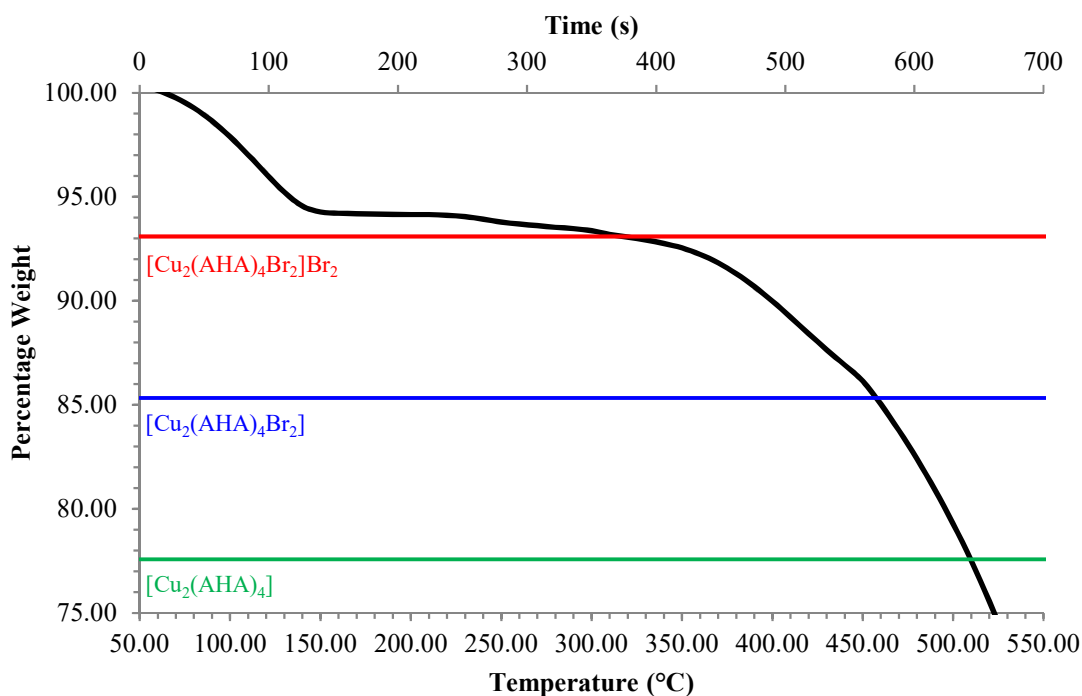


Figure 5.42 TGA results of $[\text{Cu}_2(\text{AHA})_4\text{Br}_2]\text{Br}_2 \cdot 4\text{H}_2\text{O}$ (**33**) heated at $5\text{ }^\circ\text{C}/\text{min}$ in N_2 as a graph of temperature/time vs. percentage weight. The black line indicates the weight of the sample as time/temperature increase. The red, blue, and green lines show the approximate % weight expected for the chemical species indicated next to the line.

The transformation of **32** and **33** on dehydration/rehydration was analysed using X-ray powder diffraction. Samples were analysed before and after dehydration, and after attempted rehydration. The data are plotted in Figure 5.43. Comparison of the experimental data to the simulated data clearly shows that each compound starts out as a pure form of the hydrated compound before transforming somewhat drastically to a new unknown crystalline form with very little, if any, features of the original diffraction pattern left intact. The attempted rehydration of this dehydrated compound had no effect on the diffraction pattern making this an irreversible change by solid-gas reaction, although a dissolution/precipitation process could perhaps rehydrate the complex although this was not tested.

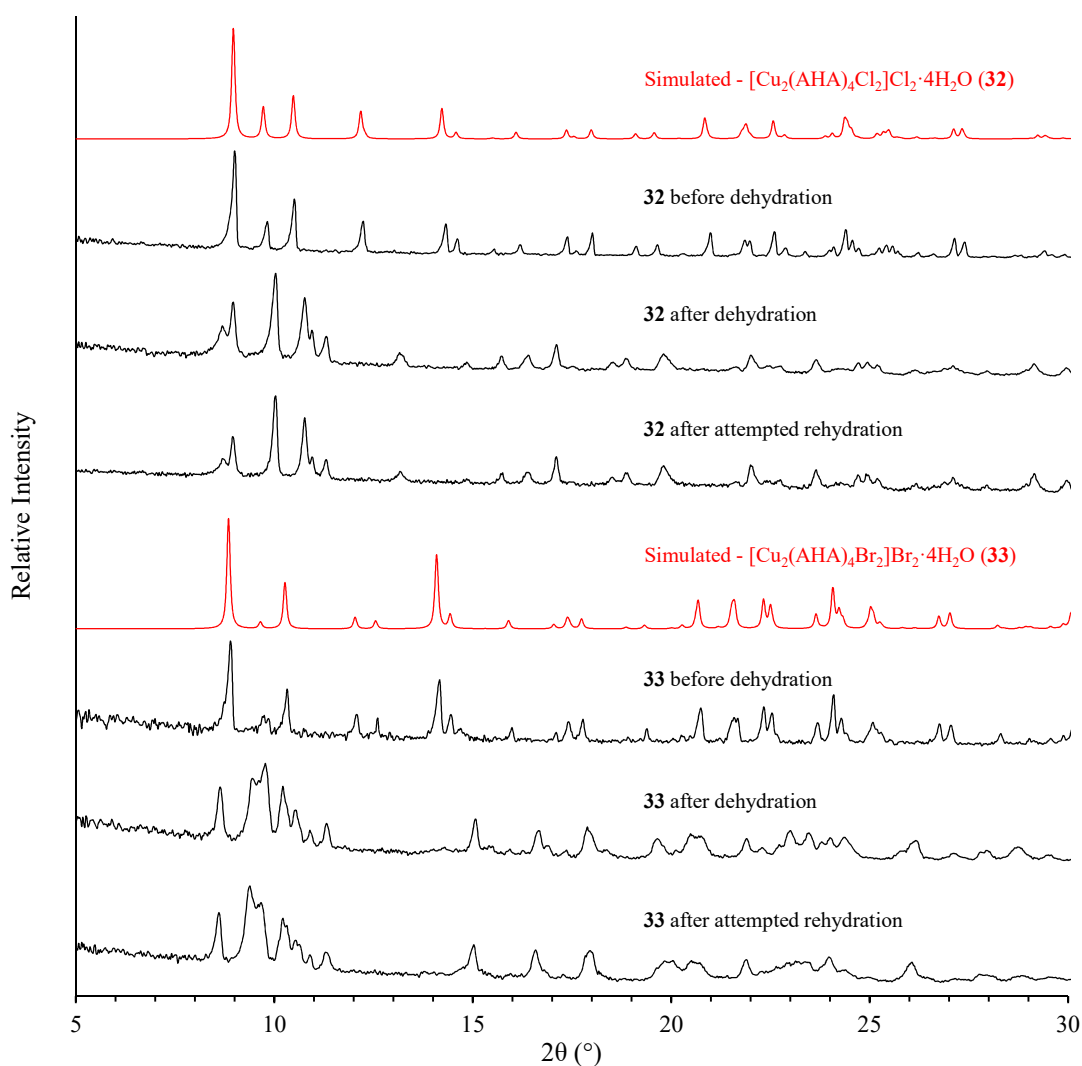


Figure 5.43 Room temperature X-ray powder diffraction data for samples of **32** and **33** Before and after dehydration, and after attempted rehydration. Experimental data are shown in black while simulated data are shown in red.

It was possible to index the diffraction patterns of dehydrated **32** and **33**. This showed that the transformation causes a loss of symmetry in the compounds from a monoclinic hydrated structure to a triclinic dehydrated structure. The unit-cells were refined using the Pawley method giving good fits to the experimental data (**32**: $R_{wp} = 0.1107$, $\chi^2 = 5.986$; **33**: $R_{wp} = 0.1333$, $\chi^2 = 13.424$) as shown in Figure 5.44 and Figure 5.45.

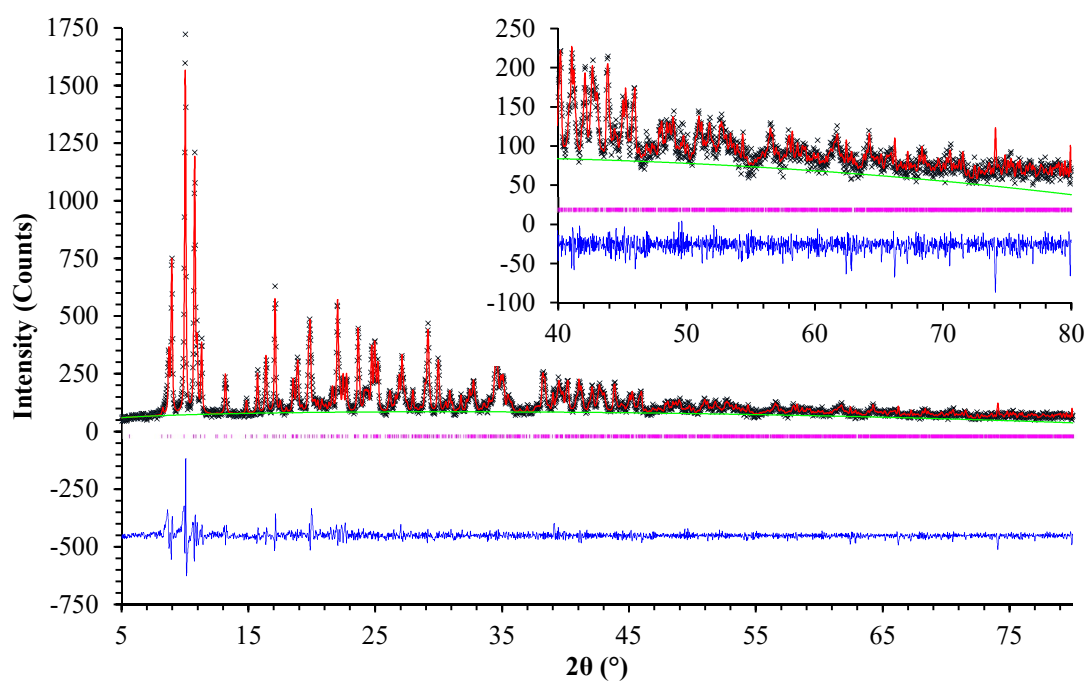


Figure 5.44 A plot of the Pawley refinement of the proposed cell for dehydrated $[\text{Cu}_2(\text{AHA})_4\text{Cl}_2]\text{Cl}_2 \cdot 4\text{H}_2\text{O}$ (32). Black crosses represent observed data, the red line calculated data, the green line background, the pink markers peak positions, and the blue line is the difference plot $[(I_{\text{obs}} - I_{\text{calc}})]$.

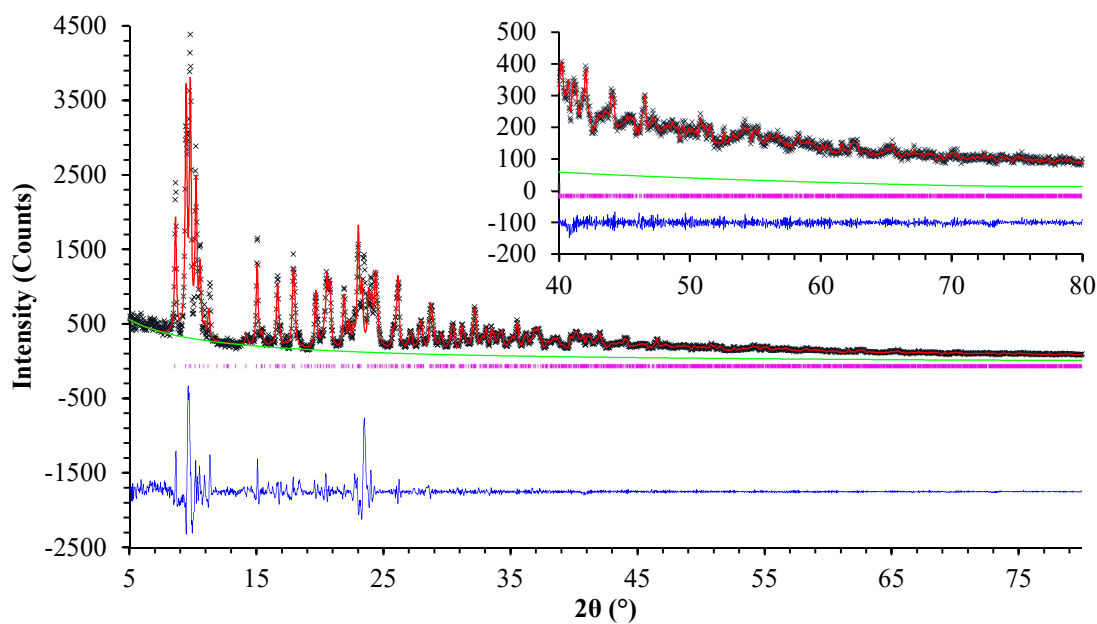


Figure 5.45 A plot of the Pawley refinement of the proposed cell for dehydrated $[\text{Cu}_2(\text{AHA})_4\text{Br}_2]\text{Br}_2 \cdot 4\text{H}_2\text{O}$ (33). Black crosses represent observed data, the red line calculated data, the green line background, the pink markers peak positions, and the blue line is the difference plot $[(I_{\text{obs}} - I_{\text{calc}})]$.

The resulting unit-cell parameters for dehydrated **32** and **33** after Pawley refinement are shown in Table 5.26 alongside the monoclinic unit-cell parameters of the hydrated structures. The two sets of unit-cell parameters are not as comparable as previous examples given the change in translational symmetry on removal of water, however it possible to see that *a* increases while *b* and *c* decrease upon dehydration of **32** with all angles altered by $\pm 10^\circ$. On the other hand, *a* and *b* decrease while *c* increases as **33** is dehydrated, and only γ shows a moderately large distortion from the original 90° angle. The difference in the response of the structures toward loss of water must be either a result of differences in hydrogen bonding strength toward bromide and chloride ions giving rise to markedly different structures, given that is the main difference between them, or simply an erroneous determination of the unit-cells. However, without a single-crystal X-ray diffraction study of the process this is simply speculation.

Table 5.26 Unit-cell parameters for the crystal structures of hydrated and dehydrated $[\text{Cu}_2(\text{AHA})_4\text{Cl}_2]\text{Cl}_2 \cdot 4\text{H}_2\text{O}$ (**32**) and $[\text{Cu}_2(\text{AHA})_4\text{Br}_2]\text{Br}_2 \cdot 4\text{H}_2\text{O}$ (**33**).

Compound	Hydrated 32	Dehydrated 32	Hydrated 33	Dehydrated 33
<i>a</i> (Å)	9.4279(7)	10.33(2)	9.5156(7)	9.313(11)
<i>b</i> (Å)	12.1456(11)	11.15(3)	12.2700(6)	10.895(10)
<i>c</i> (Å)	17.4963(12)	16.00(6)	17.8505(16)	18.94(4)
α (°)	90	101.64(2)	90	87.29(1)
β (°)	105.269(6)	92.13(2)	105.246(3)	106.14(2)
γ (°)	90	100.93(2)	90	69.79(1)

5.6.2 Anisotropic thermal expansion of $[\text{Cu}_2(\text{APA})_4\text{Cl}_2]\text{Cl}_2$ / $[\text{Cu}_2(\text{APA})_4\text{Br}_2]\text{Br}_2$ (30/31)

X-ray powder diffraction (XRPD) is a routine way of checking that the single-crystal selected for structure analysis is representative of the bulk material, and also define the purity of the crystalline portion of a sample. Diffraction data simulated from a structure

determined by single-crystal X-ray diffraction is commonly used for comparison. However, because single-crystal studies are routinely performed at low temperatures (~150 K) while powders are more commonly analysed at room temperature, some shift of the diffraction peak angles along θ is expected due to thermal expansion of the structure and material. This shift is commonly systematic, *i.e.* all peaks in the experimental data are at a lower angle than expected from the 150 K data. However, when conducting XRPD analysis on **30** and **31**, two peaks were overlapping at around $11^\circ 2\theta$ which should have occurred separately. This is shown in Figure 5.46 by comparison of the experimental and 150 K simulated data.

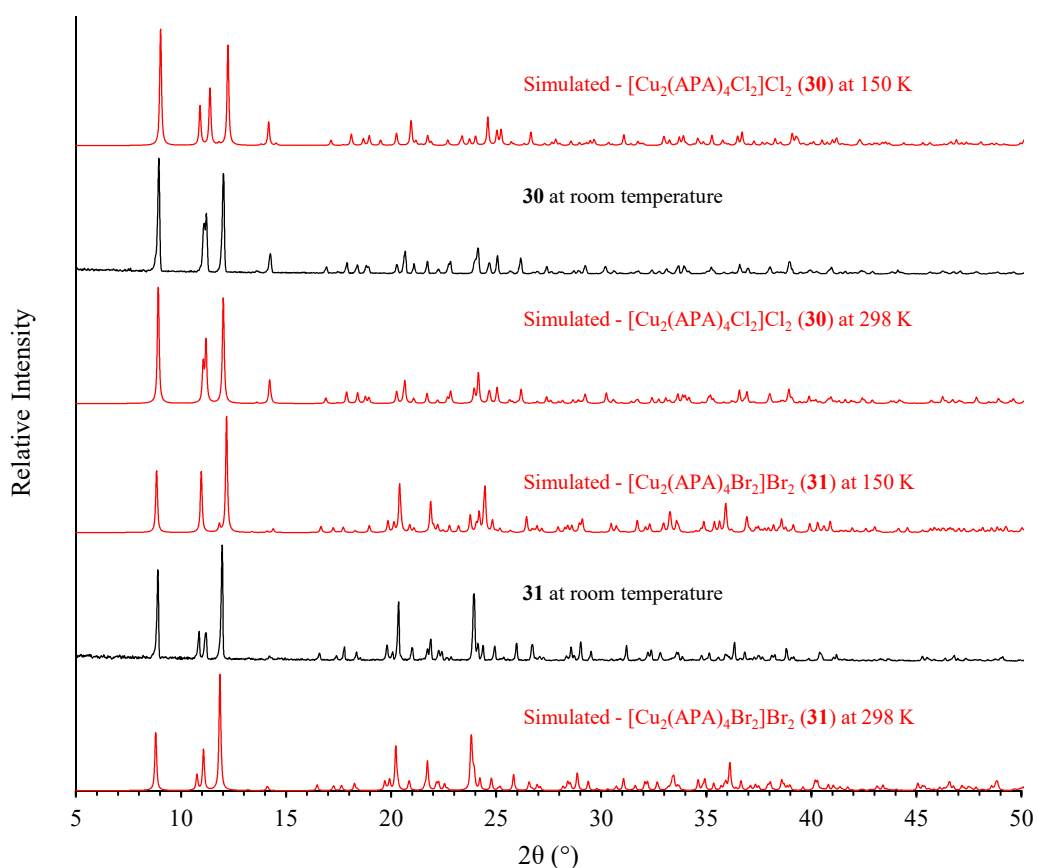


Figure 5.46 Room temperature X-ray powder diffraction data for samples of **30** and **31** against simulated data for the two structures at 150 K and 298 K. Experimental data are shown in black while simulated data are shown in red.

Crystals of each compound were re-analysed by single-crystal X-ray diffraction at room temperature (298 K) using epoxy resin to secure the crystal in place, further crystallographic details are included in Table 5.7 and Table 5.8. The refinement of the structures using the data collected at 298 K was conducted using the model at 150 K as a starting point, however the refinement resulted in a severely elongated ellipsoid for C8. Suspecting this to be a result of disorder, the atom was set to 50% occupancy and refined once more, revealing a new second position for the atom (B), as shown in Figure 5.47. The two C8 positions were refined with the same isotropic displacement parameter and the occupancies were refined as a free variable. The occupation of the two sites are almost equal in the bromide structure at 298 K, 0.470(7) and 0.530(7) for A and B respectively, but the chloride structure has a much higher occupancy for the A position at the same temperature, being 0.650(5).

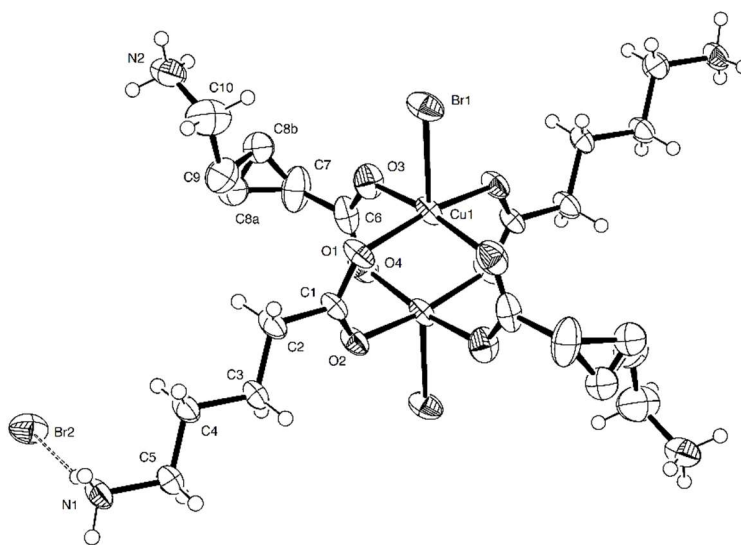


Figure 5.47 Asymmetric unit of $[\text{Cu}_2(\text{APA})_4\text{Br}_2]\text{Br}_2$ (**31**) determined at 298 K with atoms shown as thermal ellipsoids drawn at 50% probability. Hydrogen bonds are drawn as dashed lines.

The simulated data from the 298 K structures show a much better match to the experimental data, as shown in Figure 5.46 above. The unit-cell parameters extracted

from the new data are compared in Table 5.27. Each structure shows a minimal change in a and b but a much larger change in c and β , however **30** exhibits a smaller change in c and a larger change in b than the equivalent bromide structure **31**.

Table 5.27 Unit-cell parameters for the crystal structures of $[\text{Cu}_2(\text{APA})_4\text{Cl}_2]\text{Cl}_2$ (**30**) and $[\text{Cu}_2(\text{APA})_4\text{Br}_2]\text{Br}_2$ (**31**) at 150 K and 298 K.

Compound	30 (150 K)	30 (298 K)	Difference	31 (150 K)	31 (298 K)	Difference
a (Å)	9.0041(6)	8.9843(7)	-0.22%	8.8923(9)	8.9505(7)	+0.65%
b (Å)	19.5885(14)	19.8343(17)	+1.25%	20.0101(17)	20.1051(14)	+0.47%
c (Å)	9.4018(7)	9.6807(8)	+2.97%	9.7160(9)	10.0922(8)	+3.87%
β (°)	115.711(5)	117.045(6)	+1.15%	114.846(7)	116.778(5)	+1.68%

It was of interest to investigate the thermal expansion further given the difference in thermal expansion between the two structures. To do this, the unit-cell parameters were analysed at a series of different temperatures to see how the structure changes as a result of temperature and whether it is a smooth transition or if an abrupt change occurs at a specific temperature. A crystal was selected for each structure and an identical set of diffraction frames were collected at each given temperature to determine the unit-cell parameters.

The unit-cell volume was used as a guide for any structural transformations that might be occurring with a change in temperature. The graph of unit-cell volume vs. temperature for **30** is shown in Figure 5.48, and Figure 5.49 for **31**. The volume increases linearly with temperature and no abrupt changes are observed for **30** with an overall increase from 150-333 K of 3.62%. However, **31** tells a very different story. The volume increases linearly up to approximately 210 K, at which point a sharp transition in the volume occurs before increasing linearly again with an overall change from 150-333 K of 3.98%.

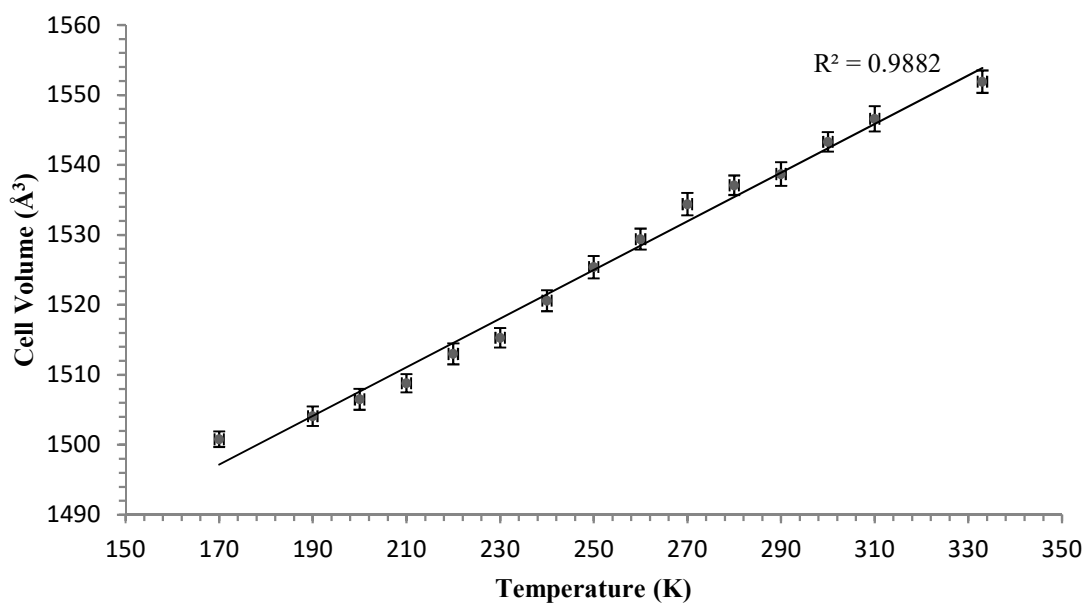


Figure 5.48 Unit-cell volume as a function of temperature for $[\text{Cu}_2(\text{APA})_4\text{Cl}_2]\text{Cl}_2$ (**30**).

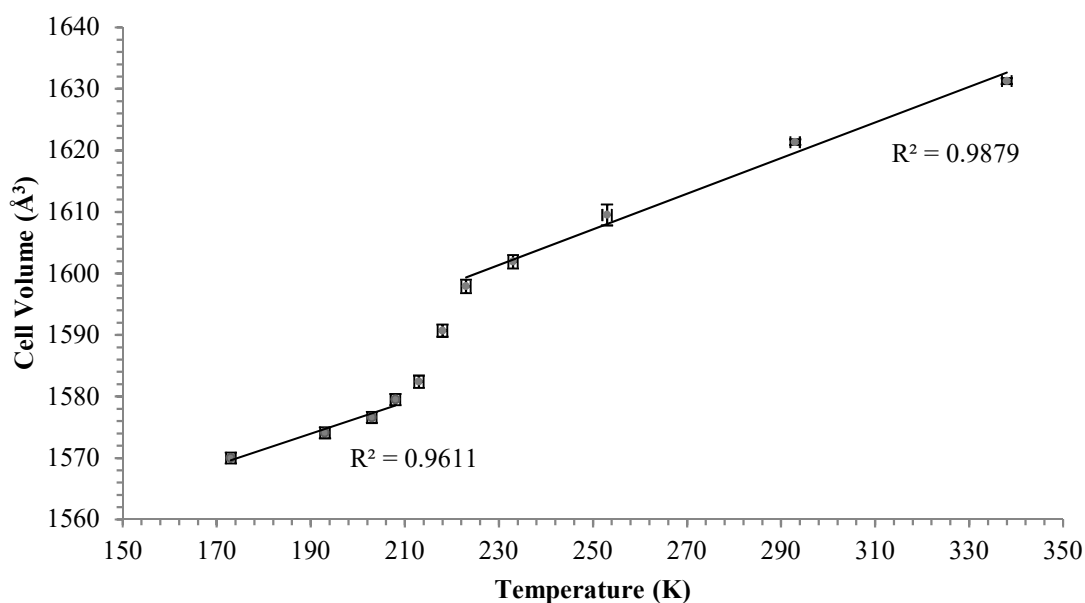


Figure 5.49 Unit-cell volume as a function of temperature for $[\text{Cu}_2(\text{APA})_4\text{Br}_2]\text{Br}_2$ (**31**).

The only difference between the two structures is the halide ions which form the majority of the hydrogen bonding interactions in the structure. It seems likely that the bromide analogue, having the weakest interactions of the two, is more susceptible to changes in temperature with respect to the packing. The alkylammonium chain that is coiled along

the *c* axis can alleviate the strain caused by thermal expansion in both compounds by relaxation, inducing an order/disorder phase transition. Since the chloride analogue has much stronger hydrogen bonding interactions it is more stable towards an increase in temperature, as evidenced by the smaller percent increase in the volume. Therefore, unlike with **31** there is no clear-cut position at which the phase transition occurs in **30**, and instead occurs gradually over a large temperature range.

5.7 Cuprate compounds and solid-gas reactions

The last set of compounds to discuss in this chapter are the tetrahalocuprate salts of the amino acids. Salts incorporating the $[\text{CuX}_4]^{2-}$ ion are very interesting for a number of reasons: different geometries of the ion are exhibited depending on the crystal packing and hydrogen bonding forces present, sometimes resulting in vivid thermochromism; structural interconversion to other copper halide compounds can occur by loss of HX; when certain hydrogen bonding groups are present, the cuprate ions can form polymeric structures through bridging halides similar to those found in layered perovskites.

Each cuprate salt was synthesised by crystallisation of $\text{CuCl}_2 \cdot 2\text{H}_2\text{O}$ or CuBr_2 and two equivalents of an amino acid from an aqueous 6M HCl or HBr solution, producing either lustrous yellow crystals of the tetrachlorocuprate salt or deep black-purple crystals of the equivalent tetrabromocuprate salt. The structures of these compounds were either already known or determined using single-crystal X-ray diffraction. They display remarkable structural similarities in both the coordination geometry of the copper ion, and the hydrogen bonding interactions of the amino acids. The main difference between the structures is the conformation of the methylene chain of the amino acids. All the structures contain $[\text{CuX}_4]^{2-}$ anions (Cu-Cl *ca.* 2.30 Å, Cu-Br *ca.* 2.45 Å) occupying a single crystallographic plane, *e.g.* (110) or (011). Due to the orientation of the anions in the

plane, long Cu-X coordinate bonds (Cu-Cl *ca.* 3.00 Å, Cu-Br *c* 3.15 Å) bridge the anions together, making the coordination geometry of the Cu centres is 4+2 (distorted octahedral) and forming a 2-D coordination polymer as shown by a representative example in Figure 5.50.

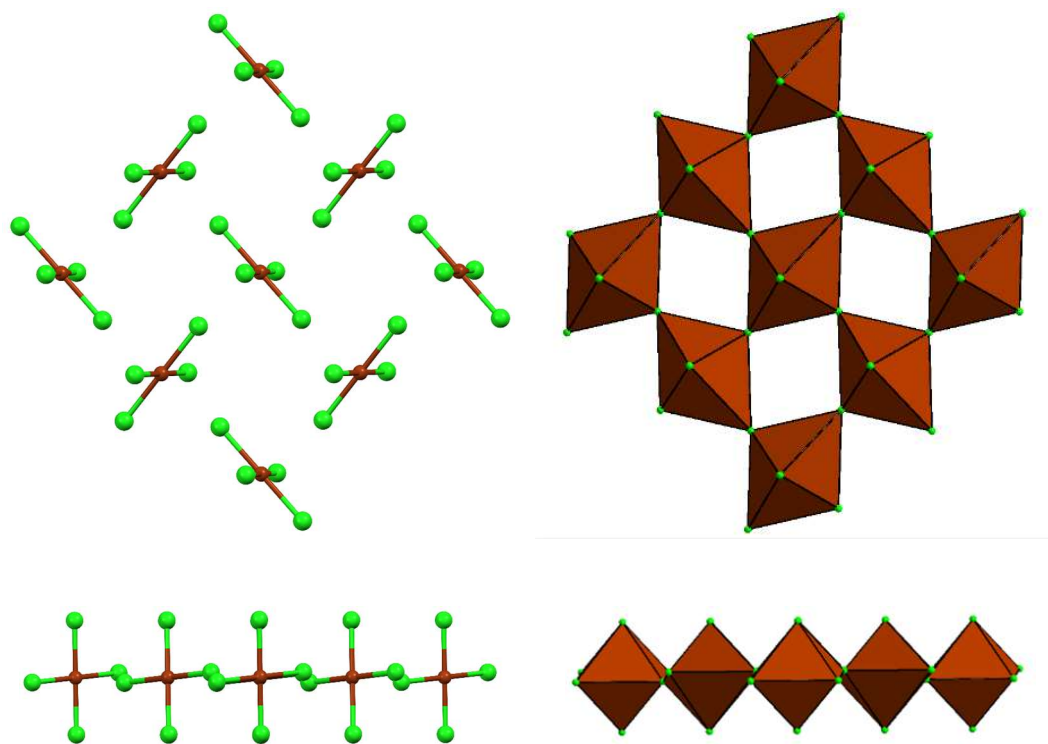


Figure 5.50 Images of the 2-D coordination polymer created by the $[\text{CuCl}_4]^{2-}$ anions in $(\text{H-}\beta\text{-Ala})_2[\text{CuCl}_4]$ (37) shown as a ball and stick diagram, left, and a polyhedral diagram, right. Top images are viewed perpendicular to the plane occupied by the polymer while bottom images are viewed parallel to the same plane. Cu atoms are shown in orange, Cl in green.

The geometry of the cuprate anions, and the arrangement of the anions into the observed coordination polymer, is a result of the $\text{N-H}\cdots\text{X}$ hydrogen bonding interactions between the ammonium groups of the cationic amino acid molecules and the halide ligands of the cuprate ions. Strong hydrogen bonds toward the halide ligands of a cuprate ion are thought to reduce the charge on the anionic ligands, reducing anion-anion repulsion allowing ligand field stabilisation energy to dictate the geometry therefore resulting in a square-planar complex.¹²⁷ The ammonium groups also bridge the cuprate ions via hydrogen

bonds to several halide ions in the cuprate layers, therefore the stable distorted octahedral geometry of copper can be produced by formation of additional long Cu-X contacts. The layers of cuprate anions and amino acid cations are then held in their respective positions by both the conformational structure of the acids, and the $R_2^2(8)$ interactions formed by mutual hydrogen bonding of two carboxylic acid moieties as shown in Figure 5.51. As mentioned earlier, it is mainly the conformational structure and length of the cations which differentiates the structures, so descriptions will focus on these factors.

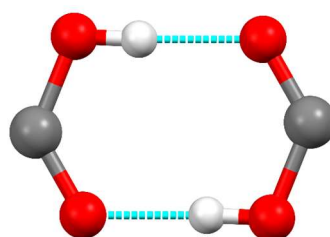


Figure 5.51 The $\text{CO}_2\text{H-HO}_2\text{C}$ supramolecular synthon found in all the $[\text{CuX}_4]^{2-}$ amino acid salts. C atoms are shown in grey, H in white, and O in red. Hydrogen bonds are drawn as light-blue dashed lines.

It has been shown in chapter 3 that compounds can have the capability to transform into cuprate salts reversibly by the absorption of gaseous HX. Noting that the only compositional difference between the paddlewheel compounds, discussed earlier in the chapter, and these cuprate salts is two HX molecules, similar solid-gas reactions to those described chapter 3 have also been attempted with the paddlewheel compounds, the results of which are also discussed below. As a reminder, the abbreviations used for the amino acids in this section of work are shown in Table 5.1.

5.7.1 $(\text{H-}\beta\text{-Ala})_2[\text{CuCl}_4]/(\text{H-}\beta\text{-Ala})_2[\text{CuBr}_4]$ (37/38)

The crystal structures of $(\text{H-}\beta\text{-Ala})_2[\text{CuCl}_4]$ (**37**) and $(\text{H-}\beta\text{-Ala})_2[\text{CuBr}_4]$ (**38**) were previously determined by Willett *et al.* as part of a study into two-dimensional magnetic materials.^{202,203} However, the hydrogen atom positions in **37** were not reported correctly.

Additionally, the quality of the model for **38** was poor ($R = 0.092$), and the provided atomic positions for C, N, and O atoms did not form a connected set as would be expected. Therefore, the crystal structures of **37** and **38** were re-determined. The hydrogen atom positions in **37** were easily determined and a good fit to observed data was obtained ($R = 0.0299$, $wR = 0.0810$), further crystallographic details are included in Table 5.9. Because the two structures have very similar unit-cells, apart from the expansion of a and b in **38** due to the length of Cu-Br bonds vs. Cu-Cl bonds, the structural model of **37** was used to refine the structure of **38** by replacing the Cl atoms with Br. Refining against the observed data for **38** gave an excellent fit when compared with the original structure determination (Original $R = 0.092$, new $R = 0.0486$), further crystallographic details are included in Table 5.10. The asymmetric units are each composed of one β -Ala cation and half a CuX_4 anion with the Cu in the 4c Wyckoff position, since they are identical only **37** is shown in Figure 5.52. Bond lengths and angles of the tetrahalocuprate ions are shown in Table 5.28 and Table 5.29 for **37** and **38** respectively, the Cu coordination geometry is 4+2 as stated in the introduction to this section.

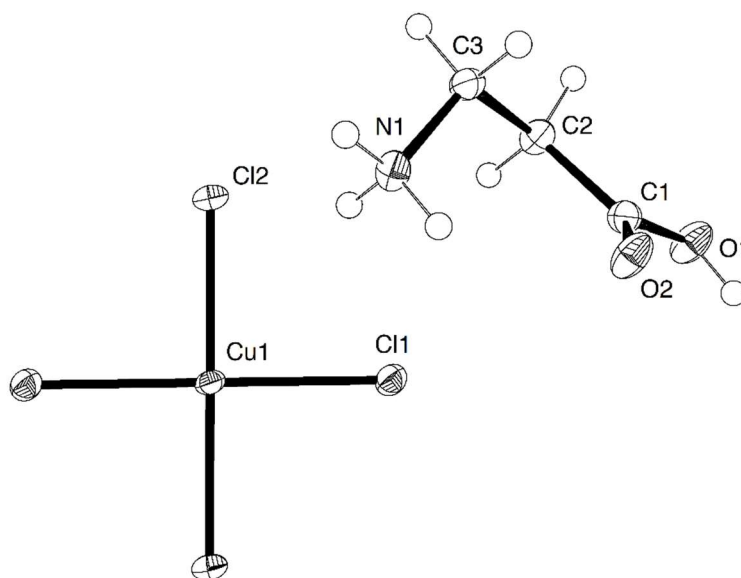


Figure 5.52 Asymmetric unit of $(\text{H-}\beta\text{-Ala})_2[\text{CuCl}_4]$ (**37**) with atoms shown as thermal ellipsoids drawn at 50% probability. The $[\text{CuCl}_4]^{2-}$ ion is completed by the symmetry operation $x - \frac{1}{2}, 2 - y, z$.

Table 5.28 Selected bond lengths (Å) and angles (°) around the Cu coordination centre for (H-β-Ala)₂[CuCl₄] (**37**).

Cu(1) – Cl(1)	2.2770(4)	Cu(1) – Cl(2)#1	3.0579(4)
Cu(1) – Cl(2)	2.3105(4)		
Cl(1) – Cu(1) – Cl(2)	89.335(14)	Cl(2) – Cu(1) – Cl(2)#1	88.264(10)
Cl(1) – Cu(1) – Cl(2)#1	89.888(14)		

#1 $x - \frac{1}{2}, 2 - y, z$

Table 5.29 Selected bond lengths (Å) and angles (°) around the Cu coordination centre for (H-β-Ala)₂[CuBr₄] (**38**).

Cu(1) – Br(1)	2.4227(5)	Cu(1) – Br(2)#1	3.1478(6)
Cu(1) – Br(2)	2.4499(6)		
Br(1) – Cu(1) – Br(2)	89.529(19)	Br(2) – Cu(1) – Br(2)#1	88.515(16)
Br(1) – Cu(1) – Br(2)#1	88.422(17)		

#1 $x, \frac{1}{2} - y, \frac{1}{2} + z$

The C and O based portion of the cation (C1, C2, C3, O1, and O2) in each structure is approximately planar: RMSD from planarity is 0.0655 Å in **37** and 0.0577 Å in **38**. The ammonium N does not occupy the plane of the rest of the molecule, but is instead rotated around the C2-C3 bond with a N1-C3-C2-C1 torsion angle of 65.5(2)° in **37** and 65.6(7)° in **38**. The lengths of axes *a* and *b* in each structure are controlled primarily by the Cu-X bond lengths in the 2-D polymeric layer. Cu-Br bonds are somewhat longer than Cu-Cl bonds, and as expected **38** has longer *a* and *b* axes; 7.3735(6) Å and 7.7223(4) Å in **37** vs. 7.7324(7) Å and 8.0011(9) Å in **38**. Remarkably though, because the cationic amino acid molecules are arranged identically in the two structures, the *c* axis lengths are almost identical; *c* is 24.080(2) Å in **37**, and 24.087(2) Å in **38**.

A comparison of the experimental X-ray powder diffraction patterns of **37** and **38** produced by solvent evaporation to the data simulated from the single-crystal structures is shown in Figure 5.53. The lack of additional peaks in the experimental data and

comparison of expected and actual composition by elemental analysis of the two samples shows they are pure.

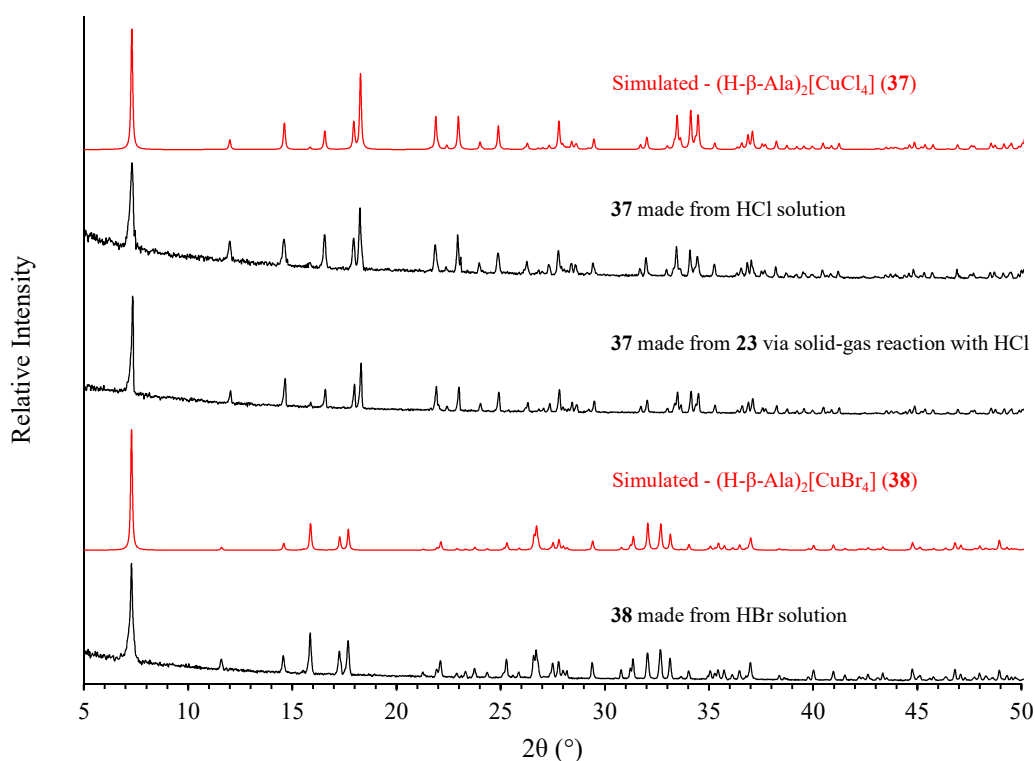


Figure 5.53 Room temperature X-ray powder diffraction data for samples of **37** and **38** made from solution, and solid-gas reaction of $[\text{Cu}_2(\beta\text{-Ala})_4\text{Cl}_2]\text{Cl}_2\cdot\text{H}_2\text{O}$ (**23**). Experimental data are shown in black while simulated data are shown in red.

The reaction of solid $[\text{Cu}_2(\beta\text{-Ala})_4\text{Cl}_2]\text{Cl}_2\cdot\text{H}_2\text{O}$ (**23**) with HCl gas produces a yellow powder in the course of approximately one hour, this was shown to be **37** by a comparison of the X-ray powder diffraction pattern to simulated data in Figure 5.53 above.. The reverse reaction was also attempted, although even after one month only a miniscule portion of the material had reverted back to a green colour. The green material was extracted as thoroughly as possible from the bulk and X-ray powder diffraction showed this sample to be composed of a mixture of **23** and **37**, as shown in Figure 5.54.

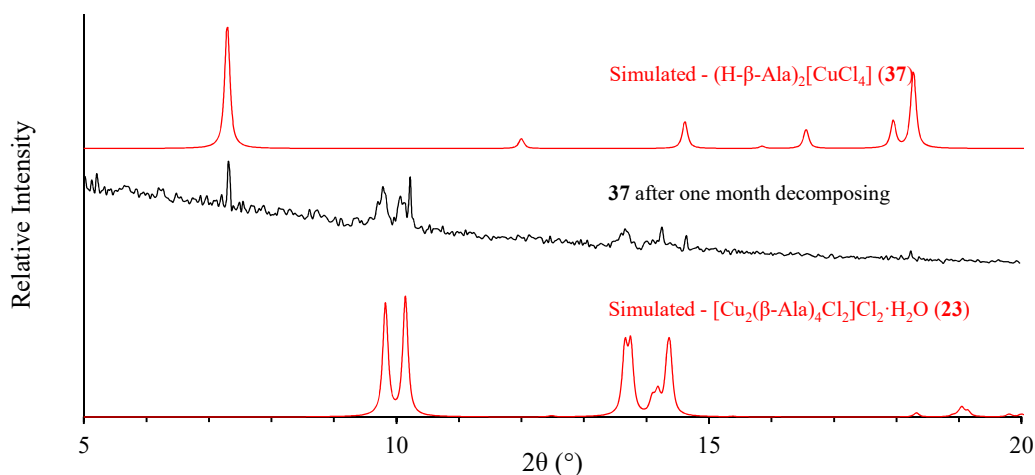


Figure 5.54 Room temperature X-ray powder diffraction data for **37** after partial decomposition. Experimental data are shown in black while simulated data are shown in red.

5.7.2 $(H-ABA)_2[CuCl_4]/(H-ABA)_2[CuBr_4]$ (**39/40**)

The structure of $(H-ABA)_2[CuCl_4]$ (**39**) was discovered and described previously by Yuan *et al.*²⁰⁴ The structure follows the general description in the introduction to this section, however unlike the β -Ala molecules in **37** the ABA molecules in **39** are almost entirely planar. The bromine equivalent to **39**, $(H-ABA)_2[CuBr_4]$ (**40**), was previously unknown until this study. While **39** is monoclinic, **40** has a triclinic unit-cell, although both are centrosymmetric. The asymmetric unit of **40** is four times larger than that of **39**, with two whole $[CuBr_4]^{2-}$ ions and four H-ABA cations, as shown in Figure 5.55, further crystallographic details are included in Table 5.10. Bond distances and angles are shown in Table 5.30, the Cu coordination geometry is 4+2 as stated in the introduction to this section.

One of the major differences between **39** and **40** is the configuration of the H-ABA cations in **40** is more similar to that found in **37** and **38** rather than entirely planar. The RMSD from the plane created by the C and O atoms of each individual cation are 0.0594 Å, 0.0590 Å, 0.0896 Å, and 0.0323 Å for the molecule containing N1 to N4 respectively.

The ammonium group then deviates from the plane in each molecule, with torsion angles of 72(2)°, 73(2)°, 76(2)°, and 76(3)° between the N atom and the three adjacent C atoms.

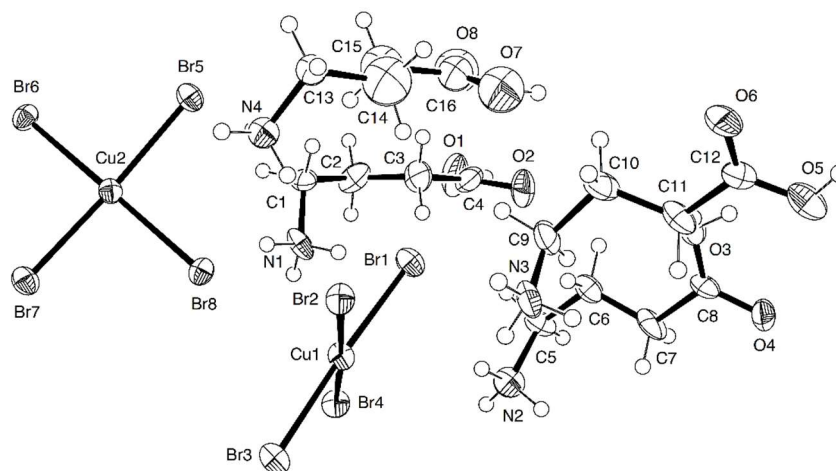


Figure 5.55 Asymmetric unit of (H-ABA)₂[CuBr₄] (**40**) with atoms shown as thermal ellipsoids drawn at 50% probability.

Table 5.30 Selected bond lengths (Å) and angles (°) around the Cu coordination centre for (H-ABA)₂[CuBr₄] (**40**).

Cu(1) – Br(1)	2.448(3)	Cu(2) – Br(2)#2	3.187(3)
Cu(1) – Br(2)	2.444(2)	Cu(2) – Br(4)#3	3.108(3)
Cu(1) – Br(3)	2.433(3)	Cu(2) – Br(5)	2.430(3)
Cu(1) – Br(4)	2.435(2)	Cu(2) – Br(6)	2.455(3)
Cu(1) – Br(6)#1	3.094(3)	Cu(2) – Br(7)	2.418(3)
Cu(1) – Br(8)	3.243(3)	Cu(2) – Br(8)	2.469(3)
Br(1) – Cu(1) – Br(2)	90.13(9)	Br(2)#2 – Cu(1) – Br(4)	176.707(91)
Br(1) – Cu(1) – Br(3)	176.82(11)	Br(2)#2 – Cu(1) – Br(5)	89.272(84)
Br(1) – Cu(1) – Br(4)	89.86(9)	Br(2)#2 – Cu(1) – Br(6)	96.623(90)
Br(1) – Cu(1) – Br(6)#1	88.006(91)	Br(2)#2 – Cu(1) – Br(7)	83.866(83)
Br(1) – Cu(1) – Br(8)	91.079(89)	Br(2)#2 – Cu(1) – Br(8)	89.719(85)
Br(2) – Cu(1) – Br(3)	91.43(9)	Br(4)#3 – Cu(1) – Br(5)	93.908(87)
Br(2) – Cu(1) – Br(4)	176.33(11)	Br(4)#3 – Cu(1) – Br(6)	84.349(85)
Br(2) – Cu(1) – Br(6)#1	86.510(89)	Br(4)#3 – Cu(1) – Br(7)	92.970(87)
Br(2) – Cu(1) – Br(8)	86.474(86)	Br(4)#3 – Cu(1) – Br(8)	89.307(86)
Br(3) – Cu(1) – Br(4)	88.77(9)	Br(5) – Cu(1) – Br(6)	88.12(9)
Br(3) – Cu(1) – Br(6)#1	89.319(90)	Br(5) – Cu(1) – Br(7)	173.04(10)
Br(3) – Cu(1) – Br(8)	91.785(90)	Br(5) – Cu(1) – Br(8)	92.19(9)
Br(4) – Cu(1) – Br(6)#1	97.159(92)	Br(6) – Cu(1) – Br(7)	91.52(9)
Br(4) – Cu(1) – Br(8)	89.855(88)	Br(6) – Cu(1) – Br(8)	173.65(10)
Br(6)#1 – Cu(1) – Br(8)	172.922(99)	Br(7) – Cu(1) – Br(8)	88.94(9)

#1 x, 1 + y, z

#2 1 – x, 1 – y, 2 – z

#3 2 – x, 1 – y, 2 – z

There is obvious pseudotranslational symmetry in the asymmetric unit, as evidenced by the decent overlap of the H-ABA cations after performing a translation of $x + \frac{1}{2}$ on half the molecules, as shown in Figure 5.56. The RMSD between the atomic positions of the overlapping molecules is 0.853 Å for those containing N1 and N4, and 0.367 Å for those containing N2 and N3. The cations containing N1 and N4 are mirror images of each other, and as a result contribute the most to the deviation from strict symmetry.

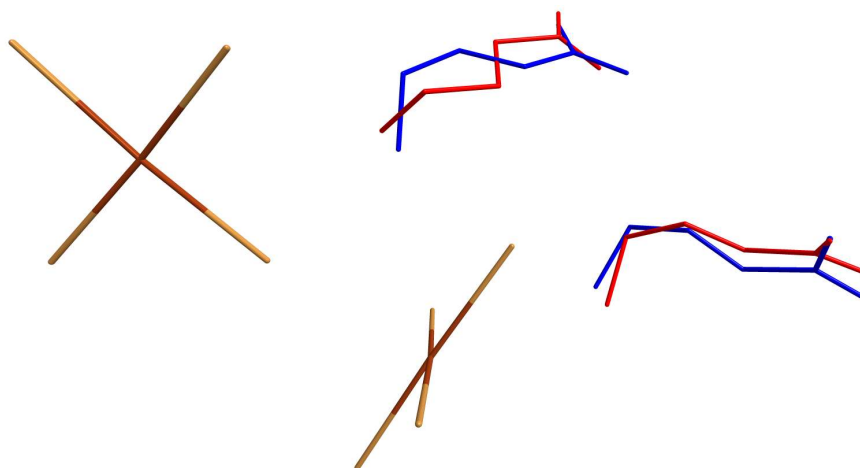


Figure 5.56 The components of the asymmetric unit in $(\text{H-ABA})_2[\text{CuBr}_4]$ (**40**) related by pseudosymmetry after performing the operator $x + \frac{1}{2}, y, z$ on one component. Br atoms are shown in brown, Cu in dark brown. One cation position is shown in blue while the other, related by pseudosymmetry, is shown in red.

The difference in the lengths of b and c in **39**, and a and b in **40** are as expected from the difference in Cu-X bond lengths between the two structures. However, the interplanar separation of the 2-D $[\text{CuX}_4]_n$ polymers in each structure are substantially different. The separation in **39** is 15.196(2) Å while in **40** it is 13.790(4) Å. The main cause of this shortening of the interplanar separation in the Br based structure is the kink in the alkylammonium chain which is otherwise straight in **39**. However why this conformation only occurs in **40** is unknown. A potential reason could be a result of the increase in Cu-X bond lengths from Cl to Br increasing the distance between Cu atoms within the 2-D polymer. The reduced packing efficiency caused by this may result in deformation of the

H-ABA molecules away from planarity to fill the void. A comparison of the crystal packing is shown in Figure 5.57.

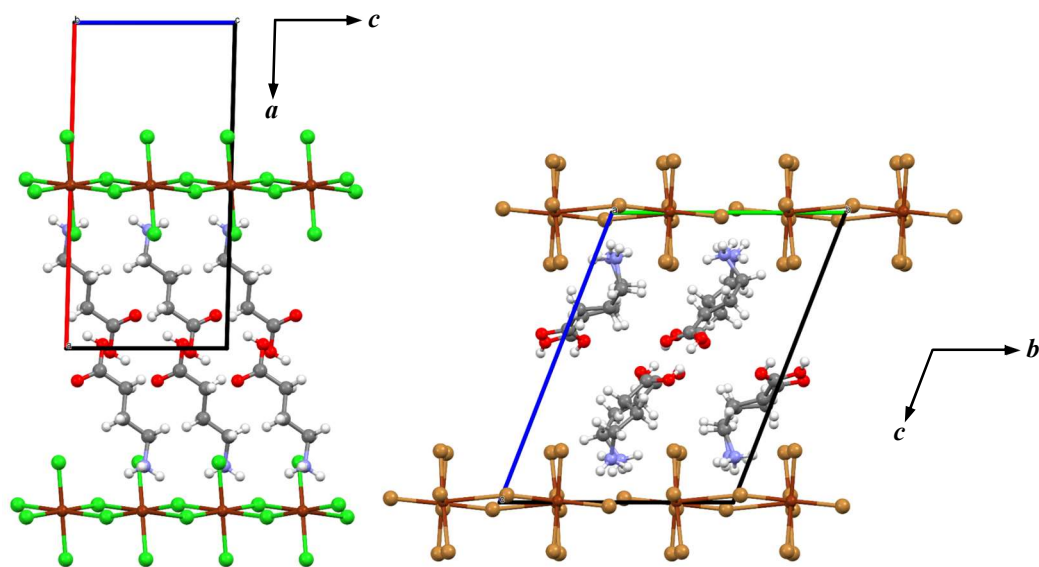


Figure 5.57 A comparison of the crystal packing of $(\text{H-ABA})_2[\text{CuCl}_4]$ (**39**),²⁰⁴ left, vs. $(\text{H-ABA})_2[\text{CuBr}_4]$ (**40**), right. C atoms are shown in grey, H in white, Br in light-brown, Cu in dark brown, Cl in green, N in light grey-blue, and O in red.

The experimental X-ray powder diffraction patterns of **39** and **40** match the simulated data from the single-crystal structures, as shown in Figure 5.58. No large unexpected peaks were observed in the experimental diffraction patterns, and elemental analysis of the two samples matches the expected composition of the pure phases. The reaction of solid $[\text{Cu}_2(\text{ABA})_4\text{Cl}_2]\text{Cl}_2 \cdot \text{H}_2\text{O}$ (**27**) with HCl gas and $[\text{Cu}(\text{ABA})_4\text{Br}_2]\text{Br}_2$ (**28**) with HBr gas produces yellow and black-purple crystalline powders of **39** and **40** respectively in approximately one hour; a similar time frame to $[\text{Cu}_2(\beta\text{-Ala})_4\text{Cl}_2]\text{Cl}_2 \cdot \text{H}_2\text{O}$ (**23**). The identification of the samples as **39** and **40** was confirmed by X-ray powder diffraction, as shown in Figure 5.58. As with **37**, the removal of HX gas from **39** was also attempted, and again, after around one month exposed to the air, only a small portion had converted from yellow to green. The green material was separated from the bulk and analysed by X-ray powder diffraction. Similar to the sample produced by decomposition of **37**, the

diffraction pattern proved the green material to be a mixture of the cuprate and paddlewheel compounds of ABA, as shown in Figure 5.59. Removal of HBr gas from **40** has not yet been attempted.

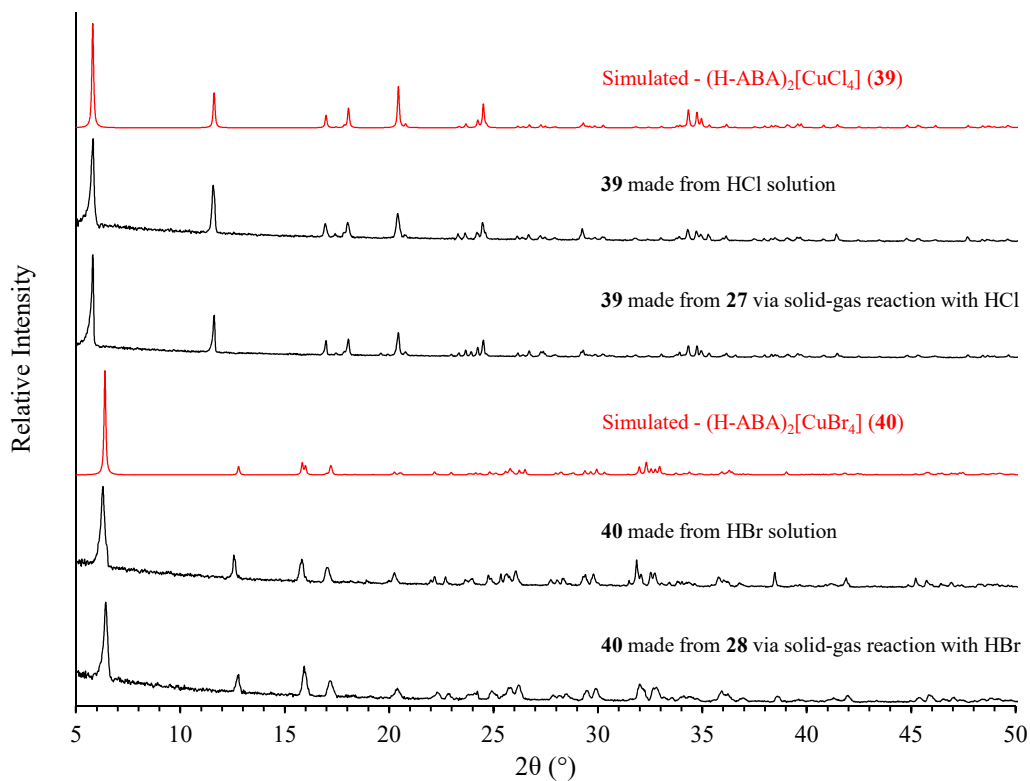


Figure 5.58 Room temperature X-ray powder diffraction data for samples of **39** and **40** made from solution, and solid-gas reaction of $[\text{Cu}_2(\text{ABA})_4\text{Cl}_2]\text{Cl}_2 \cdot \text{H}_2\text{O}$ (**27**) and $[\text{Cu}(\text{ABA})_4\text{Br}_2]\text{Br}_2$ (**28**). Experimental data are shown in black while simulated data are shown in red.

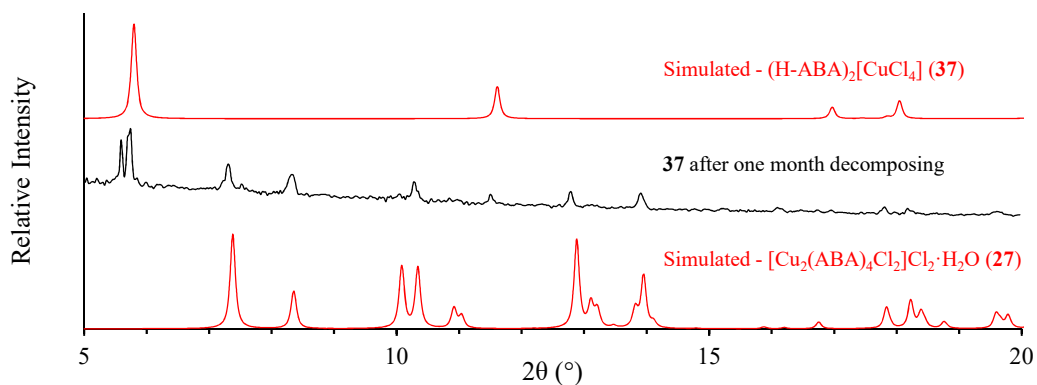


Figure 5.59 Room temperature X-ray powder diffraction data for samples of **39** after partial decomposition. Experimental data are shown in black while simulated data are shown in red.

5.7.3 (H-APA)₂[CuCl₄]/(H-APA)₂[CuBr₄] (41/42)

The crystal structures of (H-APA)₂[CuCl₄] (**41**) and (H-APA)₂[CuBr₄] (**42**) were previously unknown before this study. The structure of **41** could be determined by single-crystal X-ray diffraction, further crystallographic details are included in Table 5.10. It has a centrosymmetric triclinic unit-cell, and an asymmetric unit, shown in Figure 5.60, composed of two symmetry independent H-APA cations and CuCl₄ anions the latter of which are positioned with the Cu atoms on the 1a and 1e Wyckoff sites. Bond distances and angles for **41** are shown in Table 5.31, the Cu coordination geometry is 4+2 as stated in the introduction to this section.

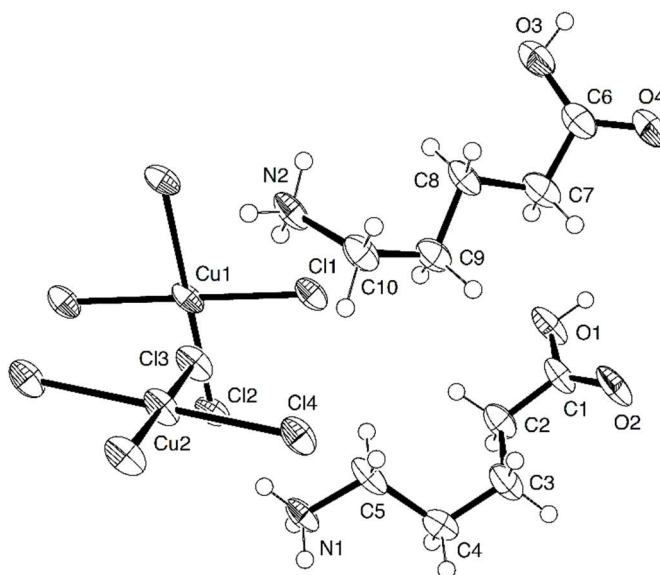


Figure 5.60 Asymmetric unit of (H-APA)₂[CuCl₄] (**41**) with atoms shown as thermal ellipsoids drawn at 50% probability. The [CuCl₄]²⁻ ions are completed by the symmetry operations $1 - x$, $1 - y$, $2 - z$ and $2 - x$, $-y$, $2 - z$.

The reason for the two symmetry independent molecules is a difference in the conformational structure of the H-APA molecules. The molecule containing N1 is planar (RMSD from planarity is 0.0155 Å) from C1-C4 (including O1 and O2) at which point C5 and N1 deviate from the plane with a C2-C3-C4-C5 torsion angle of 65.1(7)°. Conversely, the C atoms in the molecule containing N2 are planar (RMSD from planarity

is 0.0673 Å) while just the O and N atoms deviate from the plane; N2-C10-C9-C8 torsion angle is 67.9(7)° and the angle between the planes drawn through the carboxylic acid moiety and the methylene chain is 38.2(5)°.

Table 5.31 Selected bond lengths (Å) and angles (°) around the Cu coordination centre for (H-APA)₂[CuCl₄] (**41**).

Cu(1) – Cl(1)	2.3041(17)	Cu(2) – Cl(3)	2.2831(14)
Cu(1) – Cl(2)	2.3330(15)	Cu(2) – Cl(4)	2.3434(17)
Cu(1) – Cl(3)	2.9353(15)	Cu(2) – Cl(2)#1	2.9418(15)
Cl(1) – Cu(1) – Cl(2)	81.31(5)	Cl(3) – Cu(2) – Cl(2)#1	88.01(5)
Cl(1) – Cu(1) – Cl(3)	85.79(5)	Cl(3) – Cu(2) – Cl(4)	90.83(6)
Cl(2) – Cu(1) – Cl(3)	86.49(5)	Cl(4) – Cu(2) – Cl(2)#1	95.69(5)

#1 1 + x, y, z

The structure of **42** could not be determined by single-crystal X-ray diffraction as a non-twinned crystal could not be identified due to the absorbance of all plane polarised light under the microscope. The unit-cell could be determined from the X-ray powder diffraction pattern of the sample however, and a Pawley refinement provided a moderate fit to the experimental data ($R_{wp} = 0.1954$, $\chi^2 = 7.524$), as shown in Figure 5.61.

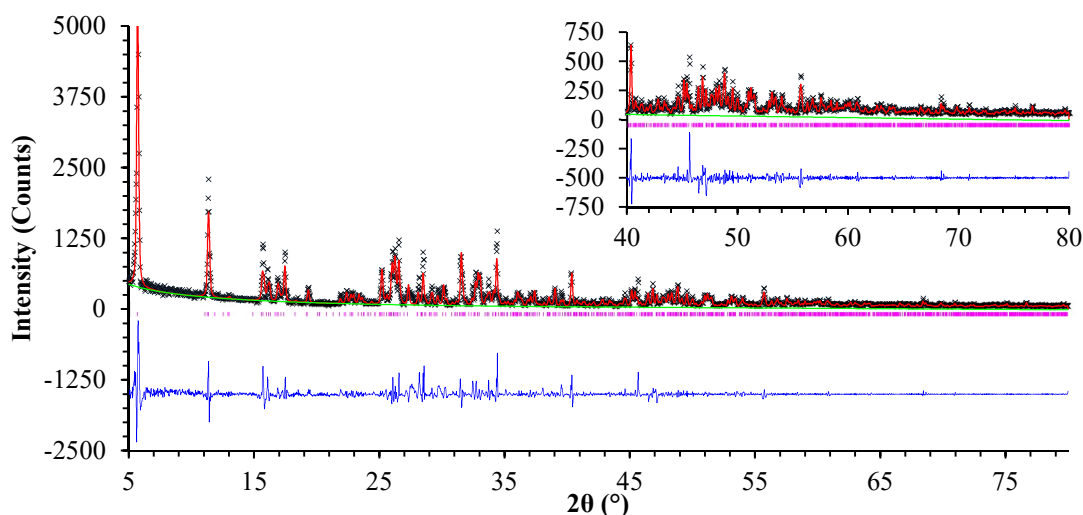


Figure 5.61 A plot of the Pawley refinement of the proposed cell for (H-APA)₂[CuBr₄] (**42**). Black crosses represent observed data, the red line calculated data, the green line background, the pink markers peak positions, and the blue line is the difference plot [$I_{obs} - I_{calc}$].

42 has a triclinic unit-cell similar to **41** although *a* and *b* are longer in **42**, as expected based on the increased length of Cu-Br vs Cu-Cl bonds, while *c* is slightly shorter, as shown in Table 5.32.

Table 5.32 Unit-cell parameters for crystal structures (H-APA)₂[CuCl₄] (**41**) and (H-APA)₂[CuBr₄] (**42**).

Compound	41	42
<i>a</i> (Å)	7.1827(13)	7.788(11)
<i>b</i> (Å)	7.5193(12)	8.040(12)
<i>c</i> (Å)	16.597(3)	15.77(3)
α (°)	86.525(13)	83.45(2)
β (°)	87.155(14)	87.68(2)
γ (°)	89.188(14)	87.79(2)

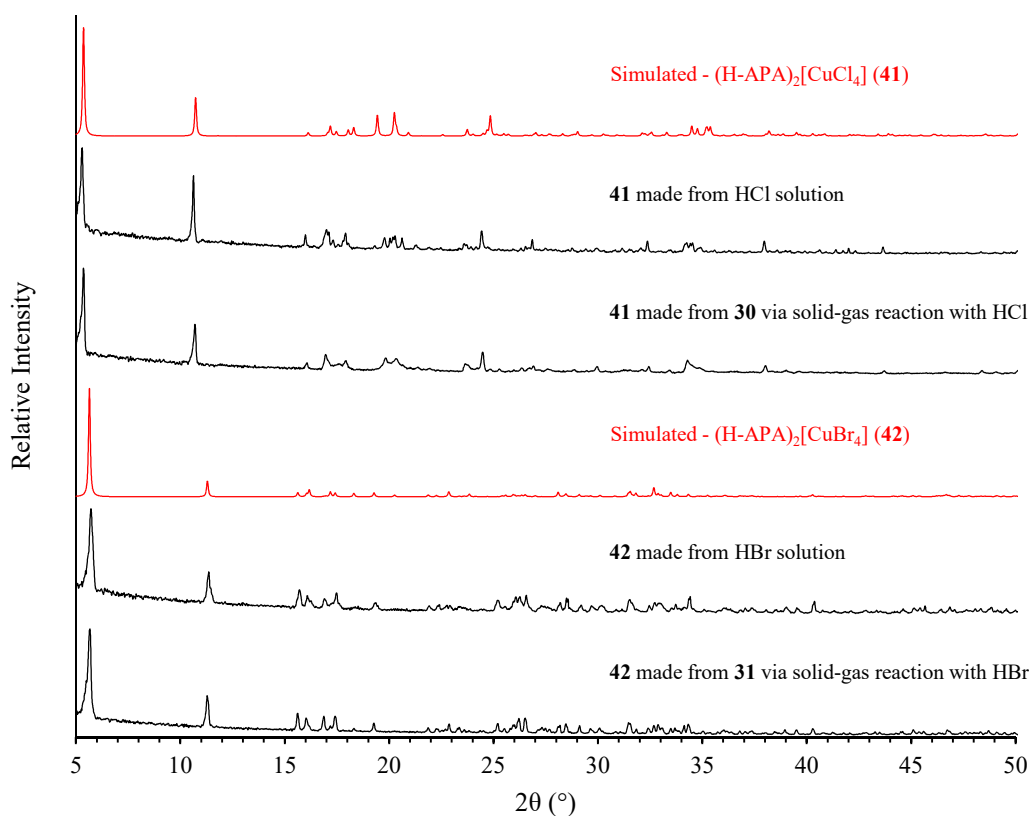


Figure 5.62 Room temperature X-ray powder diffraction data for samples of **41** and **42** made from solution, and solid-gas reaction of [Cu₂(APA)₄Cl₂]Cl₂ (**30**) and [Cu(ABA)₄Br₂]Br₂ (**31**). Experimental data are shown in black while simulated data are shown in red.

A comparison of experimental and simulated X-ray powder diffraction patterns is shown in Figure 5.62. The experimental data of **41** matches the simulated data excellently. In the case of **42**, simulated data were created by altering the crystal structure file of **41** but exchanging the unit-cell parameters for those of **42** and replacing the Cl atoms with Br. This was based on the fact that unit-cell parameters are similar in the two structures and therefore they must not be grossly different. These simulated data provided an excellent match to the experimental data obtained, backing up the idea that the structures are somewhat similar. No large unexplained peaks were seen in the observed data. Elemental analysis confirms the purity and identity of the two compounds.

Reaction of $[\text{Cu}_2(\text{APA})_4\text{Cl}_2]\text{Cl}_2$ (**30**) with HCl gas and $[\text{Cu}(\text{ABA})_4\text{Br}_2]\text{Br}_2$ (**31**) with HBr gas produces yellow and black-purple crystalline powders of **41** and **42** respectively. The reaction takes place over approximately one hour with no observed change in the colour of the samples after that time. As shown in Figure 5.62, the X-ray powder diffraction patterns of the materials match those of **41** and **42** proving their identification. Removal of HX from either material has not yet been attempted.

5.7.4 $(\text{H-AHA})_2[\text{CuCl}_4]/(\text{H-AHA})_2[\text{CuBr}_4]$ (**43/44**)

As in the above case with APA, the crystal structures of $(\text{H-AHA})_2[\text{CuCl}_4]$ (**43**) and $(\text{H-AHA})_2[\text{CuBr}_4]$ (**44**) were unknown before this study. Neither structure was readily determined by single-crystal X-ray diffraction at 150 K, as at that temperature the structures displayed an excessively large unit-cell. At approximately 298 K, the diffraction pattern of **43** became much simpler and the structure could be solved and refined with a good fit to the experimental data ($R = 0.0515$, $wR = 0.1538$), further crystallographic details are included in Table 5.10. It has a monoclinic unit-cell of space group $P2_1/c$. The asymmetric unit is composed of one disordered H-APA cation and half

a CuCl_4 anion which is positioned with the Cu atom on the 2d Wyckoff site, as shown in Figure 5.63. Bond distances and angles for **43** are shown in Table 5.33, the Cu coordination geometry is 4+2 as stated in the introduction to this section.

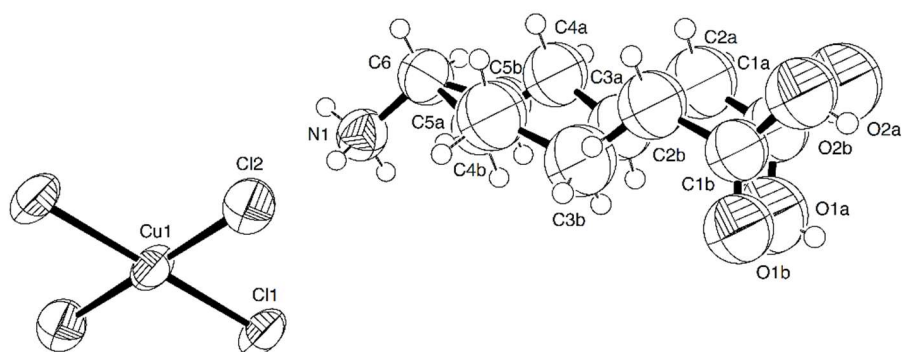


Figure 5.63 Asymmetric unit of $(\text{H-AHA})_2[\text{CuCl}_4]$ (**43**) with atoms shown as thermal ellipsoids drawn at 50% probability. The $[\text{CuCl}_4]^{2-}$ ion is completed by the symmetry operation $x, \frac{1}{2} - y, \frac{1}{2} + z$.

Table 5.33 Selected bond lengths (Å) and angles (°) around the Cu coordination centre for $(\text{H-AHA})_2[\text{CuCl}_4]$ (**43**).

Cu(1) – Cl(1)	2.2970(7)	Cu(1) – Cl(1)#1	3.0294(8)
Cu(1) – Cl(2)	2.2868(11)		
Cl(1) – Cu(1) – Cl(1)#1	91.07(2)	Cl(2) – Cu(1) – Cl(1)#1	94.13(3)
Cl(1) – Cu(1) – Cl(2)	89.62(3)		

#1 $x, \frac{1}{2} - y, \frac{1}{2} + z$

The reason for the large unit-cell of **43**, and **44**, at low temperature, and for the disorder at room temperature is due to multiple configurations of the H-AHA cations. The configuration composed of atoms labelled A is almost entirely planar with a RMSD from the plane of 0.0867 Å. The configuration labelled B is planar from the carboxylic acid to C4b (RMSD from planarity is 0.0672 Å) after which the last two C atoms and the ammonium group deviate from the plane with a C2B-C3B-C4B-C5B torsion angle of 82(2)°.

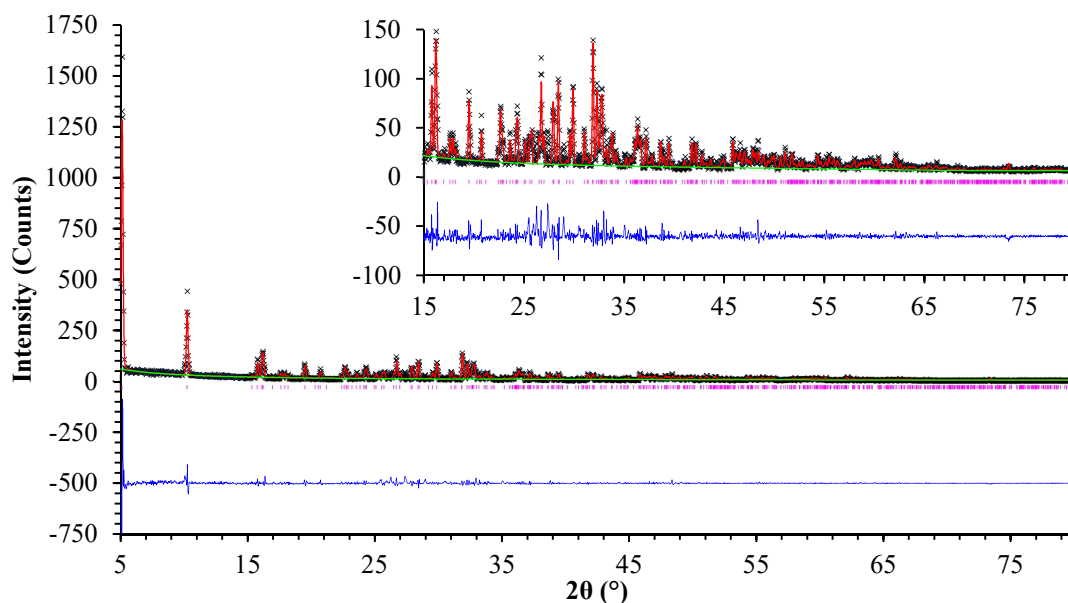


Figure 5.64 A plot of the Pawley refinement of the proposed cell for (H-AHA)₂[CuBr₄] (**44**). Black crosses represent observed data, the red line calculated data, the green line background, the pink markers peak positions, and the blue line is the difference plot [$I_{\text{obs}} - I_{\text{calc}}$].

As with **42**, the structure of **44** could not be determined by single-crystal X-ray diffraction as the crystals absorbed the majority of the plane polarised light making it almost impossible to find a non-twinned crystal. The unit-cell was determined from the X-ray powder diffraction pattern of the sample and refined with a good fit against the observed data using the Pawley method ($R_{\text{wp}} = 0.1486$, $\chi^2 = 3.036$), as shown in Figure 5.64. **44** has a triclinic unit-cell similar to **41** and **42** although all axes are longer than **41** and c is longer than **42**, as shown in Table 5.34. This is a result of Cu-Br bonds being longer than Cu-Cl bonds, and the fact that AHA is a longer molecule than APA due to an additional methylene group (-CH₂-).

In order to simulate X-ray powder diffraction data for **44**, the crystal structure file of **41** was modified to incorporate Br rather than Cl atoms, and the unit-cell parameters were exchanged for those of **44**. While the two structures will be somewhat different due to the difference in cation, the simulated data made in this way will be good enough for a

straightforward comparison. Experimental and simulated X-ray powder diffraction patterns are plotted for **43** and **44** in Figure 5.65, showing an excellent match with no unexplained peaks or gross mismatch of peak intensities. This, coupled with elemental analysis data, confirms the purity and identity of the two compounds.

Table 5.34 Unit-cell parameters for crystal structures (H-APA)₂[CuCl₄] (**41**), (H-APA)₂[CuBr₄] (**42**) and (H-AHA)₂[CuBr₄] (**44**).

Compound	41	42	44
<i>a</i> (Å)	7.1827(13)	7.788(11)	7.270(15)
<i>b</i> (Å)	7.5193(12)	8.040(12)	7.708(16)
<i>c</i> (Å)	16.597(3)	15.77(3)	17.36(3)
<i>α</i> (°)	86.525(13)	83.45(2)	83.58(2)
<i>β</i> (°)	87.155(14)	87.68(2)	88.17(2)
<i>γ</i> (°)	89.188(14)	87.79(2)	86.18(2)

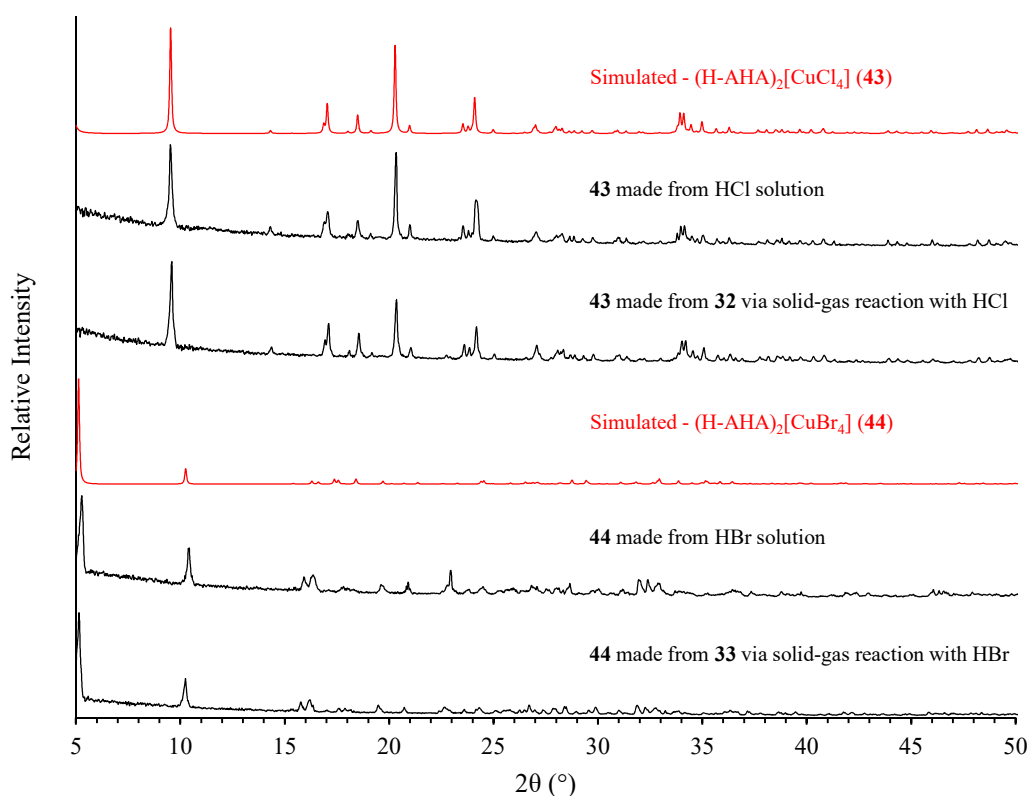


Figure 5.65 Room temperature X-ray powder diffraction data for samples of **43** and **44** made from solution, and solid-gas reaction of [Cu₂(AHA)₄Cl₂]Cl₂·4H₂O (**32**) and [Cu₂(AHA)₄Br₂]Br₂·4H₂O (**33**). Experimental data are shown in black while simulated data are shown in red.

Reaction of $[\text{Cu}_2(\text{AHA})_4\text{Cl}_2]\text{Cl}_2 \cdot 4\text{H}_2\text{O}$ (**32**) and $[\text{Cu}_2(\text{AHA})_4\text{Br}_2]\text{Br}_2 \cdot 4\text{H}_2\text{O}$ (**33**) with HCl and HBr gas, respectively, produces a yellow crystalline powder (**43**) for the chloride compound and a black-purple crystalline powder (**44**) for the bromide equivalent. As with the other compounds discussed above, the reaction takes place over approximately one hour with no observed colour change of the samples after that time. The X-ray powder diffraction patterns of the materials match those of **43** and **44**, as shown in Figure 5.65, proving the identification of the solid-gas reaction products. Removal of HX from either material has not yet been attempted.

5.8 Conclusions and future work

In summary, three distinct families of compounds have been produced in the above reactions of metal salts, predominantly copper (II) halides (CuX_2), with the amino acids (L) of general formula $\text{H}_2\text{N}-(\text{CH}_2)_n-\text{CO}_2\text{H}$, where n is an integer from 1-7.

The first family is a set of coordination polymers with the formula $[\text{M}(\text{L})_2]_n$ ($\text{M} = \text{Zn}, \text{Cu}$). A DMSO/ H_2O evaporation reaction was developed following problems with product solubility. Only one novel compound was produced in this way that could be structurally characterised, being $[\text{Zn}(\text{APA})_2]_n$ (**22**). However, two previously known compounds, $[\text{Cu}(\text{ABA})_2]_n$ (**19**) and $\{[\text{Cu}(\text{AHA})_2](\text{H}_2\text{O})_2\}_n$ (**21**), were also shown to be synthesised using the new method although only **21** was shown to be produced in a pure form. These compounds are very densely packed and the literature indicates that **21** is damaged irreversibly on removal of the water of crystallisation. No further testing of the properties of these compounds has been conducted.

The second family of compounds have the general formula $[\text{Cu}_2(\text{L})_4\text{X}_2]\text{X}_2 \cdot n\text{H}_2\text{O}$. These are paddlewheel shaped complexes, and nine novel compounds of this type have been

structurally characterised: $[\text{Cu}(\beta\text{-Ala})_4\text{Br}_2]\text{Br}_2 \cdot 2\text{H}_2\text{O}$ (**24**), $[\text{Cu}(\beta\text{-Ala})_4\text{Br}_2]\text{Br}_2 \cdot 3\text{H}_2\text{O}$ (**25**), $[\text{Cu}_2(\text{ABA})_4\text{Cl}_2]\text{Cl}_2 \cdot \text{H}_2\text{O}$ (**27**), $[\text{Cu}(\text{ABA})_4\text{Br}_2]\text{Br}_2$ (**28**), $[\text{Cu}_2(\text{APA})_4\text{Cl}_2]\text{Cl}_2 \cdot 2\text{H}_2\text{O}$ (**29**), $[\text{Cu}_2(\text{APA})_4\text{Cl}_2]\text{Cl}_2$ (**30**), $[\text{Cu}_2(\text{APA})_4\text{Br}_2]\text{Br}_2$ (**31**), $[\text{Cu}_2(\text{AHA})_4\text{Br}_2]\text{Br}_2 \cdot 4\text{H}_2\text{O}$ (**33**), and $[\text{Cu}_2(\text{AOA})_6]\text{Cl}_4$ (**34**). All of the compounds in this family exhibit a 3-D hydrogen bonded network with some similar hydrogen bonding motifs present throughout. The hydrated compounds $[\text{Cu}_2(\beta\text{-Ala})_4\text{Cl}_2]\text{Cl}_2 \cdot \text{H}_2\text{O}$ (**23**), **27**, $[\text{Cu}_2(\text{AHA})_4\text{Cl}_2]\text{Cl}_2 \cdot 4\text{H}_2\text{O}$ (**32**), and **33** were subjected to thermogravimetric analysis to determine when the water can be removed and whether HX could be removed from the compounds to produce a neutral rather than charged complex. All the compounds lost water upon heating beyond 100 °C, although no compound showed a stable state at a mass equivalent to the loss of HX. The dehydrated compounds were analysed by X-ray powder diffraction, by which the change in the unit-cell parameters was monitored. This showed that all structures collapsed on solvent removal making them potentially unsuitable for gas adsorption and hence have not been analysed for that application. **23** and **27** were shown to lose and gain water reversibly, however **32** and **33** cannot be rehydrated upon removal of the water of crystallisation. **29** would also have been analysed in a similar way to the above compounds but could not be made pure. All experiments yielded a mixture of **29** and **30**, although surprisingly these mixtures eventually transformed into pure **30** without any intervention. **30** and **31** exhibited anisotropic thermal expansion on account of the unusual configuration of one of the APA ligands. The expansion is mainly in the direction in which the ligand is projected towards in both **30** and **31**. Further studies revealed that the two compounds behave slightly differently, the chloride compound displaying a gradual transition to the high-temperature form, whereas the bromide compound exhibited a sharp change in the unit-cell parameters at around 220 K. This is thought to be the result of

differences in the strength of hydrogen bonds toward Cl^- and Br^- , the former producing stronger interactions than the latter.

Similar experiments to those which produced the above family of compounds were attempted with glycine, although this resulted in the formation of two very different compounds due to the reducing nature of the molecule: $\{[\text{Cu}_2(\text{Gly})_4][\text{Cu}_2\text{Cl}_6]\}_n$ (**35**), $[\text{Cu}(\text{CIMGly})(\text{H}_2\text{O})_2]$ (**36**). **35** is a mixed-valence compound, copper (I) produces a Cu_2Cl_6 dimer which links a chain of paddlewheel shaped complexes formed by copper (II) and glycine in a chain. **36** is the result of an addition reaction between two glycine molecules and subsequent coordination to a copper cation. The reason for the difference in products is probably a result of Br readily forming radicals which could allow the glycine molecules to react with each other. These compounds have not been isolated in a pure form yet, and further testing is still required to find the reason behind the peculiar reduction/radical reactions.

The final family of compounds have the general formula $(\text{H-L})_2[\text{CuX}_4]$. Three compounds were already structurally characterised before the present work. $(\text{H-}\beta\text{-Ala})_2[\text{CuCl}_4]$ (**37**),²⁰² $(\text{H-}\beta\text{-Ala})_2[\text{CuBr}_4]$ (**38**),²⁰³ and $(\text{H-ABA})_2[\text{CuCl}_4]$ (**39**).²⁰⁴ However, positions of the hydrogen atoms in **37** were documented on the CSD, and the non-H atoms in the CIF of **38** did not form a connected set, these were therefore re-determined. The structures of three compounds, $(\text{H-ABA})_2[\text{CuBr}_4]$ (**40**), $(\text{H-APA})_2[\text{CuCl}_4]$ (**41**), and $(\text{H-AHA})_2[\text{CuCl}_4]$ (**43**), have been determined for the first time. Additionally, the unit-cells of $(\text{H-APA})_2[\text{CuBr}_4]$ (**42**) and $(\text{H-AHA})_2[\text{CuBr}_4]$ (**44**) have been determined from X-ray powder diffraction at room temperature, however the structures have not been possible to determine by single-crystal X-ray diffraction. In light of the work discussed in chapter 3, attempts were made to synthesise all of these compounds from the equivalent

$[\text{Cu}_2(\text{L})_4\text{X}_2]\text{X}_2 \cdot n\text{H}_2\text{O}$ paddlewheel compound by solid-gas reaction with the appropriate hydrohalic acid. In each case this was successful, producing the pure tetrahalocuprate salt with exposure to the gas for approximately one hour. This is faster than the observed reactions for INAc, INAm and NAm which took approximately three hours. Additionally, the loss of HX from the amino acid cuprate salts took much longer to show any change in the material than the previous investigation. After one month of exposure to ambient conditions, **37** and **39** only showed partial decomposition of the yellow crystalline powders to the green colour of a paddlewheel complex which was the expected product in each case. X-ray powder diffraction of the discoloured material confirmed the decomposition product and the contamination with unreacted starting material. The amino acids investigated here have, on average, a similar pK_a to INAc, INAm and NAm; the pK_a is 1.77, 3.61, and 3.40 in water for INAc, INAm, and NAm respectively, although it is 4.06 on average for the amino acids. The similar pK_a , but drastically different reaction rates, reinforces the idea that the acidity of the ligand/cation (referring to the reaction $\text{R-N-H}^+ \rightleftharpoons \text{R-N} + \text{H}^+$) has very little to do with the rate of decomposition, or reaction with HX. The answer must be in the structures of the compounds, although the evidence gathered thus far does not point to a clear root cause.

Overall a great number of compounds have been synthesised from the chosen ligands, however none of these have been tested for their gas adsorption properties due to all of them being very densely packed and unlikely to accommodate guest molecules. Further work is needed to produce crystals of the neutral compounds of the ligands with various metals, especially Cu and Zn which have been shown to produce compounds that could be characterised. Given the flexibility of the methylene chain in the amino acids, it is unlikely that further work would yield permanently porous materials, although this does not preclude gas adsorption testing as the flexibility may still lead to guest inclusion at

high pressure/low temperature as has been shown in other examples of densely packed materials.

6 Copper Complexes of Benzoic Acid Based Ligands

The node and linker approach toward the design and synthesis of metal-organic frameworks has proved to be a highly successful technique for the creation of novel and functional compounds, but this relies on the predictable formation of rigid metal clusters. In the presence of a neutral ligand (L), such as H₂O, copper carboxylates are capable of forming a dinuclear paddlewheel-shaped species, [Cu₂(μ²-R-CO₂)₄(L)₂], which can be used to this effect, although in some circumstances the resulting compound adopts a mononuclear structure such as [Cu(R-CO₂)₂(L)₂] or [Cu(R-CO₂)₂(L)₃] as depicted in Figure 6.1.

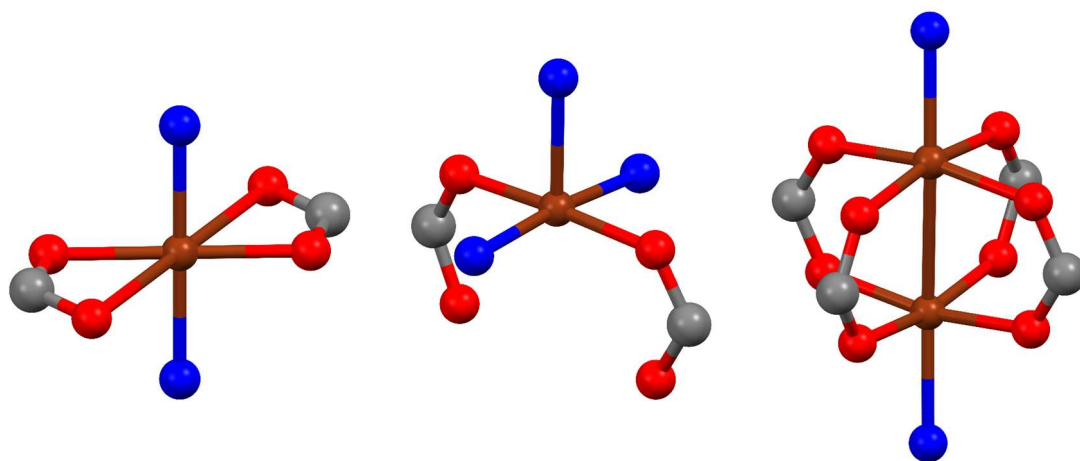


Figure 6.1 The common mononuclear and dinuclear complexes formed by copper and carboxylic acid compounds in the presence of additional neutral ligands (blue). C atoms are shown in grey, Cu in dark brown, O in red, and the coordinating atoms of the neutral ligand(s) in blue.

The dinuclear building unit has been used in the formation of many 3-D coordination polymers, chief among which is HKUST-1 or [Cu₂(BTC)₃]_n (BTC = 1,3,5-benzenetricarboxylate). However, many other compounds have since been synthesised, including {[Cu₂(5-(pyridin-4-yl)isophthalic acid)]·2H₂O·1.5DMF}_n and

[Cu₂(3,5-pyridinedicarboxylate)₂] which incorporate an equatorial to apical linkage through the design of the carboxylate ligand.^{205,206} 3-D polymers such as those above are not the only ones being investigated for their adsorptive/absorptive properties however. Takamizawa's group, among a few others, have extensively investigated the 1-D coordination polymer [Cu₂(O₂CC₆H₅)₄(Pz)]_n which is remarkably flexible allowing it to undergo single-crystal to single-crystal phase transformations to form inclusion compounds with various alcohols,^{207–210} acetone,²¹¹ acetonitrile,^{209,212,213} methane,²¹⁴ oxygen,²¹⁵ dichloromethane,²¹⁶ noble gases,²¹⁷ and, most importantly, CO₂.^{124,218–220} These studies looked in great detail at how the transformations upon guest inclusion take place, and the effect they have upon the supramolecular structure through *in situ* diffraction studies. Further studies have been conducted to expand on this body of work with similar compounds synthesised using biphenylcarboxylic acid,²²¹ 9-anthracenecarboxylic acid,²²² 1-naphthoic acid,²²³ 3-fluoro/chloro/methyl benzoate and 2,3-difluorobenzoate to name a few.²²⁴

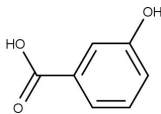
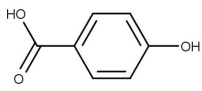
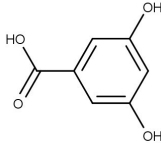
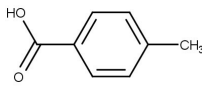
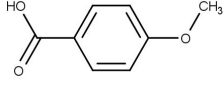
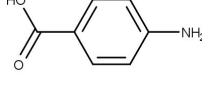
All of the work discussed above has concerned [Cu₂(μ²-R-CO₂)₄(L)₂]-type complexes which are of the most interest as they have a very rigid geometry and act as octahedral nodes. These features allow the design of functional compounds which may be 1-3 dimensional polymers, since an octahedral node can connect 3-dimensionally. However, the majority of carboxylate ligands also produce mononuclear complexes depending on the crystallising solvent or the additional ligand present, and the reasons for this have not, to the author's knowledge, been investigated in any great detail. There are currently not enough known structures which share similar features to do a systematic study into when a mononuclear or dinuclear species is produced. Therefore, the aim of the work discussed in this chapter was to attempt a series of reactions systematically with a variety of benzoic

acid derivatives, and various monotopic (terminating) and ditopic ligands, and structurally characterise the resulting compounds.

6.1 Experimental procedures

All reagents and solvents were purchased from Sigma Aldrich, BDH or Fisher Scientific and used as received. Elemental Analyses were conducted by the Elemental Analysis Service, Department of Chemistry, University of Hull on a Fisons CHN Elemental Analyser (Thermo Scientific), type EA-1108. Table 6.1 shows a list of the compounds discovered during this work, the synthetic procedures for these compounds are detailed below.

Table 6.1 A table of the newly discovered compounds for each ligand investigated shown in bold and starred.

3-Hydroxybenzoic acid (3-HBA)	* [Cu₂(3-HBA)₄(H₂O)₂](3-HBA)₂(H-DMAP)₂ (45)	
4-Hydroxybenzoic acid (4-HBA)	* [Cu₂(4-HBA)₄(H₂O)₂]·nMeOH (46) * [Cu₂(4-HBA)₂(DMAP)₂]·1.5H₂O (47) * [Cu₂(4-HBA)₄(Pz)₂]·2MeOH (48)	
3,5-Dihydroxybenzoic acid (3,5-DHBA)	* [Cu₂(3,5-DHBA)₄(MeOH)₂]·8MeOH (49) * [Cu(3,5-DHBA)₂(H₂O)₃]·5H₂O (50)	
4-Methylbenzoic acid (4-MeBA)	* [Cu₂(4-MeBA)₄(DMF)₂]·2DMF (51)	
4-Methoxybenzoic acid (4-MeOBA)	* {[Cu₂(4-MeOBA)₄(4,4'-bipy)] [Cu(4-MeOBA)₂(4,4'-bipy)]·2EtOH} _n (52)	
4-Aminobenzoic acid (4-ABA)	* [Cu₂(4-ABA)₄(4,4'-bipy)₂]·2DMF (53)	

6.1.1 $\text{Cu}_2(\text{OH})_2(\text{CO}_3)$ (Basic Copper Carbonate)

$\text{Cu}(\text{OAc})_2 \cdot \text{H}_2\text{O}$ (3.9930 g, 20 mmol) and Na_2CO_3 (2.1198 g, 20 mmol) were each dissolved in 50 mL H_2O . The sodium carbonate solution was added slowly to that of copper acetate instantly yielding a blue/green precipitate. The mixture was stirred for 1 hour before subsequent filtration and washing with water (3×50 mL) and ethanol (2×50 mL). The final product was dried in an oven at 60°C for several hours yielding 2.1964 g (Yield = 88.8%) of $\text{Cu}_2(\text{OH})_2(\text{CO}_3)$, the identity of which was confirmed by X-ray powder diffraction.²²⁵

6.1.2 $[\text{Cu}_2(3\text{-HBA})_4(\text{H}_2\text{O})_2](3\text{-HBA})_2(\text{H-DMAP})_2$ (45)

$\text{Cu}(\text{OAc})_2 \cdot \text{H}_2\text{O}$ (0.1996 g, 1 mmol), DMAP (0.1222 g, 1 mmol), and 3-HBA (0.2762 g, 3 mmol) were dissolved in methanol. No solid material was obtained until almost complete evaporation of the solvent, at which point deep blue crystals of **45** grew. Elemental anal. (%) calcd for **45**: C, 53.04; H, 4.77; N, 4.42. Found: C, 52.76; H, 4.94; N, 4.11.

6.1.3 $[\text{Cu}_2(4\text{-HBA})_4(\text{H}_2\text{O})_2] \cdot n\text{MeOH}$ (46)

$\text{Cu}_2(\text{OH})_2(\text{CO}_3)$ (0.1106 g, 0.5 mmol) and 4-hydroxybenzoic acid (0.4144 g, 3 mmol) were heated at reflux with stirring in 25 mL methanol. The resulting blue solution was left to evaporate leaving blue crystals of **46** on the sides of the glass vessel.

6.1.4 $[\text{Cu}_2(4\text{-HBA})_2(\text{DMAP})_2] \cdot 1.5\text{H}_2\text{O}$ (47)

Copper acetate (0.1996 g, 1 mmol), DMAP (0.1222 g, 1 mmol), and 4-HBA (0.2762 g, 3 mmol) were dissolved in methanol. No solid material was obtained until almost complete evaporation of the solvent, at which point bright blue crystals of **47** grew, similar in

appearance to **45**. Elemental anal. (%) calcd for **47**: C, 53.62; H, 5.62; N, 8.93. Found: C, 54.02; H, 5.50; N, 9.07.

6.1.5 $[Cu_2(4\text{-HBA})_4(\text{Pz})_2]\cdot 2\text{MeOH}$ (**48**)

$Cu(\text{OAc})_2\cdot\text{H}_2\text{O}$ (0.0499 g, 0.25 mmol) and 4-HBA (0.0691 g, 0.5 mmol) were dissolved in 20 mL MeOH with stirring, pyrazine (Pz) (0.0100 g, 0.125 mmol) was added to this solution with no noticeable change in colour. The solution was left to evaporate slowly leaving small green rectangular crystals of **48** on the sides of the glass vessel. The crystallisation of the solution is not trivial; powders are obtained at too high concentration (c. 0.5 M), and crystals only develop on the sides of the vessel by slow evaporation and none at all when evaporated too quickly.

6.1.6 $[Cu_2(3,5\text{-DHBA})_4(\text{MeOH})_2]\cdot 8\text{MeOH}$ (**49**)

Blue crystals of $[Cu_2(3,5\text{-DHBA})_4(\text{MeOH})_2]\cdot 8\text{MeOH}$ (**49**) were produced in an identical way to **46** but replacing 4-HBA with 3,5-DHBA (0.4624 g, 3 mmol).

6.1.7 $[Cu(3,5\text{-DHBA})_2(\text{H}_2\text{O})_3]\cdot 5\text{H}_2\text{O}$ (**50**)

Upon complete evaporation of the solution which produced **49**, light blue needle crystals were produced. Analysis by single-crystal X-ray diffraction showed these to be the hydrated compound $[Cu(3,5\text{-DHBA})_2(\text{H}_2\text{O})_3]\cdot 5\text{H}_2\text{O}$ (**50**).

6.1.8 $[Cu_2(4\text{-MeBA})_4(\text{DMF})_2]\cdot 2\text{DMF}$ (**51**)

4-MeBA (0.2723 g, 4 mmol) was dissolved in 10 mL DMF with addition of TEA (0.56 mL, 4 mmol). This solution was added to a glass vial and layered with a few mL of a 50/50 mixture of DMF/EtOH, and 10 mL of EtOH containing $Cu(\text{NO}_3)_2\cdot 2.5\text{H}_2\text{O}$ (0.2326 g, 1 mmol). Blue parallelogram-shaped crystals of **51** grew upon mixing of the layers.

Elemental anal. (%) calcd for **51**: C, 55.05; H, 5.88; N, 5.84. Found: C, 55.39; H, 5.86; N, 6.23.

6.1.9 $\{[Cu_2(4\text{-MeOBA})_4(4,4'\text{-bipy})][Cu(4\text{-MeOBA})_2(4,4'\text{-bipy})]\cdot 2\text{EtOH}\}_n$ (**52**)

4-MeOBA (0.0761 g, 0.5 mmol) and 4,4'-bipy (0.0195 g, 0.125 mmol) were dissolved in 5 mL DMF with addition of TEA (0.07 mL, 0.5 mmol). This solution was added to a glass vial and layered with 10 mL of a 50/50 mixture of DMF/EtOH, and 5 mL of EtOH containing $Cu(NO_3)_2\cdot 2.5 H_2O$ (0.0581 g, 0.25 mmol). Light blue-green parallelogram-shaped crystal of **52** grew upon diffusion of the layers. Elemental anal. (%) calcd for **52**: C, 57.26; H, 5.18; N, 3.51. Found: C, 57.48; H, 4.89; N, 3.54.

6.1.10 $[Cu_2(4\text{-ABA})_4(4,4'\text{-bipy})_2]\cdot 2\text{DMF}$ (**53**)

4-ABA (0.0686 g, 0.5 mmol) and 4,4'-bipy (0.0195 g, 0.125 mmol) were dissolved in 5 mL DMF with addition of TEA (0.07 mL, 0.5 mmol). This solution was added to a glass vial and layered with 10 mL of a 50/50 mixture of DMF/EtOH, and 5 mL of EtOH containing $Cu(NO_3)_2\cdot 2.5 H_2O$ (0.0581 g, 0.25 mmol). Green, elongated, octahedral-shaped crystals of **53** grew upon diffusion of the layers. The compound can also be synthesised via an adapted version of the literature method for producing $[Cu_2(4\text{-ABA})_4(\text{DMF})_2]\cdot 2\text{DMF}$ which includes half a molar equivalent, to Cu, in the upper ethanolic solution of sodium 4-aminobenzoate.²²⁶

6.2 Crystal structure and refinement information

Crystal structures were solved and refined according to the standard procedure discussed in the experimental section or as described in the above sections, apart for the following exceptions. The disordered 4-HBA ligand in **46** was modelled using a separate free

variable for the three identified positions and a SUMP command to set the total of the free variables to unity, or 100% occupation of the three sites overall. Although the guest solvent molecules were refined, the disorder of these molecules makes their identification uncertain. The apparent disorder of one of the methanol molecules identified was modelled using a free variable to refine the occupancies of the two C atom positions. The H1WA atom of the symmetrically disordered water ligand in **47** is a fixed position for the two possible orientations, therefore this atom was used to restrain the positions of both H1WB and H1WC. The latter atoms had a fixed occupancy of a half while H1WA was set as fully occupied. O3W and the two hydrogen atoms bonded to it were set to have an occupancy of a half due to H3WA being positioned on a centre of inversion. The data collected for **48** were omitted below a resolution of 0.9 Å due to weak scattering, data collected below this resolution did not have a sufficient signal to noise ratio to be considered reliable. Hydrogen atom positions in **48** were fixed, although the torsion angle of the hydroxyl groups was refined as sufficient data was present to justify doing so, and the end result was chemically sensible. Although the data collected for **50** are of sufficient quality for a good refined model, all efforts to determine the non-aromatic hydrogen positions and resolve the elongated thermal ellipsoids of O8W and O9W as two separate atoms or disorder were unsuccessful, O8W and O9W have been refined with isotropic displacement parameters as a result. The reasons for this have not yet been determined, but the model is good enough for publication as it stands so no further investigation has been conducted. The disordered DMF solvent in **51** was refined with the O atom in two positions, A and B. The isotropic thermal displacement parameter for each position was refined as equal using a free variable, and another free variable was refined to determine the occupancies of the two positions. The occupancy ratio was found to be 0.61:0.39, A:B. One of the ethanol molecules in **52** was not very well resolved so it has not been

possible to determine the hydrogen atom positions for this molecule. The crystal of **53** did not scatter well, so data were only used up to $45^\circ 2\theta$. The crystals were also determined to be twinned, most likely due to the very similar cell lengths of a and c which are 16.2001(17) Å and 16.2336(13) Å respectively. A two-fold rotation/mirror plane twin law was adopted, and the twin fraction was found to be 0.523(2):0.477(2), this improved R and wR from 0.2099 and 0.5628 to 0.0799 and 0.2268 respectively. Although the weighted R factor after final refinement is not within the normally acceptable range, the structure is chemically sensible and good enough for the extraction of general structural information which is all that is required for the present study. Further details on the crystal structure refinements are contained in Table 6.2, Table 6.3, and Table 6.4.

Table 6.2 Crystal structure data for compounds **45**, **46**, and **47**.

Compound	45	46	47
Empirical formula	C ₅₆ H ₆₀ Cu ₂ N ₄ O ₂₂	C ₃₄ H ₄₆ Cu ₂ O ₂₀	C ₂₈ H ₃₅ CuN ₄ O _{8.5}
Formula weight (g mol ⁻¹)	1268.16	901.81	627.14
Temperature (K)	150(1)	150(1)	150(1)
λ (Å)	0.71073	0.71073	0.71073
Crystal system	Monoclinic	Triclinic	Monoclinic
Space group	<i>P</i> 2 ₁ / <i>c</i>	<i>P</i> $\bar{1}$	<i>C</i> 2/ <i>c</i>
<i>a</i> (Å)	13.7715(8)	9.5665(10)	18.1824(9)
<i>b</i> (Å)	10.4084(5)	10.5001(10)	16.4129(6)
<i>c</i> (Å)	21.1358(10)	11.8307(13)	20.0580(10)
α (°)	90	66.582(8)	90
β (°)	108.865(4)	88.939(9)	106.306(4)
γ (°)	90	64.344(7)	90
<i>V</i> (Å ³)	2866.8(3)	965.90(19)	5745.1(5)
<i>Z</i>	2	1	8
Density (Mg m ⁻³)	1.469	1.55	1.450
μ (mm ⁻¹)	0.826	1.182	0.819
Crystal size (mm)	0.41 × 0.35 × 0.28	0.32 × 0.31 × 0.11	0.38 × 0.16 × 0.15
Transmission factors (max/min)	0.8141 and 0.7439	0.8831 and 0.6852	0.9200 and 0.7661
<i>F</i> (000)	1316	444	2624
θ range (°)	1.563 - 29.212	1.909 - 29.182	1.703 - 29.219
Index ranges	-18 ≤ <i>h</i> ≤ 18 -12 ≤ <i>k</i> ≤ 14 -28 ≤ <i>l</i> ≤ 22	-13 ≤ <i>h</i> ≤ 13 -14 ≤ <i>k</i> ≤ 14 -16 ≤ <i>l</i> ≤ 16	-24 ≤ <i>h</i> ≤ 22 -22 ≤ <i>k</i> ≤ 22 -27 ≤ <i>l</i> ≤ 27
Reflections collected	20300	10254	20205
Independent reflections (<i>R</i> _{int})	7708 (0.0401)	5148 (0.0536)	7727 (0.0580)
Completeness to $\theta = 25.242^\circ$	99.8%	98.9%	99.8%
Restraints/parameters	6/397	4/240	17/405
Goodness-of-fit on <i>F</i> ²	0.905	1.020	0.821
<i>R</i> ₁ [<i>I</i> > 2 σ (<i>I</i>)]	0.0410	0.0656	0.0385
<i>wR</i> ₂ (all data)	0.1112	0.1982	0.0905
Largest diff. peak and hole (e Å ⁻³)	1.621 and -0.548	1.310 and -1.123	0.600 and -0.543

Table 6.3 Crystal structure data for compounds **48**, **49**, and **50**.

Compound	48	49	50
Empirical formula	C ₃₄ H ₃₂ Cu ₂ N ₂ O ₁₄	C ₃₈ H ₆₀ Cu ₂ O ₂₆	C ₁₄ H ₂₆ CuO ₁₆
Formula weight (g mol ⁻¹)	819.69	1059.94	513.89
Temperature (K)	150(1)	150(1)	150(1)
λ (Å)	0.71073	0.71073	0.71073
Crystal system	Orthorhombic	Monoclinic	Monoclinic
Space group	<i>Pccn</i>	<i>P2₁/n</i>	<i>P2₁/m</i>
<i>a</i> (Å)	12.4866(18)	14.2444(7)	7.0156(4)
<i>b</i> (Å)	14.0866(19)	8.6721(5)	32.046(3)
<i>c</i> (Å)	19.5954(16)	18.8776(8)	9.2732(6)
α (°)	90	90	90
β (°)	90	94.776(3)	98.227(5)
γ (°)	90	90	90
<i>V</i> (Å ³)	3446.7(7)	2323.8(2)	2063.3(2)
<i>Z</i>	4	2	4
Density (Mg m ⁻³)	1.58	1.515	1.654
μ (mm ⁻¹)	1.307	1.005	1.137
Crystal size (mm)	0.32 × 0.15 × 0.11	0.24 × 0.2 × 0.07	0.37 × 0.06 × 0.05
Transmission factors (max/min)	0.9318 and 0.7667	0.9327 and 0.8335	0.9523 and 0.7038
<i>F</i> (000)	1680	1108	988
θ range (°)	2.180 - 23.255	1.868 - 29.242	2.542 - 29.217
Index ranges	-13 ≤ <i>h</i> ≤ 10 -15 ≤ <i>k</i> ≤ 14 -21 ≤ <i>l</i> ≤ 19	-16 ≤ <i>h</i> ≤ 19 -11 ≤ <i>k</i> ≤ 11 -25 ≤ <i>l</i> ≤ 25	-9 ≤ <i>h</i> ≤ 9 -37 ≤ <i>k</i> ≤ 43 -9 ≤ <i>l</i> ≤ 12
Reflections collected	6851	16014	13601
Independent reflections (<i>R</i> _{int})	2476 (0.1235)	6201 (0.0649)	5635 (0.0794)
Completeness to $\theta = 25.242^\circ$	99.6% (to 23.255°)	99.0%	99.7%
Restraints/parameters	0/241	0/312	0/283
Goodness-of-fit on <i>F</i> ²	0.738	0.818	0.852
<i>R</i> ₁ [<i>I</i> > 2σ(<i>I</i>)]	0.0457	0.0369	0.0646
<i>wR</i> ₂ (all data)	0.1046	0.0812	0.1926
Largest diff. peak and hole (e Å ⁻³)	0.380 and -0.389	0.663 and -0.735	2.413 and -1.643

Table 6.4 Crystal structure data for compounds **51**, **52**, and **53**.

Compound	51	52	53
Empirical formula	C ₄₄ H ₅₆ Cu ₂ N ₄ O ₁₂	C ₇₆ H ₈₂ Cu ₃ N ₄ O ₂₂	C ₅₄ H ₅₄ Cu ₂ N ₁₀ O ₁₀
Formula weight (g mol ⁻¹)	960.02	1594.07	1130.16
Temperature (K)	150(1)	150(1)	150(1)
λ (Å)	0.71073	1.71073	1.71073
Crystal system	Monoclinic	Triclinic	Monoclinic
Space group	<i>P2₁/c</i>	<i>P</i> $\bar{1}$	<i>P2₁/c</i>
<i>a</i> (Å)	13.2543(8)	9.9931(8)	16.2001(17)
<i>b</i> (Å)	17.4455(8)	13.5994(13)	22.5490(19)
<i>c</i> (Å)	10.0092(5)	14.0002(12)	16.2336(13)
α (°)	90	107.042(7)	90
β (°)	99.571(4)	94.489(7)	107.322(7)
γ (°)	90	97.611(7)	90
<i>V</i> (Å ³)	2282.2(2)	1789.2(3)	5661.1(9)
<i>Z</i>	2	1	4
Density (Mg m ⁻³)	1.397	1.531	1.326
μ (mm ⁻¹)	0.996	0.964	0.814
Crystal size (mm)	0.44 × 0.39 × 0.22	0.23 × 0.2 × 0.08	0.3 × 0.16 × 0.13
Transmission factors (max/min)	0.8217 and 0.6787	0.9289 and 0.7816	0.9592 and 0.8716
<i>F</i> (000)	976	817	2288
θ range (°)	1.558 - 29.219	1.837 - 29.200	1.802 - 22.499
Index ranges	-18 ≤ <i>h</i> ≤ 18 -23 ≤ <i>k</i> ≤ 20 -11 ≤ <i>l</i> ≤ 13	-11 ≤ <i>h</i> ≤ 13 -18 ≤ <i>k</i> ≤ 18 -19 ≤ <i>l</i> ≤ 19	-17 ≤ <i>h</i> ≤ 16 -22 ≤ <i>k</i> ≤ 24 -16 ≤ <i>l</i> ≤ 17
Reflections collected	16235	19939	16402
Independent reflections (<i>R</i> _{int})	6132 (0.0695)	9597 (0.0810)	7445 (0.0761)
Completeness to $\theta = 25.242^\circ$	99.8%	99.5%	99.8% (to 22.499°)
Restraints/parameters	0/258	0/465	0/638
Goodness-of-fit on <i>F</i> ²	0.932	0.881	0.902
<i>R</i> ₁ [<i>I</i> > 2 σ (<i>I</i>)]	0.0457	0.0555	0.0799
<i>wR</i> ₂ (all data)	0.1297	0.1531	0.2268
Largest diff. peak and hole (e Å ⁻³)	0.898 and -0.631	0.719 and -1.155	1.150 and -0.897

6.3 3-Hydroxybenzoic acid (3-HBA)

Discounting all complexes containing chelating ligands, a search of the CSD shows that 3-hydroxybenzoic acid (3-HBA) is known to form five complexes with copper.¹¹⁹ Those including nicotinamide,²²⁷ imidazole,²²⁸ and benzimidazole²²⁹ as the additional ligands are mononuclear. The other two incorporating 4-acetylpyridine²³⁰ and 4,4'-bipyridine²³¹ are paddlewheel-shaped, the former is a discrete complex while the latter is a 1-D coordination polymer. Reactions were only attempted with dimethylaminopyridine (DMAP), 4-aminopyridine, 3-aminopyridine, isonicotinamide, and pyridine. Although

distances and angles for this are shown in Table 6.5. The paddlewheel complex hydrogens bonds to adjacent complexes via the non-coordinated molecules. **45** is therefore a co-crystallisation of $[\text{Cu}_2(3\text{-HBA})_4(\text{H}_2\text{O})_2]$, with the DMAP salt of 3-HBA and some waters of crystallisation.

Table 6.5 Selected bond lengths (Å) and angles (°) around the Cu coordination centre for $[\text{Cu}_2(3\text{-HBA})_4(\text{H}_2\text{O})_2]$ (**45**).

Cu(1) – O(1)	1.9735(16)	Cu(1) – O(5)#1	1.9553(16)
Cu(1) – O(2)#1	1.9785(16)	Cu(1) – O(1W)	2.1417(16)
Cu(1) – O(4)	1.9537(17)	Cu(1) – Cu(1)#1	2.6360(5)
O(1) – Cu(1) – O(2)#1	168.60(6)	O(2)#1 – Cu(1) – O(1W)	101.91(7)
O(1) – Cu(1) – O(4)	89.59(7)	O(4) – Cu(1) – O(5)#1	168.38(7)
O(1) – Cu(1) – O(5)#1	89.06(7)	O(4) – Cu(1) – O(1W)	91.27(7)
O(1) – Cu(1) – O(1W)	89.45(7)	O(5)#1 – Cu(1) – O(1W)	100.26(7)
O(2)#1 – Cu(1) – O(4)	89.25(7)	O(1W) – Cu(1) – Cu(1)#1	170.06(6)
O(2)#1 – Cu(1) – O(5)#1	89.79(7)		

#1 2-x, 1-y, 1-z

The paddlewheel complexes are held in a 2-D plane parallel to (011) via two distinct hydrogen bonding motifs. The first is a $C_4^4(23)$ chain interaction composed of hydrogen bonds from a coordinated water molecule to the hydroxyl group of a free 3-HBA anion ($\text{O1W}\cdots\text{O9}$ 2.784(3) Å), the free 3-HBA molecule then hydrogen bonds to another hydroxyl group belonging to the 3-HBA ligand of a paddlewheel complex adjacent to the original ($\text{O9}\cdots\text{O3}$ 2.759(3) Å). The second interaction can be described as either a $C_4^4(32)$ chain or a $R_4^4(32)$ ring. It is composed of a non-coordinated water molecule acting as both a donor and acceptor for two hydrogen bonds to and from two 3-HBA ligands belonging to adjacent paddlewheel complexes along *b* ($\text{O3}\cdots\text{O2W}$ 2.678(4) Å and $\text{O2W}\cdots\text{O6}$ 3.304(4) Å). Each motif is shown in Figure 6.3.

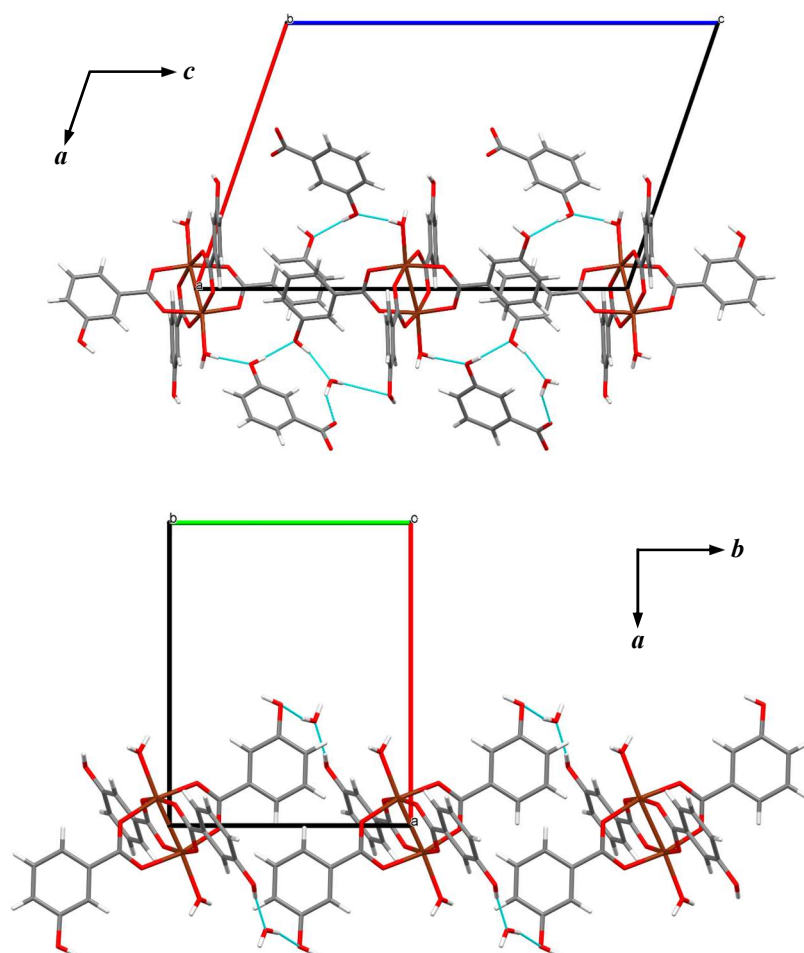


Figure 6.3 The hydrogen bonding interactions that give rise to the sheets in $[\text{Cu}_2(3\text{-HBA})_4(\text{H}_2\text{O})_2]$ (**45**). Shown left is the $\text{C}_4^4(23)$ chain interaction that extends in the $[011]$ and $[0\bar{1}1]$ directions. Shown right is the $\text{C}_4^4(32)/\text{R}_4^4(32)$ interaction that links paddlewheel complexes along b . C atoms are shown in grey, H in white, Cu in dark brown, and O in red. Hydrogen bonds are drawn as light-blue dashed lines.

Further hydrogen bonding between the 2-D sheets via the non-coordinated 3-HBA and water molecules then creates a 3-D hydrogen bonded network. The interaction can be described in its simplest form as either a $\text{C}_3^3(15)$ chain or a $\text{R}_6^6(30)$ ring and occurs between each complex and the adjacent one above or below with respect to a , as shown in Figure 6.4. The water and one of the 3-HBA ligands of one complex hydrogen bond to the carboxylate group of a non-coordinated 3-HBA molecule ($\text{O6}\cdots\text{O7}$ 2.824(4) Å, and $\text{O1W}\cdots\text{O8}$ 2.867(3) Å), this then hydrogen bonds to another complex further along a through the $\text{O9}\cdots\text{O3}$ contact mentioned previously. Additionally, the O3 hydroxyl group

hydrogen bonds to O2W, as mentioned before, and the water in turn hydrogen bonds to the carboxylate group of the same 3-HBA molecule (O2W \cdots O7 2.793(4) (3) Å). The H-DMAP cation forms a terminating hydrogen bond to a free 3-HBA anion and only seems to fill a void in the structure (N1 \cdots O8 2.798(4) Å).

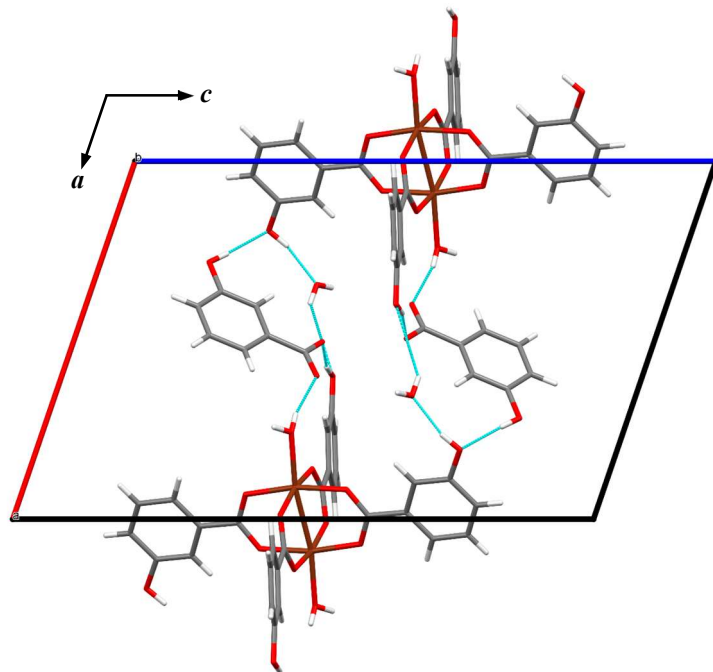


Figure 6.4 The $C_3^3(15)$, alternatively $R_6^6(30)$, hydrogen bonding interaction that occurs between the sheets in $[\text{Cu}_2(3\text{-HBA})_4(\text{H}_2\text{O})_2]$ (**45**) along a . C atoms are shown in grey, H in white, Cu in dark brown, and O in red. Hydrogen bonds are drawn as light-blue dashed lines.

X-ray powder diffraction of the blue powder of **45** matched the diffraction pattern simulated from the single-crystal structure, as shown in Figure 6.5. Elemental analysis and the lack of any additional peaks in the experimental diffraction pattern proves the product was made as a pure phase.

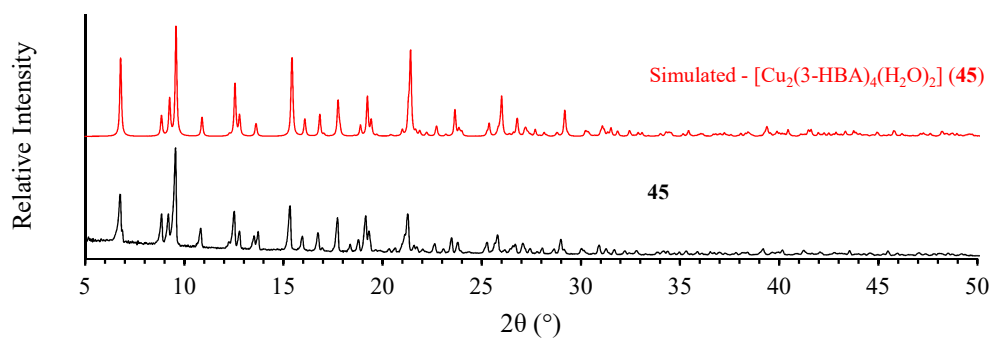


Figure 6.5 Room temperature X-ray powder diffraction data for **45**. Experimental data are shown in black while simulated data are shown in red.

6.4 4-Hydroxybenzoic acid (4-HBA)

A search of the CSD shows that there are many more complexes of Cu with 4-hydroxybenzoic acid (4-HBA) known compared to with 3-HBA.¹¹⁹ There are currently 13 on the database not including those with chelating ligands, of which only two are paddlewheel shaped: One with DMF,²³² and one with DMSO.²³³ Complexes are known with both 4,4'-bipyridine,²³⁴ and 4,4'-bipyridine N,N'-dioxide,²³⁵ although neither form linear polymers containing the paddlewheel unit. Only the reactions with methanol, DMAP, and pyrazine produced crystals that could be analysed.

6.4.1 $[Cu_2(4-HBA)_4(H_2O)_2] \cdot nMeOH$ (**46**)

46 crystallises with a triclinic cell and space group $P\bar{1}$, further crystallographic details are included in Table 6.2. The asymmetric unit, shown in Figure 6.6, contains half of a paddlewheel motif which lies upon a centre of inversion, the apical ligand in these molecules appears to be water as methanol does not give a satisfactory fit to the calculated electron density. The Cu centre has a square-pyramidal coordination geometry, bond lengths and angle of which are given in Table 6.6.

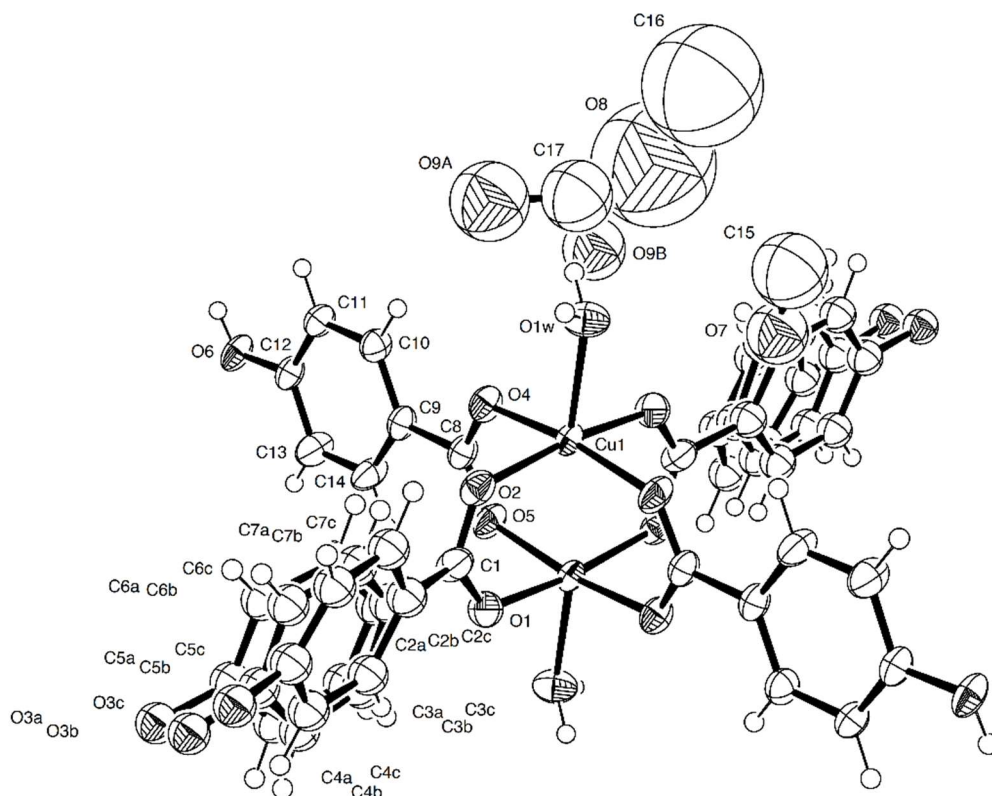


Figure 6.6 Asymmetric unit of $[\text{Cu}_2(4\text{-HBA})_4(\text{H}_2\text{O})_2] \cdot n\text{MeOH}$ (**46**) with atoms drawn as thermal ellipsoids with 50% probability. The paddlewheel fragment is completed by the symmetry operator: 1-x, 1-y, 2-z.

Table 6.6 Selected bond lengths (Å) and angles (°) around the Cu coordination centre for $[\text{Cu}_2(4\text{-HBA})_4(\text{H}_2\text{O})_2] \cdot n\text{MeOH}$ (**46**).

Cu(1) – O(1)	1.967(3)	Cu(1) – O(5)#1	1.960(2)
Cu(1) – O(2)#1	1.990(3)	Cu(1) – O(1W)	2.164(3)
Cu(1) – O(4)	1.954(2)	Cu(1) – Cu(1)#1	2.5723(9)
O(1) – Cu(1) – O(2)#1	169.94(11)	O(2)#1 – Cu(1) – O(1W)	98.89(12)
O(1) – Cu(1) – O(4)	88.96(12)	O(4) – Cu(1) – O(5)#1	170.39(11)
O(1) – Cu(1) – O(5)#1	90.49(12)	O(4) – Cu(1) – O(1W)	97.51(12)
O(1) – Cu(1) – O(1W)	91.11(12)	O(5)#1 – Cu(1) – O(1W)	92.09(12)
O(2)#1 – Cu(1) – O(4)	88.61(12)	O(1W) – Cu(1) – Cu(1)#1	172.36(10)
O(2)#1 – Cu(1) – O(5)#1	90.29(12)		

#1 1-x, 1-y, 2-z

One of the 4-HBA ligands which forms part of the complex is highly disordered with at least three discrete positions, the guest solvent molecules are also disordered. The scattering pattern from the crystal analysed displayed some diffuse scattering, this is a

phenomenon observed in disordered solids, like ice, and therefore reinforces the observed solvent disorder. The methanol molecule incorporating C17 is disordered over two positions, O9 was therefore split into two sites, O9A and O9B, and the occupancy refined under a single free variable. Despite the problematic refinement, the final model provides a relatively good fit to the experimental data ($R = 0.0656$, $wR = 0.1982$).

As shown in Figure 6.7, $C_2^2(8)$ chain interactions between molecules of the dimeric complex packing along the a and b axes in the structure lead to the formation of 2-dimensional layers. The interaction is created through hydrogen bonds from a coordinated water molecule of one complex to the hydroxyl group of a 4-HBA ligand in another complex, the latter of which then hydrogen bonds to one of the carboxylate O atoms of a further complex ($O1W \cdots O6$ 2.799(4) Å, and $O6 \cdots O2$ 2.733(4) Å). The 2-D layers stack in such a way to leave channels to be occupied by the solvent, also shown in Figure 6.7. No strong intermolecular contacts are observed which could give rise to the observed packing other than π - π stacking interactions. The solvent molecules in general are not very well refined, and this may be due to some partial evaporation of the solvent. This is further reinforced by the fact the disordered 4-HBA molecules are in a position which creates a smaller void, indicating the void was smaller in some instances. This implies that the solvent is not very strongly bonded to the structure and therefore escapes easily. X-ray powder diffraction of multiple prepared samples showed the compound could not be made phase pure, or at least decomposed between extraction from the reaction vessel and analysis.

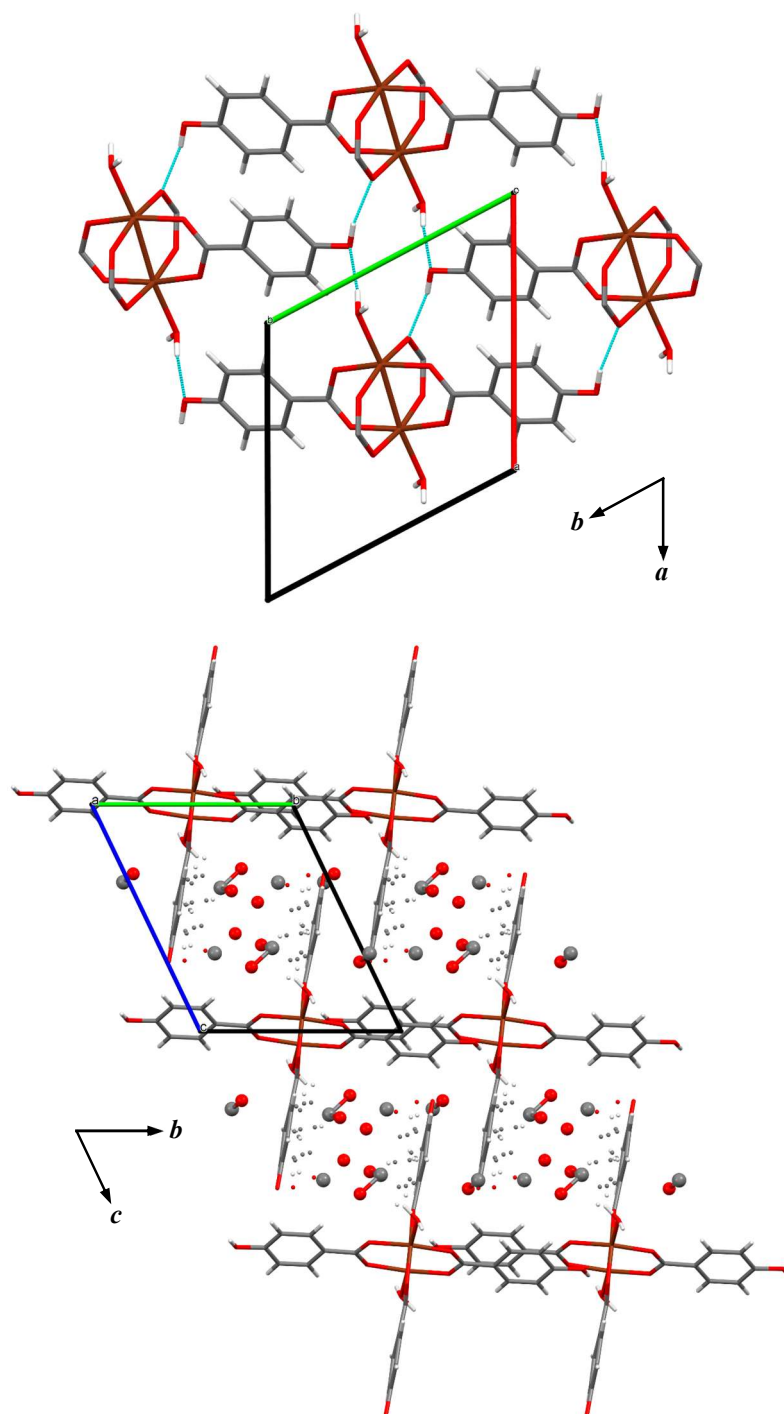


Figure 6.7 Shown left are the hydrogen bonding interactions that occur between discrete molecules of $[\text{Cu}_2(4\text{-HBA})_4(\text{H}_2\text{O})_2] \cdot n\text{MeOH}$ (**46**) creating a 2-D sheet along the ab plane. Shown right are the solvent channels along a that are created by stacking of the 2-D sheets within **46**. C atoms are shown in grey, H in white, Cu in dark brown, and O in red. Hydrogen bonds are drawn as light-blue dashed lines.

6.4.2 $[Cu_2(4-HBA)_2(DMAP)_2] \cdot 1.5H_2O$ (**47**)

47 crystallises in the monoclinic space group $C2/c$, further crystallographic details are included in Table 6.2. No problems were faced in refining the structure of **47** and final figures of merit were excellent ($R = 0.0385$, $wR = 0.0905$). The asymmetric unit is shown in Figure 6.8.

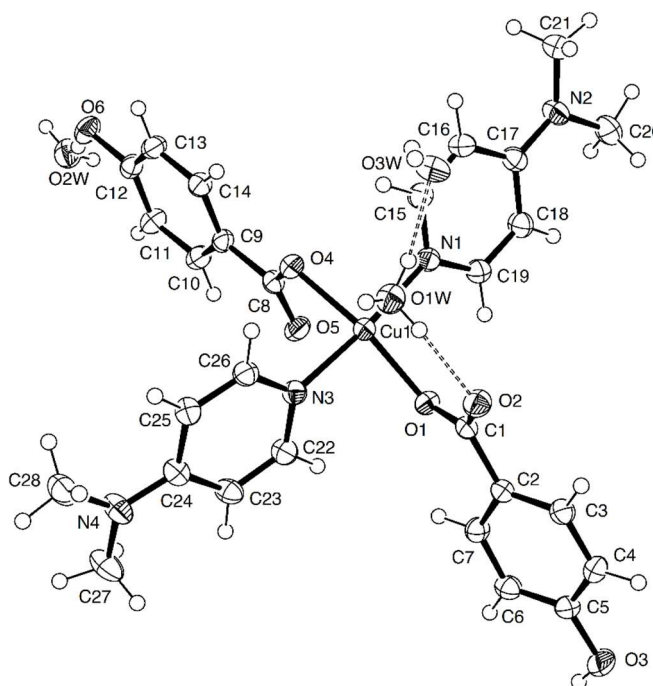


Figure 6.8 Asymmetric unit of $[Cu_2(4-HBA)_2(DMAP)_2] \cdot 1.5H_2O$ (**47**) with atoms shown as thermal ellipsoids drawn at 50% probability. Hydrogen bonds are drawn as dashed lines.

47 is composed of a Cu^{2+} cation bonded to one water, two DMAP, and two 4-HBA ligands. The coordination around the copper is either square-pyramidal or distorted octahedral, but this is uncertain as it is unknown whether a coordination bond exists between Cu1 and O5. Bond distances and angles are given in Table 6.7. In addition to this coordination compound there are also one and a half uncoordinated water molecules; one is in a general position and the other is situated with one hydrogen atom on the 4c Wyckoff position meaning it has an occupancy of a half due to symmetry. Because the

latter water molecule is disordered in this way, the coordinated water molecule which hydrogen bonds to it has three hydrogen atom positions, one is fully occupied as it only takes place in an intramolecular hydrogen bond, however the others are half occupied as their presence is linked with the position of the disordered water molecule they hydrogen bond to.

Table 6.7 Selected bond lengths (Å) and angles (°) around the Cu coordination centre for [Cu₂(4-HBA)₂(DMAP)₂] \cdot 1.5H₂O (**47**).

Cu(1) – O(1)	1.9749(13)	Cu(1) – O(5)	2.6982(17)
Cu(1) – O(1W)	2.4131(17)	Cu(1) – N(1)	1.9909(17)
Cu(1) – O(4)	1.9984(13)	Cu(1) – N(3)	1.9810(17)
O(1) – Cu(1) – O(1W)	101.09(6)	O(1W) – Cu(1) – O(5)	156.53(6)
O(1) – Cu(1) – O(4)	156.06(7)	O(1W) – Cu(1) – N(1)	87.40(7)
O(1) – Cu(1) – O(5)	101.89(6)	O(1W) – Cu(1) – N(3)	89.29(7)
O(1) – Cu(1) – N(1)	94.34(6)	O(4) – Cu(1) – O(5)	54.19(6)
O(1) – Cu(1) – N(3)	91.28(6)	N(1) – Cu(1) – N(3)	173.93(7)
O(1W) – Cu(1) – O(4)	102.83(6)		

Each complex contains an intramolecular hydrogen bonding interaction between the coordinated water and one of the 4-HBA ligands (O1W \cdots O2 2.695(2) Å). The same water molecule also forms a hydrogen bonding interaction to the same ligand in a neighbouring complex (O1W \cdots O1W 2.827(3) Å) which then has a contact in turn with the disordered non-coordinated water (O1W \cdots O3W 2.786(5) Å). The two possible configurations of all the above interactions due to symmetry are shown in Figure 6.9.

The O3W water molecule also hydrogen bonds to another complex via the hydroxyl group of one of the 4-HBA ligands which in turn forms a contact with one of the carboxylate oxygens of a neighbouring complex (O3W \cdots O3 2.970(6) Å, and O3 \cdots O5 2.730(2) Å). The other 4-HBA ligand forms an R₄⁴(8) interaction with the other uncoordinated water molecule, O2W, which links four complexes together via additional contacts between O2W and the same carboxylate oxygen which accepts the 4-HBA hydroxyl hydrogen

bond mentioned above (O6···O2W 2.637(3) Å, O2W···O6 2.800(2) Å, and O2W···O5 2.779(2) Å).

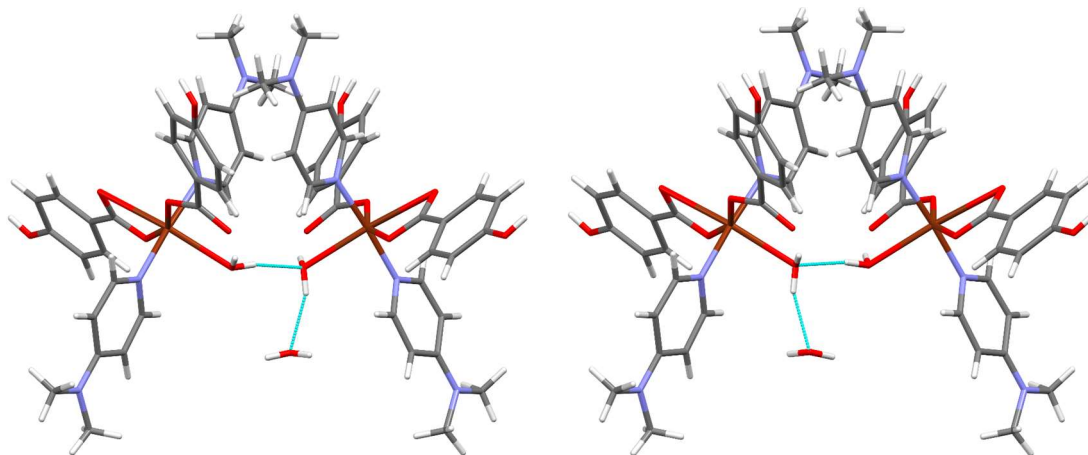


Figure 6.9 The two possible hydrogen bonding arrangements in $[\text{Cu}_2(4\text{-HBA})_2(\text{DMAP})_2] \cdot 1.5\text{H}_2\text{O}$ (**47**), involving O1W and O3W, which arise due to the hydrogen atom of O3W being on the axis of rotation for the screw axis symmetry element. C atoms are shown in grey, H in white, Cu in dark brown, N in light grey-blue, and O in red. Hydrogen bonds are drawn as light-blue dashed lines.

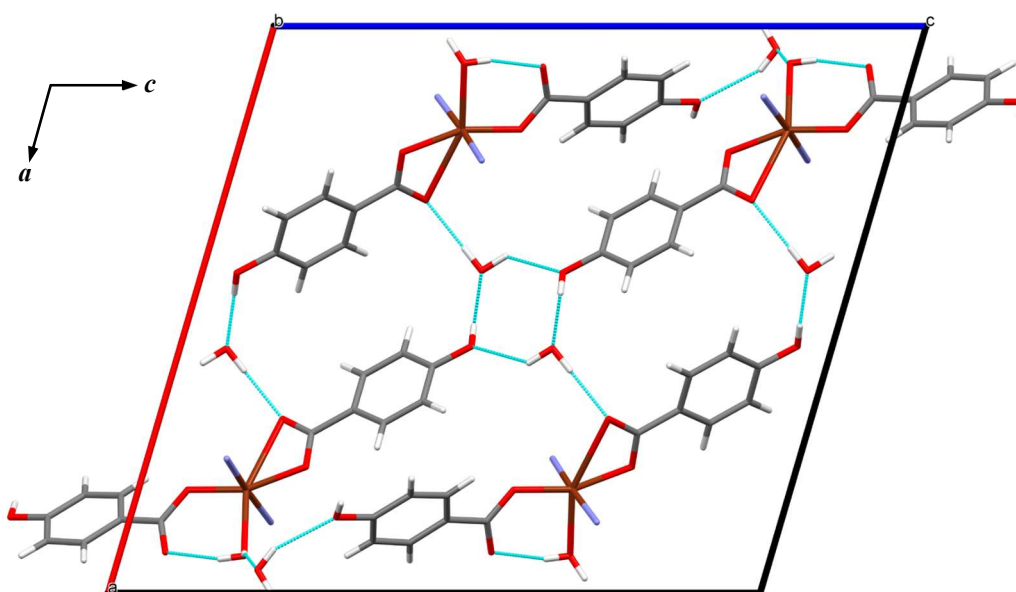


Figure 6.10 The $R_4^2(8)$ interaction, shown centre, and other hydrogen bonds which link the complexes of $[\text{Cu}_2(4\text{-HBA})_2(\text{DMAP})_2] \cdot 1.5\text{H}_2\text{O}$ (**47**). C atoms are shown in grey, H in white, Cu in dark brown, N in light grey-blue, and O in red. Hydrogen bonds are drawn as light-blue dashed lines.

A comparison of the X-ray powder diffraction pattern of the blue powder and simulated data from the single-crystal structure are shown in Figure 6.11. No additional peaks were observed in the experimental diffraction pattern when compared to the simulated data, and elemental analysis showed the sample to have the expected elemental composition indicating a pure product was made.

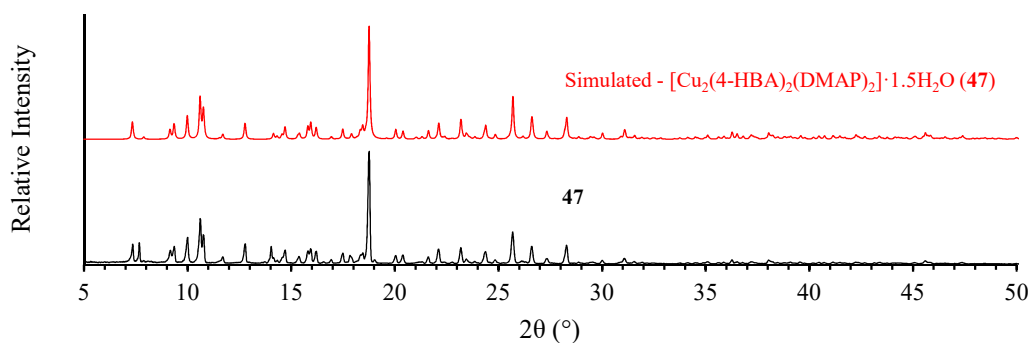


Figure 6.11 Room temperature X-ray powder diffraction data for **47**. Experimental data are shown in black while simulated data are shown in red.

6.4.3 $[Cu_2(4-HBA)_4(Pz)_2] \cdot 2MeOH$ (**48**)

48 has an orthorhombic unit-cell and crystallises in the space group $Pccn$, further crystallographic details are included in Table 6.3. Pyrazine acts as a neutral, linear, bridging ligand in this compound, creating a 1-dimensional coordination polymer which runs directly along the 2-fold rotational axis along c . This gives an asymmetric unit containing half of the paddlewheel complex along with a single uncoordinated methanol molecule, as shown in Figure 6.12. The Cu centre has a square-pyramidal coordination geometry and the bond distances and angles within the inner coordination sphere are given in Table 6.8.

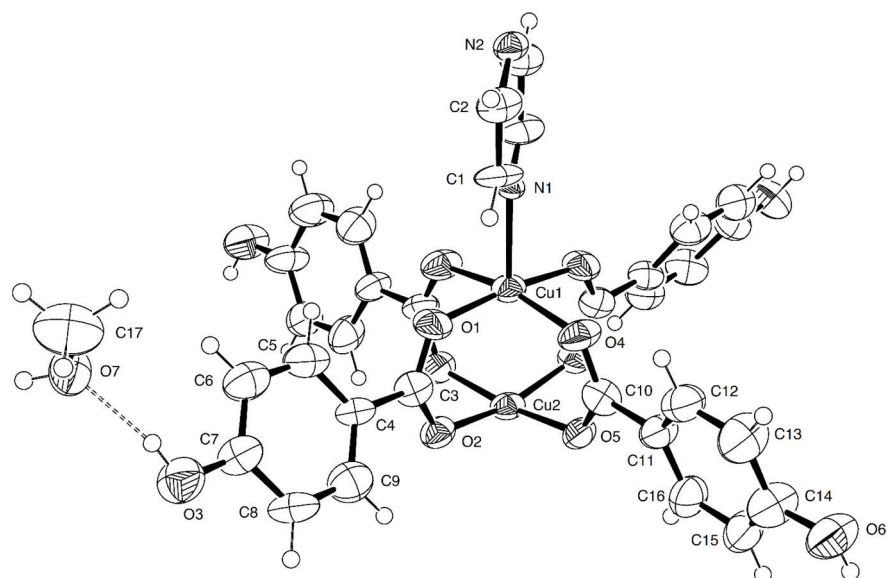


Figure 6.12 Asymmetric unit of $[\text{Cu}_2(4\text{-HBA})_4(\text{Pz})_2]\cdot 2\text{MeOH}$ (**48**) with atoms drawn as thermal ellipsoids with 50% probability. The paddlewheel fragment is completed by the symmetry operator: $\frac{1}{2}-x, \frac{3}{2}-y, z$. Hydrogen bonds are drawn as dashed lines.

Table 6.8 Selected bond lengths (Å) and angles (°) around the Cu coordination centres for $[\text{Cu}_2(4\text{-HBA})_4(\text{Pz})_2]\cdot 2\text{MeOH}$ (**48**).

Cu(1) – O(1)	1.920(6)	Cu(2) – O(2)	2.028(6)
Cu(1) – O(4)	2.000(5)	Cu(2) – O(5)	1.905(5)
Cu(1) – N(1)	2.171(7)	Cu(2) – N(2)#2	2.186(8)
Cu(1) – Cu(2)	2.6195(14)		
O(1) – Cu(1) – O(1)#1	172.3(3)	O(2) – Cu(2) – O(2)#1	165.3(3)
O(1) – Cu(1) – O(4)	90.4(3)	O(2) – Cu(2) – O(5)	88.2(2)
O(1) – Cu(1) – N(1)	93.87(14)	O(2) – Cu(2) – N(2)#2	97.34(15)
O(4) – Cu(1) – O(4)#1	166.6(3)	O(5) – Cu(2) – O(5)#1	171.2(3)
O(4) – Cu(1) – N(1)	96.72(15)	O(5) – Cu(2) – N(2)#2	94.42(15)

$$\#1 \frac{1}{2} - x, \frac{3}{2} - y, z$$

$$\#2 x, \frac{3}{2} - y, \frac{1}{2} + z$$

The polymeric chains interact with each other both directly, through hydroxyl to carboxylate hydrogen bonding interactions identical to those found in **46** ($\text{O6}\cdots\text{O2}$ 2.918(9) Å), and indirectly via a methanol molecule which mediates another hydroxyl to carboxylate interaction. The latter interaction consists of a hydrogen bond from the hydroxyl group of 4-HBA to that of the methanol guest, which in turn forms bifurcated

hydrogen bonds to two carboxylate groups in a neighbouring polymeric chain ($O3 \cdots O7$ 2.687(9) Å, $O7 \cdots O1$ 3.190(8) Å, and $O7 \cdots O4$ 3.064(9) Å). These are shown in Figure 6.13.

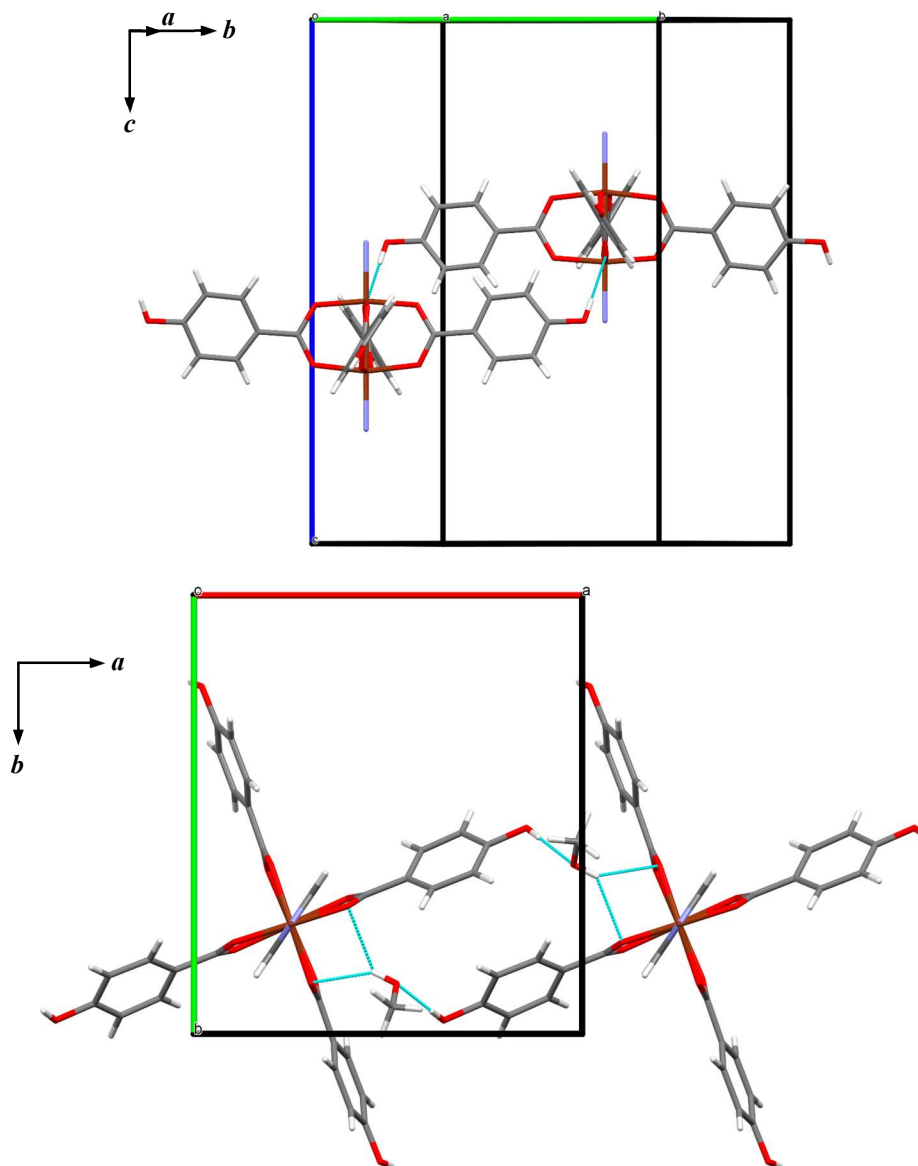


Figure 6.13 The direct (left) and indirect (right) hydrogen bonding interactions that occur between discrete polymeric strands in $[\text{Cu}_2(4\text{-HBA})_4(\text{Pz})_2] \cdot 2\text{MeOH}$ (**48**). C atoms are shown in grey, H in white, Cu in dark brown, N in light grey-blue, and O in red. Hydrogen bonds are drawn as light-blue dashed lines.

While the polymer is almost identical to that of $[\text{Cu}_2(\text{BA})_4(\text{Pz})]_n$, the packing is substantially different, and different again to that of the methanol solvate of the same

compound. The packing of **48** leads to solvent molecules which occupy channels running parallel to the *a* and *b* axes of the unit-cell, as shown in Figure 6.14.

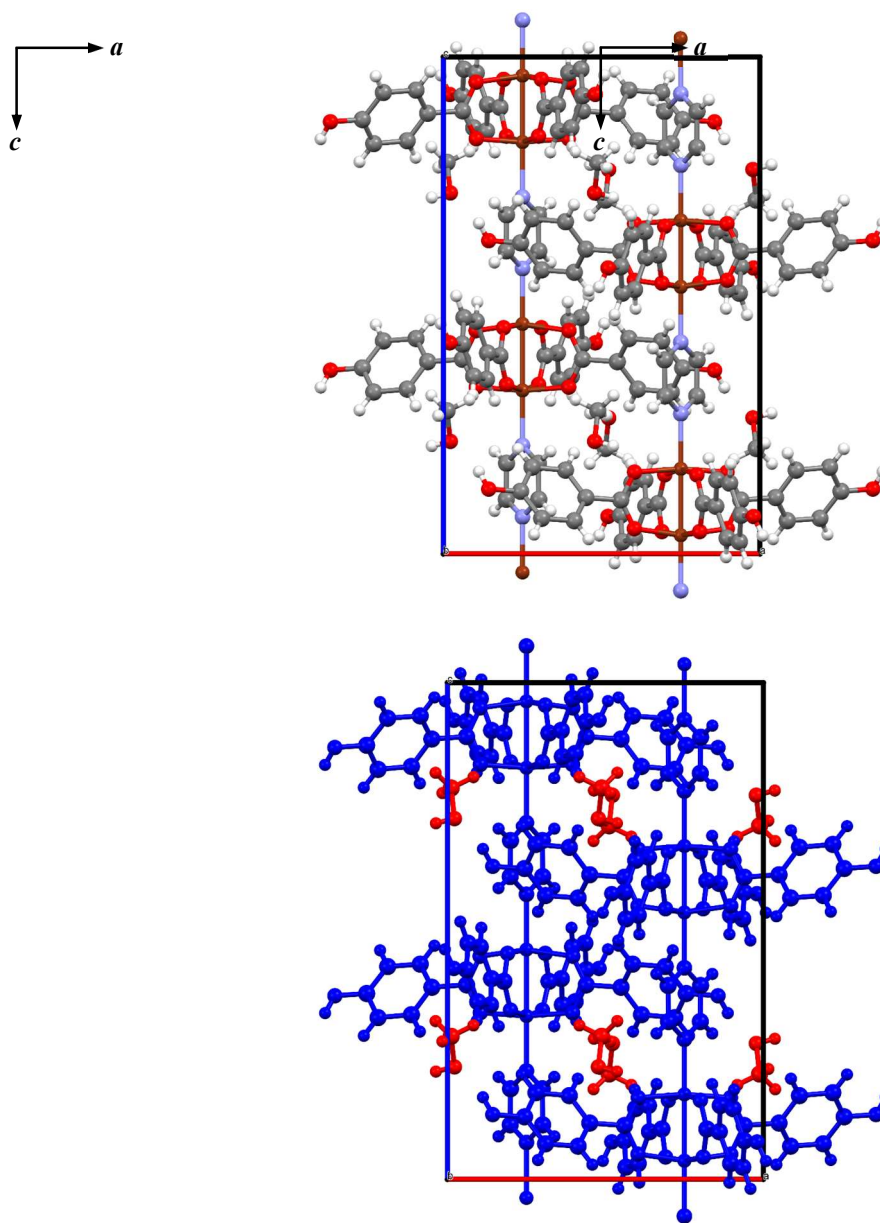


Figure 6.14 The crystal structure of $[\text{Cu}_2(4\text{-HBA})_4(\text{Pz})_2] \cdot 2\text{MeOH}$ (**48**) showing the methanol molecules residing in channels running parallel to the *a* (left) and *b* (right) crystallographic axes. C atoms are shown in grey, H in white, Cu in dark brown, N in light grey-blue, and O in red.

X-ray powder diffraction of **48**, shown in Figure 6.15, showed that the material could be made as a pure phase by the lack of any additional peaks in the experimental data which are not in simulated diffraction pattern. Changes in the diffraction patterns of compounds

are usually observed upon loss of solvent guest molecules as the structure shifts to accommodate the change. As a crude experiment to test the loss of methanol from **48**, the material was left out in ambient conditions for both 1 hour and 24 hours, and the diffraction pattern measured again at both intervals. The data from these experiments show the slow emergence of a new phase by the increasing intensity of peaks at around 9.6° , 11.1° , and 13.4° 2θ among others.

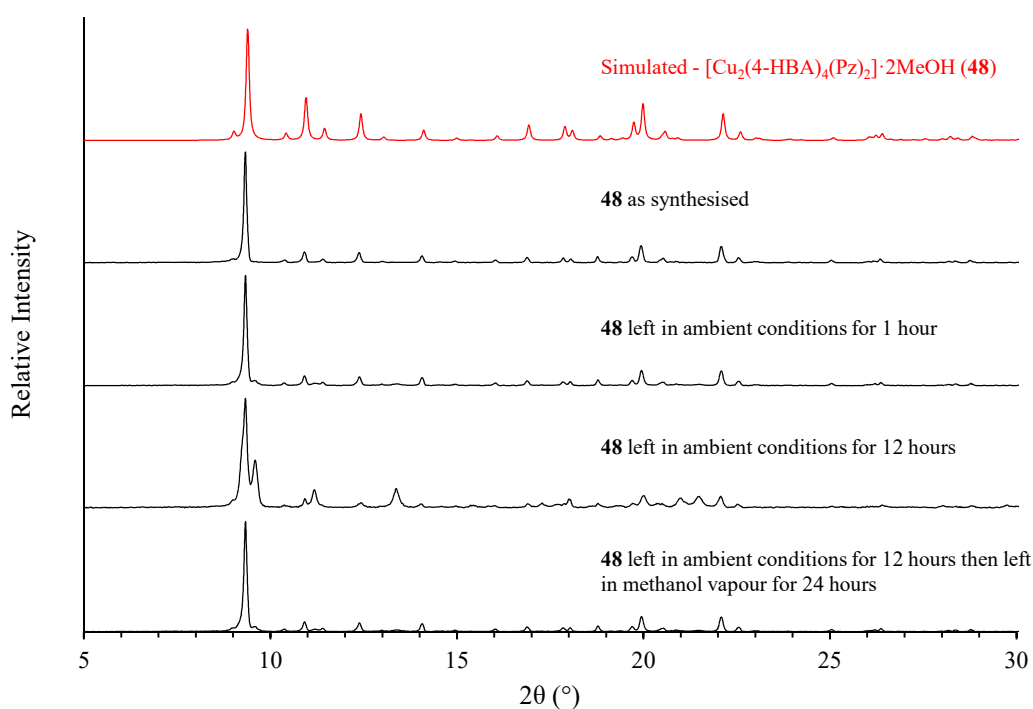


Figure 6.15 X-ray powder diffraction patterns for the desolvation and resolution of **48**. Experimental data are shown in black while simulated data are shown in red.

Predicting that evaporating methanol was the cause, the sample was left in methanol vapour for a further 24 hours resulting in the loss of these peaks and return to the original pattern. The most likely scenario is that methanol escaping from the sample induces a phase transformation through a loss of the hydrogen bonding interactions it takes place in. Whether or not this is a single-crystal to single-crystal transformation remains to be proven, but these results are very promising and require further investigation. However,

attempts to produce the sample in bulk for elemental analysis and further work have unfortunately been unsuccessful.

The same reaction which produced **48** was attempted simultaneously with 3-HBA and 3,5-DHBA, although only the reaction with 4-HBA has produced crystals of an appropriate size for structural analysis. It should be noted, however, that the reactions with 3,5-DHBA and 3-HBA do give very small crystals of a similar colour/morphology to those produced with 4-HBA.

6.5 3,5-Dihydroxybenzoic acid (3,5-DHBA)

The CSD contains six compounds formed by coordination of 3,5-dihydroxybenzoic acid (3,5-DHBA) with copper and non-chelating ligands.¹¹⁹ Two paddlewheel-shaped complexes are formed with tetrahydrofuran²³⁶ and acetonitrile,²³⁷ all others are discrete mononuclear entities or contain only 3,5-DHBA as the ligand. Reactions were attempted to see what other solvents a paddlewheel complex may form in, followed by reactions with various pyridine-based compounds although only the former experiments yielded good quality crystals.

6.5.1 $[Cu_2(3,5-DHBA)_4(MeOH)_2] \cdot 8MeOH$ (**49**)

49 has a centrosymmetric monoclinic unit-cell of $P2_1/n$ symmetry, further crystallographic details are included in Table 6.3. The asymmetric unit contains half of a paddlewheel-type complex which lies on a centre of inversion and methanol occupying the apical position, along with four uncoordinated methanol molecules, as depicted in Figure 6.16. The coordination geometry of the Cu is square-pyramidal, bond length and angle data are given in Table 6.9.

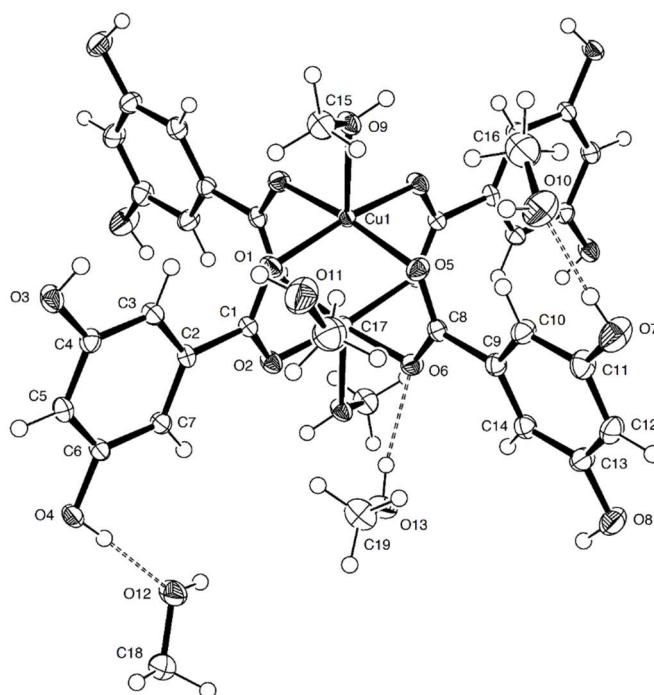


Figure 6.16 Asymmetric unit of $[\text{Cu}_2(3,5\text{-DHBA})_4(\text{MeOH})_2]\cdot 8\text{MeOH}$ (**49**) with atoms drawn as thermal ellipsoids with 50% probability. The paddlewheel fragment is completed by the symmetry operator: $1-x, 1-y, 1-z$. Hydrogen bonds are drawn as dashed lines.

Table 6.9 Selected bond lengths (Å) and angles (°) around the Cu coordination centre for $[\text{Cu}_2(3,5\text{-DHBA})_4(\text{MeOH})_2]\cdot 8\text{MeOH}$ (**49**).

Cu(1) – O(1)	1.9583(14)	Cu(1) – O(6)#1	1.9812(17)
Cu(1) – O(2)#1	1.9541(14)	Cu(1) – O(9)	2.1787(15)
Cu(1) – O(5)	1.9724(17)	Cu(1) – Cu(1)#1	2.5976(5)
O(1) – Cu(1) – O(2)#1	169.68(7)	O(2)#1 – Cu(1) – O(9)	92.97(6)
O(1) – Cu(1) – O(5)	90.52(7)	O(5) – Cu(1) – O(6)#1	169.69(7)
O(1) – Cu(1) – O(6)#1	89.50(7)	O(5) – Cu(1) – O(9)	94.97(7)
O(1) – Cu(1) – O(9)	97.29(6)	O(6)#1 – Cu(1) – O(9)	95.26(6)
O(2)#1 – Cu(1) – O(5)	89.74(7)	O(9) – Cu(1) – Cu(1)#1	179.15(5)
O(2)#1 – Cu(1) – O(6)#1	88.41(7)		

#1 $1-x, 1-y, 1-z$

There is only one direct hydrogen bond between complexes from the hydroxyl group of the apical methanol ligand to the hydroxyl group of a 3,5-DHBA ligand of another complex in either the $[111]$ or $[\bar{1}\bar{1}\bar{1}]$ direction ($\text{O9}\cdots\text{O4}$ 2.918(9) Å). All other interactions occur between complexes stacking along the b axis and are mediated by the four

uncoordinated methanol molecules. Eight O-H \cdots O hydrogen bonds are formed by these molecules and can be described as either an R₃³(11) motif at the shortest or an R₄⁴(32) at the longest (O3 \cdots O13 2.673(2) Å, O4 \cdots O12 2.630(2) Å, O7 \cdots O10 2.702(3) Å, O8 \cdots O11 2.669(3) Å, O10 \cdots O8 2.838(3) Å, O11 \cdots O13 2.987(3) Å, O12 \cdots O3 2.767(2) Å, and O13 \cdots O6 2.824(2) Å). The hydrogen bonding interactions are all shown in Figure 6.17.

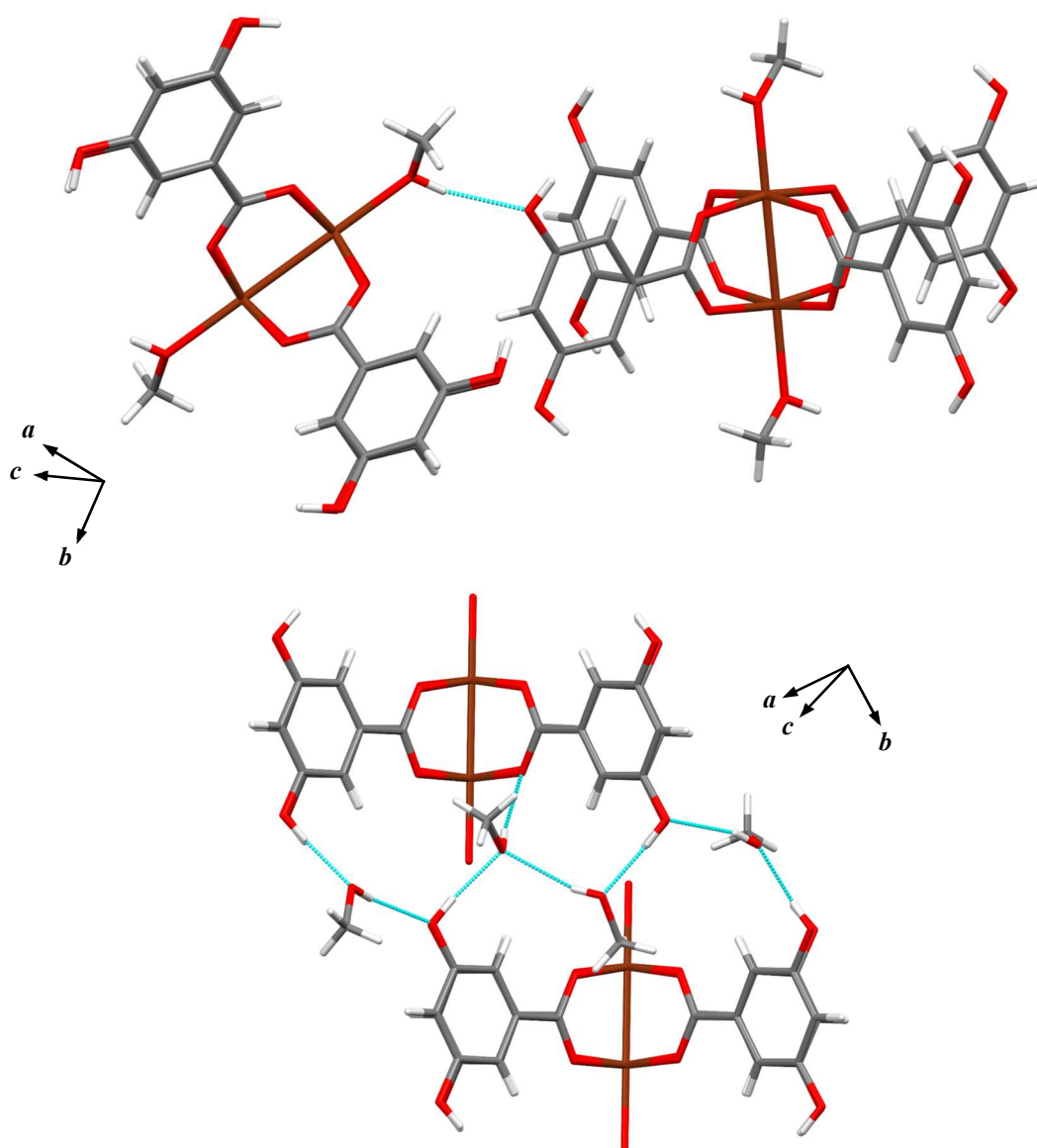


Figure 6.17 The direct, left, and indirect, right, hydrogen bonding interactions between discrete molecules in $[\text{Cu}_2(3,5\text{-DHBA})_4(\text{MeOH})_2]\cdot 8\text{MeOH}$ (**49**). C atoms are shown in grey, H in white, Cu in dark brown, and O in red. Hydrogen bonds are drawn as light-blue dashed lines.

As shown in Figure 6.18, and as seen in many other examples of how the paddlewheel complex packs, the packing of **49** creates channels which are filled with the methanol solvent. This may serve to explain why, as with **46**, the X-ray powder diffraction proved that the compound could not be made as a pure phase; the methanol solvent could easily evaporate through the channels causing the sample to change quickly into another unidentified phase.

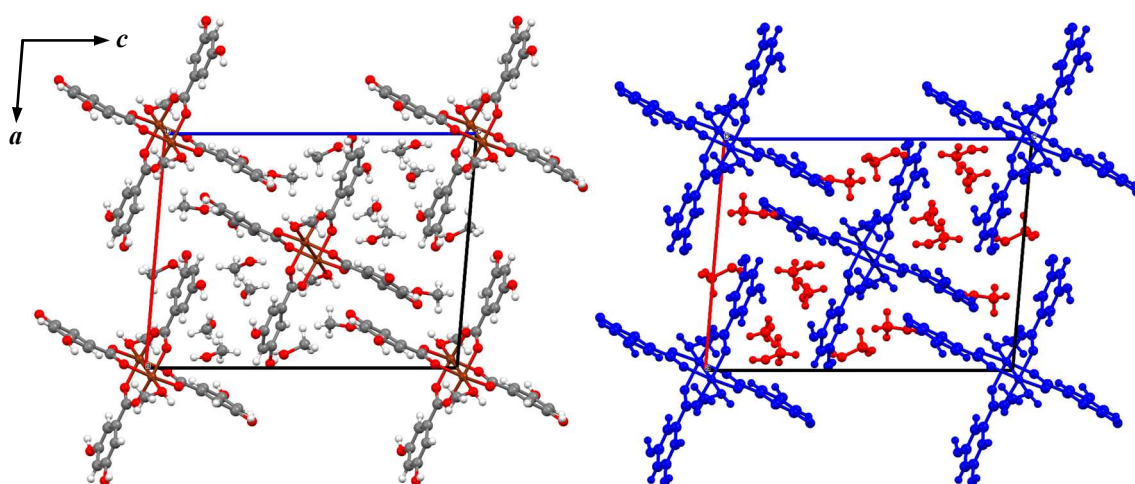


Figure 6.18 Diagrams of the overall crystal packing in $[\text{Cu}_2(3,5\text{-DHBA})_4(\text{MeOH})_2]\cdot 8\text{MeOH}$ (**49**). Shown left is a diagram with atoms coloured according to element. C atoms are shown in grey, H in white, Cu in dark brown, N in light grey-blue, and O in red. Shown right the complexes are coloured blue while the uncoordinated methanol solvent is coloured red.

6.5.2 $[\text{Cu}(3,5\text{-DHBA})_2(\text{H}_2\text{O})_3]\cdot 5\text{H}_2\text{O}$ (**50**)

50, like **49**, is monoclinic but crystallises in the space group $P2_1/m$, further crystallographic details are included in Table 6.3. The asymmetric unit contains two symmetry independent complexes and five uncoordinated water molecules, as shown in Figure 6.19. Each complex consists of a copper centre around which three water molecules and two 3,5-DHBA molecules are coordinated (all as monodentate ligands) in a square-pyramidal arrangement. Bond distance and angle data are given in Table 6.10. Each complex also lies with the three waters and Cu atom on a mirror plane and therefore

these occupy special positions. None of the hydrogen atoms of the water molecules could be resolved with the available data, so have therefore not been refined.

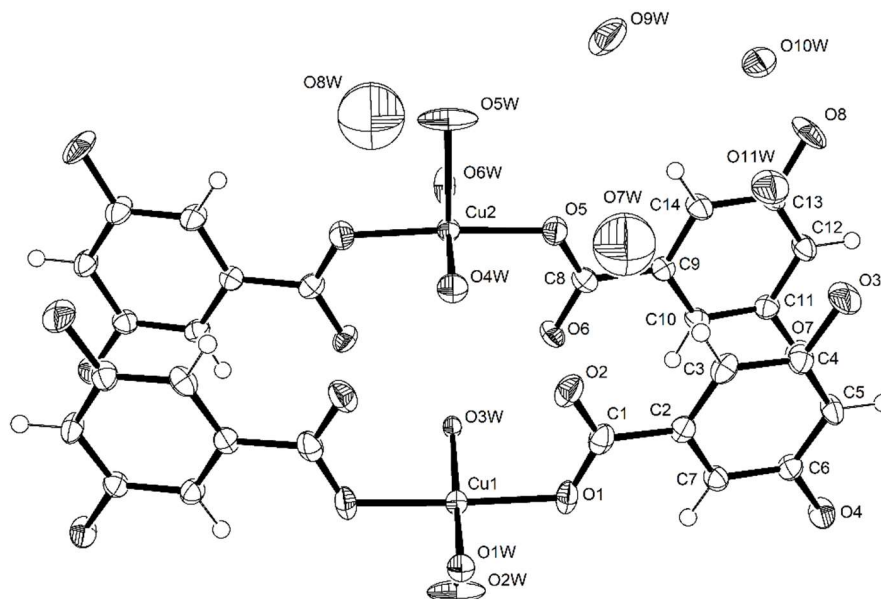


Figure 6.19 Asymmetric unit of $[\text{Cu}(3,5\text{-DHBA})_2(\text{H}_2\text{O})_3]\cdot 5\text{H}_2\text{O}$ (**50**) with atoms drawn as thermal ellipsoids with 50% probability. The fragment is completed by the symmetry operator: $x, \frac{3}{2}-y, z$.

Table 6.10 Selected bond lengths (Å) and angles (°) around the Cu coordination centres for $[\text{Cu}(3,5\text{-DHBA})_2(\text{H}_2\text{O})_3]\cdot 5\text{H}_2\text{O}$ (**50**).

Cu(1) – O(1)	1.954(3)	Cu(2) – O(5)	1.935(3)
Cu(1) – O(1W)	1.968(4)	Cu(2) – O(4W)	1.966(4)
Cu(1) – O(2W)	2.201(5)	Cu(2) – O(5W)	2.221(5)
Cu(1) – O(3W)	2.012(4)	Cu(2) – O(6W)	1.994(4)
O(1) – Cu(1) – O(1)#1	176.6(2)	O(5) – Cu(2) – O(5)#1	175.6(2)
O(1) – Cu(1) – O(1W)	89.97(9)	O(5) – Cu(2) – O(4W)	90.43(10)
O(1) – Cu(1) – O(2W)	91.67(12)	O(5) – Cu(2) – O(5W)	92.13(11)
O(1) – Cu(1) – O(3W)	89.77(9)	O(5) – Cu(2) – O(6W)	89.33(10)
O(1W) – Cu(1) – O(2W)	98.38(19)	O(4W) – Cu(2) – O(5W)	91.8(2)
O(1W) – Cu(1) – O(3W)	170.96(19)	O(4W) – Cu(2) – O(6W)	173.5(2)
O(2W) – Cu(1) – O(3W)	90.65(18)	O(5W) – Cu(2) – O(6W)	94.7(2)

$$\#1 x, \frac{3}{2} - y, z$$

A number of hydrogen bonding interactions exist between the complexes and uncoordinated water. The first of these are the $R_4^2(8)$ interactions which occur directly

between the complexes along *a*. The opposing water molecules of two complexes related by a translation of $x+1$, e.g. O1W and O3W, each form two hydrogen bonds to the uncoordinated carboxylate O atoms of the 3,5-DHBA ligands belonging to the complex between them (O1W \cdots O6 2.665(4) Å, O3W \cdots O6 2.725(5) Å, O4W \cdots O2 2.708(5) Å, O6W \cdots O2 2.734(5) Å). The second interaction is a chain occurring along *c* between the two symmetry independent complexes. This is created by hydrogen bonds between alternating 3,5-DHBA and water molecules, although the donor-acceptor arrangement cannot be described as the hydrogen atom positions are not known (O3 \cdots O8 2.668(5) Å, O3 \cdots O11W 2.719(5) Å, O4 \cdots O7 2.757(5) Å, O4 \cdots O11W 2.782(5) Å, O7 \cdots O10W 2.737(5) Å, O8 \cdots O10W 2.731(6) Å, and O10W \cdots O11W 2.757(5) Å).

The last interaction is a complicated arrangement between the apical water ligands of each symmetry independent complex, and the other uncoordinated water molecules. This connects further to the second interaction discussed above (O2W \cdots O8W 2.903(15) Å, O2W \cdots O5W 2.726(7) Å, O5W \cdots O8W 2.760(15) Å, O7W \cdots O8W 2.464(16) Å, O7W \cdots O11W 2.715(10) Å, O9W \cdots O1 2.854(7) Å, and O9W \cdots O10W 2.719(6) Å). The three groups of interactions are shown in Figure 6.20. Determination of the purity of the compound produced has not been assessed by X-ray powder diffraction.

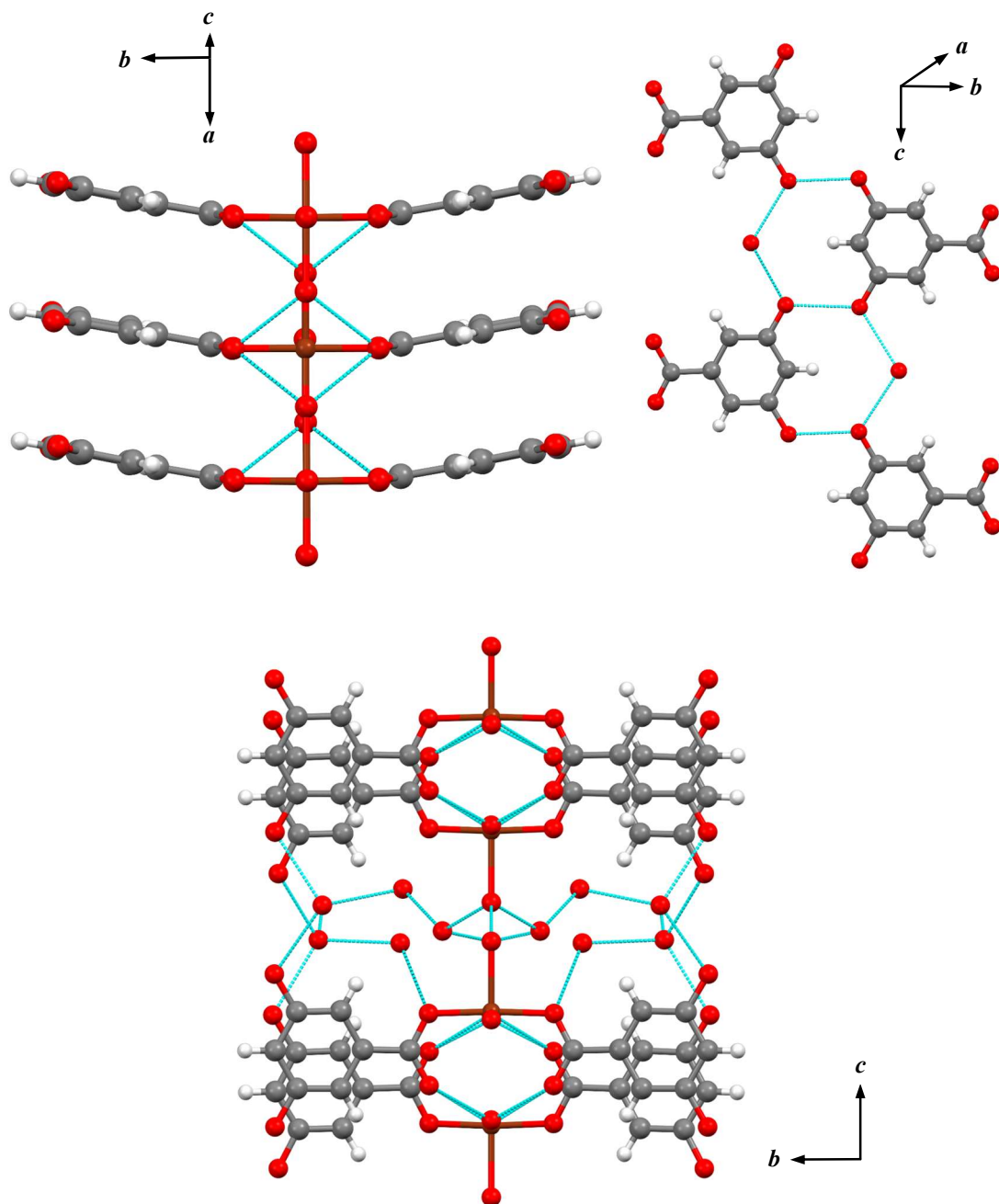


Figure 6.20 The hydrogen bonding interactions that give rise to the structure of $[\text{Cu}(\text{3,5-DHBA})_2(\text{H}_2\text{O})_3] \cdot 5\text{H}_2\text{O}$ (**50**). C atoms are shown in grey, H in white, Cu in dark brown, N in light grey-blue, and O in red. Hydrogen bonds are drawn as light-blue dashed lines.

6.6 4-Methylbenzoic acid (4-MeBA)

Eleven copper coordination complexes containing 4-MeBA without chelating ligands are contained in the CSD.¹¹⁹ Four display the paddlewheel shape,^{238–241} although the presence of water causes the formation of a non-paddlewheel complex with isonicotinamide.²⁴²

Reactions to create new pyridine-based complexes with copper and 4-MeBA were attempted with DMF, DABCO, pyrazine, and 4,4'-bipy although only the reaction with DMF produced crystals, the others only produced powders which were not analysed.

6.6.1 $[Cu_2(4-MeBA)_4(DMF)_2] \cdot 2DMF$ (**51**)

51 crystallises in the monoclinic space group $P2_1/c$, further crystallographic details are included in Table 6.4. Shown in Figure 6.21 is the asymmetric unit of **51** which consists of half a paddlewheel complex on an inversion centre, for which the apical ligand is a DMF molecule, and one uncoordinated DMF molecule. The coordination geometry of the Cu is therefore square-pyramidal, for which bond distance and angle data are given in Table 6.11.

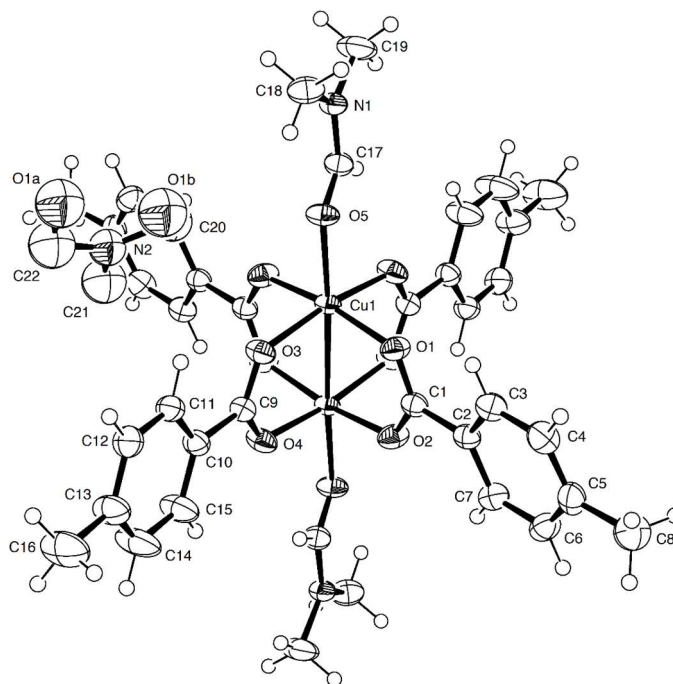


Figure 6.21 Asymmetric unit of $[Cu_2(4-MeBA)_4(DMF)_2] \cdot 2DMF$ (**51**) with atoms drawn as thermal ellipsoids with 50% probability. The paddlewheel fragment is completed by the symmetry operator: $1-x, 1-y, 2-z$.

The non-coordinated DMF molecule is disordered over two positions related by an approximate 180° turn around the N2-C21 bond. The hydrogen atom positions of this

molecule were therefore not determined, although the non-hydrogen atoms were refined normally. The occupancy for the two positions O1A and O1B were refined using a free variable. This final model gave an excellent fit to the observed data ($R = 0.0457$, $wR = 0.1297$).

Table 6.11 Selected bond lengths (Å) and angles (°) around the Cu coordination centre for $[\text{Cu}_2(4\text{-MeBA})_4(\text{DMF})_2] \cdot 2\text{DMF}$ (**51**).

Cu(1) – O(1)	1.9573(17)	Cu(1) – O(4)#1	1.9868(17)
Cu(1) – O(2)#1	1.9640(18)	Cu(1) – O(5)	2.1459(16)
Cu(1) – O(3)	1.9760(17)	Cu(1) – Cu(1)#1	2.6149(5)
O(1) – Cu(1) – O(2)#1	169.13(7)	O(2)#1 – Cu(1) – O(5)	92.37(7)
O(1) – Cu(1) – O(3)	88.65(8)	O(3) – Cu(1) – O(4)#1	169.03(7)
O(1) – Cu(1) – O(4)#1	91.19(8)	O(3) – Cu(1) – O(5)	96.36(7)
O(1) – Cu(1) – O(5)	98.50(7)	O(4)#1 – Cu(1) – O(5)	94.51(7)
O(2)#1 – Cu(1) – O(3)	90.00(8)	O(5) – Cu(1) – Cu(1)#1	176.06(5)
O(2)#1 – Cu(1) – O(4)#1	88.09(8)		

#1 1-x, 1-y, 2-z

Given the lack of any good donor groups for hydrogen bonding, no strong intermolecular interactions are observed and the packing of **51** is controlled simply by weak van der Waals' forces. **51** can be made pure as proven by comparison of the experimental X-ray powder diffraction pattern of a ground sample of **51** and data simulated from the single-crystal structure, as shown in Figure 6.22, and elemental analysis.

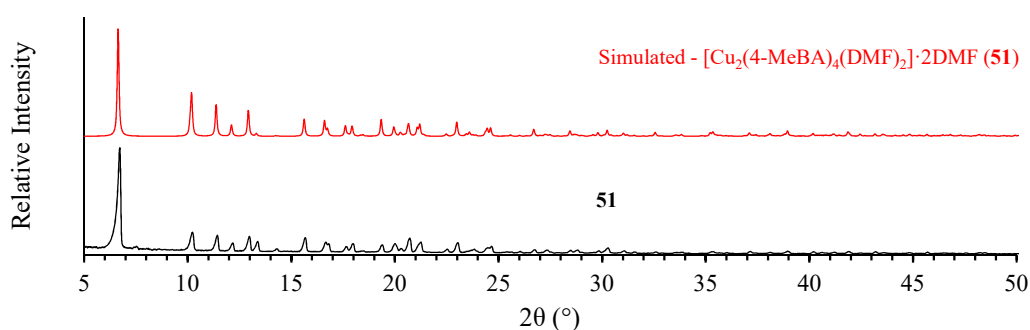


Figure 6.22 Room temperature X-ray powder diffraction data for **51**. Experimental data are shown in black while simulated data are shown in red.

6.7 4-Methoxybenzoic acid (4-MeOBA)

A search of the CSD shows that ten complexes of Cu with 4-MeOBA and non-chelating ligands are known, and those produced with acetonitrile,^{238,243} dimethylformamide,²³² and pyrazine²⁴⁴ all display the familiar paddlewheel shape.¹¹⁹ As with 4-MeBA, reactions were attempted with DMF, DABCO, pyrazine and 4,4'-bipy, although only the latter produced a novel compound with crystals good enough for analysis: the compound with DMF was already known.

6.7.1 $\{[\text{Cu}_2(4\text{-MeOBA})_4(4,4'\text{-bipy})][\text{Cu}(4\text{-MeOBA})_2(4,4'\text{-bipy})]\cdot 2\text{EtOH}\}_n$ (**52**)

52 crystallises with a centrosymmetric triclinic unit-cell, further crystallographic details are included in Table 6.4. The asymmetric unit contains two copper cations, one 4,4'-bipy molecule, three 4-MeOBA anions, and two ethanol solvent molecules acting as guests, as shown in Figure 6.23. The reaction of 4,4'-bipy with Cu and 4-MeOBA did not result in a green compound as is usual for Cu compounds containing 4,4'-bipy. Instead, the crystals of **52** are light blue-green indicating a different coordination geometry to the normal paddlewheel configuration, which is reflected by the presence of two coordination geometries coexisting in the structure: a mononuclear $[\text{Cu}(4\text{-MeOBA})_2]$ species, and a dinuclear paddlewheel-shaped $[\text{Cu}_2(4\text{-MeOBA})_4]$ species, bond distance and angle data for each are given in Table 6.12. The two monomeric units are bridged in an alternating fashion by additional Cu-N bonds to 4,4'-bipy, thereby creating a linear coordination polymer. **52** is therefore synonymous with the structure of $\{[\text{Cu}_2(3\text{-IBA})_4(4,4'\text{-bipy})][\text{Cu}(3\text{-IBA})_2(4,4'\text{-bipy})]\cdot \text{solvent}\}_n$ (3-IBA = 3-iodobenzoate) discovered by Smart *et al.*²⁴⁵

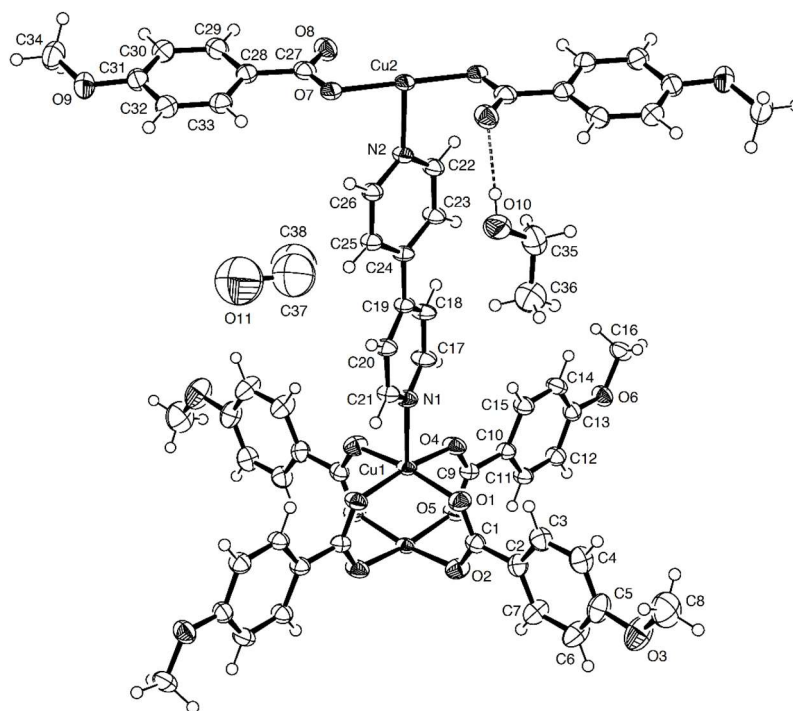


Figure 6.23 Asymmetric unit of $\{[\text{Cu}_2(4\text{-MeOBA})_4(4,4'\text{-bipy})][\text{Cu}(4\text{-MeOBA})_2(4,4'\text{-bipy})]\cdot 2\text{EtOH}\}_n$ (**52**) with atoms drawn as thermal ellipsoids with 50% probability. The paddlewheel fragment is completed by the symmetry operator: $-x, 1-y, 1-z$. The square-planar complex fragment is completed by the symmetry operator: $2-x, 1-y, -z$. Hydrogen bonds are drawn as dashed lines.

Table 6.12 Selected bond lengths (Å) and angles (°) around the Cu coordination centres for $\{[\text{Cu}_2(4\text{-MeOBA})_4(4,4'\text{-bipy})][\text{Cu}(4\text{-MeOBA})_2(4,4'\text{-bipy})]\cdot 2\text{EtOH}\}_n$ (**52**).

Cu(1) – O(1)	1.976(3)	Cu(1) – Cu(1)#1	2.6408(8)
Cu(1) – O(2)#1	1.980(3)	Cu(2) – O(7)	1.965(2)
Cu(1) – O(4)	1.965(2)	Cu(2) – O(8)	2.630(3)
Cu(1) – O(5)#1	1.965(2)	Cu(2) – N(2)	2.031(3)
Cu(1) – N(1)	2.191(3)		
O(1) – Cu(1) – O(2)#1	168.48(10)	O(4) – Cu(1) – O(5)#1	168.44(9)
O(1) – Cu(1) – O(4)	89.28(11)	O(4) – Cu(1) – N(1)	95.66(10)
O(1) – Cu(1) – O(5)#1	90.83(11)	O(5) – Cu(1) – N(1)	95.80(10)
O(1) – Cu(1) – N(1)	95.66(10)	N(1) – Cu(1) – Cu(1)#1	177.91(8)
O(2)#1 – Cu(1) – O(4)	88.58(11)	O(7) – Cu(2) – O(8)	55.76(9)
O(2)#1 – Cu(1) – O(5)#1	89.00(11)	O(7) – Cu(2) – N(2)	89.24(10)
O(2)#1 – Cu(1) – N(1)	94.53(11)	O(8) – Cu(2) – N(2)	85.35(10)

#1 $-x, 1-y, 1-z$

The mononuclear species is positioned with the Cu on the 1c Wyckoff position, whereas the dinuclear species is situated with the centre on the 1g Wyckoff position. The chains

are directed along [102] and neighbouring chains are related by unit translations along each unit-cell axis. The ethanol solvent guests are not trapped inside channels, but entirely encapsulated by the polymeric chains around them. The guests also form strong interactions with the polymer via hydroxyl to carboxylate and hydroxyl to methoxyl hydrogen bonds (O10 \cdots O8 2.809(4) Å, and O11 \cdots O3 2.755(10) Å). The structure of **52** is most similar to the benzyl alcohol solvated 3-IBA structure. However, because the two compounds do not have known structures with a common guest solvent the packing cannot be directly compared. The fact the 3-IBA compound can be crystallised with more than one solvent, and that the structure of **52** contains an entirely separate solvent again suggests that compounds of this type may be able to encapsulate several species as with the copper benzoate pyrazine polymer. Further investigation is therefore of interest into the solvation and gas adsorption properties of this compound. **52** is made pure via the diffusion method described, as confirmed by comparison of experimental and simulated X-ray powder diffraction data, as shown in Figure 6.24, and elemental analysis.

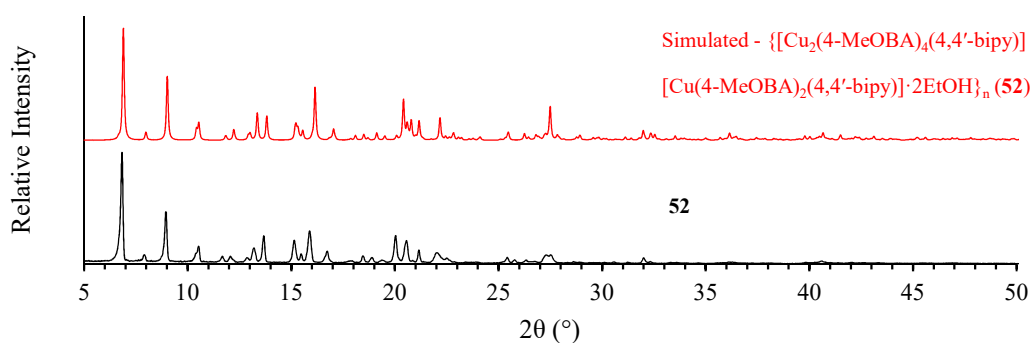


Figure 6.24 Room temperature X-ray powder diffraction data for **52**. Experimental data are shown in black while simulated data are shown in red.

6.8 4-Aminobenzoic acid (4-ABA)

Not including those with chelating ligands, there are seven known compounds of 4-ABA with copper on the CSD.¹¹⁹ Only two of these exhibit the paddlewheel shape and these are only polymorphs of the complex with DMF in the apical position.^{226,246} As with 4-MeBA and 4-MeOBA, reactions were attempted with DABCO, pyrazine and 4,4'-bipy in order to construct a 1-D coordination polymer decorated with amine groups. However, only the reaction with 4,4'-bipy produced crystals which were not one of the previously known DMF-based polymorphs.

6.8.1 $[\text{Cu}_2(4\text{-ABA})_4(4,4'\text{-bipy})_2]\cdot 2\text{DMF}$ (**53**)

The crystals **53** are monoclinic and crystallise in the space group $P2_1/c$ but have a much larger unit-cell than that of the DMF solvated structures, further crystallographic details are included in Table 6.4. The structure was determined to be that of the 4,4'-bipy complex $[\text{Cu}_2(4\text{-ABA})_4(4,4'\text{-bipy})_2]\cdot 2\text{DMF}$ (**53**). The asymmetric unit of **53** contains a whole paddlewheel complex with two Cu atoms, four 4-ABA and two 4,4'-bipy ligands, and two uncoordinated DMF solvent molecules, as shown in Figure 6.25. Each Cu centre has a square-pyramidal coordination geometry, bond lengths and angles shown in Table 6.13. Unlike the majority of 4,4'-bipy containing complexes, the ligand does not act as a bridging group in **53**. In fact, of the 5037 complexes containing a neutral 4,4'-bipy ligand, only 503, including **53**, exhibit 4,4'-bipy as a terminal ligand.

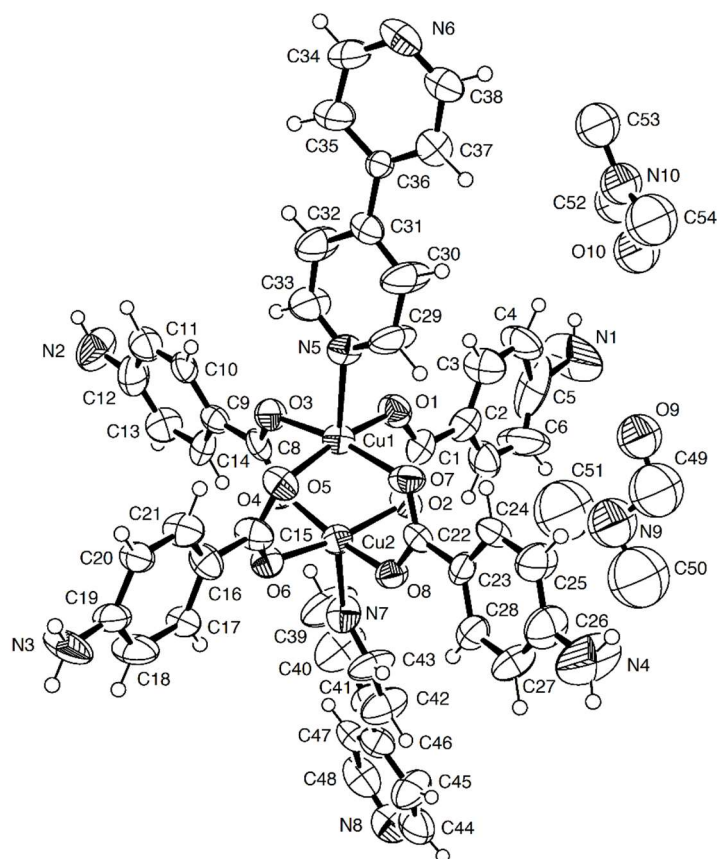


Figure 6.25 Asymmetric unit of $[\text{Cu}_2(4\text{-ABA})_4(4,4'\text{-bipy})_2]\cdot 2\text{DMF}$ (**53**) with atoms drawn as thermal ellipsoids with 50% probability.

Table 6.13 Selected bond lengths (Å) and angles (°) around the Cu coordination centres for $[\text{Cu}_2(4\text{-ABA})_4(4,4'\text{-bipy})_2]\cdot 2\text{DMF}$ (**53**).

Cu(1) – O(1)	1.974(8)	Cu(2) – O(2)	1.986(8)
Cu(1) – O(3)	1.976(6)	Cu(2) – O(4)	1.974(6)
Cu(1) – O(5)	1.967(8)	Cu(2) – O(6)	1.962(8)
Cu(1) – O(7)	1.940(7)	Cu(2) – O(8)	1.956(7)
Cu(1) – N(5)	2.185(10)	Cu(2) – N(7)	2.163(11)
Cu(1) – Cu(2)	2.6061(14)		
O(1) – Cu(1) – O(3)	88.7(3)	O(2) – Cu(2) – O(4)	89.0(3)
O(1) – Cu(1) – O(5)	168.6(4)	O(2) – Cu(2) – O(6)	168.5(4)
O(1) – Cu(1) – O(7)	89.8(3)	O(2) – Cu(2) – O(8)	90.5(3)
O(1) – Cu(1) – N(5)	91.2(4)	O(2) – Cu(2) – N(7)	88.9(4)
O(3) – Cu(1) – O(5)	90.4(3)	O(4) – Cu(2) – O(6)	89.6(3)
O(3) – Cu(1) – O(7)	167.9(4)	O(4) – Cu(2) – O(8)	169.5(4)
O(3) – Cu(1) – N(5)	94.9(3)	O(4) – Cu(2) – N(7)	95.1(4)
O(5) – Cu(1) – O(7)	88.6(3)	O(6) – Cu(2) – O(8)	88.9(3)
O(5) – Cu(1) – N(5)	100.1(4)	O(6) – Cu(2) – N(7)	102.6(4)
O(7) – Cu(1) – N(5)	97.1(3)	O(8) – Cu(2) – N(7)	95.4(4)
N(5) – Cu(1) – Cu(2)	176.1(2)	N(7) – Cu(2) – Cu(1)	172.5(3)

There is one direct hydrogen bonding interaction between complexes between the N3 amine group and the non-coordinated N atoms of the 4,4'-bipy ligands, all other interactions are toward the O atoms of the non-coordinated DMF solvent molecules, as shown in Figure 6.26 (N2···O9 3.18(2) Å, N3···N6 3.01(2) Å, N3···N8 3.01(2) Å, N4···O9 3.18(2) Å, N4···O10 3.07(2) Å, N1···O9 2.99(2) Å, and N1···O10 3.01(2) Å). The interactions create a 3-D hydrogen bonded framework which can be described as an elongated α -Po net, as shown by the simple diagram plotted in Figure 6.26. The framework is interpenetrated by a second framework related to the first by the 2_1 screw axis along b . Each attempt to make **53** as a pure compound resulted in contamination with many crystals of the DMF coordinated compound which was observed when attempting to select a crystal of **53** for structural analysis. This could be seen physically as well, as the two compounds exhibit different crystal habits: **53** crystallises almost exclusively as octahedrally shaped crystals while the DMF compounds crystallise as cuboids.

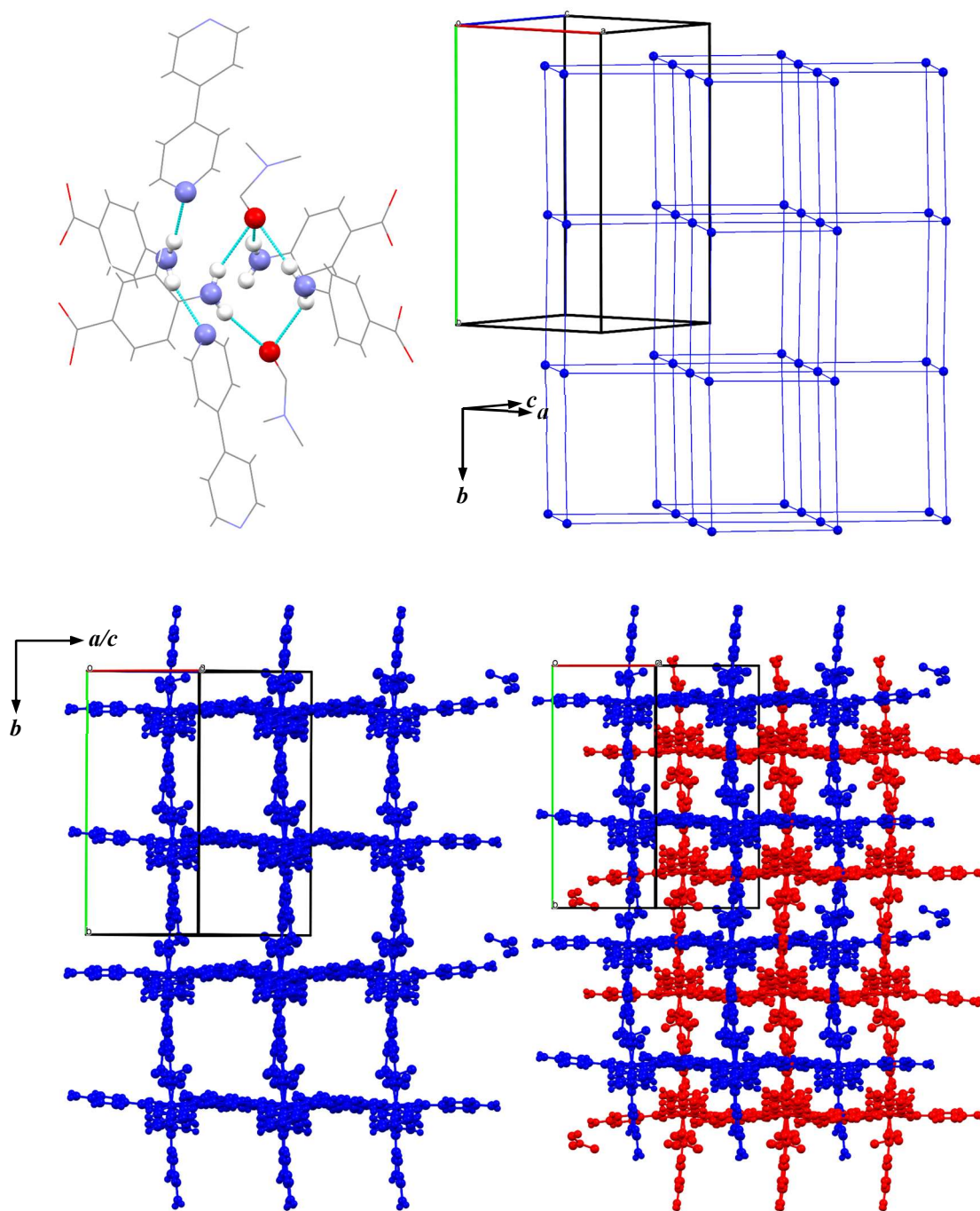


Figure 6.26 Shown top left are the hydrogen bonding interactions in $[\text{Cu}_2(4\text{-ABA})_4(4,4'\text{-bipy})_2]\cdot 2\text{DMF}$ (**53**) that connect the complexes together into an elongated α -Po framework displayed in a simplified form top right. C atoms are shown in grey, H in white, Cu in dark brown, N in light grey-blue, and O in red. Hydrogen bonds are drawn as light-blue dashed lines. Shown bottom is an individual framework drawn as a ball and stick diagram (blue), and the interpenetration of a second framework (red) related to the first by the screw axis symmetry, as viewed down (101).

6.9 Conclusions and future work

Although a systematic approach was used for the synthesis of novel copper carboxylate compounds, only nine new compounds were synthesised. Many of the reactions produced only polycrystalline powders or did not produce crystals large enough for analysis by single-crystal X-ray diffraction. Those that did have been characterised and proven to be pure samples where possible. Several of the compounds created are of interest for their potential for solvent/guest exchange, mainly **46**, **48**, **51**, and **52**. **48** was tested somewhat in this regard and showed some reversible change in the structure on apparent loss and gain of the included methanol solvent. Because of the ability for structure/compounds similar to those listed to adsorb/absorb many different molecular species, there is a potential that they too may possess this characteristic.

A search of the CSD was attempted, however the currently available data does not provide a root cause for the formation of mononuclear or dinuclear species as of yet. Additionally, due to gaps in the data, a systematic search and comparison of ligand combinations cannot be conducted currently which would help in the identification of such a cause. Further work is therefore needed to expand the library of compounds/structures available for a systematic analysis of the data to be conducted.

7 References

- 1 D. A. Lashof and D. R. Ahuja, *Nature*, 1990, **344**, 529–531.
- 2 C. U. Press, *Contribution of Working Group I to the Fourth Assessment Report of the Intergovernmental Panel on Climate Change, 2007*, Cambridge, United Kingdom, 2007.
- 3 D. M. D'Alessandro, B. Smit and J. R. Long, *Angew. Chem. Int. Ed.*, 2010, **49**, 6058–6082.
- 4 M. Rameshni, [http://stoppingclimatechange.com/Carbon%20Capture%20Overview%20\(3\).pdf](http://stoppingclimatechange.com/Carbon%20Capture%20Overview%20(3).pdf) (accessed April 2017).
- 5 R. J. Nunge and W. N. Gill, *AIChE J.*, 1963, **9**, 469–474.
- 6 R. S. Haszeldine, *Science*, 2009, **325**, 1647–1652.
- 7 S. D. Sharma and M. Azzi, *Fuel*, 2014, **121**, 178–188.
- 8 F. Closmann, T. Nguyen and G. T. Rochelle, *Energy Procedia*, 2009, **1**, 1351–1357.
- 9 X. Chen and G. T. Rochelle, *Chem. Eng. Res. Des.*, 2011, **89**, 1693–1710.
- 10 G. Rochelle, E. Chen, S. Freeman, D. Van Wagener, Q. Xu and A. Voice, *Chem. Eng. J.*, 2011, **171**, 725–733.
- 11 K. Mazloomi and C. Gomes, *Renew. Sust. Energ. Rev.*, 2012, **16**, 3024–3033.
- 12 G. Petitpas, P. Bénard, L. E. Klebanoff, J. Xiao and S. Aceves, *Int. J. Hydrog. Energy*, 2014, **39**, 10564–10584.
- 13 S. McWhorter, C. Read, G. Ordaz and N. Stetson, *Curr. Opin. Solid State Mater. Sci.*, 2011, **15**, 29–38.
- 14 H. W. Langmi, J. Ren, B. North, M. Mathe and D. Bessarabov, *Electrochim. Acta*, 2014, **128**, 368–392.
- 15 K. S. W. Sing, D. H. Everett, R. A. W. Haul, L. Moscou, R. A. Pierotti, J. Rouquerol and T. Siemieniowska, in *Handbook of Heterogeneous Catalysis*, Wiley-VCH Verlag GmbH & Co. KGaA, Weinheim, Germany, 2008.
- 16 J. Rouquerol, D. Avnir, C. W. Fairbridge, D. H. Everett, J. M. Haynes, N. Pernicone, J. D. F. Ramsay, K. S. W. Sing and K. K. Unger, *Pure Appl. Chem*, 1994, **66**, 1739–1758.
- 17 L. B. McCusker, F. Liebau and G. Engelhardt, *Pure Appl. Chem.*, 2001, **73**, 381–394.
- 18 R. W. Derlet, T. E. Albertson and C. Sacramento, *West. J. Med.*, 1986, **145**, 493–496.
- 19 M. S. Shamsuddin, N. R. N. Yusoff and M. A. Sulaiman, *Procedia Chem.*, 2016, **19**, 558–565.
- 20 H. Dolas, O. Sahin, C. Saka and H. Demir, *Chem. Eng. J.*, 2011, **166**, 191–197.
- 21 F. Fu and Q. Wang, *J. Environ. Manage.*, 2011, **92**, 407–418.
- 22 S. Zhang, T. Shao and T. Karanfil, *Water Res.*, 2011, **45**, 1378–1386.
- 23 J. Rivera-Utrilla, M. Sánchez-Polo, V. Gómez-Serrano, P. M. Álvarez, M. C. M. Alvim-Ferraz and J. M. Dias, *J. Hazard. Mater.*, 2011, **187**, 1–23.
- 24 M. M. Maroto-Valer, Z. Tang and Y. Zhang, *Fuel Process. Technol.*, 2005, **86**, 1487–1502.

- 25 A. K. Cheetham, G. Férey and T. Loiseau, *Angew. Chem. Int. Ed.*, 1999, **38**, 3268–3292.
- 26 A. Corma, M. J. Díaz-Cabañas, J. Jiang, M. Afeworki, D. L. Dorset, S. L. Soled and K. G. Strohmaier, *Proc. Natl. Acad. Sci. U. S. A.*, 2010, **107**, 13997–4002.
- 27 V. J. Inglezakis, *J. Colloid Interface Sci.*, 2005, **281**, 68–79.
- 28 F. O. M. Gaslain, K. E. White, A. R. Cowley and A. M. Chippindale, *Microporous Mesoporous Mater.*, 2008, **112**, 368–376.
- 29 S. Cavenati, C. A. Grande and A. E. Rodrigues, *J. Chem. Eng. Data*, 2004, **49**, 1095–1101.
- 30 R. S. Franchi, P. J. E. Harlick and A. Sayari, *Ind. Eng. Chem. Res.*, 2005, **44**, 8007–8013.
- 31 P. J. E. Harlick and A. Sayari, *Ind. Eng. Chem. Res.*, 2006, **46**, 446–458.
- 32 X. Du and E. Wu, *J. Phys. Chem. Solids*, 2007, **68**, 1692–1699.
- 33 N. I. Vazquez, Z. Gonzalez, B. Ferrari and Y. Castro, *Boletín la Soc. Española Cerámica y Vidr.*, 2017, **56**, 139–145.
- 34 K. Möller and T. Bein, *Chem. Mater.*, 2017, **29**, 371–388.
- 35 S. R. Batten, N. R. Champness, X.-M. Chen, J. Garcia-Martinez, S. Kitagawa, L. Öhrström, M. O’Keeffe, M. P. Suh and J. Reedijk, *Pure Appl. Chem.*, 2013, **85**, 1715–1724.
- 36 E. Wiberg, N. Wiberg and A. F. Holleman, *Inorganic Chemistry*, Academic Press, 2001.
- 37 H. J. Buser, D. Schwarzenbach, W. Petter and A. Ludi, *Inorg. Chem.*, 1977, **16**, 2704–2710.
- 38 A. Kraft, *Bull. Hist. Chem*, 2008, **33**, 61–67.
- 39 Y. Shibata, *J. Coll. Sci. Imp. Univ. Tokyo*, 1916, **37**, 1–31.
- 40 J. F. Keggin and F. D. Miles, *Nature*, 1936, **137**, 577–578.
- 41 B. F. Hoskins and R. Robson, *J. Am. Chem. Soc.*, 1990, **112**, 1546–1554.
- 42 H. Li, M. Eddaoudi, M. O’Keeffe and O. M. Yaghi, *Nature*, 1999, **402**, 276–279.
- 43 M. Eddaoudi, J. Kim, N. Rosi, D. Vodak, J. Wachter, M. O’Keeffe and O. M. Yaghi, *Science*, 2002, **295**, 469–472.
- 44 O. M. Yaghi, M. O’Keeffe, N. W. Ockwig, H. K. Chae, M. Eddaoudi and J. Kim, *Nature*, 2003, **423**, 705–714.
- 45 S. Kitagawa and M. Kondo, *Bull. Chem. Soc. Jpn.*, 1998, **71**, 1739–1753.
- 46 K. Uemura, S. Kitagawa, M. Kondo, K. Fukui, R. Kitaura, H.-C. Chang and T. Mizutani, *Chem. Eur. J.*, 2002, **8**, 3586–3600.
- 47 V. A. Blatov, M. O’Keeffe, D. M. Proserpio, J. Klinowsky, A. L. Mackay and M. Eddaoudi, *CrystEngComm*, 2010, **12**, 44–48.
- 48 M. C. Etter, J. C. MacDonald and J. Bernstein, *Acta Crystallogr. Sect. B Struct. Sci.*, 1990, **46**, 256–262.
- 49 L. Hiltunen, M. Leskelä, N. Mäkelä and L. Niinistö, *Acta Chem. Scand.*, 1987, **A 41**, 548–555.
- 50 F. Bertolotti, A. Forni, G. Gervasio, D. Marabello and E. Diana, *Polyhedron*, 2012, **42**, 118–127.
- 51 T. Sato, F. Ambe, K. Endo, M. Katada, H. Maeda, T. Nakamoto and H. Sano, *J. Am. Chem. Soc.*, 1996, **118**, 3450–3458.

- 52 D. Feng, Z.-Y. Gu, J.-R. Li, H.-L. Jiang, Z. Wei and H.-C. Zhou, *Angew. Chem. Int. Ed.*, 2012, **51**, 10307–10310.
- 53 A. Schaate, P. Roy, T. Preusse, S. J. Lohmeier, A. Godt and P. Behrens, *Chemistry*, 2011, **17**, 9320–9325.
- 54 J. H. Cavka, S. Jakobsen, U. Olsbye, N. Guillou, C. Lamberti, S. Bordiga and K. P. Lillerud, *J. Am. Chem. Soc.*, 2008, **130**, 13850–13851.
- 55 M. Bosch, M. Zhang and H.-C. Zhou, *Adv. Chem.*, 2014, **2014**, 1–8.
- 56 G. C. Shearer, S. Chavan, J. Ethiraj, J. G. Vitillo, S. Svelle, U. Olsbye, C. Lamberti, S. Bordiga and K. P. Lillerud, *Chem. Mater.*, 2014, **26**, 4068–4071.
- 57 D. Feng, Z.-Y. Gu, J.-R. Li, H.-L. Jiang, Z. Wei and H.-C. Zhou, *Angew. Chem. Int. Ed.*, 2012, **51**, 10307–10310.
- 58 H. Furukawa, N. Ko, Y. B. Go, N. Aratani, S. B. Choi, E. Choi, A. O. Yazaydin, R. Q. Snurr, M. O’Keeffe, J. Kim and O. M. Yaghi, *Science*, 2010, **329**, 424–428.
- 59 S. Bauer, C. Serre, T. Devic, P. Horcajada, J. Marrot, G. Férey and N. Stock, *Inorg. Chem.*, 2008, **47**, 7568–7576.
- 60 F. Carson, J. Su, A. E. Platero-Prats, W. Wan, Y. Yun, L. Samain and X. Zou, *Cryst. Growth Des.*, 2013, **13**, 5036–5044.
- 61 Y. Bai, Y. Dou, L.-H. Xie, W. Rutledge, J.-R. Li and H.-C. Zhou, *Chem. Soc. Rev.*, 2016, **45**, 2327–2367.
- 62 S. Kitagawa, R. Kitaura and S. Noro, *Angew. Chem. Int. Ed.*, 2004, **43**, 2334–2375.
- 63 O. K. Farha, I. Eryazici, N. C. Jeong, B. G. Hauser, C. E. Wilmer, A. A. Sarjeant, R. Q. Snurr, S. T. Nguyen, A. O. Yazaydin and J. T. Hupp, *J. Am. Chem. Soc.*, 2012, **134**, 15016–15021.
- 64 M. L. Tonnet, S. Yamada and I. G. Ross, *Trans. Faraday Soc.*, 1964, **60**, 840–849.
- 65 H. Li, M. Eddaoudi, T. L. Groy and O. M. Yaghi, *J. Am. Chem. Soc.*, 1998, **120**, 8571–8572.
- 66 C. G. Carson, K. Hardcastle, J. Schwartz, X. Liu, C. Hoffmann, R. A. Gerhardt and R. Tannenbaum, *Eur. J. Inorg. Chem.*, 2009, **2009**, 2338–2343.
- 67 A. Pariyar, J. Stansbery, R. L. Patel, X. Liang and A. Choudhury, *J. Coord. Chem.*, 2016, **69**, 1957–1969.
- 68 Y. Sakata, S. Furukawa, M. Kondo, K. Hirai, N. Horike, Y. Takashima, H. Uehara, N. Louvain, M. Meilikhov, T. Tsuruoka, S. Isoda, W. Kosaka, O. Sakata and S. Kitagawa, *Science*, 2013, **339**, 193–196.
- 69 S. S.-Y. Chui, S. M.-F. Lo, J. P. H. Charmant, A. G. Orpen and I. D. Williams, *Science*, 1999, **283**, 1148–1150.
- 70 A. G. Wong-Foy, A. J. Matzger and O. M. Yaghi, *J. Am. Chem. Soc.*, 2006, **128**, 3494–3495.
- 71 S. S. Kaye, A. Dailly, O. M. Yaghi and J. R. Long, *J. Am. Chem. Soc.*, 2007, **129**, 14176–14177.
- 72 S. Pérez-Yáñez, G. Beobide, O. Castillo, J. Cepeda, A. Luque, A. T. Aguayo and P. Román, *Inorg. Chem.*, 2011, **50**, 5330–5332.
- 73 J. Thomas-Gipson, G. Beobide, O. Castillo, J. Cepeda, A. Luque, S. Pérez-Yáñez, A. T. Aguayo and P. Román, *CrystEngComm*, 2011, **13**, 3301–3305.
- 74 J. Thomas-Gipson, G. Beobide, O. Castillo, M. Fröba, F. Hoffmann, A. Luque, S. Pérez-Yáñez and P. Román, *Cryst. Growth Des.*, 2014, **14**, 4019–4029.

- 75 J. An, S. J. Geib and N. L. Rosi, *J. Am. Chem. Soc.*, 2009, **131**, 8376–8377.
- 76 J. An, O. K. Farha, J. T. Hupp, E. Pohl, J. I. Yeh and N. L. Rosi, *Nat. Commun.*, 2012, **3**, Article no. 604, 6 pages.
- 77 T. Li, M. T. Kozłowski, E. A. Doud, M. N. Blakely and N. L. Rosi, *J. Am. Chem. Soc.*, 2013, **135**, 11688–11691.
- 78 Y. Zhang, K. Chen and H.-T. Fan, *Inorg. Chem. Commun.*, 2013, **38**, 47–49.
- 79 S. M. Cohen, *Chem. Rev.*, 2012, **112**, 970–1000.
- 80 M. Kim, S. J. Garibay and S. M. Cohen, *Inorg. Chem.*, 2011, **50**, 729–731.
- 81 Z. Chen, S. Xiang, D. Zhao and B. Chen, *Cryst. Growth Des.*, 2009, **9**, 5293–5296.
- 82 X. Song, S. Jeong, D. Kim, M. S. Lah, J.-S. Chang, M. S. Lah, S. W. Ng and O. M. Yaghi, *CrystEngComm*, 2012, **14**, 5753–5756.
- 83 X. Song, T. K. Kim, H. Kim, D. Kim, S. Jeong, H. R. Moon and M. S. Lah, *Chem. Mater.*, 2012, **24**, 3065–3073.
- 84 O. Kozachuk, K. Khaletskaya, M. Halbherr, A. Bétard, M. Meilikhov, R. W. Seidel, B. Jee, A. Pöpl and R. A. Fischer, *Eur. J. Inorg. Chem.*, 2012, **2012**, 1688–1695.
- 85 J. Zhang, L. Wojtas, R. W. Larsen, M. Eddaoudi and M. J. Zaworotko, *J. Am. Chem. Soc.*, 2009, **131**, 17040–17041.
- 86 C. Shekhah, O. Wang, H. Paradinas, M. Ocal, C. Schüpbach, B. Terfort, A. Zacher, D. Fischer, R. A. Wöll, *Nat. Mater.*, 2009, **8**, 481–484.
- 87 S. Sachdeva, A. Pustovarenko, E. J. R. Sudhölter, F. Kapteijn, L. C. P. M. de Smet and J. Gascon, *CrystEngComm*, 2016, **18**, 4018–4022.
- 88 S. Yang, X. Lin, W. Lewis, M. Suyetin, E. Bichoutskaia, J. E. Parker, C. C. Tang, D. R. Allan, P. J. Rizkallah, P. Hubberstey, N. R. Champness, K. M. Thomas, A. J. Blake and M. Schröder, *Nat. Mater.*, 2012, **11**, 710–716.
- 89 K. Mulfort, O. Farha, C. Malliakas, M. Kanatzidis and J. Hupp, *Chem. Eur. J.*, 2010, **16**, 276–281.
- 90 C. Dey, T. Kundu, B. P. Biswal, A. Mallick and R. Banerjee, *Acta Cryst.*, 2014, **B70**, 3–10.
- 91 O. M. Yaghi, G. Li and H. Li, *Chem. Mater.*, 1997, **9**, 1074–1076.
- 92 C. J. Kepert, T. J. Prior and M. J. Rosseinsky, *J. Am. Chem. Soc.*, 2000, **122**, 5158–5168.
- 93 C. Janiak, *Dalton Trans.*, 2003, 2781–2804.
- 94 J. L. C. Rowsell and O. M. Yaghi, *Angew. Chem. Int. Ed.*, 2005, **44**, 4670–4679.
- 95 J. G. Vitillo, L. Regli, S. Chavan, G. Ricchiardi, G. Spoto, P. D. C. Dietzel, S. Bordiga and A. Zecchina, *J. Am. Chem. Soc.*, 2008, **130**, 8386–8396.
- 96 O. K. Farha, A. Özgür Yazaydın, I. Eryazici, C. D. Malliakas, B. G. Hauser, M. G. Kanatzidis, S. T. Nguyen, R. Q. Snurr and J. T. Hupp, *Nat. Chem.*, 2010, **2**, 944–948.
- 97 D. A. Gómez-Gualdrón, T. C. Wang, P. García-Holley, R. M. Sawelewa, E. Argueta, R. Q. Snurr, J. T. Hupp, T. Yildirim and O. K. Farha, *ACS Appl. Mater. Interfaces*, 2017, **9**, 33419–33428.
- 98 B. Arstad, H. Fjellvåg, K. O. Kongshaug, O. Swang and R. Blom, *Adsorption*, 2008, **14**, 755–762.
- 99 A. M. Fracaroli, H. Furukawa, M. Suzuki, M. Dodd, S. Okajima, F. Gándara, J. Reimer and O. M. Yaghi, *J. Am. Chem. Soc.*, 2014, **136**, 8863–8866.

- 100 T. İslamoğlu, M. Gulam Rabbani and H. M. El-Kaderi, *J. Mater. Chem. A*, 2013, **1**, 10259–10266.
- 101 R. Haldar, S. K. Reddy, V. M. Suresh, S. Mohapatra, S. Balasubramanian and T. K. Maji, *Chem. Eur. J.*, 2014, **20**, 4347–4356.
- 102 Y. Lin, C. Kong and L. Chen, *RSC Adv.*, 2016, **6**, 32598–32614.
- 103 J. Čejka, A. Corma and S. Zones, *Zeolites and catalysis : synthesis, reactions and applications*, Wiley-VCH, 2010.
- 104 J. J. De Yoreo and P. G. Vekilov, *Rev. Mineral. Geochem.*, 2003, **54**, 57–93.
- 105 R. A. Laudise, *The Growth of Single Crystals*, Prentice-Hall Inc., Englewood Cliffs, New Jersey, 1970.
- 106 B. R. Pamplin, *Crystal Growth*, Pergamon Press Ltd., Headington Hill Hall, Oxford, 1975.
- 107 T. J. Prior and M. J. Rosseinsky, *CrystEngComm*, 2000, **2**, 128–133.
- 108 T. J. Prior and M. J. Rosseinsky, *Inorg. Chem.*, 2003, **42**, 1564–1575.
- 109 G. M. Espallargas, L. Brammer, J. Van De Streek, K. Shankland, A. J. Florence and H. Adams, *J. Am. Chem. Soc.*, 2006, **128**, 9584–9585.
- 110 J. Sundberg, L. J. Cameron, P. D. Southon, C. J. Kepert and C. J. Mckenzie, *Chem. Sci.*, 2014, **5**, 4017–4025.
- 111 X-AREA, X-RED, X-RED32, X-SHAPE, Stoe & Cie, Darmstadt, Germany, 2012.
- 112 L. J. Farrugia, *J. Appl. Cryst.*, 2012, **45**, 849–854.
- 113 G. M. Sheldrick, *Acta Cryst.*, 2008, **A64**, 112–122.
- 114 G. M. Sheldrick, *Acta Cryst.*, 2015, **A71**, 3–8.
- 115 G. M. Sheldrick, *Acta Cryst.*, 2015, **C71**, 3–8.
- 116 HighScore Plus (3.0e (3.0.5)), PANalytical, Almelo, The Netherlands, 2012.
- 117 C. F. Macrae, I. J. Bruno, J. A. Chisholm, P. R. Edgington, P. McCabe, E. Pidcock, L. Rodriguez-Monge, R. Taylor, J. van de Streek and P. A. Wood, *J. Appl. Crystallogr.*, 2008, **41**, 466–470.
- 118 K. Brandenburg and H. Putz, Endeavour - Structure Solution from Powder Diffraction (1.7g), Crystal Impact GbR, Bonn, Germany, 2015.
- 119 F. H. Allen, *Acta Cryst.*, 2002, **B58**, 380–388.
- 120 B. H. Toby, *J. Appl. Cryst.*, 2001, **34**, 210–213.
- 121 H. Furukawa, K. E. Cordova, M. O’Keeffe and O. M. Yaghi, *Science*, 2013, **341**, 974.
- 122 M. P. Suh, H. J. Park, T. K. Prasad and D.-W. Lim, *Chem. Rev.*, 2012, **112**, 782–835.
- 123 J.-R. Li, Y. Ma, M. C. McCarthy, J. Sculley, J. Yu, H.-K. Jeong, P. B. Balbuena and H.-C. Zhou, *Coord. Chem. Rev.*, 2011, **255**, 1791–1823.
- 124 S. Takamizawa, E. Nataka, T. Akatsuka, R. Miyake, Y. Kakizaki, H. Takeuchi, G. Maruta and S. Takeda, *J. Am. Chem. Soc.*, 2010, **132**, 3783–3792.
- 125 B. Xiao, P. J. Byrne, P. S. Wheatley, D. S. Wragg, X. Zhao, A. J. Fletcher, K. M. Thomas, L. Peters, J. S. O. Evans, J. E. Warren, W. Zhou and R. E. Morris, *Nat. Chem.*, 2009, **1**, 289–294.
- 126 A. Lennartson, K. Salo and M. Håkansson, *Acta Cryst.*, 2005, **E61**, m1261–m1263.

- 127 A. Kelley, S. Nalla and M. R. Bond, *Acta Cryst.*, 2015, **B71**, 48–60.
- 128 F. Neve, O. Francescangeli, A. Crispini and J. Charmant, *Chem. Mater.*, 2001, **13**, 2032–2041.
- 129 C. J. Adams, P. C. Crawford, A. G. Orpen, T. J. Podesta and B. Salt, *Chem. Commun.*, 2005, 2457–2458.
- 130 C. J. Adams, H. M. Colquhoun, P. C. Crawford, M. Lusi and A. G. Orpen, *Angew. Chem. Int. Ed.*, 2007, **46**, 1124–1128.
- 131 C. J. Adams, A. L. Gillon, M. Lusi and A. G. Orpen, *CrystEngComm*, 2010, **12**, 4403–4409.
- 132 C. J. Adams, M. F. Haddow, M. Lusi and A. G. Orpen, *Proc. Natl. Acad. Sci. U. S. A.*, 2010, **107**, 16033–16038.
- 133 W.-T. Chen, Z.-G. Luo, Y.-P. Xu, Q.-Y. Luo and J.-H. Liu, *J. Chem. Res.*, 2011, **35**, 253–256.
- 134 N. Lah and I. Leban, *Acta Cryst.*, 2005, **E61**, m1708–m1710.
- 135 W. E. Marsh, E. J. Valente and D. J. Hodgson, *Inorg. Chim. Acta*, 1981, **51**, 49–53.
- 136 C. J. Adams, M. Lusi, E. M. Mutambi and A. G. Orpen, *Chem. Commun.*, 2015, **51**, 9632–9635.
- 137 G. Mínguez Espallargas, J. van de Streek, P. Fernandes, A. J. Florence, M. Brunelli, K. Shankland and L. Brammer, *Angew. Chem. Int. Ed.*, 2010, **49**, 8892–8896.
- 138 I. J. Vitorica-Yrezabal, R. A. Sullivan, S. L. Purver, C. Curfs, C. C. Tang and L. Brammer, *CrystEngComm*, 2011, **13**, 3189–3196.
- 139 G. Mínguez Espallargas, A. J. Florence, J. van de Streek and L. Brammer, *CrystEngComm*, 2011, **13**, 4400–4404.
- 140 E. Coronado, M. Giménez-Marqués, L. Brammer and G. M. Espallargas, *Nat. Commun.*, 2012, **3**, 1–8.
- 141 A. S. Sinha, U. B. Rao Khandavilli, E. L. O'Connor, B. J. Deadman, A. R. Maguire and S. E. Lawrence, *CrystEngComm*, 2015, **17**, 4832–4841.
- 142 S. M. Fellows and T. J. Prior, *Acta Cryst.*, 2016, **E72**, 436–439.
- 143 S. Karki, T. Frišćić and W. Jones, *CrystEngComm*, 2009, **11**, 470–481.
- 144 C. J. Adams, A. Angeloni, A. G. Orpen, T. J. Podesta and B. Shore, *Cryst. Growth Des.*, 2006, **6**, 411–422.
- 145 A. I. Gubin, N. N. Nurakhmetov, M. Z. Buranbaev, R. I. Mul'kina and R. S. Erkasov, *Kristallografiya*, 1989, **34**, 238–239.
- 146 D. Krishna Kumar, A. Ballabh, D. Amilan Jose, P. Dastidar and A. Das, *Cryst. Growth Des.*, 2005, **5**, 651–660.
- 147 A. L. Spek, *Acta Cryst.*, 2009, **D65**, 148–155.
- 148 Z. Qin, H. A. Jenkins, S. J. Coles, K. W. Muir and R. J. Puddephatt, *Can. J. Chem.*, 1999, **77**, 155–157.
- 149 R. Sekiya, S. Nishikiori and K. Ogura, *J. Am. Chem. Soc.*, 2004, **126**, 16587–16600.
- 150 R. Sekiya and S. Nishikiori, *Chem. Eur. J.*, 2002, **8**, 4803–4810.
- 151 J. Xue, X. Hua, L. Yang, W. Li, Y. Xu, G. Zhao, G. Zhang, L. Liu, K. Liu, J. Chen and J. Wu, *J. Mol. Struct.*, 2014, **1059**, 108–117.

- 152 R. Sekiya, S. Nishikiori and R. Kuroda, *CrystEngComm*, 2009, **11**, 2251–2253.
- 153 F. Takusagawa and A. Shimada, *Acta Cryst.*, 1976, **B32**, 1925–1927.
- 154 C. B. Aakeröy, A. M. Beatty, B. A. Helfrich and M. Nieuwenhuyzen, *Cryst. Growth Des.*, 2003, **3**, 159–165.
- 155 J. Li, S. A. Bourne and M. R. Caira, *Chem. Commun.*, 2011, **47**, 1530–1532.
- 156 K. S. Eccles, R. E. Deasy, L. Fábán, D. E. Braun, A. R. Maguire and S. E. Lawrence, *CrystEngComm*, 2011, **13**, 6923–6925.
- 157 Y. Miwa, T. Mizuno, K. Tsuchida, T. Taga and Y. Iwata, *Acta Cryst.*, 1999, **B55**, 78–84.
- 158 K. I. Näntinen and K. Rissanen, *CrystEngComm*, 2003, **5**, 326–330.
- 159 G.-Q. Zhao, Z.-F. Pan and X.-X. Tang, *Acta Cryst.*, 2008, **E64**, o138–o138.
- 160 W. B. Wright and G. S. D. King, *Acta Cryst.*, 1954, **7**, 283–288.
- 161 R. K. Boggess and R. B. Martin, *Inorg. Chem.*, 1974, **13**, 1525–1527.
- 162 R. Lundblad and F. Macdonald, *Handbook of Biochemistry and Molecular Biology*, CRC Press, Boca Raton, United States, 4th edn., 2010.
- 163 H. G. Biedermann and K. Wichmann, *Z. Naturforsch.*, 1974, **29 b**, 360–362.
- 164 G. Stucky and R. E. Rundle, *J. Am. Chem. Soc.*, 1964, **86**, 4821–4825.
- 165 B. T. Kilbourn and J. D. Dunitz, *Inorg. Chim. Acta*, 1967, **1**, 209–216.
- 166 J. A. Bertrand, *Inorg. Chem.*, 1967, **6**, 495–498.
- 167 B. Beagley, A. G. Mackie, P. P. Matear, C. A. McAuliffe, P. T. Ndifon and R. G. Pritchard, *J. Chem. Soc., Dalton Trans.*, 1992, 1301–1304.
- 168 B. Beagley, C. A. McAuliffe, P. P. Mac Rory, P. T. Ndifon and R. G. Pritchard, *J. Chem. Soc. Chem. Commun.*, 1990, 309–310.
- 169 F. A. Cotton, C. A. Murillo and I. Pascual, *Inorg. Chem.*, 1999, **38**, 2746–2749.
- 170 Y.-Y. Liu, M. Grzywa, M. Weil and D. Volkmer, *J. Solid State Chem.*, 2010, **183**, 208–217.
- 171 C. A. Bolos and P. C. Christidis, *Acta Cryst.*, 2001, **C58**, m29–m30.
- 172 S. Löw, J. Becker, C. Würtele, A. Miska, C. Kleeberg, U. Behrens, O. Walter and S. Schindler, *Chem. Eur. J.*, 2013, **19**, 5342–51.
- 173 J. A. Bertrand and J. A. Kelley, *Inorg. Chem.*, 1969, **8**, 1982–1985.
- 174 R. C. Dickinson, F. T. Helm, W. A. Baker, T. D. Black and W. H. Watson, *Inorg. Chem.*, 1977, **16**, 1530–1537.
- 175 A. M. Atria, A. Vega, M. Contreras, J. Valenzuela and E. Spodine, *Inorg. Chem.*, 1999, **38**, 5681–5685.
- 176 G. A. Bowmaker, C. Di Nicola, F. Marchetti, C. Pettinari, B. W. Skelton, N. Somers and A. H. White, *Inorg. Chim. Acta*, 2011, **375**, 31–40.
- 177 H. tom Dieck and H.-P. Brehm, *Chem. Ber.*, 1969, **102**, 3577–3583.
- 178 D. S. Brown, T. G. Hopkins and A. H. Norbury, *Inorg. Nucl. Chem. Lett.*, 1973, **9**, 971–972.

- 179 D. D. Swank, D. O. Nielson and R. D. Willett, *Inorg. Chim. Acta*, 1973, **7**, 91–96.
- 180 R. N. Keller and H. D. Wycoff, *Inorganic Syntheses Vol. II*, McGraw-Hill Book Company, Inc., New York - London, 1946.
- 181 Ž. K. Jaćimović, V. M. Leovac and Z. D. Tomić, *Zeitschrift für Krist. - New Cryst. Struct.*, 2007, **222**, 246–248.
- 182 E. Liu, Y. Z. Zhang, L. Li, C. Yang, J. C. Fettinger and G. Zhang, *Polyhedron*, 2015, **99**, 223–229.
- 183 G. Zhang, C. Yang, E. Liu, L. Li, J. A. Golen and A. L. Rheingold, *RSC Adv.*, 2014, **4**, 61907–61911.
- 184 J. Poitras and A. L. Beauchamp, *Can. J. Chem.*, 1992, **70**, 2846–2855.
- 185 P. C. M. Duncan, D. M. L. Goodgame, M. A. Hitchman, S. Menzer, H. Stratemeier and D. J. Williams, *J. Chem. Soc., Dalton Trans.*, 1996, 4245–4248.
- 186 S. H. Lapidus, J. L. Manson, J. Liu, M. J. Smith, P. Goddard, J. Bendix, C. V Topping, J. Singleton, C. Dunmars, J. F. Mitchell and J. A. Schlueter, *Chem. Commun.*, 2013, **49**, 3558–3560.
- 187 N. Masciocchi, P. Cairati, L. Carlucci, G. Mezza, G. Ciani and A. Sironi, *J. Chem. Soc., Dalton Trans.*, 1996, 2739–2746.
- 188 E. Ahadi, H. Hosseini-Monfared and P. Mayer, *Acta Cryst.*, 2015, **E71**, m112-3.
- 189 W. E. Marsh, W. E. Hatfield and D. J. Hodgson, *Inorg. Chem.*, 1982, **21**, 2679–2684.
- 190 J. Campbell, C. Raston, J. Varghese and A. White, *Aust. J. Chem.*, 1977, **30**, 1947–1953.
- 191 F. Awwadi, R. D. Willett and B. Twamley, *Cryst. Growth Des.*, 2011, **11**, 5316–5323.
- 192 F. F. Awwadi, R. D. Willett, S. F. Haddad and B. Twamley, *Cryst. Growth Des.*, 2006, **6**, 1833–1838.
- 193 A. M. Fracaroli, H. Furukawa, M. Suzuki, M. Dodd, S. Okajima, F. Gándara, J. A. Reimer and O. M. Yaghi, *J. Am. Chem. Soc.*, 2014, **136**, 8863–8866.
- 194 B. Arstad, H. Fjellvåg, K. O. Kongshaug, O. Swang and R. Blom, *Adsorption*, 2008, **14**, 755–762.
- 195 A. Takenaka, E. Oshima, S. Yamada and T. Watanabé, *Acta Cryst.*, 1973, **B29**, 503–514.
- 196 B. Sjöberg, R. Österberg and R. Söderquist, *Acta Cryst.*, 1973, **B29**, 1136–1141.
- 197 M. Dan and C. N. R. Rao, *Chem. Eur. J.*, 2005, **11**, 7102–7109.
- 198 A. D. Mighell, *Acta Cryst.*, 2003, **B59**, 300–302.
- 199 J. Jezierska, T. Gowiak, A. Ożarowski, Y. V Yablokov and Z. Rzączyńska, *Inorg. Chim. Acta*, 1998, **275–276**, 28–36.
- 200 V. K. Sabirov, N. M. Kebets, M. A. Porai-Koshits and Y. T. Stuchkov, *Koord. Khim.*, 1994, **20**, 466–471.
- 201 N. Lah and I. Leban, *Acta Cryst.*, 2005, **E61**, m835–m837.
- 202 R. D. Willett, F. H. Jardine, I. Rouse, R. J. Wong, C. P. Landee and M. Numata, *Phys. Rev. B*, 1981, **24**, 5372–5381.
- 203 R. D. Willett, R. J. Wong and M. Numata, *Inorg. Chem.*, 1983, **22**, 3189–3194.
- 204 B.-L. Yuan, H.-C. Lan, Y.-P. Chen and Y.-B. Li, *Acta Cryst.*, 2004, **E60**, m617–m619.

- 205 S. Xiang, J. Huang, L. Li, J. Zhang, L. Jiang, X. Kuang and C.-Y. Su, *Inorg. Chem.*, 2011, **50**, 1743–1748.
- 206 T. Furuta, I. Kanoya, H. Sakai and M. Hosoe, *Polymers*, 2011, **3**, 2133–2141.
- 207 S. Takamizawa, T. Saito, T. Akatsuka and E. Nakata, *Inorg. Chem.*, 2005, **44**, 1421–1424.
- 208 S. Takamizawa, C. Kachi-Terajima, M.-A. Kohbara, T. Akatsuka and T. Jin, *Chem. Asian J.*, 2007, **2**, 837–848.
- 209 S. Takamizawa and R. Miyake, *Chem. Commun.*, 2009, 4076–4078.
- 210 S. Takamizawa, *Angew. Chem. Int. Ed.*, 2015, **54**, 7033–7036.
- 211 S. Takamizawa, T. Akatsuka and R. Miyake, *CrystEngComm*, 2010, **12**, 82–84.
- 212 R. Nukada, W. Mori, S. Takamizawa, M. Mikuriya, M. Handa and H. Naono, *Chem. Lett.*, 1999, **28**, 367–368.
- 213 S. Takamizawa and R. Miyake, *CrystEngComm*, 2010, **12**, 2728–2733.
- 214 S. Takamizawa, E.-I. Nakata and R. Miyake, *Dalton Trans.*, 2009, 1752–1760.
- 215 S. Takamizawa, E. Nakata, T. Saito, T. Akatsuka and K. Kojima, *CrystEngComm*, 2004, **6**, 197–199.
- 216 I. H. Hwang, Y. D. Jo, H. Kim, K. B. Kim, K.-D. Jung, C. Kim, Y. Kim and S.-J. Kim, *Inorg. Chim. Acta*, 2013, **402**, 39–45.
- 217 T. Ueda, K. Kurokawa, T. Eguchi, C. Kachi-Terajima and S. Takamizawa, *J. Phys. Chem. C*, 2007, **111**, 1524–1534.
- 218 S. Takamizawa, E. Nakata and H. Yokoyama, *Inorg. Chem. Commun.*, 2003, **6**, 763–765.
- 219 S. Takamizawa, E. Nakata and T. Saito, *Inorg. Chem. Commun.*, 2004, **7**, 1–3.
- 220 S. Takamizawa, Y. Takasaki and R. Miyake, *Chem. Commun.*, 2009, 6625–6627.
- 221 A. D. Burrows, M. F. Mahon, P. R. Raithby, A. J. Warren, S. J. Teat and J. E. Warren, *CrystEngComm*, 2012, **14**, 3658–3666.
- 222 Y. Takasaki and S. Takamizawa, *Chem. Commun.*, 2014, **50**, 5662–5664.
- 223 Y. Takasaki and S. Takamizawa, *Chem. Commun.*, 2015, **51**, 5024–5027.
- 224 K. Takahashi, N. Hoshino, T. Takeda, S. Noro, T. Nakamura, S. Takeda and T. Akutagawa, *Dalton Trans.*, 2014, **43**, 9081–9089.
- 225 F. Zigan, W. Joswig, H. D. Schuster and S. A. Mason, *Zeitschrift für Krist. - Cryst. Mater.*, 1977, **145**, 412–426.
- 226 J. Yang, L. Li, J.-F. Ma and Y.-Y. Liu, *Acta Cryst.*, 2005, **E61**, m237–m239.
- 227 O. Şahin, O. Büyükgüngör, D. A. Köse and H. Necefoglu, *Acta Cryst.*, 2007, **C63**, m510–m512.
- 228 J.-W. Liu, B. Zhu and S. W. Ng, *Acta Cryst.*, 2006, **E62**, m3514–m3515.
- 229 J.-R. Su and D.-J. Xu, *J. Coord. Chem.*, 2005, **58**, 629–636.
- 230 S. Youngme, A. Cheansirisomboon, C. Danvirutai, C. Pakawatchai, N. Chaichit, C. Engkagul, G. A. van Albada, J. S. Costa and J. Reedijk, *Polyhedron*, 2008, **27**, 1875–1882.
- 231 W.-G. Zhu, C.-J. Lin, Y.-Q. Zheng and H.-L. Zhu, *Transition Met. Chem.*, 2016, **41**, 87–96.

- 232 S. Gomathi and P. T. Muthiah, *Acta Cryst.*, 2013, **C69**, 1498–1502.
- 233 I. Bkouche-Waksman, C. Bois, G. A. Popovitch and P. L'Haridon, *Bull. Soc. Chim. Fr.*, 1980, 69–75.
- 234 Y.-Z. Zheng, M.-L. Tong and X.-M. Chen, *J. Mol. Struct.*, 2006, **796**, 9–17.
- 235 R. Sarma, A. K. Boudalis and J. B. Baruah, *Inorg. Chim. Acta*, 2010, **363**, 2279–2286.
- 236 L. Feng, Z. Chen, M. Zeller and R. L. Luck, *Polyhedron*, 2014, **80**, 206–215.
- 237 G. S. Papaefstathiou, B. G. Darrow and L. R. MacGillivray, *J. Chem. Crystallogr.*, 2002, **32**, 191–195.
- 238 S. Kashyap, U. P. Singh, A. K. Singh, P. Kumar and S. P. Singh, *Transition Met. Chem.*, 2013, **38**, 573–585.
- 239 H. Necefoğlu, E. Çimen, B. Tercan, H. Dal and T. Hökelek, *Acta Cryst.*, 2010, **E66**, m334–m335.
- 240 Q. Zhang, L. M. Yu, C. H. Ni, X. Li and X. Li, *Bull. Korean Chem. Soc.*, 2015, **36**, 2190–2197.
- 241 J. Zhou, L. Du, Z. Li, Y. Qiao, J. Liu, M. Zhu, P. Chen and Q. Zhao, *J. Coord. Chem.*, 2013, **66**, 2166–2177.
- 242 T. Hökelek, G. Saka, B. Tercan, E. Çimen and H. Necefoğlu, *Acta Cryst.*, 2010, **E66**, m955–m956.
- 243 F. Sama, A. K. Dhara, M. N. Akhtar, Y.-C. Chen, M.-L. Tong, I. A. Ansari, M. Raizada, M. Ahmad, M. Shahid and Z. A. Siddiqi, *Dalton Trans.*, 2017, **46**, 9801–9823.
- 244 K. Takahashi, N. Hoshino, T. Takeda, S. Noro, T. Nakamura, S. Takeda and T. Akutagawa, *Inorg. Chem.*, 2015, **54**, 9423–9431.
- 245 P. Smart, G. M. Espallargas and L. Brammer, *CrystEngComm*, 2008, **10**, 1335–1344.
- 246 J. A. Perman and M. J. Zaworotko, *J. Chem. Crystallogr.*, 2009, **39**, 78–82.